Transactions of the ASME

The Journal of Heat Transfer (ISSN 0022-1481) is published quarterly for $72 per year by The American Society of Mechanical Engineers, 345 East 47th Street, New York, N Y 10017. Second class postage paid at New York, NY and additional mailing offices. POSTMASTER: Send address changes to The Journal of Heat Transfer, c/o THE AMERICAN SOCIETY OF MECHANICAL ENGINEERS, P.O. Box 3199, Grand Central Station, New York, NY 10163.

CHANGES OF ADDRESS must be received at Society headquarters seven weeks before they are to be effective. Please send old label and new address.

PRICES: To members, $36.00, annually; to nonmembers, $90.00. Single copies, $24.00 each. Add $6.00 for postage to countries outside the United States and Canada.

STATEMENT from By-Laws. The Society shall not be responsible for statements or opinions advanced in papers or . . . printed in its publications (B7.1, para. 3).

INDEXED by the Engineering Index, Inc.

Journal of Heat Transfer

Published Quarterly by The American Society of Mechanical Engineers

VOLUME 105 • NUMBER 4 • NOVEMBER 1983

ANNOUNCEMENTS

TECHNICAL PAPERS

(contents continued on page 743)

(contents continued)

(contents continued on page 781)

(contents continued)

TECHNICAL NOTES

DISCUSSION

Two-Phase Vessel Blowdown of an Initially Saturated Liquid—Part 1: Experimental

M. N. Hutcherson
Senior Mechanical Engineer.
Assoc. Mem. ASME

R. E. Henry
Vice President.

Fauske & Associates, Inc.
Burr Ridge, Ill. 60521

D. E. Wollersheim
Professor,
Mechanical Engineering Department,
University of Missouri,
Columbia, Mo.

Experimental blowdown results for initially isothermal, saturated water from a small pressure vessel containing internal geometry are presented. This experiment simulated a break in a large duct of approximately three diameters in length which exited from the vessel. Choking only occurred at the exit of the discharge duct, and the instantaneous internal vessel pressure distribution was nearly uniform. Most of the fluid within the vessel immediately after the initiation of the blowdown became superheated liquid. This thermodynamic state together with the activated wall cavities inside the vessel maintained a nearly constant internal vessel pressure history early in the blowdown. However, in the latter stage of the depressurization, the remaining fluid within the vessel was essentially in thermodynamic equilibrium. A nonuniform distribution of fluid quality within the vessel was also detected in this experiment. In addition, this experiment illustrates that transient, two-phase, critical flow in large diameter ducts is similar to steady, two-phase, critical flow in small diameter ducts.

1 Introduction

The critical flow problem which is an integral element in the compressible blowdown phenomenon has been studied by many investigators [1–17]. The two phase critical flow from high pressure-temperature systems has been studied primarily in the steady-state case. However, some transient, two-phase critical flow work [7, 11, 18–26] has also been performed. The two-phase blowdown phenomenon is a subject of great interest to both the chemical and power industries. It is particularly pertinent to fossil-fuel fired, steam-water boilers and pressurized and boiling water nuclear reactor systems. It is also applicable to railway transportation of saturated and subcooled liquids [27]. The critical flow rate at a break in such a system is the controlling flow mechanism for most of the decompression. Hence, the critical flow phenomenon is an essential element in the analysis of the blowdown transient.

It has been shown [11] that the nature of the two-phase decompression phenomenon is strongly affected by (*i*) the configuration of the blowdown vessel, (*ii*) the internal geometry within the vessel, and (*iii*) the break location from the vessel. There has been considerable large-scale blowdown experimentation [11, 18–24, 26] primarily directed toward resolving this issue in light water nuclear reactor safety. A variety of vessel and exhaust duct arrangements have been employed, and the decompressions have been initiated from a spectrum of initial conditions. This particular study has considered a break in an "inlet line" to such a nuclear reactor vessel, and this was experimentally modeled with the apparatus illustrated in Fig. 1. A pipe break at this location in such a system has been considered to create a "worst case" blowdown for primarily two reasons:

1 The fluid entering the vessel is at a lower total temperature than the exiting fluid. Hence, the critical flow rate from an inlet duct is greater than from an outlet duct.

2 A break in an inlet line requires the core flow to stagnate and reverse flow direction in order to exhaust from an inlet duct. This flow stagnation and subsequent reversal may significantly decrease the heat transfer from the core during this period.

In the past, it has often been assumed in analyzing the two-phase decompression of such a system that the instantaneous pressure distribution inside the blowdown vessel is nearly uniform. Thermodynamic equilibrium of the remaining fluid has also been often assumed from the initiation of the blowdown. The fluid quality inside the vessel has been considered to be the isentropic quality in the absence of significant heat transfer. The two-phase critical flow phenomenon has also been assumed to be primarily the same in the transient, large duct case as in the steady-state, small duct case. This permits the models which have been verified against the steady-state, small duct data to be applied in the transient, large duct case as well. Metastable thermodynamic states have also been shown [11, 21, 28–31] to exist at the start of decompression from both saturated and subcooled liquid conditions. Choking inside the blowdown vessel and also at the break from the system is also possible under proper conditions. In reviewing the literature, these were then some of the salient questions on this topic which deserved further study. Hence, the foregoing questions served as the foundation upon which this study was formulated.

In view of the preceding discussion, the objectives of the experimental portion of this investigation [11] were to determine:

1 The effect of internal flow area changes on the possibility of choking occurring within this system

2 The effect that metastable thermodynamic states, primarily superheated liquid, have on the decompression sequence

3 Whether transient, two-phase critical flow in large diameter ducts is sufficiently similar to steady-state, two-phase critical flow in small diameter ducts to justify being modeled in a similar manner

Hence, the objective of this article is to briefly summarize the results of the experimental portion of this study and to support the major findings of the same.

2 Experimental Apparatus

The apparatus employed in this experiment was a cylindrical vessel with a volume of approximately 0.153 m^3 (5.40 $ft.^3$) as illustrated in Fig. 1. It had an attached duct which was 0.108-m (4.257-in.) i.d. and about 0.330-m (13-in.) long, (L/D = 3). This simulated a typical broken inlet duct in a

Contributed by the Heat Transfer Division for publication in the JOURNAL OF HEAT TRANSFER. Manuscript received by the Heat Transfer Division January 12, 1982.

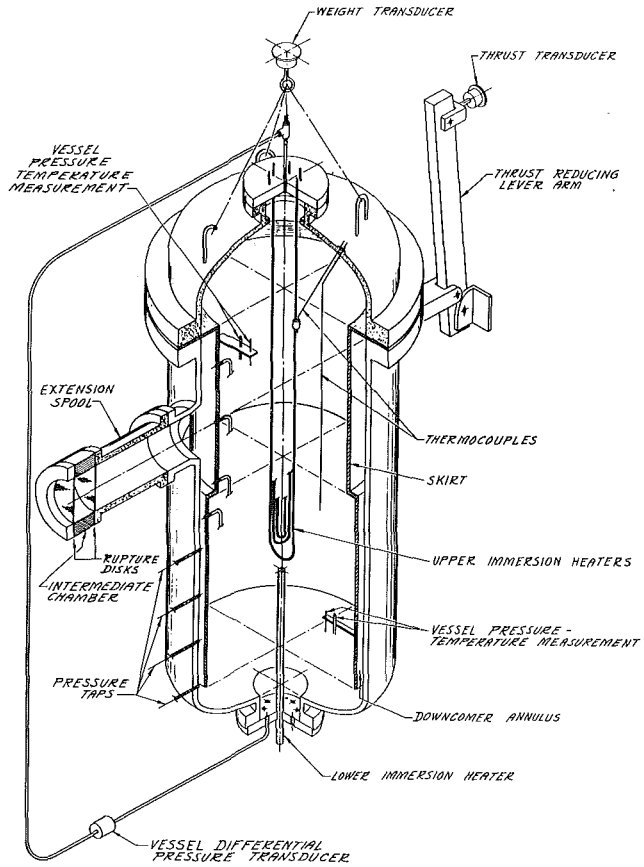

Fig. 1 Schematic of the apparatus employed in this blowdown experiment

pressurized water, nuclear reactor system. A set of two rupture disks was employed at the end of the exhaust duct to contain the fluid during heatup, and they were also used to initiate the decompressions when the desired thermodynamic conditions were established. The vessel also contained internal geometry in the form of a skirt, Fig. 1, which simulated the core barrel in a nuclear reactor vessel. For an inlet line break, the core flow is required to stagnate, reverse, and exhaust up the downcomer annulus and out the broken inlet duct.

The vessel was instrumented with two load cells and various pressure taps and thermocouples, as illustrated in Fig. 1. One of the two load cells measured the weight of the remaining fluid within the vessel, and the other one measured the thrust produced during the blowdown. Both the weight and thrust sensors were 4448 N (1000 lbf) Statham, unbounded strain gage transducers. The total suspended weight of the fluid and vessel when full of 294 K (70°F) water was approximately 2224 N (500 lbf). The maximum thrust produced in this experiment was about 31 KN (7000 lbf), and this was sensed as 3.1 KN (700 lbf) through the 10 to 1 reduction ratio lever arm. The vessel was also instrumented with 15 static pressure taps. All of these taps were 2-mm (1/16-in.) dia, with the exception of two taps near the end of the exhaust duct, P_{14} and P_{15}, which were 1-mm (1/32-in.)-dia taps. Six-mm (1/4-in.) o.d., 5-mm (0.183-in.)-i.d., stainless steel tubing connected each of the pressure taps to an individual pressure transducer. All the pressure transducers were at atmospheric conditions. They were all Statham, strain gage, diaphragm transducers, and their ranges were from 0–4.24 MPa (0–600 psig) to 0–17.2 MPa (0–2500 psig). The smaller range transducers were used to measure the pressures of greatest importance. The hard lines connecting the pressure taps and transduces were filled primarily with water during the blowdown. The longest connecting hard line was 1.12-m (44-in.), and the response time of this line and transducer was about 0.3 ms. This was well within acceptable response for the purpose of this study. There were also 14 chromel-alumel thermocouples employed in this system. Four of these thermocouples were located inside the vessel to measure the local fluid stagnation temperature (T_1, T_2, T_7, T_8), and these were 2-mm (1/16-in.) o.d. sheathed thermocouples, Fig. 1. The remaining 10 temperature sensors were 24 gage, bare wire thermocouples welded onto the exterior wall of the vessel. All the preceding measurements were recorded as analog signals with the exception of the 10 bare wire thermocouples.

3 Discussion

3.1 Calibration Test. A calibration run was performed before executing the reported two-phase tests to ensure the instrumentation was performing properly. The primary concern was with the weight and thrust measurements because of their importance in this study. The exhaust flow rate was determined by differentiating the weight decay measurement, and the thrust measurement also had to be verified. Thus, a

Nomenclature

A = flow area
C = concentration
c = specific heat capacity
D = diameter
F = force, thrust
G = mass flux, $\dot{m}/A$
h = specific enthalpy
K = Henry's concentration coefficient
k = slip ratio, u_V/u_L
m = mass, milli (10^{-3})
$\dot{m}$ = mass flow rate
P = pressure
${}_7\bar{P}_8$ = average internal vessel pressure
R = radius
s = second
T = temperature
t = time
u = flow speed
v = specific volume
x = fluid quality
(0) = time zero
α = void fraction
γ = ratio of specific heat capacities, c_p/c_v
η = throat pressure ratio (P_t/P_o or $P_t/P_{T,e}$)
ρ = fluid density
σ = surface tension
τ = arbitrary time

Subscripts

a = ambient, activation
b = bubble
c = critical or choked
d = deactivated
E = thermodynamic equilibrium
e = entrance
f = final
g = noncondensible gas, superheated vapor
h = constant enthalpy
IS = internal skirt
i = initial
L = saturated liquid
l = subcooled liquid
max = maximum
o = stagnation
p = constant pressure
s = constant entropy
sat = saturation
T = total, total thermodynamic property
t = throat
V = saturated vapor
v = constant volume
VL = saturated vapor minus liquid thermodynamic property
x = exit
1 = upstream location, thermodynamic state
2 = thermodynamic state

calibration blowdown was virtually required to validate these measurements. Such a calibration was performed by filling the vessel with 293 K (68°F) water while only leaving a gas space inside the upper region of the internal skirt, Fig. 1. This gas space was then filled with nitrogen gas. This gas then acted against the virtually incompressible water to motivate the blowdown after the rupture disks were broken. The annulus was initially full of water in this configuration, Fig. 1, and the density of the fluid at the exit of the exhaust duct during the blowdown was well known. This enabled a check to be performed on the consistency of the exhaust flow rate. It was evaluated in three ways: (*i*) from the measured remaining weight of fluid, (*ii*) the measured thrust, and (*iii*) the measured total pressure at the entrance to the exhaust duct. The pressure and temperature instrumentation were not really suspect; hence, little effort was directed at them.

The validity of the remaining mass signal was also checked against the predicted thermodynamic extremes of the expansion of the driving nitrogen gas (adiabatic and isothermal). The measured mass followed the isentropic prediction of the nitrogen expansion much more closely than the isothermal prediction particularly at the beginning of the blowdown. The measurements diverged somewhat from the isentropic prediction later in the decompression because of heat transfer from the entrained water droplets to the expanding and cooling nitrogen gas. Hence, the remaining mass measurements were bracketed by the extremes of how the nitrogen gas could have expanded during the decompression. Thus, the measurements were considered realistic. The thrust and internal vessel pressure also were analyzed in the same manner, and similar results were determined. Thus, all the measurements appeared to be realistic and consistent with each other.

The consistency of the measurements of remaining mass, thrust, and the total pressure at the entrance to the exhaust duct were checked in the following manner. This was accomplished by translating the foregoing measurements into a flow rate. The flow rate determined from the measured remaining mass is given by

$$G = \frac{1}{A_x}\frac{dm}{dt} \tag{1}$$

That from the thrust is

$$G = \sqrt{F\rho_l / A_x} \tag{2}$$

and that from the upstream total pressure considering no losses is

$$G = \sqrt{2\rho_l (P_{T,1} - P_a)} \tag{3}$$

The trends in the flow rate derived from these techniques were very similar for most of the calibration decompression. Hence, all the experimental measurements were considered to be reliable and consistent, and the system was then ready for a two phase blowdown.

3.2 Two-Phase Tests. Blowdown characteristics of a system are strongly dependent on the exhaust duct size in relation to the vessel, location of the exhaust duct from the vessel, and also the internal surface area and volume of the vessel. Experiment has shown [32] that at the beginning of subcooled and saturated liquid blowdown, the nucleation process, which is responsible for the creation of the vapor phase, occurs primarily at the interface between the liquid and containing wall rather than in the liquid freestream. In addition, the heat-up history of such a system has a significant affect on the initiation of the nucleation process and subsequent decompression. This is primarily illustrated by how far the internal vessel pressure drops below the local saturation pressure at the start of decompression. An important effect which occurs during heat-up and blowdown initiation is the action within the internal surface wall cavities. The equilibrium radius of a bubble or cavity during heatup can be approximated as

$$R_E = \frac{2\sigma(T)}{P_l - P_b} \tag{4}$$

where P_b is generally the sum of the working fluid vapor pressure, P_V or $P_{\text{sat}}(T)$, and any nonconsiderable gas pressure, P_g. The noncondensable gas pressure can be related to the concentration of that gas as

$$C(P, T) = \mathrm{K}(T) P_g \tag{5}$$

The concentration of noncondensable gases was constant within the vessel in a given test in this experiment, thus

$$P_{g,2} = P_{g,1}\frac{\mathrm{K}(T_1)}{\mathrm{K}(T_2)} \tag{6}$$

Hence, since the heat-up history of pressure and temperature was known, (4) may be used to approximate the largest remaining unflooded wall cavity before blowdown in this experiment as

$$R_{E,d} = \frac{2\sigma(T_d)}{P_{l,d} - \dfrac{\mathrm{K}(T_1)}{\mathrm{K}(T_2)} P_{g,1} - P_{\text{sat}}(T_{l,d})} \tag{7}$$

The largest remaining unflooded wall cavity at blowdown initiation, (4), is the same as that after heatup and is given by

$$R_{E,a} = \frac{2\sigma(T_{l,2})}{P_{\text{sat}}(T_{l,2}) + \dfrac{\mathrm{K}(T_1)}{\mathrm{K}(T_2)} P_{g,1} - P_{l,2}} \tag{8}$$

Equations (7) and (8) can then be combined to yield the superheat (temperature or pressure) required to activate the largest existing surface cavity at the start of decompression. This then is a simple method of yielding the extent to which the internal vessel pressure may drop below the local saturation pressure before sufficient wall cavities are activated to produce adequate vapor volume to in turn increase the vessel pressure. This is illustrated in Fig. 2 where the internal vessel pressure ($_7\bar{P}_8/P_0(0)$) dropped momentarily before recovering toward its plateau value after which it decayed in an equilibrium manner. This method was used in this experiment and produced comparable superheats as those measured at the start of these blowdowns.

The rapid decrease and subsequent recovery of the internal vessel pressure at the start of these decompressions indicate the existence of a metastable thermodynamic state during this period. The metastable decompression regime of the blowdown continued until the remaining fluid within the system became dispersed and thermodynamic equilibrium was closely approached. This is shown in this experiment by considering the two equilibrium extremes of how the remaining fluid could expand during the blowdown (isentropically and isenthalpically). These two equilibrium expansion paths were considered, and the remaining fluid mass was calculated using the measured internal vessel pressure. The calculated remaining mass based on the measured interval vessel pressure agreed with the measured remaining mass at a calculated void fraction in the internal skirt (α_{IS}) of approximately 0.5, Fig. 2. At this time, thermodynamic equilibrium was essentially established because at a void fraction of about 30 percent, a bubbly flow regime normally transactions to a dispersed one with liquid droplets suspended in a vapor continuum [33]. This then generates significant heat transfer surface area, and thus thermodynamic equilibrium is approached. At this point, the internal vessel

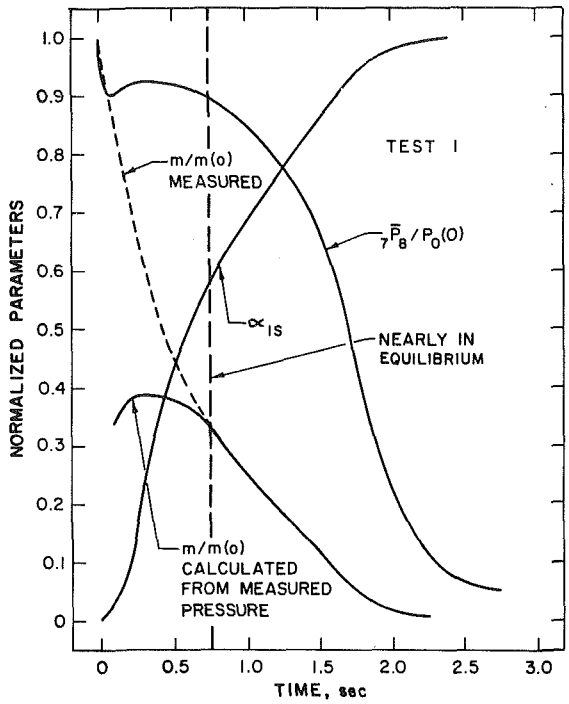

Fig. 2 An indication of when equilibrium of the remaining fluid in the internal skirt region was reached in test 1

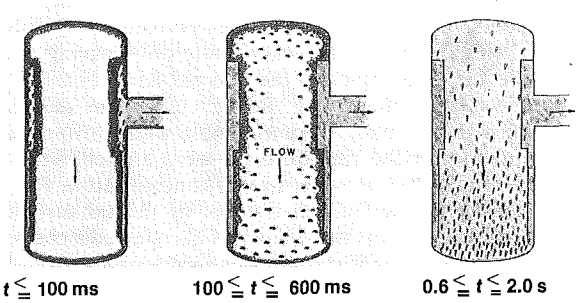

Fig. 3 Schematic of the blowdown vessel illustrating the proposed flow regimes inside the vessel during the various stages of decompression in these tests

pressure also began to decrease from its plateau value as shown in Fig. 2.

The flow regimes which most probably prevailed within this blowdown vessel during the various stages of these decompressions are illustrated in Fig. 3. The indicated time periods when the various flow regimes existed during these blowdowns are applicable to this particular geometry. Almost all the remaining fluid was in a metastable state (superheated liquid) during the first 100 ms. During this time, the surface cavities had been activated and the resulting voids were growing into the superheated liquid. Almost all the fluid within the internal skirt was superheated liquid, and that within the annulus was rapidly becoming a dispersed, two-phase, liquid-vapor mixture.

During this early period, the internal vessel pressure dropped below the saturation pressure and subsequently began to increase toward its plateau value, Fig. 2. The initial drop of the internal vessel pressure below the saturation pressure occurred because there was insufficient volume being produced by the expanding voids. The vapor volume production originating from the surface cavities could not keep pace with the volume expulsion rate. However, after only a short period, sufficient voids had expanded to adequate size to dramatically increase the volume production rate within the vessel. When this exceeded the volume exhaust rate, the internal vessel pressure then began to rise and approach a momentarily constant value, Fig. 2.

From about 100 to 600 ms, the fluid within the annulus was virtually completely dispersed, and the expanding voids originating from the walls were propagating a considerable distance into the superheated liquid within the internal skirt. During this period, the volume production rate within the vessel was approximately equal to the volume exhaust rate from the system. This was indicated by the nearly constant internal vessel pressure, Fig. 2. Once sufficient fluid had been exhausted from the system, the expanding bubbles were nearly uniformly distributed within the liquid remaining in the internal skirt. The resulting two-phase, liquid-vapor mixture was well dispersed, and equilibrium between the remaining liquid and vapor was approached. This is indicated in Fig. 2, where the internal vessel pressure decreased in a nearly equilibrium manner, and the measured and calculated remaining fluid masses agreed. During this period, the fluid volume expulsion rate greatly exceeded the production rate, hence, the internal vessel pressure decreased.

There was no evidence that the flow choked within this vessel, particularly at the annular area enlargement, Fig. 1, during these depressurizations. The pressure upstream and downstream of the annular area enlargement and the internal vessel pressure were all virtually the same. If the flow up the annulus had choked at the area enlargement, the static pressure just upstream of the area enlargement would have only been approximately 75 percent of the internal vessel pressure. The relation between the pressures immediately upstream and downstream of the area enlargement would have depended on the "back pressure" – that pressure immediately upstream of the exhaust duct. The static pressure immediately upstream and downstream of the annular area enlargement were virtually identical, hence, the flow at this location was *not* choked. This was not particularly surprising because the annular area was approximately 2.5 times larger than the exhaust duct area. The only location in this system were the exhausting flow did choke was at the minimum area section, i.e., at the exit of the exhaust duct. Motion pictures of the exhaust plane flow indicated that fully developed critical flow was established approximately 25 ms after the rupture disks had broken. The same motion pictures and the measured critical pressure ratio histories indicated that the exhausting flow was choked for about 70 percent of the 2.5 s decompressions.

The fluid quality at the entrance to the exhaust duct in this experiment deviated considerably from equilibrium conditions. The fluid quality for a uniformly distributed, homogeneous equilibrium, isentropic expansion within the vessel is given by

$$x_s = \frac{s_L(T_o) - s_L(P)}{s_{VL}(P)} \tag{9}$$

and similarly for an isenthalpic expansion

$$x_h = \frac{h_L(T_o) - h_L(P)}{h_{VL}(P)} \tag{10}$$

These two equilibrium, upstream fluid qualities as based on the measured internal vessel pressure are shown in Fig. 4. The fluid quality at the entrance to the exhaust duct was assumed to be approximately the same as at the exit. This is because the static pressure in such a short duct ($L/D = 3$) is nearly constant. Thus, there is virtually no phase change for fluid in residence in such a short length. Each of these two equilibrium fluid qualities, (9) and (10), was employed in an energy balance on the system during the blowdown given by

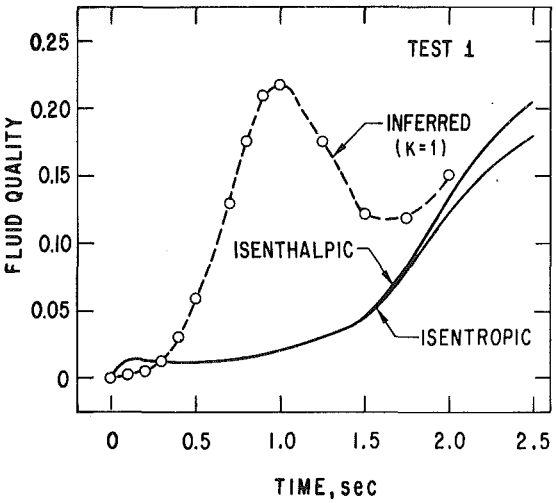

Fig. 4 Comparison of the inferred fluid quality and the entrance isentropic and isenthalpic qualities based on the measured pressure in test 1

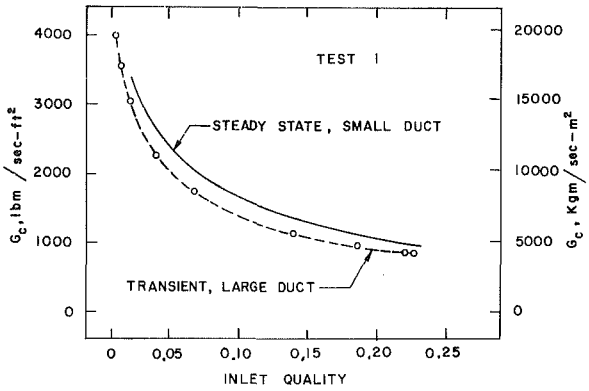

Fig. 5 Comparison of the transient, large duct, critical flow rates in test 1 and the corresponding steady-state, small duct, critical flow rates in [9]

$$m(0)h(0)-m(\tau)h(\tau)=A_x\int_0^\tau G\Big\{[h_V x+h_L(1-x)]+\frac{1}{2}G^2\Big[v_V x+v_L(1-x)\Big]^2\Big\}_x\,dt \tag{11}$$

The measured critical flow rates and the instantaneous pressures were used in (11). The balance employing the isentropic quality (9) was approximately 8 percent low, and the same employing the isenthalpic quality (10) was about 7 percent low. This indicated that the fluid quality at the entrance and exit of the exhaust duct was apparently not an equilibrium value. Fortunately, it was also possible to evaluate the fluid quality at the exit of the exhaust duct by employing a variety of the system measurements. The homogeneous exit specific volume was formulated as

$$v_x=\frac{1}{G_c^2}\left[\frac{F}{A_x}+P_a-P_x\right] \tag{12}$$

and the exit fluid quality was then determined from

$$x_x=\frac{v_x-v_L(P_x)}{v_{VL}(P_x)} \tag{13}$$

Assuming that (*i*) the fluid quality in the duct was approximately constant, (*ii*) the liquid phase was virtually incompressible, and (*iii*) the vapor phase expanded isentropically in the duct, then (13) can be recast as

$$x_1=\frac{v_x-v_L(P_{T,1})}{v_V(P_{T,1})\eta^{-1/\gamma}-v_L(P_{T,1})} \tag{14}$$

This homogeneous inferred inlet quality is also shown in Fig. 4. It is readily apparent that the shape of this inferred inlet quality curve is significantly different than that of the equilibrium qualities. This is an indication of the nonuniformity of the flow pattern within this vessel during these blowdowns. It should be noted in Fig. 4 that the inferred entrance quality began to significantly increase above the equilibrium qualities at approximately 300 ms which was after the annulus had initially been voided, Fig. 3. However, it was during this time period that the vapor phase was probably being swept up the downcomer annulus toward the exhaust duct. This vapor phase was being generated at the lower, inside wall of the internal skirt. The exhaust critical flow rate was also decreasing very rapidly at about this same time. This is consistent since the critical flow rate decreases dramatically for small increases in inlet quality in the low quality regime [9]. This homogeneous inferred inlet quality (14) was then employed in an energy balance on the system (11) to assess its validity. The energy exhausted from the system was determined from using (*i*) the homogeneous inferred inlet quality, (*ii*) the experimental critical flow rates, and (*iii*) the measured internal vessel pressure. These resulting energy balances were then within 1 percent of the initial total energy inventory. This therefore provided good confidence that the homogeneous inferred quality was a valid representation of the actual fluid quality in the exhaust duct during the blowdown.

The case of a nonhomogeneous ($k > 1$) inferred quality was also investigated, and it was determined not to be as realistic as the homogeneous ($k = 1$) case. The nonhomogeneous quality was formulated by combining the continuity equation

$$\dot{m}=\rho_V A_V u_V+\rho_L A_L u_L \tag{15}$$

and a summation of the momentum flow rates of each phase as

$$\dot{m}u=\dot{m}_V u_V+\dot{m}_L u_L \tag{16}$$

This resulted in the nonhomogeneous quality as a function of the velocity ratio (k) as

$$x=\frac{-\left[\frac{v_V}{k}+v_L(k-2)\right]+\left\{\left[\frac{v_V}{k}+v_L(k-2)\right]^2+4(v-v_L)\left[v_V\frac{k-1}{k}-v_L(k-1)\right]\right\}^{1/2}}{2\left[v_V\frac{k-1}{k}-v_L(k-1)\right]} \tag{17}$$

Assumptions (*i*) and (*iii*) that were employed in formulating (14) were also applied in (17). Once this was accomplished and (12) and (17) were combined, the energy exhausted from the system as determined from (11) increased with velocity ratio much above the 1 percent agreement obtained with the homogeneous inferred inlet quality. Thus, the actual exhausting flow was apparently very nearly homogeneous in view of the good energy balance comparison.

The transient, large duct, critical flow rates from this study compare well with the steady-state, small duct, critical flow rates of previous investigators [9], as illustrated in Fig. 5. The steady-state, critical flow rates shown in Fig. 5 are for entrance total pressures of 0.689–6.550 MPa (100-950 psia) and entrance qualities of 0.01–0.2275. These steady-state, critical flow rates were measured in convergent-divergent, axisym-

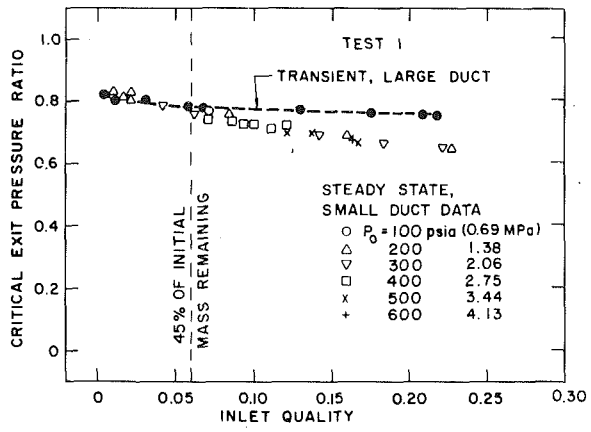

Fig. 6 Comparison of the transient, large duct, critical pressure ratio in test 1 and the steady-state, small duct, critical throat pressure ratio in [9]

metric nozzles with 6.44 and 11.1-mm (0.253 and 0.438-in.)-dia. throats. For comparison, the i.d. of the constant area exhaust duct in this study was 0.108-m (4.257-in.). The average difference between these two sets of two phase critical flow rate data is about 19 percent with the transient, large duct critical flow rates being less than the steady-state, small duct critical flow rates. The same good agreement was true of test 2 in this experiment. Based on this critical flow rate data comparison, the critical flow phenomenon appears to be quite similar in the transient, large duct and steady-state, small duct cases, as has also been inferred in [23, 25, 26].

The transient, large duct, critical exit pressure ratios from this study also compare well with steady-state, small duct, critical throat pressure ratios [9], as illustrated in Fig. 6. These two sets of critical pressure ratio data are virtually identical up to an inferred inlet quality of approximately 6 percent. At this point, less than half the initial fluid remained within the vessel during these blowdowns, Figs. 2 and 6. This was also after the critical flow rate had decreased to approximately 9800 Kgm/s-m^2 (2000 lbm/s-ft^2), Fig. 5. Thus, the critical pressure ratios of this study and the steady values compare extremely well for the major portion of these blowdowns. The transient, large duct, critical pressure ratios are somewhat greater than those for steady-state, small duct flow for entrance qualities greater than about 10 percent. However, this occurred reasonably late in these blowdowns after the most important segment of the decompressions had occurred. This was also when the homogeneous equilibrium predicted critical flow rate became similar in magnitude to the Henry-Fauske prediction [4]. This value of 10 percent entrance quality established in this transient, large duct experiment is precisely that observed in the steady-state, small duct case [4]. The internal vessel pressure started to decrease from its nearly constant value approximately when the homogeneous equilibrium critical flow rate agreed with the measured critical flow rate. This is consistent with the apparent occurrence of equilibrium of the remaining fluid, Fig. 2. The Moody model [5] significantly overpredicted the measured critical flow rates for the entire blowdown. The Henry-Fauske prediction [4] for the critical flow rate agreed well with the data while only being slightly greater than the measurements for most of the decompression.

The measured and calculated critical exit pressure ratios in tests 1 and 2 were also compared. The Henry-Fauske prediction of the overall critical pressure ratio history was best with both the homogeneous equilibrium and Moody predictions underestimating the data.

The measured and calculated remaining fluid mass within the blowdown vessel were also compared. The Moody prediction of the remaining fluid mass decreased very rapidly below the experimental results because of the excessively high predicted initial critical flow rate. The Henry-Fauske prediction of the remaining fluid mass followed the trend of the data reasonably well if not slightly underpredicting the measurements. The homogeneous equilibrium prediction of the remaining fluid mass was considerably greater than the data. This was because of the underprediction of the critical flow rate early in the blowdown.

The measured and calculated thrust histories in this experiment were also compared. The predicted thrust history obtained by employing the homogeneous equilibrium critical flow model in (12) agreed well with the data in the latter part of the decompression. However, the maximum in the predicted thrust history was later in time than the measurements indicated. This is due to the underpredicted critical flow rate early in the depressurization. The homogeneous equilibrium predicted thrust increased up to this time even with the underpredicted critical flow rate because of the increasing fluid quality, Fig. 4. The maximum thrust predicted by employing the Moody critical flow model in (12) was considerably greater than the measured maximum thrust. It was greater than the measured thrust for most of the blowdown except in the latter part of the decompression. The predicted maximum thrust obtained by using the Henry-Fauske critical flow model in (12) was only slightly greater than the measured maximum thrust. This prediction was also slightly greater than the measurements for most of the blowdown except in the latter period of the depressurization. However, it was less than the Moody prediction over the entire decompression.

Of the three cited critical flow analytical models, the measured histories in the blowdowns of this experiment were best predicted using the Henry-Fauske critical flow model.

4 Conclusions

The most significant conclusions drawn from the experimental portion of this study are as follows:

1 The fluid thermodynamic state inside the system during the blowdown is dependent on the internal vessel configuration. This is particularly pertinent at the start of blowdown from an initially subcooled or saturated liquid state. The primary vapor generation mechanism in such a system is predominately the activation and growth of bubbles originating from surface cavities. Vapor generation in the bulk liquid has not been shown to be significant. Thus, the ratio of internal vessel solid surface area to initial liquid volume is a useful criterion for assessing how quickly a dispersed, two-phase mixture is approached. The resulting local fluid compressibility greatly affects total pressure losses throughout the system and ultimately the critical flow rate from the break in the system.

2 The initial decrease of the internal vessel pressure at the start of blowdown occurs because the initial volume exhaust rate exceeds the vapor volume production rate. The initially retarded volume production rate (by bubble growth) is due to the metastable, superheated liquid state which is initially created and its subsequent relaxation toward thermodynamic equilibrium.

3 Choking only occurred at the exit of the exhaust duct in this system.

4 There was a significant nonuniform fluid quality distribution within this system early in these blowdowns. This was due to a lack of solid surface area per unit liquid volume inside the internal skirt region to aid in vapor phase generation. Hence, the liquid in the internal skirt region remained as a superheated liquid at the start of these decompressions. Once the fluid in this region became

dispersed, thermodynamic equilibrium was approached, and the internal vessel pressure began to decrease.

5 The Henry-Fauske critical flow model provides the best available prediction of the overall characteristics of the two phase decompression phenomenon observed in this experiment.

6 The two phase critical flow phenomenon is essentially the same in the transient, large duct and steady-state, small duct cases.

Acknowledgment

The authors acknowledge the financial support for this study from the United States Energy Research and Development Administration. This work was performed in the Experimental Modeling Section of the Reactor Analysis and Safety Division of Argonne National Laboratory.

References

1 Henry, R. E., Grolmes, M. A., and Fauske, H. K., "Pressure Drop and Compressible Flow of Cryogenic Liquid-Vapor Mixtures," *Heat Transfer at Low Temperatures*, edited by Walter Frost, ch. 11, Plenum Press, New York, 1975, p. 229.

2 Henry, R. E., Fauske, H. K., and McComas, S. T., "Two-Phase Critical Flow at Low Quality, Part I: Experimental," *Nuclear Science and Engineering*, Vol. 41, 1970, pp. 79–91.

3 Henry, R. E., Fauske, H. K., and McComas, S. T., "Two-Phase Critical Flow at Low Quality, Part II: Analytical," *Nuclear Science and Engineering*, Vol. 41, 1970, pp. 92–98.

4 Henry, R. E., and Fauske, H. K., "The Two-Phase Critical Flow of One Component Mixtures in Nozzles, Orifices, and Short Tubes," ASME JOURNAL OF HEAT TRANSFER, Vol. 93, No. 2, May 1971, pp. 179–187.

5 Moody, F. J., "Maximum Flow Rate of a Single Component, Two-Phase Mixture," ASME *Transactions*, Vol. 87, No. 1, Feb. 1965, p. 134.

6 Prisco, M. R., Henry, R. E., Hutcherson, M. N., and Linehan, J. L., "Nonequilibrium Critical Discharge of Saturated and Subcooled Liquid Freon-11," *Nuclear Science and Engineering*, Vol. 63, No. 4, Aug. 1977, pp. 365–375.

7 Sozzi, G. L., and Sutherland, W. A., "Critical Flow of Saturated and Subcooled Water at High Pressure," NEDO-13418, General Electric Co., San Jose, Calif., July 1975.

8 Fauske, H. K., "Some Ideas About the Mechanism Causing Two Phase Critical Flow," Appl. Sc. Res., Vol. 13, Section A, 1964, pp. 149–160.

9 Starkman, E. S., Schrock, V. E., Neusen, K. F., and Maneely, D. J., "Expansion of a Very Low Quality Two-Phase Fluid Through a Convergent-Divergent Nozzle," ASME *Journal of Basic Engineering*, Vol. 86, No. 2, June 1964, p. 247.

10 Shrock, V. E., Starkman, E. S., and Brown, R. A., "Flashing Flow if Initially Subcooled Water in Convergent-Divergent Nozzles," ASME JOURNAL OF HEAT TRANSFER, Vol. 99, May 1977, pp. 263–268.

11 Hutcherson, M. N., "Contribution to the Theory of the Two-Phase Blowdown Phenomenon," (*a*) ANL-75-82, Argonne National Laboratory, 1975: (*b*) And Interim Report, ANL/RAS 75-42, 1975: (*c*) Also, University Microfilms, 76-21951, 1976: (*d*) And University of Missouri, Mechanical Engineering Department, Ph.D. dissertation, Columbia, Mo. 1975.

12 Hutcherson, M. N., "Numerical Evaluation of the Moody Critical Flow Model," MDC N9653-110, McDonnell Douglas, St. Louis, Missouri, Sept. 1980.

13 Hutcherson, M. N., "Numerical Evaluation of the Henry-Fauske Critical Flow Model," MDC N9654-100, McDonnell Douglas, St. Louis Mo., July 1980.

14 Hutcherson, M. N., "Numerical Evaluation of the Homogeneous-Equilibrium Critical Flow Model," MDC N10437-041, McDonnell Douglas, St. Louis, Mo., Apr. 1981.

15 Hutcherson, M. N., "Numerical Evaluation of the Homogeneous Frozen Critical Flow Model," MDC N10438-041, McDonnell Douglas, St. Louis, Mo., Apr. 1981.

16 Wallis, G. B., "Critical Two-Phase Flow," *International Journal of Multiphase Flow*, Vol. 6, No. 1–2, Feb.-Apr. 1980, pp. 97–112.

17 Henry, R. E., "Two-Phase Compressible Flow," *EPRI Workshop Proceedings: Basic Two Phase Flow Modeling in Reactor Safety and Performance*, Vol. 2, Tampa, Fla., Feb. 27–Mar. 2, 1979, pp. 9-67:9–106.

18 Hutcherson, M. N., Henry, R. E., and Gunchin, R. R., "Compressible Aspects of Water Reactor Blowdown," *Transactions ANS*, Vol. 18, 1974, p. 232.

19 Hutcherson, M. N., Henry, R. E., and Wollersheim, D. E., "Experimental Measurements of Large Pipe Transient Blowdown," *Transactions ANS*, Vol. 20, Paris, France, Apr. 21–25, 1975, pp. 488–490.

20 Hutcherson, M. N., Henry, R. E., and Wollersheim, D. E., "The Two-Phase Blowdown Phenomenon in a Small LWR Geometry," *Transactions ANS*, Vol. 22, San Francisco, Calif., Nov. 16–21, 1975, pp. 466–467.

21 Hutcherson, M. N., Henry, R. E., and Wollersheim, D. E., "Two-Phase Vessel Blowdown of an Initially Saturated Liquid, Part 2-Analytical, ASME JOURNAL OF HEAT TRANSFER, Vol. 105, No. 4, pp. 694–699.

22 Morrison, A. F., "Blowdown Flow in the BWR BDHT Test Apparatus," GEAP-21656, NRC-2, General Electric Co., San Jose, Calif., 1977.

23 Hall, D. G., "A Study of Critical Flow Prediction for Semiscale Mod-1-Loss-of-Coolant Accident Experiments," TREE-NUREG-1006, EGG, Idaho, 1976.

24 Bayless, P. D., Marlow, J. B., and Averill, R. H., "Experimental Data Report for LOFT Nuclear Small Break Experiment L3-1," EGG-2007, NUREG/CR-1145, EGG, Idaho, Jan. 1980.

25 Hall, D. G., "An Evaluation of the Accuracy of Five Critical Flow Models Using Transient Data," *Proceedings of the Topical Mtg. on Thermal Reactor Safety*, CONF-770708, Sun Valley, Id., 1977, pp. 2–493.

26 Martinec, E. L., "A Comparison of the Marviken Critical Flow Tests With the Henry-Fauske Model," ANL/RAS/LWR 79-8, Argonne National Laboratory, Argonne, Ill., Dec. 1979.

27 Winters, W. S., and Merte, H., "Experiment and Nonequilibrium Analysis of Pipe Blowdown," Nucl. Sci. and Eng., Vol. 69, 1979, pp. 411–429.

28 Weisman, J., Bussell, G., Jacknani, I. L., and Hsieh, T., "The Initiation of Boiling During Pressure Transients," ASME Paper No. 73-WA/HT-25, 1973.

29 Hooper, F. C., and Abdelmessih, A. H., "The Flashing of Liquids at Higher Superheats," *Proceedings 3rd Intl. Heat Transfer Conf.*, Chicago, Ill., Vol. 4, Aug. 1966, pp. 44–50.

30 Hooper, F. C., Faucher, G., and Eidlitz, A., "Pressure Effects on Bubble Growth in the Flashing of Superheated Water," *Proceedings 4th Int. Heat Transfer Conf.*, Vol. 5, Paper No. B2.3, Paris-Versailles, France, 1970.

31 Kenning, D. B. R., and Thirunavukkarasu, K., "Bubble Nucleation Following a Sudden Pressure Reduction in Water," *Proceedings 4th Intl. Heat Transfer Conf.*, Vol. 5, Paper B2.9, Paris-Versailles, France, 1970.

32 Hoppner, G., "Experimental Study of Phenomena Affecting the Loss of Coolant Accident," Ph.D., thesis, University of California at Berkeley, 1971.

33 Radovcich, N. A., and Moissis, R., "The Transition from Two-Phase Bubble Flow to Slug Flow," MIT Report 7-7673-22, 1962.

Two-Phase Vessel Blowdown of an Initially Saturated Liquid—Part 2: Analytical

M. N. Hutcherson
Senior Mechanical Engineer.
Assoc. Mem ASME

R. E. Henry
Vice President.

Fauske and Associates, Inc.,
Burr Ridge, Ill. 60521

D. E. Wollersheim
Professor,
Mechanical Engineering Department,
University of Missouri,
Columbia, Mo.

Analytical models are presented to predict the internal vessel conditions during the decompression regimes of an initially saturated liquid. A subcooled blowdown analysis considers the elasticity of both the liquid and vessel. A bubble growth analysis for the intermediate period of blowdown is based on thermally dominated bubble growth from a solid surface into a superheated liquid. A dispersed analysis for the latter decompression period assumes the vapor bubbles have grown sufficiently so the liquid is uniformly distributed within the vapor phase. The subcooled analysis predicts the initial period of blowdown reasonably well. The bubble growth analysis predicts the rise in system pressure above that value to which it initially falls after the end of subcooled blowdown. It considers an initially "slow" depressurization rate (less than 400 MPa/s) where nucleation and bubble growth is the dominate volume producing, and thus pressure recovery, mechanism. It provides insight into why the system pressure initially drops below the saturation pressure, and it also offers an explanation for the subsequent recovery of the system pressure toward the saturation pressure. The thermodynamic equilibrium analysis provides a reasonable prediction of the latter stage of decompression. The combination of these three models predicts the overall two-phase decompression phenomenon reasonably well.

1 Introduction

This study addresses the thermodynamic and fluid dynamic aspects of two-phase blowdown of a high pressure-temperature fluid from an initial subcooled or saturated liquid state. Blowdown analysis combines a description of both the thermal-fluid behavior inside the blowdown vessel in addition to the escape flow limiting mechanism from the system. The behavior inside the blowdown vessel controls the fluid compressibility at the entrance to the exhause duct $P_{T,e}$, x_e). Hence, it controls the critical flow condition from the system and thus the depressurization rate. The two-phase blowdown phenomenon has applicability to boilers, refrigeration and cryogenic systems, chemical systems, railroad tank car transportation [1], and boiling and pressurized water nuclear reactors. It is the later, nuclear reactor safety, which has provided the primary impetus to more fully understand the two-phase decompression phenomenon. The analyses presented herein are a summary of a larger study [2]. It addressed among other questions the existence, magnitude, and effect of metastable thermodynamic states on two phase blowdown.

Metastable thermodynamic states, namely superheated liquid, exist in the early stage of decompression from an initially subcooled or saturated liquid condition [2–8]. Recent emphasis [9–10] has been to more fully understand the vapor generation (nucleation) mechanism as a result of boiling and/or flashing. Recent studies have also indicated that the nucleation mechanism at the start of subcooled and saturated liquid blowdown depends on the initial rate of pressure decay [11]. It is suggested that such blowdowns can be classified as either "fast" or "slow," depending on this criteria (normally taken to be about 400 MPa/s). Following this type classification, the decompressions reported in this study fall into the "slow" category in which nucleation from solid surfaces which contain imperfections (nucleation sites) is dominate. The effect of the magnitude of the nucleation process in the early stage of a "slow" blowdown is largely dependent on the internal vessel geometry. It is primarily related to the (*i*) internal interfacial surface area between liquid and solid surface, (*ii*) initial internal volume of liquid, (*iii*) break flow area from the system, (*iv*) internal flow area within the system, and (*v*) the location of the break in the system. A complete thermodynamic equilibrium analysis of the phenomenon [12] does not account for the superheated liquid condition at the start of blowdown. Consequently, it does not adequately describe the overall phenomenon. Even though this approach does not completely describe the phenomenon in the general case, it does become more representative of slower decompressions. Many blowdown analyses to date [13–18] has been performed in a thermodynamic equilibrium manner for the entire decompression. However, this is not a completely valid assumption [7]. Nucleation at the start of blowdown is initiated primarily from the activated surface cavities at the internal solid-liquid interfaces. It does not predominantly occur in the bulk liquid [19]. There is a fraction of the spectrum of internal surface cavities which are not flooded during heat-up and which are larger than minimum embryo size. These can subsequently function as nucleation sites upon decompression. Most initially two-phase critical flow models to date have also assumed that the expanding two-phase mixture behaves in an ideal, thermodynamic equilibrium manner. However, recently the merits of nonequilibrium critical flow analysis [20] have been recognized and implemented. There has been considerable experimental effort directed toward understanding the overall two-phase decompression phenomenon in a reactor system. This work includes that of Semiscale and LOFT, [21–24], Battelle [25, 26] (U.S. and Germany), Japan [27], and Marviken [28].

The objectives of the analytical portion of this study were primarily to understand (*i*) the transition from subcooled blowdown to the initiation of nucleation, (*ii*) the influence of the nucleation process on the early stage of decompression, and (*iii*) the transition from the bubble growth to dispersed stage of blowdown.

Contributed by the Heat Transfer Division for publication in the JOURNAL OF HEAT TRANSFER. Manuscript received by the Heat Transfer Division January 12, 1982.

2 Analysis

The two-phase decompression scenario should be divided into at least two different major classes of related phenomena [6]. The first is the fluid behavior inside the blowdown vessel upstream of the entrance to the exhaust duct, and the second is the fluid behavior inside the exhaust duct itself. The fluid behavior inside the vessel establishes the flow pattern and local fluid quality at the entrance to the exhaust duct. The presence of structure within the vessel can also significantly effect the internal flow regime. Internal structure also markedly impacts the very early stage of decompressoin by supplying additional potentially active surface cavities. These can serve as nucleation sites for the inception of vaporization. The history of previous fluid and wall pressure-temperature conditions within the vessel also effects the inception of vaporization upon depressurization. Analytical models are described herein for each of the three major decompression regimes: subcooled, bubble growth, and dispersed.

2.1 Subcooled Model. The initial period of blowdown when the fluid in the system is subcooled liquid is analyzed in this section. The assumptions employed in this model are as follows:

(*a*) The system is instantaneously opened to the ambient.

(*b*) There is frictionless, one-dimensional flow in a smooth entrance exhaust duct.

(*c*) The exhaust duct has a constant cross sectional area and internal volume.

(*d*) The flow is initially unchoked and subsequently becomes choked.

(*e*) The vessel material is elastic.

The accelerating (inertial) flow period at the start of blowdown when the flow is subcritical is small compared to the overall subcooled decompression period. It only lasts for a few milliseconds. Hence, the exhaust flow is choked during virtually all of subcooled blowdown.

The transient, subcritical flow rate in the early stage of subcooled blowdown can be described as

$$G(t) = \frac{C_d}{L}\left[P_{T,e}(t) - P_a\right]t \tag{1}$$

When the transient flow rate in (1) increases to the critical flow rate, the flow is assumed to become choked at the exit of the exhaust duct. The critical flow rate and critical exit pressure can then be determined from an initially subcooled and saturated liquid critical flow model. Such a model [29] must be evaluated at the instantaneous total thermodynamic conditions at the entrance to the exhaust duct ($P_{T,e}$, $T_{T,e}$). During this period, the thermodynamic state of the remaining fluid within the vessel is subcooled liquid. However, the state of the fluid in the exhaust duct is a compressible, two-phase, liquid-vapor mixture. It is the behavior of this compressible, two-phase, liquid-vapor mixture in the exhaust duct which limits the escape flow rate from the system.

The system response during the subcooled period of decompression is analyzed as follows. A conservation of mass in the vessel during the blowdown is

$$\frac{dm_l}{dt} = -GA_x \tag{2}$$

Equation (2) can be integrated initially with the subcritical flow rate, (1), and subsequently with the critical flow rate. The specific volume of the remaining liquid within the system is then

$$v_l = \frac{V_T}{m_l} \tag{3}$$

the influence of the elasticity of the vessel material on the subcooled blowdown is accounted for by considering the hoop stress in a thin walled vessel. This is given by

$$\sigma = \frac{1}{2\delta}\left[P_{T,e}d - P_a(d+2\delta)\right] \tag{4}$$

The vessel material is assumed to be described by Hookes Law in the elastic range. Differentiating the relation for the internal volume of a cylindrical vessel produces

$$dV_T = 2V_T\frac{dr}{r} \tag{5}$$

Equations (4) and (5) may be combined to determine the change in the original, unstressed vessel volume.

Equation (3) can be differentiated to produce

$$\frac{dv_l}{dt} = \frac{1}{m_l}\frac{dV_T}{dt} - \frac{V_T}{m_l^2}\frac{dm_l}{dt} \tag{6}$$

Nomenclature

A = cross-sectional flow area
α = void fraction, thermal diffusivity
C = coefficient, degrees Centigrade
c = specific heat capacity
d = inside diameter of vessel
Δ = finite difference
δ = vessel wall thickness
E = elasticity
F = degrees Fahrenheit
G = mass flux, $\dot{m}/A$
g = acceleration of gravity at sea level
h = specific enthalpy
η = critical exit or throat pressure ratio
J = Joule, (N − m)
Ja = Jakob number, $c_L\rho_L\ (T - T_{sat})/\rho_V h_{VL}$
K = degrees Kelvin
L = exhaust duct length
m = mass, meter
N = number of bubbles or nucleation sites in a given generation, Newtons
P = static pressure
Pa = Pascal (N/m^2)
r = radius
ρ = density
S = surface area
s = specific entropy
σ = surface tension, normal stress
T = temperature
t = time
u = flow speed
V = volume
v = specific volume
x = fluid quality

Subscripts

a = ambient
c = choked or critical flow, thermodynamic critical state or property
d = discharge, bubble departure
e = entrance
i = initial, given sector of system
L = saturated liquid
l = subcooled liquid
max = maximum
o = stagnation
p = produced
sat = saturation
Sup = superheat
T = total, total thermodynamic property
τ = arbitrary time step from start of blowdown
τ' = time step from start of growth of current bubble generation from surface
VL = saturated vapor minus liquid thermodynamic property
V = saturated vapor
x = exit
∞ = free stream

The dm_l/dt is evaluated from (2), and the dV_T/dt is determined from the change in the volume of the vessel, (5).

The depressurization rate of the liquid remaining within the system is dependent upon its elasticity according to

$$\frac{dP}{dt} = \frac{-E_l}{v_l}\frac{dv_l}{dt} \tag{7}$$

where the dv_l/dt is determined from (6). Equations (4), (5), (6), and (7) can then be combined to determine the instantaneous internal vessel stagnation pressure during the subcooled regime of decompression.

2.2 Bubble Growth Model. The system pressure recovery phenomenon during the early stage of blowdown after the pressure has dropped below the local saturation pressure is analyzed in this section. It is postulated that the volume producing mechanism within the system is initially inertially controlled and then thermally dominated vapor bubble growth.

The internal volume of the system is considered constant so that

$$V_T = V_V + V_L = m_V v_V + m_L v_L \tag{8}$$

Equation (8) is differentiated to produce

$$\frac{dv_V}{dt} = \frac{-1}{m_V}\left[v_L\frac{dm_L}{dt} + v_V\frac{dm_V}{dt} + m_L\frac{dv_L}{dt}\right] \tag{9}$$

The factor dv_L/dt is determined from the elasticity of the liquid phase as

$$\frac{dv_L}{dt} = \frac{-1}{E_L v_L}\frac{dP}{dt} \tag{10}$$

The behavior of the saturated vapor phase is approximated as Pv_V = constant, so the left side of (9) becomes

$$\frac{dv_V}{dt} = \frac{-v_V}{P}\frac{dP}{dt} \tag{11}$$

Substituting (10) and (11) into (9) gives the following relation for the time rate of change of the internal vessel pressure

$$\frac{dP}{dt} = \frac{PE_L}{m_V v_V E_L + v_L P}\left[v_L\frac{dm_L}{dt} + v_V\left(\frac{dm_V}{dt}\right)_{\text{net}}\right] \tag{12}$$

The total mass flow rate from the system is

$$\frac{dm}{dt} = -GA_x \tag{13}$$

For homogeneous, incompressible flow, which is a good approximation during the early, low void fraction period of the blowdown, the flow rate is

$$G = \rho u = [2\rho(1-\eta_c)P_{T,e}]^{1/2} \tag{14}$$

The η_c is the saturated liquid critical exit pressure ratio, and the fluid density is

$$\rho = \rho_V\alpha + \rho_L(1-\alpha) \tag{15}$$

The mass flow rate of the liquid phase from the system is then

$$\frac{dm_L}{dt} = -\rho_L A_x(1-\alpha)\left[\frac{2(1-\eta_c)P_{T,e}}{\rho_V\alpha + \rho_L(1-\alpha)}\right]^{1/2} \tag{16}$$

and that of the vapor phase from the system is

$$\frac{dm_{V,x}}{dt} = -\rho_V A_x\alpha\left[\frac{2(1-\eta_c)P_{T,e}}{\rho_V\alpha + \rho_L(1-\alpha)}\right]^{1/2} \tag{17}$$

Equation (16) can be substituted directly into (12). However, the change in the mass of the vapor phase within the system in (12) is a net difference. It is the result of the production of vapor mass by bubble nucleation minus the rate of vapor mass exhausted from the system (17).

The inertially dominated bubble growth period given by

$$r = \left\{\frac{2}{3}v_l[P_{\text{sat}}(T) - P_l]\right\}^{1/2} t \tag{18}$$

is very short for most fluids. It was approximately 10^{-8} s in the tests reported in this study. Thus, the bubble growth is assumed to be primarily thermally controlled as given by

$$r = \left[\frac{12}{\pi}\alpha_l \text{Ja}\right]^{1/2} t^{1/2} \tag{19}$$

where the Jakob number, Ja, is

$$\text{Ja} = \frac{c_L\rho_L(T - T_{\text{sat}})}{\rho_V h_{VL}} \tag{20}$$

The volume of an individual spherical bubble growing in a thermally dominated manner (19) is

$$V_b = \frac{4}{3}\pi\left[\frac{12}{\pi}\alpha_l \text{Ja}^2\right]^{3/2} t^{3/2} \tag{21}$$

where (t) is the time for inception.

The departure diameter of steam bubbles growing from a surface in pool boiling conditions has been correlated [30] as

$$D_d = 1.5\times 10^{-4}\left[\frac{\sigma}{g(\rho_L - \rho_V)}\right]^{1/2}\left[\frac{c_L\rho_L T_{\text{sat}}}{\rho_V h_{VL}}\right]^{5/4} \tag{22}$$

The surface tension (σ) of saturated water against its own vapor (steam) in (22) has been correlated by White [31] as

$$\sigma(N/m) = 0.2358\left[1 - \frac{T}{T_c}\right]^{1.256}\left[1 - 0.625\left(1 - \frac{T}{T_c}\right)\right] \tag{23}$$

A simplification of (23) which is within 1 percent of it over the range of 366–566 K (200–560°F) is

$$\sigma(N/m) = 0.14783\left[1 - \frac{T}{T_c}\right]^{1.053} \tag{24}$$

The departure diameter is then used in (19) to determine when a bubble will separate from the surface. By knowing the departure bubble diameter and the total surface area within the system, the maximum number of nucleation sites can be determined as

$$N_{\max} = \frac{2}{\sqrt{3}}\frac{S_T}{{D_d}^2} \tag{25}$$

This assumes that the bubbles on the wall at departure are just touching each other, spherical in shape, and arranged in a triangular array. The increasing diameter of a bubble on the wall can be determined from (19) for time greater than the inertially controlled period (18). When the diameter of the bubbles on the surface reach the departure diameter, that generation is assumed to leave the surface and continues to grow in the liquid.

The incremental vapor volume production is the increase in volume of the vapor bubbles in the free stream and also those growing from the solid surface. This is given by

$$\Delta V_{V,\tau} = \Delta V_{V,\infty,\tau} + \Delta V_{V,\omega,\tau'} \tag{26}$$

The incremental mass of vapor produced within the system can then be approximated as

$$\Delta m_{V,P,\tau} = \rho_{V,\tau}\Delta V_{V,\tau} \tag{27}$$

The net change in the mass of the vapor phase within the system is then

$$\Delta m_{V,\tau} = \Delta m_{V,P,\tau} + \Delta m_{V,x,\tau} \tag{28}$$

This net change in the mass of the vapor within the system (28), where the second term is negative, is then used in (12).

If the bubbles growing from the surface have not yet reached departure size, their growth is determined by the instantaneous Jakob number (19, 20). However, if the growing bubbles have reached departure size, they separate from the surface. The current internal vessel pressure then determines a new departure bubble diameter from (22). This then determines the current number of vapor bubbles growing from the surface in the next generatoin, (25). This analysis

then applies to the period of blowdown in which the fluid configuration remains to be vapor bubbles growing in a superheated liquid.

2.3 Dispersed Model. This section considers the liquid-vapor mixture when it closely approaches thermodynamic equilibrium conditions. This occurs when the fluid configuration in the system changes from vapor bubbles growing in a superheated liquid toward a dispersed, two-phase mixture. It is assumed that the bubbly to dispersed fluid configuration transitition occurs at a void fraction of approximately 0.3 [32]. The remaining fluid is then assumed to expand isentropically. The pressure and quality at this condition then determines the initial entropy from which the fluid expands in the dispersed regime as given by

$$s_i = s_V(P_i)x_i + s_L(P_i)(1-x_i) \tag{29}$$

For a homogeneous fluid, the quality in (29) when the fluid configuration transition occurs can be determined from

$$x_i = \frac{v_L(P_i)\alpha_i}{v_L(P_i)\alpha_i + v_V(P_i)(1-\alpha_i)} \tag{30}$$

The continuity equation for flow from the system is given in (13) when employing the critical flow rate, G_c. It can then be integrated to determine the instantaneous fluid mass remaining with the system. The two-phase critical flow rate in (13) is determined from the Henry-Fauske critical flow model [33] in this analysis. The instantaneous specific volume of the remaining mixture is determined from $v = V/m$. This specific volume can then be used to determine the homogeneous fluid quality from

$$x = \frac{V/m - v_L(P)}{v_{VL}(P)} \tag{31}$$

The remaining homogeneous mixture is assumed to expand isentropically so

$$s_i = s[P(t)] = s_V(P)x + s_L(1-x) = \text{constant} \tag{32}$$

where the fluid quality in (32) is that from (31). Equations (29), (30), (31), and (32) are then combined to determine the internal vessel pressure history during the homogeneously dispersed regime of blowdown.

3 Discussion

The proposed subcooled blowdown model compares reasonably well with measured internal vessel pressure histories as illustrated in Fig. 1. This particular test was performed in a large-scale, reactor simulator vessel which contained internal structure in the form of a separator plate. Even with this large blowdown vessel and its internal complexities, this simple model still predicted the pressure decay during the subcooled period of this blowdown reasonably well.

In the bubble growth blowdown model, vapor nuclei are assumed to originate at the wall and continue to grow while being limited by thermal conduction to the liquid-vapor interface. The bubbles are then assumed to continue to expand and pressurize the system. *The net effect of the volume production rate within and the volume escape rate from the system is then assumed to be the controlling mechanism of the system pressure.* This only applies while the fluid configuration is vapor bubbles growing in a superheated liquid, i.e., for $\alpha \leq 30$ percent [32]. This proposed model is illustrated and validated in more detail as follows.

The predicted system pressure history in the bubble growth regime of blowdown is nearly independent of the initial liquid superheat for a given system geometry. However, the predicted system pressure is more sensitive to the number of potential nucleation sites per unit surface area (N/S) for a given initial liquid superheat. Decreasing the N/S decreases the predicted pressure history. This effect on the predicted

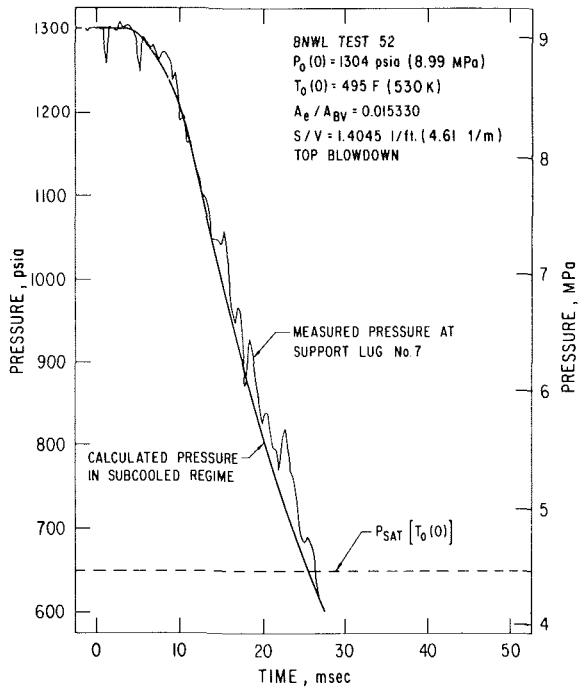

Fig. 1 Comparison of the subcooled blowdown model to the data of BNWL run 52 [25]

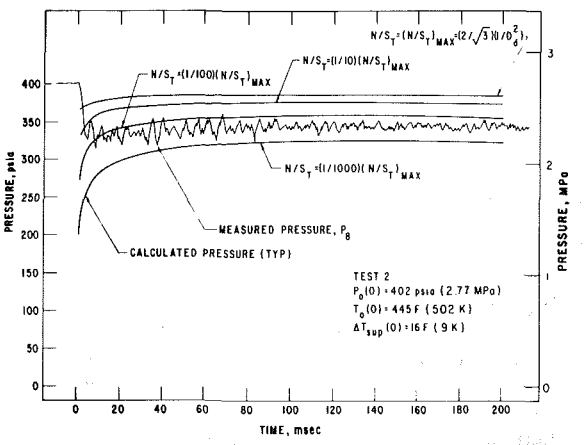

Fig. 2 Comparison of the measured and predicted internal vessel pressure by the bubble growth blowdown model for various *N/S* in test 2

pressure history for test 2 of this study is shown in Fig. 2. A range of three decades of the maximum N/S in Fig. 2 approximately brackets the measured pressure history. However, Fig. 2 illustrates that 1 percent of the maximum N/S best predicts the measured system pressure history.

The vapor volume within the system during the decompression is given by

$$V_V = V_T - mv_L \tag{33}$$

where m is the measured remaining mass inside the vessel. The predicted vapor volume within the system for 1 percent of the maximum N/S compared well with the inferred vapor volume from (33). Thus, *the vapor volume producing mechanism during the early period of the decompression appears to be thermally dominated bubble growth in a superheated liquid.*

The predicted pressure and void fraction histories in the vessel in test 2 for 1 percent of the maximum N/S are shown in Fig. 3. Since this analysis only considers bubble growth in a superheated liquid, it applies only during the period this fluid

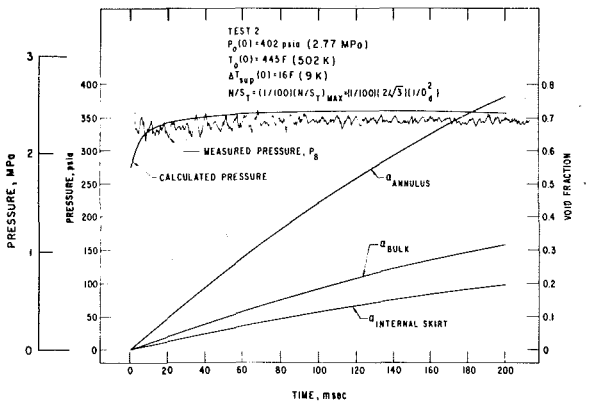

Fig. 3 Comparison of the measured and calculated internal vessel pressure by the bubble growth blowdown model in test 2

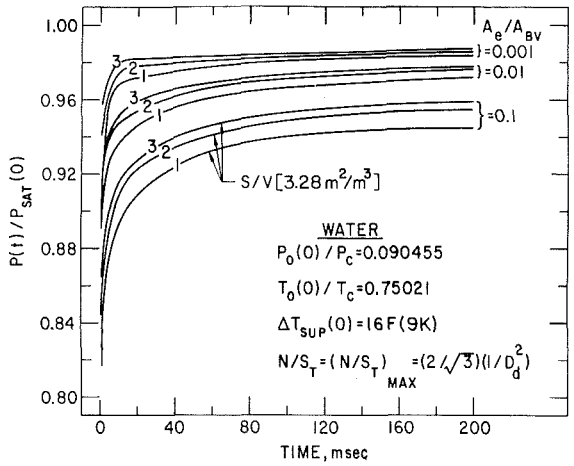

Fig. 4 Prediction of the internal vessel pressure history during the early stage of decompression by the proposed bubble growth blowdown model

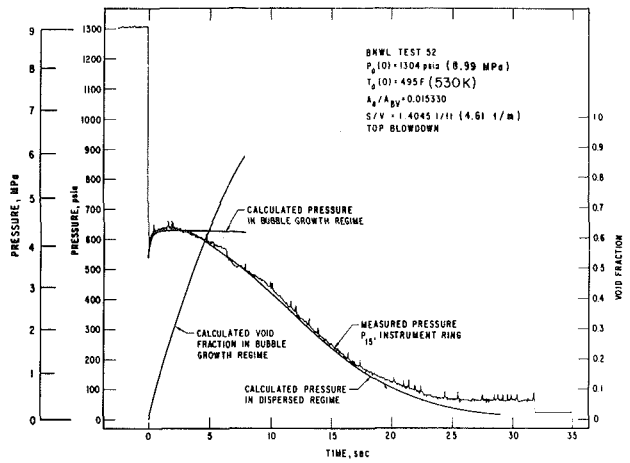

Fig. 5 Comparison of the dispersed regime blowdown model prediction to the measured pressure history of BNWL run 52 [25]

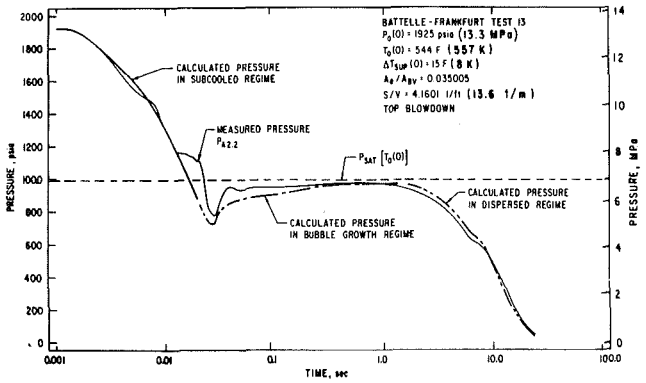

Fig. 6 Comparison of the subcooled, bubble growth, and dispersed blowdown models to the measured pressure in the Battelle-Frankfurt run 13 [26]

configuration exists during the decompression. The maximum void fraction in a bubbly fluid configuration without bubble coalescence is about 70 percent. However, in practice the bubbly fluid configuration is not sustained beyond a void fraction of approximately 30–40 percent [32]. Hence, the predictions in Fig. 3 are applicable primarily in the range of the void fraction in the downcomer annulus from zero to about 30 percent. These predictions compare well with the measured internal vessel pressure histories in this experiment. The void fraction in the downcomer annulus is used in determining the mass flow rates of the liquid and vapor phases escaping from the system. It is the best indicator of a flow regime transition in this region of the system.

The pressure during the bubble growth period of decompression is dependent upon the internal surface area and size of the exit from the system. The system pressure is greater for reduced area ratios (A_e/A_{BV}) for a given ratio of internal solid surface area per unit volume (S/V) as shown in Fig. 4. The volume of the vessel employed in this study was used for illustration. The instantaneous system pressure is also greater for increased S/V at a given area ratio. As illustrated in Fig. 4, the system pressure is more sensitive to S/V as the area ratio is increased, and the pressure also recovers slower as the area ratio is increased and S/V is decreased. The system pressure is typically more sensitive to S/V than it is to the area ratio.

This bubble growth analysis can be applied to each sector within a system during depressurization. Once the bubbly to dispersed fluid configuration transition occurs, the vaporization of superheated liquid droplets is the only remaining mechanism to sustain the pressure. This bubble growth blowdown model can also be used to predict the decompression characteristics in an initially nonisothermal system.

The proposed dispersed regime blowdown model is compared to the measured pressure history in the BNWL top blowdown run 52 [25] in Fig. 5. As illustrated, the dispersed model prediction compares well with the measured pressure history. This is particularly noteworthy considering that this model assumes a completely dispersed fluid, and this was a top blowdown which influences phase separation during blowdown [34]. Also, this dispersed regime blowdown model is based only on simple thermodynamics, and it pedicts the measurements quite well. This good agreement of model and experiment is also demonstrated in additional comparisons in this study.

The combined pressure history predictions of the three foregoing models are compared to the measured pressure history of Battelle-Frankfurt [26] run 13 in Fig. 6. The comparison is reasonably good even though the predictions deviate somewhat from the measurements at about 25 ms. This is attributed to dissolved gas coming out of solution.

4 Conclusions

The most significant conclusions drawn from the analytical portion of this study are as follows:

1 The subcooled blowdown model reasonably well predicts the early period of decompression when significant amounts

of dissolved, noncondensable gases do not come out of solution.

2 The bubble growth blowdown model predicts the recovering internal vessel pressure history after surface cavity activation when most of the remaining fluid is superheated liquid. This model indicates proper trends, and it also compares well with available data.

3 The recovering internal vessel pressure at the start of blowdown is dependent upon (*a*) the internal vessel surface area, (*b*) the internal vessel volume, (*c*) the exit or break flow area, and (*d*) the flow area within the vessel. Phase separation increases as the exit flow area decreases relative to the internal vessel flow area.

4 The recovering internal vessel pressure history at the start of decompression is more sensitive to S/V than it is to A_x/A_{BV}.

5 As the S/V decreases, the liquid in the vessel remains superheated longer, which promotes the internal vessel pressure to remain nearly constant for a longer period particularly for small A_x/A_{BV}.

6 The proposed dispersed regime blowdown model compares well with available data.

Acknowledgment

The authors acknowledge the financial support for this study from the U.S. Energy Research & Development Administration. This work was performed in the Experimental Modeling Section of the Reactor Analysis & Safety Division of Argonne National Laboratory.

References

1 Sallet, D. W., Hannemann, R. J., and Guhler, M., "An Investigation Into Unsteady Two Phase Depressurization of Vessels Through Orifices and Short Pipes," ASME 78-WA/HT-35, 1978.

2 Hutcherson, M. N., "Contribution to the Theory of the Two Phase Blowdown Phenomenon," ANL-75-82, Argonne National Laboratory, 1975; also, University Microfilms, 76-21951, 1976; and University of Missouri, Mechanical Engineering Department (Ph.D. dissertation) Columbia, Mo. 1975.

3 Edwards, A. R., and O'Brien, T. P., "Studies of Phenomena Connected With the Depressurization of Water Reactors," *Journal of Brit. Nucl. Energy Soc.*, Vol. 9, No. 2, April 1970, pp. 125–135.

4 Tanger, G. E., Vachon, R. I., and Pollard, R. B., "Pool Boiling Response to Pressure Decay," *Proc. Third Intl. Heat Transfer Conf.*, Vol. 4, 1966, pp. 38–43.

5 Brown, E. A., "Explosive Decompression of Water," *Proceedings Heat Transfer and Fluid Mechanics Inst.*, Stanford, Calif., June 15–17, 1960, pp. 135–146.

6 Hutcherson, M. N., Henry, R. E., and Wollersheim, D. E., "Two-Phase Vessel Blowdown of an Initially Saturated Liquid—Part 1: Experimental," ASME JOURNAL OF HEAT TRANSFER, Vol. 105, No. 4, pp. 687–693.

7 Winters, W. S., and Merte, H., "Experiment and Nonequilibrium Analysis of Pipe Blowdown," *Nucl. Sci. and Eng.*, Vol. 69, 1979, pp. 411–429.

8 Edwards, A. R., and Jones, C., "An Analysis of Phase IIA Blowdown Tests—the Discharge of High Enthalpy Water from a Simple Vessel into a Containment Volume," SRD-R-27, Safety and Reliability Directorate, United Kingdom Atomic Energy Authority, Warrington, Lancashire, England, 1974.

9 Leslie, D. C., "The Development of Flashing Flow from Existing Nucleation Sites," AEEW-R505, United Kingdom Atomic Energy Authority, Reactor Group, Winfrith, Dorchester, Dorset, England, 1966.

10 Hunt, D. L., "The Effect of Delayed Bubble Growth on the Depressurization of Vessels Containing High Temperature Water," Report AHSB(S)R189, United Kingdom Atomic Energy Authority, Nov. 1970.

11 Alamgir, M. D., Kan, C. Y., and Lienhard, J. H., "An Experimental Study of the Rapid Depressurization of Hot-Water," ASME JOURNAL OF HEAT TRANSFER, Vol. 102, No. 5, 1981.

12 Rasmussen, J., Rasmussen, L., Malnes, D., Imset, O., "Simulation of Blowdown from Pressure Vessels Based on Nonisothermal Equilibrium Effects. Comparison with Experimental Data," European Two Phase Flow Group Mtg., Harwell, England, June 1974.

13 Moore, K. V., and Rettig, W. H., "RELAP4-A Computer Program for Transient Thermal Hydraulic Analysis," ANCR-1137 Rev. 1, Aerojet Nucl. Co., Mar. 1975.

14 Katsma, K. R., *et al.*, "RELAP4/Mod5, A Computer Program for Transient Thermal Hydraulic Analysis of Nuclear Reactor and Related Systems," ANCR-NUREG 1335, Aerojet Nucl. Co., Sept. 1976.

15 Moore, K. V., et al., "RETRAN—A Program for One-Dimensional Transient Thermal Hydraulic Analysis of Complex Fluid Flow Systems," EPRI-NP-408, Electric Power Research Institute, Jan. 1977.

16 Gido, R. G., Grimes, C. I., Lawton, R. G., and Kudrick, J. A., "COMPARE—A Computer Program for the Transient Calculation of a System of Volumes Connected by Flowing Vents," LA-NUREG-6488-MS, also NRC-4, Los Alamos Laboratory, Sept. 1976.

17 Wheat, L. L., Wagner, R. J., Neiderauer, G. F., and Obernchain, C. G., "CONTEMPT-LT, A Computer Program for Predicting Containment Pressure-Temperature Response to a Loss of Coolant Accident," ANCR-1219, Aerojet Nucl. Co., June 1975.

18 Broadus, C. R., James, S. W., Lee, W. H., Lime, J. F., and Pate, R. A., "BEACON/Mod 2—A Program for Analyzing the Flow of Mixed Air, Steam, and Water in a Containment System," CDAP-TR-002, EGG, Dec. 1977.

19 Hoppner, G., "Experimental Study of Phenomena Affecting the Loss of Coolant Accident," Ph.D. thesis, University of California at Berkeley 1971.

20 Vigil, J. C., and Pryor, R. J., "Transient Reactor Analysis Code (TRAC) Development and Assessment," *Journal of Nucl. Safety*, Vol. 21, No. 2, Mar.-Apr. 1980.

21 Alder, R. S., Feldman, E. M., and Pinson, P. A., "Experimental Data Report for 1-1/2 Loop Semiscale System Isothermal Test 1011," ANCR-1146, Aerojet Nucl. Co., Mar. 1974.

22 Zender, S. N., Crapo, H. S., Jensen, M. F., Sackett, K. R., "Experimental Data Report for Semiscale Mod-1, Test S-01-1," ANCR-1198, Aerojet Nucl. Co., Apr. 1975.

23 Hall, D. G., "A Study of Critical Flow Prediction for Semiscale Mod-1 Loss of Coolant Accident Experiments," TREE-NUREG-1006, USNRC, Dec. 1976.

24 Prassinas, P. G., Galvsha, B. M., Jarrell, D. B., "Experimental Data Report for LOFT Nonnuclear Small Break Experiment L3-0," NUREG/CR-0959, TREE-1390, EGG Idaho, Aug. 1979.

25 Allemann, R. T., McElfresh, A. J., Neuls, A. S., Townsend, W. C., Wilburn, N. P., and Witherspoon, M. E., "Coolant Blowdown Studies of a Reactor Simulator Vessel Containing a Perforated Sieve Plate Separator," BNWL-1463, Battelle Northwest Lab., Richland, Wash., Feb. 1971.

26 Kanzleiter, T., Koehn, J., Sauberlich, C., Stein, K., and Zimmermann, M., "Untersuchung der Vorgange bei der Druckentlastung Wassergekuhlter Reaktoren," 8. Bericht, Band I, Battelle Institut, Germany, July 1971.

27 Hugie, H., Yamanauchi, A., Sagawa, N., Ogasawara, H., and Tagami, T., "Studies for Safety Analyses of Loss of Coolant Accidents in Light Water Reactors," *J. Japan Soc. Mech. Eng.*, Vol. 69, (571), Aug. 1966, p. 1068.

28 Ericsen, L., Gros Daillon, L., Hall, D., Kilpi, K., Ravnsbova, J., Sandervag, O., and Vidarsson, J., "The Marviken Full Scale Critical Flow Tests: Interim Report; Results from Tests 1-7," Marviken Power Station, Sweden.

29 Henry, R. E., "Two-Phase Critical Discharge of Initially Saturated and Subcooled Liquid," *Nucl. Sci. Eng.*, Vol. 41, 1970, p. 336.

30 Cole, R., and Rohsenow, W. M., "Correlation of Bubble Departure Diameters for Boiling of Saturated Liquids," *Chem. Eng. Prog. Sym. Series*, AIChE, Vol. 65, 1969, p. 92.

31 White, H. J., "International Representation of the Surface Tension of Water Substance," Office of Std. Ref. Data, NBS, Washington, D. C., Dec. 1976.

32 Radovcich, N. A., and Moissis, R., "The Transition from Two-Phase Bubble Flow to Slug Flow," MIT Report 7-7673-22, 1962.

33 Henry, R. E., and Fauske, H. K., "The Two-Phase Critical Flow of One Component Mixtures in Nozzles, Orifices, and Short Tubes," ASME JOURNAL OF HEAT TRANSFER, Vol. 93, No. 2, May 1971, p. 179.

34 Grolmes, M. A., and Fauske, H. K., "An Evaluation of Incomplete Phase Separation in Freon Vented Depressurization Experiments," 3rd Multiphase Flow and Heat Transfer Symposium, Miami, Fla., Apr. 18–20, 1983.

A. G. Ostrogorsky[1]
Rensselaer Polytechnic Institute,
Troy, N.Y. 12181

R. R. Gay
NUS Corporation,
Menlo Park, Calif. 94025
Assoc. Mem. ASME

R. T. Lahey, Jr.
Rensselaer Polytechnic Institute,
Troy, NY, 12181,
Fellow ASME

The Prediction of Pressure Drop and CCFL Breakdown in Countercurrent Two-Phase Flow

A steady-state analytical model has been developed to predict channel pressure drop as a function of inlet vapor flow rate and applied heat flux during conditions of countercurrent two-phase flow. The interfacial constitutive relations utilized are flow structure dependent and allow for the existence of either smooth or wavy liquid films. A computer code was developed to solve the analytical model. Predictions of Δp versus vapor flow rate were found to agree favorably with experimental data from adiabatic, air/water systems. In addition, the model was used to predict countercurrent flow conditions in heated channels characteristic of a BWR/4 nuclear reactor fuel assembly.

Introduction

Countercurrent flow (CCF) in vertical channels is a special case of annular flow. The maximum flow rates of the gas and liquid film are not independent, but can be adequately correlated. Following Wallis [1] it is convenient to express the velocities of the two-phases in terms of the following dimensionless groups

$$j_g^* = j_g \rho_g^{1/2} [gD(\rho_f - \rho_g)]^{-1/2} \quad (1)$$

$$j_f^* = j_f \rho_f^{1/2} [gD(\rho_f - \rho_g)]^{-1/2} \quad (2)$$

Wallis [1] found that for countercurrent flow limited (CCFL) conditions these dimensionless groups were related by

$$j_g^{*1/2} + m j_f^{*1/2} = C_1 \quad (3)$$

Equation (3) is known to be in good agreement with many data taken in tubes, in which the parameter, D, in equations (1) and (2) is the inside diameter of the tube.

For geometries typical of Boiling Water Reactor (BWR) fuel rod bundles, the choice of the characteristic length, D, is more complex. In this case the so-called natural characteristic length, $D = (\sigma/g(\rho_f - \rho_g))^{1/2}$ was used to obtain a modified Kutateladze correlation of the form [2].

$$(K_g)^{1/2} + m(K_f)^{1/2} = C \quad (4)$$

where

$$K_g = j_g [\rho_g^2 / g(\rho_f - \rho_g)]^{1/4} \quad (5)$$

$$K_f = j_f [\rho_f^2 / g(\rho_f - \rho_g)]^{1/4} \quad (6)$$

The parameter, K_k, is called the Kutateladze number of phase-k. A CCFL condition occurs when the flow rate of gas exceeds some critical value which causes liquid hold-up. The limiting value of vapor flow rate for which compete hold-up occurs at the exit (i.e., no liquid flow into the top of the channel) can be obtained from equations (3), or (4), by setting $j_f = 0$. CCFL breakdown occurs when liquid is first able to enter the flow channel after a period of zero liquid flow.

Countercurrent Flow Structure. The possible flow structures for both adiabatic and diabatic countercurrent flow are illustrated in Figs. 1 and 2, respectively.

Adiabatic Flow. It is assumed that in adiabatic flow there is no significant phasic mass interchange between the liquid and vapor.

- Region 1 is a liquid falling film type regime. The vapor/liquid interface is smooth. As j_g^* increases, j_f^* slowly decreases. The liquid film thickness decreases, thus the liquid fraction decreases also.
- Region 2 forms when $j_g^* \simeq j_{g,\text{lim}}^*$. It is a combination of a smooth film (Region 1) and wavy film (Region 3). For adiabatic flows, the rough interface first forms at the lower part of the tube.
- Region 3 is a wavy film flow. The liquid fraction, $(1-\alpha)$, is high, j_f^* is very low, and j_g^* is greater than $j_{g,\text{lim}}^*$.
- Region 4 is wavy film flow with $j_{f,\text{in}}^* = 0$. A hanging film is shown, in which part of the channel is wetted by a wavy film and part is dry. As j_g^* increases from $j_{g,\text{crit}}^*$ to $j_{g,\text{dry}}^*$, the liquid film thickness decreases so that the interface becomes more stable (i.e., less wavy). In addition, the position of the hanging film recedes.
- Region 5 is a single-phase flow of vapor, (i.e, there is no liquid in the channel).

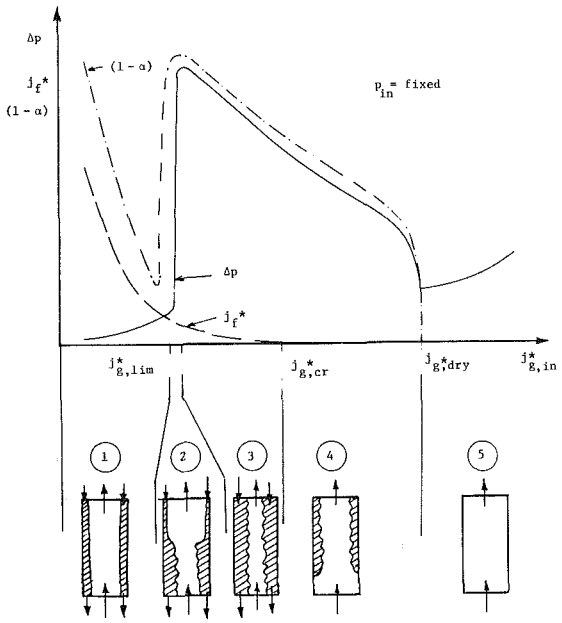

Fig. 1 Variation of liquid velocity, liquid fraction and pressure drop with inlet vapor velocity in an adiabatic tube

Diabatic Flow. The major difference between adiabatic and diabatic flow is that there can be mass interchange between the two phases causing both j_v and j_f to vary in the axial direction. As shown schematically in Fig. 2, a region having $j_{f,\text{in}}^* = 0$ and $\alpha < 1.0$ cannot exist (i.e., when there is no liquid inflow, all the liquid in the heated channel evaporates). It should be noted that significant values of the *exit* (rather than inlet) vapor volumetric flux are plotted on the abcissa of Fig. 2. This is valid if the system geometry, heat flux (q'') and inlet

[1] Presently Research Assistant, Heat Transfer Laboratory, Mechanical Engineering Department, Massachusetts Institute of Technology, Cambridge, Mass. 02139.

Contributed by the Heat Transfer Division for publication in the JOURNAL OF HEAT TRANSFER. Manuscript received by the Heat Transfer Division April 19, 1982.

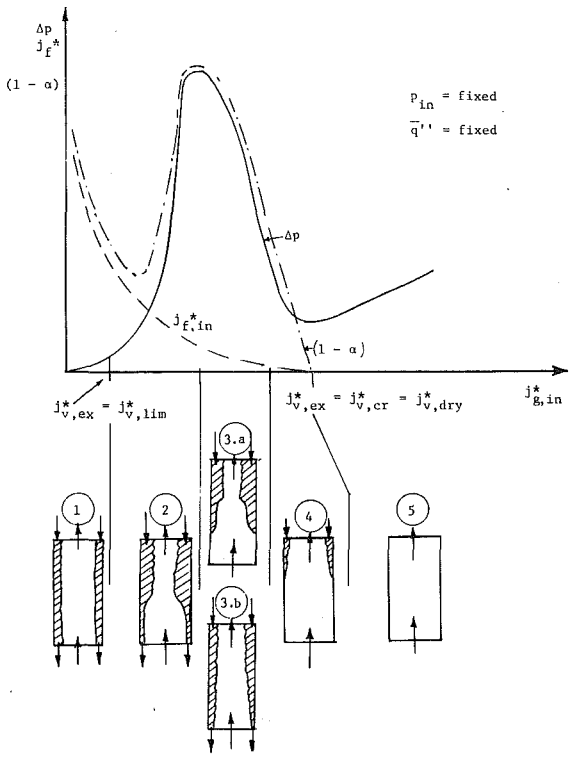

Fig. 2 Variation of liquid velocity, liquid fraction and pressure drop with inlet vapor velocity in a diabatic tube

pressure (p_{in}) are fixed, since for this case there is a unique relationship between $j_{v,ex}^*$ and $j_{g,in}^*$.

- Region 1 has the same characteristics as for adiabatic flow.
- Region 2 exists over a larger range of $j_{g,in}^*$ than for adiabatic flow, because the maximum vapor velocity is at the top. Thus, the wavy film structure starts at the top of the tube, and as $j_{g,in}^*$ increases, the discontinuity between the smooth and wavy regions moves from the top to the bottom of the tube.
- Region 3(a) is for a situation in which dryout of the liquid film has occurred, so the lower part of the tube is dry.
- Region 3(b) is possible for short tubes and/or low heat flux. The inlet, j_v^*, is greater than $j_{v,lim}^*$; thus, the entire interface is rough but dryout of the liquid film has not occurred.
- Region 4 is the same as for a hanging film case in adiabatic flow. Both $(1-\alpha)$ and j_f^* approach zero at the same point, $j_{v,crit}^*$.
- Region 5 is a region in which there is no liquid in the heated channel, only superheated vapor.

It can be noted that the shape of both Δp versus j_g^* curves is similar to a boiling curve [3]. Indeed, the $j_{v,dry}^*$ point plays a role similar to the rewetting temperature. That is, although some hysteresis may occur [3], it is essentially the boundary for the breakdown of CCFL conditions in a Δp-controlled system.

Flow Structure Transitions. Between cases 4 and 5, shown in Fig. 1, there is a steep pressure drop decrease which occurs for adiabatic countercurrent flow. The value of j_g^*, at which the liquid film can no longer be present in a tube, can be derived from a force balance on the liquid film. Defining F_i as the interfacial shear force and F_{gr} as the gravitational force on the liquid, and neglecting the wall shear (since $j_f = 0$), a momentum analysis yields

$$F_i - F_{gr} = 0 \tag{7}$$

where

$$F_i = \tau_i A_i = \frac{f_i}{2}\frac{j_g^2}{\alpha^2} D\sqrt{\alpha}\,\pi L \rho_g \tag{8}$$

$$F_{gr} = D^2(1-\alpha)\frac{\pi}{4} L(\rho_f - \rho_g)g \tag{9}$$

F_i and F_{gr} are both functions of void fraction, but F_i is also a

Nomenclature

A = flow area, m^2
A_{x-s} = flow channel cross-sectional area, m^2
C_P = heat capacity, J/m^3-K
D = diameter, m
D_H = $4A_{x-s}/P_f$ = hydraulic diameter, m
D_{rod} = fuel rod outside diameter
F = force, N
f = friction factor
G = mass flux, kg/m^2-s
H = heat transfer coefficient, W/m^2-K
h = specific enthalpy, J/kg
j = $j_g + j_f$ = volumetric flux (homogeneous velocity) of two-phase mixture, m/s
j_f = volumetric flux of liquid phase, m/s
j_g = volumetric flux of gas or saturated vapor, m/s
j_v = volumetric flux of superheated vapor, m/s
K_{exp} = expansion pressure loss coefficient
K_{cont} = contraction loss coefficient
L = length, m
m = dimensionless constant in flooding correlation
N = number of parallel channels being modeled
P = perimeter, m
p = pressure, N/m^2
Q = volumetric flow rate, m^3/s, or direct heat addition, J/s
q'' = heat flux, W/m^2
Re = Reynolds number
T = temperature, K
v_k = velocity of phase -k, m/s
w = mass flow rate, kg/s
x = flow quality
z = axial position, measured from top (exit) of channel downward, m

Greek

α = void fraction
β = fraction of wall heat transferred directly to the liquid phase
δ = thickness, m
κ = thermal conductivity, W/m-K
λ = nonboiling length, m
μ = viscosity, N-s/m^2
τ = shear stress, N/m^2
σ = surface tension, N/m
σ_j = flow area ratio defined by equation (52)
ξ = distance from bottom of channel, m

Subscripts

B = boiling
CL = centerline
cond = condensation
conv = convection
crit = critical (also where $j_f = 0$)
dry = dry or dryout conditions (also where $\alpha = 1$)
e = thermodynamic equilibrium
ex = exit
F = liquid film
f = saturated liquid
H = heated
i = interfacial
l = subcooled liquid
in = inlet
g = saturated vapor or gas
gr = gravitational
lim = limiting condition
sat = saturation condition
subc = subcooling
sup = superheated
v = vapor
W = wall

Superscripts

* = dimensionless form

function of j_g. Note that as void fraction approaches unity, F_{gr} approaches zero while F_i approaches a finite value, dependent upon j_g. Thus, for high enough values of j_g, F_i is greater than F_{gr}, for any α, and no solution exists to equation (7), implying that the liquid is blown out of the tube. Thus, from equations (7–9)

$$j^*_{g,\text{dry}} = \left[\frac{\alpha^{3/2}_{\max}(1-\alpha_{\max})}{2f_i}\right]^{1/2} \tag{10}$$

where $\alpha_{\max}$ is the void fraction which satisfies the equation, $dj^*_g/d\alpha = 0$. Thus, $\alpha_{\max}$ depends on the void dependence of the interfacial friction factor, f_i. The dimensionless vapor velocity $j^*_{g,\text{dry}}$ is the value above which the liquid is blown out of the tube causing the void fraction to equal unity.

The Analytical Model

The general case of single-component, diabatic, two-phase flow will be considered here. It is assumed that both the vapor and liquid can simultaneously be in direct contact with portions of the heated surface. The total heat addition is therefore partitioned into the wall heat added to the liquid phase and that added to the vapor phase. At the vapor/liquid interface, convective heat transfer or condensation is also allowed to take place.

When there is mass transfer at the vapor/liquid interface (i.e., for diabatic flow), the vapor volumetric flux, j^*_v, increases as we move up the channel, and the liquid volumetric flux, j^*_f, decreases as we move down the channel. Thus, both j^*_v and j^*_f will normally have a maximum at the top of a heated channel. If the liquid inflow is highly subcooled, then the maximum vapor velocity may occur before the exit of the channel (due to condensation of vapor on the liquid film). The liquid volumetric flux, at the axial position where j_v is a maximum, can be determined by using either the Wallis or the modified Kutateladze CCFL correlation. For instance, if the CCFL point is at the top of the channel

$$j^*_{f_{\text{in}}} = [C_1 - (j^*_{v,\text{ex}})^{1/2}]^2\, m^{-2} \tag{11a}$$

or

$$K_{f_{\text{in}}} = [C_2 - (K_{v,\text{ex}})^{1/2}]^2\, m^{-2} \tag{11b}$$

The liquid film dryout and non-dryout conditions are treated separately, because in the case of film dryout, the exit mass flow rate of vapor can be directly determined from

$$w_{v,\text{ex}} = w_{g,\text{in}} + w_{f,\text{in}} \tag{12}$$

Thus, the boundary conditions at the top of the channel can be determined without considering the conditions within the channel. When dryout does not occur, the situation is more complex because some amount of liquid is evaporated, while the rest of the liquid drains into the lower plenum.

Evaluation of Parameters When Dryout Has not Occurred. Let us consider a general case in which we have superheated vapor at the inlet, with multiple surfaces within the heated channel. A liquid film can flow on some surfaces while others are dry. The change in vapor volumetric flux is caused by the change in density of the flowing superheated vapor and by the mass transfer at the interface (evaporation or condensation).

To provide information about the local enthalpy and density of the vapor, the steady-state, vapor energy equation can be used

$$h_v(z) = h_{v,\text{in}}\left[\frac{w_{v,\text{in}}}{w_v(z)}\right] + \frac{1}{w_v(z)}[Q_v(z) - Q_{\text{conv}}(z) - Q_{\text{cond}}(z)] \tag{13}$$

where $Q_v(z)$ is the direct heat addition to the vapor phase

$$Q_v(z) = (1-\beta)P_H\int_0^z q''(z')dz' \quad (0 \le z \le L_H) \tag{14}$$

and β ($0 \le \beta \le 1$) is a constant which defines the fraction of the wall heat going to the liquid phase. Q_{conv} (z), is the (convective) heat transferred from the superheated vapor to the saturated liquid. It is given by

$$Q_{\text{conv}}(z) = P_i\, H_{\text{conv}}\int_0^z (T_v - T_{\text{sat}})dz' \quad (\lambda \le z \le L_H) \tag{15}$$

The Dittus-Boelter correlation was used for H_{conv}, and the expression for the interfacial perimeter (P_i) is based on the geometry under consideration. Finally, Q_{cond} (z) is the vapor phase heat loss due to condensation on the subcooled liquid film's interface

$$Q_{\text{cond}(z)} = P_i\, H_{\text{cond}}\int_0^z (T_v - T_l)dz \quad (0 \le z \le \lambda) \tag{16}$$

where, from [5]

$$H_{\text{cond}} = 0.065\,\frac{\kappa_l \rho_l^{1/2}}{\mu_l}\left[\frac{C_p\mu}{\kappa}\right]_l \tau_i^{1/2} \tag{17}$$

The mass transfer at the interface due to condensation is

$$\Delta w_f(z) = -\Delta w_v(z) = \frac{Q_{\text{cond}}(z)}{h_{fg}} \tag{18}$$

where Q_{cond} is defined by equation (16). Using equation (13) and the appropriate fluid property functions, the vapor density and temperature, as a function of the axial position, can be obtained.

The mass transfer at the interface also depends on the liquid enthalpy, which from an energy balance on the liquid is

$$h_l(z) = h_{l,\text{in}}\left[\frac{w_{f,\text{in}}}{w_{f(z)}}\right] + \frac{1}{w_{f(z)}}[Q_l(z) + Q_{\text{conv}}(z) + Q_{\text{cond}}(z)] \tag{19}$$

where $Q_l(z)$ is the direct heat addition to the liquid.

The position of the boiling boundary (λ) is implicitly defined by

$$\beta P_H\int_0^\lambda q''(z)dz + P_i H_{\text{cond}}\int_0^\lambda (T_v - T_l)dz = h_f[w_{f,\text{in}} + \Delta w_f(\lambda)] - h_{l,\text{in}}\, w_{f,\text{in}} \tag{20}$$

Knowledge of the inlet liquid flow rate, $w_{f,\text{in}}$, is required in order to evaluate the length of the boiling boundary, λ. Fortunately, we know, $w_{f,\text{in}} = j_{f,\text{in}}\rho_l A_{x-s}$, where the liquid volumetric flux at the inlet, $j_{f,\text{in}}$, is determined as a function of the exit vapor volumetric flux, $j_{v,\text{ex}}$, by a CCFL correlation.

Once $j_{f,\text{in}}$ has been found, $j_v(z)$ can be evaluated from the following expression[1]

$$j_v(z) = \begin{cases} j_{v,\text{in}}\,\dfrac{\rho_{v,\text{in}}}{\rho_v(z)} + \dfrac{P_H\beta}{\rho_v(z)h_{fg}A_{x-s}}\displaystyle\int_z^{L_H} q''(z')dz', & (\lambda \le z \le L_H) \\ j_{v,\lambda}\,\dfrac{\rho_v(\lambda)}{\rho_v(z)} - \dfrac{P_i}{\rho_v(z)h_{fg}A_{x-s}}H_{\text{cond}}\displaystyle\int_z^{\lambda}(T_v - T_l)dz', & (0 < z < \lambda) \end{cases} \tag{21}$$

In equation (21) the velocity of the vapor increases because of the boiling process and decreases because of condensation.

Similarly, we can compute j_f (z) as,

[1] Recall the axial position, z, is measured as positive in the downward direction.

$$j_f(z)=\begin{cases} j_{f,\text{in}}+\dfrac{P_i}{\rho_f h_{fg} A_{x-s}} H_{\text{cond}} \displaystyle\int_0^z (T_v - T_l)dz', & (0\le z\le \lambda) \\ j_{f,\lambda}-\dfrac{P_H \beta}{\rho_f h_{fg} A_{x-s}} \displaystyle\int_\lambda^z q''(z')dz', & (\lambda < z < L_H) \end{cases} \tag{22}$$

Evaluation of Parameters When Dryout Has Occurred. When dryout occurs (i.e., $j_{f,\text{ex}} = 0$), the entire amount of liquid that enters the channel from the top is evaporated within the flow channel. Moreover, the single-phase vapor is heated by an amount, Q_v, below the dryout location, thus the vapor will always be superheated below the dryout point.

The liquid flowing into the channel from the upper plenum may be saturated or subcooled, however, since $\rho_l \simeq \rho_f$.

$$j_{f,\text{in}} = w_{f,\text{in}}/\rho_f A_{x-s} \tag{23}$$

For this case, the vapor flow rate at the exit comes directly from equation (12), written in the form

$$j_{v,\text{ex}} = j_{g,\text{in}} \frac{\rho_{g,\text{in}}}{\rho_{v,\text{ex}}} + j_{f,\text{in}} \frac{\rho_f}{\rho_{v,\text{ex}}} \tag{24}$$

Thus, the CCFL correlation, given in equation (3), becomes

$$\left[\left(j^*_{g,\text{in}} \frac{\rho_{g,\text{in}}}{\rho_{v,\text{ex}}} + j^*_{f,\text{in}} \frac{\rho_f}{\rho_{v,\text{ex}}}\right)\right]^{1/2} + m[j^*_{f,\text{in}}]^{1/2} = C_1 \tag{25}$$

In equation (25), $j_{f,\text{in}}$ and $\rho_{v,\text{ex}}$ are unknown, since the vapor is superheated. Once the exit density of the superheated vapor, $\rho_{v,\text{ex}}$, is known, $j_{f,\text{in}}$ can be evaluated from equation (25), which can be substituted into equation (24) to get $j_{v,\text{ex}}$. Let us now consider the evaluation of $\rho_{v,\text{ex}}$.

The mixture energy equation for the heated channel yields

$$w_{v,\text{ex}} h_{v,\text{ex}} - w_{f,\text{in}} h_{l,\text{in}} - w_{g,\text{in}} h_{g,\text{in}} - Q = 0 \tag{26}$$

where, Q is the total channel heat addition. Using equation (12)

$$h_{v,\text{ex}} = \frac{w_{f,\text{in}} h_{l,\text{in}} + w_{v,\text{in}} h_{v,\text{in}} + Q}{[w_{g,\text{in}} + w_{f,\text{in}}]} \tag{27}$$

Since the system pressure is assumed known and the superheated vapor enthalpy can be computed from equation (27), $\rho_{v,\text{ex}}$ can be computed from the state equation. The local liquid volumetric flux can be evaluated by

$$j_f(z)=\begin{cases} j_{f,\text{in}}+\dfrac{P_i}{\rho_f h_{fg} A_{x-s}} H_{\text{cond}} \displaystyle\int_0^z (T_v - T_l)dz', & (0<z<\lambda) \\ j_{f,\lambda}-\dfrac{1}{\rho_f h_{fg} A_{x-s}}\left[P_H \beta \displaystyle\int_\lambda^z q''(z')dz' + P_i H_{\text{conv}} \right. & \\ \left. \times \displaystyle\int_\lambda^z (T_v - T_{\text{sat}})dz'\right], & (\lambda < z < \lambda + L_B) \\ 0, & (z > \lambda + L_B) \end{cases} \tag{28}$$

The parameters L_B (the length over which film evaporation occurs) and λ can be computed from an energy balance

$$\beta P_H \int_0^\lambda q''(z)dz + P_i H_{\text{cond}} \int_0^\lambda (T_v - T_l)dz = h_f(w_{f,\text{in}} + \Delta w_f(\lambda)) - h_{l,\text{in}} w_{f,\text{in}} \tag{29}$$

$$\beta P_H \int_\lambda^{L_B+\lambda} q''(z)dz + P_i H_{\text{conv}} \int_\lambda^{L_B+\lambda} (T_v - T_{\text{sat}})dz = (w_{f,\text{in}} + \Delta w_f(L_B+\lambda)) h_{fg} \tag{30}$$

It is interesting to note that when $j_{g,\text{in}}$ increases, $w_{f,\text{in}}$ decreases, thus the length of the "hanging film", $(L_B + \lambda)$, is less. Conversely, when $j_{g,\text{in}}$ decreases, the length of the "hanging film" will increase.

The change of the volumetric vapor flux with distance can be computed from

$$j_v(z)=\begin{cases} \dfrac{j_{v,\text{ex}}\rho_{v,\text{ex}}}{\rho_v(z)} + \dfrac{H_{\text{cond}} P_i}{h_{fg}\rho_v(z) A_{x-s}} \displaystyle\int_0^z (T_v - T_l)dz', & (0\le z\le\lambda) \\ \dfrac{j_v(\lambda)\rho_v(\lambda)}{\rho_v(z)} - \dfrac{1}{h_{fg}\rho_v(z) A_{x-s}}\left[P_H \beta \displaystyle\int_0^z q''(z')dz' \right. & \\ \left. + P_i H_{\text{conv}} \displaystyle\int_\lambda^z (T_v - T_{\text{sat}})dz'\right], & (\lambda \le z \le L_B + \lambda) \\ \dfrac{j_{g,\text{in}}\rho_{g,\text{in}}}{\rho_v(z)}, & (L_B + \lambda \le z \le L_H) \end{cases} \tag{31}$$

As before, the local density of the superheated vapor can be obtained from a state equation, which has pressure and enthaply as the argument. The static pressure is known, and the local vapor enthalpy can be evaluated by

$$h_v(z)=\begin{cases} h_{v,\text{ex}} \dfrac{w_{v,\text{ex}}}{w_v(z)} - \dfrac{(1-\beta)P_H}{w_v(z)} \displaystyle\int_0^z q''(z)dz' & \\ + \dfrac{H_{\text{cond}} P_i}{w_v(z)} \displaystyle\int_0^z (T_v - T_l)dz, & (0\le z\le\lambda) \\ h_v(\lambda)\dfrac{w_v(\lambda)}{w_v(z)} - \dfrac{(1-\beta)P_H}{w_v(z)} \displaystyle\int_\lambda^z q''(z')dz' & \\ + \dfrac{H_{\text{conv}} P_i}{w_v(z)} \displaystyle\int_\lambda^z (T_v - T_{\text{sat}})dz, & (\lambda \le z \le \lambda + L_B) \\ h_{g,\text{in}} + \dfrac{P_H}{w_{g,\text{in}}} \displaystyle\int_z^L q''(z')dz', & (\lambda + L_B \le z \le L) \end{cases} \tag{32}$$

Equations (23–32) allow one to evaluate all the flow parameters of interest for the case in which a dryout has occurred.

Evaluation of Pressure Drop. For pressure drop calculations, the flow channel was divided up into a number of axial nodes. The most important unknown parameter in each node is the void fraction, since the pressure drop is directly dependent on this parameter. Once the void fraction is evaluated, all other terms in the momentum equations may be easily determined. The model assumes constant j_v and j_f within each axial node for the void fraction and pressure drop calculations. Hence, for diabatic flow, the channel must be divided into a sufficiently large number of axial nodes in order to adequately predict variations of flow properties with distance. The flow regime transition from smooth film to wavy film in a given node was assumed to occur at $j^*_{g,\text{lim}} = 0.202$, in agreement with experimental observations [3].

Evaluation of the Void Fraction in the Smooth Interface Region. In the smooth film region, the interfacial shear stress is negligible compared to the wall shear stress (i.e., $f_w > f_i$, and $\rho_f >> \rho_v$); thus, we can evaluate the void fraction by a falling film analysis [1].

Defining a dimensionless liquid film thickness as

$$\delta^* = \frac{\delta}{D_H}\left[\frac{D_H\sqrt{\rho_f(\rho_f - \rho_v)g D_H}}{\mu_f}\right]^{2/3} \tag{33}$$

The film thickness in laminar flow ($\text{Re} \le 1000$) is [1]

$$\delta^* = 0.909\ \text{Re}^{1/3} \tag{34}$$

where

$$\text{Re} = j_f \frac{\rho_f D_H}{\mu_f} \tag{35}$$

For turbulent flow, the appropriate result is given by [1]

$$\delta^* = 0.115\ \mathrm{Re}^{0.6} \tag{36}$$

This equation is equivalent to

$$\frac{\delta}{D_H} = 0.063\, j_f^{*2/3} \tag{37}$$

Once δ/D_H is known, α can be determined. For example, in a tube ($D_H = D$) equation (37) yields

$$\alpha = D_i^2/D^2 = [1 - 2\delta/D]^2 = [1 - 0.126\, j_f^{*2/3}]^2 \tag{38}$$

Equation (38) can be used to calculate the void fraction in a tube during countercurrent annular flow with a smooth liquid film interface.

The Evaluation of the Void Fraction in the Wavy Interface Region. If we wish to integrate from the bottom of the conduit, it is convenient to define a spatial variable (ξ) which is referenced to the bottom of the channel, $\xi \triangleq L - z$.

For steady-state conditions, a force balance on the vapor core yields

$$-\frac{\partial p}{\partial \xi}\alpha A_{x-s} - \rho_v g \alpha A_{x-s} - \tau_i P_i = \frac{\partial}{\partial \xi}(\rho_v \alpha v_v^2) A_{x-s} \tag{39}$$

where, in general, the interfacial perimeter can be written as

$$P_i = C_1 [A_{x-s}\alpha + N\frac{\pi}{4} D_{\mathrm{rod}}^2]^{1/2} \tag{40}$$

Dividing both sides of equation (39) by αA_{x-s} yields

$$\frac{\partial p}{\partial \xi} + \rho_v g + \frac{\rho_v}{\alpha}\left(v_v^2 \frac{\partial \alpha}{\partial \xi} + \alpha \frac{\partial v_v^2}{\partial \xi}\right) + \frac{\tau_i P_i}{\alpha A_{x-s}} = 0 \tag{41}$$

The steady mixture momentum equation is

$$\frac{\partial p}{\partial \xi} A_{x-s} - g[\rho_v \alpha + \rho_f(1-\alpha)]A_{x-s} + \tau_w P_w = \frac{\partial}{\partial \xi}[\rho_v \alpha v_v^2 - \rho_f(1-\alpha)v_f^2]A_{x-s} \tag{42}$$

Combining equations (41) and (42) yields

$$\frac{\tau_i P_i}{\alpha A_{x-s}} + \frac{\tau_W P_W}{A_{x-s}} = (1-\alpha)(\rho_f - \rho_v)g - \rho_f\left[(1-\alpha)\frac{\partial v_f^2}{\partial \xi} + v_f^2 \frac{\partial(1-\alpha)}{\partial \xi}\right] - \rho_v\left[v_v^2 \frac{\partial \alpha}{\partial \xi} + \alpha \frac{\partial v_v^2}{\partial \xi}\right]\frac{(1-\alpha)}{\alpha} \tag{43}$$

where

$$\tau_i = \frac{f_i \rho_v v_v^2}{2} = f_i \frac{\rho_v j_v^2}{2\alpha^2} \tag{44}$$

$$\tau_W = f_W \frac{\rho_f v_f^2}{2} = f_W \frac{\rho_f j_f^2}{2(1-\alpha)^2} \tag{45}$$

The void fraction may be obtained from equation (43) and a CCFL correlation. A constitutive relation of f_i is also required to complete the system of equations. In our analysis, an empirical correlation proposed by Bharathan [4] was used. This correlation is given by

$$f_i = 0.005 + A(\delta^*)^B \tag{46}$$

where

$$\mathrm{Log}_{10} A = -0.56 + \frac{9.07}{D^*} \tag{47}$$

$$B = 1.63 + \frac{4.74}{D^*} \tag{48}$$

$$\delta^* = \frac{\delta}{\left[\frac{\delta}{(\rho_f - \rho_v)}\right]^{1/2}} \tag{49}$$

$$D^* = \frac{D_H}{\left[\frac{\delta}{(\rho_f - \rho_v)}\right]^{1/2}} \tag{50}$$

Evaluation of Inlet and Exit Pressure Drop. The static pressure change due to sudden contraction at the inlet of conduit, $-j$, can be written as

$$\Delta p_{\mathrm{in}_j} = \left[(1-\sigma_j^2) + K_{\mathrm{cont}_j}\right]\frac{G_j^2}{2\rho_{g,\mathrm{in}}} \tag{51}$$

where G_j is the mass flux in the jth channel, and σ_j is the flow area ratio

$$\sigma_j \triangleq \frac{A_{g_j}}{A_{x-s,\mathrm{plenum/N}}} = \frac{\alpha_j A_{j,\mathrm{channel}}}{A_{x-s,\mathrm{plenum}/N}} \tag{52}$$

and N is the number of parallel channels.

Similarly, the static pressure change due to a sudden expansion at the exit of channel -j is,

$$\Delta p_{\mathrm{ex}} = [(\sigma_j^2 - 1) + K_{\mathrm{exp}}]\frac{G_j^2}{2\rho_{v,\mathrm{ex}}} \tag{53}$$

Discussion of Results

A computer code was written to solve the model just described. As shown in Fig. 3, the predictions of this code for adiabatic, air/water flow are in good agreement with the experimental pressure drop data obtained by Bharathan [4]. Moreover, this figure shows a typical normalized $\{\Delta p^* \triangleq (\Delta p - g\rho_g L)/g(\rho_f - \rho_g)D_H)\}$ adiabatic pressure drop versus j_g^* curve. The j_g^* is constant in the axial direction, and when it becomes greater than $j_{g,\mathrm{lim}}^*$, the interface switches from smooth to wavy. At that point, for a stiff vapor supply, relative maximum values of the film thickness, interfacial friction factor, liquid fraction, and pressure drop are reached. Experimental data were not available to test the code predictions for diabatic flow situations; however, since heat addition does not affect the pressure drop directly, but only changes the vapor and liquid flowrates and fluid properties, one can assume that the pressure drop should be properly predicted.

Steam/water predictions were made of pressure drop, liquid fraction $(1-\alpha)$ and $j_{f,\mathrm{in}}^*$ for conditions typical of a BWR/4 fuel rod bundle (having a 1.4 peak-to-average axial heat flux profile), for 1, 2, 3, and 5 percent decay heat power levels [6]. Figures 4 and 5 illustrate the results for 1 and 5 percent power levels, respectively. Since the parameters j_f^* and $(1-\alpha)$ are not constant in the axial direction, only the values at the exit of the channel are plotted (i.e., $j_{f,\mathrm{in}}^*$ and $1-\alpha_{\mathrm{ex}}$). The transition from a smooth to a wavy interface first takes place at the top of the channel when $j_{v,\mathrm{ex}}$ becomes greater than $j_{v,\mathrm{lim}}^*$. At the same time, the maximum local liquid fraction $(1-\alpha_{\mathrm{ex}})$ is reached. The maximum Δp is reached when the whole interface is wavy ($j_{g,\mathrm{in}}^* = j_{g,\mathrm{lim}}$). In Figs. 4 and 5, one can see that as the rod power level increases, the Δp versus j_g^* curve moves to the left. This result occurs because the higher heat addition implies a higher exit vapor velocity, $j_{v,\mathrm{ex}}^*$, for the same $j_{g,\mathrm{in}}^*$. It is interesting to note that a BWR/4 fuel rod bundle should be completely dry at a 5 percent decay heat power level, independent of the inlet vapor velocity, $j_{g,\mathrm{in}}^*$ (other than zero inlet flow). Any decrease in inlet j_g^* would cause an increase in the exit (superheated) vapor enthalpy and thus a decrease in density, so that the exit velocity, $j_{v,\mathrm{ex}}^*$, is always higher than $j_{g,\mathrm{cr}}^*$.

Figure 6 illustrates a series of runs in which a BWR/4

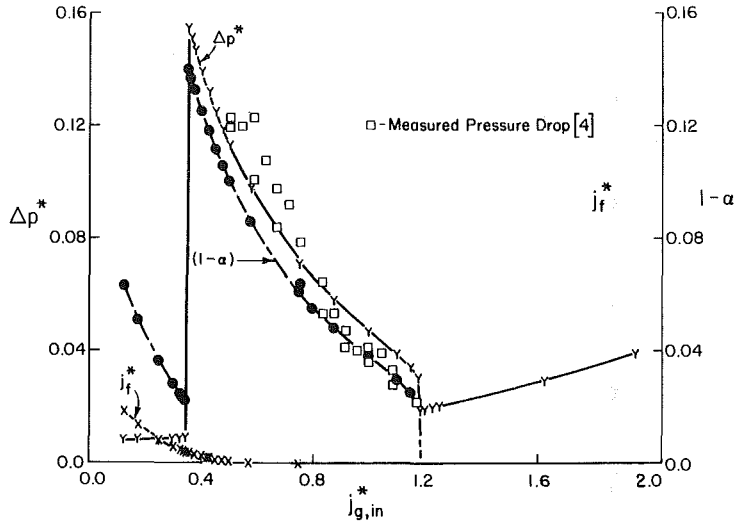

Fig. 3 Typical adiabatic variation of liquid velocity, liquid fraction and pressure drop with vapor velocity (air/water)

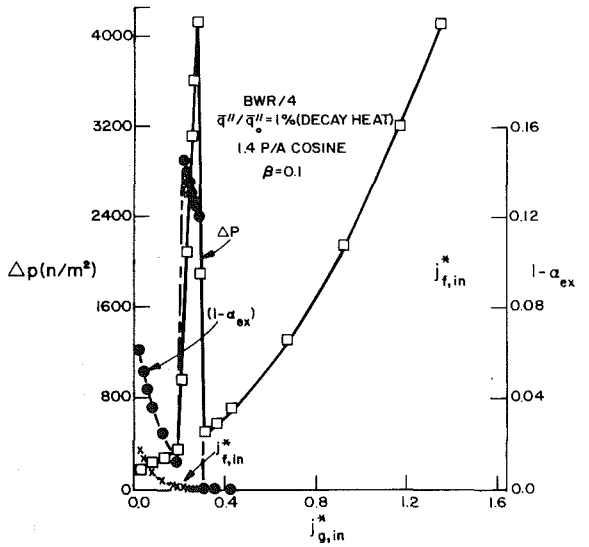

Fig. 4 BWR/4: 1 percent decay heat, 90 percent of wall heat to vapor (β = 0.1)

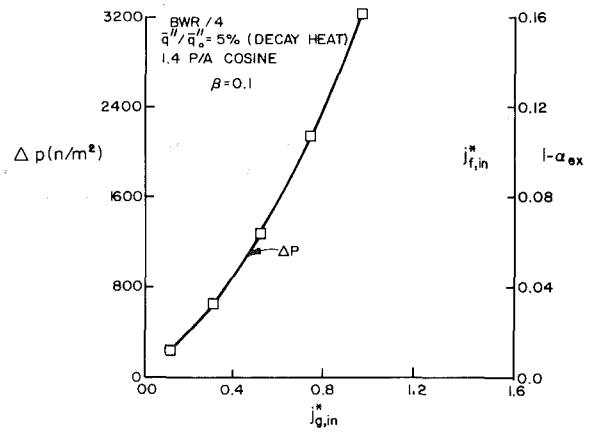

Fig. 5 BWR/4: 5 percent decay heat, 90 percent of wall heat to vapor ($\beta = 0.1$)

bundle at 1 percent decay heat power level was evaluated for several values of β, the fraction of wall heat transferred directly to the liquid. It can be seen as β is increased (i.e., more heat is added directly to the liquid), the transition to a wavy film occurs at a higher value of $j^*_{g,in}$ and the (local) peak

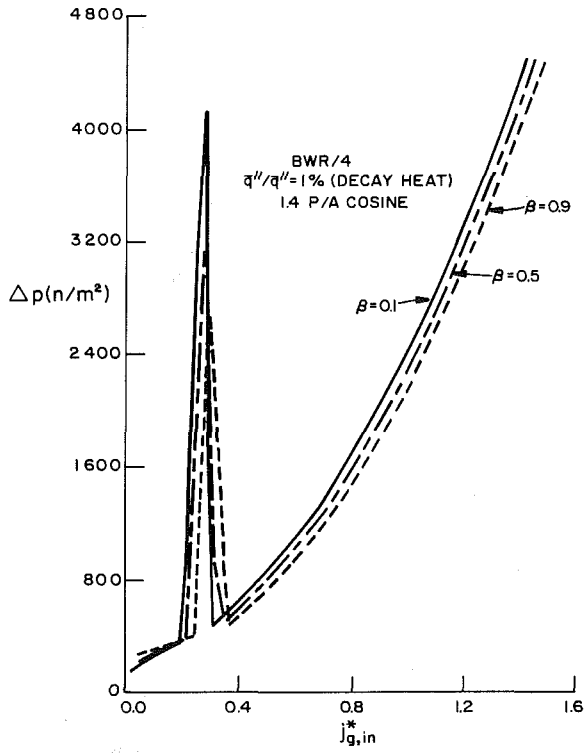

Fig. 6 Comparison of the effect of β on the countercurrent pressure drop in a BWR/4 bundle (1 percent decay heat)

Δp decreases. As discussed previously, this occurs because of the effect of vapor superheat on $j_{v,ex}$.

References

1 Wallis, G. B., *One-Dimensional Two-Phase Flow*, McGraw-Hill, New York, 1969.

2 Sun, K. H., and Fernandez, R. T., "Countercurrent Flow Limitation Correlations for BWR Bundles During LOCA," *Transactions. Am. Nucl. Soc.*, Vol. 27, 1977.

3 Wallis, G. B., Karlin, A. S., Clark, C. R., Bharathan, D., Hagi, Y., Richter, H. J., "Countercurrent Gas-Liquid Flow in Parallel Vertical Tubes," *International Journal of Multiphase Flow*, Vol. 7, 1981.

4 Bharathan, D., "Air-Water Countercurrent Annular Flow," EPRI Report NP-1165, 1979.

5 Collier, J. G., *Convective Boiling and Condensation*, 1972.

6 Ostrogorsky, A. G., Gay, R. R., Lahey, R. T., USNRC Topical Report NRC-04-80-236, 1981.

H. J. Kim
Graduate Student,
Mechanical and Nuclear
Engineering Department.

S. G. Bankoff

Walter P. Murphy Professor,
Chemical Engineering Department and
Mechanical and Nuclear Engineering
Department.
Mem. ASME

Northwestern University,
Evanston, Ill. 60201

Local Heat Transfer Coefficients for Condensation in Stratified Countercurrent Steam-Water Flows

A study of steam condensation in countercurrent stratified flow of steam and subcooled water has been carried out in a rectangular channel inclined 33 deg to the horizontal. The variables in this experiment were the inlet water and steam flow rates, and the inlet water temperature. Condensation heat transfer coefficients were determined as functions of local steam and water flow rates, and the degree of subcooling. Correlations are given for the local Nusselt number for the smooth and for the rough interface regimes, and also for the dimensionless wave amplitude. A turbulence-centered model is also developed. It is shown that better agreement with the data can be obtained if the characteristic scales in the turbulent Nusselt number and Reynolds numbers are related to measured interfacial parameters rather than the bulk flow parameters. The important effect of interfacial shear, missing in previous eddy-transport models, is thus implicitly included.

1 Introduction

In a small-break, loss-of-coolant accident in a pressurized water reactor, with the main pumps inoperative, the primary side of the steam generators go into the reflux condenser mode, before the primary pressure falls substantially below the secondary system pressure. Condensate then drains back through the hot legs toward the reactor. At about the same time, the emergency core coolant water is injected into the hot legs. Hence, a countercurrent stratified flow of steam and subcooled water is set up within the hot leg(s). If the differential pressure between the reactor upper plenum and the hydrostatic leg in the downcomer can be kept sufficiently low, the core will not uncover. This is a consequence most devoutly to be desired, as the Three Mile Island experience showed. The upper plenum pressure is determined by the balance between the rate of production of steam in the overheated core, and the rate of condensation in the steam generators, hot legs, and downcomer. For this reason the study of local condensation heat transfer coefficients in stratified countercurrent flow of steam and cold water is of considerable current interest.

Previous Investigations. There are only two studies of stratified countercurrent steam-water local condensation rates known to the authors. Cook et al. [1] measured condensation rates in a nearly vertical (83 deg) flat-plate geometry. Considerable entrainment of fluidized droplets was observed in the lower portion of the test section at the higher steam and water flow rates. Segev et al. [2] estimated local heat transfer coefficients, by measuring local bulk water temperatures by means of thermocouples set flush into the test section wall, in an inclined countercurrent flow of steam and water. Further discussion and comparison will be given later.

2 Experimental Procedure

The steam-water countercurrent flow contactor is made up of three sections, consisting of an upper and a lower plenum, together with a test section (Fig. 1). The upper and lower plena are designed to insure smooth exit and entry of steam and water. The test section is provided with the appropriate instrumentation to determine the local condensation rates, heat transfer coefficients and interfacial wave amplitude. The test section was completely insulated, and pyrex windows were fitted into both side plates for visual observation.

Liquid entry is through a porous stainless steel plate, with thickness 2.4 mm and porosity 100 microns. The steam entrance region in the lower plenum contains a set of screens and a perforated plate to establish uniform flow. In addition, honeycomb material is inserted to act as turning vanes through the 90 deg bend. The water leaving the test section is drained by gravity through a set of fine mesh screens. The residual water which has not been thus removed is trapped in a small water receptable formed by the side wall and a flow divider, and is drained into a holding tank. The water level in the holding tank is controlled by a magnetic level controller and a solenoid valve. The water circulates through the heat exchanger into the water entrance plenum. The inlet water temperature can be controlled to any desired temperature by means of a heat exchanger. Steam from the building supply is throttled down to a slightly superheated temperaure at atmospheric pressure after removing any condensate in the supply line by means of a steam separator. This arrangement made it possible to have dry, slightly superheated steam join smoothly in parallel flow with the water film at the bottom of the test section. The presence of a uniform velocity profile at the steam entrance to the test section was verified by electrically heated pitot tube measurements. The steam flow rates were measured at six stations: 0.22 m, 0.4 m, 0.58 m, 0.76 m, 0.93 m, and 1.27 m from the steam entrance along the channel centerline. This was accomplished by integrating the

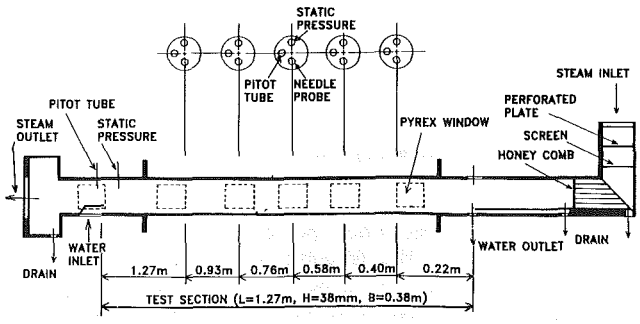

Fig. 1 Sketch of test section

Contributed by the Heat Transfer Division and presented at the ASME Winter Annual Meeting, Phoenix, Arizona, November 14-19, 1982. Manuscript received by the Heat Transfer Division November 5, 1982. Paper No. 82-WA/HT-24.

measured steam velocity profile at each station, assuming two-dimensional flow. The two-dimensionality assumption was verified by pitot tube traverses across the width of the test section, and the integration method was checked by measuring the steam velocity profiles with zero water flow across the height of the test section. Upon comparing the measured inlet steam flow rate with the calculated local steam flow rates, it was found that the deviation was less than ±2 percent. The pitot tubes, which were electrically heated to prevent steam from condensing inside the tubes, were all attached to a common traversing table, allowing them to be positioned at selected elevations in the test section within 0.05 mm. The inlet steam flow rate was calculated from measurements of the differential pressure, absolute pressure, and the thermodynamic state of the incoming steam, using a 50-mm inlet steam venturi. The pressure difference and absolute pressure were measured with diaphragm-type differential pressure transducers. The static pressures at the same locations as the pitot tubes in the test section were measured by wall-mounted pressure taps. Inlet and outlet temperatures of the steam and water were measured by using K-type (Chromel-Alumel) thermocouples connected to a zero point reference junction. The water inlet flow rate was determined by measuring the pressure drop across a 32-mm venturi meter.

The interfacial structure was obtained by traversing micrometer-mounted conductivity probes, consisting of a 0.5-mm stainless steel needle with a sharpened tip, made nonwetting by application of a teflon coating, except at the very tip. The probe was connected to a 12 V d-c circuit, containing a trigger circuit. The probe output was quite close to a series of step functions, so that a trigger voltage of 6 V was adequate to give an accurate local void fraction. Using these probes, the mean water layer thickness and the probability density function for liquid contact with the probe as a function of probe elevation could be measured. This is equivalent to the time-average liquid volume fraction, $1 - \alpha$, as a function of height, where the mean thickness is taken to be at the point where $\alpha = 0.5$. Only the maximum wave amplitude, a, is here reported, corresponding to the elevation difference between 0 and 100 percent probability of liquid contact. The transducer signals were fed directly into a PDP-11/34 computer through a 16-channel A/D converter, with a usual sampling time and sampling frequency of about 10 s and 120 Hz (500 Hz for the conductivity probes), and the reduced data were transferred to magnetic disks for permanent storage.

The data are reported here for a test section angle of inclination of 33 deg to the horizontal at atmospheric pressure. The range of test conditions was restricted for two reasons: (*i*) high water and/or steam flow rates produce surface instabilities, leading to bridging and/or flooding; (*ii*) with cold water and low steam flow rates, complete condensation occurs within the test section, which results in large pressure pulses (water hammer). For these reasons, the experimental ranges in the present geometry were restricted to: liquid Reynolds number 800–5000, and gas Reynolds number 3000–18,000. The reproducibility of the steam flow measurements was checked by duplicate measurements at each station on different days, resulting in agreement within ±2 percent.

3 Typical Data

Typical steam flow rates as a function of axial position are shown in Figs. 2 and 3, together with curves obtained by fitting a fourth-order polynomial to the data.

As expected, the steam condensation rates increase with increasing steam inlet flow rates, increasing water inlet flow rates, and decreasing inlet water temperatures. Little or no condensation occurs in the region between the steam entrance and the first station (0.22 meters downstream of the entrance) in these runs, since the exit water is nearly at the saturation temperature. The R_T values for the 31 tests conducted varied from 0.43 to 1.06, where

$$R_T = \frac{C_{pl}(T_{\text{sat}} - T_{l,\text{in}})W_l}{h_{fg}W_g} \tag{1}$$

For $R_T > 1$, the water has the potential for condensing all the steam within the test section, which can lead to bridging and water hammer.

A typical set of velocity profiles along the channel is shown

Nomenclature

a = maximum wave amplitude
a' = dimensionless wave amplitude defined by equation (9)
B = channel width
C_p = specific heat
f = friction coefficient
$F(\alpha_e)$ = weakly varying function given by [15]
g = acceleration of gravity
H = channel height
h = local heat transfer coefficient
h_{fg} = latent heat of evaporation
k = thermal conductivity
L = length of test section
m = mass flow rate
Nu = Nusselt number, $h\delta/k$
Nu_t = turbulent Nusselt number, $h\lambda_t/k$
n_1, n_2, n_3, n_4 = constants in equation (4)
P = static pressure
Pr = Prandtl number
R_T = parameter defined by equation (1)
Re = Reynolds number, W/μ
Re_t = turbulent Reynolds number, $u_t\lambda_t/\nu$
St_t = turbulent Stanton number
T = temperature
t_{exp} = exposure time
u = velocity
u_t = turbulent velocity scale
u_* = shear velocity
W = mass flow rate per unit width
x = coordinate of steam flow direction
y = coordinate normal to the flow
z = distance from water inlet

Greek Symbols

α = void fraction
α_e = dimensionless exposure time for a single eddy, $t_{\text{exp}}u_t/\lambda_t$
δ = mean water layer thickness
θ = inclination angle
λ_t = turbulent length scale
μ = viscosity
ν = kinematic viscosity
ρ = density
σ = surface tension
τ = shear stress
ϕ = Reynolds momentum flux

Subscripts

a = adiabatic
b = wall surface
g = vapor
i = interface
in = inlet
l = liquid
sat = saturation

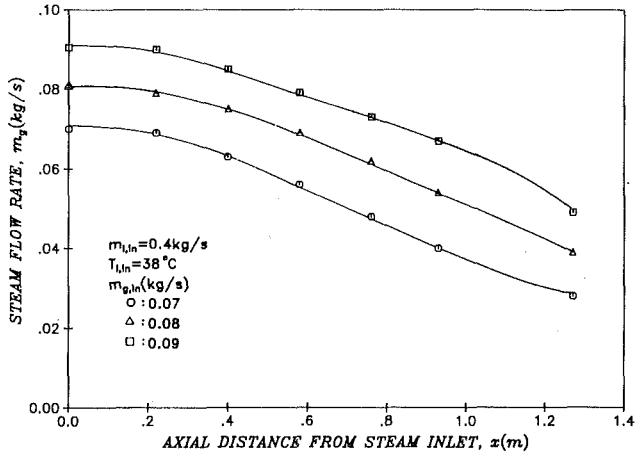

Fig. 2 Axial steam flow rate profile as a function of inlet steam flow rate

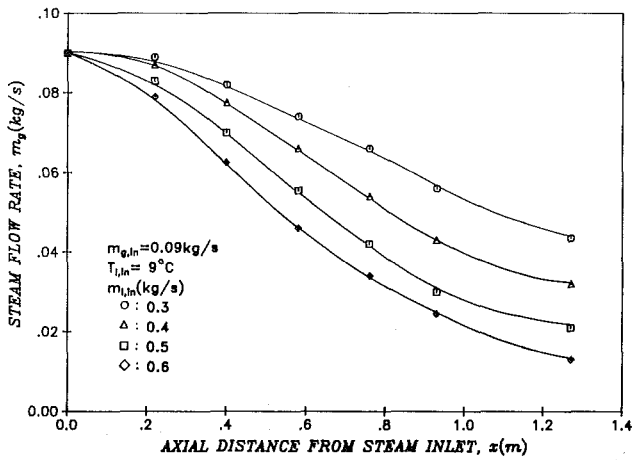

Fig. 3 Axial steam flow rate profile as a function of inlet water flow rate

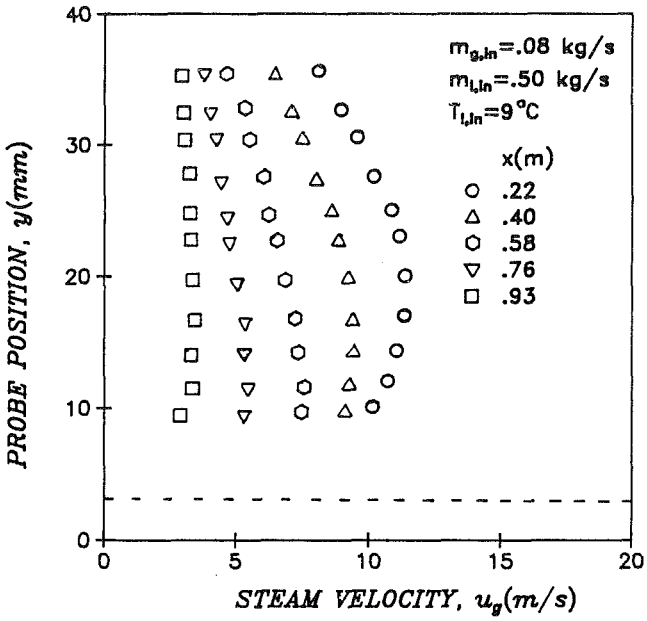

Fig. 4 Steam velocity profiles

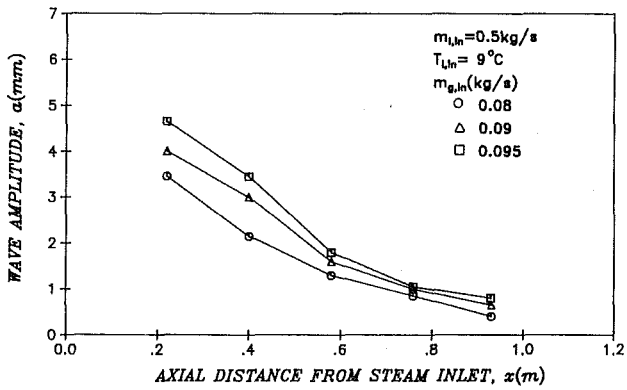

Fig. 5 Wave amplitude measurement for different steam flow rates

in Fig. 4. In cocurrent, noncondensing, gas-liquid flows, it has been shown [3, 4, 5] that for a wavy interface regime, the plane of maximum velocity shifts progressively toward the smooth upper wall as the gas flow is increased. The interfacial region exhibits characteristics similar to turbulent flow over a rough surface. This is not observed in the steam/water experiments of this study. At least for the first three stations from the steam entrance, the steam/water interface can be classified as a rough, pebbly surface, and the steam velocity boundary layer at the interface decreases in thickness with distance from the entrance. Condensation at the steam/water interface accounts for this result. However, the surface is smooth, with small two-dimensional waves, at the last two stations, and the steam velocity profile is so flat that it is difficult to make any judgment as to boundary layer thickness.

Figure 5 shows the distribution of wave amplitudes at the five measuring stations. As expected, the wave amplitude is largest at the steam entrance region, where the interfacial shear stress is largest, and decreases monotonically up the channel. Likewise, upon increasing the inlet steam flow rate, the wave amplitude increases. Complete data will be found in reference [6].

4 Data Correlation and Analysis

4.1 Local Heat Transfer Coefficients. Local heat transfer coefficients were calculated by defining

$$h = \frac{h_{fg}}{T_{\text{sat}} - T_l} \frac{dW_l}{dz} \tag{2}$$

where T_l is the bulk water temperature at the distance z from the water entrance, calculated from an energy balance

$$T_l = T_{l,\text{in}} + \frac{(W_l - W_{l,\text{in}})\{h_{fg} + C_{pl}(T_{\text{sat}} - T_{l,\text{in}})\}}{C_{pl} W_l} \tag{3}$$

dW_l/dz was calculated by differentiating the fourth-order polynomial fitted through the measured steam flow rate data. Typical local heat transfer coefficients, shown in Fig. 6, have the expected trends. The local heat transfer coefficient decreases smoothly from $z = L$ (water exit), where the shear stress and wave amplitudes are maximum, towards a minimum at $z = 0$. Increasing the steam flow rate increases the heat transfer coefficient. In the tests reported here, h varied from about 5 to 25 kw/m^2°C, whereas in a comparable study Segev et al. [2] obtained local heat transfer coefficients ranging from 8 to 28 kw/m^2°C. On the other hand, the data of Cook et al. [1] were higher (5–45 kw/m^2°C). This is to be expected, since the water flow rates were higher (W_l = 2.1 ~ 4.67 kg/m•s versus W_l = 0.78 ~ 1.57 kg/m•s in the present experiment) and the test section was nearly vertical (83 deg inclination versus 33 deg in the present experiments).

The local Nusselt number can be considered to be principally a function of the local gas and liquid Reynolds

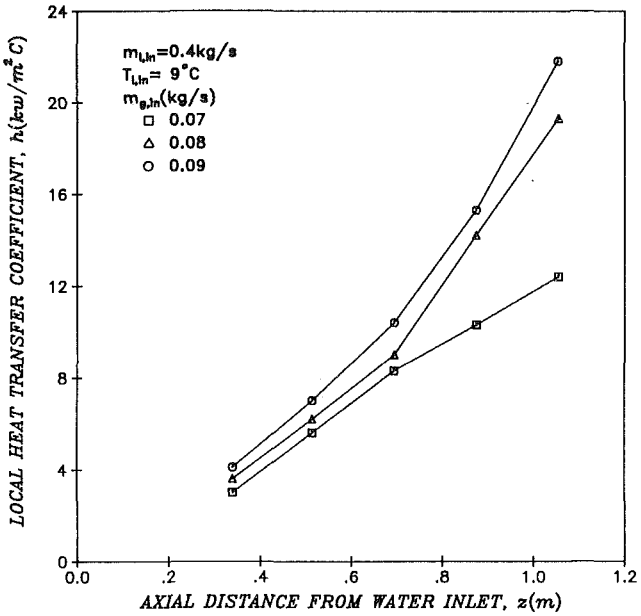

Fig. 6 Axial heat transfer coefficient profile as a function of inlet steam flow rate

numbers, and possibly the liquid Prandtl number, since the thermal resistance lies principally on the liquid side. An empirical power-law correlation would then be of the form

$$\mathrm{Nu} = n_1 \mathrm{Re}_g^{n_2} \mathrm{Re}_l^{n_3} \mathrm{Pr}^{n_4} \tag{4}$$

The data were separated according to wave structure and correlated by least-square fitting, giving the equations

$$\mathrm{Nu} = 0.173\ \mathrm{Re}_g^{0.027} \mathrm{Re}_l^{0.49} \mathrm{Pr}^{0.42} \tag{5}$$

(smooth interface regime)

$$\mathrm{Nu} = 3.43 \times 10^{-10} \mathrm{Re}_g^{2.1} \mathrm{Re}_l^{0.56} \mathrm{Pr}^{1.16} \tag{6}$$

(rough interface regime)

The classification of data according to wave structure was done mainly by visual observations. Most of the data in the smooth interface regime had gas Reynolds numbers less than 6000. It should be recognized, however, that the range of variation of the Prandtl number was at most a factor of three, so that no significance is attached to the variation in Prandtl number exponent in passing from a smooth to a rough interface. The liquid Reynolds number exponent is about 0.5 for both regions, which is in accordance with the small eddy model of Banerjee et al. [7] and Lamont and Scott [8]. The important result is the abrupt increase in gas Reynolds number exponent from a value near zero for smooth interfaces, indicating negligible shear stress effects, to a value greater than two for rough interfaces. The wave structure is thus controlling when three-dimensional pebbly waves, merging eventually into a series of roll waves, are present. This result differs from that of Segev et al. [2], who also classified their condensation data into several groups, corresponding to smooth interface, rough interface, and bypass region (flooding). Since none of our data were in the flooding region, this last region is not of present concern, although a companion paper [9] deals with steam-water flooding. In the smooth interface region the findings are in agreement, in that the influence of the steam Reynolds number is negligible. However, the exponent of the steam Reynolds number is greater than two for the rough interface region in equation (6), whereas the Segev et al. correlation for their region B (corresponding to the appearance of pebbled surface and roll waves), with fixed inlet water temperature of 23°C, was

$$\mathrm{Nu} = 1.16 \times 10^{-3} \mathrm{Re}_g^{0.28} \mathrm{Re}_l^{0.87} \mathrm{Pr}^{0.05} \tag{7}$$

Important differences exist in the two experiments, which may account for this discrepancy. The aspect ratio and height of the test section were 10 and 38 mm, respectively, in the present work, as compared to 3 and 51 mm in the cited reference. There were also some differences in technique, the condensation rate in the Segev work being determined by measuring the water temperature with flush-mounted bottom thermocouples. Also, the inlet water temperatures, angle of inclination and test section lengths differed somewhat. Nevertheless, it appears from the present data that the interfacial wave structure controls the transport mechanism when significant roll waves are present. We therefore suggest that there were significant wave structure differences in the two experiments, which may be attributed, in large part, to the differing aspect ratios and differing steam-water relative velocities at the same values of gas and liquid Reynolds number. The latter point is reinforced by the observation that at similar gas and liquid Reynolds numbers the heat transfer coefficients were 50–90 percent higher in the present experiments. Note, however, that even if a different dimensionless gas velocity, such as the Froude number, were used to take into account the differing aspect ratios, the exponent on the dimensionless gas velocity would remain unchanged.

A correlation for this geometry encompassing both the smooth and rough interface regions can be found by incorporating another dimensionless group, consisting of a dimensionless wave amplitude range, a'. The result is given by

$$\mathrm{Nu} = 9.36 \times 10^{-3} \mathrm{Re}_g^{0.47} \mathrm{Re}_l^{0.4} \mathrm{Pr}^{0.89} a'^{0.82} \tag{8}$$

$$\text{where } a' = \frac{a}{\left\{\dfrac{\sigma}{(\rho_l - \rho_g) g}\right\}^{1/2}} \tag{9}$$

The Nusselt number data all lie within a ±30 percent band from this correlation line. This is not unreasonable, since a single local Nusselt number correlation is here being applied to data from five different axial positions in the countercurrent flow test section. A much smaller spread can be obtained if only the data from a single test station are correlated at any one time. More complete data can be found in [10]. This correlation shows the importance of interfacial wave structure, but requires some predictive capability on wave amplitude before it can be used. Therefore, the measured wave amplitudes were similarly correlated using a least-square fitting, giving the equation

$$a' = 3.03 \times 10^{-8} \mathrm{Re}_g^{1.85} \mathrm{Re}_l^{0.006} \mathrm{Pr}^{-0.23} \tag{10}$$

It is seen that the steam Reynolds number has a powerful effect on the wave amplitudes, whereas that of the liquid Reynolds number is negligible. Upon substituting equation (10) into equation (8), one obtains a similar value for the gas Reynolds number exponent given in equation (6) for the rough interface region. The result can be ascribed to the small variation of the gas Reynolds number for the smooth interface region data, in contrast to the wide variation for the rough interface region.

4.2 Interfacial Shear Stress. The interfacial shear stresses were calculated, using measured steam flow rates, pressure gradients, and water layer thicknesses, and assuming that the flow is steady, incompressible and nonentraining. The temperature of the vapor phase is assumed to be the saturation temperature. The momentum balance for the control volume on the steam side gives

$$\tau_i = -\frac{d}{dx}\int_\delta^H \rho u_g^2 dy + u_i \frac{dw}{dx} - (H-\delta)\frac{\partial P_g}{\partial x} - \rho g \sin\theta (H-\delta) - \tau_b \tag{11}$$

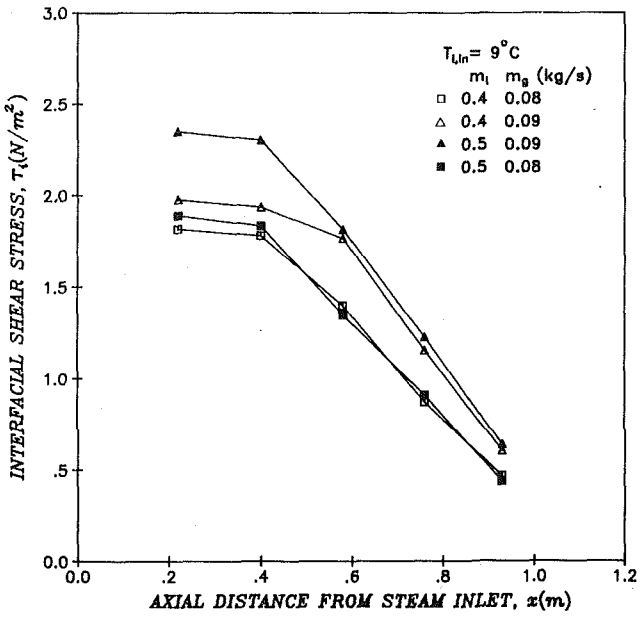

Fig. 7 Axial distribution of interfacial shear stress

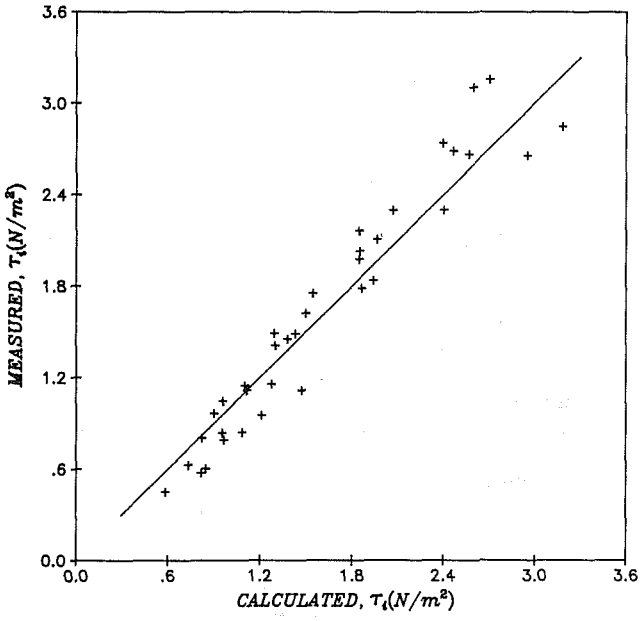

Fig. 8 Comparison of measured interfacial shear stress with the calculated value

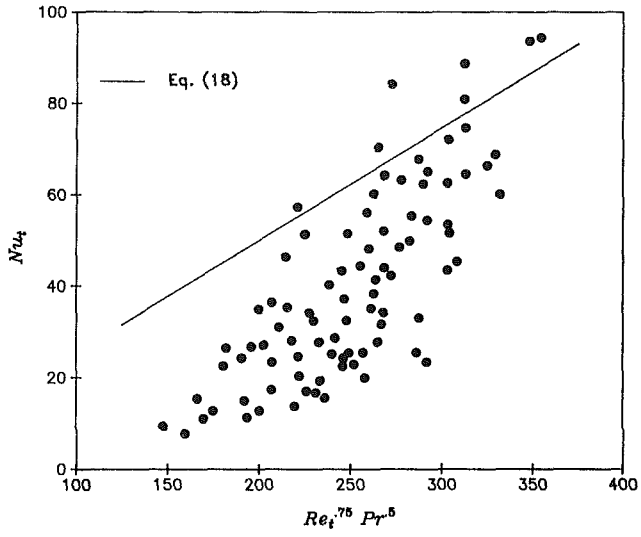

Fig. 9 Comparison with turbulence equation using $u_t = 0.3\bar{u}_l$, $\lambda_t = \delta$

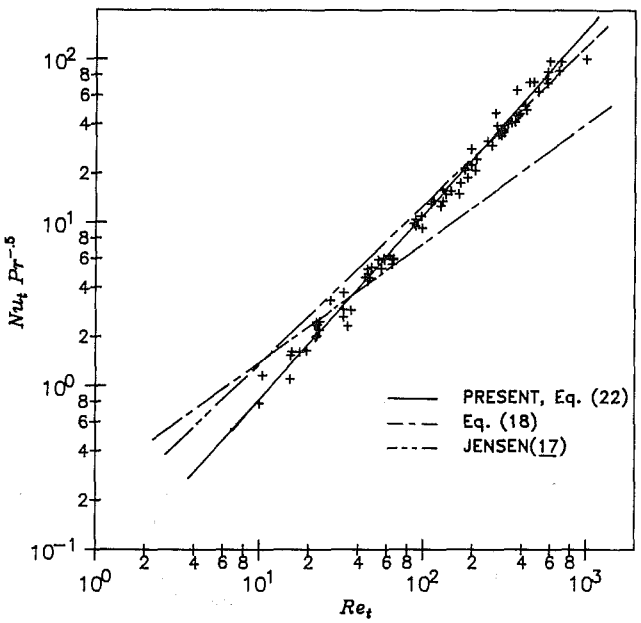

Fig. 10 Comparison with other equations for turbulence-centered model

Hanratty and Engen [3] found, for the fully developed flow of a horizontal, stratified, turbulent gas and liquid, that the velocity profile in the gas phase near the wall was unaffected by the presence of the moving liquid phase. Therefore, the wall shear stress at the gas phase may be calculated from the Blasius equation for the friction factor in turbulent flow

$$f_b = 0.079\ \mathrm{Re}_g^{-1/4} \tag{12}$$

The results, shown in Fig. 7, show that the interfacial shear stress increases with increasing steam and liquid flow rates and decreasing liquid temperature, in a similar fashion as the condensation rate. This suggests that the interfacial shear stress and the condensation rate may be governed by the same mechanism. Linehan [11] proposed a simple relationship for the interfacial shear stress in the presence of mass transfer

$$\frac{f_i}{f_{i,a}} = 1 - \frac{\phi}{f_{i,a}} \tag{13}$$

which is equivalent to

$$\tau_i = \tau_{i,a} - \bar{u}_g \frac{dW_g}{dx} \tag{14}$$

This relationship indicates that the interfacial shear stress in the presence of condensation is simply augmented by an amount equal to the condensation rate times the average vapor velocity, where the interface has been neglected in comparison with the vapor velocity. A more exact expression would thus be

$$\tau_i = \tau_{i,a} - (\bar{u}_g - u_i) \frac{dW_g}{dx} \tag{15}$$

For this turbulent liquid flow with wavy interface, the interface velocity is assumed to be the average liquid velocity. The friction factor, $f_{i,a}$, in the absence of condensation was

calculated from the correlation suggested by Linehan [11], who used Cohen's data [12], despite the fact that they were obtained for cocurrent flow. This is allowable since the adiabatic shear stress was much smaller than the condensation-induced shear stress in the present steam-water flows. This correlation may be written as

$$f_{i,a} = 0.23 \times 10^{-5} \mathrm{Re}_l + 0.0131 \text{ for } \mathrm{Re}_l > 340 \quad (16)$$

where

$$f_{i,a} = \frac{\tau_{i,a}}{\rho_g \bar{u}_g^2/2} \quad (17)$$

The present data are compared with this model (Fig. 8). The results are in good agreement with the values predicted by this modified model, substantiating the assumptions.

4.3 Turbulence-Centered Model. It is interesting to see whether a turbulence-centered model for steam condensation can be developed, which is similar to those which have been presented for absorption of slightly soluble gases at smooth interfaces of cocurrent flows of gases and turbulent liquids. Several turbulent gas absorption models relating the mass transfer coefficient to the local turbulent properties have been suggested for different Reynolds number ranges [8, 13]. Brumfield, et al. [14] and Theofanous et al. [15] presented a synthesis of the large-eddy model [13] (energy-containing motions) and the small-eddy model [8] (energy-dissipating motions). In terms of the analogous dimensionless heat transfer equations [16], the correlation is

$$\mathrm{Nu}_t = 0.25\ \mathrm{Re}_t^{3/4}\mathrm{Pr}^{1/2} \qquad \mathrm{Re}_t > 500 \quad (18)$$

$$= 0.7\, F(\alpha_e)\mathrm{Re}_t^{1/2}\mathrm{Pr}^{1/2} \qquad \mathrm{Re}_t < 500 \quad (19)$$

Evaluation of the model depends on the accuracy with which the turbulent velocity and length scales, u_t and λ_t, can be predicted. For horizontal cocurrent steam-water flow, the scales used in gas absorption [15], $u_t = 0.3\ \bar{u}_l$ and $\lambda_t = \delta$ (water thickness), result in a good fit of the measured h and the value predicted by equation (18) [16]. However, for countercurrent steam-water flow in an inclined channel, the comparison between measured and predicted values reveal large discrepancies, as shown in Fig. 9. Appropriate values are difficult to define for the turbulent intensity, u_t, and turbulent length scale, λ_t, due to the highly agitated steam-water interface and large condensation rates, which affect the interfacial shear stress. This is not considered explicitly in the turbulence equation.

Considering the strong effect of the sheared and disturbed interface on the turbulence properties, the turbulent velocity and length scales may be defined in terms of interfacial parameters as follows

$$u_t = u_* = \sqrt{\tau_i/\rho} \quad (20)$$

$$\lambda_t = a \quad (21)$$

An improved correlation, using these interfacial scales, is shown in Fig. 10, and is expressed as follows

$$\mathrm{Nu}_t = 0.061\ \mathrm{Re}_t^{1.12}\mathrm{Pr}^{0.5} \quad (22)$$

The dependence upon the turbulent Reynolds number has been increased compared to the smooth-interface, eddy-cell models. This is reasonable, however, since the influence of the gas Reynolds number, which is crucial for the rough interface, appears only in the length and velocity scales. This implies, in turn, a larger Reynolds number exponent. The square-root dependency of the Prandtl number is considered to be fortuitous. This correlation is compared in Fig. 10 with the turbulence equation (18) and the Jensen [17] correlation for cocurrent steam-water flow. Linehan [11] suggested that the Stanton number for condensation of steam at the surface of cocurrent-flow water layer was a constant, based upon the hypothesis of constant eddy diffusivity. Jensen [17] argued that the appropriate constant grouping was St $\mathrm{Pr}^{0.5}$, based upon an examination of some gas absorption data, together with his own cocurrent steam-water data. In either case the Nusselt number is then proportional to the Reynolds number. As noted above, the range of Prandtl number in the present steam-water data is too narrow to allow meaningful determination of the Prandtl number exponent, but the Reynolds number exponent is greater than one, as expected. This is because the influence of the steam flow on the interfacial transport and wave structure is greater in countercurrent flow at an inclination of 33 deg than in horizontal cocurrent flow. The increase in Reynolds number exponent for the Linehan model over that for the model of Brumfield et al. can be attributed to the dominant effect of the interfacial condensation on the interfacial shear stress, and hence on the Stanton number. The Brumfield et al. equation was based entirely on data for the absorption of slightly soluble gases, where such an effect would be negligible. Note that the very weak (or zero) dependence of the Stanton number on the Reynolds number implies that the choice of turbulent length scale has little effect. On the other hand, the frictional characteristics come into play in the choice of the velocity scale.

5 Concluding Discussion

Local heat transfer measurements in inclined stratified countercurrent flow of steam and cold water have shown that in all cases the local heat transfer coefficient increases with distance from the water inlet. This coincides with the development of interfacial waves, pointing to the strong influence of turbulence generated by the interfacial waves, which completely dominates the normal growth of the thermal boundary layer in the liquid. Empirical correlations have been given for the heat transfer coefficients in the smooth (capillary waves) and rough (pebbly three-dimensional waves or roll waves) regimes. Measurements of maximum wave amplitude have also been performed, using conductivity probes, and have been also correlated. The powerful effect of the steam Reynolds number in the rough regime, particularly near the steam entrance, is shown in these correlations, and indicates the importance of interfacial shear, as well as form drag, in enhancing the heat transfer. To obtain the interfacial shear, a simple model due to Linehan, with slight modifications, shows good agreement with the data. An alternative approach for the heat transfer coefficient uses turbulence scales, consisting of the wave amplitude and the friction velocity, to formulate the correlation. This approach appears promising, since it employs scales which are local to the interfacial region, but needs further development and testing.

6 Acknowledgment

This work was supported by the U.S. Nuclear Regulatory Commission. Professors R. S. Tankin and M. C. Yuen, and Mr. S. C. Lee are thanked for their helpful cooperation.

References

1 Cook, D., Bankoff, S. G., Tankin, R. S., and Yuen, M. C., "Countercurrent Steam-Water Flow in a Vertical Channel," NUREG/CR-2056, 1981.

2 Segev, A., Flanigan, L. J., Kurth, R. E., and Collier, R. P., "Experimental Study of Countercurrent Steam Condensation," ASME JOURNAL OF HEAT TRANSFER, Vol. 103, 1981, pp. 307-311.

3 Hanratty, T. J., and Engen, J. M., "Interaction Between a Turbulent Air Stream and a Moving Water Surface," *AIChE Journal*, Vol. 3, 1957, pp. 299-304.

4 Ellis, S. R. M., and Gay, B., "The Parallel Flow of Two Fluid Streams: Interfacial Shear and Fluid-Fluid Interaction," *Trans. Instn. Chem. Engrs.*, Vol. 37, 1959, pp. 206–213.

5 Akai, M., Inoue, A., Aoki, S., and Endo, K., "A Cocurrent Stratified Air-Mercury Flow with Wavy Interface," *International Journal of Multiphase Flow*, Vol. 6, 1980, pp. 173–190.

6 Kim, H. J., Ph.D. thesis, Department of Mechanical and Nuclear Engineering, Northwestern University, 1983.

7 Banerjee, S., Scott, D. S., and Rhodes, E., "Mass Transfer to Falling Wavy Liquid Films in Turbulent Flow," *I&EC Fundamentals*, Vol. 7, 1968, pp. 22–27.

8 Lamont, J. C., and Scott, D. S., "An Eddy Cell Model of Mass Transfer into the Surface of a Turbulent Liquid," *AIChE Journal*, Vol. 16, 1970, pp. 513–519.

9 Lee, S. C., and Bankoff, S. G., "Stability of Steam-Water Countercurrent Flow in an Inclined Channel," ASME JOURNAL OF HEAT TRANSFER, Vol. 105, Nov. 1983,

10 Bankoff, S. G., and Kim, H. J., "Countercurrent Steam-Water Flow in a Flat Plate Geometry," Rept. NU-8201B, Chem. Eng. Dept., Northwestern Univ., Evanston, Ill., to appear as NUREG report, Nuclear Reg. Comm., 1982.

11 Linehan, J. H., "The Interaction of Two-Dimensional, Stratified, Turbulent Air-Water and Steam-Water Flows," Ph.D. thesis, Department of Mechanical Engineering, University of Wisconsin, 1968.

12 Cohen, L. S., "Interaction Between Turbulent Air and a Flowing Liquid Film," Ph.D. thesis, Department of Chemistry and Chemical Engineering, University of Illinois, 1964.

13 Fortescue, G. E., and Pearson, J. R. A., "On Gas Absorption Into a Turbulent Liquid," Chemical Engineering Science, Vol. 22, 1967, pp. 1163–1176.

14 Brumfield, L. K., Houze, R. N., and Theofanous, T. G., "Turbulent Mass Transfer at Free Gas-Liquid Interfaces, with Applications to Film Flows," *International Journal of Heat and Mass Transfer*, Vol. 18, 1975, pp. 1077–1081.

15 Theofanous, T. G., Houze, R. N., and Brumfield, L. K., "Turbulent Mass Transfer at Free, Gas-Liquid Interfaces, with Applications to Open-Channel, Bubble and Jet Flows," *International Journal of Heat and Mass Transfer*, Vol. 19, 1976, pp. 613–624.

16 Bankoff, S. G., "Some Condensation Studies Pertinent to LWR Safety," *International Journal of Multiphase Flow*, Vol. 6, 1980, pp. 51–67.

17 Jensen, R. J., "Interphase Transport in Horizontal Stratified Cocurrent Flow," Ph.D. thesis, Department of Mechanical and Nuclear Engineering, Northwestern University, 1981.

S. C. Lee
Graduate Student,
Mechanical and Nuclear
Engineering Department

S. G. Bankoff
Walter P. Murphy Professor,
Chemical Engineering Department and
Mechanical and Nuclear
Engineering Department
Mem. ASME

Northwestern University,
Evanston, Ill. 60201

Stability of Steam-Water Countercurrent Flow in an Inclined Channel: Flooding[1]

Flooding of stratified countercurrent steam-water flow in nearly-horizontal and in inclined flat-plate geometries is investigated. An envelope theory for onset of flooding in inclined stratified flow is developed, which agrees better with the experimental data than other theories. In addition, some basic flow parameters, such as mean film thickness and interfacial friction factor in the roll-wave regime (near-flooding) have been measured. Empirical correlations for these parameters were sought, which are essential in the flooding analysis.

Introduction

During a postulated loss-of-coolant accident (LOCA) in a pressurized-water reactor (PWR), countercurrent flow of steam and cold water may take place either in a vertical tube or in an inclined channel when the emergency core cooling (ECC) water is injected into the reactor vessel. The stability of this flow is a matter of concern, particularly if it limits delivery of water to the hot reactor core.

Two important instabilities have been observed in inclined countercurrent flow of steam and cold water [1]: condensation-induced waterhammer and flooding. Waterhammer will be discussed in detail in a following paper [2]. The onset of flooding (sometimes called "countercurrent flow limitation" (CCFL)) corresponds to the limiting condition where the flow rates of neither the gas nor the liquid phase can be increased further without altering the flow pattern. Various authors have given different definitions of flooding, but the *flooding point* generally refers to the onset of flooding. On the other hand, we may define the *flooding range* as the range from 100 percent to 0 percent downward delivery of the entering liquid. Most small-scale studies of flooding have dealt with vertical annular flow, but stratified flow occurs in a number of applications, such as in the PWR hot leg in a small-break accident. Further, the relative simplicity and flexibility of inclined-channel flooding may lead to important additions to our understanding of the flooding process. This flexibility results from the independent variations of void fraction, aspect ratio and inclination angle which are possible in this mode.

The present study deals with stratified steam-water flow in rectangular ducts at various angles to the horizontal. A flooding analysis based on the envelope of possible operating lines, using hydrodynamic and energy equations for inclined countercurrent flow, is presented and also compared with the data for the onset of flooding. In addition, some key flow parameters, such as mean film thickness and interfacial friction factor, were measured in order to furnish empirical correlations for the flooding analysis.

Experimental System and Procedure

A schematic diagram of the experimental apparatus is shown in Fig. 1. It includes a test section, two water storage tanks, heat exchanger, and two circulating pumps. The test section is a rectangular channel approximately 2.13-m long and 0.38-m wide with adjustable depth. The distance between the water inlet and outlet is 1.27 m. The test section has its own support system which permits any inclination between 0 and 90 deg. Two channel depths (H = 0.076 m and 0.038 m) and three inclination angles (θ = 2.9, 4.5 and 33.5 deg from the horizontal) were employed. Measurements of temperatures, pressure drops, flow rates, and film thicknesses were made. Details on the apparatus and measurements are found elsewhere [1, 3]. A summary of the experimental parameter ranges in the present study is given in Table 1.

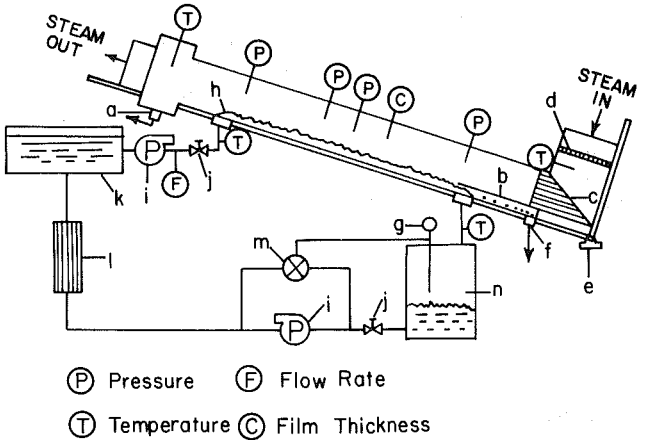

Fig. 1 Schematic diagram of experimental apparatus: (*a*) bypass liquid outlet; (*b*) divider wall; (*c*) honeycomb; (*d*) perforated plate; (*e*) journal bearing; (*f*) auxiliary drain; (*g*) level meter; (*h*) guide vane; (*i*) pump; (*j*) control valve; (*k*) storage tank; (*l*) heat exchanger; (*m*) solenoid valve; (*n*) water holding tank

The data for onset of flooding were obtained by increasing the steam flow rate at a given water flow rate. Most water flow rates under investigation lay in the turbulent region in order to maintain uniform liquid film thicknesses across the width of the channel. The onset of flooding was determined mainly by visual observation, but occasional checks by means of pressure drop measurements were made to assure the reliability of the data.

Measurement of Basic Flow Parameters

It is important to have some understanding of basic flow parameters in countercurrent flow when investigating flooding, partly because some empirical information is essential, and partly because sudden changes in the flow parameters represent a flow regime transition which in many cases can be identified with flooding. Therefore, some experimental results for key parameters will be presented here. These were measured in a nearly horizontal countercurrent flow (H = 0.076 m and θ = 4.5 deg).

Pressure Drop. Pressure drop has always been a good

Contributed by the Heat Transfer Division and presented at the ASME Winter Annual Meeting, Phoenix, Arizona, November 14-19, 1982. Manuscript received by the Heat Transfer Division November 5, 1982. Paper No. 82-WA/HT-6.

Table 1 Summary of experimental conditions for figures and correlations

Measurements	Geometrical conditions H(m)	θ	Experimental condition Liquid flow	Vapor flow	Result	Note
Pressure drop	0.076	4.5	$W_{f,in} = 2.19$ kg/ms	up to the onset of flooding	Fig. 1	
Mean film thickness	0.076	4.5	$600 \le Re_f \le 9600$	no steam flow	eq. (3)	smooth film
	0.076	4.5	$1400 \le Re_f \le 12000$	$23{,}000 < Re_g < Re_g^*$	eq. (5)	three-dimensional wave region
	0.076	4.5	$1800 \le Re_f \le 11000$	$Re_g^* \le Re_g \le 51{,}000$	eq. (6)	roll-wave regime
Interfacial friction factor	0.076	4.5	$2000 \le Re_f \le 12000$	$23{,}000 < Re_g < Re_g^*$	Fig. 5	three-dimensional wave region
	0.076	4.5	$2000 \le Re_f \le 12000$	$Re_g^* \le Re_g \le 51{,}000$	eq. (9)	roll-wave regime
Onset of flooding	0.076	4.5, 2.9			Figs. 6, 7	
	0.038	4.5, 33.5			Fig. 6	

indicator for predicting flow pattern changes, either in adiabatic or in condensing flows. In steam-water, countercurrent flow, the interface becomes more disturbed, due to condensation, than in air-water flow, so that visual observation alone cannot allow an accurate detection of the onset of flooding. Pressure drop measurements were employed, together with visual observations, in order to determine the onset of flooding in the present study.

The vapor phase momentum balance, from equation (A1) leads to

$$\Delta P_g = \rho_g g L \sin\theta + \int_0^L \frac{\tau_{ia} + \tau_{wg}}{(H-\delta)}\, dx - \int_{W_{g,out}}^{W_{g,in}} \frac{W_g\, dW_g}{\rho_g (H-\delta)^2} \qquad (1)$$

(I) (II) (III)

with the expression for the interfacial shear stress for the condensing flow due to Linehan [4]

$$\tau_i = \tau_{ia} + (\tilde{U}_g + U_i)\,(dW_g/dx) \qquad (2)$$

Of these three terms, the gravity term (I) is usually negligible compared to the other two terms. There is an increase in pressure due to the loss of vapor phase momentum by condensation, which monotonically increases to an asymptotic value as the vapor flow rate is increased. Therefore, the pressure drop is at first negative, decreasing in the low steam flow region with increasing steam flow rate because the pressure gain term (III) is dominant in this region. However, when the steam flow approaches the flooding velocity, the frictional loss term (II) begins to rise sharply because of the build-up of roll waves. Thus the pressure drop exhibits a sharp increase near the flooding point, becoming strongly positive. The steam flow rate at the minimum pressure drop corresponds to the point of inception of roll waves on the interface. Typical pressure drops are shown in Fig. 2.

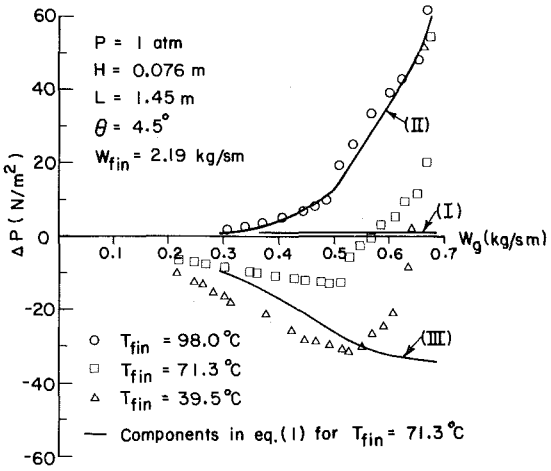

Fig. 2 Pressure drop in steam-water countercurrent flow

Mean Film Thickness. The relative fractions of contact time between the tip of a needle probe and the gas phase were monitored while traversing the tip from the minimum wave height to the maximum, as shown in Fig. 3. The mean film thickness was then obtained by integrating the curve connecting these data points. It can be seen in Fig. 3 that the gas Reynolds number does not affect the mean film thickness

Nomenclature

D^* = dimensionless length scale
f = friction factor
H = channel depth (m)
h = heat transfer coefficient (kW/m²K)
i_{fg} = latent heat (kJ/kg)
j = superficial velocity (m/s)
J_m^* = modified Wallis parameter
L = channel length (m)
N_m = modified two-phase Grashof number
Nu = Nusselt number, hx/k_f
Pr = Prandtl number, ν_f/α_f
Re = Reynolds number, W/μ
Re_g^* = critical gas Reynolds number
St = Stanton number, $Nu/(PrRe_f)$
U = velocity (m/s)
W = mass flow rate per unit width (kg/ms)

Greek Letters

α = void fraction or thermal diffusivity (m²/s)
β = ratio of interface velocity to average liquid velocity
δ = mean film thickness (m)
θ = inclination angle
μ = viscosity (Ns/m²)
ν = kinematic viscosity (m²/s)
ρ = density (kg/m³)
ρ^* = density ratio, ρ_g/ρ_f
σ = surface tension (N/m)
τ = shear stress (N/m²)

Subscripts

a = adiabatic
f = liquid
g = gas
i = interface
in = inlet
k = g or f
L = total length
out = outlet
s = saturation
w = wall
x = coordinate

Superscripts

$*$ = dimensionless
$-$ = average

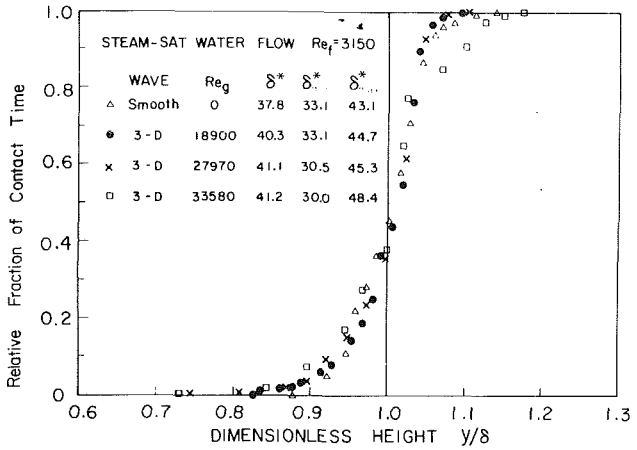

Fig. 3 Distribution of fraction of relative contact time between the tip of a needle probe and the gas phase as a function of probe height

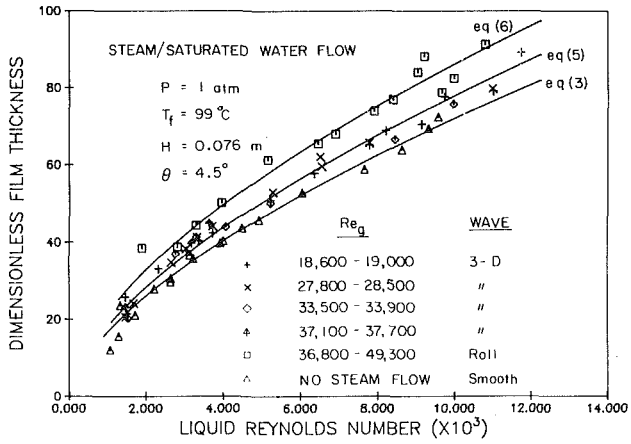

Fig. 4 Mean film thicknesses for three distinct regimes in a nearly horizontal flow

significantly, despite the fact that the interface becomes rougher with increasing gas flow rate, so long as the three-dimensional wave regime is maintained.

Three distinct film regimes were identified visually: smooth film, three-dimensional wave, and roll wave. For the smooth film regime, where the liquid film flows down alone, the dimensionless mean film thickness can be correlated as follows

$$\delta^* = 0.208\,\mathrm{Re}_f^{0.635} \quad 600 \le \mathrm{Re}_f \le 9600 \tag{3}$$

where the dimensionless film thickness is defined by

$$\delta^* = \delta[g\sin\theta(\rho_f - \rho_g)\rho_f/\mu_f^2]^{1/3} \tag{4}$$

For the rough film regime, two different correlations were obtained, which reflects the experimental result in this range that the effect of the upwards gas flow on the mean film thickness is negligible. For the three-dimensional wave regime

$$\delta^* = 0.229\,\mathrm{Re}_f^{0.633} \quad 1400 \le \mathrm{Re}_f \le 12{,}000 \tag{5}$$

For the roll wave regime,

$$\delta^* = 0.334\,\mathrm{Re}_f^{0.603} \quad 1800 \le \mathrm{Re}_f \le 11{,}000 \tag{6}$$

The experimental results on the mean film thickness are shown in Fig. 4. The dimensionless mean film thicknesses with countercurrent gas flow increase by approximately 10 and 20 percent, respectively, for the rough three-dimensional wave and roll wave regimes over the smooth film thickness without gas flow. Thus the presence of the upwards gas flow does not alter significantly the liquid film thickness in nearly horizontal countercurrent flow, except close to the flooding condition.

Interfacial Shear Stress. From the momentum balance for developed gas flow in the absence of mass transfer, it follows

$$\tau_{ia} = \left(\frac{\Delta P}{\Delta L}\right)(H-\delta) - \tau_{wg} - \rho_g g(H-\delta)\sin\theta \tag{7}$$

Thus, the adiabatic interfacial friction factor, f_{ia}, defined by

$$f_{ia} = \frac{2\tau_{ia}}{\rho_g(\bar{U}_g + U_i)^2} \tag{8}$$

can be determined by measurements of pressure drop and mean film thickness. One may use the Blasius equation for the evaluation of the wall friction factor in equation (7) based on the experimental result of Hanratty and Engen [5] that the wall shear stress in the gas phase is not affected significantly by the presence of the moving interface for a turbulent gas flow over a liquid film.

Figure 5 shows the interfacial friction factors for nearly horizontal steam/saturated-water countercurrent flow. It was found that the interfacial friction factor for the three-dimensional wave regime is of the same order of magnitude as for the smooth film regime, but that it is strongly dependent upon the gas Reynolds number, as well as the liquid Reynolds number, for the roll wave regime. The interfacial friction factor during the build-up of the roll waves, which is closely related to the limit of countercurrent flow, can be correlated by the following equation

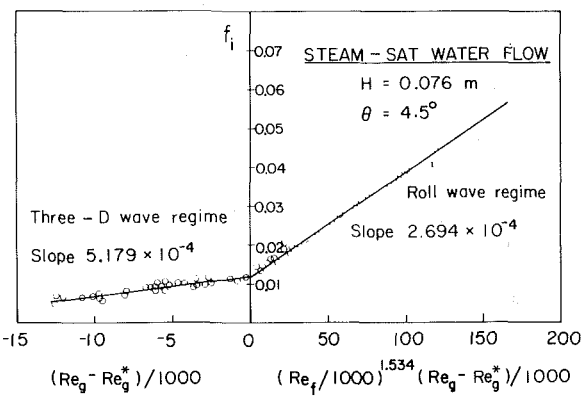

Fig. 5 Interfacial friction factors measured in nearly horizontal steam-saturated water countercurrent flow

$$f_{ia} = 0.012 + 2.694\times 10^{-4}(\mathrm{Re}_f/1000)^{1.534}(\mathrm{Re}_g - \mathrm{Re}_g^*)/1000 \tag{9}$$

where Re_g^* represents the critical gas Reynolds number as a function of liquid Reynolds number for the transition to the roll wave regime in this geometry.

$$\mathrm{Re}_g^* = 1.837\times 10^5\,\mathrm{Re}_f^{-0.184} \tag{10}$$

It should be recognized that a dimensionless interfacial relative velocity may be a more appropriate number than the gas Reynolds number to characterize these transitions.

Interfacial shear stresses for fully developed roll waves are difficult to measure because of the significant entrainment of liquid droplets torn from the tips of the waves. Nevertheless, it is thought that the interfacial friction factor may be described by equation (9) reasonably well, since it is observed that the frequency of the roll waves continues to increase up to the flooding point as the gas flow rate is increased beyond the inception of entrainment.

Flooding Analysis

Several different viewpoints have been expressed for analytical models, which are described in some detail by Bankoff and Lee [6]. The envelope theory considers flooding to be the limiting condition for countercurrent flow, which

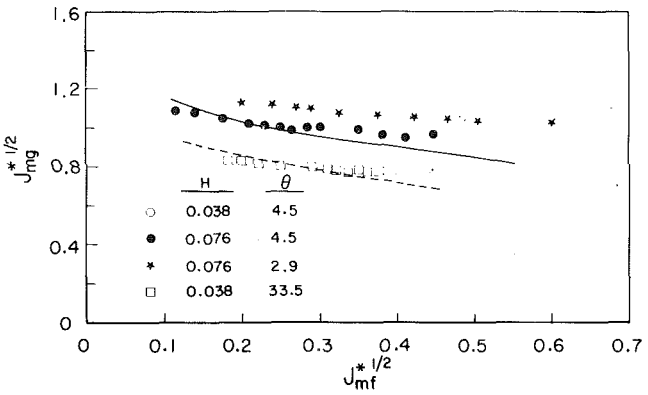

Fig. 6 Comparison of the envelope theory with flooding data: —— prediction for H = 0.076 m and θ = 4.5 deg; - - - prediction for H = 0.038 m and θ = 33.5 deg

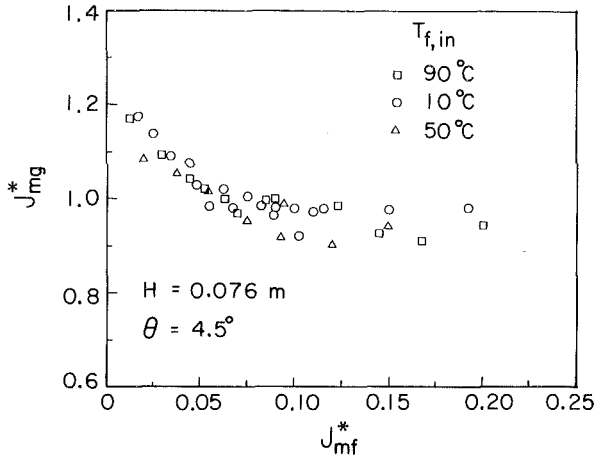

Fig. 7 Effect of water inlet temperature on the vapor flooding velocity. Experimental data for H = 0.076 m and θ = 4.5 deg.

can be described by the locus of tangents in the (J_g^*, J_f^*) plane to the operating lines for constant void fraction, based on the steady hydrodynamic equations. The envelope thus separates the attainable and unattainable regions for countercurrent flow. This theory, suggested originally by Wallis [7], and then employed by Bharathan et al. [8] and Dobran [9], has been modified to account for the effect of inclination angle and condensation in the present study.

Flooding equations based on this modified theory are derived in detail in the Appendix. In this analysis, a modified Wallis parameter, which considers the effect of inclination angle, was introduced

$$J^*_{mk} = j_k \left[\frac{\rho_k}{2gH\sin\theta(\rho_f - \rho_g)} \right]^{1/2} \tag{11}$$

where the hydraulic diameter of the test section is chosen as the length scale.

Flooding equations (A5) and (A10) contain the interfacial friction factor, f_{ia}, which must be obtained empirically. Two empirical correlations were employed. For nearly horizontal inclinations, the following equation, which is combined from equations (6) and (9) was developed

$$f_{ia} = 0.012 + 6.091 \times 10^{-8}(1-\alpha)^{2.544} \mathrm{N_{mf}}^{0.848} \cdot [N_{mg} J^*_{mg} - 1.837 (N_{mf} J^*_{mf})^{-0.184}] \tag{12}$$

where the modified, two-phase Grashof number is defined by

$$N_{mk} = [2gH^3 \sin\theta \rho_k (\rho_f - \rho_g)/\mu_k^2]^{1/2} \tag{13}$$

For a moderately steep inclination, the empirical correlation presented by Bharathan et al. [8] was modified by employing the effective gravity component in the definition of the Laplace capillary length scale. It is argued that the interfacial structure may not be altered significantly by the inclination angle, except for nearly horizontal angles. Thus, the results lead to

$$f_{ia} = 0.005 + A\,(D^*/2)^B (1 - \sqrt{\alpha})^B \tag{14}$$

where the coefficients, A and B, are given by

$$\log A = -0.56 + 9.07/D^* \tag{15}$$

$$B = 1.63 + 4.74/D^* \tag{16}$$

and

$$D^* = 2H[(\rho_f - \rho_g) g \sin\theta/\sigma]^{1/2} \tag{17}$$

For the evaluation of the wall shear stress in the steam phase, the Blasius equation was employed, as mentioned earlier. The calculation of the liquid wall shear stress requires knowledge concerning the turbulent behavior of the film. Utilizing von Karman's universal velocity distribution, the equation for the friction factor can be expressed as follows

$$1.0 - 3.0\sqrt{\frac{f_{wf}}{2}} = 2.5\sqrt{\frac{f_{wf}}{2}} \ln\left(\mathrm{Re}_f \sqrt{\frac{f_{wf}}{2}}\right) - \frac{64}{\mathrm{Re}_f} \tag{18}$$

In countercurrent flow, the velocity profile of the liquid film is distorted near the interface due to the upwards gas flow. However, the use of equation (18) should not produce a significant error in the wall friction because of the thin interface layer.

For flooding in a condensing flow, the heat transfer analysis of countercurrent steam-water flow is included in the Appendix. Therefore, if a specifically pertinent correlation for the heat transfer coefficient is available, the flooding velocity in a condensing flow can also be predicted.

Visual Observations for Onset of Flooding

Visual observations made in flooding tests show that the flooding characteristics appear to vary from one geometrical condition to another. When the channel depth was 0.038 m and the inclination angles were 4.5 and 33.5 deg, the onset of flooding was clearly marked by the formation of water slugs and bridging. As a preliminary to slug formation, a rough thick liquid film developed, with well-developed roll waves superimposed on the three-dimensional pebbly interface which caused considerable augmentation of the interfacial shear stress. The water slugs, which originated at the water exit, then propagated backwards with increasing steam flow rate, followed by rupture of the interface and bridging in the middle of the test channel. During slug propagation, the flow could be characterized as an oscillatory plug flow with continuous entrainment of water droplets. However, for relatively high water flow rates, the transition to flooding occurred very rapidly with a small increase of the steam flow rate after the formation of water slugs, and thus it was hard to distinguish between the point of slug formation and the flooding threshold. For H = 0.076 m and θ = 4.5 and 2.9 deg, roll waves also appeared when the flooding point was approached. Similarly, slugs were formed at the water exit of the test channel, but no backwards propagation of a slug was observed. Instead, the slug grew to a height several times the mean film thickness, and a mist of water droplets was entrained from the tops of the water slugs. This resulted in an oscillatory plug flow, owing to the internal circulation of water droplets deposited onto the liquid film. Consequently, the onset of flooding for H = 0.076 m appeared to be not so abrupt as that for H = 0.038 m.

Results and Discussion

Comparisons of the flooding data with the envelope theory

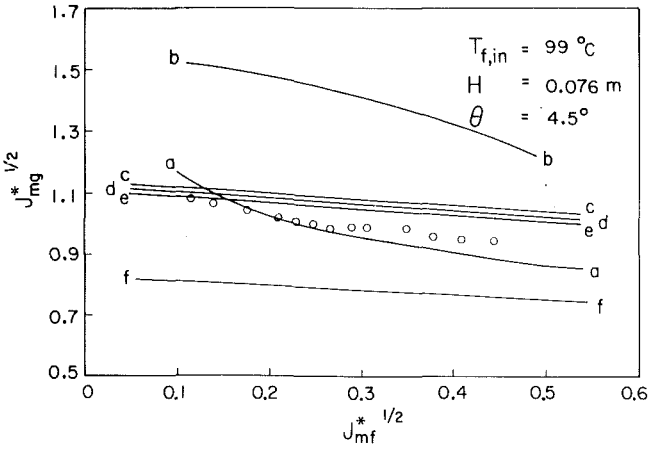

Fig. 8 Comparison of various analytical models with flooding data for nearly horizontal flow: (a) Present theory; (b) Taitel and Dukler [14]; (c) Gardner [15]; (d) Wallis and Dobson [13]; (e) Mishima and Ishii [11]; (f) Kordyban and Ranov [12]

are shown in Fig. 6. Good agreement is seen for both the steep and the nearly horizontal inclinations. It is not surprising that the modified correlation (14) appears to be valid for inclined countercurrent flow, because it turns out that the flooding curve calculated with equation (14) for the nearly vertical inclination is very close to that for the present steep angle (33.5 deg). This indicates that the dimensionless velocity defined by equation (11) may incorporate the gravity effect well for steep angles. However, for moderately-inclined or nearly horizontal flow, the dimensionless gas flooding velocity generally rises as the inclination angle decreases. This rise seems to be related to the $(g\sin\theta)^{-1/2}$ term in equation (11), since the dependence of the superficial gas flooding velocity on the inclination angle appears to be not significant so long as the void fraction is large enough. The channel depth may change the dimensionless gas flooding velocity, as seen from the experimental data for $H = 0.076$ m and 0.038 m at $\theta = 4.5$ deg. Some difference in J^*_{mg} between $H = 0.076$ m and 0.038 m may be noted. Recent observations by Bankoff and Lee [6] show that the dimensionless gas flooding velocity decreases monotonically at a fixed liquid velocity in vertical annular flow with increasing tube diameter, but the effect is not significant for large tube diameters. A similar result may also hold for inclined stratified flow.

Figure 7 shows the influence of the liquid inlet temperature on the flooding velocity. There are only small deviations between condensing and adiabatic flows. In the present test section, the exit water temperature reaches nearly saturation, regardless of initial subcooling. Thus, the water inlet temperature plays an insignificant role in altering the vapor flooding flux. This result agrees with the observation by Wallis et al. [9] that the onset of flooding in vertical condensing flow may be considered to be hydrodynamics-limited, rather than heat-transfer-limited.

The effect of water inlet temperature can also be described by the envelope theory. When the water exit temperature rises to saturation, the flow rate approaches a limiting value, $(1 + K)\, J^*_{mf,\text{in}}$. The dimensionless condensation rate, dJ^*_{mg}/dx^*, becomes very small, as seen from equation (A7). Therefore, it can be neglected compared to the other terms in the flooding equations (A5) and (A10). Thus, it may be concluded that the initial subcooling has an unimportant effect on the vapor flooding flux in a long channel, as in the present system. However, this is true only for bottom flooding. If top flooding takes place, as in vertical annular flow with upper head injection, the condensation effect will be an important factor. This case can also be predicted by the envelope theory, wherein the dimensionless condensation rate term becomes important in equation (A5), partly because of higher heat transfer coefficient and also partly because of low value of x^* in equation (A7) for top flooding.

Comparison With Slug Formation Models

The formation of a water slug was observed at the bottom just before the onset of flooding in nearly horizontal countercurrent flow. Therefore, it is interesting to compare the present data with the slug formation models proposed by several investigators. Five theoretical studies on this subject are available to compare directly with the flooding data: Mishima and Ishii model [11], Kordyban and Ranov model [12], Wallis and Dobson model [13], Taitel and Dukler model [14] and Gardner model [15]. These studies apply to cocurrent horizontal flow, but can be extended to nearly horizontal countercurrent flow with minor modifications [1].

It is shown in Fig. 8 that the onset of flooding in nearly horizontal flow can be successfully predicted by the following three models: Mishima and Ishii model [11], Wallis and Dobson Model [13], and Gardner model [15]. It is interesting to note that these three models are based on quite different assumptions. The first model employs the concept of the most dangerous wave, which implies that the finite-amplitude wave with the largest growth rate is responsible for slug formation. The second model is derived semi-empirically, using Kelvin-Helmholtz theory for the stability of a small amplitude wave. Finally, the third model focuses on energy transfer from the mean gas flow to produce the instability. On the other hand, the prediction by the Taitel-Dukler model [14] results in a much higher flooding curve. This discrepancy may be attributed to ignoring the frictional loss at the interface in the Bernoulli-type equation. If the interfacial shear were taken into consideration in calculating the gas pressure at the wave crest, the prediction would be closer to the flooding data. The Kordyban-Ranov theory [12] predicts a considerably lower flooding curve compared to the experimental data. This seems to be partly because the critical wavelength, which was estimated to be 0.025–0.050 m from their cocurrent-flow experimental observations, may change significantly in nearly horizontal countercurrent flow. It thus seems likely from this comparison that the slug formation model in cocurrent horizontal flow can be successfully employed for the prediction of the onset of flooding in nearly horizontal countercurrent flow, after suitable modifications.

Summary and Conclusions

Flooding in inclined stratified countercurrent flow has been investigated. An envelope theory, which is based on the hydrodynamic and energy equations for the onset of flooding in a condensing flow, is developed and found to agree very well with the data. Various slug formation models are also compared with the present data. A noteworthy result is that some of these models, which were developed basically for horizontal cocurrent flow, can also be employed to predict the onset of flooding in nearly horizontal countercurrent flow. Condensation has little effect on the onset of flooding if flooding is initiated at the bottom of the tube. Measurements of some key flow parameters have been made in nearly horizontal countercurrent flow. The mean film thicknesses in countercurrent flow increase only slightly compared to those without upwards gas flow, depending upon the interfacial wave regime. The interfacial friction factor for the roll-wave regime (near-flooding) in nearly horizontal flow is strongly dependent upon both liquid and gas Reynolds numbers, whereas for the three-dimensional wave regime it is of the same order of magnitude as for the smooth film regime.

References

1 Lee, S. C., "Stability of Steam-Water Countercurrent Stratified Flow," Ph.D. thesis, Northwestern University, Evanston, Ill., 1983.

2 Lee, S. C., and Bankoff, S. G., "Stability of Steam-Water Countercurrent Flow in an Inclined Channel: II. Condensation-Induced Waterhammer," to be submitted to ASME JOURNAL OF HEAT TRANSFER, 1983.

3 Lee, S. C., and Bankoff, S. G., "Stability of Steam-Water Countercurrent Flow in an Inclined Channel," ASME, 82-WA/HT-6, 1982.

4 Linehan, J. H., "The Interaction of Two-Dimensional Stratified, Turbulent Air-Water and Steam-Water Flows," Ph.D. thesis, University of Wisconsin, 1968.

5 Hanratty, T. J., and Engen, J. M., "Interaction between a Turbulent Air Stream and a Moving Water Surface," *AIChE Journal*, Vol. 3, 1957, pp. 299-304.

6 Bankoff, S. G., and Lee, S. C., "A Comparison of Flooding Models for Air-Water and Steam-Water Flow," presented at NATO Advanced Research Workshop on Advances in Two-Phase Flow and Heat Transfer, Aug. 31-Sept. 3, 1982, Schliersee, West Germany.

7 Wallis, G. B., *One-Dimensional Two-Phase Flow*, McGraw-Hill, N.Y., 1969.

8 Bharathan, D., Wallis, G. B., and Richter, H. J., "Air-Water Countercurrent Annular Flow," EPRI NP-1165, 1979.

9 Dobran, F., "Condensation Heat Transfer and Flooding in a Counter-Current Subcooled Liquid and Saturated Vapor Flow," *Thermal-Hydraulics in Nuclear Power Technology*, ASME, New York, 1981, pp. 9-19.

10 Wallis, G. B., deSieyes, D. C., Rosselli, R. J., and Lacombe, J., "Countercurrent Annular Flow Regimes for Steam and Subcooled Water in a Vertical Tube," EPRI NP-1336, 1980.

11 Mishima, K., and Ishii, M., "Theoretical Prediction of Onset of Horizontal Slug Flow," ASME *Journal of Fluids Engineering*, Vol. 102, 1980, pp. 441-445.

12 Kordyban, E. S., and Ranov, T., "Mechanisms of Slug Formation in Horizontal Two-Phase Flow," ASME *Journal of Basic Engineering*, Vol. 92, 1970, pp. 857-864.

13 Wallis, G. B., and Dobson, J. E., "The Onset of Slugging in Horizontal Stratified Air-Water Flow," *Int. J. Multiphase Flow*, Vol. 1, 1973, pp. 173-193.

14 Taitel, Y., and Dukler, A. E., "A Model for Predicting Flow Regime Transitions in Horizontal and Near Horizontal Gas-Liquid Flow," *AIChE Journal*, Vol. 22, 1976, pp. 47-55.

15 Gardner, G. C., "Onset of Slugging in Horizontal Ducts," *Int. J. Multiphase Flow*, Vol. 5, 1979, pp. 201-209.

16 Hewitt, G. F., and Wallis, G. B., "Flooding and Associated Phenomena in Falling Film Flow in a Vertical Tube," UKAEA Report, AERE-R4022, 1963.

APPENDIX

The flooding equations based on the envelope theory will be derived in this section.

Hydrodynamic Equations

Under the assumption that the flow is one-dimensional without any entrainment, the momentum balances for the gas and liquid phases can be written as follows

$$\tau_{wg}+\tau_i-(H-\delta)\frac{dP_g}{dx}+\rho_g g(H-\delta)\sin\theta = \frac{d}{dx}(W_g\tilde{U}_g)+U_i\frac{dW_g}{dx} \tag{A1}$$

$$-\tau_{wf}-\tau_i-\delta\frac{dP_f}{dx}+\rho_f g\delta\sin\theta=\frac{d}{dx}(W_f\tilde{U}_f)-U_i\frac{dW_f}{dx} \tag{A2}$$

From a mass balance, it follows that

$$\frac{dW_f}{dx}=\frac{dW_g}{dx} \tag{A3}$$

From the normal momentum jump balance, neglecting the curvature of the interface and the normal component of the liquid momentum flux, the pressure discontinuity due to the condensation at the interface becomes

$$P_f-P_g=\frac{1}{\rho_g}\left(\frac{dW_g}{dx}\right)^2 \tag{A4}$$

Eliminating the pressure gradients in equations (A1) and (A2) with equation (A4), and then substituting equation (A3), the following dimensionless equation is obtained

$$F=f_{wg}J^{*2}_{mf}/\alpha^3+f_{wf}J^{*2}_{mf}/(1-\alpha)^3 + \frac{f_{ia}}{\alpha(1-\alpha)}[J^*_{mg}/\alpha+\beta\rho^{*1/2}J^*_{mf}/(1-\alpha)]^2 + 2(H/L)\left[\frac{(2\alpha-1)}{\alpha^2(1-\alpha)}J^*_{mg}+2\rho^{*1/2}\frac{J^*_{mf}}{(1-\alpha)^2} + 2(H/L)^2\left(\frac{d^2J^*_{mg}}{dx^{*2}}\right)\right]\left(\frac{dJ^*_{mg}}{dx^*}\right)-1=0 \tag{A5}$$

where f_{wg} and f_{wf} are the wall friction factor for the steam and liquid side, respectively. In equation (A5), β denotes the ratio of the interface velocity to the average liquid velocity, which, following Hewitt and Walls [16], may be taken to be unity when flooding takes place. However, this has a negligible effect on the flooding solution, since the first term in the brackets of the interfacial shear term is much greater than the second term.

Heat Transfer Equations

From the definition of the heat transfer coefficient and the energy balance for the liquid film [1], one obtains

$$h=\frac{C_{pl}W_f}{(1+K)W_{f,\text{in}}-W_f}\left(\frac{dW_f}{dx}\right) \tag{A6}$$

or in dimensionless form

$$\frac{dJ^*_{mg}}{dx^*}=\frac{1}{x^*}(1/\rho^*)^{1/2}\text{St}[(1+K)J^*_{mf,\text{in}}-J^*_{mf}] \tag{A7}$$

where K is the dimensionless subcooling number, defined by

$$K=C_{pl}(T_s-T_{f,\text{in}})/i_{fg} \tag{A8}$$

Upon differentiating equation (A7) with respect to x^* one obtains

$$\frac{d^2J^*_{mg}}{dx^{*2}}=-\frac{1}{x^*}\left[1+\text{St}+\frac{x^*}{\text{St}}\frac{d\text{St}}{dx^*}\right]\left(\frac{dJ^*_{mg}}{dx^*}\right) \tag{A9}$$

One notes that the condensation rate term in equation (A5) consists of three terms: vapor momentum change, liquid momentum change and momentum transfer at the interface. However, the last two terms can be neglected compared to the first term, as can be seen from equation (A5), since $\rho^* << 1$ and $(H/L) << 1$. The effect of the vapor momentum term on the flooding solution depends upon the magnitude of dJ^*_{mg}/dx^*. From equation (A7), however, one can see that dJ^*_{mg}/dx^* is, in general, small, since J^*_{mf} is almost identical to $(1+K)J^*_{mf,\text{in}}$ when the temperature at the liquid exit approaches saturation. Thus, one may expect that the solution for bottom flooding in a condensing flow is to be very similar to that in an adiabatic flow.

Flooding Analysis

The envelope which represents a limiting curve separating the operating region from an unattainable region for countercurrent flow, can be described by the locus of tangents in the (J^*_{mg}, J^*_{mf}) plane to the operating lines for constant void fraction. Thus the flooding solution in stratified flow can be deduced from equation (A5) and its derivative with respect to α by eliminating the void fraction

$$F(J^*_{mg}, J^*_{mf}, \alpha)=0 \tag{A5}$$

$$G(J^*_{mg}, J^*_{mf}, \alpha)=\frac{\partial F}{\partial\alpha}=0 \tag{A10}$$

Since both equations, (A5) and (A10), are nonlinear in α, the solution is determined numerically by a generalized Newton method.

Reflux Condensation and Transition to Natural Circulation in a Vertical U-Tube

S. Banerjee
Professor of Chemical and Nuclear Engineering, University of California, Santa Barbara, Calif. 93106
Mem. ASME

J-S. Chang

R. Girard

Department of Engineering Physics, McMaster University, Hamilton, Ontario L8S 4M1

V. S. Krishnan
Atomic Energy of Canada, Ltd., Pinawa, Manitoba ROE 1L0

Reflux and natural circulation condensation in vertical inverted U-tube steam generators form an important heat removal mechanism for nuclear reactors in certain accidents. As a first step in understanding the behavior of such steam generators, condensation was studied in a single vertical tube with a cooling jacket. Steam was fed into the tube from an inlet plenum and condensed in the jacketed region. The inlet and outlet pressures and cooling jacket conditions were controlled to give well-defined boundary conditions. The amount of steam condensed and the flow patterns obtained were determined. The steam flow rate into the tube initially increased with pressure differences between the inlet and outlet plenums. The condensate ran back to the inlet plenum countercurrent to the steam flow (reflux flow). At a certain pressure difference, no further increase in steam inlet flow rate was observed though pure refluxing was maintained. Instead, a column of liquid formed above the two-phase condensing region. The length of this column increased as the pressure difference was increased. At a sufficiently large pressure difference the liquid column carried over the top of the vertical U-bend and there was a dramatic change in flow regime to natural circulation condensation in which the bulk of the condensate flowed cocurrently with the steam. The behavior of the system was explained by postulating that "flooding" conditions were reached at the inlet when the pressure difference became large enough for a liquid column to form above the condensing region. A small perturbation analysis of the stability of the condensing and liquid column regions was done using a lumped parameter approach and constant pressure boundary conditions. Experimental results on the frequency of oscillations in a single tube followed the qualitative trends predicted by the linear analysis, but the predicted frequencies were about twice as high as those observed.

Introduction

Steam generators in pressurized water reactors may act as important heat sinks in certain postulated accidents, such as small break loss of coolant accidents and anticipated transients without scram. To illustrate the importance of this heat removal process, consider a situation in which heat (perhaps at decay heat levels) is generated in the reactor core, but the leak or break in the primary heat transport system is so small that only a portion of the heat generated can be transported out. In this case, there may be some additional heat loss through system piping and components, but the steam generators become a major heat sink. For systems with no coolant loss, the heat can be transported by single-phase natural or forced circulation from the core to the steam generator. The prediction of single-phase natural circulation velocities and heat transfer, while not easy, is within the capability of existing methods provided high accuracy is not required. On the other hand, if the primary heat transport system has lost some coolant and is partially filled with vapor, then prediction becomes much more difficult.

For the two-phase situation, several overall flow patterns may occur. In the first, steam may be generated in the core, and provided it can escape from the reactor vessel, flow to the steam generators which contain relatively cold water on their secondary sides. There the steam could condense and the condensate flow back countercurrent to the steam flow. This mode of heat removal is called reflux condensation, implying countercurrent flow of steam and water. The second possibility is that the steam may flow to the steam generators, condense, and under certain conditions, all or part of the condensate may be carried along cocurrently with the steam. This cocurrent steam-water flow pattern is called natural circulation (though this is not a strictly accurate term). There are, of course, several intermediate possibilities. The flow may oscillate between reflux condensation and natural circulation, or a mixture of these flow patterns may be obtained with some condensate flowing countercurrent to the steam, and some cocurrent. The behavior of multitube systems and multiple steam generators is very complex.

In general, heat removal capability in natural circulation is greater than in reflux condensation. Therefore, it is of interest to determine the mechanisms governing heat removal in reflux condensation and to investigate the factors affecting transition to natural circulation. Also, it is of importance to understand how and why liquid (condensate) is held up in the steam generators in various modes of condensation, because this liquid is then unavailable for reactor core cooling. This is illustrated schematically in Fig. 1 for a loop in which the steam flow rate is sufficient to hold up some water in the steam generator tubes.

To this end, reflux condensation was studied in a single vertical tube to simplify the system as much as possible. It was understood that such a geometry would eliminate the possibility of tube-to-tube instabilities and oscillations. In addition, the elimination of the return U-bend or down leg would not allow investigation of the natural circulation mode. However, such a study was considered a necessary first step to understanding the mechanisms governing heat removal and

Contributed by the Heat Transfer Division and presented at the ASME Winter Annual Meeting, Washington, D.C., November 15-20, 1981. Manuscript received by the Heat Transfer Division April 19, 1982. Paper No. 81-WA/HT-59.

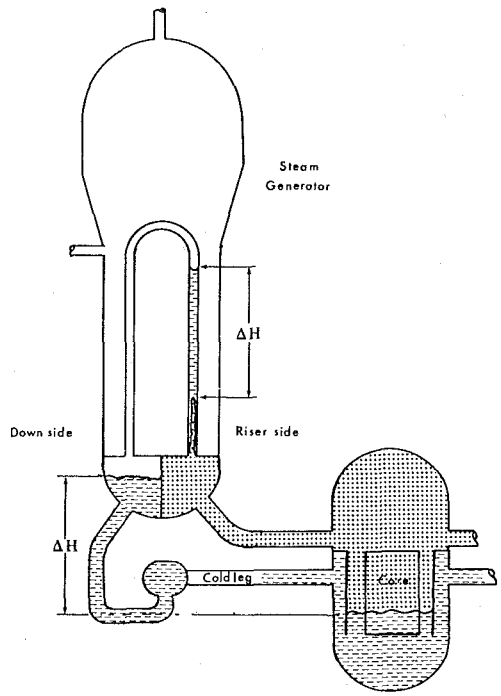

Fig. 1 Schematic of a pressurized water reactor loop showing refluxing in a steam generator under partial coolant inventory conditions

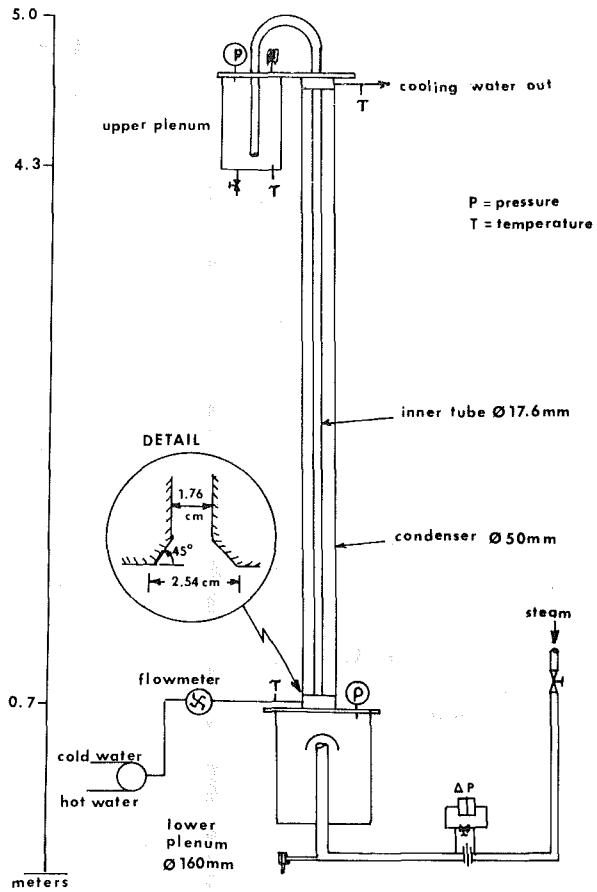

Fig. 2 Schematic of experimental apparatus

liquid holdup in reflux condensation, and the factors affecting transition to natural circulation. Furthermore, the stability of a single-tube condensation system with constant pressure boundary conditions was investigated as a prelude to consideration of multiple-tube systems. A program to investigate more complex systems is underway at the University of California, Santa Barbara. Other investigators have also done work contemporary with that in this paper, and the results are reported in [1-3]. Oscillations in direct contact condensation have also been investigated [4].

This paper is the first in a series which will deal systematically with the effects of noncondensibles, oscillations between refluxing and natural circulation, multiple tube systems, and multiple steam generators. The present paper first deals with various aspects of reflux condensation and transition to natural circulation. The stability of a single-tube condensation system is then discussed. This work is not meant to directly simulate the course of events in a full-sized steam generator, but rather to elucidate the phenomena that may occur and the mechanisms that govern them.

Nomenclature

A = tube inside cross-sectional area, m^2
C_L, C_V = constant coefficient
D = tube inside diameter, m
f = two-phase friction factor
f_q = heat removal rate per unit circumferential area of condenser tube, w/m^2
g = gravitational acceleration, m/s^2
h = specific enthalpy, J/kg
$j^*_{g_f}$ = nondimensional flooding parameter = $m_c/[A(gD\rho_{g_f}(\rho_f - \rho_g))^{1/2}]$
m^* = mass flow rate relative to the moving two-phase /single phase boundary, kg/s
m_o = mass flow rate at inlet to condensing section, kg/s
m_c = mass rate of condensation, kg/s
m_i = mass flow rate of steam to plenum, kg/s
m = mass flow rate in test section, kg/s
p_o = pressure at inlet plenum, kPa
p_1 = pressure at test-section inlet, kPa
p_e = pressure at exit plenum, kPa
P = perimeter of condenser tube, m
R = gas constant, 0.46×10^{-3} kPa • m^3/kg °K
s = Laplace transform variable
t = time, s
T_p = temperature in inlet plenum, °C
x_o = flow quality in plenum
z = distance variable, m
$\alpha \equiv \bar{\alpha}$ = system mean void fraction
$\delta(i)$ = perturbed variable
η = length, m
ρ = area mean density, kg/m^3
ρ_{fg} = (liquid density - vapor density) kg/m^3
ω = angular frequency

Subscripts

o = inlet conditions to test-section or in plenum
a = acceleration component
aV = average
f = frictional component when used with pressure
f,L = liquid
g,v = vapor
fg = difference between vapor and liquid property, except where noted otherwise
i = plenum inlet
p = conditions in inlet plenum
2ϕ = two-phase
overbar = steady state

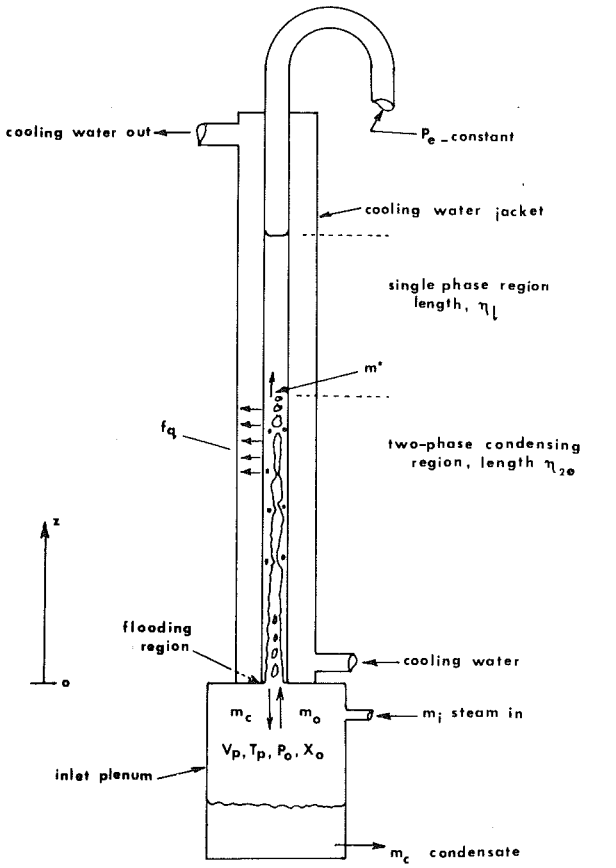

Fig. 3 Reflux condensation in vertical tube showing flow patterns in inner tube

Experimental Apparatus and Procedure

The objective of these experiments was to study single-tube reflux condensation in isolation from possible interactions with other system components, i.e., the boundary conditions at each end of the condenser tube were controlled to give constant plenum pressures. Also the secondary side conditions were controlled to give well-defined boundary conditions. Essentially, two sets of experiments were done. The first dealt with various factors affecting reflux condensation and the transition to natural circulation. The second dealt with oscillations in a reflux condensation system (but not oscillations between refluxing and natural circulation, which will be discussed in a subsequent paper).

The apparatus was made of two concentric glass tubes, as shown schematically in Fig. 2. Some of the important dimensions are shown on the figure. The test section was a long vertical double-pipe heat exchanger made of pyrex glass. The inner tube, in which condensation of steam takes place, was a single piece connected at the bottom to a steam inlet plenum and at the top to an outlet plenum. The connection to the outlet plenum was through a small section of stainless steel tubing in the form of an inverted U. The plenums were constructed of plexiglass. The outer pipe, which carried the flow of cooling water, was made of pyrex glass sections that were clamped to one another.

Pressures were measured by reluctance pressure transducers and temperatures by copper-constantan thermocouples. Steam flow rates were directly determined by collecting condensate from the plenum over a known period of time under constant operating conditions. The inlet and outlet plenum pressures were kept constant during a run. The pressure difference between the inlet and outlet, and the absolute pressure level at the inlet were two of the variables for the test matrix. The temperature of the cooling water was also a variable for the test matrix. The cooling water temperature determined the heat flux between the condensing flow and the cooling water. This was because the shell side cooling water flow was laminar, and the tube side condensation heat transfer coefficient was very high. This led to an overall heat transfer coefficient that was essentially constant for the conditions studied. The heat flux therefore depended on the log mean temperature difference between the condensing flow and the cooling water.

The test matrix explored the effects of pressure difference between the inlet and outlet plenums, and wall heat flux in the condensing region. Further details of the apparatus and measurements may be obtained from Banerjee et al. [5].

Besides pressures and temperatures at various points, measurements were made of the amount of steam condensed per unit time, the length of the condensing region and the liquid column above it (if any), and the frequency with which these lengths oscillated during reflux condensation. The lengths of the two-phase and single-phase regions were measured by using a meter scale. If the lengths oscillated, then the maximum and minimum values were taken and averaged. The frequency of oscillation was measured by examining the pressure difference traces.

Results on Reflux Condensation

As explained in the introduction, factors affecting reflux condensation and transition to natural circulation were investigated in one series of experiments. These, together with an interpretation of the results, are presented in this section. Theoretical and experimental results on the stability of a single tube condensation system with constant pressure boundary conditions are presented later.

Effects of Pressure Difference Between Inlet and Outlet Plenums. The flow patterns observed in reflux condensation (countercurrent steam-condensate flow) have the general character shown in Fig. 3. Above the inlet of the tube, a two-phase condensing region is formed. Above this two-phase region, a single-phase (liquid) region may be present. The single-phase region does not occur unless the pressure difference is sufficient to give "flooding" velocities at the inlet, as shown later.

Under steady operating conditions, the lengths of the two-phase region and single-phase region, if any, oscillate about average values. Observations regarding the frequency of these oscillations are presented in the next section. In this section, the results relate to the average lengths of the two-phase and single-phase regions.

The first experimental observation of significance is that the steam inlet mass flow rate (which is equivalent to the condensation rate for reflux flows) remains relatively constant with changes in pressure difference between the inlet and outlet plenums. This is shown in Fig. 4. Also the secondary side temperature, which governs heat flux in the condensing region in these experiments, has no significant effect on the inlet mass flow rate. The scatter in the results is, to some extent, caused by the plot being in dimensional form. As shown later, the values of j_g^* are relatively constant.

The second observation is that the average length of the single-phase region (the water column above the two-phase region) increases with increases in pressure difference between the inlet and outlet plenums as shown in Fig. 5. For the secondary side temperature being kept constant, the average length of the two-phase condensing region does not change with pressure difference. This, of course, is to be expected since the average inlet mass flow rate (as shown in Fig. 4) does not change significantly with pressure difference.

Effects of Secondary Side Conditions. As mentioned

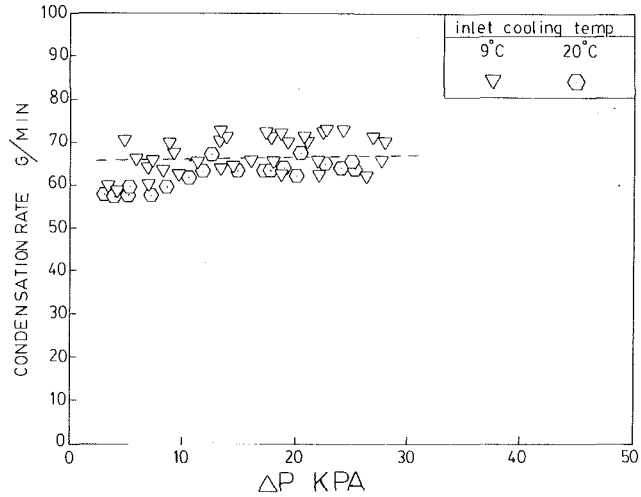

Fig. 4 Condensation rate (or inlet mass flow rate) as a function of cooling water inlet temperature in jacket

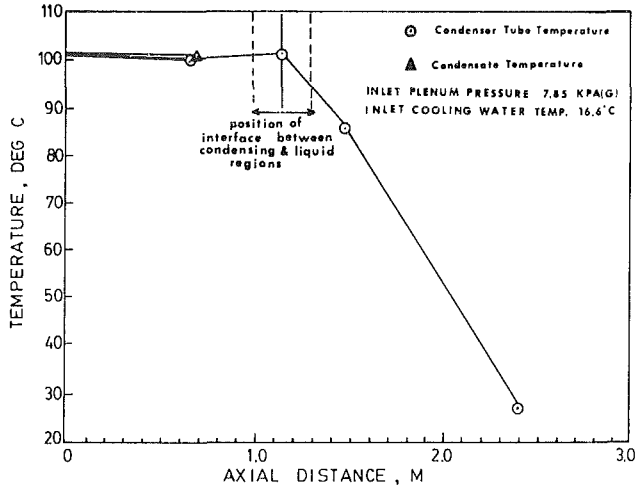

Fig. 6 Temperature profiles in tube during reflux condensation

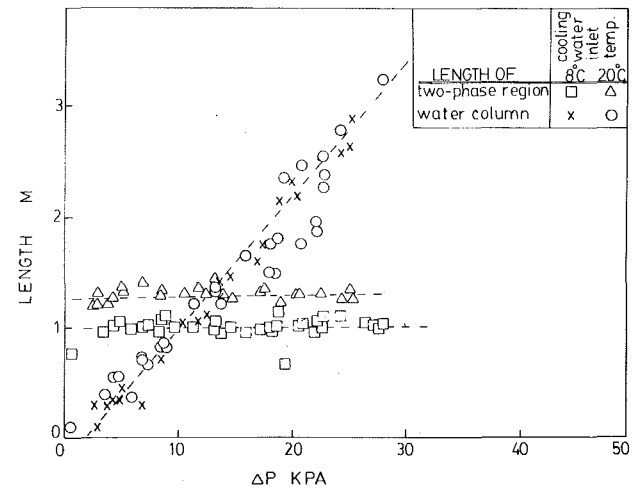

Fig. 5 Lengths of single-phase and two-phase regions as a function of cooling water inlet temperature and pressure difference

earlier, the oveall heat transfer coefficient between the tube and shell side is relatively constant in the condensing region, because the shell side cooling water flow is laminar and the tube side condensation heat transfer coefficient is high. Consequently, the heat flux in the condensing region is proportional to the log mean temperature difference between the tube-side and the shell-side temperatures. The effects of cooling water inlet temperature (which is a measure of the log mean temperature difference at constant flow rate) are shown in Fig. 5. It is clear that the length of the single-phase region does not depend on cooling water inlet temperature, but the length of the two-phase condensing region does. Colder cooling water leads to a shorter condensation length at a given pressure difference. However, as noted previously, the pressure difference by itself does not affect the length of the condensing region.

Temperature Profiles. Typical axial temperature profiles within the condenser tube are shown in Fig. 6. The temperature at the centerline of the tube T_c, and the temperature 1 mm from the wall, T_w, are indicated by triangles and circles respectively. The location of the averaged, minimum, and maximum positions of the interface between the two-phase and single-phase regions are shown by vertical lines. The temperatures actually reflect values close to saturation temperatures, except well into the single-phase region. Complete results on temperature profiles for various conditions may be found in Banerjee et al. [5]. The following trends were generally observed:

- The temperature near the tube wall increases slightly with increasing axial distance in the two-phase region. This temperature, in general, refers to the falling liquid film temperatures. This small effect is to be expected since the flow of the falling liquid film is in general countercurrent to the cooling water flow in the jacket. The cooling water heats up as it flows up the annulus, i.e., it is colder at the bottom than at the top. The liquid film on the condensing (or tube) side flows downwards and is colder at the bottom than at the top. The fact that the liquid film cools slightly as it falls must be due to heat loss to the cooling water in the jacket which is not quite made up by heat transfer from the vapor core.
- The temperature profile in the single-phase region has a sharp gradient near the edge of the two-phase region, and the liquid is significantly subcooled. This indicates that axial mixing in the single-phase region is poor, in spite of the oscillations discussed in the next section. An important consequence is that the vapor pressure of steam above the liquid column would be expected to reflect the average temperature at the top surface of the single-phase region. This is turn depends on the secondary side temperature. Therefore, in reflux condensation the secondary side temperature will govern the primary side pressure in the absence of noncondensibles.
- Finally, the temperature at the centerline is at saturation and increases with system pressure. This effect is not shown in the figure, but is evident when the results are examined.

Interpretation of Results. The results obtained may be interpreted in terms of a simple model. The model postulates that the maximum inlet steam flow rate for reflux condensation is governed by "flooding" (or liquid carry up) at the inlet. This explains all the phenomena observed as follows:

1 Consider an increase in pressure difference from one operating state to another. This would initially lead to an increase in steam inlet flow rate to values above that for "flooding." Liquid would be carried up into the single-phase region, and the length of this region would increase. As the length of the single-phase region increases, the gravitational head (or static component of pressure drop) would increase, resulting in a reduction in inlet steam flow rate. This process

Table 1 Conditions at flooding

Run[a]	Plenum pressure Bottom kPa(g)	Plenum pressure Top kPa(g)	Inlet steam temp[a] °C	j_g^*	j_f^*	V_{flood} (m/s)
1	3	0	103	.3899	1.024	6.02
2	5	0	104	.3844	1.027	5.84
3	3	0	103	.4027	1.058	6.22
4	7	0	103	.3899	1.024	6.02
5	8.5	0	105	.3907	1.062	5.84
6	12.5	0	106	.4330	1.196	6.36
7	17.5	0	107	.4035	1.133	5.83
8	22.5	0	108	.4091	1.167	5.82
9	25.0	0	109	.4035	1.170	5.65
10	9.5	5.6	105	.3793	1.028	5.65
11	14.5	6.0	106	.3846	1.062	5.66
12	21.5	6.8	108	.3979	1.135	5.65
13	24.5	5.6	110	.3864	1.139	5.32
14	29.0	4.8	110	.3864	1.139	5.32
15	17.5	10.2	106	.3846	1.062	5.66
16	16.0	10.8	107	.3793	1.065	5.49
17	22.0	10.8	108	.3979	1.135	5.65
18	27.5	10.2	109	.3918	1.136	5.48
19	31.5	11.0	111	.4032	1.208	5.47
20	36.0	10.8	112	.3818	1.143	5.01
21	18.5	15.8	108	.3741	1.068	5.32
22	25.5	15.0	110	.3749	1.105	5.16
23	29.0	15.2	111	.4146	1.242	5.62
24	34.0	14.0	112	.3704	1.109	4.86

[a] Inlet steam temperature taken at plenum

would continue until the inlet steam flow rate returned to the "flooding" value when no net liquid carry up would occur and the average length of the single-phase region would reach a constant value.

Thus, the proposed model explains why the length of the single-phase region increases with increases in pressure difference between the inlet and outlet plenums (see Fig. 5). It also explains why the inlet steam flow rate for reflux condensation does not change with pressure difference (see Fig. 4). (These remarks, of course, pertain to the situation when a steady operating condition is obtained; they do not apply to the transient situation that obtains for a period of time when the pressure difference is changed from one value to another).

A decrease in pressure difference simply results in a decrease in inlet steam flow rate until the single-phase region has drained sufficiently to reduce the static pressure drop, and thus allows the steam inlet flow rate to rise to the "flooding" value.

It should also be noted that flooding flow rates are only weakly dependent on thermophysical properties. Therefore, while there should be an effect of the inlet plenum absolute pressure level, this effect is small unless a wide range of inlet absolute pressure levels is studied.

2 Consider the effect of a change in cooling water temperature which results in a change in wall heat flux. The first order effect is to leave the steam flow for "flooding" at the inlet unchanged (see Fig. 4). Downstream effects may have some influence on flooding because of "history" effects on the liquid film, but in general, the flooding velocity depends mainly on "local" conditions. (This is why flooding correlations that do not take tube length into account work quite well.) Thus, changes in cooling water temperature, and hence in heat flux, do not change the inlet steam flow rate.

On the other hand, the same amount of steam is condensed per unit time over a different length because of the changed heat flux. This explains why the two-phase region changes in length with changes in heat flux (see Fig. 5). Furthermore, if the accelerational and frictional components of pressure drop are relatively small in comparison to the static head component, then changes in the two-phase length only lead to relatively small changes being required in the static head component. Thus, the single-phase region does not change in length (within experimental error) when the heat flux is changed. This situation may not work for rather small tube diameters or small single-phase region lengths.

Thus, inlet "flooding" controlling the maximum steam flow rate in reflux condensation explains all the observed results, i.e., that the inlet steam flow rate does not change with pressure difference or wall heat flux once the single-phase (liquid column) region is established; that the single-phase region length changes with pressure difference but not wall heat flux; and that the two-phase region length changes with wall heat flux but not pressure difference.

That the proposed mechanism is correct is further supported by values of j_g^* and j_f^* calculated from the measurements. The calculated values of some of the runs are tabulated in Table 1. The rest are available in [5]. The values of j_f^* are small compared to j_g^* in all cases because the liquid density is much higher than the vapor density. In any case, $j_g^* \sim 0.4$ in all the runs. This is to be expected from available flooding correlations, e.g., that of Wallis [6].

Effect of Noncondensibles. Noncondensible gas (air) was mixed with the steam flow and the effects determined qualitatively the mass concentration of the noncondensibles. To a first approximation, low concentrations of noncondensibles (< 5 percent) do not appear to affect any of the phenomena observed. The only discernible effect is that small gas bubbles become dispersed through the single-phase region. The bubbles rise slowly and vent to the upper plenum. Typical void fractions are ~ 10–20 percent. If the upper plenum is not vented, the overall effect is to gradually increase the back pressure and hence reduce the pressure difference. This results in a reduction in the length of the single-phase region, but there is no discernible effect on the inlet steam flow rate. However, as explained in the next subsection, the presence of noncondensibles has a major effect on the transition to natural circulation.

Transition to Natural Circulation. By natural circulation

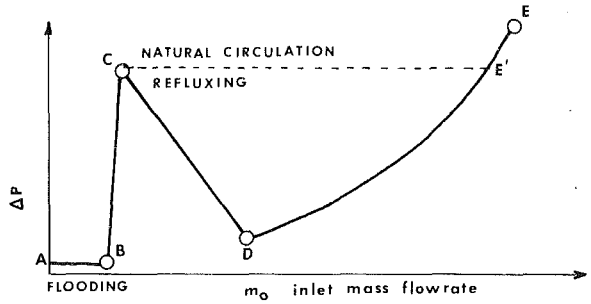

Fig. 7 Pressure drop – inlet mass flow rate characteristics for vertical inverted U-tube condenser

we mean the regime in which steam, and at least some portion of the condensate, flow cocurrently. From the experiments, this regime always occurs when the liquid column carries over the top of the U-bend. True natural circulation cannot be established in the apparatus shown in Fig. 2, because the inlet and outlet pressures are controlled, and the plenums are not connected. However, a set of experiments has been done in which the inlet and outlet plenums are connected to make a closed system, and a heater is placed in the inlet plenum to produce steam. This system goes into natural circulation when the liquid column carries over the top of the U-bend. These experiments will be described in detail in a later paper (Nguyen and Banerjee [7]).

To understand why the system goes into natural circulation, the pressure drop characteristics of the system must be considered. Qualitative pressure drop characteristics are shown in Fig. 7. (The details will depend on the particular system.) In the region AB, the system is in reflux condensation but no liquid column has built up because the inlet steam flow rate is below the value for flooding. In the region BC, the pressure drop can be increased, but the inlet flow rate stays constant at the flooding value as discussed previously. The increase in pressure drop results in an increase in the liquid column length until it carries over the U-bend at point C.

The region CD corresponds to a situation where some of the condensate and steam flows over the top of the U-bend. It is an unstable region and oscillations between refluxing and natural circulation are always observed because the mass flow rate in a real system cannot be controlled since capacitances from plenums and piping exist. The pressure drop characteristic has a negative slope with mass flow rate because only part of the condensate is carried over in this region leaving a thick wavy film on the up leg and a very thin film on the down leg of the inverted U-tube. As the steam flow rate is increased the gravity head pressure difference between the up and down leg decreases and the system becomes friction pressure drop dominated at point D.

The region DE corresponds to a friction dominated "natural circulation" flow in which the steam and liquid flow cocurrently.

If the pressure difference is controlled then the mass flow rate increases to point C and then jumps to point E′ on the curve DE. This sudden increase in inlet steam flow rate was always obtained in the present set of experiments. On the other hand, if the mass flow rate is controlled, then the system goes into oscillations between refluxing and natural circulation until the mass flow exceeds that at point D. The reasons for this will be discussed in a later paper (Nguyen and Banerjee [7]).

The main effect of noncondensible gases is to accumulate above the single-phase region in reflux condensation, and hence to increase the back pressure. Our later experiments (not reported here) show that the qualitative form of the pressure drop characteristic, illustrated in Fig. 7, is preserved. However, for fixed secondary side conditions, the absolute pressure level on the primary side is raised if the noncondensibles are not vented. The reason for this is that the pressure above the single-phase region in reflux condensation is no longer the vapor pressure of steam corresponding to the liquid surface temperature, but the sum of the partial pressures of steam and noncondensibles.

Stability of Vertical Single Tube Refluxing Systems

Description of Phenomena and Analysis. For the single-tube reflux condensation system discussed in the previous section, two types of oscillatory phenomena were observed. First, sharp pressure waves travelled through the system, at times shattering the inner glass tube. These pressure waves appeared to be caused by rapid collapse of vapor slugs or bubbles near the two-phase/single-phase interface region. These were clearly "condensation shocks" and the magnitude of the pressure spikes increased with increasing heat flux to the secondary side. While the qualitative behavior was clear from observations, no systematic study of the phenomena was made. This was not because these shocks were not of interest but because they did not appear to affect the main parameters investigated in these experiments, i.e., they appeared to have a relatively small effect on liquid distribution and heat removal capability in reflux condensation.

Second, the single- and two-phase regions oscillate about their average lengths. These oscillations were of some significance because if they were of large enough amplitude, the possibility of "dumping" some of the liquid into the lower plenum existed. For this reason an analytical study was made of stability of a single tube reflux condensation system. The work was confined at this stage to a linear analysis which should give the right qualitative trends for the oscillations. These were then compared with experimental results. However, no analysis was done for finite amplitude oscillations, so analytical results regarding the possibility of "dumping" could not be obtained. Experiments could not be done under conditions where "dumping" might occur because the heat fluxes were too high and the glass tubes invariably shattered due to condensation shocks. "Dumping" is important because it is a mechanism by which the heat removal capability in reflux condensation could be increased beyond the "flooding" limited capability. For example, once the single-phase liquid region "dumped" some of its content into the lower plenum, the vapor velocity would increase above the "flooding" value and the length of the liquid column would start increasing. If dumping continued periodically, the overall effect would be an average inlet steam flow rate above the "flooding" value, and hence increased heat removal capability.

The linear stability analysis is first presented followed by experimental results and discussion. The analysis is condensed because of space limitations but is completely described in [5]. It yields criteria for the onset of oscillations as well as the frequency of small oscillations. Data on the oscillation frequency were taken, in the experiments described here, but no data were obtained on the onset of oscillations. Therefore, only the analysis with regard to frequency is presented here.

Stability Analysis for Single Tube Refluxing Governing Equations. From experimental observations an idealized schematic of the reflux condensation system can be drawn as shown in Fig. 3 which defines the symbols. The system can be separated into four sections, the lower plenum, the two-phase region, the water column, and the upper plenum. We will assume that p_e, f_q, m_i, and the volume of vapor (assumed to behave ideally) in the plenum are not changing with time and a uniform temperature obtains inside the single-phase region. Therefore, the energy balance in the single-phase region can

be ignored. This is also equivalent to assuming that heat transfer from the single-phase region is negligible in comparison to the condensation heat transfer from the two-phase region. In general, this is good assumption. The approach followed here in writing the mass and heat balances in the two-phase region is somewhat similar to that of other investigators' efforts to model horizontal condensing flows [8, 9]. The governing equations describing the dynamics of the phenomena can be expressed as follows:

Mass balance in two-phase region:

Integrating the mass conservation equation over the two-phase region, we obtain

$$\frac{d}{dt}\{(\rho_f - \rho_{fg}\alpha)A\eta_{2\phi}\} = m_o - m_c - m^* \tag{1}$$

where α is the system mean void fraction and $\rho_{fg} = \rho_f - \rho_g$ to keep it positive.

Heat balance in two-phase region:

$$\frac{d}{dt}\{[\rho_f h_f(1-\alpha) + \rho_g h_g \alpha]A\eta_{2\phi}\} =$$

$$-f_q P\eta_{2\phi} + (h_f + h_{fg}x_o)m_o - h_f(m^* + m_c) \tag{2}$$

Mass balance in water column:

$$\frac{d}{dt}[\rho_f A\eta_L] = m^* \tag{3}$$

Test-section momentum balance:

$$p_1 - p_e = \int_0^{\eta_{2\phi}+\eta_L}\left[\frac{1}{A}\frac{\partial m}{\partial t} + \frac{1}{A^2}\frac{\partial(m^2/\rho)}{\partial z} + \frac{f}{2DA^2}(m^2/\rho) + g\rho\right]dz \tag{4}$$

Plenum mass balance:

$$\frac{dp_o}{dt} + \frac{RT_p}{V_p}m_o = \frac{RT_p}{V_p}m_i \tag{5}$$

Condensate net drain rate:

$$m_c = C_L\left(\frac{\rho_{\text{av}}}{\rho_f}\eta_{2\phi} + \eta_L\right)^{1/2} - m^* \tag{6}$$

where $\rho_{\text{av}} = (\rho_f - \rho_{fg}\alpha)$

Test-section inlet flow rate:

$$m_o = C_v(p_o - p_1)^{1/2} \tag{7}$$

Overall pressure drop balance:

$$p_o - p_e = (p_o - p_1) + (p_1 - p_e) \tag{8}$$

Note that quite simple expressions, equations (6) and (7), are used to describe the flow rate of condensate into the plenum and flow rate of vapor into the condensing section, respectively, as functions of pressure drops. $m^*(t)$ has been included in equation (6) in a rather simple manner to account for liquid movement across the point of complete condensation. Equation (8) states that the overall pressure drop is the sum of the pressure drop across the inlet boundary and that across the entire test-section. Equations (1) and (2) can be rearranged to yield

$$\frac{Ah_{fg}\rho_g\rho_f}{\rho_{fg}f_q p}\frac{d\eta_{2\phi}}{dt} + \eta_{2\phi} = \frac{h_{fg}}{f_q p}\left[m_o x_o + \frac{\rho_g}{\rho_{fg}}(m_o - m_c - m^*)\right] \tag{9}$$

$$\eta_{2\phi}\frac{d\alpha}{dt} + \left(\alpha - \frac{\rho_f}{\rho_{fg}}\right)\frac{d\eta_{2\phi}}{dt} = -\frac{1}{A\rho_{fg}}(m_o - m_c - m^*) \tag{10}$$

The test section momentum balance equation (4) can be simplified to remove its distributied nature by using suitable averages. The axial variations in $m(t,z)$ and $\rho(t,z)$ are written as overall averages $(m_o(t) + m^*(t))/2$ and $\rho_{\text{av}}(t)$, respectively. $m(t)$ in the water column is approximated by $(m^*(t) + 0)/2 = m^*(t)/2$. We further ignore the frictional pressure drop in the water column. Equation (4) can thus be simplified as follows

$$p_1 - p_e \sim \int_0^{\eta_{2\phi}}\left[\frac{1}{A}\frac{\partial m}{\partial t} + \frac{1}{A^2}\frac{\partial}{\partial z}(m^2/\rho) + \frac{f}{2DA^2}(m^2/\rho) + g\rho\right]dz$$

$$+\int_{\eta_{2\phi}}^{\eta_{2\phi}+\eta_L}\left(\frac{1}{A}\frac{\partial m}{\partial t} + \frac{1}{A^2}\frac{\partial}{\partial z}(m^2/\rho_f) + g\rho_f\right)dz \tag{11}$$

$$\sim \frac{\eta_{2\phi}}{2A}\frac{d}{dt}(m_o + m^*) + \frac{1}{A^2}\frac{(m^{*2} - m_o^2)}{(\rho_f - \rho_{fg}\alpha)}$$

$$+\frac{f}{8DA^2}\frac{(m_o + m^*)^2}{(\rho_f - \rho_{fg}\alpha)}\cdot\eta_{2\phi}$$

$$+ g(\rho_f - \rho_{fg}\alpha)\eta_{2\phi} + g\rho_f\eta_L + \frac{\eta_L}{2A}\frac{dm^*}{dt} - \frac{m^{*2}}{A^2\rho_f}$$

Steady-State Solution. The steady-state solution of the model equations can be obtained by setting the time derivative equal to zero. Thus

$$\bar{m}^* = 0$$

$$\bar{m}_o = m_i$$

$$\bar{m}_c = m_i$$

$$\bar{\eta}_{2\phi} = \frac{h_{fg}x_o m_i}{f_q P}$$

$$\bar{\eta}_l = \frac{m_i^2}{C_L{}^2} - \frac{\bar{\rho}_{\text{av}}\bar{\eta}_{2\phi}}{\rho_f} = \frac{m_i^2}{C_L{}^2} - \frac{h_{fg}x_o m_i}{f_{q_l}}\left(1 - \frac{\rho_{fg}\bar{\alpha}}{\rho_f}\right) \tag{12}$$

$$\bar{p}_o - p_e = \frac{m_i^2}{C_v^2} - \frac{m_i^2}{A^2\bar{\rho}_{\text{av}}} + \frac{fm_i^3 h_{fg}x_o}{8DA^2\bar{\rho}_{\text{av}}f_q p}$$

$$+ g\bar{\rho}_{\text{av}}\bar{\eta}_{2\phi} + g\rho_f\bar{\eta}_L$$

$$= \Delta\bar{p}_{01} + \Delta\bar{p}_a + \Delta\bar{p}_f + \Delta\bar{p}_g + g\rho_f\bar{\eta}_L$$

$$= m_i^2\left[\left(\frac{1}{C_v^2} + \frac{g\rho_f}{C_L^2} - \frac{1}{A^2\bar{\rho}_{\text{av}}}\right) + \frac{fh_{fg}x_o}{8DA^2 f_q P\bar{\rho}_{\text{av}}}m_i\right] \tag{13}$$

where $\bar{\rho}_{\text{av}} = (\rho_f = \rho_{fg}\bar{\alpha})$

Equation (13) represents the steady-state pressure drop characteristic of the system. This is cubic in m_i and reminiscent of that obtained in boiling systems [10–12].

The acceleration pressure drop $m_i{}^2/A^2\bar{\rho}_{\text{av}}$ influences the pressure drop characteristic significantly. If this term is ignored the characteristic has one local minimum at $m_i = 0$ as given by

$$\frac{\partial(\bar{p}_o - p_e)}{\partial m_i} = 2m_i\left(\frac{1}{C_v^2} + \frac{g\rho_f}{C_L^2} - \frac{1}{A^2\bar{\rho}_{\text{av}}}\right)$$

$$+ 3m_i^2\frac{fh_{fg}x_o}{8DA^2\bar{\rho}_{\text{av}}f_q P} = 0 \tag{14}$$

and

$$\frac{\partial^2(\bar{p}_o - p_e)}{\partial m^2} = 2\left(\frac{1}{C_v^2} + \frac{g\rho_f}{C_L^2} - \frac{1}{A^2\bar{\rho}_{\text{av}}}\right.$$

$$\left. + 6m_i\frac{fh_{fg}x_o}{8DA^2\bar{\rho}_{\text{av}}f_q P}\right) < 0 \tag{15}$$

However, when $m_i{}^2/A^2\bar{\rho}_{\text{av}}$ is large enough, and its magnitude

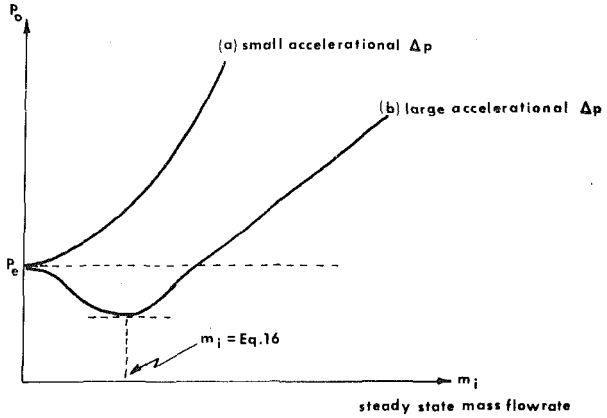

Fig. 8 Steady-state pressure drop characteristics in reflux condensation with inlet mass velocities less than flooding values

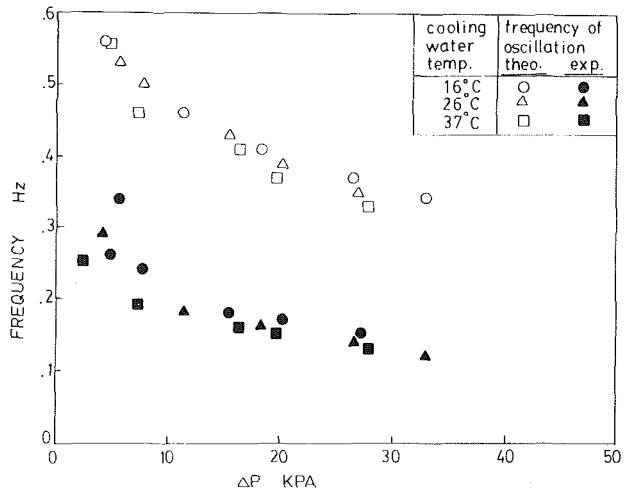

Fig. 9 Predicted and experimentally measured frequencies of oscillation in a reflux condensation system

greater than $m_i^2(1/C_v^2 + g\rho_f/C_L^2)$, $m_i = 0$ becomes a local maximum and a local minimum can be found at

$$m_i = \frac{2\left(\dfrac{1}{A^2\bar{\rho}_{av}} - 1/C_v^2 - g\rho_f/C_L^2\right)}{\dfrac{3}{8}\dfrac{fh_{fg}x_o}{DA^2\bar{\rho}_{av}f_q p}} \tag{16}$$

Thus, in general, the pressure drop characteristic will be shown as in Fig. 8.

Linear Analysis. One approach commonly adopted in studying the dynamic behavior of nonlinear systems is to linearize the model equations about the steady-state solution and examine the stability of the linearized system about this steady state using Laplace transform techniques [10]. Following this approach, the linearized form of equations (3-11) may be written as

$$\underset{\sim}{A}(\delta m_i \delta m^* \delta\eta_{2\phi} \delta\eta_L \delta\alpha \delta\Delta P_{01} \delta p_0)^T = \underset{\sim}{b}\delta m_o \tag{17}$$

where $\delta y(s) = [y(t) - \bar{y}]$ represents the Laplace transformed time domain perturbation. The coefficients $\underset{\sim}{A}$ and $\underset{\sim}{b}$ are functions only of the steady-state solution, system parameters, and the complex Laplace variables. Equation (17) describes the response of the perturbations on the left-hand side to a disturbance, δ_{m_o}, in the flow rate at the inlet of the test section. The stability of the response is determined by the roots of $\underset{\sim}{A}(s) = 0$. For the sake of brevity, we will not present here the complete forms of $\underset{\sim}{A}$ and $\underset{\sim}{b}$. These are available in [5]. Instead, we will concern ourselves only with a limiting case of interest. This is the situation when the total gravitational pressure drop in the system $g(\rho_f - \rho_{fg}\bar{\alpha})\bar{\eta}_{2\phi} + g\rho_f\bar{\eta}_L$, dominates all other pressure drops, a roughly correct assumption for our experiments. Then, system stability is determined by

$$s^2 + \frac{2g}{(\bar{u}_{2\phi} + \bar{\eta}_L)} = 0 \tag{18}$$

Equation (18) represents an undamped second-order system of frequency

$$\omega = \left[\frac{1}{\pi}\frac{g}{(\bar{\eta}_{2\phi} + \bar{\eta}_L)}\right]^{1/2} (Hz) \tag{19}$$

The oscillation mechanism is as follows. A momentary increase in the flow rate of steam to the test section increases the volume of the two-phase condensing region. The resulting increase in heat transfer area is more than adequate to condense the increased flow (because the ratio of area increase to volume increase is equal to $4/D >> 1$). This results in a greatly increased gravitational head and, therefore, a lowering of the steam inflow rate to the test section and increased drainage of condensate into the plenum. This causes the gravitational head to fall below its original level. The increased pressure differentual now causes the steam flow rate into the test section to increase, thus restarting the oscillation cycle. Thus, the oscillation is the result of heat transfer rate, pressure drop, and system inertia interaction.

Experimental Results. The analysis in the previous section should give a rough estimate of the frequency of the oscillations observed. Without a finite amplitude analysis, a more exact estimate is not possible.

The experimentally observed frequency of the oscillations (measured from the pressure drop traces) are shown as a function of pressure difference for various cooling water temperatures (and hence, heat fluxes) in Fig. 9. The frequencies determined by measurement are compared with the results of the analysis in the previous subsection (equation (19)) in Fig. 9. In general, the measured frequencies and those predicted by the analysis agree within a factor of two. This discrepancy can be attributed to the use of a highly simplified model and several approximations to describe a rather complex countercurrent condensing flow problem, e.g., the gravitational head may not completely dominate in our experiments. Furthermore, the experimentally measured frequency of the oscillations may not correspond to that predicted by the linear stability analysis but could correspond to the most unstable finite amplitude oscillation.

As shown in Fig. 9, the measured frequencies follow the same general pattern as the predictions. At low pressure differences, which correspond to a short single-phase region, the frequency of oscillations is high. This is explained by the fact that at low pressure differences, a short single-phase region is obtained, and this does not present a large inertia to resist pressure oscillation. The reverse is true for larger pressure differences.

Furthermore, it appears that at low cooling water inlet temperatures (16°C) frequencies of oscillations are higher than for warmer cooling water, for the whole range of pressure differences considered. This can be explained by considering equation (19) which indicates that the frequency of oscillations is inversely related to the two-phase and single-phase region lengths. As discussed previously, for a given pressure difference, the length of the two-phase region increases with increases in cooling water temperature. Therefore, from equation (19) the frequency of oscillations will decrease with an increase in length of the two-phase region (and hence increase in cooling water temperature). At

high pressure difference, the difference does not show up as clearly because the length of the two-phase region is small compared to the length of the single-phase region (see equation (19)).

Conclusions

Reflux condensation in a single vertical tube has been experimentally investigated using constant inlet and outlet pressure boundary conditions. The flow patterns that are usually obtained consist of a two-phase condensing region above the inlet followed by a single-phase (liquid) region. The average length of the two-phase region varies linearly with pressure difference between the inlet and outlet. The average length of the two-phase region depends on the coolant temperature and hence heat flux through the tube wall, but not on the pressure difference. These observations were explained by postulating that the inlet flow rate during refluxing is limited to the "flooding" flow rate. The single-phase region adjusts its length to give rise to a gravity head that balances any changes in the impressed pressure difference such that the inlet flow rate is maintained at flooding values. Transition to natural circulation occurs if the single-phase region is long enough to carry over the top of the U-bend. The maximum amount of liquid that can be held up in the tube occurs just before this transition. Thus, the maximum heat removal capability in reflux condensation may be estimated from the flooding flow rate, i.e., it will be $m_o\ h_{fg}$ per tube. (As explained earlier, this value may be somewhat increased by tube-to-tube instabilities or oscillations that cause dumping in the lower plenum). Another important parameter that can be estimated from this work is the liquid that is held up in a vertical tube during reflux condensation. Finally, the pressure difference at which transition to natural circulation will occur can be estimated if the wall heat flux can be estimated (so that the length of the two-phase region may be calculated) and the vertical tube height is known.

Low concentrations of noncondensibles do not appear to affect the pressure difference at which transition occurs but do increase the absolute pressure level. This is because the pressure above the single-phase region is then given by the sum of the partial pressures of steam (in equilibrium with the liquid surface) and the noncondensibles. In the absence of noncondensibles, the absolute pressure level is determined by the vapor pressure above the liquid column which in turn depends on the secondary side temperature (because the liquid column is not well mixed).

The stability of reflux condensation in a single vertical tube with constant pressure boundary conditions has also been investigated in this study using a linearized lumped parameter approach. The frequency of oscillations is found to be inversely proportional to the square root of the sum of the lengths of the two-phase and single-phase regions. The analysis predicts the trends in the oscillations observed in experiments, but the experimental frequencies are lower than predicted by a factor of two.

Results on system oscillations between refluxing and natural circulation, the effect of noncondensibles, multiple tubes, and multiple steam generators are being investigated and will be reported in the future.

References

1 Calia, C., and Griffith, P., "Modes of Circulation in an Inverted U-Tube Array with Condensation," HTD-Vol. 15, ASME, New York, 1981.

2 Dobran, G., "Condensation Heat Transfer and Flooding in a Counter-Current Subcooled Liquid and Saturated Vapour Flow," *Thermally-Hydraulics in Nuclear Power Technology*, HTD-Vol. 15, ASME, New York, 1981.

3 Hein, D., Rippel, R., and Weiss, P., "The Distribution of Gas in a U-Tube Heat Exchanger and its Influence on the Condensation Process," *Proceedings of the 7th International Heat Transfer Conference*, Vol. 5, 1982, pp. 467–474.

4 Westendorf, W. H., and Brown, W. F., "Stability of Intermixing of High-Velocity-Vapour With its Subcooled Liquid in Concurrent Streams," NASA-TND-3553, 1966.

5 Banerjee, S., Change, J.-S., Girard, R., Nijhawan, S., Krishnan, V-S., and Vandenbroek, M. A., "Transient Two-Phase Flow," Final Report to Ontario Hydro, Toronto, for period Aug. 1, 1979 to July 31, 1980.

6 Wallis, G. B., *One-Dimensional Two-Phase Flow*, McGraw-Hill, N.Y., 1969.

7 Nguyen, Q., Banerjee, S., "Flow Regimes and Heat Removal Mechanisms in a Single Inverted U-Tube Steam Condenser," ANS Transactions, Vol. 43, 1982, pp. 788–789.

8 Wedekind, G. L., Bhatt, B. L., and Beck, B. T., "A System Mean Void Fraction Model for Predicting Various Transient Phenomena Associated with Two-Phase Evaporating and Condensing Flows," *Int. J. Multiphase Flow*, Vol. 4, 1978, pp. 97–114.

9 Bhatt, B. L., and Wedekind, G. L., "A Self-Sustained Oscillatory Flow Phenomenon in Two-Phase Condensing Flow Systems," ASME JOURNAL OF HEAT TRANSFER, Vol. 102, No. 4, 1980, pp. 694–700.

10 Friedly, J. C., *Dynamic Behavior of Processes*, Prentice-Hall, Englewood Cliffs, N. J., 1972.

11 Ledinegg, M., "Instability of Flow during Natural and Forced Circulation," USAEC Report AEC-tr-1861, translated from Die Warme, Vol. 61, 1938, pp. 891–898.

12 Tong, L. S., *Boiling Heat Transfer and Two-Phase Flow*, John Wiley, New York, 1965.

Numerical Modeling of Wet Cooling Towers—Part 1: Mathematical and Physical Models

A. K. Majumdar
Mem. ASME

A. K. Singhal
Mem. ASME

CHAM of North America, Inc.,
Huntsville, Ala. 35810

D. B. Spalding
Mem. ASME
Imperial College,
London, England

The paper discusses the limitations of current practices of evaluating thermal performance of wet cooling towers and describes a more advanced mathematical model for mechanical and natural draft cooling towers. The mathematical model computes the two-dimensional distributions of: air velocity (two components); temperature, pressure, and moisture content; and water temperature. The downward direction of water flow is presumed. The local interphase heat and mass transfer rates are calculated from empirical correlations for which two options are provided. In the first option, only one constant (Ka, based on Merkel's approximations) is employed; in the second option, two separate constants for heat and mass transfer are used. Boundary conditions can be either of the prescribed cooling range or of the prescribed hot water temperature types. The governing equations are solved by a finite difference method. The model is embodied into a computer code (VERA2D) which is applicable for the natural and mechanical draft towers of both the crossflow and counterflow arrangements. Several applications of the code are described in Part II of the paper.

Introduction

The function of a wet cooling tower is to cool water by bringing it into direct contact with air. This cooling is accomplished by a combination of sensible heat transfer and evaporation of a small proportion of water. The contact time and area between air and water are increased by spraying water over a fill (a grid of bars or plates), and passing air through the fill. Two flow arrangements, counterflow and crossflow, are commonly used. The air flow is maintained by the buoyancy (chimney) effect in a natural draft tower, and by a fan in a mechanical draft tower. Schematic representations of commonly used designs are shown in Fig. 1.

In order to predict the thermal performance of a given design, one needs:

(*a*) A Mathematical model which provides an accurate solution of the conservation equations for mass, momentum, and energy

(*b*) Physical models to express resistance to airflow and interphase heat and mass transfer

The current methodology of cooling tower design lacks in both respects. The present paper describes a mathematical model to meet the first requirement and also provides suggestions for improvement in the second. It is also argued that the development of an accurate mathematical model is a primary requirement, since it aids in the development of physical models and associated empirical correlations.

Review of Existing Methods

Table 1 presents a summary of the capabilities and limitations of the existing methods of thermal performance analysis of cooling towers. In the conventional methods [1, 2], the ratio of water to air mass flow rate (L/G) to accomplish a specified cooling requirement is obtained from the solution of the following three equations:

1 Heat balance equation

2 Merkel's [3] equation expressing heat transfer being proportional to the enthalpy difference between saturated vapor and air

3 An empirical expression relating overall heat and mass transfer coefficient, Ka, with L/G

The set of equations is solved by graphical method (see Fig. 2). Merkel's equation is substituted into the heat balance equation, and the resulting equation is numerically integrated for a given cooling range. The integral is plotted against L/G. This is known as *demand curve* since it represents cooling requirement at a particular ambient condition. The heat and mass transfer coefficient of the fill, which is also expressed as a function of L/G, is superimposed on the same plot; this is known as the *characteristic curve*. The intersection of the demand and characteristic curves indicates the value of L/G for accomplishing the required cooling.

Cooling Tower Institute [1] has published a set of demand

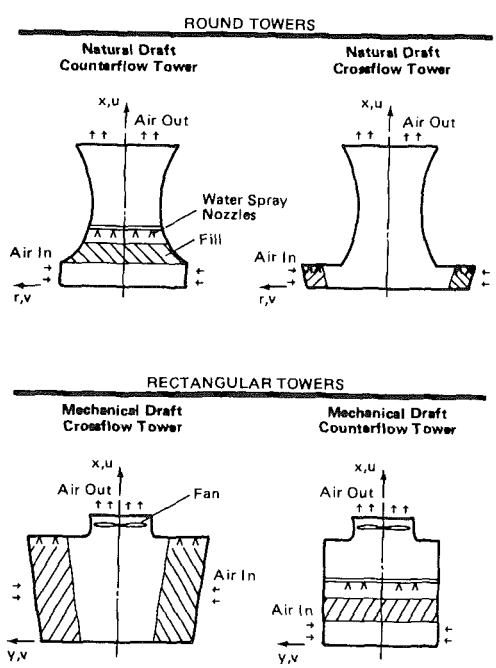

Fig. 1 *The coordinate systems for round and rectangular towers*

Contributed by the Heat Transfer Division and presented at the 21st ASME/AIChE National Heat Transfer Conference, Seattle, Washington, July 24-28, 1983. Manuscript received by the Heat Transfer Division July 19, 1982.

Table 1 A summary of the available mathematical models for analyzing wet cooling towers

Authors	Year	Applicability to the Types of Tower				Mathematical Models		Coupled (?)
		Natural		Mechanical		Heat Transfer	Air Flow	
		Counter	Cross	Counter	Cross			
Chilton (4)	1952	●				0D*	0D	Yes
Rish (5)	1961	●				0D	0D	Yes
Singham & Spalding (6)	1965	●				0D	0D	Yes
Foster & Wheeler	1943			●		0D	0D	No
Pritchard & Co. (8)	1957			●		0D	0D	No
Cooling Tower Inst. (1)	1967			●		0D	0D	No
Mesarovic (9)	1973	●				1D	0D	No
Zivi & Brand (10)	1956				●	2D	Not Solved	–
Baker & Shryock (11)	1961				●	2D	Not Solved	–
Cross et al (12)	1976			●	●	1D for Counter 2D for Cross	Not Solved	–
Kelly (2)	1970				●	2D	0D	No
Winnarski & Tichenor (13)	1978	●	●			1D for Counter 2D for Cross	0D	Yes
Penny, Rosten & Spalding (14)	1979	●	●			2D	2D	Yes
I.A. Furzer (15)	1978	●				2D	2D	Yes
Majumdar, Singhal and Spalding (VERA2D Code)	1981	●	●	●	●	2D	2D	Yes

*0D = Zero Dimensional (Global) Model

curves for counterflow towers by integrating the one-dimensional thermal equation by Tchebycheff's method. Zivi and Brandt [10] developed a numerical method for integrating this equation for crossflows in two dimensions. By making use of this method, Kelly [2] generated a similar set of demand curves for crossflow towers. The main limitations of these simplified methods are discussed below.

Lack of Flexibility to Accept Empirical Input in a General Form. The graphical method of performance evaluation makes a presupposition that heat and mass transfer coefficient (KaV/L) is a function of L/G only (Fig. 2). This assumption is questionable and restricts the applicability of data. A rigorous processing of test data could reveal that it is more appropriate to express heat and mass transfer coefficients in terms of fundamental dimensionless parameters such as Reynolds number, Prandtl number, and other geometrical parameters. It is difficult, however, to generalize the graphical methods [1, 2] to use different forms of empirical correlations.

Simplifying Assumptions of Merkel's Equation. Merkel [2] expressed the heat and mass transfer process as a combined process by considering the enthalpy difference as the basic driving force. Therefore, Merkel's equation expresses heat transfer as a product of overall heat and mass transfer coefficient (Ka) and the difference between the enthalpy of

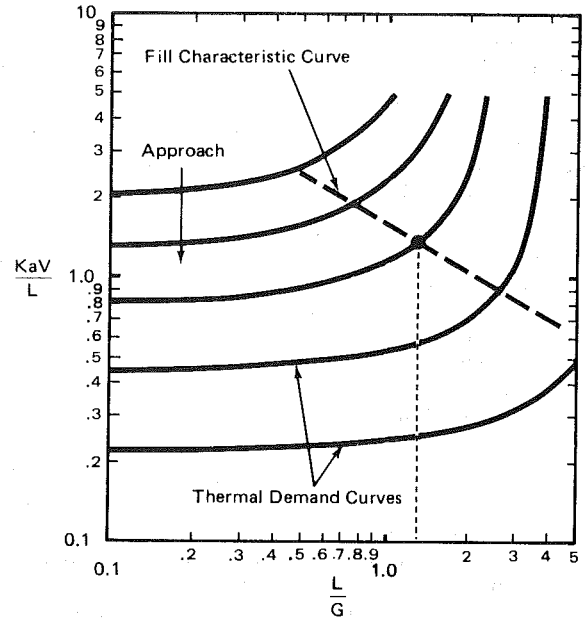

Fig. 2 Graphical solution of thermal equation at a given range and wet-bulb temperature

saturated air at the water temperature (h_S), and the enthalpy of the main air stream (h_G). Mathematically,

$$q''' = \mathrm{Ka}(h_S - h_G) \tag{1}$$

Since, in reality, total heat transfer from water to air consists of sensible as well as evaporative heat transfer, a general expression of heat transfer should at least have:

(*a*) Two separate coefficients for heat and mass transfer
(*b*) Two driving forces: temperature difference and vapor fraction difference

A recognition of two driving forces calls for the solution of an additional conservation equation of moisture fraction, which is not feasible in most of the existing methods.

Nonuniformity of Flow. In both natural and mechanical draft towers, air changes its direction as it enters the tower horizontally and leaves vertically. Therefore, the air flow

Nomenclature

a = area of transfer surface per unit volume, m^2/m^3
a_E, a_W, a_N, a_S = coefficients of finite difference equation (13), kg/s
A = cross-sectional area, m^2
$C_{P,\mathrm{air}}$ = specific heat of dry air, J/kg°C
$C_{P,\mathrm{vapor}}$ = specific heat of vapor, J/kg°C
C_G = specific heat of moist air, J/kg°C
D = diameter of the tower, m
f_G = moisture fraction of moist air, kg/kg
f_G^* = moisture fraction of dry air, kg/kg
f_S = moisture fraction of saturated moist air, kg/kg
f_x, f_y = resistances to air flow in x- and y-directions respectively, N/m^3
G = mass flow rate of dry air, kg/s
G' = mass flux of dry air, kg/m^2s
g = gravitational acceleration, m/s^2
H = heat transfer coefficient, $W/m^2\,°C$
H_{Fill} = height of the fill, m
h_G = specific enthalpy of moist air, J/kg
h_G^* = specific enthalpy of dry air, J/kg
h_F = specific enthalpy of water, J/kg
h_S = specific enthalpy of saturated moist air, J/kg
h_T = specific enthalpy of transferred substance, J/kg
h_{fg} = latent heat of vaporization, J/kg
h_{stack} = height of the stack, m
K = mass transfer coefficient, kg/m^2s
L = mass flow rate of air, kg/s
L' = mass flux of water, kg/m^2s
m_v''' = rate of mass transfer

through the tower deviates significantly from uniformity. Nonuniformity in flow distribution can be accounted for only by performing two- or three-dimensional analysis of fluid flow and heat transfer inside the tower.

Coupling Between Fluid Flow and Heat Transfer. The fluid flow and heat transfer processes in a natural draft tower are strongly coupled, because:

(*a*) The amount of air flow through the tower depends on the difference between the density of air inside the tower and that of ambient air

(*b*) The density of air inside the tower depends on the extent of heat and mass transfer from water to air in the fill and spray region

(*c*) Heat and mass transfer from water to air depends on the available air flow rate

A schematic representation of this coupling of process is shown in Fig. 3. Similar coupling exists in mechanical draft towers; however, its influence on airflow rate is not so important because of the presence of a fan.

Earlier mathematical models, such as Singham and Spalding [6] and Winnarski and Tichenor [13], attempted to account for this coupling by solving a simplified equation called a "buoyancy equation." This equation is based on the postulation that the hydrostatic pressure difference, caused by the difference in densities of the warm moist air inside the tower and that of the cooler drier air outside, is equal to the pressure loss that would be experienced by the air stream flowing through the tower in the absence of hydrostatic pressure difference. Mathematically,

$$(\rho_{amb} - \rho_{tower})gH = N_v\left[\frac{1}{2}\rho_{amb}\left(\frac{\dot{m}_G}{\pi D^2/4}\right)^2\right] \qquad (2)$$

The left-hand side of equation (2) represnets the driving force due to buoyancy. The right-hand side represents the resistance to flow of air through the tower. While calculating ρ_{tower}, air is assumed saturated above the fill. Since equation (2) neglects several terms such as due to convection, pressure gradient, and wall friction, and since it does not account for spatial variation, the coupling of processes is not represented adequately.

Effect of Ambient Pressure Variation on Evaporation. The rate of evaporation from water depends on temperature of water as well as pressure. Thus in Merkel's equation, h_S is a function of water temperature and pressure. Current methods [1, 2] employ a polynomial expression to calculate enthalpy of saturated air, and therefore, they are applicable for standard atmospheric pressure only. In order to account for the effect of ambient pressure, one needs to:

(*a*) Express h_S as a function of the moisture fraction of saturated air, f_S

(*b*) Evaluate f_S from fundamental equations, e.g., Clasius-Clapeyron equation and law of ideal gas mixture

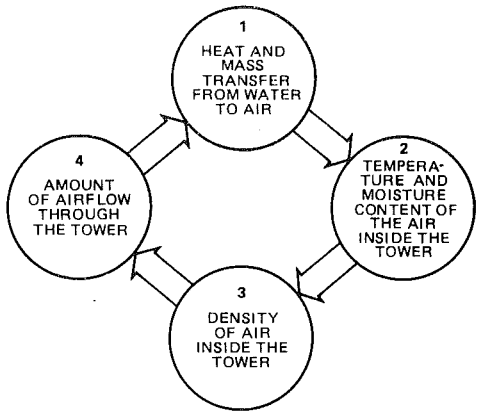

Fig. 3 Schematic representation of the coupling between fluid flow and heat transfer processes in a natural draft tower

Present Mathematical Model

The present model treats airflow to be two-dimensional and elliptic, while the water flow is considered to be one-dimensional. It obtains simultaneous solution of conservation equations for:

(*a*) Mass continuity of air
(*b*) Mass fraction of moisture in air
(*c*) Mass continuity of water
(*d*) Air momentum in vertical direction
(*e*) Air momentum in active horizontal direction
(*f*) Enthalpy of air
(*g*) Enthalpy of water

Nomenclature (cont.)

per unit volume, kg/m^{3}s
N_v = number of velocity heads lost in the tower
n = empirical constant for fill
p = pressure, Pa
P = input power to fan, W
q''' = rate of heat transfer per unit volume, W/m^3
R = universal gas constant, J/kg-mol K
$\dot{q}''$ = rate of heat transfer per unit area of transfer surface, W/m^2
r = radial coordinate, m
S_u, S_ρ = components of source term of finite difference equation
T = temperature, °C
u = vertical component of velocity, m/s
v = horizontal component of velocity, m/s
V = tower volume per unit plan area, m^3/m^2
V_G = specific volume of air, m^3/kg
W = molecular weight
W_{Fill} = width of the fill, m
x = vertical Cartesian coordinate, m
y = horizontal Cartesian coordinate, m
Γ_{eff} = effective exchange coefficient, kg/ms
λ = empirical constant for fill, m^{-1}
μ_{eff} = effective viscosity, kg/ms
ρ = density of moist air, kg/m^3
σ_{eff} = effective Prandtl number, dimensionless
ϕ = dependent variable

Subscript

amb = ambient
bs = base of the fan stack
DB = dry bulb
elim = eliminator
F = water
G = moist air
S = saturated
WB = wet bulb

The calculation domain extends from the vertical inlet section to the horizontal outlet plane and thus covers the entire cooling tower. For the sake of generality, both polar and Cartesian coordinates are considered (Fig. 1). Following are the governing conservation equations in polar coordinates.

Mass of Air:

$$\frac{\partial}{\partial x}(\rho u) + \frac{1}{r}\frac{\partial}{\partial r}(\rho r v) = \dot{m}_v''' \tag{3}$$

Mass of Water:

$$\frac{\partial}{\partial x}(\rho_F u_F) = \dot{m}_v''' \tag{4}$$

x-Direction Momentum:

$$\frac{\partial}{\partial x}(\rho u^2) + \frac{1}{r}\frac{\partial}{\partial r}(\rho r v u) - \frac{\partial}{\partial x}\left(\mu_{\text{eff}}\frac{\partial v}{\partial x}\right) - \frac{1}{r}\frac{\partial}{\partial r}\left(r\,\mu_{\text{eff}}\frac{\partial v}{\partial r}\right) = -\frac{\partial p}{\partial x} - f_x - (\rho - \rho_{\text{amb}})g \tag{5}$$

r-Direction Momentum:

$$\frac{\partial}{\partial x}(\rho u v) + \frac{1}{r}\frac{\partial}{\partial r}(\rho r v^2) - \frac{\partial}{\partial x}\left(\mu_{\text{eff}}\frac{\partial v}{\partial x}\right) - \frac{1}{r}\frac{\partial}{\partial r}\left(r\,\mu_{\text{eff}}\frac{\partial v}{\partial r}\right) = -\frac{\partial p}{\partial r} - f_y \tag{6}$$

Air Enthalpy:

$$\frac{\partial}{\partial x}(\rho u h_G) + \frac{1}{r}\frac{\partial}{\partial r}(\rho r v h_G) - \frac{\partial}{\partial x}\left(\Gamma_{\text{eff}}\frac{\partial h_G}{\partial x}\right) - \frac{1}{r}\frac{\partial}{\partial r}\left(r\,\Gamma_{\text{eff}}\frac{\partial h_G}{\partial r}\right) = \dot{q}''' \tag{7}$$

Water Enthalpy:

$$\frac{\partial}{\partial x}(\rho_F u_F h_F) = -\dot{q}''' \tag{8}$$

Moisture Fraction of Air:

$$\frac{\partial}{\partial x}(\rho u f_G) + \frac{1}{r}\frac{\partial}{\partial r}(\rho r v f_G) - \frac{\partial}{\partial x}\left(\Gamma_{\text{eff}}\frac{\partial f_G}{\partial x}\right) - \frac{1}{r}\frac{\partial}{\partial r}\left(r\Gamma_{\text{eff}}\frac{\partial f_G}{\partial r}\right) = \dot{m}_v''' \tag{9}$$

Equation of State:

$$\rho = \frac{p W_G}{R(T_{DB} + 273)} \tag{10}$$

The following features of the conservation equations (3-10) may be noted.

- All conservation equations for air are coupled through convective fluxes (ρu and ρv), In addition, momentum equations (5) and (6) are coupled through pressure.
- The gravity term in equation (5) uses a density difference ($\rho - \rho_{\text{amb}}$) rather than density (ρ). This is in accordance with the reduced pressure method [19]. The pressure, p, used in these equations is the reduced pressure, i.e., the relative pressure with reference to the ambient pressure at the same elevation. This practice of using reduced pressure and density difference is based on the exact transformations employing the following relation:

$$p = p_{\text{static}} + \rho_{\text{amb}} g\, x$$

- By setting r to unity and changing $\partial/\partial r$ to $\partial/\partial y$, the above set of equations become appropriate for the Cartesian coordinates in rectangular towers.

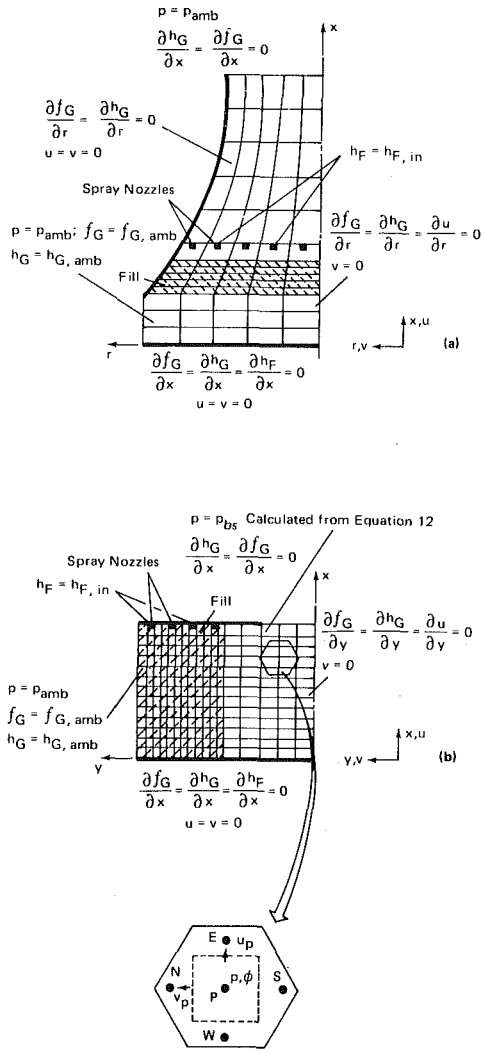

Fig. 4 Calculation domain, grid layout and boundary conditions for (a) natural-draft counterflow tower and (b) mechanical-draft crossflow tower

- $\dot{m}_v'''$ and $\dot{q}'''$ represent the sources of mass and enthalpy, and f_x and f_y represent resistances to air flow due to the presence of solid obstacles. Expressions for calculating $\dot{m}_v'''$, $\dot{q}'''$, f_x, and f_y are described later in the section entitled "Physical Models."
- h_G is the specific enthalpy of moist air, and f_G is the fraction of vapor content of moist air. Since hydrodynamic equations solve for velocities and pressure of moist air, it is appropriate to solve for specific enthalpy and moisture fraction of moist air. However, specific enthalpy of dry air, h_G^*, and moisture fraction of dry air, f_G^*, can be evaluated from the following expression:

$$h_G^* = \frac{h_G}{1 - f_G} \tag{11}$$

$$f_G^* = \frac{h_G}{1 - f_G} \tag{12}$$

Finite Difference Equations. The calculation domain is subdivided into finite number of control cells (Fig. 4). The finite difference equations are obtained by integrating the partial differential equation over the finite volume represented by a cell [20].

Typical grid distributions for a natural draft counterflow

tower and a mechanical draft crossflow tower have been shown in Fig. 4. Nonuniform grid distributions are employed with larger number of control cells located in the fill region. Grid is nonorthogonal to suit the hyperbolic shape of natural draft tower. All scalar quantities (such as p, h_G, f_G, etc.) are calculated at the center of the control cells; and velocity components (u and v) are calculated at the cell faces.

The general form of finite difference equations is

$$\phi_P = \frac{a_E\phi_E + a_W\phi_W + a_N\phi_N + a_S\phi_S + S_U}{a_E + a_W + a_N + a_S - S_P} \tag{13}$$

where ϕ stands for any dependent variable such as u, v, h_G, h_F, and f_G; and link coefficients a_E, a_W, a_N, and a_S express the effects of convection and diffusion between the grid point, P, and its neighboring grid nodes in East, West, North and South directions, respectively. S_U and S_P are the components of source term, S, which is linearized as:

$$S = S_U + S_P\phi$$

Boundary Conditions. The following quantities are specified as system boundary conditions:

1 Hot water flow rate
2 Either cooling range or hot water temperature
3 Dry-bulb temperature, T_{DB}
4 Wet-bulb temperature, T_{WB}
5 Ambient pressure

The specified conditions for each dependent variable at all four boundaries of the calculation domain are also shown in Fig. 4.

The moisutre fraction and enthalpy of inlet air are calculated from the dry-bulb and wet-bulb temperatures by employing the following thermodynamic relations.

$$f_{G,\text{amb}} = f_s - \frac{C_G L_e (T_{DB} - T_{WB})(1 - f_s)}{h_{fg}} \tag{14}$$

$$h_{G,\text{amb}} = (1 - f_{G,\text{amb}})\, C_G\, T_{DB} + f_{G,\text{amb}}\, h_{fg} \tag{15}$$

Equation (14) has been derived from the thermal equilibrium equation for a wet bulb temperature [21]. Equation (15) follows from the definition of specific enthalpy of moist air. Calculation of f_s is to be described in the section of Physical Models.

Pressures are specified at the inlet and outlet boundaries, while the velocities are calculated from the local differences between the ambient pressure and the pressure inside the tower. Pressures at the inlet and outlet sections of a tower are the same as that of ambient. For mechanical draft towers, the fan and stack are simulated by way of a "point" model, i.e., no distributions of flow variables are calculated in the stack. The pressure at the bottom of the stack, p_{bs}, is calculated from Bernoulli's equation by considering the input power and efficiency of fan and the area changes in stack. Appendix A describes the calculation steps for p_{bs}. The final form is

$$p_{bs} = p_{\text{amb}} - \frac{\rho\eta_{\text{fan}} P}{\dot{m}_G} - \frac{1}{2}\rho\, u_{\text{fan}}^2 \left[\left(\frac{A_{\text{fan}}}{A_{\text{plenum}}}\right)^2 - \left(\frac{A_{\text{fan}}}{A_{\text{stack}}}\right)^2 - N_{\text{stack}}\right] - (\rho_{\text{amb}} - \rho) g\, h_{\text{stack}} \tag{16}$$

where P is the input power to fan and N_{stack} is the number of velocity heads ($= \rho\, u_{\text{fan}}^2/2$) lost in the stack.

Solution Procedure. Since the governing equations are coupled and nonlinear, they have to be solved by means of an iterative procedure. An implicit solution scheme based on the procedures of [17] and [18] is employed. The main steps of the calculation procedure are depicted in Fig. 5. The convergence of numerical scheme is checked by the normalized residual errors of all conservation equations in each control cell of the calculation domain.

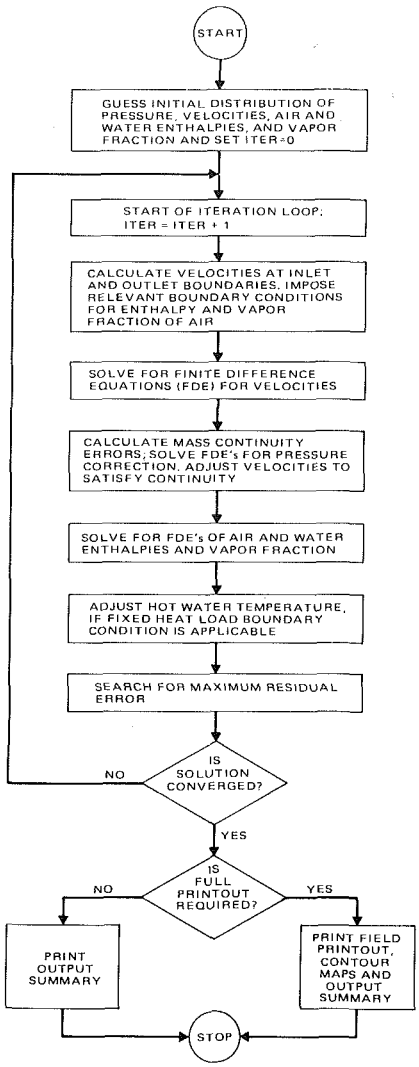

Fig. 5 Illustration of the main calculation steps in VERA2D

Physical Models

Resistances to Air Flow. The flow resistances offered by various solid obstacles and water flow within the tower are expressed for each control cell in the following integrated form.

$$\int f_x dV = N \cdot \frac{1}{2}\rho u^2 \Delta V + N_{\text{louver}} \frac{1}{2}\rho u^2 \Delta A + N_{\text{elim}} \frac{1}{2}\rho u^2 \Delta A \tag{17}$$

$$\int f_y dV = N \cdot \frac{1}{2}\rho v^2 \Delta V + N_{\text{louver}} \frac{1}{2}\rho v^2 \Delta A + N_{\text{elim}} \frac{1}{2}\rho v^2 \Delta A \tag{18}$$

where ΔV is the volume, and ΔA is the area of the control cell face normal to the velocity component. N is the number of velocity heads lost per unit air travel distance in the fill or in the spray region. N_{louver} and N_{elim} are the total number of

velocity heads lost in the louver and eliminator, respectively. Available empirical data for coefficients of resistances to airflow in cooling towers have been compiled and presented in a separate report [23].

Turbulence Model for Air Flow. The effective viscosity of air is calculated from an algebraic model of turbulence [24] which states $\mu_{\text{eff}} = C\,\rho_{\text{amb}}\,u_{\text{avg}}\,y_l$, where u_{avg} is the average flow velocity in the tower, y_l is characteristic length, and C is an empirical constant (= to 0.06). The length scale, y_l, is taken to be equal to the pitch of fill elements. Effective exchange coefficients (Γ_{eff}) for enthalpy and moisture fraction are calculated as

$$\Gamma_{\text{eff}} = \frac{\mu_{\text{eff}}}{\sigma_{\text{eff}}} \tag{19}$$

where σ_{eff} is the effective Prandtl number and has been assumed to be unity.

More sophisticated models of turbulence [24] will not be useful unless control cell dimensions are smaller than the pitch of the fill element. The typical grids in a natural draft counterflow tower are 2 to 3 m wide, whereas the pitch of the fill elements are in the order of 2 to 5 cm. Computations with several control cells between successive fill elements would be extremely expensive, and cannot be justified unless the accuracy of empirical correlations for pressure drop and heat and mass transfer are significantly improved.

Psychrometric Property for Air. The calculation of $\dot{m}_v'''$ [equation (9)] and $f_{G,\text{amb}}$ [equation (14)] requires a knowledge of moisture fraction of saturated air, f_s. This f_s is a function of pressure and temperature and is determined with the help of Clausius-Clapeyron equations and the equation of ideal gas mixture. These equations are

$$\frac{d\,p_S}{dT} = \frac{h_{fg}}{T\,V_G} \tag{20}$$

$$\frac{f_S}{1-f_S} = \frac{W_{\text{water}}}{W_{\text{air}}}\,\frac{p_S}{p_{\text{amb}}-p_S} \tag{21}$$

where p_S and V_G are the saturation pressure of water vapor at the water temperature and specific volume of moist air. Further details on integration of equation (20) appear in Appendix B. The use of fundamental equations, rather than tables or polynomial curve fits, increases the range of applicability of the method. Equations (20) and (21) are applicable to all ambient pressures.

Heat and Mass Transfer Models.

The Current Practices. Equations (7) and (9) require the expressions for the rates of heat and mass transfer from water to air (i.e., for $\dot{q}'''$ and $\dot{m}'''$). The current practice for $\dot{q}'''$ is based on the use of Merkel's model, which is

$$\dot{q}''' = \text{Ka}(h_S - h_G) \tag{22}$$

where Ka is an empirical mass transfer coefficient, and $h_S - h_G$ is the difference between the enthalpies of the saturated air and dry air. For counterflow fills and sprays, Lowe and Christie [16] have reported empirical data in the following form

$$\frac{\text{Ka}}{L'} = \lambda\left(\frac{L'}{G'}\right)^{-n} \tag{23}$$

where L' and G' are the mass fluxes of water and dry air, and λ and n are empirical constants. Different fills have different values of λ and n.

For crossflow fills, Kelly [2] has reported data for Ka values as a function of L/G for different heights and widths of a fill. As a result, a large number of fill characteristic curves appear in [2]. Further analysis of this data has indicated that Ka can be expressed as a function of the product of water and dry air mass flow ratio (L/G) and fill aspect ratio ($H_{\text{Fill}}/W_{\text{Fill}}$). For example, Fig. 6 shows the data for the plastic wedge fill. Therefore, the Ka correlation is considered to be of the following form

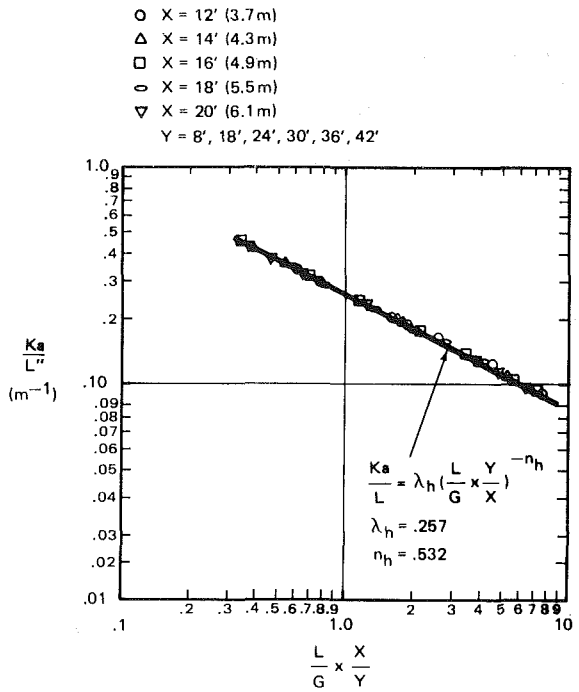

Fig. 6 Heat transfer characteristics of standard wood lath crossflow fill (vertical pitch = 10.16 cm, horizontal pitch = 20.32 cm)

$$\frac{\text{Ka}}{L'} = \lambda\left(\frac{L}{G}\,\frac{H_{\text{Fill}}}{W_{\text{Fill}}}\right)^{-n} \tag{24}$$

It may be noted that for round towers, $L' \neq L/W_{\text{Fill}}$ and $G' \neq G/H_{\text{Fill}}$. Available data for both counterflow and crossflow fills have been compiled and reported [23].

An expression of evaporation rate, $\dot{m}_v'''$, consistent with equation (22), is

$$\dot{m}_v''' = \text{Ka}(f_S - f_G) \tag{25}$$

Remarks on the Current Practice. The current practice of calculating $\dot{q}'''$ employs only one coefficient (Ka) to represent both sensible and evaporative heat transfer processes. Also, the coefficient, Ka, is expressed as a function of water to dry air mass flow ratio, (L/G), only. Such simplifications have narrowed down the range of applicability of the empirical data. Strictly speaking, the data are applicable only for the conditions at which they were deduced from the experiments. Evidence of such restrictions can be seen from the need of ad hoc corrections, such as the hot water correction [11, 25, 26].

Suggestions for Improvement. These limitations can be removed by employing a more accurate expression for heat and mass transfer from water to air and by expressing the coefficients of heat and mass transfer in terms of fundamental dimensionless parameters, such as Reynolds number, Prandtl number, and Weber number.

The complete expression of heat transfer can be written as

$$\dot{q}''' = \frac{T_F - T_G + \dfrac{\text{Ka}}{Ha_{\text{air}}}\left(\dfrac{f_s - f_G}{1-f_s}\right)h_T}{\dfrac{1}{Ha_{\text{water}}} + \dfrac{1}{Ha_{\text{air}}}} \tag{26}$$

where

$$h_T = C_P, \text{vapor } T_G + h_{fg}. \quad (27)$$

Equation (26) has been derived from the Reynolds flow model [21, 22]. Ha_{water}, Ha_{air} are the heat transfer coefficients for water and air side, and Ka is the mass transfer coefficient. These three coefficients are required to be determined from experiments. The assumption of $Ha_{\text{water}} >> Ha_{\text{air}}$ simplifies equation (26) to

$$\dot{q}''' = Ha_{\text{air}}(T_F - T_G) + \text{Ka}\frac{f_s - f_G}{1 - f_s} h_T \quad (28)$$

Equation (28) requires only two empirical coefficients, namely, Ka and Ha_{air}.

Two further assumptions, namely, $f_s << 1$ and $h_{fg} \cong h_T$, reduce equation (28) to

$$\dot{q}''' = Ha_{\text{air}}(T_F - T_G) + \text{Ka}(f_s - f_G) h_{fg} \quad (29)$$

Finally, with the additional assumption that Lewis number H/KC_G unity, equation (29) reduces to Merkel's equation (25), which involves only one empirical constant.

Further discussion and analysis of the abovementioned models of heat and mass transfer and possible ways of evaluating necessary coefficients will be the subject of a future communication.

The present mathematical model (embodied into a computer code VERA2D) has built-in options for employing equations (25), (28), or (29). Option for equation (26) can be easily included. Therefore, VERA2D provides a framework for the development of a suitable heat and mass transfer model and associated empirical coefficients. Until such developments, the option of Merkel's model [equation (25)] must be used for consistency with the available empirical data.

Summary

A general, two-dimensional mathematical model applicable for natural and mechanical draft towers of counterflow or crossflow arrangements has been described. The main features of the present model are the following:

(*a*) Simultaneous solutions of coupled nonlinear equations governing fluid flow, heat transfer and mass transfer are obtained.

(*b*) Physical model for heat and mass transfer has been incorporated in a manner which permits separate calculation for sensible and evaporative heat transfer.

(*c*) Any form of empirical correlation for heat and mass transfer can be inserted in the computer program.

(*d*) The model has been embodied in a user-oriented computer code VERA2D [22] which can be used for performance evaluations as well as for developing physical models and associated empirical correlations. Some applications of the computer code have been described in Part 2 of the paper [28].

(*e*) The model is extensible for three-dimensional and transient analysis to account for effects such as cross wind, blockages inside the tower, and changes in operational and climatic conditions.

Acknowledgment

The work has been supported by Electric Power Research Institute, Palo Alto, California under the contract number RP 1262-1. The authors wish to acknowledge Mr. Hugh E. Reilly of EPRI for his comments and suggestions. Thanks are due to Kelli King and Lynn Wilson for the preparation of the typescript.

References

1 "Cooling Tower Performance Curves," Cooling Tower Institute, Houston, Texas, 1967.

2 Kelly, N. W., "Kelly's Handbook of Crossflow Cooling Tower Performance," Neil W. Kelly and Associates, Kansas City, Mo., 1976.

3 Merkel, F., "Evaporative Cooling," *Zeits. Verein deutscher Ingenieure*, Vol. 70, 1926, pp. 123–128.

4 Chilton, H., "Performance of Natural Draught Water Cooling Towers," *Proceedings Inst. Elec. Eng. London*, Vol. 99, 1952, pp. 440–452.

5 Rish, R. F., "The Design of a Natural Draught Cooling Tower," *Proceedings International Heat Transfer Conference*, Colorado, pt. V, 1961, pp. 951–958.

6 Singham, J. R., and Spalding, D. B., "The Performance of Natural Draught Cooling Towers: Comparison of Theory with Experiment," *Second Int. Congress on Chem. Eng., Chem. Equipment and Automation*, Marienbad, Czechoslovakia, 1965; (reprinted by Department of Mechanical Engineering Imperial College, Aug. 1965, Report No. ED/TN/1).

7 Foster Wheeler Corporation, New York, Bulletin CT43-2, 1943.

8 J. F. Pritchard and Co. of California. "Counterflow Cooling Tower Performance," 1957.

9 Mesarovic, M. M., "Ararat—A Computer Code for Thermal Design of Cooling Towers," *Nuclear Engineering and Design*, Vol. 24, 1973, pp. 57–70.

10 Zivi, S. M., and Brand, B. B., "An Analysis of the Crossflow Cooling Tower," *Refrigerating Engineering*, Vol. 64, 1956, pp. 31–34 and 90–92.

11 Baker, D. R., and Shryock, H. A., "A Comprehensive Approach to the Analysis of Cooling Tower Performance," ASME JOURNAL OF HEAT TRANSFER, Vol. 83, 1961, pp. 339–349.

12 Cross, K. E., Park, J. E., Vance, J. M., and Van Wie, N. H., "Theory and Application of Engineering Models for Crossflow and Counterflow Induced Draft Cooling Towers," Union Carbide Report No. K/CSD-1, May 1976.

13 Winniarski, L. D., and Tichenor, B. A., "Model of Natural Draft Cooling Tower Performance," *Journal of the Sanitary Engineering Division*, Proceedings of the American Society of Civil Engineers, Vol. 96, 1970, pp. 927–943.

14 Penney, T. R., Rosten, H. I., and Spalding, D. B., "Validation of Cooling Tower Analyzer," Vol. 1 and 2, EPRI Report No. FP-1279, Dec. 1979.

15 Furzer, I. A., "An Improved Thermodynamic Analysis of Hyperbolic Cooling Towers," *Proceedings of Sixth International Heat Transfer Conference*, Toronto, Aug. 7–11, 1978, pp. 103–109.

16 Lowe, H. J., and Christie, D. G., "Heat Transfer and Pressure Drop Data on Cooling Tower Packings, and Model Studies of the Resistance of Natural Draught Towers to Air Flow," *Proceedings International Heat Transfer Conference*, Colorado, pt. V, 1961, pp. 933–950.

17 Patankar, S. V., and Spalding, D. B., "A Calculation Procedure for Heat Mass and Momentum Transfer in Three Dimensional Parabolic Flows," *International Journal of Heat and Mass Transfer*, Vol. 15, 1972, pp. 1787–1806.

18 Singhal, A. K., and Spalding, D. B., "Mathematical Modeling of Multiphase Flow and Heat Transfer in Steam Generators," *Multiphase Transport Fundamentals, Reactor Safety, Applications*, Vol. 1–5, Hemisphere Publishing Corporation, Washington, D.C., 1980, pp. 373–406.

19 Spalding, D. B., "The Calculation of Free-Convection Phenomena in Gas-Liquid Mixtures Heat Transfer," *Heat Transfer and Turbulent Buoyant Convection*, Vol. II, Hemisphere Publishing Corporation, Washington, D.C., 1976, pp. 569–586.

20 Patankar, S. V., *Numerical Heat Transfer*, Hemisphere Publishing Corporation, Washington, D.C., 1980.

21 Spalding, D. B., *Convective Mass Transfer*, Edward Arnold Limited, London, 1963.

22 Majumdar, A. K., Singhal, A. K., and Spalding, D. B., "VERA2D—A Computer Program for Two-Dimensional Analysis of Flow, Heat and Mass Transfer in Evaporative Cooling Towers: Vol. 1—Mathematical Formulation, Solution Procedure, and Applications," EPRI report, Contract No. RP 1262-1, 1983.

23 Majumdar, A. K., and Singhal, A. K., "VERA2D—A Computer Program for Two-Dimensional Analysis of Flow, Heat and Mass Transfer in Evaporative Cooling Towers: Vol. II—User's Manual," EPRI Report No. CS-2923, Contract No. RP 1262-1, 1983.

24 Launder, B. E., and Spalding, D. B., *Mathematical Model of Turbulence*, Academic Press, 1972.

25 Kelly, N. W., "A Blue Print for the Preparation of Crossflow Cooling Tower Characteristics," Cooling Tower Institute Paper TP-146A, Jan. 1976.

26 Hallet, G. F., "A Review of Present and Recently Proposed Methods for Thermal Evaluation of Atmospheric Water Cooling Equipment," Cooling Tower Institute Paper No. 224A, Jan. 1980.

27 Keenan, J. H., Keyes, F. G., Hill, P. G., and Moore, J. G., *Steam Tables*, John Wiley and Sons, 1979.

28 Majumdar, A. K., Singhal, A. K., Reilly, H. E., and Bartz, J. A., "Numerical Modeling of Wet Cooling Towers—Part 2: Application to Natural and Mechanical Draft Towers," ASME JOURNAL OF HEAT TRANSFER, Vol. 105, No. 4, Nov. 1983, pp. 736–743.

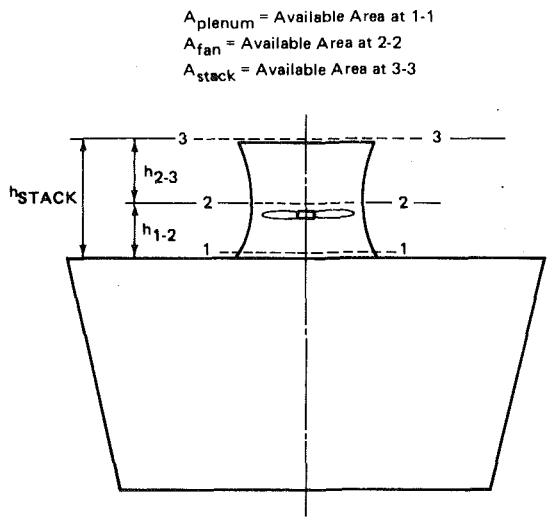

Fig. 7 Schematic representation of fan and stack in a mechanical draft tower

APPENDIX A

Modeling of Fan and Its Stack

The fan and stack have been schematically shown in Fig. 7. p_{bs} of equation (16) is determined from Bernoulli's equation applied in the stack; this accounts for:

(*a*) Energy supplied by fan
(*b*) Energy available due to buoyancy in the stack
(*c*) Energy loss due to skin friction and form drag
(*d*) Energy leaving tower

Calculation of P_{bs}. Pressure at plane 2 (p_2), shown in Fig. 7, is related with the ambient pressure (= to p_{amb}) by applying Bernoulli's equation and continuity equation between plane 2 and 3.

$$p_2 = p_{amb} - \frac{1}{2}\rho u_{fan}^2\left[1-\left(\frac{A_{fan}}{A_{stack}}\right)\right] - (\rho_{amb}-\rho)g\,h_{2-3} + h_{L_{2-3}} \quad \text{(A1)}$$

Similarly, pressure at plane 1 (= to p_{bs}) is related with the pressure at plane 2 (p_2).

$$p_{bs} = p_2 - \frac{\rho\,\eta_{fan}P}{G} + \frac{1}{2}\rho u_{fan}^2\left[1-\left(\frac{A_{fan}}{A_{plenum}}\right)^2\right] - (\rho_{amb}-\rho)g\,h_{1-2} + h_{L_{1-2}} \quad \text{(A2)}$$

Substituting equation (A2) in equation (A1) and introducing the following definitions

$$h_{stack} = h_{1-2} + h_{2-3} \quad \text{(A3)}$$

$$h_L = h_{L_{1-2}} + h_{L_{2-3}} = N_{stack}\frac{1}{2}\rho u_{fan}^2 \quad \text{(A4)}$$

The final expression of p_{bs} is written as

$$p_{bs} = p_{amb} - \frac{\rho\,\eta_{fan}P}{G} - \frac{1}{2}\rho u_{fan}^2\left[\left(\frac{A_{fan}}{A_{plenum}}\right)^2 - \left(\frac{A_{fan}}{A_{stack}}\right)^2 - N_{stack}\right] - (\rho_{amb}-\rho)g\,h_{stack} \quad \text{(A5)}$$

APPENDIX B

Integration of Clausius-Clapeyron Equation

The Clausius-Clapeyron equation (20) is integrated by using the equation of state

$$V_G = \frac{R}{W_{water}}\frac{T}{p_S} \quad \text{(B1)}$$

and the correlation of latent heat with temperature

$$h_{fg} = A_o - B_o T \quad \text{(B2)}$$

where A_o (= 3.148856×10^6) and B_o (= 2.372×10^3) are curve fit constants for h_{fg} in J/kg and T is in K. The values of A_o and B_o as given above are appropriate for 0°C to 80°C temperature range [27]. The integration of equation (20) provides the following expression

$$p_S = p_{ref}\exp\left\{\frac{W_{water}}{R}\left[A_o\left(\frac{1}{T_{ref}}-\frac{1}{T_S}\right) - B_o\,(Ln\,T_{ref})\right]\right\} \quad \text{(B3)}$$

where T_{ref} and p_{ref} is the absolute temperature and vapor pressure of a given reference point. The computer program employs 273 K as the reference temperature and 610 Pa as corresponding vapor pressure [27].

A. K. Majumdar
Mem. ASME

A. K. Singhal
Mem. ASME

CHAM of North America Incorporated,
Huntsville, Ala. 35810

H. E. Reilly

J. A. Bartz
Mem. ASME

Electric Power Research Institute,
Palo Alto, Calif. 94303

Numerical Modeling of Wet Cooling Towers—Part 2: Application to Natural and Mechanical Draft Towers

This paper presents several applications of the mathematical model described in Part 1 of the paper. Natural and mechanical draft towers of counterflow and crossflow arrangement have been considered. Predicted thermal performances compare well with the available data from operating towers. The distributions of air velocities, pressure, temperature, moisture fraction, and water temperature have been assessed from the considerations of physical plausibility only, since no experimental data are available for comparison. Some sample parametric computations for a mechanical draft crossflow tower are also presented. The parameters studied are: (a) air travel dimension of fill; (b) aspect ratio of fill; (c) fan power; and (d) atmospheric pressure. The results are self-consistent and demonstrate the applicability of the model as an analysis tool.

Introduction

A general mathematical model for predicting thermal performance of wet cooling towers has been described in Part I of the paper [1]. The purpose of Part II is to demonstrate, by way of specific examples, the flexibility and accuracy of the model. To this effect, several calculations for the natural and mechanical draft towers of both counterflow and crossflow designs are presented. The order of presentation satisfies, in sequence, the following objectives:

1 To demonstrate the stability and accuracy of the numerical scheme
2 To provide comparison of predicted performance parameters with Kelly's method [3], as well as with test data of operating towers
3 To present and analyze the predicted distributions of air velocity components, pressure, temperature, moisture fraction, and water temperature
4 To present and analyze results of parametric computations
5 To indicate the computer storage and execution time requirements for typical calculations

All calculations employ Merkel's model of heat transfer, in conformity with the available fill data.

Stability and Accuracy of the Numerical Scheme

As explained in Part 1 of the paper, the mathematical model requires simultaneous solution of a set of second-order, nonlinear, coupled partial differential equations which represent the conservation of mass, momentum, and energy in each control cell of a cooling tower. An iterative calculation scheme is used to solve these equations. The test and usability of such a solution scheme lies in the certainty and speed of convergence of the iterative procedure. Another important consideration is the capability of producing practically grid-independent solutions, so that the calculations show accurate manifestations of the supplied flow and geometric conditions. For studying these features, two typical natural and mechanical daft towers were selected. Figure 1 shows schematic representation of these towers together with sample grid distributions. The main geometrical and flow parameters are:

Natural Draft Tower

Radius at the base	= 28.00 m
Radius at the exit	= 16.00 m
Radius at the throat	= 15.00 m
Tower height	= 80.00 m
Inlet port height	= 6.00 m
Fill height	= 2.50 m
Spray height	= 1.50 m
Fill type	– Asbestos louver

Mechanical Draft Tower

Mean half-width of the tower in air travel direction	= 11.00 m
Longitudinal width of the cell	= 11.00 m
Fill height	– 11.00 m
Fill width in air travel direction	– 4.57 m
Fan diameter	– 9.14 m
Fan hub diameter	= 2.74 m
Stack diameter at exit	= 10.67 m
Stack height	= 4.27 m

Fill type: Standard wood lath (Vertical pitch = 20.32 cms, Horizontal pitch = 20.32 cms)

All computations were performed with the following values of property data.

Specific heat of dry air	= 1004.832 J/kg °C
Specific heat of vapor	= 1814.8 J/kg °C
Molecular weight of dry air	= 28.97
Molecular weight of water	= 18.
Lewis Number	= 1.

Ka values were calculated from equations (23) and (24) of [1] for counterflow and crossflow, respectively.

Convergence Behavior of Solutions. Figures 2 and 3 present the convergence behavior of the solutions for the natural draft counterflow tower. The following points may be noted from these figures.

Contributed by the Heat Transfer Division and presented at the 21st ASME/AIChE National Heat Transfer Conference, Seattle, Washington, July 24–28, 1983. Manuscript received by the Heat Transfer Division July 19, 1982.

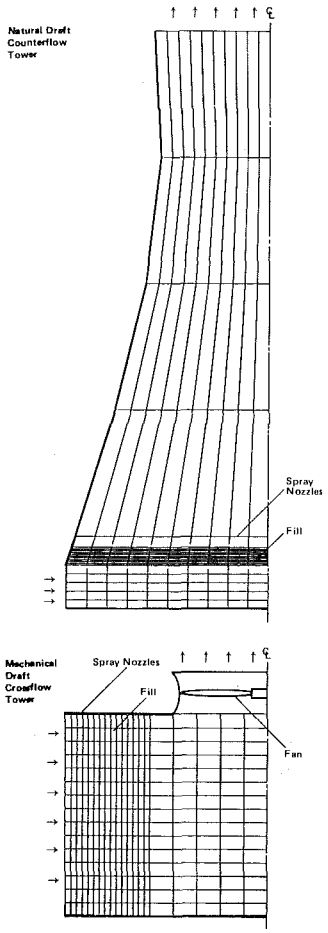

Fig. 1 Sample grid distribution for (*a*) natural draft counterflow and (*b*) mechanical draft crossflow tower

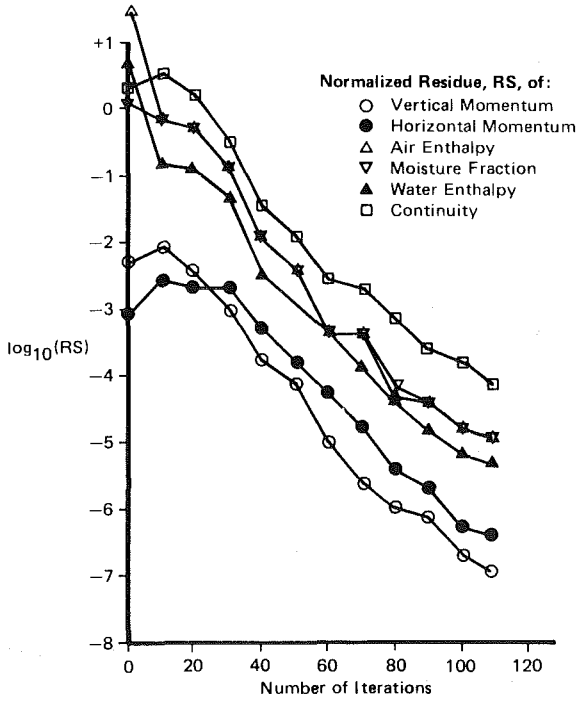

Fig. 2 Reduction of normalized residual errors in a natural draft counterflow tower

(*a*) The logarithmic values of normalized residual errors of each conservation equation are plotted on the ordinates, at an interval of ten iterations.

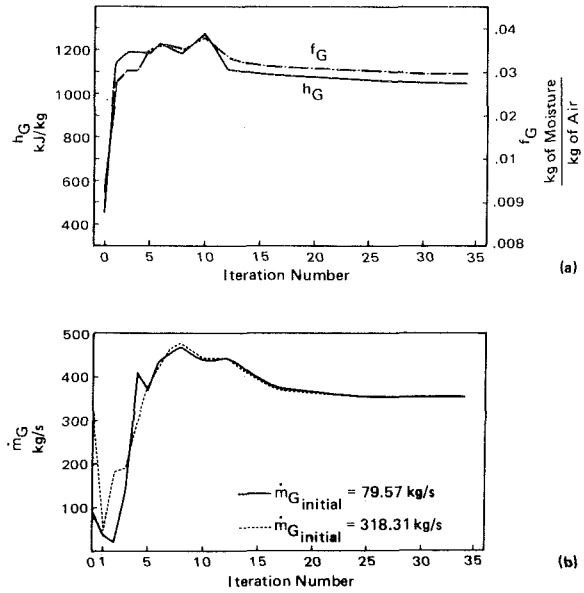

Fig. 3 The variation of (*a*) air enthalpy and moisture fraction at a point near axis at the base plane and (*b*) total air flow rate with iterations for a natural draft tower

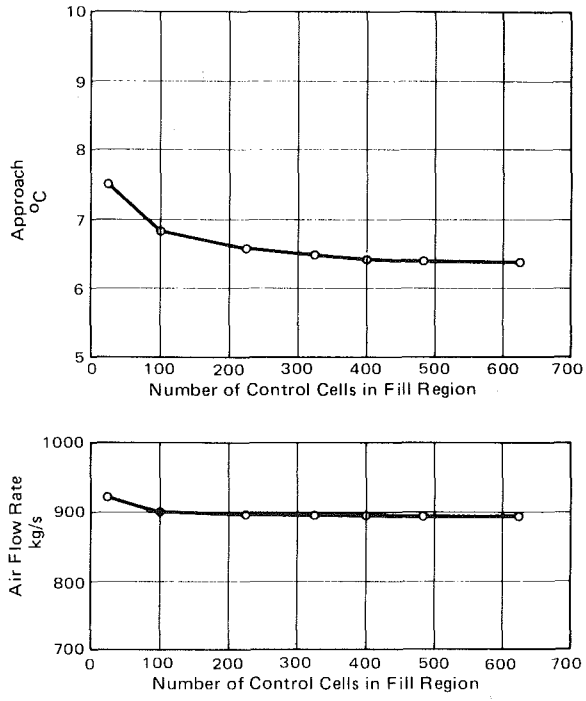

Fig. 4 The effect of grid distribution on the predicted approach and air flow rate in a mechanical draft crossflow tower

(*b*) All residuals have been reduced by at least 5 decades (5 orders of magnitudes) in 100 iterations.

(*c*) Air flow rate is settled in about 30 iterations.

(*d*) The moisture fraction and air enthalpy at a typical point also show a settled behavior after the same number of iterations.

In Fig. 3, dotted and full lines present the calculated air flow rates for two runs, which employed two different values of the initial (guessed) air mass flow rates (80 and 320 kg/s). In spite of this large difference, after about 10 iterations both runs show nearly the same values of air flow rate. Similar checks were made for different initial guesses of the hot water temperature (cooling range is prescribed as a boundary condition).

Calculation of the mechanical draft tower also showed satisfactory convergence behavior; details are provided in [4].

Grid Independence of Solutions. A series of computations has been performed to examine the sensitivity of predicted tower performance on grid distribution. Figure 4 shows the effect of grid distribution on predicted approach and air flow rate in the mechanical draft crossflow tower. This study shows that with 400 controls cells in the fill region the predicted tower performance is practically independent of grid distribution. Figure 5 shows the effect of grid distribution on tower performance for the natural draft counterflow tower. For counterflow towers, practically grid independent solutions were obtained with 25 control cells in the vertical direction (21 in the fill and spray region) and 12 cells in the horizontal direction.

Comparison With Kelly's Method

Cooling Tower Institute [2] and Kelly [3] provided methods for calculating thermal performance of counterflow and crossflow cooling towers, respectively. Both methods employ a graphical solution of demand and fill-characteristic curves as explained in [1]. The present mathematical model requires empirical correlations to determine mass transfer coefficient, Ka. However demand curves are not required since the model calculates fluid flow, heat transfer, and thermodynamic properties from basic physical laws.

Figure 6 provides the comparison of predicted approach by present mathematical model with those obtained with Kelly's method [3] for the mechanical draft crossflow tower. The present model predicts slightly higher values of approach, i.e., poorer performance of the tower. The observed differences are within 2.5 percent in thermal effectiveness, (η = Range/Range + Approach) of the tower. There are several factors which could contribute to the discrepancies as described below.

No.	Present model	Kelly's method
1	Accounts for loss of water due to vaporization; this leads to nonuniform water distribution	Does not account for loss of water due to vaporization
2	Heat transfer rate depends upon atmospheric pressure	Heat transfer rate is independent of atmospheric pressure
3	Calculates nonuniform air distribution throughout the tower	Assumes uniform air distribution
4	Allows for air density variation	Assumes uniform air density
5	Obtains grid independent solution by refining mesh size	Obtains grid independent solution by extrapolating coarse mesh size solution to zero mesh size

The above remarks about Kelly's method are made on the basis of [3].

Comparison With Field Test Data

Table 1 provides a comparison between the model's prediction of performance and existing field test data on a mechanical draft crossflow tower. Specific details of the tower are given below.

Mean half-width of the tower	= 9.70 m	Fan diameter	= 8.53 m
Longitudinal width of the cell	= 10.97 m	Hub diameter	= 1.22 m
Cell height	= 11.98 m	Stack diameter	= 9.68 m
Air travel width of the fill	= 5.15 m	Stack height	= 4.27 m

Type of fill: Splash bar (Fill H of Kelly's [3] Handbook)

Number of Velocity Heads Lost at Drift Eliminator	= 9.93
Number of Velocity Heads Lost at inlet louver	= 2.06
Fan Horsepower	= 177.60

The comparison of measured and predicted approach values shows a reasonable agreement.

Predicted Flow Distributions

Figures 7–10 show the predicted distributions of water temperature, air temperature, vapor fraction, relative humidity, presure, density, and velocity in the mechanical draft crossflow tower. The main observations are summarized below:

- Figure 7 shows a significant variation in water temperature at the cold water basin level.
- Air temperature, moisture fraction and relative humidity increase as air passes through the fill.
- Both pressure and density of the air decrease as air passes through the fill. The density contours are similar to that of vapor fraction, implying a strong dependence of density on the vapor fraction.
- The predicted air flow distribution shows an expected trend, i.e., practically uniform flow in the fill (because of high resistance), very low motion in the lower part of the plenum (i.e., near the centerline of the tower), and a smooth turning and acceleration of flow towards the exit. It should be reminded here that the fan stack has been simulated as a point model; its detailed simulation may show different velocity distribution near the exit.

Figures 11–13 show the predicted velocity distributions for the cooling towers of other three designs, namely, mechanical draft counterflow, natural draft counterflow, and natural draft crossflow, respectively.

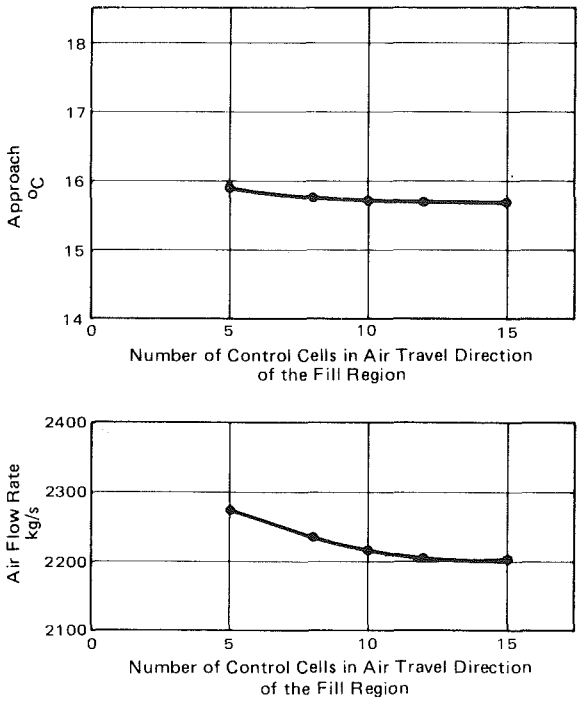

Fig. 5 The effect of grid distribution on the predicted approach and air flow rate in a natural draft counterflow tower

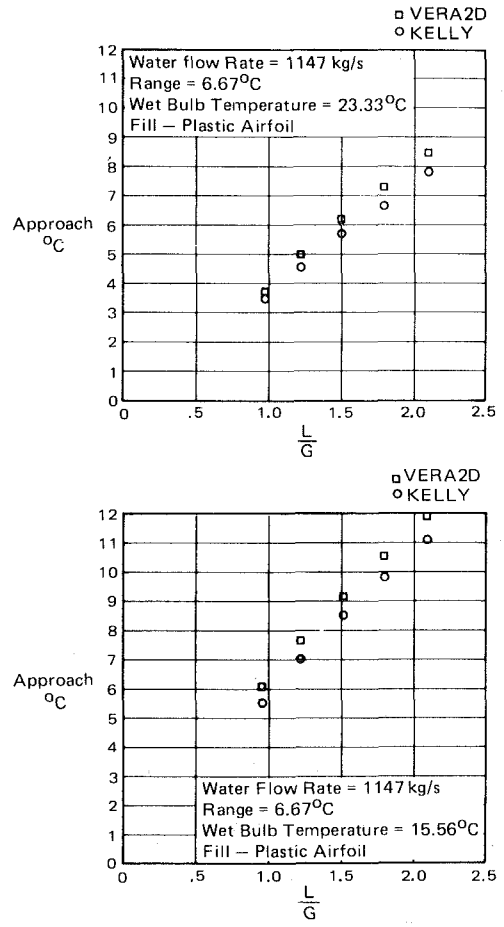

Fig. 6 Comparison of predicted approach (by VERA2D) with that of Kelly for a mechanical draft crossflow tower

It is interesting to note that in the counterflow fills, the predicted flow distributions are far from being uniform or vertical, i.e., flow is really not countercurrent to waterflow,

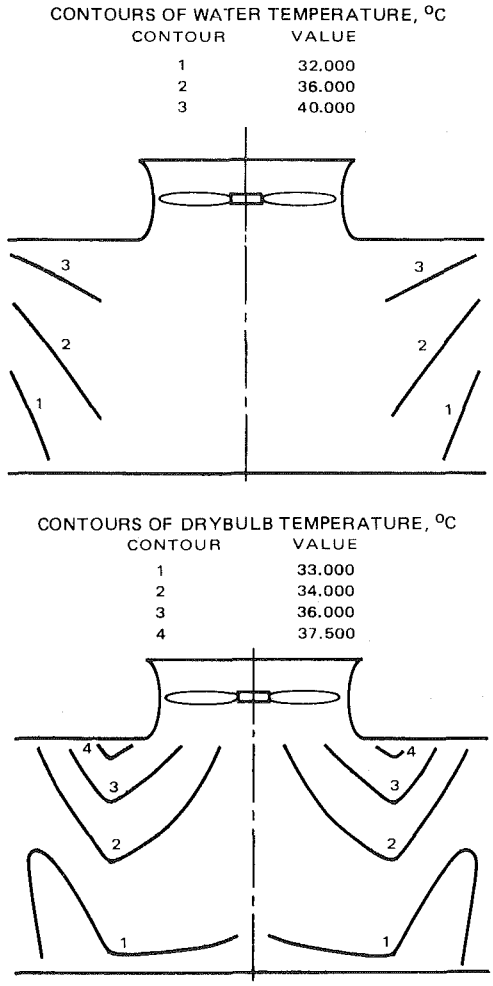

Fig. 7 Predicted contours of air and water temperature

but at a significant angle. It clearly shows the need of improving empirical data base for fills.

Also, the velocity distribution approaching the fill is considerably nonuniform. This nonuniformity is due to the right angle turn of the air stream immediately after its entry to the tower. Finally, in Fig. 12, exit air velocity is fairly nonuniform (with low velocities near the wall).

Performance Curves

Figure 14 shows the predicted performance curves for a typical mechanical draft crossflow tower at two different flow rates. At each flow rate, computations are performed for different ranges and wet-bulb temperatures. The predictions show that cold water temperature increases with the increase in cooling range, wet-bulb temperature, and water flow rate.

Figure 15 shows the predicted performance curve for a typical natural draft counterflow tower. For a given cooling range, the predicted cold water temperatures are plotted against wet-bulb temperature for different ambient relative humidities. Lower cold water temperatures are predicted at higher relative humidity. For natural draft towers, ambient relative humidity plays a major role in tower performance, since the amount of air flow through the tower directly depends on the density of ambient air. For a given cooling range, the tower performance deteriorates at lower relative humidity due to the reduction in air flow rate. The air flow rate reduces because the drier air is heavier than the moist air. These performance curves show the same trends as reported in [6]

Table 1 Comparison of VERA2D predictions with field test data for a mechanical draft crossflow tower

Test Number	Specified Conditions				Approach (°C)			Predicted Air Flow Rate (kg/sec)
	Range (°C)	Dry Bulb Temperature (°C)	Wet Bulb Temperature (°C)	Water Flow Rate (kg/sec)	Measured	Predicted	Difference Between Measured & Predicted	
1	8.33	29.00	21.38	1118.25	9.16	9.279	−0.119	647.2
2	8.29	29.80	21.87	1148.57	8.94	9.301	−0.361	644.5
3	8.10	30.25	22.25	1153.68	8.85	9.045	−0.195	643.8
4	8.11	30.30	22.28	1148.96	8.76	9.003	−0.243	644.0
5	8.06	30.50	22.39	1152.51	8.64	8.950	−0.310	643.7
6	7.78	32.00	23.85	1143.45	7.34	8.108	−0.768	642.3
7	7.73	30.25	22.26	1132.82	8.48	8.594	−0.114	645.5
8	7.56	31.00	22.67	1130.46	8.16	8.289	−0.129	644.9
9	7.31	31.80	23.56	1126.52	7.54	7.740	−0.200	644.1
10	8.02	30.15	22.16	1155.66	8.70	9.035	−0.335	644.0
11	8.20	29.55	21.75	1153.29	8.96	9.318	−0.358	644.6
12	8.09	29.45	21.66	1137.94	8.97	9.146	−0.176	645.8
13	8.15	28.85	21.26	1137.94	9.14	9.352	−0.212	646.5
14	7.79	30.00	22.02	1137.94	8.65	8.773	−0.123	645.5
15	8.11	28.95	21.31	1137.94	8.94	9.301	−0.361	646.4

Table 2 Effect of changing the air travel dimension of fill

Case Number	Predictions	
	Approach (°C)	Air Flow Rate (kg/s)
Base Case	8.46	792.5
1.1	8.64	732.2
1.2	9.34	644.9

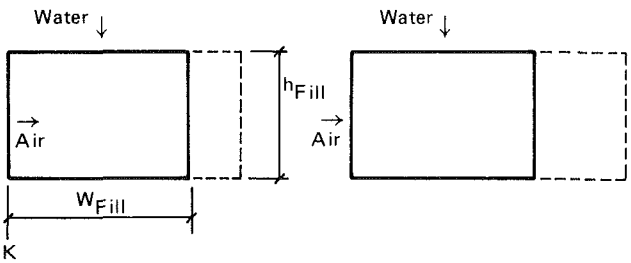

Case 1.1
W_{Fill} is Increased by 25%

Case 1.2
W_{Fill} is Increased by 50%

Sample Parametric Studies

Effect of Increasing Air Travel Dimension of a Fill. Table 2 shows the predictions of approach and air flow rate for three cases:

Case 1: Base case, mechanical draft crossflow tower with conditions described in section 1 of this paper

Case 2: Air travel dimension of fill increased by 25 percent from that of base case

Case 3: Air travel dimension of fill increased by 50 percent from that of base case

The results show that in spite of the increase of fill dimension (and hence volume of the fill), the tower performance deteriorates. This is because for the selected fill, an increase in flow resistances reduces air flow significantly; i.e. 10 to 20 percent. The results could be different for different fills, which will have different heat transfer and pressure drop characteristics. However, for a given fill, the optimum dimensions can be found by a more detailed parametric study.

Table 3 Effect of alternative fill arrangements

Case Number	Predictions	
	Approach (°C)	Air Flow Rate (kg/s)
Base Case	8.46	792.5
2.1	7.691	883.0
2.2	10.52	634.4

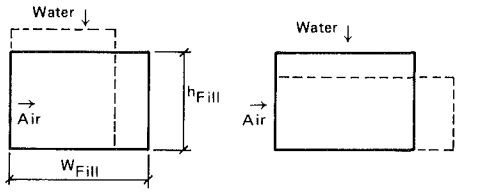

Case 2.1
W_{Fill} is Decreased by 25%
h_{Fill} is Increased by 25%

Case 2.2
W_{Fill} is Increased by 25%
h_{Fill} is Decreased by 25%

Table 4 Effect of ambient pressure

Run Number	Description of the Run	Predictions	
		Approach	Air Flow Rate (kg/s)
Base Case	Ambient Pressure (At Sea Level Altitude) = 101323 N/M^2 Fan HP = 180.0 L/G = 1.12	6.45	894.8
3.1	Ambient Pressure [At 2500 Feet (762M) Altitude]=91109.64 N/M^2 Fan HP = 180.00 (Fixed) L/G = 1.22 (Calculated)	6.24	821.5
3.2	Ambient Pressure = 91109.64 N/M^2 Fan HP = 222.39 (Calculated) L/G = 1.12 (Fixed)	5.69	892.5

Effect of Alternative Fill Arrangement. The predictions for two alternative fill arrangements (maintaining the same fill volume) and their comparison with the base case is shown in Table 3. The predictions clearly show that the taller and slender arrangement of fill performs better than the shorter and thicker arrangement. Once again, optimum fill arrangements can be determined by performing similar parametric computations over a wider range.

Effect of Fan Power. The predicted effect of varying the power input to fan on the approach and air flow rate of an induced draft crossflow tower is shown in Fig. 16. As expected, the air flow rate increases and approach decreases with the increase in fan horsepower. Figure 16(*b*) also shows that approach, like air flow rate, can be related with fan horse power by a power law expression.

Effect of Ambient Pressure. The effect of ambient pressure has been studied by performing two additional runs (Table 4). At lower ambient pressure pertinent to a higher altitude, for example, in run 3.1, the fan power was retained constant, while in run 3.2 the flow rate was retained constant, i.e., equal to that of the base case. Following are the observations.

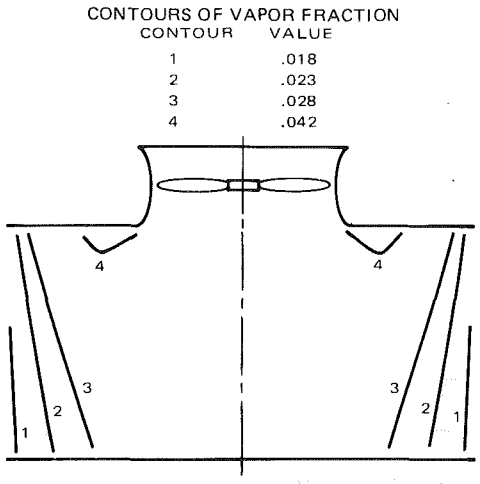

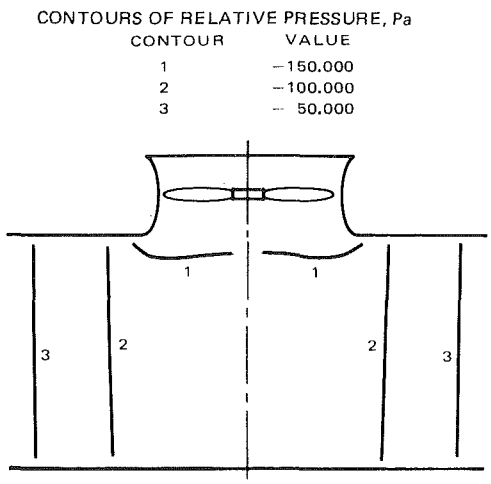

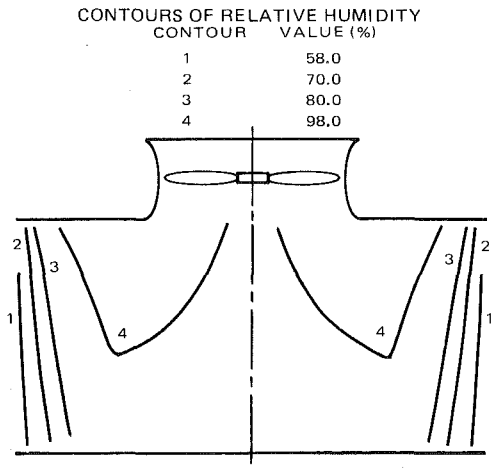

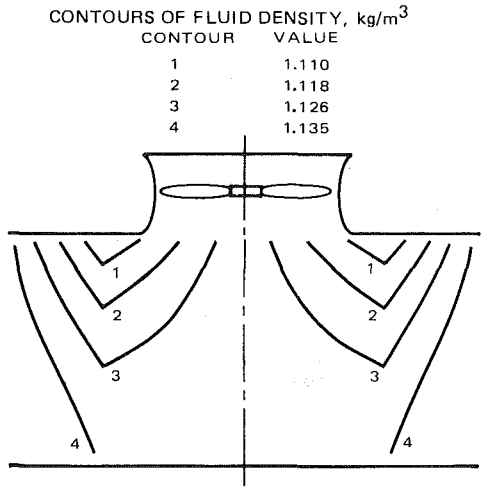

Fig. 8 Predicted contours of vapor fraction and relative humidity in a mechanical draft crossflow tower

Fig. 9 Predicted contours of pressure and density in a mechanical draft crossflow tower

1 Same fan (with identical input power) at a higher altitude draws less amount of air. In spite of this, tower performance improves due to the enhancement of evaporation rate at the reduced ambient pressure.

2 The tower operation with a constant L/G shows a significant improvement in the tower performance at higher altitudes, due to the reduction in ambient pressure.

Computational Details

All computations have been performed with the aid of the VERA2D computer code which is written in standard FORTRAN IV and is described in [3] and [4]. The code requires about 37K decimal words SCM storage, and about 4 $\times$ 10^{-4} s per cell per iteration execution (CPU) time on a CDC 7600 computer. For a typical mechanical draft tower with 500 control cells, about 50 iterations are needed and the corresponding execution time is 11 s. The calculations are regarded as converged when the maxima of normalized residual errors in all conservation equations become less than 0.001. Computation of a natural draft tower with the same number of control cells requires about 20 percent more time (i.e., about 13 s on a CDC 7600 computer).

Concluding Remarks

The paper has described several applications of the mathematical model described in [1]. The presented examples demonstrate:

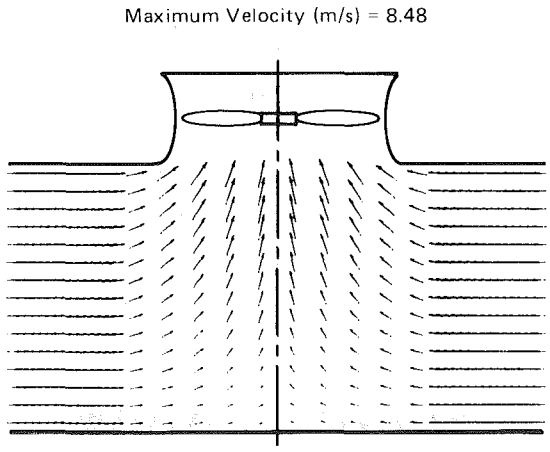

Fig. 10 Predicted velocity vectors for the mechanical draft crossflow tower

(*a*) The accuracy and stability of the numerical solution scheme

(*b*) The physical realism of predicted global and local quantities

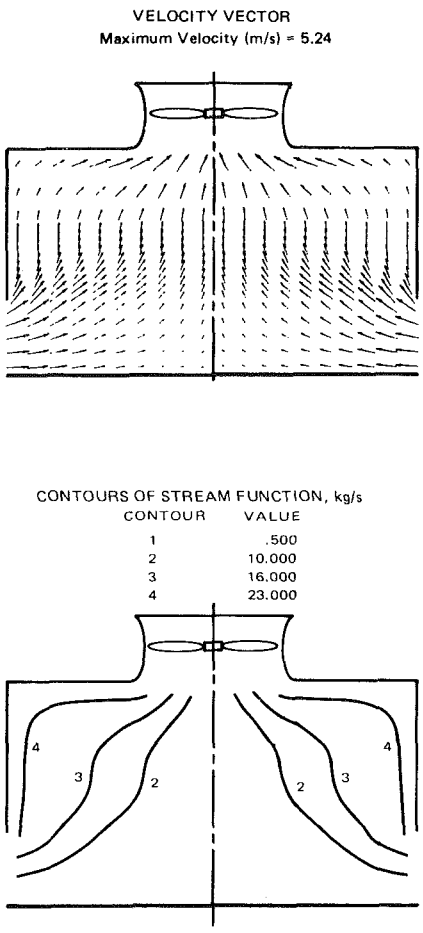

Fig. 11 Predicted velocity vectors and stream function in a mechanical draft counterflow tower

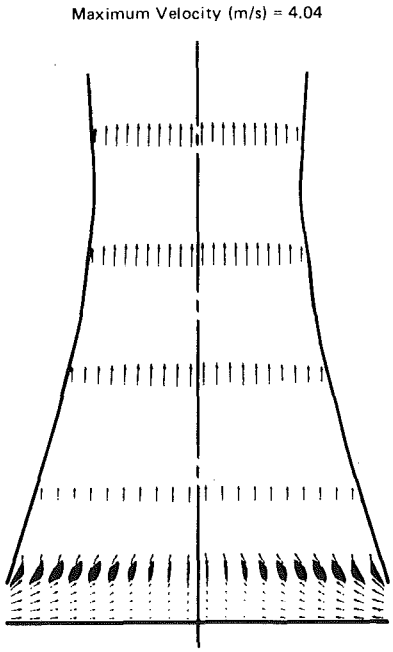

Fig. 12 Predicted velocity vectors in a natural draft counterflow tower

(*c*) Sample performance curves

(*d*) Self-consistent and physically plausible results for the parametric studies

(*e*) The modest computer time requirements for both mechanical and natural draft towers

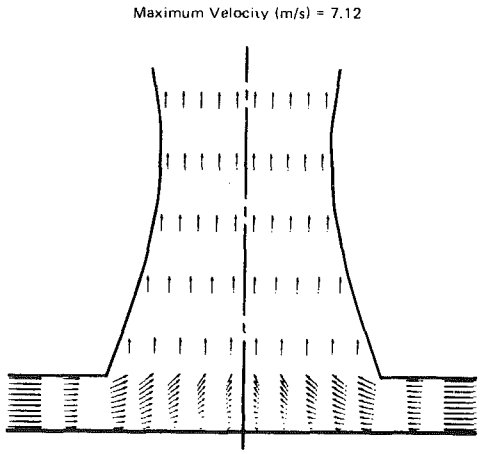

Fig. 13 Predicted velocity vectors in a natural draft crossflow tower

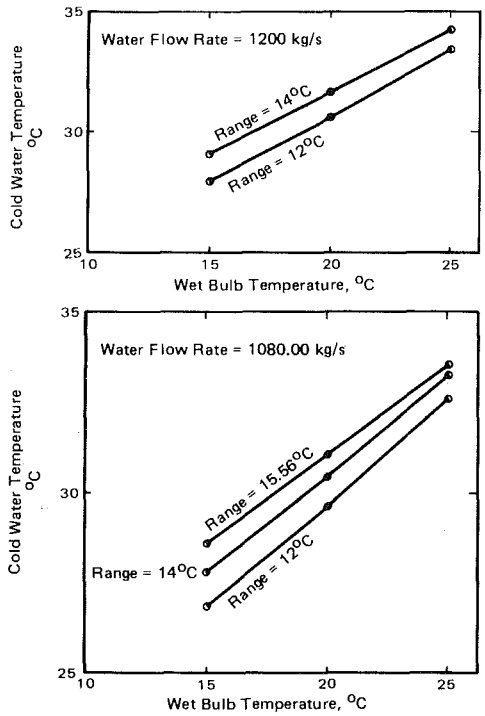

Fig. 14 Performance curves for a mechanical draft crossflow tower

The model can be used for relative performance evaluation, and design optimization studies. It can also be used as a research tool for the development of adequate heat and mass transfer models and associated empirical data, which are very much needed for more accurate performance predictions.

Acknowledgment

The work has been supported by Electric Power Research Institute (EPRI), Palo Alto, California under the contract no. RP 1262-1. The developed code "VERA2D" is available from Electric Power Software Center, University Computing Company, Dallas, Texas 75207. The authors wish to thank Dr. L. T. Tam for providing computer graphics and Mr. N. K. Agrawal for assistance in computations. Thanks are also due to Lynn Wilson and Kelli King for the preparation of the typescript.

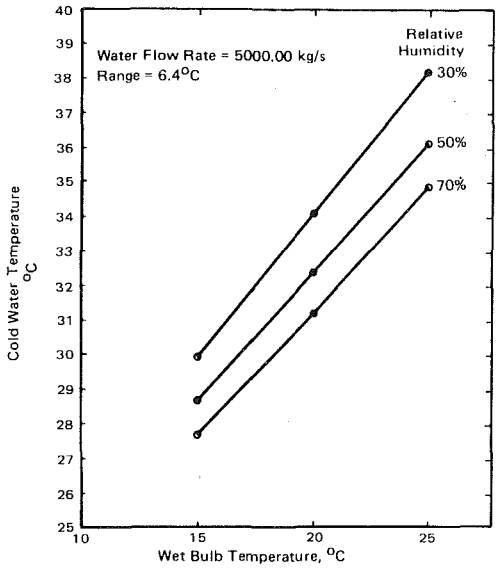

Fig. 15 Performance curves for a natural draft counterflow tower

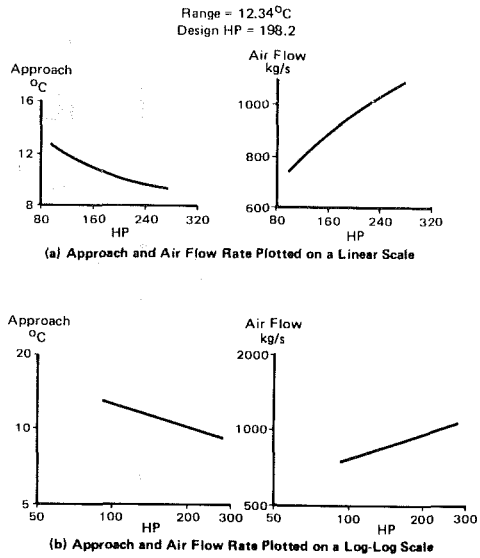

Fig. 16 Predicted effect of fan horsepower on approach and air flow rate

References

1 Majumdar, A. K., Singhal, A. K., and Spalding, D. B., "Numerical Modeling of Wet Cooling Towers; Part 1: Mathematical & Physical Models," ASME JOURNAL OF HEAT TRANSFER, Vol. 105, No. 4, Nov. 1983, pp. 728-735.

2 Cooling Tower Institute, "Cooling Tower Performance Curves," Cooling Tower Institute, Houston, Texas, 1967.

3 Kelly, N. W., *Kelly's Handbook of Crossflow Cooling Tower Performance*, Neil W. Kelly and Associates, Kansas City, Missouri, 1976.

4 Majumdar, A. K., Singhal, A. K., and Spalding, D. B., "VERA2D—A Compuer Program for Two-Dimensional Analysis of Flow, Heat, and Mass Transfer in Evaporative Cooling Towers: Vol. 1—Mathematical Formulation, Solution Procedure and Applications," EPRI Report No. CS-2923, Project 1262-1, Mar. 1983.

5 Majumdar, A. K., and Singhal, A. K., "VERA2D—A Computer Program for Two-Dimensional Analysis of Flow, Heat and Mass Transfer in Evaporative Cooling Towers: Vol. 2—User's Manual," EPRI Report No. CS-2923, Project 1262-1, Mar. 1983.

6 Cooling Tower Institute, "Acceptance Test Code for Water Cooling Towers," CTI Code ATC-105, Feb. 1975.

The Effect of Tube Layout on the Fluid-Elastic Instability of Tube Bundles in Crossflow

B. M. H. Soper[1]
Heat Transfer and Fluid Flow Service,
AERE Harwell,
Oxon, England

Fluid-elastic instability is widely recognized as a mechanism which can cause rapid failure of tubes in shell and tube heat exchangers. The shellside flow velocity for the onset of the fluid-elastic whirling is commonly calculated from Connors' formula provided that the instability factor is known. The literature contains several reported values of the instability factor for different tube bundles but these have been obtained from a variety of test configurations and this has led to some large discrepancies. This paper describes a systematic study of the effect of tube layout on the instability factor for sixteen tube bundles. The results presented show that the instability factor varies by a factor of 3 over the range of tube layouts tested. This paper concludes with a comparison of the results of the present study with values taken from the open literature.

Introduction

The quest for increased thermal performance of shell and tube heat exchangers has led to an increase in shellside flow velocities which, in turn, has given rise to an increase in the incidence of flow induced vibration. Whilst the number of heat exchangers that experience flow induced vibration is small in proportion to the total number manufactured [1], the occurrence of this problem can be sufficiently violent to cause tube failure within a short period of time and may result in the closing down of costly process plants or power generating stations. For this reason, the subject has attracted much research effort in recent years, and whilst great advances have been made, there are still many aspects of the problem which have yet to be explained.

Flow induced vibration of closely spaced tubes in crossflow can be caused by a number of separate mechanisms. Of these, there is one class which are self excited in that they depend upon the interaction between the fluid flow and the motion of the structure, i.e., they are fluid-elastic in origin. Fluid-elastic vibration sets in at a critical flow velocity and can become of large amplitude if the flow is increased further. Unlike tube resonances caused by some fluid dynamic effects, e.g., vortex shedding, increasing the flow velocity during fluid-elastic instability is very unlikely to result in a reduction of vibration amplitude to an acceptable level but rather is likely to result in tube failure. The critical velocity for fluid-elastic vibration is therefore of great importance to designers of heat exchangers and can be regarded as the upper limiting flow.

Much of the pioneering work on fluid-elastic vibration of tubes in crossflow was done by Connors [2]. He developed a semiempirical model, based on the motion of tubes which he had observed commonly in a single tube row. His analysis related the critical velocity, V_c, to the properties of the fluid and the structure as follows

$$\frac{V_c}{f_n d} = K\left[\frac{m_e \delta}{\rho d^2}\right]^{0.5} \tag{1}$$

where K is a stability parameter at 9.9 for Connors's single tube row for which P/d was 1.41. In tube bundles, the assumed tube motions upon which equation (1) was based do not generally occur, and an equation of the following form is more appropriate

$$\frac{V_c}{f_n d} = \phi(G)\left[\frac{m_e}{\rho d^2}\right]^a \delta^b \tag{2}$$

and a and b may be less than 0.5 [3, 4, 6]. To evaluate these parameters, an extensive experimental program would be required in which tube layout, m_e, ρ, d, and δ were varied systematically. Because the object of the work described in this paper was to study the effect of tube layout, the other parameters being kept essentially constant, it was decided to use equation (1) as a means of reducing the experimental data. This approach has been used widely in other studies and allowed comparisons to be made with published data.

Since the work described in this paper was carried out, there have been some significant contributions to this field. In particular, Price and Paidoussis [4] have extended the quasi-static theory, Tanaka and Takahara [5] have developed an unsteady theory which makes extensive use of measured fluid force coefficients, and Weaver and El Kashlan [6] have published further experimental results on the effects of tube mass ratio. All of these results support the contention that the simple Connors relationship has no general validity for tube bundles.

Experimental Facility

Use was made of an existing wind tunnel which had been built for an earlier study of fluid dynamic forces in tube bundles. This restricted the available air flow velocities and maximum tube span for the design of a suitable test section. It was considered undesirable to use tubes of small diameter because little is known about scaling of flow-induced vibration. Design of a suitable test section therefore centered around achieving a sufficiently low tube natural frequency to allow tube vibration to occur within the flow available.

Wind Tunnel. The wind tunnel is shown schematically in Fig. 1. The working section measures 0.457-m square and the contraction ratio is 3.2. Air is drawn through the wind tunnel by a centrifugal fan which is capable of giving a maximum empty tunnel velocity of 30 m/s with a turbulence intensity of approximately 1 percent. The fan is run at constant speed and control of the flow through the test section is achieved by bleeding air into the tunnel downstream of the test section. There are four bleed ports, one in each wall of the tunnel to ensure that the symmetry of the flow is not disturbed. The bleed flow is regulated by moving a sleeve which partially blanks off the ports. A flexible coupling between the fan and

[1] Present address: AEE Winfrith, Dorchester, Dorset, England

Contributed by the Heat Transfer Division and presented at the ASME Winter Annual Meeting, Chicago, Illinois, November 16-21, 1980. Manuscript received by the Heat Transfer Division November 17, 1980.

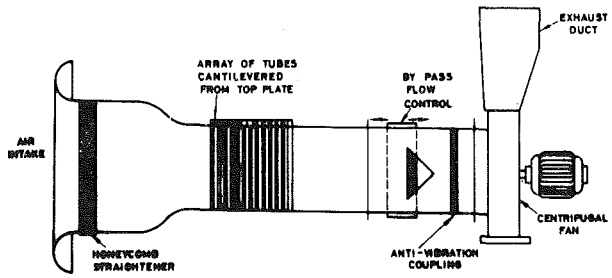

Fig. 1 General arrangement of vibration rig

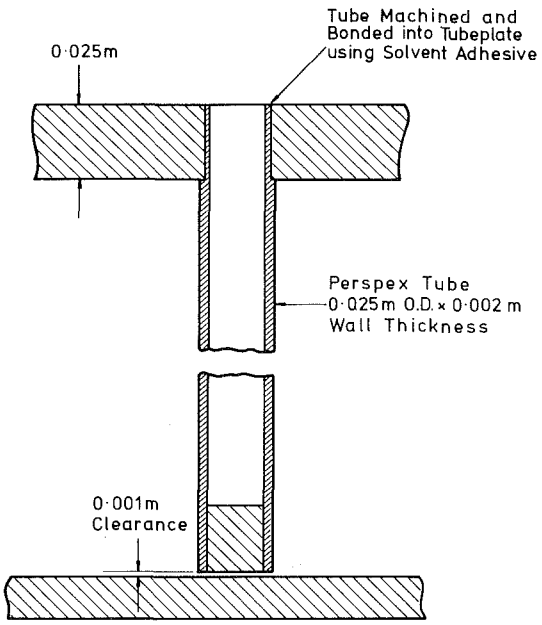

Fig. 2 Tube mounting arrangement

the wind tunnel ensures there is no transmission of mechanical vibrations to the test sections.

Test Sections. Several test section designs were considered that would enable low stiffness to be achieved whilst maintaining a tube outside diameter of 0.025 m. In the final design, Fig. 2, low stiffness was achieved by using cantilevered tubes made of "Perspex" (polymethyl methacrylate). It has been shown in an earlier paper [7] that the use of cantilevered tubes does not affect the critical flow velocity for a tube bundle of given tube layout. The use of Perspex as the tube material simplified the construction of the test sections, because it was possible to use Perspex also as the tube plate material and to bond the tubes into the 0.025-m thick tube plate. This technique gave good consistency between tubes and resulted in tube natural frequencies within 2 percent. To allow the tubes

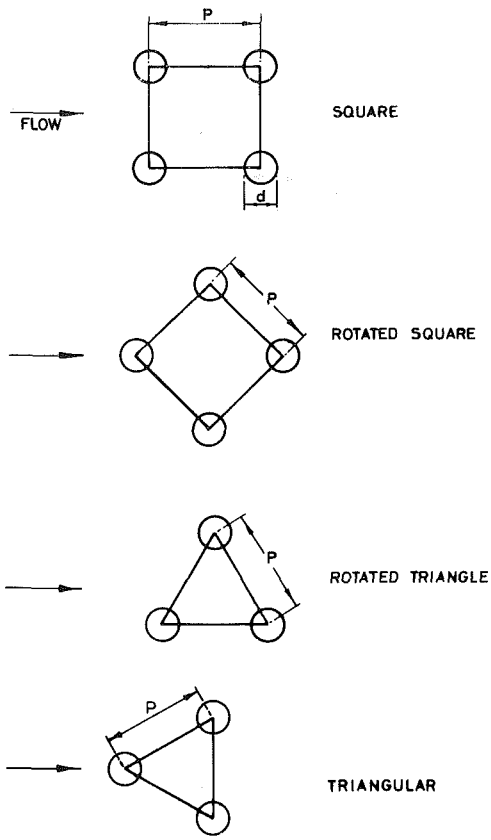

Fig. 3 Geometric configurations

to vibrate freely, a clearance of 1 mm was provided between the free end of the cantilevered tubes and the adjacent bottom wall of the test section. Rubber bungs in the bore of the free end of each tube prevented flow leakage from the bundle[2].

Tube Layout Configuration. Sixteen test sections have been built, representing the geometries shown in Fig. 3, each with pitch to diameter ratios (P/d) of 1.27[3], 1.35, 1.52, and 1.78. The lattice is continued right up to each side wall by using dummy tube segments where appropriate. Ten rows of tubes are provided in the flow direction.

It should be noted that the critical velocity used to calculate the instability factor has been based on the maximum intertube velocity, i.e., through the minimum gap between tubes. For the square and triangular configurations, the maximum intertube velocity always occurs between tubes in

[2]The mass of the rubber bung was considered to be uniformly distributed along the length of the tube for the purpose of calculating K from equation (1)

[3]The value of P/d for the triangular geometry was 1.25 due to the use of 1-in. o.d. tubing.

Nomenclature

a = exponent in equation (2)
b = exponent in equation (2)
d = tube outside diameter, m
f_n = tube fundamental frequency, Hz
K = instability factor, dimensionless
m_e = tube effective mass (tube plus contained and displaced fluid with added mass effects) per unit length, kg/m
P = tube pitch, m
S_a = Strouhal number based on acoustic resonance, dimensionless
S_v = Strouhal number based on vortex shedding resonance, dimensionless
V_c = flow velocity through the minimum gap between tubes at the onset of fluid-elastic instability, m/s
V_g = flow velocity through the minimum gap between tubes, m/s
V_s = superficial flow velocity, m/s
δ = logarithmic decrement of damping, dimensionless
ρ = density of fluid outside the tubes, kg/m^3
$\phi(G)$ = function of tube layout geometry

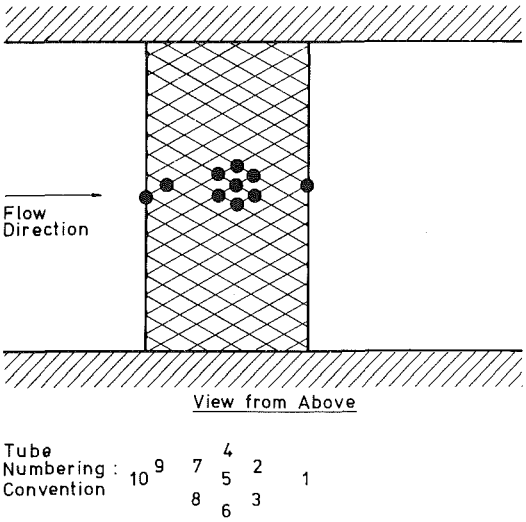

Fig. 4 Position of instrumented tubes in tube bundle

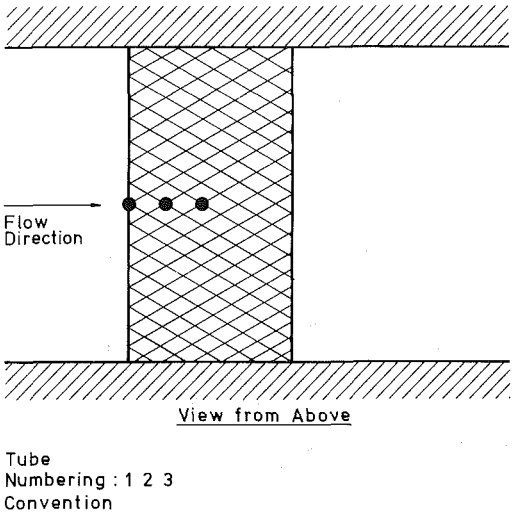

Fig. 5 Revised position of instrumented tubes in tube bundle

the same row, whereas for the rotated variants this is not the case. The maximum intertube velocity is related to the superficial velocity as follows:

Square and triangular configurations (TEMA designation):

$$V_g = \frac{P/d}{(P/d-1)} V_s \tag{3}$$

Rotated triangular configurations:

$$V_g = \frac{\sqrt{3}P/d}{2(P/d-1)} V_s$$

Rotated square configurations[4] (for $P/d < 1.71$):

$$V_g = \frac{P/d}{\sqrt{2}(P/d-1)} V_s$$

where $V_c = V_g$ at the onset of fluid-elastic instability.

In addition, a single row test section has been built having $P/d = 1.41$. Constructional details are similar to those for the tube bundles.

Instrumentation. The air flow velocity was obtained from the pressure drop across the contraction in the wind tunnel.

[4]This definition of V_g was used also for the bundle with $P/d = 1.78$ although V_g is then 3 percent lower than the maximum intertube velocity.

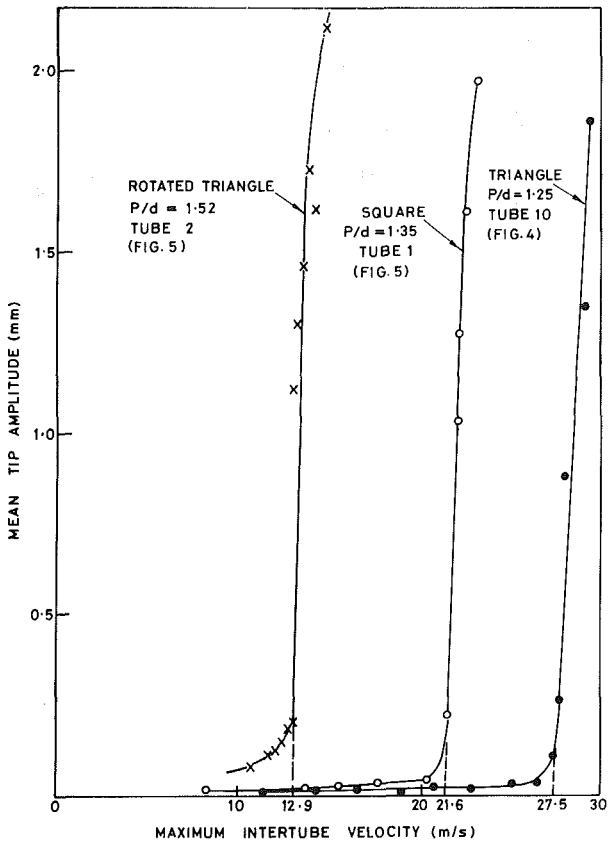

Fig. 6 Typical tube response curves

The contraction pressure drop had been calibrated by comparison with the velocity measured using a pitot static tube.

The amplitudes of selected tubes were measured using wire resistance strain gauges, bonded to the tube bore at the position of maximum bending strain. Maximum sensitivity was achieved by the use of two diametrically arranged strain gauges. The strain gauge signal was amplified and then fed to a RMS meter with a 30 s time constant or to an ultraviolet recorder. For each instrumented tube, strain gauges were provided to measure the components of the tube motion normal to and parallel with the flow direction.

For the triangular configuration test sections with $P/d = 1.25$ and 1.35, ten tubes were instrumented and located at the positions shown in Fig. 4. Because of the consistency of the results obtained from these two test sections, later test sections were fitted with only three instrumented tubes at the locations shown in Fig. 5.

Test Carried Out and Results

For each of the wind tunnel test sections, the vibration response of the instrumented tubes was recorded over a range of airspeed sufficient to cause self-excited vibration. A stroboscope was used to observe the motion of each tube which was found to vibrate at its fundamental frequency. Typical response curves are shown in Fig. 6, from which can be seen the sudden increase in amplitude when a critical value of intertube velocity is exceeded. The critical velocity was obtained from each response curve as the point at which a tangent to the post critical response intersects the velocity axis.

The damping of each of the instrumented tubes was determined from simple "plucking" tests in still air. The natural frequency of each instrumented tube was obtained from recordings of the tube motion during fluid-elastic instability. No significant coupling of tube vibrations, via the

Table 1 Summary of test results

Geometry	$\frac{P}{d}$	V_c,m/s	f_n, H_z	$\frac{m_e}{\rho d^2}$	δ
Triangular	1.25	24.6	36.4	359	0.30
"	1.35	21.7	34.0	236	0.26
"	1.52	30.6	35.1	236	0.24
"	1.78	41.5	36.4	236	0.22
Rotated triangular	1.27	13.9	33.8	236	0.24
" "	1.35	16.0	33.3	236	0.25
" "	1.52	12.9	33.7	236	0.25
" "	1.78	13.7	33.4	236	0.24
Square	1.27	23.1	32.8	236	0.25
"	1.35	21.4	33.3	236	0.24
"	1.52	19.6	32.8	236	0.23
"	1.78	23.7	32.1	236	0.18
Rotated square	1.27	23.3	33.5	236	0.24
" "	1.35	27.4	33.2	236	0.24
" "	1.52	31.4	32.4	236	0.22
" "	1.78	34.8	32.4	236	0.22
Single row	1.41	52.3	33.6	236	0.18

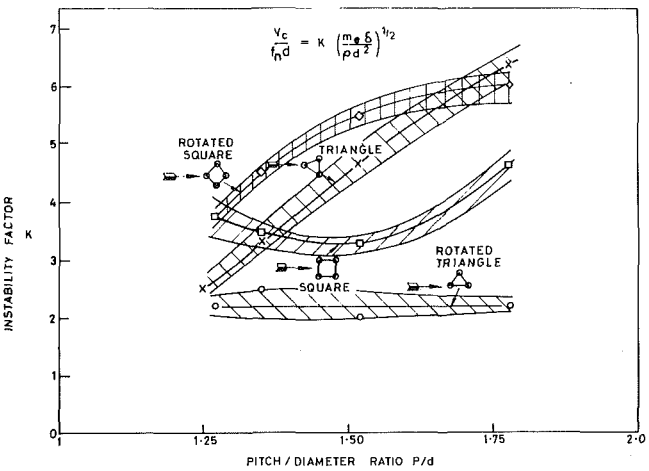

Fig. 7 Instability factors for bundles tested

common tube support plate, was observed during these tests.

Mean values of V_c, f_n, δ, and $m_e/\rho d^2$, for each of the test sections, are given in Table 1.

Triangular Geometry. The values of K obtained from the tests on the triangular geometry arrays are shown in Fig. 7. It can be seen that increasing the tube spacing was found consistently to increase the K value and so render the bank less prone to self-excited vibration. A study of the tube motion revealed no obvious phase relationships between tubes and the amplitude of each tube varied with time, and so the response was plotted as the RMS displacement taken over a period of several minutes.

The hatched zones in Fig. 7 indicate the possible cumulative error in K arising from inaccuracies in the measurement of the parameters that were used to calculate K.

The tube bank with $P/d = 1.25$ yielded a mean value of critical velocity of 24.6 m/s and the coefficient of variation of the results from each of the 20 channels was only 2.6 percent. A similar consistency was found in the results for the banks with $P/d = 1.35$ and 1.52. For the wider spaced tube bank ($P/d = 1.78$), however, it was possible to exceed, by a significant amount, the flow velocity required to cause the first tube to vibrate without achieving vibration in the last few rows of the bundle.

Rotated Triangle Geometry. Figure 7 shows that, unlike the nonrotated variant, this configuration was equally prone to self-excited vibration for all tube spacings within the test range. Moreover, tube banks of this geometry were always more susceptible to self-excited vibration than their nonrotated counterparts.

The tube motion was more ordered with this geometry, and it was often possible to identify "cells" in which tubes vibrated according to the pattern described by Connors [2]. For the banks with $P/d = 1.27$ and $P/d = 1.35$, the worst vibration occurred in the second row whereas for the wider spaced banks, it was the third row. In every case, however, the tubes in the worst row vibrated predominantly transverse to the flow, adjacent tubes being in antiphase. As for the triangular geometry, the widest spaced bundle required a large increase in flow velocity (factor of 3.6) following the first tube starting to vibrate before the whole bundle was vibrating.

Square Geometry. The bundle of square tube layout exhibited interesting behavior in that it was the intermediate spacing ratios which appeared to be most susceptible to fluid-elastic instability. The close packed bundles ($P/d = 1.27$ and 1.35) exhibited vibration throughout the bundle and again there were "cells" in which Connors-type motion could be seen. For the wider spaced bundles, a different type of motion was observed. Tubes in the same row all moved in phase perpendicular to the flow direction but the motion in adjacent rows was in antiphase. This type of motion has been observed also by Gross [8] who applied the term "galloping" to it. The second and third tube rows (in flow direction) vibrated most violently, whereas successive downstream rows vibrated less violently such that the last few rows were essentially stationary. In order to excite the whole bundle into vibration, it was necessary to limit the amplitude of the tubes in the second row by inserting close fitting brass tubes into the tube bores before the flow was increased. The bundle with $P/d = 1.52$ required almost twice the flow velocity before every tube was vibrating, and for the bundle with $P/d = 1.78$, vibration throughout the bundle was not achieved within the flow available.

These results suggest that there are two mechanisms which give rise to self-excited vibration in square lattice tube banks, each applicable to a different range of tube spacing.

Rotated Square Geometry. For most spacing ratios, the rotated square tube geometry was the least likely to vibrate, due to fluid-elastic instability, as shown in Fig. 7. With this tube layout, however, acoustic standing waves were set up in the wind tunnel as described more fully in a later section.

For the wider spaced bundles of this geometry, it was found again that not every tube went unstable at the same intertube velocity. For the bundle with $P/d = 1.52$, the ratio of velocities for the first and last tubes to go unstable was 0.75.

Single Row of Tubes. The single row test section showed

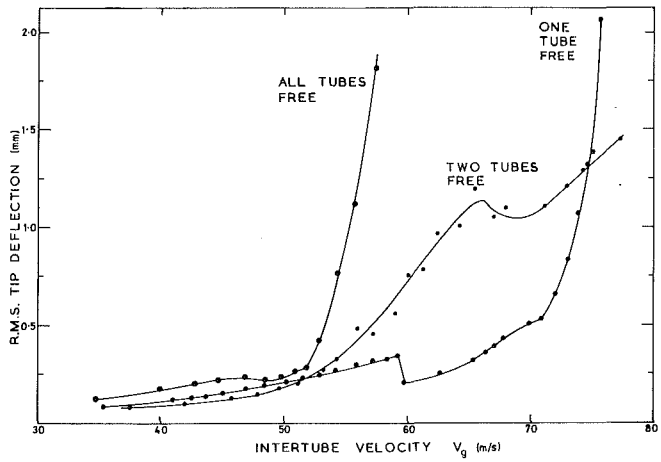

Fig. 8 Vibration of a row of tubes with $P/d = 1.41$

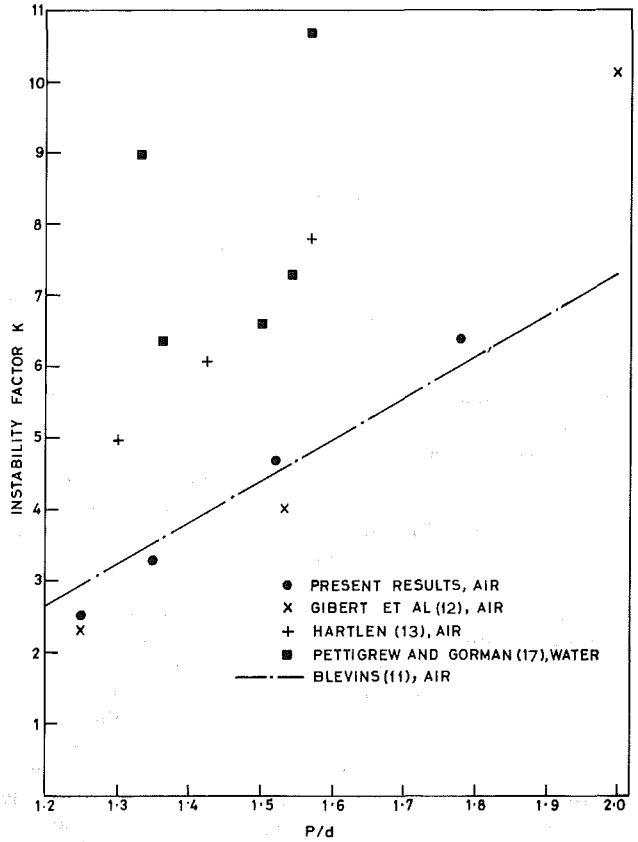

Fig. 9 Instability factors for bundles with triangular tube layout

similar amplitude versus velocity response curves to those from tests on tube bundles. The main difference was in the pattern of tube motion which was predominantly in the flow direction, with adjacent tubes in antiphase. This motion is in accordance with the jet switch mechanism postulated by Roberts [9], although no attempt has been made to verify this.

The mean value of instability factor, obtained from tests on this test section, was 10.1 with a coefficient of variation of 8.4 percent.

Because the mechanism of fluid-elastic instability is not well-understood, the opportunity was taken to see if one flexible tube in a row of rigid tubes will still go unstable. Figure 8 shows results for one, two, and all tubes flexible. It can be seen that a single flexible tube can become unstable but at 40 percent higher critical flow velocity. Goyder [10] has analysed a single tube row and has shown that there are

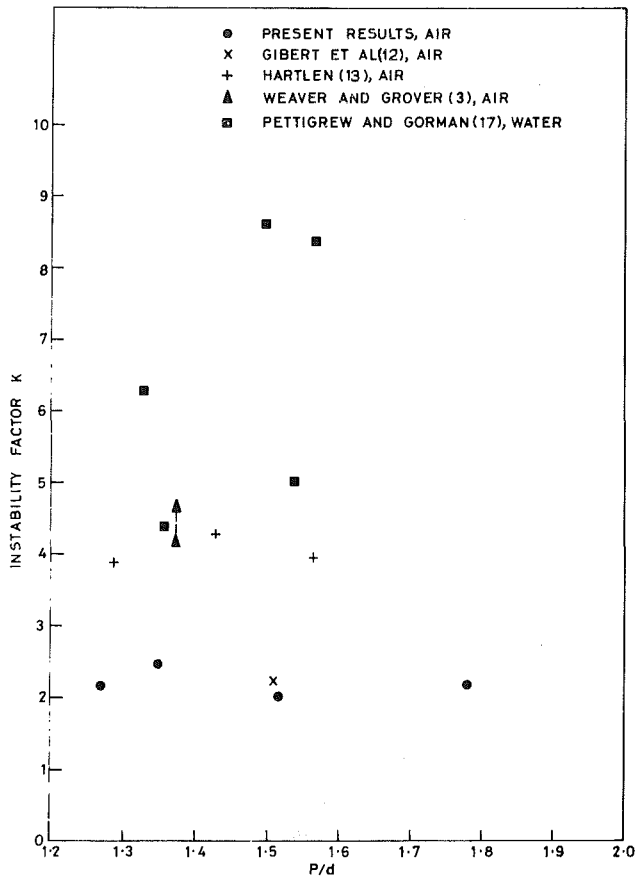

Fig. 10 Instability factors for bundles with rotated triangular tube layout

several possible critical velocities depending on the number of flexible tubes and the pattern of vibration between adjacent tubes. His theory predicts the vibration of two flexible tubes not one. Blevins [11] has also shown that a single flexible tube is theoretically stable but for a more specific assumed motion of the tube. The motion of a single flexible cylinder is predominantly in the flow direction, which would suggest that the instability arises from changes in the drag force on the tube, brought about by shifting separation points of the boundary layer as the tube vibrates upstream and downstream.

Comparison of Instability Factors with Published Data. The instability factors presented here are compared with values from other sources (corrected as necessary so that the reference gap velocity is in line with equation (3)) in Figs. 9–13. It is evident that there are large discrepancies between reported values, although this is reduced if data are compared only with other data from tests using the same fluid. This is an important point because there is increasing evidence that the exponent in equation (1) is less than 0.5 and may be as small as 0.21 [3]. For most cases, the results of the present study form the lower bound of the values plotted and therefore tend towards the values that should be used for design purposes.

The value of $K = 10.1$ for a single tube row with $P/d = 1.41$ compares favourably with Connors's results (see Fig. 13) and this adds credibility to the values obtained for the tube bundles.

Acoustic Resonance. During tests on bundles of the rotated triangle tube layout, a note at a frequency of 380 Hz was audible over a small range of flow velocities. This was identified as an acoustic standing wave, of wavelength equal to twice the width of the test section, perpendicular to both the tube axis and the flow [18]. This standing wave did not

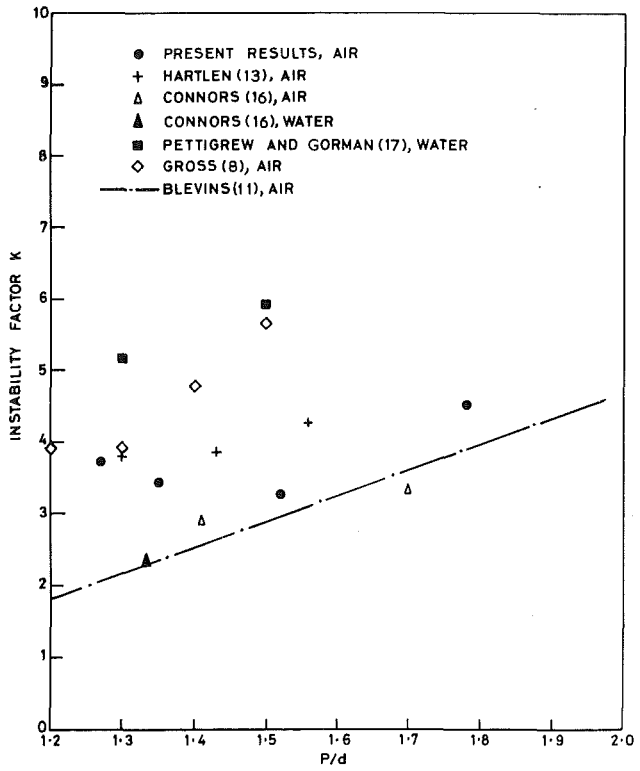

Fig. 11 Instability factors for bundles with square tube layout

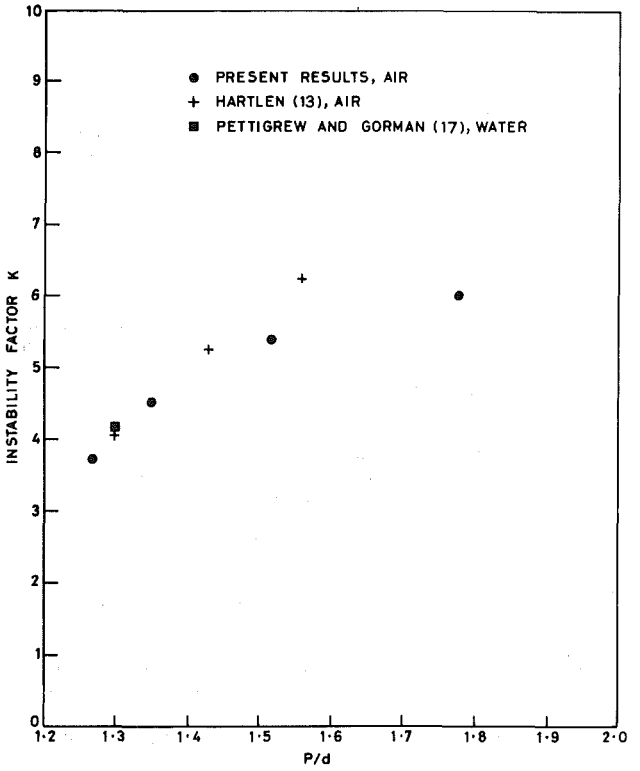

Fig. 12 Instability factors for bundles with rotated square tube layout

significantly increase the emitted noise level, nor did it apparently interfere with the formation of self-excited vibration, and so it was not investigated further.

Acoustic resonance was encountered again when bundles of the rotated square geometry were tested. For the bundle with $P/d = 1.27$, a loud note of frequency equal to 384 Hz was initiated when the intertube velocity exceeded 19 m/s but there was no significant tube motion. The noise intensity increased

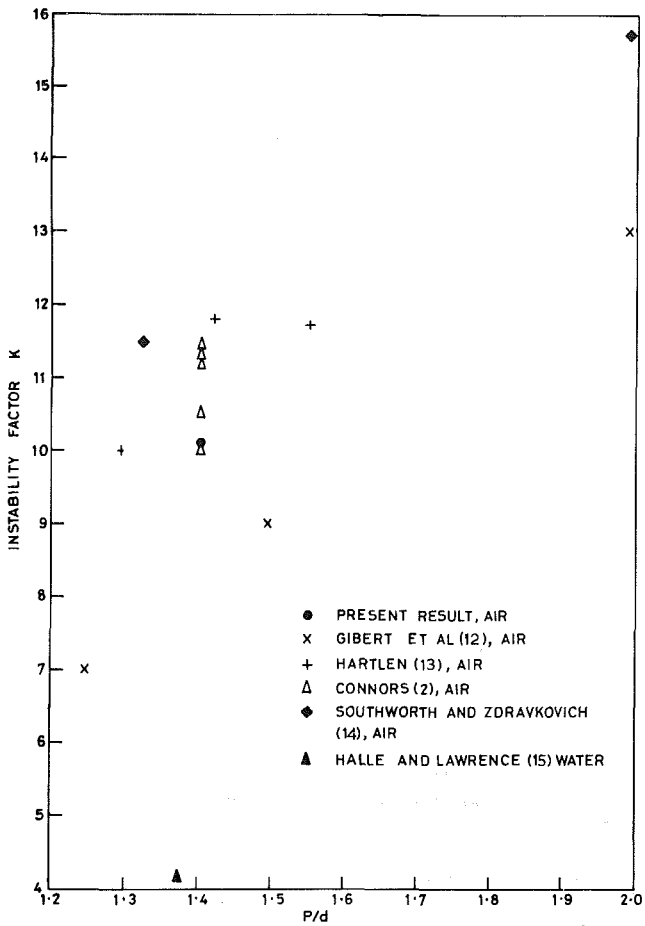

Fig. 13 Instability factors for single tube rows

with flow, reaching a maximum of 145 dBA inside the wind tunnel, until at an intertube velocity of 23 m/s the noise disappeared to give way to extremely violent tube vibration. This vibration persisted until the flow had been reduced by 30 percent and the acoustic wave returned. The violent nature of the vibration caused early tube failure whilst attempting to produce tube response curves. After repair, tests were carried out in which the flow was steadily increased until the vibration was initiated, the flow was noted and the tunnel was immediately shut down. Use of acoustic baffles situated along the centerline of the wind tunnel, both upstream and downstream of the bundle and parallel with the flow, gave 40 dBA attenuation of the emitted noise. It was found that the upstream baffle could be removed without much effect on noise level, but the critical speed measured with the downstream baffle was 5 percent different from that without a baffle.

The tube bank with $P/d = 1.35$ exhibited somewhat different characteristics. In this case, the onset of the acoustic standing wave was accompanied by significant tube vibration as shown in Fig. 14, but at a frequency of 380 Hz, which corresponds to the vortex shedding frequency and the resultant acoustic resonance. Increasing the flow caused the noise and vibration to diminish until the onset of self-excited vibration was ultimately reached, characterised by motion at the tube fundamental frequency. The resulting vibration was again extremely violent and necessitated the same test technique as described above. It is interesting that vortex shedding, reinforced by the acoustic standing wave, was able to cause significant tube vibration at a frequency well away from the natural frequencies of the tube (33, 206, 579 Hz).

As tube spacing increased, so did the separation between vortex shedding resonance, enhanced by acoustic resonance,

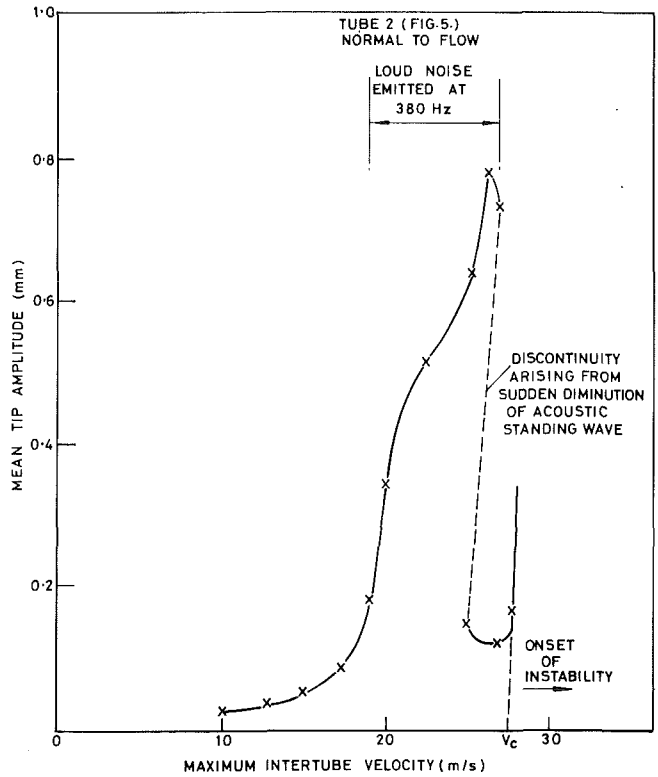

Fig. 14 Tube response for rotated square layout bundle with $P/d = 1.35$

and the onset of fluid-elastic instability. For the bundle with $P/d = 1.52$, vortex shedding/acoustic resonance occurred for intertube velocities between 19 and 25 m/s, whereas fluid-elastic instability did not occur until the intertube velocity reached 31 m/s. For the widest spaced bundle ($P/d = 1.78$), the vortex shedding/acoustic resonance occurred in the velocity range 20 to 26 m/s and the critical velocity for this bundle was 36 m/s.

Strouhal numbers, based on the measured frequency of the acoustic standing wave and an average intertube velocity, are given in Table 2 for each of the rotated square tube bundles. These values agree reasonably well with Strouhal numbers based on vortex shedding data taken from reference [19].

Barrington [20] has reported that heat exchangers that suffer acoustic resonance are frequently of the rotated square tube layout geometry, and this is in accordance with the author's experience of practical heat exchangers.

Conclusions

1 The rotated triangle geometry was the most prone to fluid-elastic instability, having a value for K of approximately 2.2 for P/d in the range 1.27 to 1.78.

2 The triangular geometry became less prone to fluid-elastic instability as the tube spacing was increased, K increasing from 2.5 to 6.4 as P/d was increased from 1.25 to 1.78.

3 For the square geometry, vibration occurred at the lowest critical velocity for $P/d = 1.52$, both closer and wider tube spacings being more resistant to fluid-elastic instability.

4 Although the rotated square geometry exhibited the greatest resistance to fluid-elastic whirling, this was marred by the presence of intense acoustic standing waves. This casts some doubt as to their suitability for applications with gas as the shellside fluid.

Tests on a single tube row have highlighted the need for further research if the mechanism of fluid-elastic instability is to be fully understood.

Table 2 Comparison of Strouhal number data

P/d	S_a	S_v
1.27	0.45	0.50
1.35	0.44	0.45
1.52	0.43	0.40
1.78	0.41	0.35

Acknowledgments

The author is grateful to Mr. I. M. Lockey for his assistance with the wind tunnel test work. He also wishes to thank UKAEA and HTFS for permission to publish this work. The HTFS vibration work is supported by the Chemicals and Minerals Requirements Board of the U.K. Department of Industry.

References

1 Paidoussis, M. P., "Flow Induced Vibrations in Nuclear Reactors and Heat Exchangers—Practical Experiences and State of Knowledge," *Proceedings of the Symposium on Practical Experiences with Flow Induced Vibrations*, IAHR/IUTAM, Karlsruhe, Germany, Sept. 3-6, 1979.

2 Connors, H. J., Jr., "Fluid-elastic Vibration of Tube Arrays Excited by Crossflow," *Proceedings of Symposium on Flow Induced Vibration in Heat Exchangers*, ASME, Dec. 1970, pp. 42-46.

3 Weaver, D. S., and Grover, L. K., "Crossflow Induced Vibrations in a Tube Bank—Turbulent Buffeting and Fluidelastic Instability," *Journal of Sound and Vibration*, Vol. 59, No. 2, 1978, pp. 277-294.

4 Price, S. J., and Paidoussis, M. P., "Fluid-elastic Instability of an Infinite Double Row of Circular Cylinders Subject to a Uniform Crossflow," ASME Design Engineering Technical Conference, Hartford, Conn., Sept. Paper No. 81-DET-24.

5 Tanaka, H., and Takahara, S., "Fluid-Elastic Vibration of a Tube Array in Crossflow," *Journal of Sound and Vibration*, Vol. 77, No. 1, 1981, pp. 19-37.

6 Weaver, D. S., and El Kashlan, M., "The Effects of Damping and Mass Ratio on the Stability of a Tube Bank," *Journal of Sound and Vibration*, Vol. 76, No. 2, 1981, pp. 283-294.

7 Franklin, R. E., and Soper, B. M. H., "An Investigation of Fluid-Elastic Instabilities in Tube Bundles Subjected to Fluid Crossflow," Paper F6/7, *Proceedings of 4th International Conference on Structural Mechanics in Reactor Technology*, Vol. 6, San Francisco, Calif., Aug. 1977, North Holland Publishing Co., pp. 1-14.

8 Gross, H. G., "Investigations in Aeroelastic Vibration Mechanisms and Their Application in Design of Tubular Heat Exchangers," dissertation (in German), Technical University of Hannover, 1975.

9 Roberts, B. W., "Low Frequency, Aeroelastic Vibrations in a Cascade of Circular Cylinders," Mechanical Engineering Science Monographs, No. 4, Sept. 1966.

10 Goyder, H. G. D., "Unstable Vibrations of a Bundle of Cylinders Due to Crossflow," International Conference on Recent Advances in Structural Dynamics," Institute of Sound and Vibration Research, University of Southampton, England, July 7-11, 1980.

11 Blevins, R. D., *Flow Induced Vibration*, 1st ed., Van Nostrand Reinhold, 1977.

12 Gibert, R. J., Chabrerie, J., and Sagner, M., "Tube Bundle Vibrations in Transversal Flow," Paper 2.2, *Proceedings of International Conference on Vibration in Nuclear Plant*, BNES/UKAEA, Keswick, England, May 9-12, 1978.

13 Hartlen, R. T., "Wind Tunnel Determination of Fluid-Elastic Vibration Thresholds for Typical Heat Exchanger Tube Patterns," Report No. 74-309-K, Aug. 1974, Ontario Hydro, Toronto, Canada.

14 Southworth, P. J., and Zdravkovich, M. M., "Crossflow Induced Vibrations of Finite Tube Banks in In-line Arrangements," *Journal of Mechanical Engineering Science*, Vol. 17, 1975, pp. 190-198.

15 Shin, Y. S., and Wambsganss, M. W., "Flow Induced Vibration in LMFBR Steam Generators—A State of the Art Review," *Nuclear Engineering and Design*, Vol. 40, No. 2, 1977, pp. 235-284.

16 Connors, H. J., Jr., "Fluid-elastic Vibration of Heat Exchanger Tube Arrays," *ASME Journal of Mechanical Design*, Vol. 100, No. 2, Apr. 1978, pp. 347-353.

17 Pettigrew, M. J., and Gorman, D. J., "Vibration of Heat Exchange Components in Liquid and Two Phase Crossflow," Paper 2.3, *Proceedings of International Conference on Vibration in Nuclear Plant*, BNES/UKAEA, Keswick, England, May 1978.

18 Hill, R. S., "Tube Vibration in Boilers and Other Heat Exchangers," *Transactions of North East Coast Institution of Engineers and Shipbuilders*, Vol. 92, 1976, pp. 91-100.

19 Fitz-Hugh, J. S., "Flow Induced Vibration in Heat Exchangers," Paper No. 427, *International Symposium on Vibration Problems in Industry*, Keswick, England, Organized by UKAEA Windscale/NPL Teddington, 1973.

20 Barrington, E. A., "Acoustic Vibrations in Tubular Exchangers," *Chemical Engineering Progress*, Vol. 69, No. 7, July 1973, pp. 62-68.

The Use of Porous Baffles to Control Acoustic Vibrations in Crossflow Tubular Heat Exchangers

K. P. Byrne
Senior Lecturer,
School of Mechanical and Industrial Engineering,
The University of New South Wales,
Sydney, Australia
and Visiting Scholar,
Ray W. Herrick Laboratories,
Purdue University,
West Lafayette, Ind. 47907

This paper describes how a single porous baffle can be used to prevent the occurrence of acoustic vibration in a crossflow tubular heat exchanger. A method for determining the optimum location and the optimum specific flow resistance of the porous baffle is presented. Finally, a description of how a porous baffle was successfully applied to control acoustic vibration which was occurring in the heat recovery region of a 375-MW brown coal steam generator is given.

Introduction

A commonly used heat exchanger construction consists of a parallel bundle of tubes which is immersed in a fluid whose flow direction over the outside of the tubes is perpendicular to the tube axes. This type of heat exchanger is often described as a crossflow tubular heat exchanger. Fluid flowing inside the tubes is heated or cooled by the fluid flowing across the outside of the tubes. Occasionally, the fluid flowing across the outside of the tubes in this type of heat exchanger produces a vibration of the heat exchanger. This vibration is usually associated with either the vibration of the tubes, or if the fluid which surrounds the tubes is a gas, this gas may vibrate in a resonant manner. The vibration of the tubes is often harmful in that it can cause fretting wear, either at the tube supports or at the tube center spans due to tube-to-tube contact. Further, fatigue failures of the tubes may also occur. The resonant vibration of the gas around the tubes, which is commonly called acoustic vibration, may also cause failures of the tubes if it occurs at a frequency which is close to one of the natural frequencies of the tubes. Even if the resonant vibration of the gas does not produce tube failures, it generally produces an intense, low frequency, pure tone noise which is usually considered to be unacceptable. It may also induce fatigue damage to the casing of the heat exchanger. A good summary of the methods for controlling vibration in crossflow tubular heat exchangers is given by Eisinger [1].

The purpose of this paper is to describe a novel method of preventing acoustic vibration from occurring in a crossflow tubular heat exchanger. The usual method of preventing this vibration from occurring is to fit solid baffles between the tubes so that the baffles are parallel to the direction of the crossflow over the tubes. Generally, in crossflow tubular heat exchangers such as those used in the economizer region of large fossil fuel steam generators, a number of baffles must be fitted. These baffles can be expensive to fit, especially if they are retrofitted, and they may seriously inhibit inspection and maintenance operations. The method for preventing acoustic vibration described in this paper involves the use of a single porous baffle located at a particular plane in the heat exchanger. This porous baffle is installed between the tubes so that it is parallel to the direction of the crossflow of the gas over the tubes. This paper describes how the proper location and specific flow resistance of the porous baffle can be determined. The application of the porous baffle to overcoming an acoustic vibration problem in a large brown coal fired steam generator is also described.

Review of the Acoustic Vibration Phenomenon

Acoustic vibration in crossflow tubular heat exchangers has been the subject of extensive study. A review of this topic has been recently made by Blevins [2]. Aspects of acoustic vibration in crossflow tubular heat exchangers which are relevant to the porous baffle described in this paper are outlined in this section.

Consider a single cylindrical tube centrally located in a large flow duct such that the axis of the tube is perpendicular to the direction of the flow in the duct. As the fluid in the duct flows past the tube, vortices will be formed in the wake behind the tube if the Reynolds number, $\mathrm{Re}=\rho VD/\eta$, is within a certain range. Here, ρ is the fluid density, V is the free-stream velocity, D is the tube diameter, and η is the dynamic viscosity of the fluid. The frequency, f_v, of the vortex shedding can be determined from the Strouhal number, $S=f_vD/V$, which remains nearly constant with a value of 0.2 for Reynolds numbers from about 300 to 200,000.

Consider now the arrangement of tubes shown in Fig. 1. This arrangement shows the cross section of an in-line crossflow tubular heat exchanger. Although it has been accepted that vortices are shed in a discrete periodic manner from the first few rows of tubes encountered by the crossflow entering a heat exchanger such as that represented in Fig. 1, some skepticism has been expressed about the existence of vortices which are shed in a discrete periodic manner from further rows of tubes encountered by the crossflow. Owen [3] has proposed that turbulent buffeting of these spatially periodic further rows of tubes generates a spectrum of the fluctuating quantities in the gas around the tubes, such as the gas particle velocity, which exhibits a peak at a buffeting frequency, f_b, given by

$$f_b = V_{\max} D\left[3.05\left[\frac{T-D}{T}\right]^2 + 0.28\right]/TL \qquad (1)$$

$V_{\max}$ is the intertube gas velocity, D is the tube diameter, L is the tube pitch in the longitudinal or flow direction, and T is the tube pitch in the transverse direction.

Although the previously outlined turbulent buffeting theory is based on sound reasoning, it has been traditional engineering practice to assume that vortices will be shed from all of the tubes in a group of tubes, such as those shown in Fig. 1, at a vortex shedding frequency, f_v, given by equation (2). The Strouhal number, S, is, in general, not equal to 0.2.

Contributed by the Heat Transfer Division for publication in the JOURNAL OF HEAT TRANSFER. Manuscript received by the Heat Transfer Division October 18, 1982.

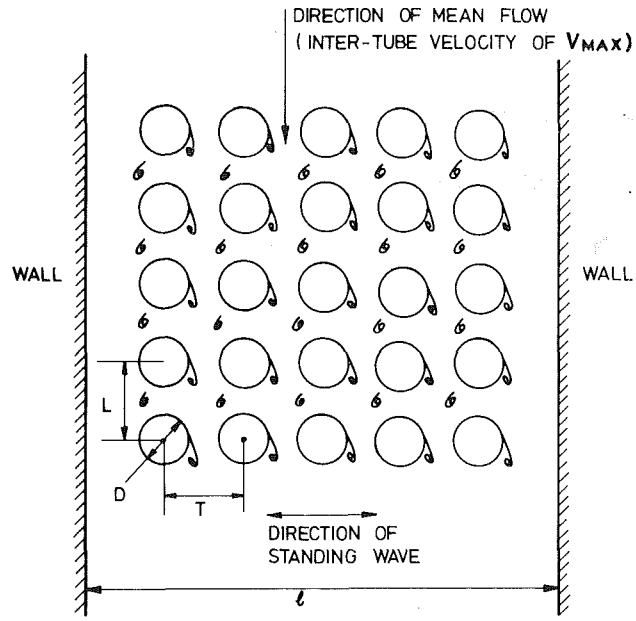

Fig. 1 Cross section of an in-line crossflow tubular heat exchanger showing nomenclature

$$f_v = SV_{\max}/D \tag{2}$$

$V_{\max}$ is the intertube gas velocity, and D is the tube diameter.

Experimental data have been compiled, for example, by Fitz-Hugh [4], to give the Strouhal numbers, S, for various tube bank geometries. In these data, the Strouhal numbers are given for various L/D and T/D ratios, where L is the tube pitch in the longitudinal or flow direction and T is the tube pitch in the transverse direction. Other investigators have also assembled similar data. Unfortunately, there is not always close agreement between the data published by various investigators. The most recent readily obtained data are those given by Murray et al. [5].

It has been noted by Païdoussis [6] that, despite the evident differences in the mechanisms associated with turbulent buffeting and vortex shedding, it is found that f_b computed from equation (1) is usually approximately equal to f_v computed from equation (2). Thus, an excitation frequency, f_e, can be defined by

$$f_e \approx f_b \approx f_v \tag{3}$$

Although turbulent buffeting or vortex shedding in a tube arrangement such as that shown in Fig. 1 is associated with a particular excitation frequency, f_e, fluctuating quantities, such as the gas particle velocities around different tubes, will in general not be synchronized. However, at certain frequencies, it is possible for these fluctuating quantities to become synchronized around all the tubes. These frequencies are given by the frequencies, f_s, at which standing waves can exist between the walls shown in Fig. 1. Disturbances in the gas at a frequency which is close to a standing wave frequency tend to promote the generation of the corresponding standing wave. Suppose that a standing wave is present between the walls. The gas which is flowing across the tubes has, in addition to its mean velocity in the flow direction, a fluctuating velocity transverse to the mean flow direction. This fluctuating transverse velocity is associated with the standing wave. It is this fluctuating transverse velocity that, if sufficiently large, will cause the fluctuating quantities around all the tubes to become synchronized. These synchronized fluctuating quantities reinforce and sustain the standing wave. The standing wave frequencies, f_s, are given by

$$f_s = \frac{nc_{\text{eff}}}{2l} \qquad n = 1,2,3, \ldots . \tag{4}$$

l is the span between the walls as shown in Fig. 1 and c_{eff} is the effective speed of sound. It has been shown by Parker [7] that the tubes reduce the actual speed of sound, c, in the gas to an effective speed of sound, c_{eff}, in planes normal to the axes of the tubes.

The spatial variation of the fluctuating transverse gas velocity and the fluctuating pressure for $n = 1,2$ and 3 is shown in Fig. 2. When $n = 1$, the standing wave is composed of one half-wave between the walls, and the maximum value of the fluctuating transverse gas velocity occurs at the "half-span" point between the walls. When $n = 2$, the standing wave is composed of two half-waves between the walls, and the maximum fluctuating transverse gas velocity occurs at the "quarter-span" points between the walls. When $n = 3$, the standing wave is composed of three half-waves between the walls, and the maximum fluctuating transverse gas velocity occurs at the "sixth-span" points and the "half-span" point. The fluctuating pressure associated with any standing wave can be seen from Fig. 2 to have a maximum value at the walls. It is this fluctuating pressure which, in practical crossflow tubular heat exchangers, causes the casing to vibrate and radiate sound.

Although it is essential that the intertube gas velocity $V_{\max}$

Nomenclature

c = speed of sound (m/s)
c_{eff} = effective speed of sound (m/s)
d = distance of porous baffle from wall of heat exchanger (m) (see Fig. 3)
D = tube diameter (m) (see Fig. 1)
f = frequency (Hz)
f_b = buffeting frequency (Hz)
f_e = excitation frequency (Hz)
f_s = standing wave frequency (Hz)
f_v = vortex shedding frequency (Hz)
k = wave number (1/m)
l = span between heat exchanger walls (m) (see Fig. 1)
L = tube pitch in longitudinal flow direction (m) (see Fig. 1)
n = number of half waves between heat exchanger walls (integer) (see Fig. 2)
$\tilde{P}_i$ = complex representation of the acoustic pressure at point i modulus (Pa) argument (radians)
R = specific flow resistance (rayls)
Re = Reynolds number (dimensionless)
S = Strouhal Number (dimensionless)
T = tube pitch in the transverse direction (m) (see Fig. 1)
V = free-stream velocity (m/s)
$V_{\max}$ = intertube gas velocity in the minimum gap between two neighboring tubes (m/s)
$\tilde{z}_i$ = complex representation of the specific acoustic impedance at point i modulus (rayls) argument (radians)
ρ = density (kg/m^3)
ρc = characteristic impedance (rayls)
Ψ = Chen number (dimensionless)
η = dynamic viscosity (Pa•s)
ω = angular frequency (rad/s)

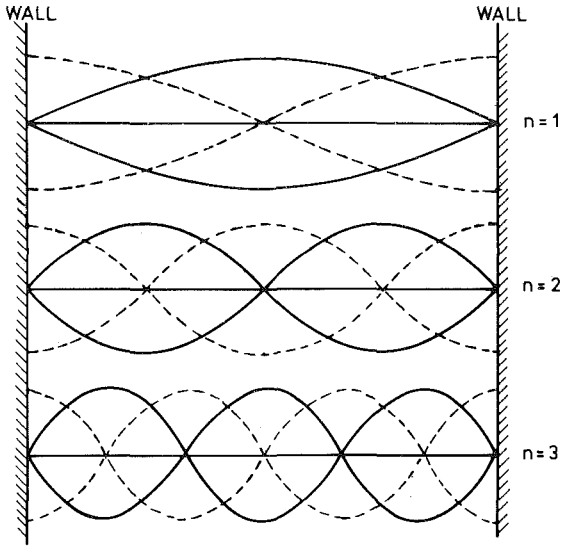

Fig. 2 Variation of the fluctuating transverse velocity and the fluctuating pressure associated with standing waves composed of one, two, and three half-waves (___ velocity ···· pressure)

be such that equation (5) is satisfied before acoustic vibrations can occur, it is not a sufficient condition.

$$f_e = f_s \tag{5}$$

Chen [8] has proposed a number, Ψ, which has been found useful in assessing whether or not a crossflow tubular heat exchanger is likely to exhibit acoustic vibrations at the frequencies given by equation (4). The Chen number, Ψ, is given by

$$\Psi = \frac{\mathrm{Re}}{\mathrm{S}} \left[\frac{L-D}{L} \right]^2 \frac{D}{T} \tag{6}$$

Re is the Reynolds Number, and S is the Strouhal Number. These numbers are defined in terms of the intertube gas velocity, $V_{\max}$. L is the tube pitch in the longitudinal or flow direction, and T is the tube pitch in the transverse direction. D is the tube diameter.

Chen and Young [9] have analyzed the acoustic vibration potential of the crossflow tubular heat exchangers in a large number of steam generators. They concluded that if Ψ for a particular heat exchanger is greater than about 2000, acoustic vibration is likely to occur in this heat exchanger.

It can be concluded, in summary, that, if acoustic vibrations are to occur in crossflow tubular heat exchangers, not only must there be matching between the excitation frequency, f_e, and a standing wave frequency, f_s, but, at this condition, the Chen number, Ψ, given by equation (6) must exceed some value.

The Porous Baffle Concept

It was seen in the previous section that the generation of acoustic vibration in a crossflow tubular heat exchanger is closely related to the development of standing waves. It is necessary to have standing waves to produce synchronization of fluctuating quantities, such as the fluctuating gas particle velocity, around all of the tubes. If standing waves are inhibited from developing, this synchronization and the associated acoustic vibration will not occur. The basic aim of the porous baffle is to provide a means of inhibiting the development of standing waves. The porous baffle consists of a single flow resistive element which is inserted between the tubes so that it is parallel to the flow direction. The porous baffle inhibits the transverse motion of the gas particles that is associated with the standing waves. The advantage of a porous baffle over solid baffles is that a single porous baffle can be used to inhibit the development of a number of standing waves, whereas several solid baffles are required to inhibit the development of a number of standing waves. The method of determining the optimum location and specific flow resistance of the porous baffle is described in the following sections.

The Optimum Location of the Porous Baffle

The correct location of a porous baffle in a crossflow tubular heat exchanger can be deduced from the preceding results. It can be seen from equations (1) and (2) that as the intertube gas velocity, $V_{\max}$, is increased the excitation frequency, f_e, increases in a proportional manner. There is a possibility that acoustic vibrations will arise at all the flow velocities that produce excitation frequencies matching the standing wave frequencies. However, it is most likely that the acoustic vibrations will occur at the higher flow velocities. This can be seen by substituting $\mathrm{Re} = \rho V_{\max} D/\eta$ in equation (6) and noting that, since S and the other terms are constant, high values of Ψ are associated with high values of $V_{\max}$. This suggests that the porous baffle should be located at a position which will produce maximum damping of the highest frequency standing wave. The maximum damping which can be produced by a given resistive element will be obtained when the resistive element is located at a point where the transverse particle velocity in the standing wave is a maximum. Thus, for example, suppose that on the basis of the maximum intertube gas velocity, $V_{\max}$, there can be a maximum of three half-waves across the span between the walls. The maximum transverse particle velocity for this standing wave will occur at the "one-sixth" span points and at the "one-half" span point. This can be seen from Fig. 2. However, it is not satisfactory to place the porous baffle at the "one-half" span point, as at a lower flow velocity there could be a standing wave comprised of two half-waves between the walls. The "one-half" span point is a velocity node in this standing wave and so no damping of this standing wave will be produced. However, at the "one-sixth" span points, there is a substantial transverse particle velocity associated with a standing wave comprised of two half-waves and so substantial damping of this standing wave will also be produced.

It can be seen that, in general, if the maximum number of half-waves between the walls is n, the porous baffle should be located at a distance from one wall equal to the wall to wall span divided by $2n$. This recommendation is based on the assumption that the specific flow resistance of the porous baffle is not high enough to substantially alter the frequencies and velocity distributions of the standing waves.

Generally, in crossflow tubular heat exchangers such as those used in the economizer area of large fossil fuel steam generators where the distance, l, between the walls may be approximately 20 m, the tube geometry and gas velocities are such that the maximum value of n does not usually exceed 5.

It is of interest, by way of comparison, that if solid baffles are to be used to prevent acoustic vibration from occurring in a tubular heat exchanger in which the maximum number of half-waves that can occur between the walls is n, then n solid baffles should, in theory, be used to prevent the acoustic vibration occurring.

The Optimum Flow Resistance of the Porous Baffle

The function of the porous baffle is to produce the maximum damping of standing waves so that they do not develop and cause synchronization in the fluctuating quantities around all of the tubes. It is evident that, if the porous baffle has a very low flow resistance, it will extract little energy from the standing waves, and so they will only be lightly damped. It is also evident that, if the porous baffle has

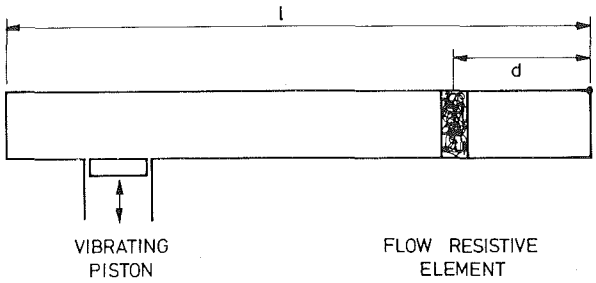

Fig. 3 Model used to investigate the effect of the specific flow resistance of the porous baffle

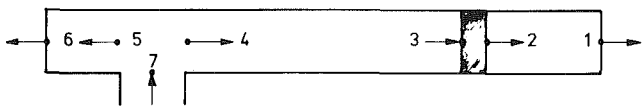

Fig. 4 Impedance and pressure calculation points for model

a very high flow resistance, it will act like a solid wall and standing waves will develop between the walls and the porous baffle. Thus, between these two extremes of flow resistance values there will be an optimum value. The simple model shown in Fig. 3 can be used to determine this optimum value. The model consists of a pipe of length, l, which is closed at both ends. The closed ends represent the walls shown in Fig. 1. The pipe contains a gas of density, ρ, and sonic velocity, c, and so the characteristic impedance of the gas is ρc. At a distance, d, from one end of the pipe is a flow resistive element which represents the porous baffle. The specific flow resistance of this element is R. The specific flow resistance of the element is the differential pressure across the element needed to produce a unit particle velocity through the element. Thus the normalized specific flow resistance is $R/\rho c$. A piston located at some point along the pipe excites longitudinal acoustic vibrations in the gas in the pipe. The point at which the piston is located must be such that it is not at a node. The analysis is simplified by having the cross-sectional area of the piston the same as the cross-sectional area of the pipe.

An easily measured quantity in an actual crossflow tubular heat exchanger is the amplitude of the acoustic pressure at the casing wall, and so it is appropriate to use the amplitude of the acoustic pressure at the closed end adjacent to the piston as the measure of the response of the gas in the system shown in Fig. 3. The basic aim of the analysis is to find how the frequency dependent acoustic pressure varies at the closed end as the normalized specific flow resistance of the flow resistive element is varied. It is convenient in doing this to keep the velocity amplitude of the piston constant at a value of unity.

Simple acoustic transmission line theory can be used for the analysis and an outline of how the analysis is done is now given with reference to Fig. 4. Details of some useful acoustic transmission line formulae are given in Appendix A. At points 1 and 6 on Fig. 4, the normalized specific acoustic impedances $\tilde{z}_1/\rho c$ and $\tilde{z}_0/\rho c$ in the directions shown are infinite. The impedance formula from Appendix A can be used with the infinite normalized specific acoustic impedances at points 1 and 6 to find, in the directions shown on Fig. 4, the normalized specific acoustic impedances at points 2 and 5, $\tilde{z}_2/\rho c$ and $\tilde{z}_5/\rho c$. The normalized specific acoustic impedance at point 3 in the direction shown, $\tilde{z}_3/\rho c$, can then be found from

$$\tilde{z}_3/\rho c = \tilde{z}_2/\rho c + R/\rho c \tag{7}$$

The impedance formula from Appendix A can then be applied to obtain, in the direction shown on Fig. 4, the normalized specific acoustic impedance at point 4 from that at point 3.

The equality of the acoustic pressures at points 4, 5, and 7 on Fig. 4 and the equality of the volume velocities entering and leaving the T joint on Fig. 4 lead to the parallel impedances formula and so at the piston

$$\tilde{z}_7/\rho c = \frac{(\tilde{z}_4/\rho c)(\tilde{z}_5/\rho c)}{\tilde{z}_4/\rho c + \tilde{z}_5/\rho c} \tag{8}$$

Since the piston has a unit velocity amplitude, the complex representation of the acoustic pressure at the piston is given by $\tilde{z}_7$ and so the "normalized" pressure per unit amplitude of the piston velocity is

$$\tilde{P}_7/\rho c = \tilde{z}_7/\rho c \tag{9}$$

The equality of the acoustic pressures at the T junction leads to

$$\tilde{P}_5/\rho c = \tilde{z}_7/\rho c \tag{10}$$

The pressure formula given in Appendix A allows the "normalized" acoustic pressure at point 6, $\tilde{P}_6/\rho c$, to be found from the corresponding result at point 5. The amplitude of $\tilde{P}_6/\rho c$ is the required result.

A computer program was written so that the preceding calculations could be readily performed. The results of the calculations are given in Figs. 5, 6, and 7. The horizontal axis

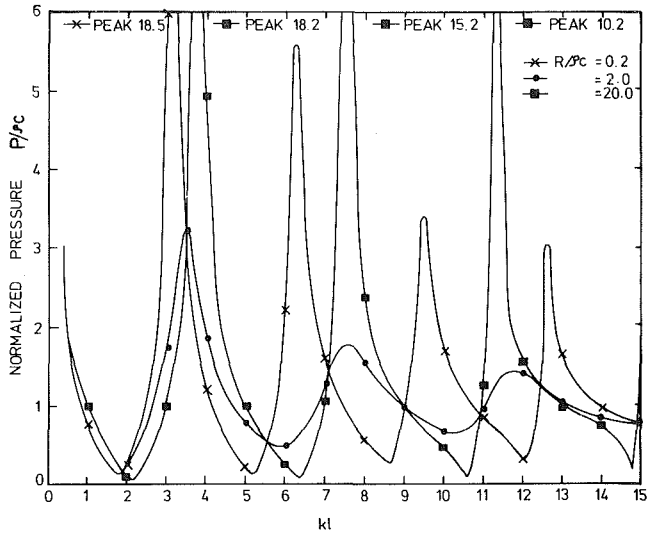

Fig. 5 Variation of the normalized pressure at point 6 with k for $d = l/6$ and $R/\rho c = 0.2$, 2.0, and 20.0

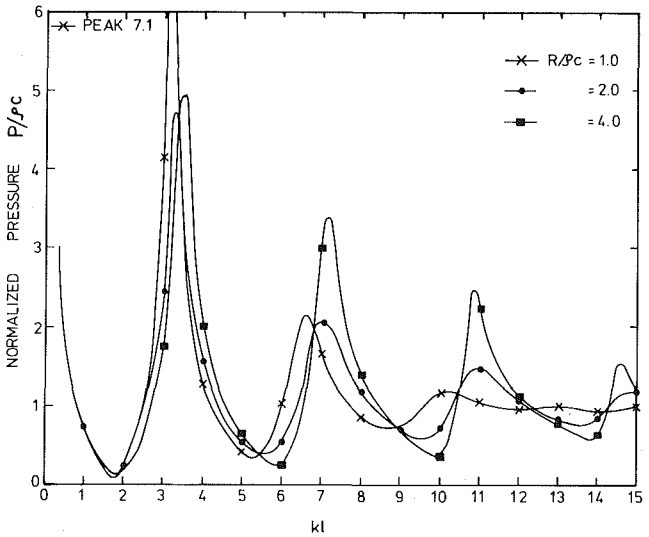

Fig. 6 Variation of the normalized pressure at point 6 with k for $d = l/6$ and $R/\rho c = 1.0$, 2.0 and 4.0

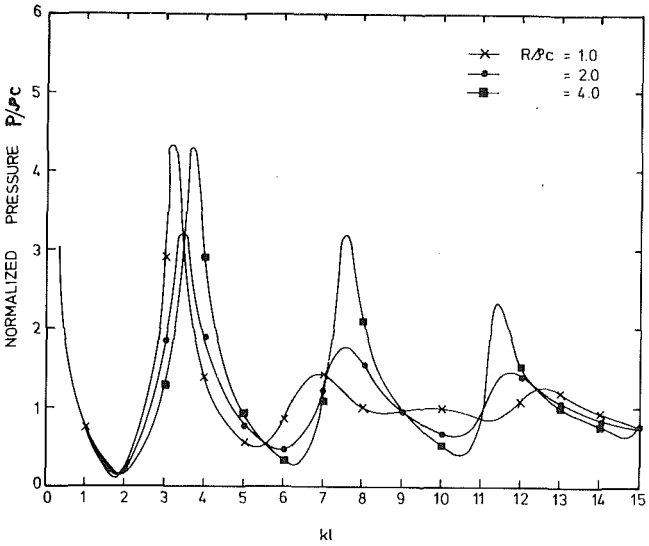

Fig. 7 Variation of the normalized pressure at point 6 with k for $d = l/8$ and $R/\rho c = 1.0$, 2.0 and 4.0

in these figures is the quantity $kl = \omega l/c = 2\pi fl/c$. In this last expression, f is the frequency, l is the distance between the ends of the pipe, and c is the sonic velocity. The vertical axis in these figures is the "normalized" pressure amplitude per unit piston velocity amplitude. The "normalized" pressure amplitude is the actual pressure amplitude divided by ρc. The parameter in the figures is the normalized specific flow resistance of the flow resistive element. The piston was located at a distance of $l/11$ from the closed end of the pipe shown in Fig. 3 for all of the calculations. The distance, d, the flow resistive element was located from the closed end of the pipe shown in Fig. 3, was $l/6$ for Figs. 5 and 6 and $l/8$ for Fig. 7.

Inspection of Figs. 5, 6, and 7 shows that, in terms of reducing the dynamic response of the gas in the pipe, the most effective value of the normalized specific flow resistance is approximately 2. Further, it can be seen from Figs. 6 and 7 that when the normalized specific flow resistance is considerably different from 2, the effectiveness of the flow resistive element in reducing the dynamic response of the gas is not greatly degraded. This fact is of considerable importance in a practical porous baffle.

It is not surprising that the optimum value of the normalized specific flow resistance of the porous baffle is 2. A standing wave can be considered to be the superposition of two progressive waves which are traveling in opposite directions. It is shown in Appendix B that the dissipation of acoustic energy produced per unit area by a thin flow resistive element of specific flow resistance, R, which is placed in the path of a plane progressive wave, is proportional to

$$\frac{4R/\rho c}{[R/\rho c + 2]^2} \tag{11}$$

The maximum value of this quantity occurs when $R/\rho c$ is 2.

The Use of a Porous Baffle in a 375-MW Brown Coal Steam Generator

It was found during the commissioning of a 375-MW brown coal steam generator at Yallourn in Australia that severe acoustic vibration occurred in the heat recovery area at about 68 percent of the CMR load. The heat recovery area of this steam generator incorporates a number of different in-line crossflow tubular heat exchangers of the type shown in Fig. 1. The acoustic vibration occurred at a frequency of 35 Hz and traverses across the tube banks with a probe microphone revealed that the acoustic vibration was

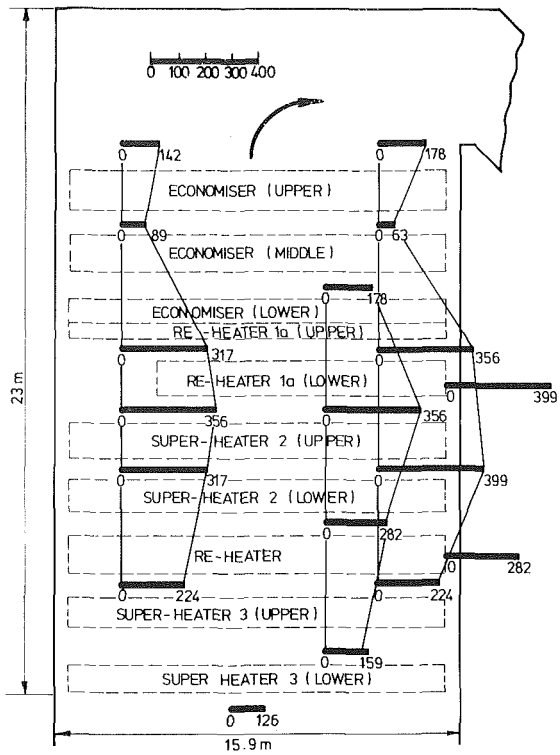

Fig. 8 Measured RMS acoustic pressures in Pa at a wall parallel to the tubes of a vibrating 375-MW steam generator at 68 percent of CMR load

associated with a standing wave of two half waves across the 15.9-m span between the walls parallel to the tubes. Thus, n was equal to 2. The RMS values of the harmonically fluctuating pressures in the gas were measured at a wall parallel to the tubes with a probe microphone inserted through the ports in the access doors. The pressures are shown in Fig. 8. The variation of these pressures in the flow direction suggests that, in addition to the standing wave between the walls, a standing wave was also present in the flow direction.

The dimensions, D, T, and L for the various tube banks shown in Fig. 8 are listed in Table 1 along with the Strouhal numbers, S, obtained from the data of Fitz-Hugh [4]. The design gas temperatures entering and leaving the various tube banks at 100 percent of the CMR load are shown in Table 2 along with the corresponding densities, ρ, sonic velocities, c, and intertube gas velocities, V_{max}, derived by assuming that the flue gas was a perfect gas with a gas constant of 306 J/kg°K, a specific heat ratio of 1.4 and an absolute pressure of 100 kPa. The data given in Tables 1 and 2 can be used to calculate the excitation frequencies, f_e, by use of equation (2) and the standing wave frequencies, f_s, by use of equation (4). The effective sonic velocity, c_{eff}, used in equation (4) was made equal to c because of the small differences between c_{eff} and c and the large tube-less chambers between the different tube banks. The span, l, was made equal to 15.9 m. The results of these calculations are given in Table 3. It was then assumed that the percentage of the CMR load was proportional to the flow velocity, and the data given in Table 3 was used to compute the percentage of the CMR load needed to produce matching between the excitation frequencies, f_e, and the standing wave frequencies, f_s. The corresponding Chen numbers at these conditions were also computed, and the results are shown in Table 4. It can be seen from equation (6) that the Reynolds number must be used to compute the Chen number. The dynamic viscosity used in computing the Reynolds number was extracted from the values given by Raznjevic [10] for air at various temperatures. The other data required for this computation are given in Table 1 and 2.

Table 1 Strouhal numbers, S, for various tube banks (after Fitz-Hugh [4])

Tube bank	D (mm)	T (mm)	L (mm)	T/D	L/D	S
Economizer	44.5	120	92	2.70	2.07	0.22
Reheater (1a)	63.5	120	110	1.89	1.73	0.26
Superheater 2	44.5	120	90	2.70	2.02	0.22
Reheater (1b)	57	120	110	2.11	1.93	0.24
Superheater 3	44.5	120	90	2.70	2.02	0.22

Table 2 Gas temperatures, densities, sonic velocities, and intertube velocities at 100 percent CMR load

Tube bank	Location	Temperature (°C)	Density (kg/m^3)	Sonic Velocity (m/s)	Intertube Velocity (m/s)
Economizer	outlet	338	0.535	512	8.22
	inlet	430	0.465	549	9.45
Reheater (1a)	outlet	430	0.465	549	12.58
	inlet	464	0.443	562	13.20
Superheater 2	outlet	464	0.443	562	9.92
	inlet	539	0.402	590	10.93
Reheater (1b)	outlet	539	0.402	590	13.10
	inlet	592	0.378	609	13.93
Superheater 3	outlet	592	0.378	609	11.63
	inlet	747	0.320	661	13.69

Table 3 Excitation frequencies and standing wave frequencies at 100 percent CMR load

Tube bank	Location	Excitation frequency (Hz)	Standing wave frequencies (Hz)			
			One 1/2 wave	Two 1/2 waves	Three 1/2 waves	Four 1/2 waves
Economizer	outlet	40.6	16.1	32.2	48.3	64.4
	inlet	46.7	17.3	34.5	51.8	69.1
Reheater (1a)	outlet	51.5	17.3	34.5	51.8	69.1
	inlet	54.0	17.7	35.3	53.0	70.7
Superheater 2	outlet	49.0	17.7	35.3	53.0	70.7
	inlet	54.0	18.6	37.1	55.7	74.2
Reheater (1b)	outlet	55.2	18.6	37.1	55.7	74.2
	inlet	58.7	19.2	38.3	57.4	76.6
Superheater 3	outlet	57.5	19.2	38.3	57.4	76.6
	inlet	67.7	20.8	41.6	62.4	83.2

Table 4 Percentage of CMR load needed to produce matching of the excitation frequencies and the standing wave frequencies along with the corresponding Chen numbers, Ψ

Tube bank	Location	Standing wave condition							
		One 1/2 wave		Two 1/2 waves		Three 1/2 waves		Four 1/2 waves	
		%	Ψ	%	Ψ	%	Ψ	%	Ψ
Economizer	outlet	39.7	1155	79.3	2310	>110	–	>110	–
	inlet	36.9	980	73.9	1959	>110	–	>110	–
Reheater 1a	outlet	33.5	1359	67.1	2719	100.6	4078	>110	–
	inlet	32.7	1282	65.4	2564	98.1	3846	>110	–
Superheater 2	outlet	36.1	881	72.2	1763	108.2	2644	>110	–
	inlet	34.4	838	68.8	1677	103.1	2515	>110	–
Reheater 1b	outlet	33.6	1257	67.3	2514	100.9	3772	>110	–
	inlet	32.6	1172	65.2	2343	97.8	3515	>110	–
Superheater 3	outlet	33.3	726	66.7	1451	100.0	2177	>110	–
	inlet	30.7	604	61.4	1208	92.2	1811	>110	–

Inspection of Table 4 shows that, on the basis of the Chen numbers, the standing wave involving one half-wave is unlikely to develop between the walls parallel to the tubes, as the Chen numbers are considerably smaller than 2000. However, the standing wave involving two half-waves is likely to develop at a load of between 60 and 70 percent of the CMR load as the Chen numbers are above 2000 in some tube banks. This standing wave did in fact develop and the measured frequency of 35 Hz in the range of the predicted values shown in Table 3.

After a temporary porous baffle constructed of a 50-mm-thick blanket of high temperature mineral wool was found to be successful in preventing the acoustic vibration, a permanent porous baffle was fitted. This permanent porous baffle was constructed of two parallel sheets of perforated stainless steel. The space between the sheets was loosely filled with ceramic fiber to give the desired specific flow resistance. The desired specific flow resistance at a particular location is twice the characteristic impedance of the gas at that location, that is, twice the product of the density and sonic velocity values given in Table 2. Although this baffle could not be located in the optimum position because of support restrictions and was in fact located at the "one-fifth" span point, it was found to be successful in preventing acoustic vibration from occurring, even at high gas flow rates which would have produced a standing wave composed of three half-waves. This final porous baffle, which was approximately 23 m long by 15 m wide, contained 29 holes, 0.75 m in diameter. These holes were for the soot blower lances and were found not to affect the functioning of the porous baffle. However, it was found necessary to continue the baffle well above the upper economizer tube bank to prevent a relatively weak vibration from occurring in this tube bank.

Conclusions

The work described in this paper has shown how a single porous baffle can be used to prevent acoustic vibrations from occurring in a crossflow tubular heat exchanger. Further, a logical procedure for determining the optimum location and specific flow resistance of the porous baffle has been discussed. Briefly, if at the maximum flow condition, a standing wave of n half-waves is produced between the walls of the heat exchanger, then the optimum location of the porous baffle is at a distance of the wall to wall span divided by $2n$ from one wall, and the specific flow resistance of the baffle should be approximately equal to twice the characteristic impedance of the medium in which the baffle is operating.

Acknowledgment

The assistance of International Combustion Australia Limited in undertaking the work described in this paper is gratefully acknowledged. International Combustion Australia Limited holds certain patents relating to the porous baffle described in this paper.

References

1 Eisinger, F. L., "Prevention and Cure of Flow-Induced Vibration Problems in Tubular Heat Exchangers," ASME *Journal of Pressure Vessel Technology*, Vol. 102, 1980, pp. 138-145.

2 Blevins, R. D., "A Review of Acoustic Resonance in Heat Exchanger Tube Bundles," Third Keswick International Conference on Vibration in Nuclear Plant, sponsored by UKAEA and BNES, May 1982.

3 Owen, P. R., "Buffeting Excitation of Boiler Tube Vibration," *Journal of Mechanical Engineering Science*, Vol. 7, No. 4, 1965, pp. 431-439.

4 Fitz-Hugh, J. S., "Flow-Induced Vibration in Heat Exchangers," International Symposium on Vibration Problems in Industry, Keswick, U.K., Apr. 1973.

5 Murray, B. C., Bryce, W. B., and Rae, G., "Strouhal Numbers for Tube Arrays," Third Keswick International Symposium on Vibration in Nuclear Plant, Sponsored by UKAEA and BNEW, May 1982.

6 Païdoussis, M. P., "Flow-Induced Vibrations in Nuclear Reactors and Heat Exchangers," *Practical Experiences With Flow-Induced Vibrations*, edited by E. Naudascher and D. Rockwell, Springer-Verlag, 1980, pp. 1-81.

7 Parker, R., "Acoustic Resonances in Passages Containing Banks of Heat Exchanger Tubes," *Journal of Sound and Vibration*, Vol. 57, No. 2, 1978, pp. 245-260.

8 Chen, Y. N., "Flow-Induced Vibration and Noise in Tube Bank Heat Exchangers Due to von Kármán Streets," ASME *Journal of Engineering for Industry*, Vol. 90, 1968, pp. 134-146.

9 Chen, Y. N., and Young, W. C., "The Orbital Movement and the Damping of the Fluidelastic Vibration of Tube Banks Due to the Vortex Formation, Part 3—Damping Capability of the Tube Bank Against Vortex Excited Sonic Vibration in the Fluid Column," ASME *Journal of Engineering for Industry*, Vol. 96, 1974, pp. 1072-1075.

10 Raznjevic, K., *Handbook of Thermodynamic Tables & Charts*, Hemisphere Publishing Corporation.

11 Kinsler, L. E., and Frey, A. R., *Fundamentals of Acoustics*, John Wiley and Sons, 1962.

APPENDIX A

Acoustic Transmission Line Formulae

This appendix provides a brief outline of how two useful acoustic transmission line formulae are developed. The development of the simple harmonic solution of the acoustic plane wave equation on which these formulae are based is in given books on physical acoustics, such as Kinsler and Frey [11].

It is convenient to represent the wave elements associated with traveling harmonic plane acoustic waves by the complex notation. Suppose, for example, that the acoustic pressure associated with a plane harmonic wave traveling in the positive x-direction is given by

$$p_+(x,t) = P_+ \cos(\omega t - kx + \phi_+) \tag{A1}$$

P_+ is the amplitude of the acoustic pressure, ω is the angular frequency, k is the wave number, and ϕ_+ is the phase relative to some time and position origins. The complex representation of this acoustic pressure is

$$\tilde{p}_+ = \tilde{P}_+ e^{j(\omega t - kx)} \tag{A2}$$

The amplitude and phase information have been grouped into the complex quantity, $\tilde{P}_+$, as

$$\tilde{P}_+ = P_+ e^{j\phi} \tag{A3}$$

The real part of the right-hand side of equation (A2) has physical significance and is equal to the right-hand side of equation (A1).

The complex representation of the acoustic pressure of a harmonic plane acoustic wave traveling in the negative x-direction is

$$\tilde{p}_- = \tilde{P}_- e^{j(\omega t + kx)} \tag{A4}$$

The corresponding complex representations of the particle velocities associated with the positive and negative traveling harmonic plane acoustic waves $\tilde{u}_+$ and $\tilde{u}_-$ are related to the complex representations of the acoustic pressures by the characteristic impedance ρc of the gas in which the waves are traveling by

$$\tilde{u}_+ = \tilde{p}_+ / \rho c \tag{A5}$$

$$\tilde{u}_- = -\tilde{p}_- / \rho c \tag{A6}$$

At each value of x, the actual acoustic pressure is composed of the acoustic pressures associated with the waves traveling in the positive and negative x-directions, and then, the complex representation of the actual acoustic pressure is

$$\tilde{p} = \tilde{p}_+ + \tilde{p}_- \tag{A7}$$

Similarly

$$\tilde{u} = \tilde{u}_+ + \tilde{u}_- \tag{A8}$$

The specific acoustic impedance, $\tilde{z}$, is the ratio of the complex pressure, $\tilde{p}$, to the complex particle velocity, $\tilde{u}$, and so

$$\tilde{z} = \frac{\tilde{p}}{\tilde{u}} \tag{A9}$$

The modulus of $\tilde{z}$ represents the amplitude of the acoustic pressure needed to produce a unit amplitude of the particle velocity, and the argument of $\tilde{z}$ represents the phase

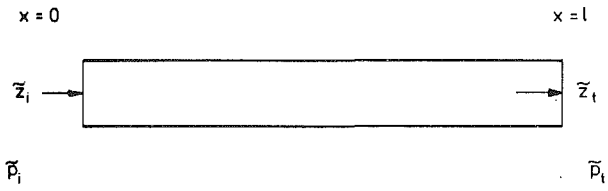

Fig. 9 Model for acoustic transmission line formulae

relationship between the acoustic pressure and the particle velocity.

The preceding results can be used to develop two useful acoustic transmission line formulae.

The Impedance Formula

A pipe length, l, is shown in Fig. 9. The pipe contains a gas with a characteristic impedance of ρc. At the end $x=l$, the pipe is terminated by a specific acoustic impedance of $\tilde{z}_t$. It is required to find the specific acoustic impedance at the end $x=0$.

Application of equations (A2) and (A4) to (A9) yields

$$\tilde{z}_t = \frac{[\tilde{P}_+ e^{-jkl} + \tilde{P}_- e^{jkl}]}{[\tilde{P}_+ e^{-jkl} - \tilde{P}_- e^{jkl}]/\rho c} \tag{A10}$$

Manipulation of this equation yields

$$\tilde{P}_- = \tilde{P}_+ \frac{(1-\rho c/\tilde{z}_t)e^{-j2kl}}{(1+\rho c/\tilde{z}_t)e^{+j2kl}} \tag{A11}$$

At $x=0$, the specific acoustic impedance, $\tilde{z}_i$, is given by

$$\tilde{z}_i = \frac{(\tilde{P}_+ + \tilde{P}_-)}{(\tilde{P}_+ - \tilde{P}_-)/\rho c} \tag{A12}$$

The substitution of equation (A11) into equation (A12) yields the required result

$$z_i = \rho c\left[\frac{(1+\rho c/\tilde{z}_t)e^{jkl} + (1-\rho c/\tilde{z}_t)e^{-jkl}}{(1+\rho c/\tilde{z}_t)e^{jkl} - (1-\rho c/\tilde{z}_t)e^{-jkl}}\right] \tag{A13}$$

Division of both sides of this equation by ρc gives the normalized specific acoustic impedance $\tilde{z}_i/\rho c$ at the inlet of the pipe. Equation (A13) is referred to as the impedance formula.

The Acoustic Pressure Formula

A pipe of length, l, is shown in Fig. A1. The pipe contains a gas with a characteristic impedance of ρc. At the end $x=0$, the pipe has an input impedance of $\tilde{z}_i$ and the complex representation of the acoustic pressure is $\tilde{P}_i$. It is required to find the complex representation of the acoustic pressure at the end $x=l$.

The previous nomenclature can be used to give the following equations at $x=0$

$$\tilde{P}_i = \tilde{P}_+ + \tilde{P}_- \tag{A14}$$

$$\tilde{z}_i = \frac{(\tilde{P}_+ + \tilde{P}_-)}{(\tilde{P}_+ - \tilde{P}_-)/\rho c} \tag{A15}$$

At $x=l$, the acoustic pressure, $\tilde{P}_t$, is given by

$$\tilde{P}_t = \tilde{P}_+ e^{-jkl} + \tilde{P}_- e^{jkl} \tag{A16}$$

Substitution of equations (A14) and (A15) into this equation yields the required result

$$\tilde{P}_t = \frac{\tilde{P}_i}{2}[[1+\rho c/\tilde{z}_i]e^{-jkl} + [1-\rho c/\tilde{z}_i]e^{jkl}] \tag{A17}$$

Equation (A17) is referred to as the pressure formula.

APPENDIX B

Acoustic Energy Dissipation Formula

Suppose that a thin flow resistive element of specific flow resistance, R, is placed at $x=0$ in the path of a traveling harmonic plane acoustic wave whose acoustic pressure can be represented by

$$\tilde{p}_i = \tilde{P}_i e^{j(\omega t - kx)} \tag{B1}$$

A reflected and transmitted wave will be generated at the flow resistive element. The complex representations of the acoustic pressures of the reflected transmitted waves are, respectively

$$\tilde{p}_r = \tilde{P}_r e^{j(\omega t + kx)} \tag{B2}$$

$$\tilde{p}_t = \tilde{P}_t e^{j(\omega t - kx)} \tag{B3}$$

The corresponding particle velocities are represented by

$$\tilde{u}_i = \tilde{p}_i/\rho c \tag{B4}$$

$$\tilde{u}_r = -\tilde{p}_r/\rho c \tag{B5}$$

$$\tilde{u}_t = \tilde{p}_t/\rho c \tag{B6}$$

At the flow resistive element, where $x=0$, the differential pressure across the flow resistive element, $\tilde{P}_i + \tilde{P}_r - \tilde{P}_t$, is equal to the product of the specific flow resistance of the flow resistive element and the particle velocity through it. The particle velocity through the flow resistive element is equal to the particle velocity of the transmitted wave. These facts lead to

$$\tilde{P}_i + \tilde{P}_r - \tilde{P}_t = \frac{R}{\rho c}\tilde{P}_t \tag{B7}$$

Since the particle velocity entering the flow resistive element must equal that leaving it, equation (B8) can be written

$$\tilde{P}_i - \tilde{P}_r = \tilde{P}_t \tag{B8}$$

These two equations can be used to express $\tilde{P}_r$ and $\tilde{P}_t$ in terms of $\tilde{P}_i$ to give

$$\tilde{P}_t = \frac{2}{(R/\rho c + 2)}\tilde{P}_i \tag{B9}$$

$$\tilde{P}_r = \frac{R/\rho c}{(R/\rho c + 2)}\tilde{P}_i \tag{B10}$$

The acoustic intensity, I, of a traveling harmonic plane acoustic wave whose acoustic pressure amplitude is P is $P^2/2\rho c$. Thus, by finding the acoustic intensities of the reflected and transmitted waves and subtracting these from the intensity of the incident wave, the energy dissipation rate per unit area, E_d, in the flow resistive element can be found. It is

$$E_d = \frac{4R/\rho c}{(R/\rho c+2)^2} \times \frac{P_i^2}{2\rho c} \tag{B11}$$

Natural Convective Heat Transfer on an Unheated Vertical Plate Attached to an Upstream Isothermal Plate

K. Kishinami
Associate Professor,
Department of Industrial Mechanical Engineering,
Muroran Institute of Technology,
Muroran, Japan

N. Seki
Professor,
Department of Mechanical Engineering,
Faculty of Technology,
Hokkaido University,
Sapporo, Japan

A numerical and experimental investigation on natural convective heat transfer with the coupling of heat conduction and thermal radiation from a vertical unheated plate connected to an upstream isothermal plate is carried out. The governing equations for conduction in the unheated plate and for convection in the boundary layer are written in finite difference form and are analyzed numerically by using an iterative technique coupled through the common heat flux with thermal radiation. The numerical results are discussed after comparing with the experimental results of temperature and velocity profiles and heat transfer coefficient. The coupling effects of heat conduction in the unheated plate and thermal radiation from the surface on laminar natural convective heat transfer from the plate connected to an isothermal heated upstream plate is greatly influenced by the plate-fluid thermal conductivity ratio and plate thickness, and the radiation emissivity of the plate.

1 Introduction

Natural convection from a plate with an arbitrarily curved surface [1, 2] or with complex thermal conditions [3] plays an important role in the field of heat transfer engineering. However, the coupling effects of conduction in an unheated plate and thermal radiation from the plate, which is connected to an upstream heated plate, on natural convective heat transfer along it seem to be an open question.

In an earlier work concerning the problem as mentioned here, Yang [4], using an integral technique in the wake region studied the laminar free convection wake above a heated finite vertical plate using an asymptotic series expansion by which the velocity and temperature profiles were found in the immediate neighborhood of the trailing edge. Zinnes [5] studied analytically the problem of laminar natural convective heat transfer from a vertical flat plate with an arbitrary surface heating. He used a numerical technique that considered heat conduction in the plate and stated that the computational procedure by finite difference method, which he described in detail, gave a reliable, convergent, and economic solution to a wide class of similar problems. He pointed out that the most important factor for this case was the plate-fluid conductivity ratio. Hayday et al. [6] studied analytically a similar problem of heat transfer from a vertical plate with discontinuous wall temperature by using a numerical technique in which the streamwise derivatives were approximated by finite differences. The method developed by them promised to be useful in solving a wide variety of problems. Kelleher [7] explored the same problems using a classical asymptotic expansion, in which his numerical results for various wall-temperature ratios were compared with the numerical work of Hayday et al. and with experimental data. To determine the laminar free convection wake above an isothermal vertical plate, Hardwick et al. [8] used numerical analysis for a fluid region that was described by both parabolic equations and elliptic equations. They compared their predictions with experimental results obtained by using a laser holographic interferometer and a hot wire anemometer. For the effect of thermal radiation on natural convective heat transfer, Fujii et al. [9] studied numerically and experimentally the natural convective heat transfer from a uniform heat flux vertical plate subjected to thermal radiation. They proposed a simple prediction for the surface temperature distribution on the plate. For steady buoyancy-induced upflow above a uniformly heated vertical plate, which is referred to as a natural convection plume, Sparrow et al. [10] studied numerically this problem for the values of Pr = 0.7 and 10, and they pointed out that the fully developed free plume was symmetric about the vertical plane.

In this paper the problem of natural convective heat transfer in air around an unheated vertical plate connected to an upstream isothermal plate is studied taking into account both the effects of heat conduction in the unheated plate and thermal radiation from the plate. Results predicted with a finite difference method are compared with experimental ones. The velocity boundary layer was measured by a photographic technqiue that uses the trajectories of fine zinc stearate particle injected at relatively low speed on the leading edge by means of micro particle ejector. Detailed discussions are given to clarify the characteristic behavior of the flow and heat transfer with results obtained for a broad range of parameters.

2 Experimental Apparatus and Measurement

Figure 1 illustrates the outline of the present experimental apparatus composed of an isothermal heated vertical plate followed by an unheated plate, and equipment for the measurement of the velocity and temperature profiles. This apparatus is placed in a thermostatic chamber of dimensions 3.32 × 2.71 × 2.23 m, which possesses good thermal isolation. Its wall and ceiling are covered with asbestos plates which fulfill the requirements of a blackbody enclosure, and concrete floors are each backed by a 100-mm thickness of styrofoam block insulation.

The air temperature is closely controlled by thermostat and a wollen cloth curtain serves as a screen damper to suppress stray air currents in the chamber. The temperature control cycle during the run operates on and off at the successive intervals of 30 and 1200 s, respectively,. The wall of the room

Contributed by the Heat Transfer Division for publication in the JOURNAL OF HEAT TRANSFER. Manuscript received by the Heat Transfer Division May 13, 1982.

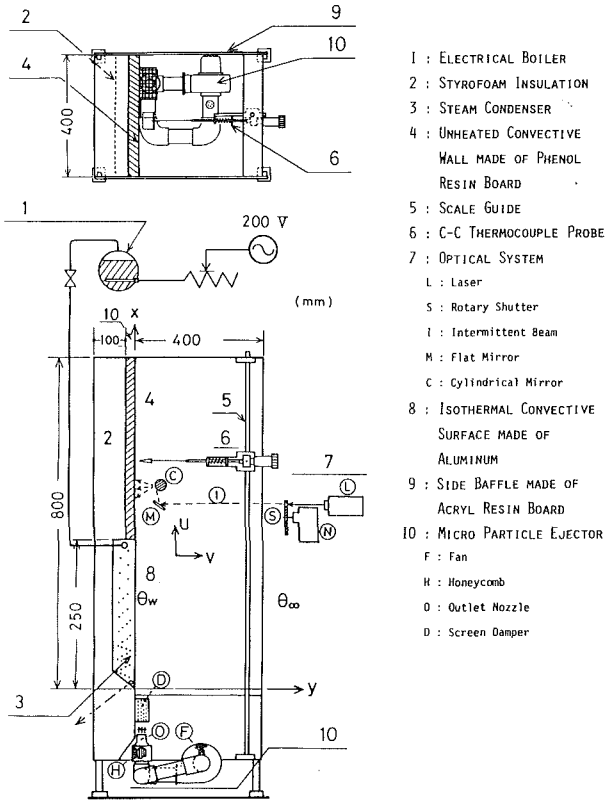

Fig. 1 Experimental apparatus

is nearly equal to the air temperature, ϑ_∞, which is very steady over long periods of time. A steady laminar natural convection boundary layer develops on the heated upstream surface which was made of aluminum. The temperature of this surface was maintained at 99.4°C during the experiments by saturated steam generated with an electric boiler (1). Natural convective heat transfer is caused by the steady buoyancy-induced upflow on the unheated plate connected to the aforementioned plate, which is made of phenol resin of 10 mm in thickness, and the backside is thermally isolated from the surroundings by styrofoam block insulation of 100 mm in the unheated plate, which also exchanges heat by radiation with isothermal nonreflecting surroundings at the ambient temperature. The measurement of the surface temperature is carried out with copper-constantan thermocouples set at 11 points along the heated and unheated surfaces. A steady-state condition is obtained after 3 or 4 hrs from the starting of the run. The temperature measurement of the boundary layer is performed with a copper-constantan thermocouple probe of 0.1 mm in diameter (6). The velocity distribution in the fluid layer is measured with the optical system (7), which consists of laser (L), rotary shutter (S), flat mirror (M), and cylindrical mirror (C), and with the trajectories of fine zinc stearate visualized by the intermittent beam (I). For the measurement of the velocity distribution in this study, the fine zinc stearate particles are ejected directly at the leading edge of the heated surface at low speed by micro particle ejector (10). The photographic technique uses a camera lens with aperture set at f 1.2, high-speed ASA 400 film, and a high intensity laser beam. The optical system for the velocity measurement (7) as shown in this figure generates intermittent beams obtained from a neon-laser point source with a rotating disk shutter intercepting the beams at the rates of 180 to 240 times per s. Subsequently, the beams irradiate an arbitrary convective boundary layer by means of flat mirror (M), and cylindrical mirror (C). The particle trajectories are recorded by camera with f 1.2 and 1/30 second. As shown in this figure, side baffles made of transparent acrylic resin boards (9) of 5 mm in thickness (800-mm height and 400-mm width) are installed on both sides of the apparatus to prevent transverse fluid flows along the lateral edges of the plate. The fine zinc stearate particles are stirred by a fan (A) in the micro particle ejector, sent continuously into honeycomb (H), and ejected from the outlet nozzle (0) of 20 mm in diameter at a velocity 20–50 mm/s. A screen damper (D) is set up above the outlet nozzle so that the velocity boundary layer can be stabilized at the time of ejection.

Nomenclature

L = length of isothermal vertical heated plate
L_t = fictitious length to trailing edge of unheated plate
b = plate thickness
x,y = longitudinal and transverse length coordinates
u,v = longitudinal and transverse velocities
g = acceleration of gravity
c_p = specific heat at constant pressure
X,Y = nondimensional longitudinal and transverse length coordinates $= x/L, y/L$
U,V = nondimensional longitudinal and transverse velocities $= uL/\upsilon, vL/\upsilon$
T = nondimensional temperature $= (\vartheta - \vartheta_\infty)/(\vartheta_w - \vartheta_\infty)$
B = nondimensional plate thickness $= b/L$
Pr = Prandtl number $= \upsilon/\alpha$
Gr_L = Grashof number based on L and $(\vartheta_w - \vartheta_\infty) = g\beta L^3(\vartheta_w - \vartheta_\infty)/\upsilon^2$
q_r = radiation heat flux between an area element on the unheated convective surface and nonreflecting surroundings
R_λ = plate-fluid thermal conductivity ratio
h_c = local convective heat transfer coefficient based on $(\vartheta_w - \vartheta_\infty)$
h_r = local heat transfer coefficient by radiation based on $(\vartheta_w - \vartheta_\infty)$
Nu_c = nondimensional local convective heat transfer coefficient defined in equation (9)
Nu_r = nondimensional local radiative heat transfer coefficient defined in equation (8)
Θ_w^{4*} = nondimensional radiation factor of the fourth power of the absolute temperature between the isothermal plate and surroundings defined in equation (12)
L^* = nondimensional length of the isothermal plate defined in equation (13)

Greek

ρ = fluid density
λ = thermal conductivity
υ = kinematic viscosity
α = thermal diffusivity
β = coefficient of volumetric expansion
ϑ = temperature
ϵ = radiation emissivity

Subscripts

j,k = nodal indices in the X- and Y- directions
k_w = node index of the plate surface in the Y-direction
∞ = ambient conditions
w = isothermal heated plate surface conditions
ex = the conditions corresponding to experiment

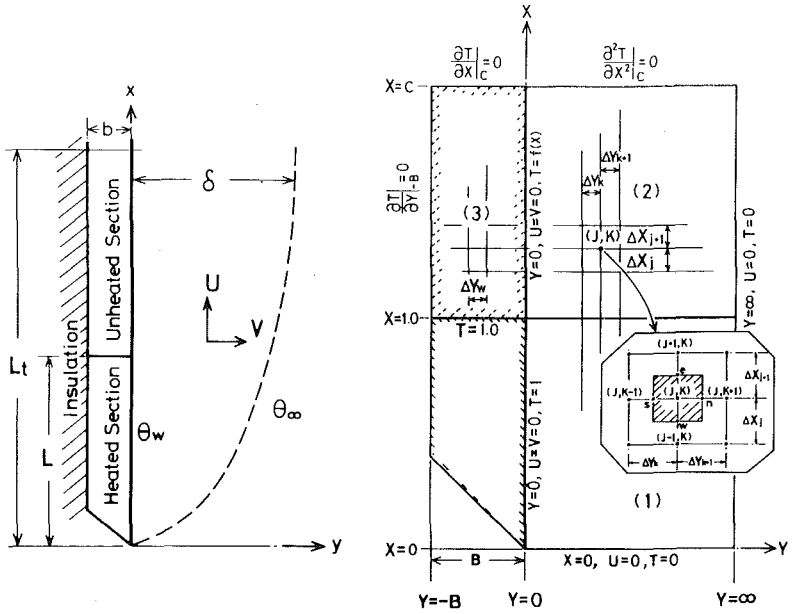

Fig. 2 Physical model: (*a*) dimensional coordinate system, (*b*) nondimensional finite difference model with boundary conditions

3 Numerical Analysis and Solution

The problem discussed here is a complex phenomenon of heat transfer with coupling effects of heat conduction in the unheated plate and radiation on the surface.

Generally, in the analysis of convective boundary layer, an elliptic equation derived from momentum equations in the X- and Y-directions can be applied to obtain a steady solution. However, the equations which must be solved in this case are the parabolic momentum equation only in the X-direction and the elliptic energy equation because of a moderate change in the velocity profile and an abrupt change in the temperature profile in the immediate neighborhood of the contact boundary between the isothermal plate and the unheated one. Also, the radiation heat flux from unheated convective surface elements to nonreflecting surroundings is expressed in one-dimensional form with an emissivity coefficient, ϵ, of the plate.

Governing Equations. The physical situations for this case are illustrated in Figs. 2(*a*) and 2(*b*), the former is the dimensional coordinate system whose lower portion ($0 \le x < L$) is a heated plate maintained at a uniform temperature ϑ_w, and the upper portion ($x > L$) is an unheated plate, and the latter is a nondimensional model for the finite difference computation, in which the regions expressed as (1) and (2) are natural convective zones on the isothermal heated plate and the unheated plate, respectively, and the region (3) is a heat conductive one in the unheated plate.

The zero point of coordinates in the X- and Y-directions is fixed to the front edge of the plate and to the surface of the wall, respectively. The fluid region is divided into nonuniformly spaced horizontal- and vertical-strips of width ΔX_j, ΔY_K at each node index (j,k) in the X- and Y-directions in this figure, while the unheated plate region is divided into uniform node spacing, ΔX_j. Specially, a fine longitudinal node spacing near the conjugated boundary between the regions (1) and (2) and a fine transverse node spacing in the vicinity of the wall are employed, as well as a fine longitudinal node spacing near the leading edge. At a fictitious trailing edge of the unheated plate ($X = L_t$) as shown in Fig. 2(*a*) an adiabatic condition in the X-direction is adopted in the plate region (3) and also the parabolic energy equation is adopted in the fluid region (2). L_t is taken to be more than three times as large as the isothermal heated length L in this calculation procedure.

The governing equations are nondimensionalized by introducing the following dimensionless variables.

$$X = x/L, Y = y/L, B = b/L, U = uL/\nu, V = vL/\nu, R_\lambda = \lambda_w/\lambda_f$$

$$T = (\theta - \theta_\infty)/(\theta_w - \theta_\infty), \mathrm{Gr}_L = g\beta L^3(\theta_w - \theta_\infty)/\nu^2, \mathrm{Pr} = \nu/\alpha \quad (1)$$

where U and V are the dimensionless longitudinal and transverse velocity, T is the nondimensional temperature in which ϑ_w and ϑ_∞ are the temperatures of the isothermal heated wall and of the ambient air, respectively, B is the nondimensional unheated plate thickness, and also R_λ the plate-fluid thermal conductivity ratio in which λ_w and λ_f are thermal conductivities of the unheated plate and fluid, respectively. The characteristic length, L, in the above equations is taken to be the length of the upstream isothermal heated plate. It should be noted that the aforementioned nondimensional variable Gr_L is not in the same form as a conventional Grashof number, even though Gr_L times X^3 corresponds well to a conventional local Grashof number for the region of the isothermal plate.

The nondimensional boundary layer equations expressing conservation of mass, momentum, and energy for two-dimensional steady laminar natural convective heat transfer from this vertical plate are as follows.

$$\frac{\partial U}{\partial X} + \frac{\partial V}{\partial Y} = 0 \quad (2)$$

$$U\frac{\partial U}{\partial X} + V\frac{\partial U}{\partial Y} = \mathrm{Gr}_L \cdot T + \frac{\partial^2 T}{\partial Y^2} \quad (3)$$

$$U\frac{\partial T}{\partial X} + V\frac{\partial T}{\partial Y} = \frac{1}{\mathrm{Pr}} \cdot \left(\frac{\partial^2 T}{\partial X^2} + \frac{\partial^2 T}{\partial Y^2}\right) \quad (4)$$

The nondimensional energy equation for steady conduction in the unheated plate is given as follows

$$\frac{\partial^2 T}{\partial X^2} + \frac{\partial^2 T}{\partial Y^2} = 0 \quad (5)$$

The nondimensional equation expressing the continuity of

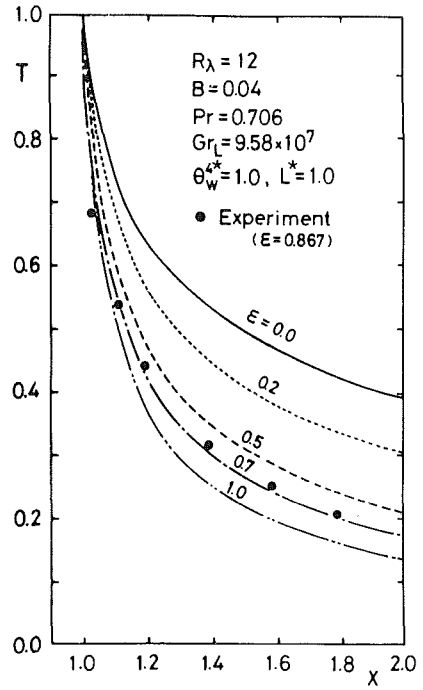

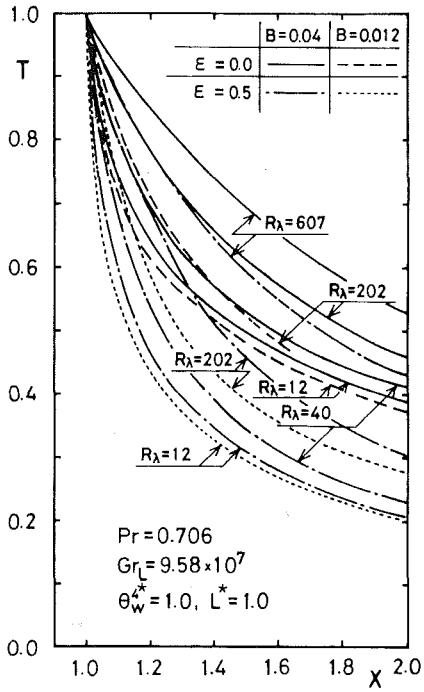

Fig. 3 Surface temperature distribution on the unheated plate: (*a*) effect of ϵ on the surface temperature under experimental conditions, (*b*) effects of parameters R_λ, ϵ, and B on surface temperature distribution

heat flux at the unheated plate-fluid interface is coupling equation of the heat transmission between the plate and fluid, expressed as follows.

$$\frac{\lambda_w}{\lambda_f}\cdot\frac{\partial T}{\partial Y}\bigg|_{-0} = \frac{\partial T}{\partial Y}\bigg|_{+0} - q_r\cdot L/[\lambda_f\cdot(\theta_w-\theta_\infty)] \quad (6)$$

where q_r is the radiation heat flux from unheated convective surface elements.

Radiation heat flux of $q_r(j,k)$ from an area element on the unheated surface (j,k_w) in Fig. 2(*b*) to environmental surroundings is expressed as follows by using the emissivity of the plate

$$q_r(j,k_w) = 4.88\cdot\epsilon\cdot\left[\left(\frac{273+\theta(j,k_w)}{100}\right)^4 - \left(\frac{273+\theta_\infty}{100}\right)^4\right] \text{kcal/m}^2\text{h} \quad (7)$$

In this study, the wall temperature of the surroundings is equivalent to that of the ambient air, and the term of $\vartheta(j,k_w)$ in the foregoing equation is the temperature of the unheated surface. Local radiative and convective heat transfer coefficients, h_r and hc, are defined and transformed in dimensionless form as follows, which are connected with local Nusselt numbers Nu_r and Nu_c.

$$\mathrm{Nu}_r = \frac{h_r\cdot L}{\lambda_f} = \frac{4.88\cdot\epsilon\cdot\left[\left(\frac{273+\theta(j,k_w)}{100}\right)^4 - \left(\frac{273+\theta_\infty}{100}\right)^4\right]}{\theta_w-\theta_\infty}\cdot\frac{L}{\lambda_f} \quad (8)$$

$$\mathrm{Nu}_c = \frac{h_c\cdot L}{\lambda_f} = -\frac{\partial T}{\partial Y}\bigg|_{+0} \quad (9)$$

$$R_\lambda\cdot\frac{\partial T}{\partial Y}\bigg|_{-0} = -\mathrm{Nu}_c - \mathrm{Nu}_r \quad (10)$$

The nondimensional heat balance equation (10) is the interface coupling condition adopted for the region of $1 < X \le L_t/L$, and $Y=0$, which is obtained by substituting dimensionless equations (8) and (9) into equation (6). The nondimensional equations (2–6) transformed into finite difference form using an up-wind difference technique, which was similar to that given by Zinnes [5].

The following boundary conditions are employed in this calculation

$$\begin{aligned}
&0\le X\le L_t/L\ ,\quad Y=\infty: && U=0, T=0\\
&\qquad\quad ,\quad Y=-B: && \frac{\partial T}{\partial Y}=0\\
&\qquad\quad ,\quad Y=0: && U=0, V=0\\
&0\le X\le 1\ ,\quad Y=0: && T=1\\
&0\le Y\le\infty\ ,\quad X=0: && U=0, T=0\\
&\qquad\quad ,\quad X=L_t/L: && \frac{\partial^2 T}{\partial X^2}=0\\
&-B\le Y\le 0\ ,\quad X=1: && T=1\\
&\qquad\quad ,\quad X=L_t/L: && \frac{\partial T}{\partial X}=0
\end{aligned} \quad (11)$$

The solution involves a step-by-step marching procedure in the streamwise direction and successive iteration from the leading edge until a satisfactory convergence is obtained, since the energy equation is elliptic. In any given steps, finite difference equations of the conduction plate region (3) and the convection region (2) are simultaneously solved by an iterative technique coupled through the common heat flux, including thermal radiation. In this calculation, it is most important to compute iteratively the plate region (3) which takes precedence over the convection region (2). In this procedure, the coupling equation between the unheated convective surface and fluid is a nonlinear equation because of the fourth power of the absolute temperature in the radiation term, and its finite difference form is transformed into a linear equation by substituting a value of the surface temperature at the previous step.

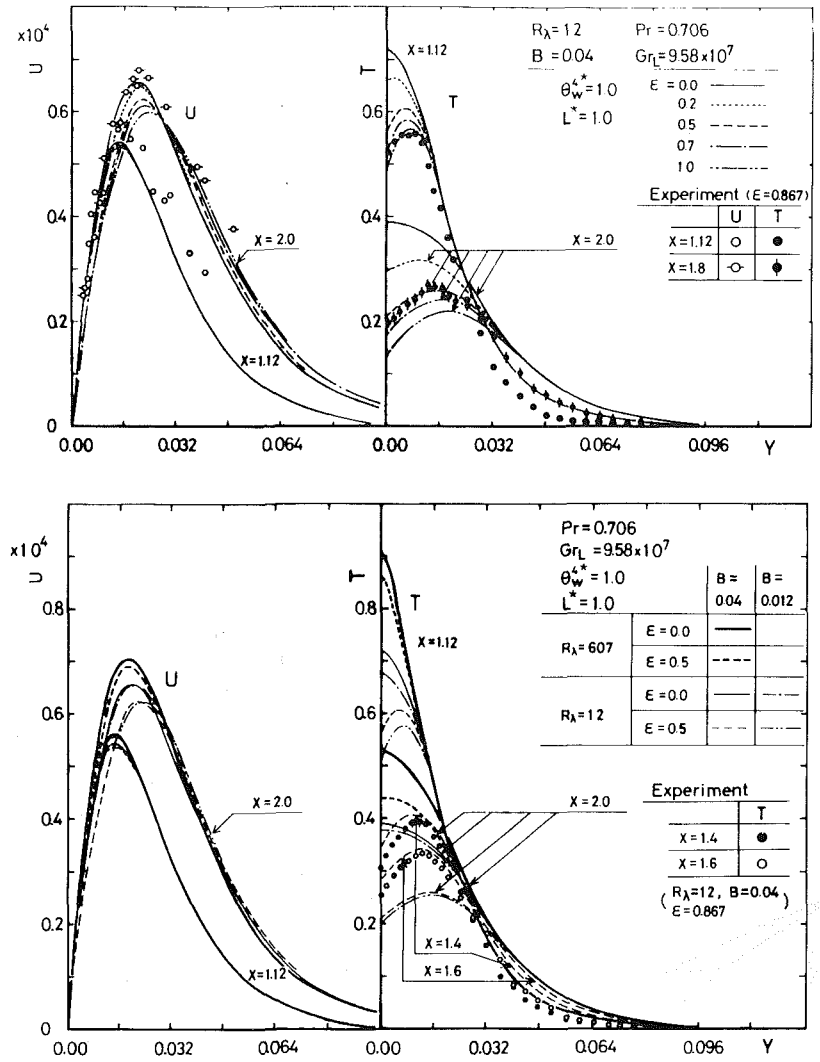

Fig. 4 Temperature and velocity profiles in the boundary layer on the unheated plate: (*a*) comparison of the measured temperature and velocity profiles with numerical results, (*b*) effects of parameters R_λ, ϵ, and B on both temperature and velocity profiles

The present analysis deals with nonsimilar temperature and velocity profiles, and therefore, local heat transfer calculations are complicated. In particular, heat flux by radiation between the unheated plate and the wall of surroundings defined in equation (7) and the characteristic length of isothermal plate are important factors. However, the parameter of radiation heat flux is not simply expressed since the surface temperature of unheated plate is unknown. Therefore, a dimensionless parameter of the fourth power of the absolute temperature, which indicates the degree of heat flux by radiation from an unheated convective surface element, is introduced on the basis of the present experimental conditions.

$$\vartheta_w^{4*} = [(\theta_w + 273)^4 - (\vartheta_4 + 273)^4]/[(\theta_{w_{ex}} + 273)^4 - (\vartheta_{\infty_{ex}} + 273)^4] \quad (12)$$

where ϑ_{wex} and $\vartheta\infty_{ex}$ correspond to this experimental temperatures of the isothermal plate and the ambient air, respectively, that is , $\vartheta_{w_{ex}} = 99.4$ °C, $\vartheta_{\infty_{ex}} = 25$ °C. Similarly, a dimensionless characteristic length of the isothermal vertical plate is introduced as follows

$$L^* = L/L_{ex} \quad (13)$$

where L_{ex} is equal to 0.25 m corresponding to the length of the isothermal plate in the experiment.

The functional dependent factors for this case are expressed as follows.

$$\left.\begin{matrix} \theta\ , & \theta_w(X), \\ U, & \mathrm{Nu}_c, \\ V, & \mathrm{Nu}_r \end{matrix}\right\} = F(X, Y, B, R_\lambda, \mathrm{Pr}, \mathrm{Gr}_L, \epsilon, \Theta_w^{4*}, L^*) \quad (14)$$

where the function of $\theta_w(X)$, Nu_c, and Nu_r correspond to the case of $Y = 0$.

In this numerical heat transfer model, the convective fluid is restricted to a transparent fluid of air, and the values of Prandtl number, Pr and thermal conductivity, λ_f, are taken to be constant.

To ascertain the accuracy of the numerical analysis, it is very important to properly choose a fine transverse node spacing in the vicinity of the wall as well as a fine longitudinal node spacing near the leading edge. The choice of the length to a fictitious trailing edge, L_t, which defines the end of computations is also important. As a check on the finite difference computations, the results of the temperature and velocity profiles, by using very fine nodal spacings, are in good agreement with Ostrach's result [13] in the isothermal plate region. It should be noted that the accuracy of prediction for wall temperatures in the unheated plate

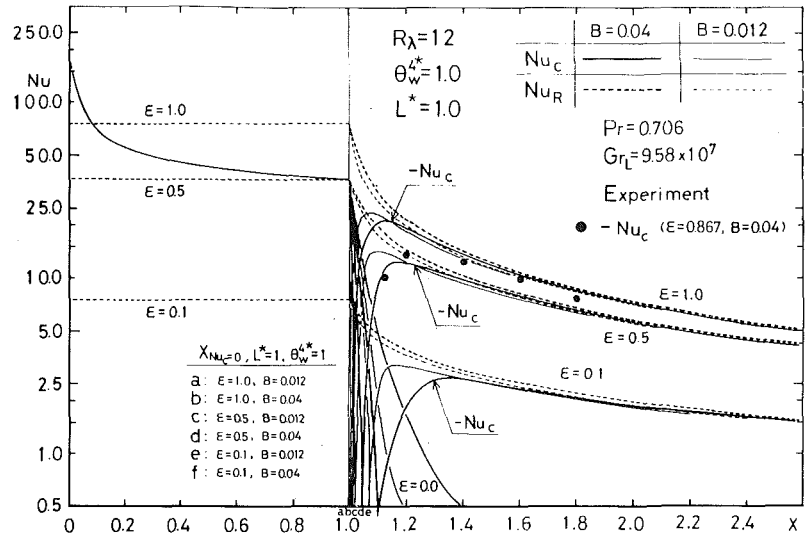

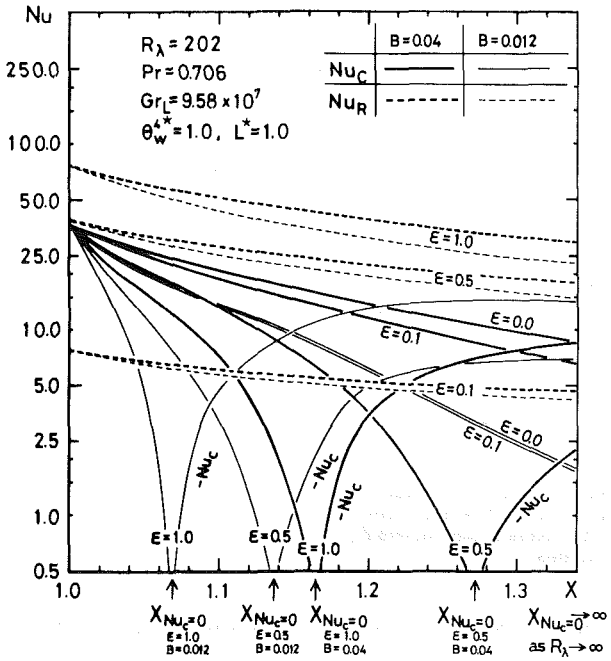

Fig. 5 Local nondimensional convective and radiative heat transfer coefficients, Nu_c and Nu_r: (*a*) comparison of the predicted results of Nu_c and Nu_r as parameters E_1 and B with the experimental data, (*b*) effects of parameters R_λ, ϵ, and B on Nu_c and Nu_r

depends significantly on the choice of length, L_l, especially for large values of R_λ.

4 Results and Discussions

The numerical computations under the experimental conditions, Pr = 0.706, L = 0.25 m, θ_w = 99.4°C, and θ_∞ = 25°C; therefore, L^* = 1.0 and Θ_w^{4*} = 1.0, are carried out to clarify the characteristics of the flow and heat transfer for various combination of plate-fluid thermal conductivity ratio, R_λ, radiation emissivity, ϵ, and nondimensional plate thickness B.

The Surface Temperature Distribution on the Unheated Plate. The surface temperature distribution on the unheated plate for the present experimental conditions of R_λ = 12, Gr_L = 9.58 × 10^7, and B = 0.04 are shown in Fig. 3(*a*) in terms of the parameter ϵ, (ϵ = 0.0, 0.2, 0.5, 0.7, and 1.0). It is clear that the prediction for ϵ = 0.7 corresponds to the experimental results even though the emissivity of the phenol resin plate is measured to 0.867 by the spectroscopic monochrometers ranging from 50 to 100°C. A slight discrepancy may be caused mainly by an angle factor for radiation traveling between the side baffles and an area element of the unheated convective surface. All properties related to this numerical analysis are assumed to be constant except for density variation in the buoyancy term of the momentum equation, and all properties in comparing the analytical and experimental results have been chosen at the mean temperature, $(\theta_{wex} + \theta_{\infty ex})/2$. The prediction of the surface temperature distribution on the unheated plate for the plate-fluid conductivity ratio, R_λ = 607, 202, 40, and 12 are shown in Fig. 3(*b*) for ϵ = 0.5 and 0. It can be quantitatively concluded from this figure that the decrease in the surface temperature of the unheated plate with increasing X becomes small for the large values of R_λ, and the effect of the radiation emissivity on the surface temperature distribution is considerable for small values of R_λ. The dependence of the plate thickness (B = 0.04 and 0.012 on the surface temperature is also given in this figure. It appears that for small values of R_λ the effect of B on the surface temperature is very small so that the difference tends to converge with increasing X regardless of the radiation heat flux.

The Temperature and Velocity Profiles in the Boundary Layer on the Unheated Plate. The effects of the radiation heat flux on the velocity and temperature profiles in the boundary layer on the unheated plate are shown in Figs. 4(*a*) and 4(*b*). From Fig. 4(*a*), it is clear that the temperature profiles in the vicinity of the wall are considerably affected by the value of ϵ as it approaches unity. However, the effect of ϵ on the velocity profiles is not so much as that on the temperature profiles and appears larger with increasing of X. For ϵ > 0.5, there is little difference in the profiles. The experimental results of the velocity and temperature profiles as shown in this figure for X = 1.12 and 1.8 appear to be in good agreement with the present prediction considering the radiation emissivity of ϵ = 0.7. The effect of the plate-fluid conductivity ratio on the velocity and temperature profiles in the boundary layers for R_λ = 12 and 607 is shown in Fig. 4(*b*). There is a considerable effect of both R_λ and ϵ on the temperature profile in the vicinity of the wall, but little effect on the velocity profile. The effect of R_λ on both profiles begins to appear larger with increasing X in the same manner as before. The dependence of the plate thickness B on both profiles for B = 0.04 and 0.012 is given in this figure. From the results of Fig. 3(*b*) and Fig. 4(*b*), the effect of B for small

R_λ is not as significant as that for large R_λ. A comparison between the analytical prediction ($\epsilon = 0.5$) and the experimental results of temperature for $X = 1.4$ and 1.6 are given in Fig. 4(*b*).

Nusselt Number Nu_c and Nu_r. According to the heat balance equation (10) at the unheated plate-fluid interface, the conduction heat flux in the plate should be essentially equivalent to the total heat flux by radiation and convection at every position of X. In this case, the numerical results for Nu_r and Nu_c under the experimental conditions of $Gr_L = 9.58 \times 10^7$, $Pr = 0.706$, $B = 0.04$, $\Theta_w^{4*} = 1.0$, $L^* = 1.0$, and $R_\lambda = 12$ are shown in Fig. 5(*a*) for $\epsilon = 1.0$, 0.5, 0.1, and 0. The effect of the direct conduction from the isothermal plate to the unheated plate on Nu_c and Nu_r extends to the location of about $X = 1.4$, regardless of the existence of the radiation heat flux. However, the effect of radiation on Nu_c and Nu_r yields a distinguishable difference for various values of ϵ. On the isothermal heated surface, Nu_r is constant depending only on ϵ, and Nu_c varies with $X^{-0.25}$, but on the unheated surface an inversion of Nu_c from heat release to heat absorption takes place at around $X = 1.04$. With increasing X beyond this point, the released heat flux by radiation balances gradually with the absorbed convective heat flux, and this difference between the two fluxes corresponds to the conduction heat flux in the unheated plate. The comparison between the numerical results of Nu_c and experimental data is also given in Fig. 5(*a*). The experimental results of Nu_c agree reasonably with the predictions in the range of $\epsilon = 0.5$–1.0. The effect of the unheated plate thickness ($B = 0.04$ and 0.012) on Nu_c and Nu_r is very small because of the low value of R_λ, as shown also in the figure. The predicted results of Nu_c and Nu_r at the same conditions as just mentioned, except for the high value of $R_\lambda = 202$, are shown in Fig. 5(*b*) in the neighborhod of the inversion of Nu_c for $\epsilon = 1.0$, 0.5, 0.1, 0.0, and $B = 0.04$ and 0.012. In view of both Fig. 5(*a*) and 5(*b*), it is clear that the inversion of Nu_c is closer to the position at $X = 1.0$, which corresponds to the contact point between the isothermal vertical plate and unheated one, as the value of ϵ approaches unity with small B. For large values of R_λ, as shown in Fig. 5(*b*), the inversion of Nu_c takes place in a region far from the contact point. For the case of $B = 0.04$ and $\epsilon = 0.1$, it is clear that the inversion of Nu_c arises beyond the position of $X = 2.0$. Consequently, the temperatures on the unheated surface are seen to decrease less rapidly as the case in Fig. 5(*a*). As a matter of fact, the inversion of Nu_c from heat release to heat absorption does not take place at any position of X when radiation is neglected.

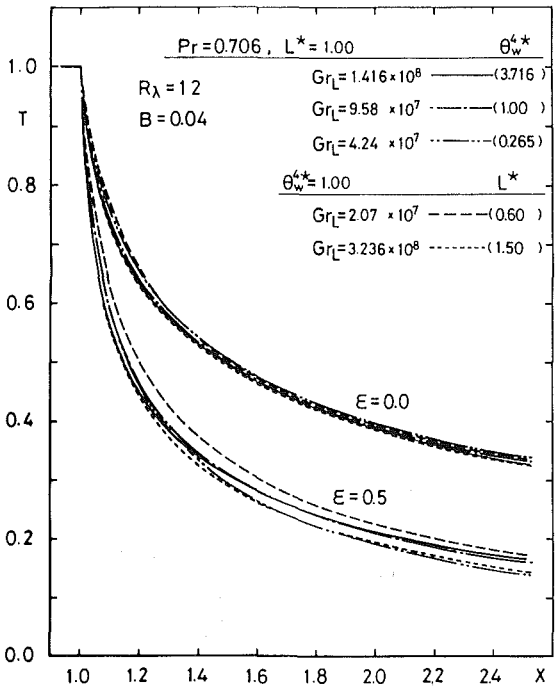

Further Discussion. Further discussions on the effects of the isothermal plate length, L, and the isothermal plate temperature, θ_w, in the problem are needed. For this purpose, dimensionless parameters, L^* and Θ_w^{4*}, are introduced, the former being the nondimensional length of the isothermal vertical plate and the latter, the nondimensional radiation factor already mentioned. Figures 6(*a*) and 6(*b*) show the numerical results of the surface temperature and of Nu_c and Nu_r on the unheated plate for two values with various combinations of Θ_w^{4*} (0.265, 1.00, 3.716) and L^* (0.6, 1.00, 1.50, each of which corresponds to the isothermal plate

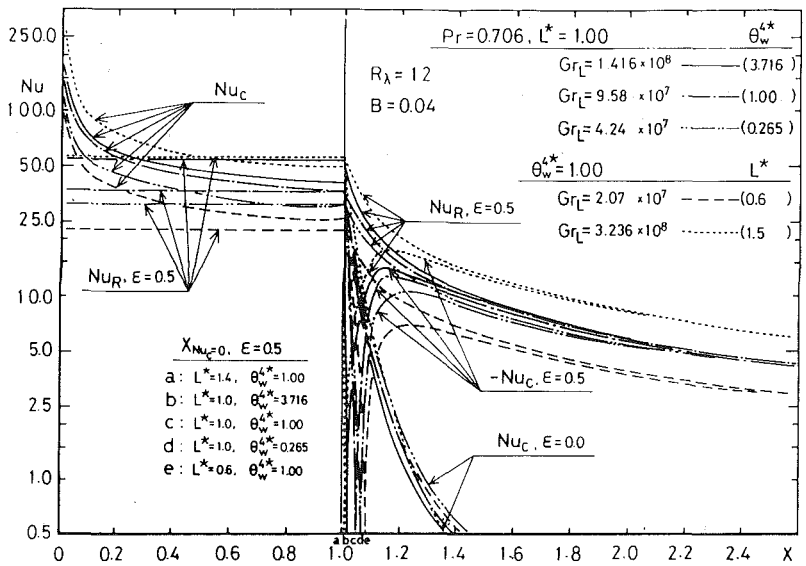

Fig. 6 Effects of L^* and Θ_w^{4*}; (*a*) surface temperature distribution on the unheated plate for various Gr_L, (*b*) local nondimensinal convective and radiative heat transfer coefficients, NU_c and Nu_r, for various Gr_L

temperature of θ_w = 50, 99.4 and 200°C and to the isothermal plate length of L = 0.15, 0.25, 0.375 m, respectively.

As shown in Fig. 6(*a*), the surface temperature distribution on the unheated plate shows a similar trend for various Gr_L, regardless of the different values of L^* and $\Theta_w^4{}^*$, especially when the radiation is ignored. The analytical results of Nu_c and Nu_r, corresponding to the cases shown in Fig. 6(*a*), are given in Fig. 6(*b*). Notwithstanding the fact that Gr_L varies with $\Theta_w^4{}^*$ for constant L^*, Nu_c, and Nu_r for a constant emissivity converge to the same value with increasing X, except in the neighborhood of the inversion point of Nu_c. On the contrary, when Gr_L varies with L^* for constant $\Theta_w^4{}^*$, the prediction of Nu_c and Nu_r are considerably different from each other. The values of Nu_c and Nu_r in this case become slightly higher in proportion to the magnitude of L^*. It should also be noted from the experimental observation ($Gr_L = 9.58 \times 10^7$) that stable laminar flow along the unheated plate reaches as high as $X > 2.8$ ($x > 700$ mm).

From the aforementioned discussion it is clear that the predicted results of Nu_c and Nu_r with radiation are different from each other as a result of the different values of L^* and $\Theta_w^4{}^*$, even though the values of Gr_L and other parameters remain the same. On the other hand, the results without radiation are nealy the same in spite of different values of L^* and $\Theta_w^4{}^*$.

5 Conclusions

In the present numerical and experimental study, natural convective heat transfer from an unheated plate connected to the upstream isothermal plate is considered. Numerical calculation are carried out for a wide range of Grashof numbers, emissivity of the plate, and several other parameters. Results are compared to experimental data for a Prandtl number of 0.706.

The following conclusions may be made:

1 The most influential factors in this problem are the plate-fluid thermal conductivity ratio, R_λ, and the radiation emissivity, ϵ, of the unheated plate. The effects of R_λ on the surface temperature of the unheated plate are as follows: when the value of R_λ is large, the surface temperature does not decrease as much as that for small values of R_λ. The effect of ϵ on the decrease in the surface temperature with increasing X is considerably larger for the range of R_λ considered here when ϵ approaches more closely to unity, but it is not the case for $R_\lambda \to \infty$. The effect of the plate thickness, B, on the surface temperature of the unheated plate is larger for larger values of R_λ.

The effect of ϵ on the temperature profile in the boundary layer is that the temperatures in the vicinity of the unheated wall drop sharply as ϵ approaches unity. Subsequently, an inversion of the nondimensional convective heat transfer coefficient, Nu_c, from heat release to heat absorption conditions takes place in the immediate neighborhood of the contact point between the isothermal plate and the unheated one. The effect of ϵ on the velocity profile in the boundary layer is not as large as that on the temperature profile and appears larger with increasing X.

2 The distribution of local heat transfer coefficient on the unheated plate does not have a similar trend. However, such a trend is observed for Gr_L with constant L^*, except in the neighborhood of X = 1.0, and also for the no radiation case. On the contrary, the distribution of surface temperature on the unheated plate shows a similar trend for any values of Gr_L as long as other conditions remain the same.

3 An inversion of nondimensional convective heat transfer coefficient, Nu_c, from heat release to heat absorption conditions takes place at a position approaching more closely to the contact point between the isothermal heated plate and the unheated one, as the values of $\Theta_w^4{}^*$, ϵ, and L^* increase, or as the values of B and R_λ decrease.

Reference

1 Kishinami, K., Saito, H., and Tokura, I., "Natural Convective Heat Transfer From an Arbitrarily Curved Isothermal Surface," *Transactions JSME*, Vol. 45, No. 399, Nov. 1980, pp. 1613-1621.

2 Lienhard, J., Eichhorn, R., and Dhir, V., "Laminar Natural Convection Under Nonuniform Gravity," ASME JOURNAL OF HEAT TRANSFER, Vol. 94, Feb. 1972, pp. 80-86.

3 Seki, N., Fukusako, S., and Nakaoka, N., "Experimental Study On Natural Convection Heat Transfer With Density Inversion of Water Between Two Horizontal Concentric Cylinders," ASME JOURNAL OF HEAT TRANSFER, Vol. 97, Nov. 1975, pp. 556-561.

4 Yang, K —T., "Laminar Free Convection Wake Above a Heated Vertical Plate," ASME JOURNAL OF HEAT TRANSFER, Vol. 86, Mar. 1964, pp. 131-138.

5 Zinnes, A. E., "The Coupling of Conduction With Laminar Natural Convection From a Vertical Plate With Arbitrary Surface Heating," ASME JOURNAL OF HEAT TRANSFER, Vol. 92, Aug. 1970, pp. 528-535.

6 Hayday, A. A., Bowlus, D. A., and Mcgraw, R. A., "Free Convection From a Vertical Flat Plate With Step Discontinuities in Surface Temperature," ASME JOURNAL OF HEAT TRANSFER, Vol. 89, Aug. 1967, pp. 244-250.

7 Kelleher, M., "Free Convection From a Vertical Plate With Discontinuous Wall Temperature," ASME JOURNAL OF HEAT TRANSFER, Vol. 93 Nov. 1971, pp. 349-356.

8 Hardwick, N. E., and Levy, E. K., "Study of Laminar Free-Convection Wake Above an Isothermal Vertical Plate," ASME JOURNAL OF HEAT TRANSFER, Vol. 95, Aug. 1973, pp. 289-294.

9 Fujii, T., Fujii, F., and Tanaka, H., "Laminar Natural Convective Heat Transfer From a Vertical Surface With Uniform Heat Flux to Air," *Transactions JSME*, Vol. 44, No. 387, Nov. 1979, pp. 3832-3837.

10 Sparrow, E. M., Patankar, S. V., and Abdel-Washed, R. M., "Development of Wall and Free Plumes Above a Heated Vertical Plate," ASME JOURNAL OF HEAT TRANSFER, Vol. 100, May. 1978, pp..184-190.

11 Eichhorn, R., "Measurement of Low-Speed Gas Flows by Particle Trajectories: A New Determination of Free Convection Velocity Profiles," *International Journal of Heat and Mass Transfer*, Vol. 5, 1962, pp. 915-928.

12 Aihara, T., and Saito, E., "Measurement of Free Convection Velocity Field Around the Periphery of a Horizontal Torus," ASME JOURNAL OF HEAT TRANSFER, Vol. 92, Feb. 1972, pp. 95-98.

13 Ostrach, S., "An Analysis of Laminar Free-Convection Flow and Heat Transfer About a Flat Plate Parallel to the Direction of the Generating Body Force," NACA Report 1111, 1953, pp. 63-79.

The Stability of Vertical Buoyancy-Induced Flow in Cold Water

J. M. Higgins
Eastman Kodak Company,
Rochester, N.Y.

B. Gebhart
University of Pennsylvania,
Department of Mechanical Engineering
and Applied Mechanics,
Philadelphia, Pa. 19104
Fellow ASME

Calculations of the stability of the buoyancy-induced flow of cold water, adjacent to a vertical surface, have been carried out. The disturbance equations, for an isothermal boundary condition, have been formulated with a new density relation for pure and saline water, of very high accuracy. Buoyancy terms in the base flow and disturbance equations, thereby, accurately express the buoyancy forces in water at low temperatures. Stability results are presented for a Prandtl number of 12.6 for a variety of ambient and surface temperature conditions. The anomalous cold water density behavior was found to produce important differences in stability from the Boussinesq solutions. The Boussinesq approximation consistently overpredicts the buoyancy force in upflow circumstances. The resulting neutral stability prediction lies upstream of the accurate ones. For temperature conditions which result in downflow, the predictions lie downstream of the accurate values. The effects may be very large.

1 Introduction

Buoyancy-induced flows in pure and saline water are much in evidence in the world around us. The short term circulations of water due to the sun's heating, as well as the seasonal thermal inversion of lakes, are buoyancy-induced flow processes. The transition of these flows from laminar to turbulent depends on their stability characteristics. A balance of pressure, viscous, and buoyancy forces will determine whether a transition to turbulence will occur.

In technology, the buoyancy-induced flows encountered are usually on a much smaller scale than those seen in nature. Transition for laminar flow to turbulence often occurs quickly and within the confines of the same system. The need for an understanding of this complex process is evident. Analytically, turbulence models are still largely dependent on empirical bases, and the later stages of the transition process are not very well understood. Studies of the early parts of transition, however, have made considerable progress in the last several decades.

Most stability analyses and experiments have studied flows in air, water, and waterlike silicone fluid at room temperature. Water has a density extremum condition near 4°C. This behavior has been found to have drastic effects on laminar stability, even though flow vigor is substantially decreased from that at room temperature levels. The process of buoyancy force reversal, possibly leading to convective inversion of the flow, was expected to complicate their stability dynamics. This study analyzes the stability of the buoyancy-induced flow of cold water adjacent to a vertical, isothermal surface.

Earlier studies of the stability of buoyancy-induced flow have established basic principles that have helped guide later analytical and experimental work. A summary of these studies may be found in Higgins [1]. Dring and Gebhart [2], by a direct numerical integration, obtained solutions to the coupled Orr-Sommerfeld equations. Neutral stability curves as well as disturbance amplification contours for a constant flux surface condition (Pr = 6.7) were determined. Temperature and velocity disturbance amplification rates were then measured and the predicted frequency filtering mechanism supported. Hieber and Gebhart [3] used a simpler numerical technique to compute neutral curves and amplification contours for a constant flux surface for a wide range of Prandtl numbers.

The buoyancy term of the governing equations has traditionally been dealt with by treating the density as a linear function of temperature, the so-called second Boussinesq approximation. This treatment is inappropriate in the extremum region. More appropriate density representations have been the subject of much study. Perhaps the first realistic attempt to represent the density extremum of pure water was made by Mendeleef [11]. A density relation was written in terms of $(t-t_m)$, where t_m is the extremum temperature. Dumoré, Merk, and Prins [12] observed convective inversion during experiments with melting ice spheres. Many studies utilized a buoyancy term quadratic in temperature to describe behavior near the extremum. Merk [13] utilized an integral technique to solve the boundary layer equations with that form. The predictions were in agreement with the ice sphere observations. Goren [14] determined that convective velocities near the extremum are much less vigorous than those at room temperature. Govindarajulu [18] extended the work of Goren to show that similarity solutions exist adjacent to vertical and horizontal porous plates. Soundalgekar [19] obtained approximate solutions to these equations with a Karman-Pohlhausen integral technique for a wall temperature which varies with distance along the plate. Soundelagekar [20] also provided a numerical solution to the one-dimensional unsteady problem. However, Bryden [15] determined polynomial correlations for sea water properties using the data of Bradshaw and Schleicher [16]. The thermal expansion term, although cubic in temperature, was complicated in pressure and salinity dependence and contained 22 terms.

Gebhart and Mollendorf [4] developed a simple, effective and very accurate density relation for pure and saline water. It accurately correlates density as a function of temperature, salinity, and pressure. It contains only one temperature term, as an expansion around the extremum temperature, t_m. The simplicity of this equation is very convenient in boundary layer analysis for many flow conditions. Buoyancy force reversals and convective inversions are accurately predicted. The significant effect of the density extremum on heat and momentum transport is shown.

The recent study of Qureshi and Gebhart [5], investigated the stability of flow in ambient water at the density extremum temperature, t_m, adjacent to a uniform heat flux vertical surface. A similarity solution had been indicated by Gebhart and Mollendorf [6] for $t_\infty = t_m$. No buoyancy force reversals arise for this condition. The base flow and disturbance

Contributed by the Heat Transfer Division for publication in the JOURNAL OF HEAT TRANSFER. Manuscript received by the Heat Transfer Division February 5, 1982.

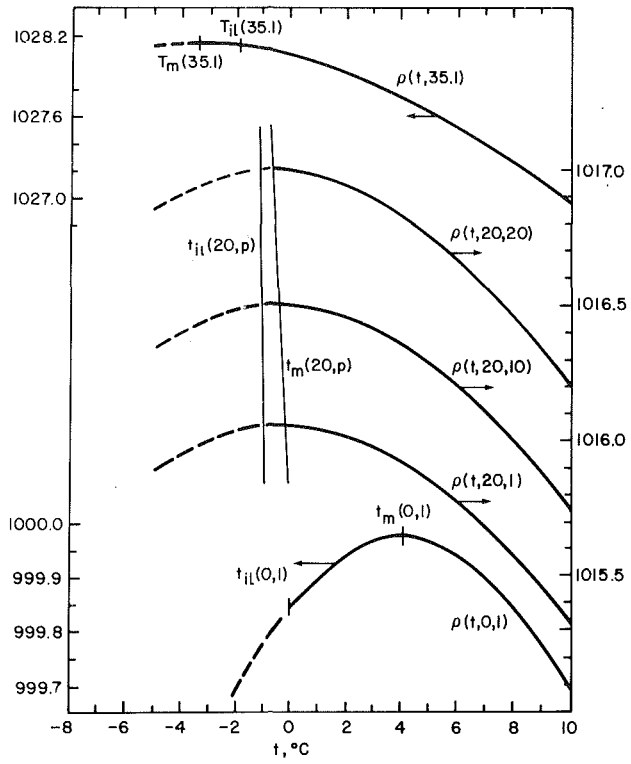

Fig. 1 The density-temperature dependence at various s and p, in kg m^{-3}. Both t_m and t_{il} are shown.

equations were solved for the similarity condition, for Pr = 11.6, the value at 4°C. The computations indicated that the low temperature ambient initially stabilizes the flow, although farther downstream the amplification rate increases.

Measurements of disturbance quantities compared favorably with the computations. The density extremum behavior was found to delay transition, compared to results in room temperature water. It also resulted in simultaneous velocity and thermal transition, that is, transition for both occurring at the same values of the streamwise distance dependent parameter, G. A new parameter was suggested to correlate beginning of transition. Also, the selective downstream frequency amplification mechanism was found to be less sharp for this kind of flow.

The present work considers the stability of a buoyancy induced flow in cold water adjacent to a vertical isothermal surface, at t_o. Similarity solutions may be found for any values of t_∞ and t_o. For $t_\infty \neq t_m$ buoyancy force and local flow reversals may arise. Neutral curves are presented for various ambient temperature levels other than 4°C and several values of surface temperature, for Pr = 12.6. Comparisons with Boussinesq results show that important differences occur for temperature conditions near 4°C. The direction of these deviations from the Boussinesq equivalents are reasoned both qualitatively and quantitatively.

2 The Density Relation

It has been known that water experiences an extremum of density $\rho_m(s,p)$ at moderate salinity and pressure levels. Density variations are seen in Fig. 1, for several values of s and p. The density-temperature relationship is thought to be almost symmetric about t_m (s,p) in this region.

Any linear, or Boussinesq approximation of density, is an inadequate description of the density-temperature behavior in this region. The relation of Gebhart and Mollendorf [4] accurately correlates density in the ranges t = 0–20°C, s = 0–40 ppt., and p = 1–1,000 bars. The expression conveniently contains a single temperature term

$$\rho(t,s,p) = \rho_m(s,p)\{1-\alpha_t(s,p)[|t-t_m(s,p)|]^{q(s,p)}\} \quad (1a)$$

$$R = \frac{t_m(s,p)-t_\infty}{t_o-t_\infty} \quad (1b)$$

where $\rho_m(s,p)$, $\alpha_t(s,p)$, $t_m(s,p)$, and $q(s,p)$ are polynomial functions of pressure and salinity, and R, in (1b), arises to position t_o and t_∞ with respect to t_m. These polynomials were determined by a nonlinear regression fit to the relation of Fine and Millero [7] and to the data of Chen and Millero [8].

The simplicity of equation (1) enabled Gebhart and Mollendorf [6] to assess buoyancy force and flow reversals. Very large density extremum effects on heat and momentum transport were found. The results of Qureshi and Gebhart [5] also indicate large effects on the stability of flow adjacent to a vertical uniform heat flux surface. The calculations applied to $t_\infty = t_m$, i.e., R = 0, as defined above. This condition is not necessary for similarity for isothermal surfaces.

3 Base Flow

(i) Development of Equations. The boundary layer equations for the steady, thermally induced base flow shown in Fig. 2 are well known [17]. From the density relation in equation (1a), the buoyancy term is

Nomenclature

B_1, B_2, B_3 = complex constants
B = frequency parameter
c_p = specific heat
f = similarity stream function
F = a temperature parameter
g = gravity
G = $4\sqrt{\mathrm{Gr}_x/4}$
Gr_x = local Grashof number
i = $\sqrt{-1}$
k = thermal conductivity
K = a constant
M = a temperature parameter
$p, \bar{p}, p'$ = pressure
Pr = Prandtl number
q = exponent in ρ equation
R = temperature parameter
s = salinity, temperature disturbance
$t, \bar{t}, t'$ = temperature, °C
T = generalized temperature
$u, \bar{u}, u'$ = x-direction velocity components
U = characteristic velocity
$v, \bar{v}, v'$ = y-direction velocity components
x, y = coordinates
Z = a temperature parameter

Greek

α = complex wave number
α_t = coefficient (°C)$^{-q}$
β = frequency
β_t = thermal expansion coefficient
Δ = difference
δ = bounary region thickness
ρ = density, kg/m^3
τ = time
ν = kinematic viscosity
ϕ = disturbance amplitude
ψ = stream function

Subscripts

B = Boussinesq
f = "film" condition
Im = imaginary
m = at density extremum condition
o = surface condition
Re = real
∞ = ambient medium

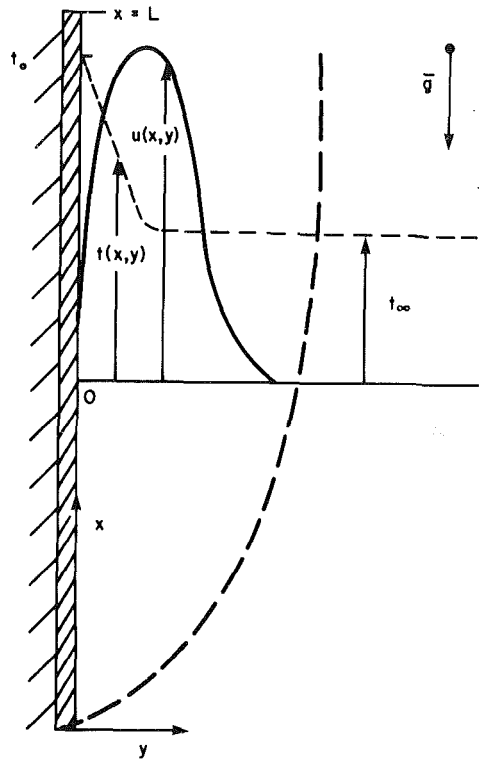

Fig. 2 Isothermal vertical surface, showing boundary layer with velocity profile $u(x,y)$ and temperature profile $t(x,y)$. The horizontal scale is expanded for clarity.

$$g(\rho_\infty - \rho) = g\rho_m \alpha_t [|t - t_m|^q - |t_\infty - t_m|^q] \tag{2}$$

The following similarity variables apply

$$\eta = \frac{y}{x}\sqrt[4]{\frac{\mathrm{Gr}_x}{4}} = \frac{y}{4x}G$$

where

$$\mathrm{Gr}_x = \frac{g\alpha_t}{\nu^2}x^3 |t_o - t_\infty|^q$$

and α_t here is the thermal expansion coefficient from the density relation (1*a*). For conditions at 1 atm and no salinity, the value of q is 1.89. The stream function is introduced

$$\psi = \nu G f(\eta)$$

where $u = \psi_y$; $v = -\psi_x$. The temperature variable is written as

$$T = \frac{t - t_\infty}{t_o - t_\infty} \tag{3}$$

where t_o is the assigned isothermal surface temperature. The equations in similarity form become

$$f''' + 3ff'' - 2f'^2 \pm \{|T - R|^q - |R|^q\} = 0 \tag{4a}$$

$$T'' + 3\mathrm{Pr} f T' = 0 \tag{4b}$$

with boundary conditions

$$f'(0) = f(0) = 1 - T(0) = f'(\infty) = T(\infty) = 0 \tag{4c}$$

The ($\pm$) denotes upflow and downflow, respectively, and Pr is an appropriate fluid Prandtl number. This fifth-order system is coupled through the buoyancy term.

Asymptotic solutions provide effective starting values to an integration scheme, beginning at large η and proceeding inward to $\eta = 0$. The constants are guessed initially and the integration performed. With correct guesses, the specified boundary conditions at the wall, $\eta = 0$, will be satisfied. Calculated distributions of T and $f' \propto u$ are shown in Fig. 3,

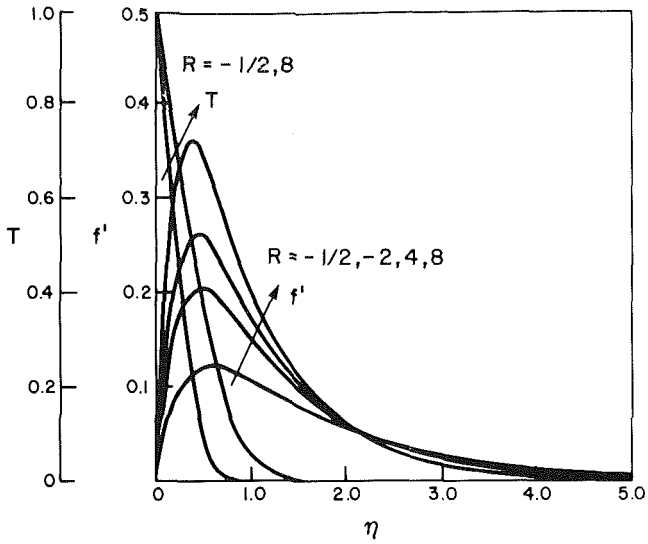

Fig. 3 Base flow results for various values of R and Pr of 12.6

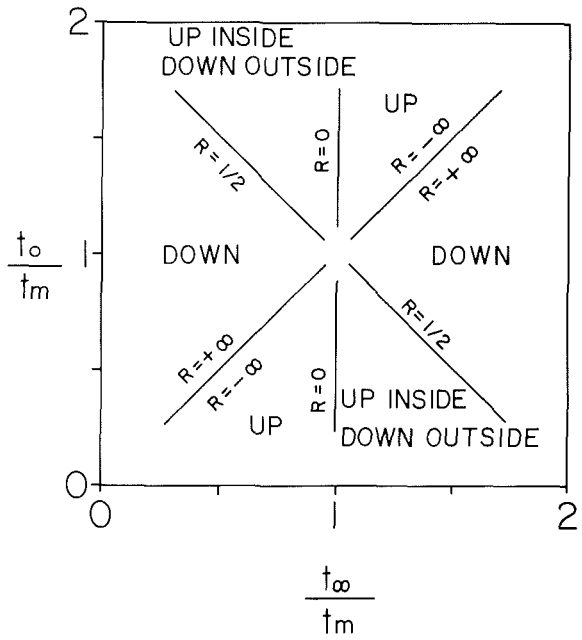

Fig. 4 The direction of the buoyancy force, determined by the values of t_o, t, and t_m, and therefore, of R

for a Prandtl number Pr = 12.6, for several values of the temperature parameter, R, pertinent to this study.

(ii) Flow Regimes. The temperature parameter, R, is a convenient indicator of the location of imposed temperatures t_o and t_∞, with respect to t_m. Referring to equation (1*b*), it is seen that for large R, ($R \to \pm\infty$), with moderate ($t_o - t_\infty$), the imposed conditions t_o and t_∞, and all temperatures between, are far removed from the extremum region. The situation may accurately be treated as Boussinesq. However, for moderate values of R, several anomalous flow regimes arise. Figure 4, from Gebhart and Mollendorf [6], summarizes these regimes, where the labels UP and DOWN refer to buoyancy force direction, and INSIDE and OUTSIDE refer to boundary layer locations adjacent to the heated surface, and far from it, respectively. It is seen that for all values of R, other than the range $0 < R < 1/2$, the buoyancy force is unidirectional and in a direction consistent with the location of t_o and T_∞ with respect to t_m.

For all values of R in the range $0 < R < 1/2$, a bidirectional buoyancy force arises across the thermal transport

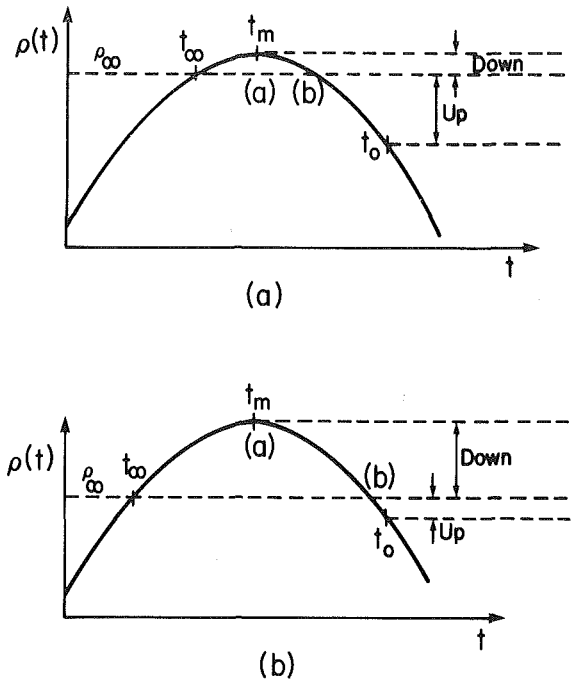

Fig. 5 Illustration of density behavior near t_m; (a), $R = 0^+$, outside buoyancy force reversal; (b), $R = 1/2^-$, inside buoyancy force reversal

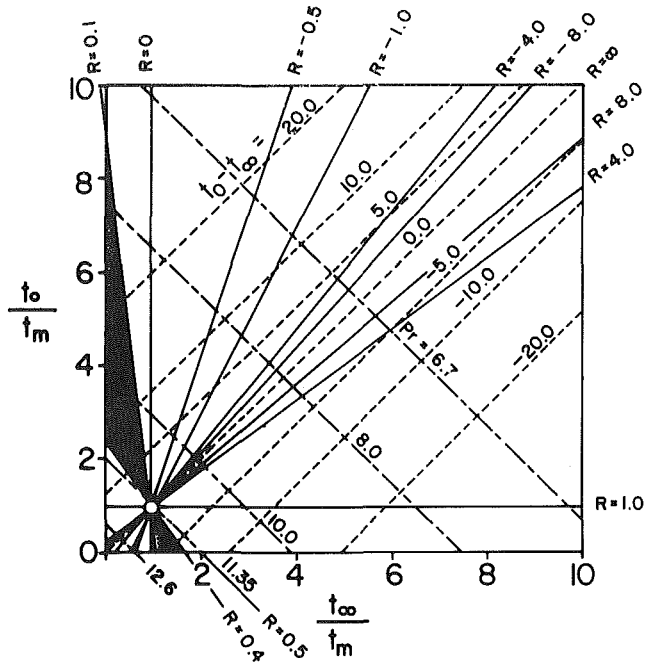

Fig. 6 Relationship between system temperatures t_o/t_m and t/t_m, and temperature parameter $R = (t_m - t_\infty)/(t_o - t_\infty)$: — constant R; —·— constant Pr; ··· constant $(t_o - t_\infty)$. The shaded area indicates, approximately, the local flow reversal region.

region. Figure 5(*a*) illustrates that, for $R = 0^+$, the density across the boundary layer, beginning at the plate surface is less than ρ_∞ until point (*b*) is reached. The buoyancy force is upward to this point. From point (*b*), through point (*a*) to t_∞, the density is greater than ρ_∞ and the buoyancy force, correspondingly, is downward. Because the downward force occurs over a small section of the boundary layer near the outer edge, this is referred to as an "outside buoyancy force reversal." Figure 5(*b*) shows that, approaching the bidirectional regime from the $R = 1/2^-$ direction, an "inside buoyancy force reversal" occurs.

It is the balance of viscous, pressure, and buoyancy forces which determine the flow direction, and not the buoyancy force alone. The buoyancy force may eventually overcome the viscous and pressure forces, and local flow reversal, or complete "convective inversion" does occur, somewhere within the range of $0.12 < R < 0.32$. Low Grashof numbers (Gr) characterize the nonvigorous nature of this flow regime. The boundary layer approximations may become inapplicable. The numerical solutions to the stability equations become increasingly unstable in this regime.

Figure 6 shows, in more detail, the relationship between the parameter R, the chosen system temperatures t_o and t_∞ and buoyancy force reversal. Constant Prandtl number contours are also shown corresponding to the intermediate or film temperature $t_f = (t_o + t_\infty)/2$. Specifying $\Pr(t_f)$ and R, determines $\Delta t = t_o - t_\infty$. Constant Δt lines are shown. The shaded area is, approximately, the local flow reversal region. The line $R = 0.5$ is seen to correspond only to $\Pr = 11.35$, the value of Pr at about 4°C. For this circumstance, t_o and t_∞ are centered about $t_f = t_m$ for any Δt. There is no equivalent Boussinesq solution for this condition, since, at $t_f = t_m$, the thermal expansion coefficient, β_t, is zero.

4 Disturbance Equations

Linear disturbance theory and development of the disturbance equations is well established and can be found in sufficient detail in (1).

The disturbance quantities are normalized in the following manner, where δ and U are the characteristic length and velocity.

$$\phi(\eta) = \frac{\bar{\phi}(y)}{U}, \quad s(\eta) = \frac{\bar{s}(y)}{\Delta t}, \quad \alpha = \bar{\alpha}\delta, \quad \beta = \frac{\bar{\beta}\delta}{U}$$

$$\mathrm{Gr}_x = \frac{g\alpha_t}{\nu^2} x^3 |t_o - t_\infty|^q, \quad G = 4\sqrt[4]{\frac{\mathrm{Gr}_x}{4}}, \quad \delta = \frac{4x}{G}, \quad U = \frac{\nu G^2}{4x}$$

$\bar{\alpha}$ is the complex wave number; $\bar{\beta}$, wavelength; $\bar{\phi}$ and $\bar{s}$, the velocity and temperature disturbance amplitude functions, respectively. The bars indicate dimensional quantities.

Some aspects of the x-dependence of U and δ are neglected, the so-called parallel flow approximation. This has been discussed in detail in [3].

The vorticity form of the Navier-Stokes equation is utilized to eliminate pressure as a variable. The resulting Orr-Sommerfeld momentum and energy equations, for buoyancy-induced flow with the new buoyancy term are

$$(\phi'' - \alpha^2\phi)(f' - \beta/\alpha) - \phi f''' = \frac{1}{i\alpha G}\left[\alpha^4\phi - 2\alpha^2\phi'' + \phi'''' \pm \left\{q\frac{(T-R)}{|T-R|}|T-R|^{q-1}s' + q(q-1)|T-R|^{q-2}sT'\right\}\right] \tag{5a}$$

$$s'' = i\alpha \Pr G[(f' - \beta/\alpha)s - T'\phi] + \alpha^2 s \tag{5b}$$

The boundary conditions for an isothermal surface are

$$\phi(0) = \phi'(0) = s(0) = \phi(\infty) = \phi'(\infty) = s(\infty) = 0 \tag{5c}$$

The foregoing system is a sixth-order eigenvalue problem, linear in the disturbance amplitude eigenfunctions $\phi(\eta)$, and $s(\eta)$. The eigenvalues of the system are chosen to be the nondimensional wave number, α, and frequency, β. The singular points, where $(f' - \beta/\alpha) = 0$, are defined as the critical layers. These were the subject of the limited analysis which preceded the availability of numerical methods of solution. The f and T are the previously defined base flow quantities. The density relation used in the analysis is seen to produce two buoyancy terms, coupling the momentum

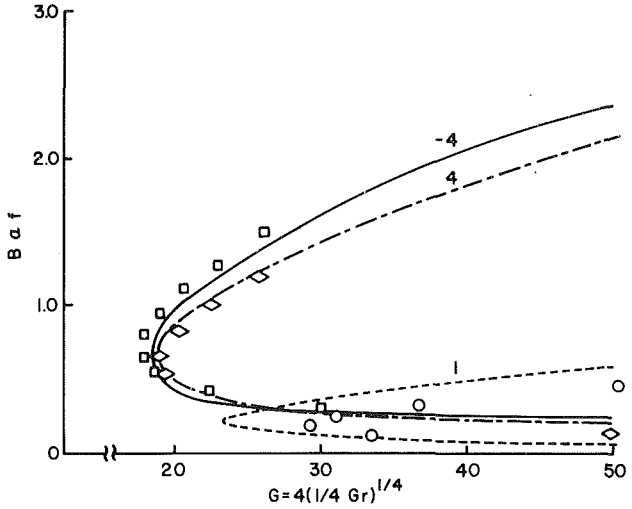

Fig. 7 Stability plane for various values of R, Pr = 12.6; nonBoussinesq results: — $R=-4.0$; —·— $R = 4.0$; ··· $R = 1.0$. Boussinesq results: □, $R = -4.0$; ◇, $R = 4.0$; ○, $R = 1.0$.

equation to the energy equation. For the Boussinesq approximation, $q = 1$, and the buoyancy terms reduce to the conventional ones seen in previous analyses. Again, asymptotic solutions, valid as $\eta \to \infty$, are used as input values to a numerical integration scheme.

5 Numerical Solution and Results

The homogeneous, linear, sixth-order system is solved by separately integrating six linearly independent integrals. As discussed in detail in [3], the eigenfunctions are expressible as linear combinations of the six independent integrals

$$\phi(\eta) = B_1\,\phi_1 + B_2\,\phi_2 + B_3\,\phi_3$$

$$s(\eta) = B_1\,s_1 + B_2\,s_2 + B_3\,s_3$$

where B_1, B_2, and B_3 are complex constants. B_1 is usually chosen as unity, fixing the scale of the disturbance level arbitrarily.

A fourth-order, Runge-Kutta integration routine was used to obtain the base flow solution, dependent on R and Pr. Then, the corresponding sixth-order disturbance equations were integrated. Both integrations used a fixed step size of $\eta = 0.05$, beginning with the asymptotic solutions at large η and proceeding inward to the wall at $\eta = 0$. Typically, values of G and α_{Im} are specified for a particular integration. The remaining eigenvalues, α_{Re} and β, are then guessed. The six independent integrals are integrated separately, and two of the three boundary conditions at $\eta = 0$ are applied to determine B_2 and B_3. The third boundary condition is satisfied only for appropriate values of the eigenvalues α_{Re} and β. This method of solution, originally employed in [3] has the distinct advantage of guessing only two initial eigenvalues, rather than six, as was necessary in earlier numerical solutions.

Recall that the temperature parameter R indicates the proximity of the imposed temperature levels t_o and t_∞ to the extremum temperature, t_m. Large values of R indicate conditions remote from the extremum region, where an appropriate Boussinesq density approximation may be sufficient. For all small values of R, say less than $|R| = 8$, an accurate density relationship produces important differences from the simpler Boussinesq treatment. The midrange of the interval $0 < R < 1/2$ also encompasses several bidirectional flow regimes.

Stability results are presented here, for several sets of temperatures t_o and t_∞, in terms of the eigenvalue parameter, B

$$B = \beta\,G^{1/3} = \frac{2\pi f}{\nu}\left[\frac{g}{\nu^2}\,\alpha_t\,|t_o - t|^q\right]^{-2/3}$$

The parameter B has no x-dependence and is proportional to physical frequency, f. Constant frequency paths to large values of G are then merely horizontal lines in a stability plane in terms of B versus G. It is recalled from the similarity transformation that the quantity, G, is directly proportional to $\sqrt[4]{\mathrm{Gr}_x}$. For a particular circumstance, with t_o and t_∞ specified, the properties α_t and ν are also specified. G may then be considered to be an explicit indicator of x, distance along the surface, for a given flow.

The definition of the Grashof number arises in the transformation of the base flow equations. The Boussinesq formulation produces the following traditional Grashof number

$$\mathrm{Gr}_{x_B} = \frac{g\beta_t}{\nu^2}\,x^3\,(t_o - t_\infty) \tag{6a}$$

The cold water formulation results in the following different Grashof number

$$\mathrm{Gr}_x = \frac{g\alpha_t}{\nu^2}\,x^3\,|t_o - t_\infty|^q \tag{6b}$$

The two values of Gr_x are related, as seen in Appendix A, as

$$\mathrm{Gr}_x = K\mathrm{Gr}_{x_B} \tag{6c}$$

where

$$K = \frac{1}{q}\,Z\,|t_f - t_m|^{1-q}\,\frac{|t_o - t_\infty|^q}{(t_o - t_\infty)}, \quad Z = \frac{t_f - t_m}{|t_f - t_m|}$$

In like manner, G, α, and B may be expressed in terms of G_B, α_B, and B_B

$$G = K^{1/4}\,G_B$$

$$\alpha = K^{-1/4}\,\alpha_B$$

$$B = K^{-2/3}\,B_B$$

All results are presented in terms of the variables G, α, and B, as appropriate for cold water.

Three neutral curves for Pr = 12.6 are shown in Fig. 7. This value of Pr corresponds to $t_f = 1.3°\mathrm{C}$. The curves shown are for $R = \pm 4$ and 1. The resulting temperatures t_o and t_∞ are close to t_m. For example, for $R = 4$, $t_0 = 1.69°\mathrm{C}$ and $t_\infty = 0.91°\mathrm{C}$. Deviations in the nose region arise for $R = \pm 4$. For the subcooled ambient condition, $R = 1$, $t_o = t_m$, and $t_\infty = -1.43°\mathrm{C}$, the nonBoussinesq behavior causes large effects. Also note that, as R decreases from 4 to 1, the neutral curves shift to the right. This indicates that initial instabilities occur further downstream as conditions approach the less vigorous flow reversal regime, $0.12 < R < 0.32$.

The disagreement between Boussinesq and cold water computations is further illustrated in Fig. 8, again for Pr = 12.6, but for $R = \pm 2$ and $-1/2$. It is apparent that, for both upflows $R = -2$ and $R = -1/2$, the Boussinesq based calculations significantly underpredict the values of G for which neutral stability occurs. However, for downflow at $R = 2$, the Boussinesq calculation overpredicts these values. Qureshi and Gebhart [5] present results for the isothermal boundary condition for $R=0$ ($t_\infty = t_m$) and upflow circumstance, for Pr = 11.6, that show the same trend. They also present disturbance profiles and phase distributions that are qualitatively similar to those for the conditions presented here.

Figure 9 explains the under- and overpredictions qualitatively. An upflow circumstance is shown in Fig. 9(*a*), with temperatures t_o and t_∞ to the left of t_m. A line representing the Boussinesq approximation of $(\rho_\infty - \rho)$ is drawn tangent to the film temperature, t_f. Consider any

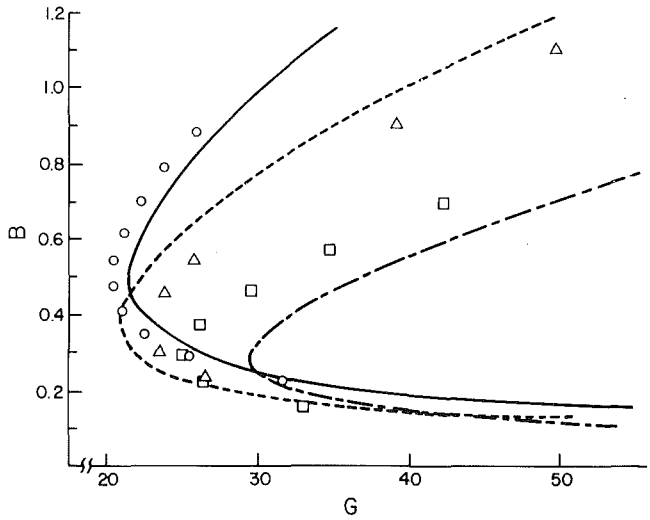

Fig 8 Stability plane for various values of R, Pr = 12.6; non-Boussinesq results; — $R = -2.0$; ··· $R = 2.0$; —·— $R = -1/2$. Boussinesq results: ○, $R = -2.0$; △, $R = 2.0$; □ $R = -1/2$.

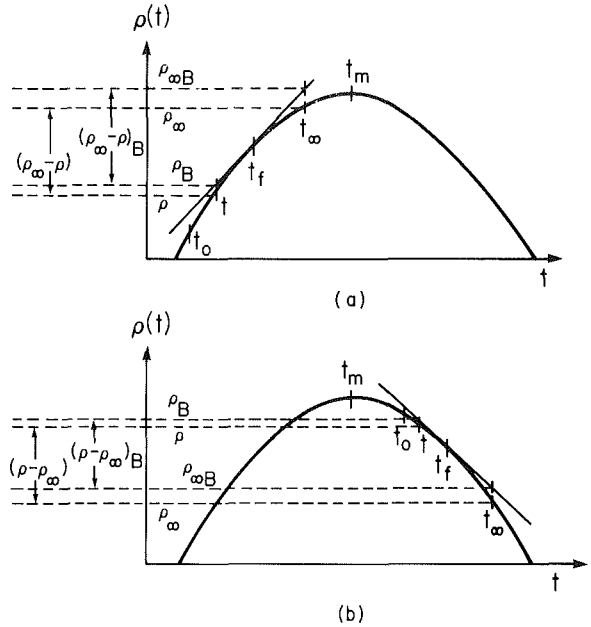

Fig. 9 Illustration of the disparity between Boussinesq and true buoyancy forces near t_m: (a) upflow, $(\rho_\infty - \rho)_B > (\rho_\infty - \rho)$; (b) downflow, $(\rho_\infty - \rho)_B < (\rho_\infty - \rho)$.

particular point in the thermal boundary layer, with temperature, t, and corresponding density, $\rho(t)$. The density difference predicted by the Boussinesq approximation, $(\rho_\infty - \rho)_B$, is shown. Also shown is the correct value of $(\rho_\infty - \rho)$. Clearly

$$(UP), (\rho_\infty - \rho)_B > (\rho_\infty - \rho).$$

This applies for any t chosen between t_o and t_∞. Thus, the linear approximation overpredicts the buoyancy force. Since buoyancy is the driving force, a larger value increases flow vigor, with earlier destabilization, that is, at a smaller value of G. The predicted neutral curve is displaced to the left, as the points show.

Figure 9(*b*), downflow, illustrates the opposite characteristic, seen in Fig. 8 for $R = 2$. Clearly

$$(\text{DOWN}), (\rho_\infty - \rho)_B > (\rho_\infty - \rho)$$

Flow vigor is reduced and the predicted neutral conditions lie to the right of the actual neutral curve. This may be quantitatively illustrated by considering an approximation to the ratio of Boussinesq to nonBoussinesq buoyancy forces, as determined in Appendix B

$$\frac{g(\rho_\infty - \rho)_B}{g(\rho_\infty - \rho)} = \frac{g\beta_l (t - t_\infty)}{g(\rho_\infty - \rho)} = \frac{q}{Z_f} \frac{(t_o - t_\infty)}{|t_o - t_\infty|} |T_f$$

$$-R|^{q-1} \frac{T}{[|T-R|^q - |R|^q]}$$

or

$$\frac{g(\rho_\infty - \rho)_B}{g(\rho_\infty - \rho)} = \frac{1}{K}$$

where K relates the Boussinesq to the cold water Grashof numbers in equation (6*c*).

For given values of R and Pr, t_0, t_∞, and t_f are determined. The $T(\eta)$ dependence is computed across the boundary layer. Table I shows $1/K$ for the R values corresponding to the results in Fig. 8. Overpredictions of the upflows, $R = -2$ and $R = -1/2$, are indicated by the result $1/K > 1$, and correspond to the left-shifted neutral curves. Underprediction indicated by $1/K < 1$, for the downflow $R = 2$, coincides with the right-shifted curve. The quantity $1/K$ may be used in this manner to determine whether the Boussinesq approximation over- or underpredicts the buoyancy force for a given set of conditions.

6 Summary

The new accurate density relation, describing the anomalous behavior of water near t_m, has been incorporated into the base flow and disturbance equations for flow adjacent to a vertical isothermal surface. The new disturbance equations contain special buoyancy terms, allowing an accurate stability analysis to be performed in cold water flows. Neutral conditions for Pr = 12.6 for a variety of ambient and surface temperatures have been presented.

The results show that the Boussinesq and cold water calculations have significant differences in the nose regions of the neutral curves. The Boussinesq approximation is shown to consistently overpredict the buoyancy force in upflow circumstances, with the resulting neutral stability curve lying to the left of the true one. For downflow circumstances, the opposite is true. The ratio of the Grashof numbers, $1/K$, is shown to be an indicator of over- or underprediction.

References

1 Higgins, J. M., "Stability of Buoyancy-Induced Flow of Water Near the Density Extremum, Adjacent to a Vertical, Isothermal Surface," Doctoral disseration, State University of New York at Buffalo, 1981.

2 Dring, R. P., and Gebhart, B., "A Theoretical Investigation of Disturbance Amplification in External Laminar Natural Convection," *Journal of Fluid Mechanics*, Vol. 34, 1968, pp. 551–564.

3 Hieber, C. A., and Gebhart, B., "Stability of Vertical Natural Convection Boundary Layers," *Journal of Fluid Mechanics*, Vol. 48, 1971, pp. 625–646.

4 Gebhart, B., and Mollendorf, J. C., "A New Density Relation for Pure and Saline Water," *Deep-Sea Res.*, Vol. 24, 1977, pp. 831–848.

5 Qureshi, Z. H., and Gebhart, B., "The Stability of Vertical Buoyancy-Induced Flow in Cold, Pure, and Saline Water, to appear in JOURNAL OF HEAT TRANSFER; see also Qureshi, Z. H., Stability and Measurements of Fluid and Thermal Transport in Vertical Buoyancy-Induced Flows in Cold Water," Doctoral dissertation, SUNYAB, Buffalo, N.Y., 1980.

6 Gebhart, B., and Mollendorf, J. C., "Buoyancy-Induced Flows in Water Under Conditions in Which Density Extrema May Arise, *Journal of Fluid Mechanics*, Vol. 89, 1978, pp. 673–707.

7 Fine, R. A., and Millero, F. J., "Compressibility of Water as a Function of Temperature and Pressure," *Journal of Chemical Physics*, Vol. 59, 1973, p. 5529.

8 Chen, C. T., and Millero, F. J., "The Specific Volume of Seawater at High Pressures," *Deep-Sea Res.*, Vol. 23, 1976, pp. 595–612.

9 Plapp, J. E., "Laminar Boundary Layer Stability in Free Convection," Doctoral dissertation, Calif. Instit. Tech., 1957.

10 Polymeropoulos, C. E., and Gebhart, B., "Incipient Instability in Free Convection Laminar Boundary Layers," *Journal of Fluid Mechanics*, Vol. 30, 1967, pp. 225–239.
11 Mendeleef, D. I., "On the Variation of the Density of Water at Different Temperatures," Royal Soc. of London, *Phil. Mag.*, Vol. 33, 1892, pp. 99–132.
12 Dumoré, J. M., Merk, H. J., and Prins, J. A., "Heat Transfer From Water to Ice by Thermal Convection," *Nature*, Vol. 172, 1953, pp. 460–461.
13 Merk, H. J., "The Influence of Melting and Anomalous Expansion on the Thermal Convection in Laminar Boundary Layers," *Appl. Sci. Res.*, sect. A, Vol. 4, 1954, pp. 435–452.
14 Goren, S. L., "On Free Convection in Water at 4°C," *Chemical Engineering Science*, Vol. 21, 1966, pp. 515–518.
15 Bryden, H. L., "New Polynomials for Thermal Expansion, Adiabatic Temperature Gradient and Potential Temperature of Sea Water," *Deep-Sea Res.*, Vol. 20, 1973, pp. 401–408.
16 Bradshaw, A., and Schleicher, K. E., "Direct Measurement of Thermal Expansion of Seawater Under Pressure,' *Deep-Sea Res.*, Vol. 17, 1970, pp. 691–706.
17 Gebhart, B., *Heat Transfer*, 2d ed., McGraw-Hill, 1971.
18 Govindarajulu, T., "Free Convection Flow of Water at 4°C on Vertical and Horizontal Plates," *Chemical Eng. Sc.*, Vol. 25, 1970, pp. 1827–1828.
19 Soundalgekar, V. M., "Laminar Free Convection Flow of Water at 4°C From a Vertical Plate With Variable Wall Temperature," *Chem. Eng. Sci.*, Vol. 28, 1973, pp. 307–309.
20 Soundalgekar, V. M., "A Note on the Unsteady Free Convection of Water at 4°C Past an Infinite Vertical Plate," *Chem. Eng. Sci.*, Vol. 25, 1980, pp. 750–752.

APPENDIX A

Conversion From Boussinesq to Cold Water Formulation Coordinates

The definition of the Grashof number arises from the nondimensionalization of the base flow equations. In a Boussinesq formulation

$$\mathrm{Gr}_{x_B} = \frac{g\beta_t}{\nu^2} x^3 (t_o - t_\infty) \tag{A1}$$

The formulation utilizing the new density relation results in

$$\mathrm{Gr}_x = \frac{g\alpha_t}{\nu^2} x^3 |t_o - t_\infty|^q \tag{A2}$$

For comparisons, (A2) is written in terms of (A1) as

$$\mathrm{Gr}_x = \left(\frac{\alpha_t}{\beta_t}\right) \frac{|t_o - t_\infty|^q}{(t_o - t_\infty)} \mathrm{Gr}_{x_B}$$

The density at reference temperature, t_f, is

$$\rho(t_f) = \rho_m [1 - \alpha_t |t_f - t_m|^q]$$

The Boussinesq volumetric expansion coefficient becomes

$$\beta_t = -\frac{1}{\rho}\frac{\partial \rho}{\partial t}\bigg|_{t=t_f} = \frac{1}{Z_f}\frac{\rho_m \alpha_t q |t_f - t_m|^{q-1}}{\rho_m [1 - \alpha_t |t_f - t_m|^q]}$$

$$\approx \frac{1}{Z_f} \alpha_t q |t_f - t_m|^{q-1}$$

where

$$Z_f = \frac{|t_f - t_m|}{(t_f - t_m)}$$

If $|t_f - t_m|^q << 1$

Table 1 Buoyancy force parameter $1/K$, as a function of T and R

T	$R = 2.0$	$R = -2.0$	$R = -1/2$
0.1	0.7908	1.1943	1.7076
0.2	0.8094	1.1689	1.5802
0.3	0.8290	1.1446	1.4715
0.4	0.8496	1.1213	1.3778
0.5	0.8714	1.0991	1.2959
0.6	0.8945	1.0778	1.2237
0.7	0.9189	1.0573	1.1597
0.8	0.9448	1.0377	1.1024
0.9	0.9724	1.0188	1.0508
1.0	1.0018	1.0006	1.0041

$$\left(\frac{\alpha_t}{\beta_t}\right) = \frac{Z_f \alpha_t}{\alpha_t q |t_f - t_m|^{q-1}} = \frac{1}{q} Z_f |t_f - t_m|^{1-q}$$

and

$$\mathrm{Gr}_x = \frac{1}{q} Z_f |t_f - t_m|^{1-q} \frac{|t_o - t_\infty|^q}{(t_o - t_\infty)} \mathrm{Gr}_{x_B}$$

Or, restating, this in terms of $K(\mathrm{Pr}_f, R)$

$$\mathrm{Gr}_x = K \mathrm{Gr}_{x_B}, \; K = \frac{1}{q} Z_f |t_f - t_m|^{1-q} \frac{|t_o - t_\infty|^q}{(t_o - t_\infty)}$$

Using these results, the parameters, G, α, α and B are related as

$$G = K^{1/4} G_B, \quad \alpha = K^{-1/4} \alpha_B, \quad \alpha = K^{-3/4} \beta_B$$
$$\text{and } B = K^{-2/3} B_B$$

APPENDIX B

Comparison of the Boussinesq and Cold Water Buoyancy Force Formulations

The base flow buoyancy force in the traditional Boussinesq treatment is approximated with a linear relationship in temperature as

$$g(\rho_\infty - \rho)_B = g\rho\beta_t (t - t_\infty)$$

Using the new density relation, the buoyancy force becomes:

$$g(\rho_\infty - \rho) = g\rho_m \alpha_t |t_o - t_\infty|^q [|T - R|^q - |R|^q] \tag{B1}$$

The Boussinesq form, using β_t at t_f, from the new density equation, becomes

$$g(\rho_\infty - \rho) = \frac{1}{Z_f} g q \rho_m \alpha_t (t_o - t_\infty) |t_o - t_\infty|^{q-1} |T_f - R|^{q-1} T \tag{B2}$$

Dividing (B2) by (B1) gives

$$\frac{g(\rho_\infty - \rho)_B}{g(\rho_\infty - \rho)} = \frac{1}{K}$$

where K is the ratio of the cold water Gr_x to the Boussinesq Gr_{xB} from equation (6c). For $1/K > 1$, $g(\rho_\infty - \rho)_B > g(\rho_\infty - \rho)$, and for $1/K < 1$, $g(\rho_\infty - \rho)_B > g(\rho_\infty - \rho)$. Computations for several cases pertinent to this study are summarized in Table 1.

Vortex Instability of Horizontal and Inclined Natural Convection Flows From Simultaneous Thermal and Mass Diffusion

T. S. Chen
Mem. ASME

K. L. Tzuoo[1]

A. Moutsoglou[2]

Department of Mechanical and Aerospace Engineering, University of Missouri-Rolla, Rolla, Mo. 65401

An analysis is performed to study the heat/mass transfer and vortex instability characteristics of buoyancy induced flows that result from simultaneous diffusion of heat and mass in laminar boundary layers adjacent to horizontal and inclined surfaces. Numerical results are obtained for a Prandtl number of 0.7 over a range of Schmidt numbers and various angles of inclination from the horizontal, ϕ. For a given ϕ, it is found that when the two buoyancy forces from thermal and mass diffusion act in the same direction, both the surface heat and mass transfer rates increase, causing the flow to become more susceptible to the vortex mode of instability. These trends are reversed when the two buoyancy forces act in the opposite directions. On the other hand, as ϕ is increased, the heat and mass transfer rates are enhanced, but the instability of the flow to the vortex mode of disturbances decreases and eventually vanishes at $\phi = 90$ deg.

Introduction

In many convective flows over a heated surface, the effect of buoyancy force may play an important role in the transport process. If, in addition, there exists a concentration gradient in the fluid, the buoyancy force effect from species diffusion may also be of significance. Thus, buoyancy forces may be induced simultaneously by thermal diffusion and diffusion of species in a transport process. The problems of combined effects of thermal and mass diffusion in natural convection flow have been studied for vertical and horizontal flat plates (see, for example [1, 2]). More recently, Chen and Yuh [3] have generalized the analysis to flow over an inclined plate, in which they neglected the streamwise pressure gradient term in the momentum equation and obtained similarity solutions for the flow, thermal, and concentration fields. Their analysis is valid under the condition when $(\delta/x)\tan\gamma << 1$ (where δ is the boundary-layer thickness and γ is the angle of inclination from the vertical) and therefore fails at $\gamma = \pi/2$ (i.e., a horizontal plate). Their results are thus good for inclination angles from the vertical that are not very large (say, $\gamma < 60$ deg) and poor for larger angles (i.e., for inclined plates that are closer to the horizontal orientation).

The instability of vertical, inclined, and horizontal natural convection flows has also been analyzed extensively by many investigators (see, for example, [4–12]). A good summary of the buoyancy-induced flows and their stability characteristics has been given by Gebhart [13]. Some of the previous studies have treated the wave mode of instability, while the others the vortex mode of instability. However, the majority of these studies, except for [8] and [11], have considered the flow situation in which the buoyancy force is induced solely by the temperature variations in the fluid. The wave instability of natural convection flows with combined buoyancy modes of thermal and mass diffusion has been investigated by Pera and Gebhart [8] for a horizontal plate, with both Prandtl and Schmidt numbers equal to 0.7, and by Boura and Gebhart [11] for a vertical plate, with a Prandtl number of 0.7 and Schmidt numbers of 0.2, 0.94, and 2.0. The vortex instability of natural convection flows under the combined thermal and mass diffusion processes, however, seems not to have been investigated, either for flow over a horizontal plate or an inclined plate. This has motivated the present investigation.

In contrast to the analytical studies, experimental work on the instability of inclined natural convection flows has been confined to situations in which there is no mass diffusion (see, for example, [14–16]). From the experimental study of Lloyd and Sparrow [14] for natural convection of water over a heated, inclined surface, it has been verified that the first onset of the instability of the flow is due to the wave mode of disturbances when the angle of inclination from the vertical is less than 17 deg, whereas for angles larger than 17 deg the first onset of the instability is due to the vortex mode of disturbances. Because of this finding and of the fact that analytical results of the instability of flow depend on the accuracy of the main flow solutions, an analysis of the vortex instability of natural convection flows over horizontal and inclined surfaces should be preceded with an accurate and complete solution of the main flow. Such a main flow solution under the simultaneous effects of thermal and mass diffusion has not been carried out, and it constitutes the first phase of the present investigation.

In the main flow analysis, both the streamwise and the normal components of the buoyancy forces from thermal and mass diffusion are taken into account. However, attention is focused on flow with low concentration levels such that the diffusion-thermo and thermo-diffusion effects, as well as the interfacial velocity due to the mass diffusion, can be neglected. The relative effect of the buoyancy forces between thermal and mass diffusion appears as a parameter $N = \mathrm{Gr}_{x,c}/\mathrm{Gr}_{x,t}$, where $\mathrm{Gr}_{x,c}$ and $\mathrm{Gr}_{x,t}$ denote, respectively, the local concentration Grashof number and the local thermal Grashof number. The governing conservation equations for the laminar boundary layer are transformed into a system of dimensionless equations such that the nonsimilarity parameter $\xi(x)$ varies with x to a positive power and depends also on the angle of inclination from the horizontal, ϕ. This system of equations is then solved by an efficient finite difference method.

The stability analysis is based on the linear theory. The

[1] Presently a Ph.D. candidate at the Department of Mechanical Engineering, Stanford University, Stanford, Calif.

[2] Presently at the Department of Mechanical Engineering, Virginia Polytechnic Institute and State University, Blacksburg, Va., Mem. ASME

Contributed by the Heat Transfer Division and presented at the ASME Winter Annual Meeting, Washington, D.C., November 15–20, 1981. Manuscript received by the Heat Transfer Division June 21, 1982. Paper No. 81-WA/HT-64.

disturbance quantities are assumed to be of the form of a stationary vortex roll that is periodic in the spanwise direction, with its amplitude function depending only on the normal coordinate. The resulting eigenvalue problem consisting of four coupled differential equations for the velocity, temperature, and concentration disturbances, along with their boundary conditions, is solved by the fourth-order, Runge-Kutta integration scheme in conjunction with Newton-Raphson shooting technique.

Numerical results for the main flow quantities, such as the local wall shear stress, the local Nusselt number, and the local Sherwood number, are presented for a Prandtl number of 0.7, with Schmidt numbers of 0.6, 1, and 2 and values of the relative buoyancy parameter, N, equal to -0.5, 0, 1, and 2. Neutral stability curves for representative values of N and Schmidt number are shown for various angles of inclination from the horizontal. Critical thermal Grashof numbers are also presented and compared with available analytical results from the wave mode of instability for flow over horizontal and vertical plates.

Analysis

The Main Flow, Thermal, and Concentration Fields. Consideration is given to an inclined flat plate that forms an acute angle, ϕ, from the horizontal and is situated in an otherwise quiescent fluid with free stream temperature, T_∞, and free-stream species concentration, C_∞. The plate is maintained at a uniform temperature, T_w, and a uniform concentration C_w, with its heated surface facing upward. Let the x-coordinate be measured in the streamwise direction from the leading edge of the plate and the y-coordinate be measured normal to the plate. Under the assumptions of negligible diffusion-thermo and thermo-diffusion effects, along with Boussinesq approximation, the governing conservation equations of the laminar boundary layer flow can be written as [3]

$$\frac{\partial U}{\partial x}+\frac{\partial V}{\partial y}=0 \tag{1}$$

$$U\frac{\partial U}{\partial x}+V\frac{\partial U}{\partial y}=g\beta\cos\phi\frac{\partial}{\partial x}\int_y^\infty (T-T_\infty)\,dy + g\beta^*\cos\phi\frac{\partial}{\partial x}\int_y^\infty (C-C_\infty)\,dy + g\beta\sin\phi(T-T_\infty)+g\beta^*\sin\phi(C-C_\infty)+\nu\frac{\partial^2 U}{\partial y^2} \tag{2}$$

$$U\frac{\partial T}{\partial x}+V\frac{\partial T}{\partial y}=\kappa\frac{\partial^2 T}{\partial y^2} \tag{3}$$

$$U\frac{\partial C}{\partial x}+V\frac{\partial C}{\partial y}=D\frac{\partial^2 C}{\partial y^2} \tag{4}$$

where all notations are defined in the nomenclature. The first two terms on the right-hand side of equation (2) represent the streamwise pressure gradient induced by the normal component of the buoyancy forces, respectively, from the temperature and concentration variations in the fluid, and the third and fourth terms represent the axial component of the respective buoyancy forces. The boundary conditions for equations (1-4) are

$$\begin{aligned} U=0,\ V=v_w,\ T=T_w,\ C=C_w \quad &\text{at} \quad y=0 \\ U\to=0,\ T\to T_\infty,\ C\to C_\infty \quad &\text{as} \quad y\to\infty \end{aligned} \tag{5}$$

It is noted that equation (2) reduces to that for a vertical plate [1] when $\phi=\pi/2$ and to that for a horizontal plate [2] when $\phi=0$ deg.

Nomenclature

C = mass fraction of the diffusing species
D = binary diffusion coefficient
D^n = $d^n/d\eta^n$, differential operator
f = reduced stream function
g = gravitational acceleration
$\mathrm{Gr}_{x,t}$ = $g\beta(T_w-T_\infty)x^3/\nu^2$, thermal Grashof number
$\mathrm{Gr}_{x,c}$ = $g\beta^*(C_w-C_\infty)x^3/\nu^2$, Grashof number for mass diffusion
k = thermal conductivity of fluid
L = x, characteristic length
$\dot{m}$ = mass flux of the diffusing species
N = $\mathrm{Gr}_{x,c}/\mathrm{Gr}_{x,t}$, ratio of Grashof numbers
Nu_x = $q_w x/[(T_w-T_\infty)k]$, local Nusselt number
p' = perturbation pressure
P = mainflow pressure
Pr = ν/κ, Prandtl number
q_w = local surface heat flux
Sc = ν/D, Schmidt number
Sh_x = $\dot{m}_w x/[\rho D(C_w-C_\infty)]$, local Sherwood number
t = dimensionless amplitude function of temperature disturbances
t' = perturbation temperature
T = fluid temperature
u,v,w = dimensionless amplitude functions of velocity disturbances
u',v',w' = axial, normal, and spanwise components of velocity disturbances
U,V = mainflow velocity components in x- and y-directions
x,y,z = axial, normal, and spanwise coordinates
Y,Z = dimensionless normal and spanwise coordinates, $Y=\eta$
α = dimensionless wave number of disturbances
β = $[-(\partial\rho/\partial T)_{p,C}]/\rho$, volumetric coefficient of thermal expansion
β^* = $[-(\partial\rho/\partial C)_{p,T}]/\rho$, volumetric coefficient of expansion with mass fraction
γ = angle of inclination from the vertical
δ = boundary layer thickness
η = $(y/x)(\mathrm{Gr}_{x,t}\cos\phi/5)^{1/5}$, pseudo-similarity variable
η_δ = dimensionless boundary layer thickness
θ = $(T-T_\infty)/(T_w-T_\infty)$, dimensionless temperature
κ = thermal diffusivity of fluid
λ = dimensionless mass fraction
μ = dynamic viscosity of fluid
ν = kinematic viscosity of fluid
ξ = $(\mathrm{Gr}_{x,t}\cos\phi/5)^{1/5}\tan\phi$, buoyancy force and inclination parameter
ρ = density of fluid
τ = shear stress
ϕ = angle of inclination from the horizontal
ψ = stream function

Superscripts

$+$ = dimensionless disturbance quantity
$*$ = critical condition
$\hat{}$ = resultant quantity

Subscripts

w = condition at the wall
∞ = condition at the free stream

Equations (1–5) can be transformed into a dimensionless form by employing the dimensionless coordinates $\xi(x)$ and $\eta(x,y)$ [12]

$$\xi=\left(\frac{\mathrm{Gr}_{x,t}\cos\phi}{5}\right)^{1/5}\tan\phi,\quad \eta=\frac{y}{x}\left(\frac{\mathrm{Gr}_{x,t}\cos\phi}{5}\right)^{1/5} \tag{6}$$

along with the reduced stream function $f(\xi,\eta)$, the dimensionless temperature $\theta(\xi,\eta)$, and the dimensionless mass fraction $\lambda(\xi,\eta)$ defined, respectively, by

$$f(\xi,\eta)=\psi(x,y)\Big/5\nu\left(\frac{\mathrm{Gr}_{x,t}\cos\phi}{5}\right)^{1/5},$$

$$\theta(\xi,\eta)=\frac{T-T_\infty}{T_w-T_\infty},\quad \lambda(\xi,\eta)=\frac{C-C_\infty}{C_w-C_\infty} \tag{7}$$

in which $\psi(x,y)$ is the stream function that satisfies the continuity equation (1) with $u=\partial\psi/\partial y$ and $v=-\partial\psi/\partial x$, and $\mathrm{Gr}_{x,t}$ is the local Grashof number defined by $\mathrm{Gr}_{x,t}=g\beta(T_w-T_\infty)x^3/\nu^2$. Upon transformation, the system of equations assumes the following form

$$f'''+3ff''-(f')^2+\frac{2}{5}\left[\eta(\theta+N\lambda)+\int_\eta^\infty(\theta+N\lambda)d\eta+\frac{3}{2}\xi\int_\eta^\infty\left(\frac{\partial\theta}{\partial\xi}+N\frac{\partial\lambda}{\partial\xi}\right)d\eta\right]+\xi(\theta+N\lambda)=3\xi\left[f'\frac{\partial f'}{\partial\xi}-f''\frac{\partial f}{\partial\xi}\right] \tag{8}$$

$$\frac{1}{\mathrm{Pr}}\theta''+3f\theta'=3\xi\left[f'\frac{\partial\theta}{\partial\xi}-\theta'\frac{\partial f}{\partial\xi}\right] \tag{9}$$

$$\frac{1}{\mathrm{Sc}}\lambda''+3f\lambda'=3\xi\left[f'\frac{\partial\lambda}{\partial\xi}-\lambda'\frac{\partial f}{\partial\xi}\right] \tag{10}$$

$$f'(\xi,0)=f(\xi,0)=0,\ \theta(\xi,0)=1,\ \lambda(\xi,0)=1$$
$$f'(\xi,\infty)=\theta(\xi,\infty)=\lambda(\xi,\infty)=0 \tag{11}$$

In the foregoing equations, the primes indicate partial differentiation with respect to η and N is defined as

$$N=\frac{\beta^*(C_w-C_\infty)}{\beta(T_w-T_\infty)}=\frac{\mathrm{Gr}_{x,c}}{\mathrm{Gr}_{x,t}} \tag{12}$$

with $\mathrm{Gr}_{x,c}=g\beta^*(C_w-C_\infty)x^3/\nu^2$ denoting the local Grashof number for mass diffusion. The parameter N measures the relative importance of the buoyancy forces between mass and thermal diffusion that drive the flow. There is no mass diffusion when $N=0$. The buoyancy forces from mass and thermal diffusion act in the same direction when $N>0$, whereas they act in the opposite directions when $N<0$. It is noted here that the dimensionless coordinate ξ is a measure of the plate inclination as well as the thermal buoyancy force intensity.

In writing the boundary condition $f(\xi,0)=0$ in equation (11), the normal velocity, v_w, at the wall associated with the species diffusion process has been assumed to be negligibly small. This assumption is valid when the condition

$$\frac{v_w x}{\nu}<<3\left(\frac{\mathrm{Gr}_{x,t}\cos\phi}{5}\right)^{1/5} \tag{13}$$

or, from the use of Fick's law, the condition

$$\frac{1}{3\mathrm{Sc}}(C_w-C_\infty)[-\lambda'(\xi,0)]<<1 \tag{14}$$

is fulfilled.

The physical quantities of interest are the local wall shear stress, τ_w, the local Nusselt number, Nu_x, and the local Sherwood number, Sh_x. They are defined, respectively, by

$$\tau_w=\mu\left(\frac{\partial u}{\partial y}\right)_{y=0},\quad \mathrm{Nu}_x=\frac{q_w}{T_w-T_\infty}\frac{x}{k},$$

$$\mathrm{Sh}_x=\frac{\dot m_w}{C_w-C_\infty}\frac{x}{\rho D} \tag{15}$$

With $q_w=-k(\partial T/\partial y)_{y=0}$ and $\dot m_w=-\rho D(\partial C/\partial y)_{y=0}$, equation (15) can be written in terms of the dimensionless variables as

$$\tau_w\frac{x^2}{5\mu\nu}\left(\frac{\mathrm{Gr}_{x,t}\cos\phi}{5}\right)^{-3/5}=f''(\xi,0) \tag{16}$$

$$\mathrm{Nu}_x\left(\frac{\mathrm{Gr}_{x,t}\cos\phi}{5}\right)^{-1/5}=-\theta'(\xi,0) \tag{17}$$

$$\mathrm{Sh}_x\left(\frac{\mathrm{Gr}_{x,t}\cos\phi}{5}\right)^{-1/5}=-\lambda'(\xi,0) \tag{18}$$

Formulation of the Stability Problem. As discussed in [12] and [17], the disturbance quantities u', v', w', p', t', and c', which are taken as functions of (y,z), are superimposed on the mainflow quantities U, V, $W=0$, P, T, and C to form the following resultant quantities $\hat u$, $\hat v$, $\hat w$, $\hat p$, $\hat t$, and $\hat c$

$$\begin{aligned}\hat u&=U(x,y)+u'(y,z)\\ \hat v&=V(x,y)+v'(y,z)\\ \hat w&=w'(y,z)\\ \hat p&=P(x,y)+p'(y,z)\\ \hat t&=T(x,y)+t'(y,z)\\ \hat c&=C(x,y)+c'(y,z)\end{aligned} \tag{19}$$

These resultant quantities satisfy the continuity equation, the Navier-Stokes equations, the energy equation, and the mass-fraction equation for an incompressible, steady three-dimensional natural convection flow over an inclined plate under the simultaneous thermal and mass diffusion. When they are substituted into the aforementioned conservation equations and the resulting equations are linearized with respect to the disturbance quantities, one arrives at

$$\frac{\partial v'}{\partial y}+\frac{\partial w'}{\partial z}=0 \tag{20}$$

$$u'\frac{\partial U}{\partial x}+v'\frac{\partial U}{\partial y}+V\frac{\partial u'}{\partial y}=g\beta\sin\phi\,t'+g\beta^*\sin\phi\,c'+\nu\left(\frac{\partial^2u'}{\partial y^2}+\frac{\partial^2u'}{\partial z^2}\right) \tag{21}$$

$$u'\frac{\partial V}{\partial x}+v'\frac{\partial V}{\partial y}+V\frac{\partial v'}{\partial y}=-\frac{1}{\rho}\frac{\partial p'}{\partial y}+g\beta\cos\phi\,t'+g\beta^*\cos\phi\,c'+\nu\left(\frac{\partial^2v'}{\partial y^2}+\frac{\partial^2v'}{\partial z^2}\right) \tag{22}$$

$$V\frac{\partial w'}{\partial y}=-\frac{1}{\rho}\frac{\partial p'}{\partial z}+\nu\left(\frac{\partial^2w'}{\partial y^2}+\frac{\partial^2w'}{\partial z^2}\right) \tag{23}$$

$$u'\frac{\partial T}{\partial x}+v'\frac{\partial T}{\partial y}+V\frac{\partial t'}{\partial y}=\kappa\left(\frac{\partial^2t'}{\partial y^2}+\frac{\partial^2t'}{\partial z^2}\right) \tag{24}$$

$$u'\frac{\partial C}{\partial x}+v'\frac{\partial C}{\partial y}+V\frac{\partial c'}{\partial y}=D\left(\frac{\partial^2c'}{\partial y^2}+\frac{\partial^2c'}{\partial z^2}\right) \tag{25}$$

Next, the pressure terms in the y- and z-momentum equations, equation (22) and (23), are eliminated, and the resulting system of five coupled equations are then transformed into a dimensionless form by introducing the following dimensionless quantities

$$Y=\frac{y}{L}\left(\frac{\mathrm{Gr}_{L,t}\cos\phi}{5}\right)^{1/5},\quad Z=\frac{z}{L}\left(\frac{\mathrm{Gr}_{L,t}\cos\phi}{5}\right)^{1/5} \tag{26}$$

$$u^+=\frac{u'}{\frac{\kappa}{L}\left(\frac{\mathrm{Gr}_{L,t}\cos\phi}{5}\right)^{2/5}},\quad v^+=\frac{v'}{\frac{\kappa}{L}\left(\frac{\mathrm{Gr}_{L,t}\cos\phi}{5}\right)^{1/5}},$$

$$w^+=\frac{w'}{\frac{\kappa}{L}\left(\frac{\mathrm{Gr}_{L,t}\cos\phi}{5}\right)^{1/5}},\quad t^+=\frac{t'}{T_w-T_\infty},$$

$$c^+=\frac{c'}{C_w-C_\infty} \tag{27}$$

where $\mathrm{Gr}_{L,t}=g\beta(T_w-T_\infty)L^3/\nu^2$ is the thermal Grashof number based on the characteristic length, $L(x)$. In order to have $Y=\eta$, one lets $L(x)=x$. It then follows that $\mathrm{Gr}_{L,t}=\mathrm{Gr}_{x,t}$. Furthermore, the main flow quantities appearing in equations (20-25) are expressed in terms of $f(\xi,\eta)$, $\theta(\xi,\eta)$, $\lambda(\xi,\eta)$ and their derivatives. The resulting dimensionless disturbance equations are further simplified by introducing

$$u^+=u(Y)e^{i\alpha Z},\quad v^+=v(Y)e^{i\alpha Z},\quad w^+=w(Y)e^{i\alpha Z},$$
$$t^+=t(Y)e^{i\alpha Z},\quad c^+=c(Y)e^{i\alpha Z} \tag{28}$$

where α is the dimensionless wave number of the disturbances. That is, the disturbances are taken to have the form of stationary vortex rolls that are periodic in the spanwise direction, with their amplitude functions u, v, w, t, and c depending only on Y. The result of the aforementioned operations leads to the following system of equations for the disturbance amplitude functions

$$[(D^2-\alpha^2)-B_1D+B_2]u$$
$$=B_3v-5\mathrm{Pr}\left(\frac{\mathrm{Gr}_{x,t}\cos\phi}{5}\right)^{1/5}\tan\phi(t+Nc) \tag{29}$$

$$[(D^2-\alpha^2)^2-B_1D(D^2-\alpha^2)-B_2(D^2-\alpha^2)]v$$
$$=B_4\alpha^2u+5\alpha^2\mathrm{Pr}\left(\frac{\mathrm{Gr}_{x,t}\cos\phi}{5}\right)^{2/5}(t+Nc) \tag{30}$$

$$[(D^2-\alpha^2)-B_1\mathrm{Pr}D]t=B_5u+B_6v \tag{31}$$

$$[(D^2-\alpha^2)-B_1\mathrm{Sc}D]c=B_7\frac{\mathrm{Sc}}{\mathrm{Pr}}u+B_8\frac{\mathrm{Sc}}{\mathrm{Pr}}v \tag{32}$$

with the boundary conditions

$$u=v=Dv=t=c=0\quad\text{at}\quad\eta=0\quad\text{and}\quad\eta=\infty \tag{33}$$

In equations (29-33), $D^n=d^n/d\eta^n$ and the boundary conditions arise from the vanishing of the disturbances at the wall and in the free stream, in which $Dv=0$ results from the continuity equation $\partial v^+/\partial Y+\partial w^+/\partial Z=0$ along with $w^+=0$ at $\eta=0$ and $\eta=\infty$. The coefficients $B_1(\xi,\eta)$ through $B_8(\xi,\eta)$ in the foregoing equations have the expressions

$$B_1=2\eta f'-3f-3\xi\partial f/\partial\xi \tag{34a}$$

$$B_2=2\eta f''-f'-3\xi\partial f'/\partial\xi \tag{34b}$$

$$B_3=5f'' \tag{34c}$$

$$B_4=\frac{1}{5}(4\eta^2f''+2\eta f'-6f-12\xi\eta\partial f'/\partial\xi$$
$$+12\xi\partial f/\partial\xi+9\xi^2\partial^2f/\partial\xi^2) \tag{34d}$$

$$B_5=-\frac{1}{5}(2\eta\theta'-3\xi\partial\theta/\partial\xi) \tag{34e}$$

$$B_6=\theta' \tag{34f}$$

$$B_7=-\frac{1}{5}(2\eta\lambda'-3\xi\partial\lambda/\partial\xi) \tag{34g}$$

$$B_8=\lambda' \tag{34h}$$

The system of equations (29-32), along with their boundary conditions, equation (33), forms an eigenvalue problem of the form

$$E(\mathrm{Gr}_{x,t},\alpha;\mathrm{Pr},\mathrm{Sc},N,\phi)=0 \tag{35}$$

For given values of Prandtl number, Pr, Schmidt number, Sc, relative buoyancy parameter, N, and angle of inclination, ϕ, the value of α satisfying equation (35) is sought as the eigenvalue for a prescribed value of $\mathrm{Gr}_{x,t}$.

Numerical Method of Solutions

The system of equations for the main flow, thermal, and concentration fields, equations (8-11), was solved by a finite difference technique modified from that described in [18]. Its details are omitted here. However, it is worthwhile to mention the treatment of the integrals involving θ, $\partial\theta/\partial\xi$, λ, and $\partial\lambda/\partial\xi$ in equation (8). Introduction of

$$G=\int_\eta^\infty\theta d\eta,\quad H=\int_\eta^\infty\lambda d\eta \tag{36}$$

gives rise to two additional equations

$$G'+\theta=0,\quad G(\xi,\infty)=0 \tag{37}$$

$$H'+\lambda=0,\quad H(\xi,\infty)=0 \tag{38}$$

and simplifies equation (9) to

$$f'''+3ff''-(f')^2+\frac{2}{5}\left[\eta(\theta+N\lambda)+(G+NH)\right.$$
$$\left.+\frac{3}{2}\xi\frac{\partial}{\partial\xi}(G+NH)\right]+\xi(\theta+N\lambda)$$
$$=3\xi\left(f'\frac{\partial f'}{\partial\xi}-f''\frac{\partial f}{\partial\xi}\right) \tag{39}$$

Thus, the finite difference solution was performed on equations (39), (9-11), (37), and (38) to obtain the main flow quantities. This approach gives a better rate of convergence and hence reduces the numerical computation time.

In the stability calculations, a fourth-order, Runge-Kutta integration scheme was used to solve equations (29-33). The integration was started from $\eta=\infty$ to $\eta=0$ by using the asymptotic solutions of equations (29-32) at $\eta=\eta_\infty$ as the starting values. The asymptotic solutions for u, v, t, and c at $\eta=\eta_\infty$ consist of five sets of independent solutions (u_i, v_i, t_i, c_i), with $i=1, 2, 3, 4$, and 5, that can be easily obtained. In addition, the numerical solution of the eigenvalue problem parallels that described in [19], and it suffices to mention only its highlights. In determining the neutral stability curve for given values of Pr, Sc, N, and ϕ, the eigenvalue problem is to find the value of α for a specified value of $\mathrm{Gr}_{x,t}$. This is done as follows. First, the main flow solution is obtained to provide the coefficients B_1 to B_8 for a preassigned value of $\xi=(\mathrm{Gr}_{x,t}\cos\phi/5)^{1/5}\tan\phi$ with given values of Pr, Sc, and N. Next, with the angle ϕ specified, the parameter $\mathrm{Gr}_{x,t}\cos\phi/5=(\xi/\tan\phi)^5$ in equations (29) and (30) is known and integration of equations (29-32) can be performed from $\eta=\eta_\infty$ to $\eta=0$ for each set of the five independent solutions by assuming a value of α, starting with the asymptotic solutions at η_∞. Newton-Raphson shooting method is then used to obtain a converged eigenvalue α for the particular $\mathrm{Gr}_{x,t}$. This completes a solution of the eigenvalue problem. The same process is repeated to obtain different values of the (α, $\mathrm{Gr}_{x,t}$) pair in mapping out a neutral stability curve.

Numerical computations were carried out for Pr = 0.7 and Sc = 0.6, 1, 2, with N ranging from -0.5 to 2. The Schmidt number range covers typically diffusion into air of water vapor (Sc = 0.6), carbon dioxide (0.94), methanol (0.97), and ethyl benzene (2.01). In the calculations, the values of η_∞ were found to depend on the Schmidt number Sc and the N value.

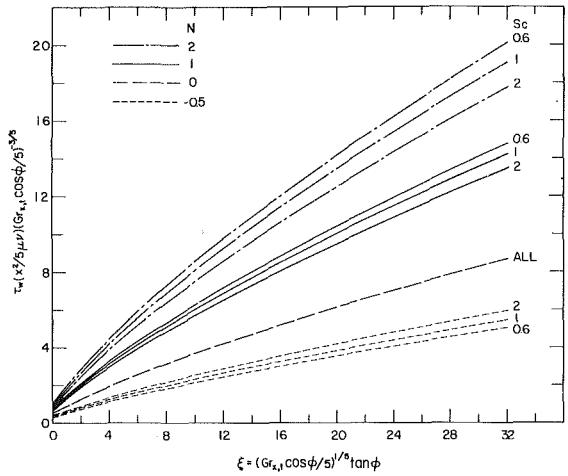

Fig. 1 Local wall shear stress results

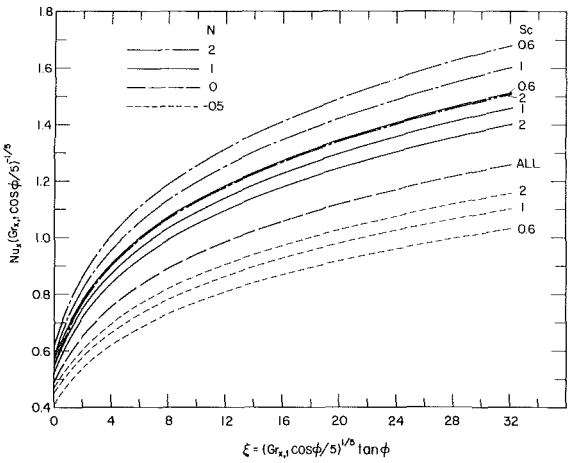

Fig. 2 Local Nusselt number results

For both Sc = 1 and 2, the η_∞ values of 7 for $N = 1$, 2, and 8 for $N = -0.5$ were found to be sufficient in both the main flow and stability calculations, whereas for Sc = 0.6, $\eta_\infty = 8$ for $N = 1$, 2, and 10 for $N = -0.5$ were required. In the main flow solutions by the finite difference method, variable step sizes were used in the ξ-direction. The step size was increased gradually with increasing ξ and ranged from $\Delta\xi = 0.1$ for $0 \le \xi \le 1$ to $\Delta\xi = 2.0$ for $\xi \ge 30$. On the other hand, a uniform step size of $\Delta\eta = 0.02$ in the η-direction was used in the main flow calculations. In the stability calculations, $\Delta\eta$ was taken to be 0.04 for $0 \le \eta \le \eta_\infty$.

Results and Discussion

Numerical results for the local wall shear stress, the local Nusselt number, and the local Sherwood number are shown in terms of $\tau_w(x^2/5\mu\nu)(Gr_{x,l}\cos\phi/5)^{-3/5}$, $Nu_x(Gr_{x,l}\cos\phi/5)^{-1/5}$, and $Sh_x(Gr_{x,l}\cos\phi/5)^{-1/5}$, respectively, in Figs. 1, 2, and 3. An inspection of these figures reveals that these three quantities increase with increasing value of ξ; that is, the wall shear stress and the surface heat/mass transfer rates either increase with increasing angle of inclination ϕ for a fixed local thermal Grashof number $Gr_{x,l}$ or increase with increasing thermal Grashof number for a fixed angle, ϕ. These trends are to be expected physically, because when the local thermal Grashof number is increased or when the angle ϕ is increased from the horizontal (i.e., $\phi = 0$ deg) toward the vertical ($\phi = 90$ deg) orientation, the buoyancy forces will become more pronounced. This causes an increase in the wall shear stress and the surface heat/mass transfer rates. This condition will prevail as long as the N value is such that the combined buoyancy forces from thermal and mass diffusion produce a positive effect.

Figures 1, 2, and 3 also show that, for a given Schmidt number, the wall shear stress and the surface heat/mass transfer rates increase with increasing value of N when $N > 0$. This is because the buoyancy force from mass diffusion assists the thermal buoyancy force when $N > 0$. On the other hand, when $N < 0$, the buoyancy force from mass diffusion opposes the thermal buoyancy force and the values of these three quantities become lower than those for $N = 0$ (i.e., when there is no buoyancy force from mass diffusion). In addition, as the Schmidt number decreases, the local wall shear stress and the local Nusselt number are seen to increase when $N > 0$ and to decrease when $N < 0$. The reason for this is that a smaller Schmidt number corresponds to a larger binary diffusion coefficient, which in turn exerts a larger influence on the flow field and hence the thermal field. The Sherwood number results indicate, however, that for a fixed N value, larger Sherwood numbers are associated with larger

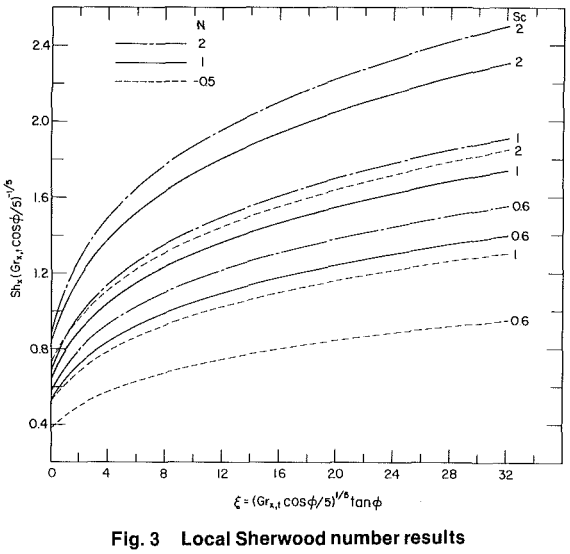

Fig. 3 Local Sherwood number results

Schmidt numbers. That is, the surface mass transfer rate increases with increasing Schmidt number. This is because a larger Schmidt number provides a thinner concentration boundary-layer thickness relative to the flow boundary-layer thickness, thereby resulting in a larger concentration gradient at the wall and hence an enhancement in the surface mass transfer rate. This trend is analogous to the heat transfer process in which the surface heat transfer rate increases as the Prandtl number increases.

To show the variations of the local Nusselt number Nu_x and the local Sherwood number Sh_x with the local thermal Grashof number $Gr_{x,l}$, the angle of inclination, ϕ, and the relative buoyancy force intensity, N, Figs. 4 and 5 have been prepared for a representative case of Sc = 1. It can be seen from the figures that both Nu_x and Sh_x increase with increasing values of $Gr_{x,l}$, ϕ, and N, as has already been discussed. Plotted with dotted lines in the figures for comparisons are the results for $\phi = 15$ and 45 deg from the approximate similarity solutions that were obtained by neglecting the streamwise pressure gradient terms in the momentum equation (2), as was done by Chen and Yuh [3]. As is expected, the approximate solution deviates from the new solution as ϕ decreases, with a considerably larger deviation occurring at a smaller value of $Gr_{x,l}$. This can be gleamed from the condition for which the similarity solution is valid; that is, $(\delta/x)\tan(\pi/2-\phi) << 1$ or $\tan(\pi/2-\phi) << (Gr_{x,l}\cos\phi/5)^{1/5}/\eta_\delta$.

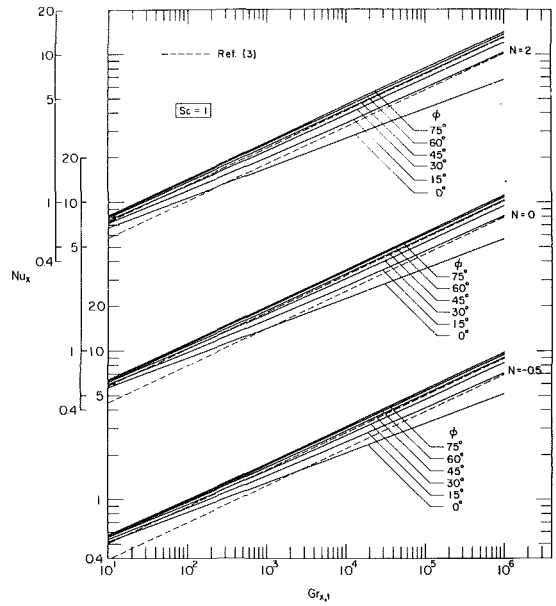

Fig. 4 Local Nusselt number versus local thermal Grashof number for various angles of inclination, Sc = 1

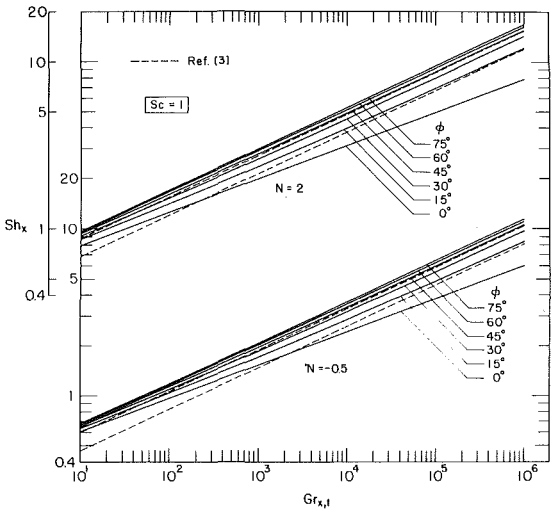

Fig. 5 Local Sherwood number versus local thermal Grashof number for various angles of inclination, Sc = 1

Neutral stability curves and critical wave and Grashof numbers were obtained for various angles of inclination ϕ ranging from 0 deg (i.e., the horizontal plate) to 75 deg. Representative neutral stability curves are plotted in Fig. 6 for Pr = 0.7 and Sc = 1 at ϕ = 0, 30, and 60 deg. It is seen from the figure that for a fixed N value, as the angle ϕ increases from 0 deg, the neutral stability curve shifts right-upward, indicating a stabilization of the main flow to the vortex mode of instability at a larger wave number. On the other hand, at a given angle of inclination ϕ, as N increases from a negative to a positive value, the neutral stability curve shifts left-upward, indicating a destabilization of the flow at a larger wave number. This phenomenon is to be expected from the physical reasoning that a larger N value gives rise to a stronger effect of combined buoyancy forces, which in turn contributes to a less stable flow. It is interesting to note from Fig. 6 that for a fixed angle ϕ the locus of the critical points (i.e., the points of minimum thermal Grashof numbers) on the neutral stability curves for different N values forms a straight line in an α versus $\mathrm{Gr}_{x,l}$ semilogarithmic plot.

In order to examine the effect of Schmidt number on the

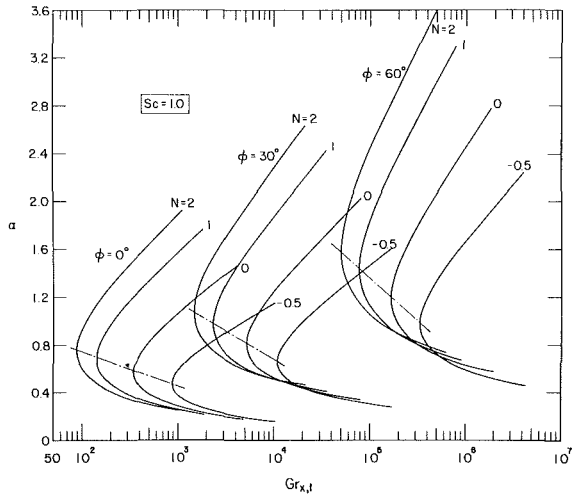

Fig. 6 Representative neutral stability curves for ϕ = 0, 30, and 60 deg, Sc = 1

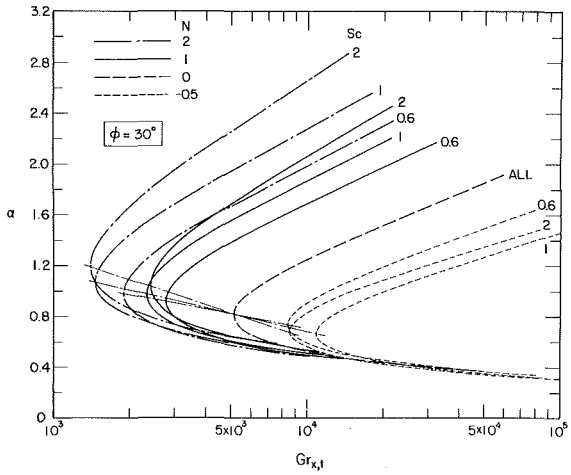

Fig. 7 Neutral stability curves for ϕ = 30 deg and Sc = 0.6, 1, and 2

vortex instability of the flow, neutral stability curves for Pr = 0.7 and Sc = 0.6, 1, and 2 at a fixed angle ϕ = 30 deg, with N = −0.5, 0, 1, and 2, are brought together in Fig. 7. Although the critical points on the neutral stability curves for different N values at a given Schmidt number are seen to lie on a particular straight line, which is different for a different Schmidt number, the relative position of the critical points for different Schmidt numbers appears to shift with a change in the N value. In general, a decrease in the N value contributes to the stabilization of the flow, and a decrease in the Schmidt number from 1 to 0.6 for a fixed N value tends to stabilize the flow when $N > 0$ and to destabilize the flow when $N < 0$. However, such a definite trend does not exist as the Schmidt number is increased from 1 to 2. This type of behavior is due to the combined effects of Sc and N on the stability characteristics of the flow.

The critical thermal Grashof numbers $\mathrm{Gr}^*_{x,l}$ and the critical wave numbers α^* at various angles of inclination ϕ are listed in Table 1. They are for Pr = 0.7 and Sc = 0.6, 1, and 2, with N = −0.5, 0, 1, and 2. The angular variation of these critical thermal Grashof numbers are also plotted in Fig. 8. From the table and the figure, it is seen that an inclined natural convection flow with mass diffusion becomes less susceptible to the vortex mode of instability as the plate is tilted from the horizontal toward the vertical orientation. The flow is the most susceptible to the vortex mode of instability when the plate is horizontal, and this susceptibility diminishes as ϕ

Table 1 Critical thermal Grashof numbers and wave numbers for Pr = 0.7

				Sc = 0.6				
	$N=2$		$N=1$		$N=0$		$N=-0.5$	
ϕ	$Gr^*_{x,t}$	α^*	$Gr^*_{x,t}$	α^*	$Gr^*_{x,t}$	α^*	$Gr^*_{x,t}$	α^*
0°	132	0.702	191	0.652	340	0.583	544	0.516
15°	497	0.834	724	0.775	1.32×10^3	0.682	2.13×10^3	0.620
30°	1.90×10^3	0.981	2.78×10^3	0.908	5.17×10^3	0.805	8.42×10^3	0.730
45°	8.87×10^3	1.163	1.30×10^4	1.084	2.45×10^4	0.965	4.03×10^4	0.870
60°	5.99×10^4	1.435	8.84×10^4	1.335	1.67×10^5	1.184	2.74×10^5	1.070
75°	1.13×10^6	1.942	1.67×10^6	1.800	3.14×10^6	1.610	5.19×10^6	1.450
				Sc = 1.0				
	$N=2$		$N=1$		$N=0$		$N=-0.5$	
ϕ	$Gr^*_{x,t}$	α^*	$Gr^*_{x,t}$	α^*	$Gr^*_{x,t}$	α^*	$Gr^*_{x,t}$	α^*
0°	88	0.757	143	0.685	340	0.583	880	0.473
15°	360	0.905	577	0.820	1.32×10^3	0.682	3.03×10^3	0.563
30°	1.47×10^3	1.071	2.33×10^3	0.972	5.17×10^3	0.805	1.09×10^4	0.662
45°	7.21×10^3	1.280	1.13×10^4	1.158	2.45×10^4	0.965	4.92×10^4	0.791
60°	4.98×10^4	1.578	7.80×10^4	1.430	1.67×10^5	1.184	3.29×10^5	0.975
75°	9.45×10^5	2.135	1.47×10^6	1.923	3.14×10^6	1.610	6.21×10^6	1.320
				Sc = 2.0				
	$N=2$		$N=1$		$N=0$		$N=-0.5$	
ϕ	$Gr^*_{x,t}$	α^*	$Gr^*_{x,t}$	α^*	$Gr^*_{x,t}$	α^*	$Gr^*_{x,t}$	α^*
0°	60	0.829	114	0.733	340	0.583	846	0.475
15°	295	1.000	529	0.885	1.32×10^3	0.682	2.54×10^3	0.572
30°	1.41×10^3	1.190	2.41×10^3	1.035	5.17×10^3	0.805	8.53×10^3	0.680
45°	7.38×10^3	1.431	1.23×10^4	1.240	2.45×10^4	0.965	3.75×10^4	0.818
60°	5.22×10^4	1.775	8.63×10^4	1.520	1.67×10^5	1.184	2.44×10^5	1.005
75°	9.98×10^5	2.362	1.64×10^6	2.068	3.14×10^6	1.610	4.58×10^6	1.362

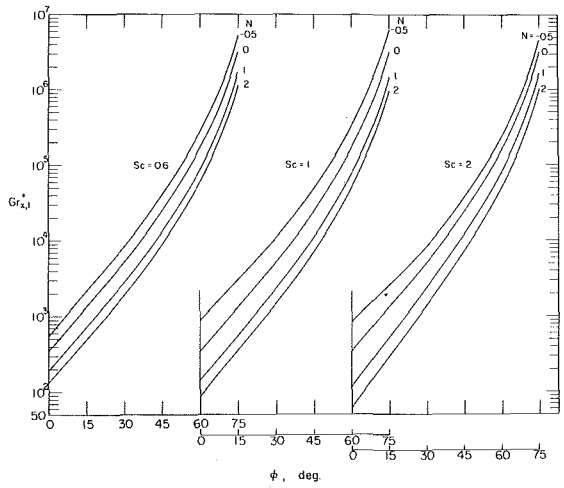

Fig. 8 Critical thermal Grashof number versus angle of inclination, Sc = 0.6, 1, and 2

increases, atttaining a maximum critical thermal Grashof number of infinity when the plate is vertical. This is because when the plate is vertical, there is no buoyancy force component that acts normal to the plate and, as a result, vortex mode of instability does not take place. The instability of the flow is seen to be affected strongly by the buoyancy force from mass diffusion. The flow becomes less or more stable to the vortex mode of instability, depending on whether the buoyancy force from mass diffusion assists or opposes the thermal buoyancy force (that is, depending on whether $N > 0$ or $N < 0$).

It is interesting to compare the present vortex instability results with the horizontal wave instability results of Pera and Gebhart [8] for the case of a horizontal plate and of Boura and Gebhart [11] for the case of a vertical plate. For the horizontal plate [8], the critical values of $5[(1+N)Gr^*_{x,t}/5]^{1/5}$ for Pr = Sc = 0.7 were found to be about 49, 53, 64, and 77 when N = 2, 1, 0, and −0.5. These values correspond to critical thermal Grashof numbers, $Gr^*_{x,t}$, of about 1.51×10^5, 3.35×10^5, 1.72×10^6, and 8.66×10^6, respectively. For a vertical plate [11], the critical values of $4(Gr^*_{x,t}/4)^{1/4}$ for Pr = 0.7 and Sc = 0.94 are about 60, 66, and 73 when N = 0.5, 0, and −0.2. The corresponding critical thermal Grashof numbers are, respectively, 2.03×10^5, 2.96×10^5, and 4.44×10^5. A comparison between the present vortex instability results for the inclined plate with the wave instability results for the horizontal and vertical plates indicates that the first onset of the instability of the flow is due to the vortex mode of disturbances when the plate is horizontal, whereas in a vertical plate it is due to the wave mode of disturbances. Thus, a crossover from the vortex to the wave mode of instability is expected to occur as the plate is tilted from the horizontal toward the vertical position. However, an accurate assessment of the inclination angles at which the crossover takes place cannot be made at present because there is a lack of wave instability results for inclined free convection flows with combined buoyancy mode of thermal and mass diffusion. As a final note, it is mentioned that there appears to be no experimental instability data available for comparison with the present analytical results except for the case of N = 0 (i.e., without mass diffusion effect). Such a comparison for the case of N = 0 has already been made in [12] and is therefore not repeated here.

Conclusions

A study has been conducted to analyze the flow and heat/mass transfer as well as the vortex instability characteristics of buoyancy-induced flows that result from simultaneous diffusion of heat and mass in laminar boundary layers adjacent to horizontal and inclined surfaces. The analysis is restricted to situations in which low concentration levels exist such that the diffusion-thermo/thermo-diffusion effects and the interfacial velocities due to mass diffusion are neglected. In general, it has been found that when the buoyancy force from mass diffusion assists the thermal buoyancy force, the heat/mass transfer rates increase and the flow becomes less stable to the vortex mode of instability. These trends are reversed when the two buoyancy forces oppose each other. As the angle of inclination from the

horizontal is increased, the buoyancy force effects become more pronounced. This gives rise to an increase in the surface heat/mass transfer rates, but to a stabilization of the main flow to the vortex mode of disturbances.

Acknowledgments

The present study was supported by a grant (NSF ENG 75-15033 A01) from the National Science Foundation.

References

1 Gebhart, B., and Pera, L., "The Nature of Vertical Natural Convection Flows Resulting From the Combined Buoyancy Effects of Thermal and Mass Diffusion," *International Journal of Heat and Mass Transfer*, Vol. 14, 1971, pp. 2025-2050.

2 Pera, L., and Gebhart, B., "Natural Convection Flows Adjacent to Horizontal Surfaces Resulting from the Combined Buoyancy Effects of Thermal and Mass Diffusion," *International Journal of Heat and Mass Transfer*, Vol. 15, 1972, pp. 269-278.

3 Chen, T. S., and Yuh, C. F., "Combined Heat and Mass Transfer in Natural Convection on Inclined Surfaces," *Numerical Heat Transfer*, Vol. 2, 1979, pp. 233-250.

4 Kahawita, R. A., and Meroney, R. N., "The Vortex Mode of Instability in Natural Convection Flow Along Inclined Plates," *International Journal of Heat and Mass Transfer*, Vol. 17, 1974, pp. 541-548.

5 Haaland, S. E., and Sparrow, E. M., "Vortex Instability of Natural Convection Flow on Inclined Surfaces," *International Journal of Heat and Mass Transfer*, Vol. 16, 1973, pp. 2355-2367.

6 Iyer, P. A., and Kelly, R. E., "The Stability of the Laminar Free Convection Flow Induced by a Heated Inclined Plate," *International Journal of Heat and Mass Transfer*, Vol. 17, 1974, pp. 517-525.

7 Nachtsheim, P. R., "Stability of Free-Convection Boundary-Layer Flows," *NASA*, TN D-2089, 1963.

8 Pera, L., and Gebhart, B., "On the Stability of Natural Convection Boundary Layer Flow over Horizontal and Slightly Inclined Surfaces," *International Journal of Heat and Mass Transfer*, Vol. 16, 1973, pp. 1147-1163.

9 Hwang, G. J. and Cheng, K. C., "Thermal Instability of Laminar Natural Convection Flow on Inclined Isothermal Plates," *Canadian Journal of Chemical Engineering*, Vol. 51, 1973, pp. 659-666.

10 Haaland, S. E., and Sparrow, E. M., "Wave Instability of Natural Convection on Inclined Surfaces Accounting for Nonparallelism of the Basic Flow," ASME *Journal of Heat Transfer*, Vol. 96, 1973, pp. 405-407.

11 Boura, A. R., and Gebhart, B., "The Stability of a Vertical Flow which Arises from Combined Buoyancy Modes," *AIChE Journal*, Vol. 22, 1976, pp. 94-102.

12 Chen, T. S., and Tzuoo, K. L., "Vortex Instability of Free Convection Flow Over Horizontal and Inclined Surfaces," ASME *Journal of Heat Transfer*, Vol. 104, 1982, pp. 637-643.

13 Gebhart, B., "Buoyancy Induced Fluid Motions Characteristics of Applications in Technology—The 1978 Freeman Scholar Lecture," ASME *Journal of Fluid Engineering*, Vol. 101, 1979, pp. 5-28.

14 Lloyd, J. R., and Sparrow, E. M., "On the Instability of Natural Convection Flow on Inclined Plates," *Journal of Fluid Mechanics*, Vol. 42, 1970, pp. 465-470.

15 Shaukatullah, H., and Gebhart, B., "An Experimental Investigation of Natural Convection Flow on an Inclined Surface," *International Journal of Heat and Mass Transfer*, Vol. 21, 1978, pp. 1481-1490.

16 Lock, G. S. H., Gort, C., and Pond, G. R., "A Study of Instability in Free Convection from an Inclined Plate," *Applied Scientific Research*, Vol. 18, 1967, pp. 171-182.

17 Wu, R. S., and Cheng, K. C., "Thermal Instability of Blasius Flow Along Horizontal Plates," *International Journal of Heat and Mass Transfer*, Vol. 19, 1976, pp. 907-913.

18 Cebeci, T., and Bradshaw, P., *Momentum Transfer in Boundary Layers*, ch. 7, Hemisphere Publishing Corp., Washington, D.C., 1977.

19 Moutsoglou, A., Chen, T. S., and Cheng, K. C., "Vortex Instability of Mixed Convection Flow over a Horizontal Flat Plate," ASME *Journal of Heat Transfer*, Vol. 103, 1981, pp. 257-261.

H. Ozoe
Associate Professor.

M. Ohmuro
Graduate Student.

A. Mouri
Undergraduate Student.

S. Mishima
Undergraduate Student.

H. Sayama
Professor.

Department of Industrial and Mechanical Engineering, Okayama University, Okayama, Japan

S. W. Churchill
The Carl V.S. Patterson Professor, Department of Chemical Engineering, University of Pennsylvania, Philadelphia, Pa., 19104

Laser-Doppler Measurements of the Velocity Along a Heated Vertical Wall of a Rectangular Enclosure

The horizontal and vertical velocity profiles near a heated vertical wall of rectangular enclosure were measured for the laminar regime of natural convection with a laser-Doppler anemometer. The horizontal temperature profiles near the heated wall were measured with a thermocouple. An almost perfect two-dimensional mode of flow was confirmed for the central regime of the box. A minimum in the temperature profile between the hot wall and the thermally stratified central core resulted in a downward flow just outside the boundary layer of upward flow, but the central core was stagnant. Visualization of the flow with a phenolphtalein tracer confirmed the two-dimensionality of the flow along the vertical heated wall and revealed a zone of three-dimensional flow in the form of spiral streaklines along the insulated top plate toward the opposing cooled vertical wall. Measurements such as these provide for the first time the basis for a critical test of the accuracy of numerical solutions.

Introduction

The extensive literature on natural convection in rectangular enclosures, heated on one vertical wall and cooled on the opposing one, has been reviewed by Ostrach [1] and more recently by Catton [2]. Hence, only those investigations directly relating to the measurements of the temperature and/or velocity field will be mentioned herein.

Schmidt and Beckmann [3] measured the temperature field using a small thermocouple, and the velocity field using the deflection of a quartz thread, for laminar natural convection near an electrically heated vertical plate. The first velocity measurements of free convection using tracer particles were apparently made by Cheesewright [4] for the turbulent regime. He also measured the temperature field. Recently a number of measurements of the velocity profile and the turbulent intensity by a laser-Doppler anemometer have been reported. Such measurements by Steinberner and Reineke [5] are in fair agreement with the theoretical work of Ostrach [6] for the laminar regime. In the near future such measurements may be expected to provide a test for two-dimensional, finite difference solutions of Plumb and Kennedy [7], Lin and Churchill [3], and Steinberner and Reineke, and others for the turbulent regime.

There have been many measurements of the average heat flux for natural convection inside an enclosure but only a few, e.g., by Martini and Churchill [9], of both the temperature and velocity fields. Schinkel and Hoogendoorn [10] measured the temperature field only, using an interferogram. Apparently this method gives an integrated density in the direction of the beam and hence is appropriate only for two-dimensional flow. Oertel and Kirchartz [11] measured the density variation interferometrically as well as the velocity for a horizontal fluid layer but at the central plane only. A number of investigators, including the present ones, have carried out numerical solutions for two- and three-dimensional laminar natural convection, primarily for rectangular and cylindrical enclosures, but experimental data to

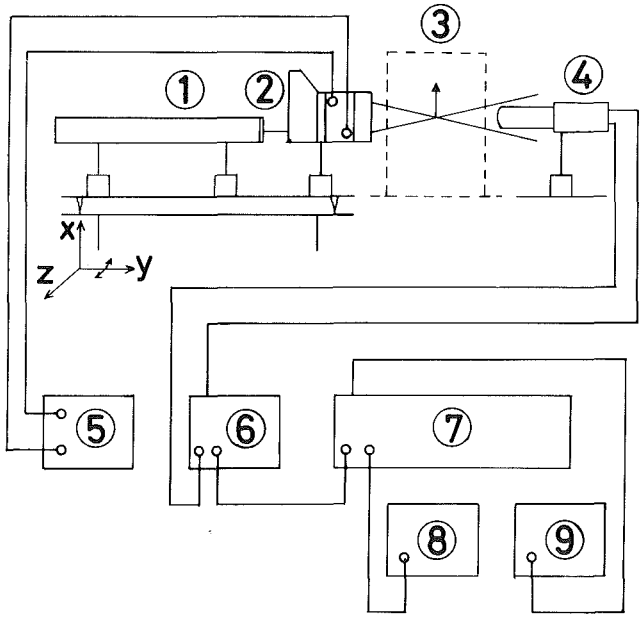

Fig. 1 Schematic of the laser-Doppler anemometer:
1 laser emitter
2 optical unit
3 measuring point
4 photomultiplier
5 flow direction adapter
6 high voltage supply
7 signal processor
8 Doppler signal monitor
9 frequency counter

Contributed by the Heat Transfer Division for publication in the JOURNAL OF HEAT TRANSFER. Manuscript received by the Heat Transfer Division July 27, 1981.

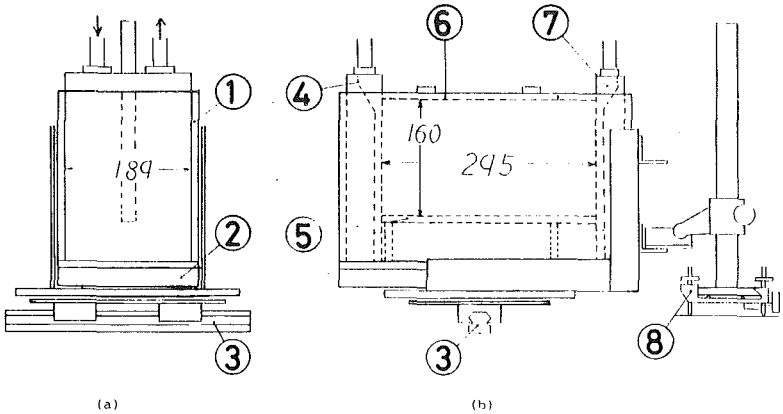

Fig. 2 Schematic of the experimental apparatus
(a) end view (b) side view
1 side wall of convection cell
2 bottom insulation
3 precision, sliding guide rail
4 hot-water jacket
5 bottom plate of convection cell
6 top plate of convection cell
7 cold-water jacket
8 traveling microscope

test the predicted temperature and velocity fields critically are not yet available.

In this paper, results are reported for two-dimensional flow fields using both a laser-Doppler anemometer and visualization with phenolphtalein, and for the corresponding temperature fields using a thermocouple.

1 The Laser-Doppler Anemometer

The anemometer used is a DISA-Mark I with a flow-direction adapter. Figure 1 shows the accessories of the anemometric system for measurements in the convection cell.

This device and setup were first tested by comparing measured velocities with pitot-tube measurements of a steady water jet. The cross-point of the laser beams was 1 mm above the exit from the pitot tube. The average differences between the velocities obtained from the laser-Doppler anemometer and those from the pitot tube were -1.20, $+0.50$, and 0.37 percent for velocities of 0.21, 0.50, and 0.857 m/s, respectively. The anemometer was therefore concluded to perform satisfactorily.

2 Experimental Apparatus for Natural Convection

Figure 2 consists of end and side views of the experimental apparatus. The circulating jacket (1) at one end is shown in Fig. 2(*a*), and both jackets, (4) and (7), are shown on the left-hand and right-hand sides of the cell in Fig. 2(*b*). Hot water was circulated through the left-hand jacket and cold water through the right. 79 × 240 × 5-mm channels were built into both jackets to produce a downward then upward flow of water at a velocity of 24.5 cm/s, thus producing an estimated heat transfer coefficient of 1260 W/m^2. The vertical wall of the jackets adjacent to the convection cell was made of 5-mm-thick copper to minimize the temperature variation.

The bottom plate (5) was elevated as shown, in the further interest of isothermality on the heated and cooled walls of the cell. The bottom and top plates, (5) and (6), of 10-mm-thick plexiglass were thermally isolated from the heating and cooling plates with water-proof tape. The resulting inner dimensions of the convection cell were 160-mm high (in the x-direction), by 295-mm wide (in the y-direction) by 189-mm deep (in the z-direction). The internal dimensions of the heated and cooled surfaces were thus 160 × 189 mm. The two vertical walls perpendicular to the jackets were of 10 mm plexiglass, covered by a further 2-mm thick layer of plexiglass. A Styrofoam plate 50-mm-thick (2) was placed beneath the cell for thermal insulation.

The entire apparatus was placed on a precision sliding guide rail (3) and joined to the mounting of a traveling microscope (8) so that movement in the z-direction could be measured precisely. The optical unit of the laser-Doppler anemometer was placed on a three-dimensional mounting (from a grinding machine), permitting lateral and vertical movement with an accuracy of 0.02 mm.

The temperature fields were measured with a thermocouple

Nomenclature

f_D = Doppler frequency [1/s]
f_{vco} = output frequency from a voltage-controlled local oscillator in a mixer stage of a frequency tracker [1/s]
g = acceleration due to gravity [m/s^2]
H = height of experimental box [m]
Ra_H = Rayleigh number $= g\beta(T_w - T_c)H^3/\alpha\nu$ [−]
t = time [s]
T = temperature [K]
T_c = cold wall temperature [K]
T_w = hot wall temperature [K]
u = vertical velocity [m/s]
v = horizontal velocity away from heated wall [m/s]
x = vertical distance above bottom plate [m]
y = horizontal distance from heated wall [m]
z = horizontal coordinate parallel to heated wall [m]
α = thermal diffusivity of fluid [m^2/s]
β = volumetric coefficient of expansion [1/K]
ν = kinematic viscosity [m^2/s]
θ = central angle between two laser beams at a measuring point [rad]
Φ = oblique angle of laser beam from the heated wall [rad]
λ = wavelength of laser light [m]

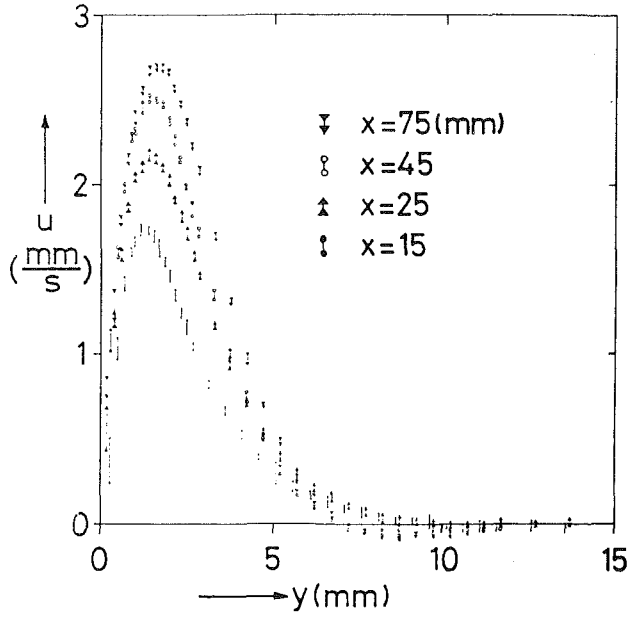

Fig. 3 Profiles of the vertical component of the velocity at elevations below the midplane

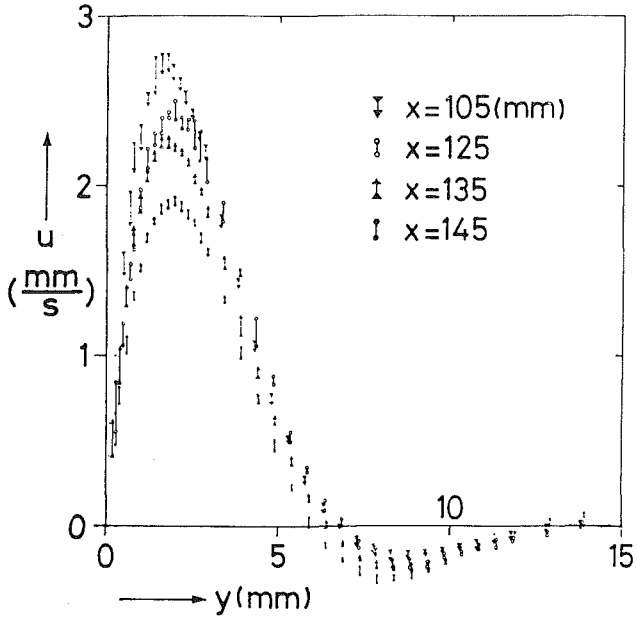

Fig. 4 Profiles of the vertical component of the velocity at elevations above the midplane

of 0.1-mm copper and constantan. The junction was supported by two thin bamboo pieces. It could be traversed in two directions with 0.01 mm accuracy. The thermocouple output was read from the digital voltmeter and was accurate within ±0.01 K.

Owing to the presumed and observed antisymmetry of the velocity and temperature fields, the measurements were confined to the heated half of the enclosure.

3 Experimental Conditions

The test water was boiled prior to use to prevent the formation of air bubbles within the enclosure. The circulating water for the heated plate came from a bath at 288.2 K and for the cooled plate from a bath at 281.0 K.

The laser-Doppler signal from the photomultiplier was fed to a signal processor and the f_{vco} signal was measured with a frequency counter. The digital value of the frequency, f_D, is translated to velocity, u, by the equation

$$u = \frac{\lambda f_D}{2 \sin \frac{\theta}{2}} = \frac{6.328 \times 10^{-7}}{2 \times 0.2035} f_D = 1.555 \times 10^{-6} f_D (\text{m/s})$$

Here λ is the characteristic wavelength of the He-Ne laser beam, and θ is the central angle of the two beams at the point of measurement. A small amount of milk ($<10^{-4}$ml/ml) was mixed with the water in the test cell to seed the laser measurement.

The wavelength λ of the He-Ne laser beam was 632.8 mm with an uncertainty of ±0.03 percent. The central angle θ was determined from a measured distance of 111 ± 0.5 cm between the two laser beams on a screen located 267 ± 0.5 cm from the cross-point of the beams, with a resulting error of ±0.65 percent in sin (θ/2). According to the manufacturer's manual [12] the error in the Doppler frequency was ±0.25 percent. The measured velocity is thus presumed to have a possible total error of ±0.93 percent.

The velocity and temperature measurements were made at eight different heights from the bottom plate, such as at $x=15$, 25, 45, 75, 105, 125, 135, and 145 mm. The horizontal and vertical velocities were measured separately. The measurements were made only after a stationary state, as indicated by the thermocouple output, had been attained.

The temperature distribution on the heated wall was concurrently measured as 14.67°C, 14.82°C, and 15.02°C at $x=10$, 80 and 150 mm, yielding an integrated mean temperature of 14.84°C for the hot plate. The corresponding mean temperature of the cold plate was 7.8°C, giving a mean temperature difference of 7.04°C. Physical properties were computed at 11.32°C, the arithmetic mean of the plate temperatures. This resulted in an overall Rayleigh number, $Ra_H = 1.52 \times 10^8$ and Pr = 9.08. The error in the velocity due to the nonisothermality of the heated and cooled plates is discussed and bounded in the Appendix.

4 Results

4.1 Vertical Velocity. The frequency counter gives a perturbed digital output for each measurement. The upper and lower values are recorded and plotted to suggest the range of uncertainty of the data. The vertical velocity, u, is plotted versus the corrected distance from the heated wall, y, in Fig. 3 for four lower heights, and in Fig. 4 for four upper heights. (The location of the point of measurement, the cross-point of the laser beams, was corrected for deflection of the laser beams due to the gradient in the index of refraction [see Appendix].) The velocities are plotted only out to $y=15$ mm, although the measurements generally extended to 20 mm. The peak velocity occurred at $y=1.2$ mm for an elevation $x=15$ mm and at $y=2.0$ mm for $x=145$ mm. This movement of the y-location of the peak with x was monotonic. A maximum vertical velocity 2.77 (mm/s) occurred at $x=105$ mm and $y=1.6\sim1.8$ mm. The profiles in Fig. 3 are similar to those for boundary layer, but those in Fig. 4 exhibit a region of downward flow. This reverse flow, which has been noted by Elder [13] and others, is characteristic of natural convection in enclosures as compared to free convection along an isolated, vertical heated plate. A monotonic increase in the velocity gradient with height is observed in Fig. 3 for $x \leq 75$ mm, and a monotonic decrease in the velocity gradient with height in Fig. 4 for $x \geq 105$ mm, but with some irregularity, and with a slight upward flow for $x=145$ mm and $y \cong 15$ mm.

At $x=75$ mm, the y-profiles of the vertical velocity were measured at a number of locations along side wall, i.e., at $z=72.51$, 75.19, 77.88, 80.56, and 83.25 mm. The profiles of the vertical velocity at these locations almost coincided, as shown in Fig. 5, thus confirming the two-dimensionality of

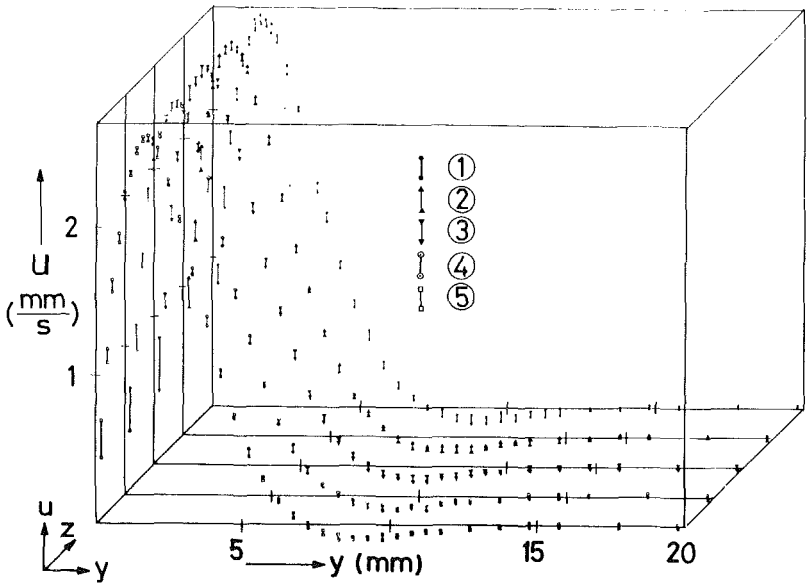

Fig. 5 Profiles of the vertical component of the velocity at an elevation of $x = 75$ mm.

Depths					
No.	1	2	3	4	5
z(mm) =	72.51	75.19	77.88	80.56	83.25

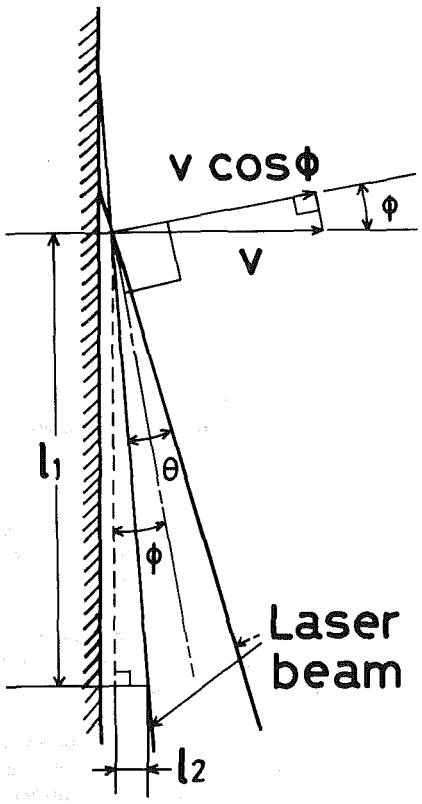

Fig. 6 Top view of the orientation of the laser beams used to measure the horizontal component of the velocity:

$$\phi + \frac{\theta}{2} = 0.459 \text{ rad} \quad \phi - \frac{\theta}{2} = 0.050 \text{ rad}$$

the vertical velocity near the central plane ($z = 94.5$ mm) of the enclosure.

4.2 Horizontal Velocity. A schematic of the laser beams used to measure the component of the velocity perpendicular to the wall is shown in Fig. 6. The centerline of the two beams was oblique to the heated wall at an angle $\phi = 0.2548$ rad (14.6 deg) so that the velocity could be measured right up to the wall. The measured velocity is then divided by $\cos\phi = 0.9677$ to obtain the horizontal component. These velocities are plotted in Fig. 7 versus distance from the wall for several elevations. (Positive values indicate flow away from the wall.)

Near the bottom of the enclosure the horizontal velocity is negative (towards the heated wall). At an elevation of $x = 75$ mm, it becomes essentially zero for all y. Thus, as further confirmed by the vertical component in Fig. 3, a stagnant core exists at this elevation. For $x \geq 105$ mm the main flow is away from the wall. Along the lower half of the heated wall, $\partial u/\partial x > 0$ with $\partial v/\partial y < 0$ and along the upper half $\partial u/\partial x < 0$ with $\partial v/\partial y > 0$, thus satisfying two-dimensional continuity, at least qualitatively. The horizontal distribution of the horizontal velocity toward the hot plate at an elevation $x = 75$ mm and several depths, $z = 56.95$, 58.34, 59.72, 61.11, 62.49, and 91.59 mm is shown in Fig. 8. Over this range of z, the horizontal velocity is essentially zero for all y.

The horizontal velocities away from the wall along the top horizontal cover plate are plotted in Fig. 9 versus the distance from the top wall at $y = 5$ mm, 20 mm, and 40 mm. The profile of the horizontal velocity with height is almost the same at these distances, although the boundary layer thickness and the maximum velocity appear to increase slightly with y. The maximum velocity is about 0.5 mm/s and the boundary layer thickness is about 30–50 mm. Integration of the values in Fig. 9 and of the vertical velocities for large x in Fig. 4 gives comparable volumetric flow rates, as would be expected.

4.3 Temperature Distribution. The surface temperature on the heated plate was determined from thermocouples attached to the plate. The temperature distribution within the fluid was determined with a traveling thermocouple. The location of the measuring point within the fluid was somewhat uncertain, owing to the 0.5 mm thickness of the thermocouple junction. Therefore, the measured profiles were plotted versus the tentative distance from the wall and extrapolated to the wall. A correction of 0.2 mm was deter-

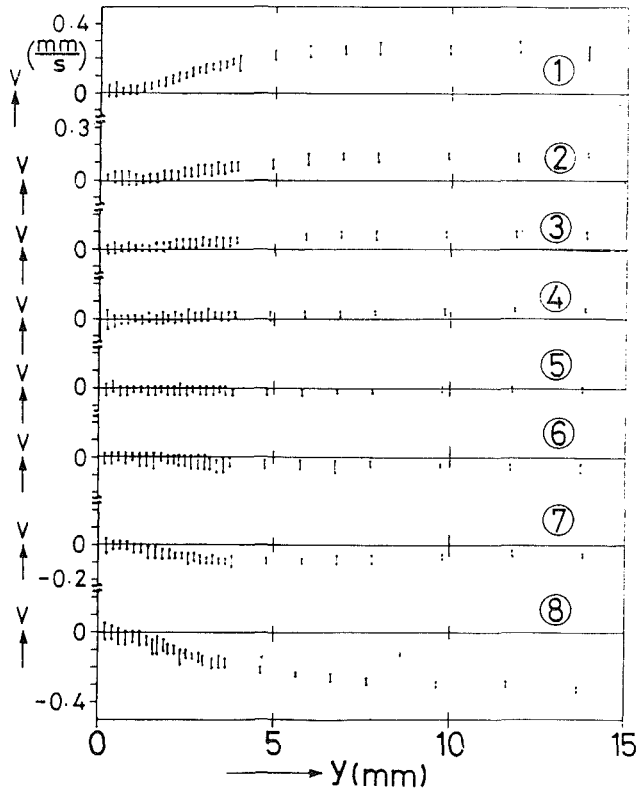

Fig. 7 Profiles of the horizontal component of the velocity at various elevations

Elevations

No.	x (mm)	No.	x (mm)
1	145	5	75
2	135	6	45
3	125	7	25
4	105	8	15

mined by comparison with the corresponding measured surface temperature. The corrected profiles are shown in Fig. 10 for the same elevations as the velocity profiles in Figs. 3, 4, and 7. The temperature of the heated surface varied slightly, resulting in different terminal points for these profiles. Thermal stratification is apparent for $y > 10$ mm. The minimum in the temperature profiles occurs between the heated wall and the stagnant central region. This minimum is due to heating of the rising current of cold water near the wall and is responsible for the downward flow observed in Fig. 4.

4.4 Flow Visualization. A number of flow visualization studies have previously been carried out for free convection along a vertical hot plate in a large volume of fluid and inside a rectangular box. Most of the studies were for the same physical case as studied herein but with the observations confined to a single two-dimensional plane. In this study, the phenolphtalein illumination method was adopted. The heated vertical copper plate was connected to a negative electrode and the cold plate to a positive electrode. Phenolphtalein indicator was mixed into an aqueous solution of sodium hydroxide which was then converted to a weak acid by the addition of a dilute hydrogen chloride solution. 100 ml of this indicator solution was mixed into the test water and a direct current of 10 V was impressed. The red color of phenolphtalein appeared along the heated plate. The color was so thin and uniform on the heating copper plate that it could not be photographed. After flowing up along the copper plate the flow turned and proceeded horizontally along the top cover plate. For $0 < y < 20$ mm, the whole top area was red, but for greater distances the streaks, as shown here in

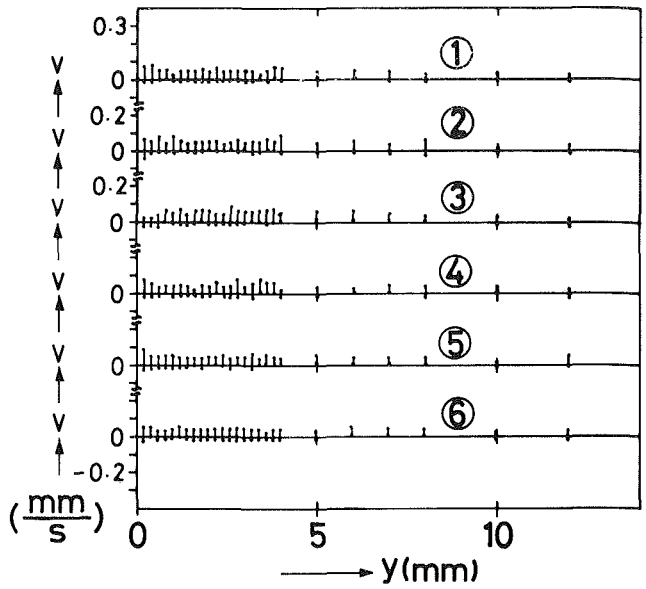

Fig. 8 Profiles of the horizontal component of the velocity at an elevation $x = 75$ mm:

Depth

No.	1	2	3	4	5	6
z (mm)	56.95	58.34	59.72	61.11	62.49	91.59

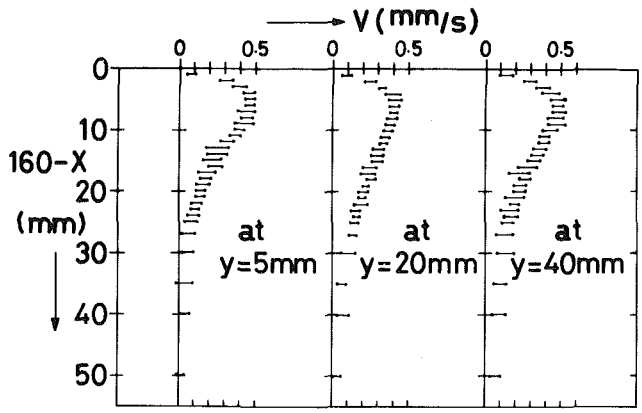

Fig. 9 Profiles of the horizontal component of the velocity at several distances from the wall

black and white in Fig. 11, were observed indicating a series of roll cells. The total number of roll cells was 17 to 22 over the total width of 189 mm in the z-direction.

The dyed layer increases slightly in thickness with distance in the direction of flow. Two possible explanations are offered for this vortical behavior: (*i*) the centrifugal force produced by the transition from vertical to horizontal flow generates Görtler-type vortices; or (*ii*) the temperature difference between the heated fluid layer and the plexiglass cover plate, generates Bénard-type vortices. According to Pellow and Southwell [14], the critical Rayleigh number for a fluid layer with one free and one rigid horizontal boundary is 1100. The visible thickness of the dyed layer was about 30 mm. The corresponding critical temperature difference would then be only 0.0028 K.

This vortical, three-dimensional behavior has apparently not been reported before for rectangular enclosures heated and cooled on opposite sides.

4.5 Comparison of Measured Velocity Profile With That of Boundary Layer Theory. Comparison of the experimental measured values of the x-component of the velocity with the

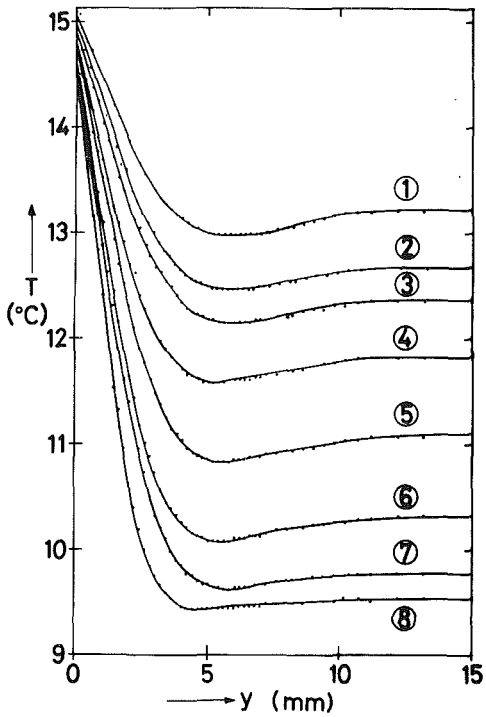

Fig. 10 Measured temperature profiles at different heights (same elevations and code as in Fig. 7)

predictions of laminar boundary layer for a vertical isothermal plate (for $Pr = 9.08$) reveals excellent agreement near the wall at all intermediate elevations. However, in the outer region the experimental measurements fall increasing below this solution for increasing elevations. These deviations are presumed to be due to the downward flow in the enclosure outside the boundary layer.

5 Conclusions

Laser-Doppler measurements of the velocity components and thermocouple measurements of the temperature have been utilized to characterize the nearly two-dimensional laminar natural convection along the vertical heated wall of an enclosure. Such measurements provide the basis for a more critical test of numerical solutions than either heat flux measurements at the wall or photographs of streaklines.

The measured velocities were found to be in numerical agreement with the theoretical solution for an isolated vertical plate very near the heated vertical wall and at low elevations, but not elsewhere. The agreement, even in a limited region is a confirmation of the accuracy and generality of the measurements. The difference elsewhere between the enclosed and unconfined flows is in part due to the top and bottom plates but also to the small downward flow observed at the edge of the boundary layer.

The temperature profiles reveal a minimum between the heated wall and the thermally stratified core. This minimum is responsible for the aforementioned downflow.

Phenolphtalein flow visualization confirmed the two-dimensionality of the motion inside the boundary layer along the heated vertical wall but indicated that the horizontal flow across the top plate consisted of longitudinal roll cells. This motion may be due to the centrifugal force generated by the change in direction, or Bénard-like convection superimposed on the horizontal flow.

The measured and observed flow field can be summarized as follows. The fluid rises rapidly along the hot wall in a boundary-layerlike flow with a thickness of about 10 mm. A maximum velocity of about 2.7 mm/s is attained at

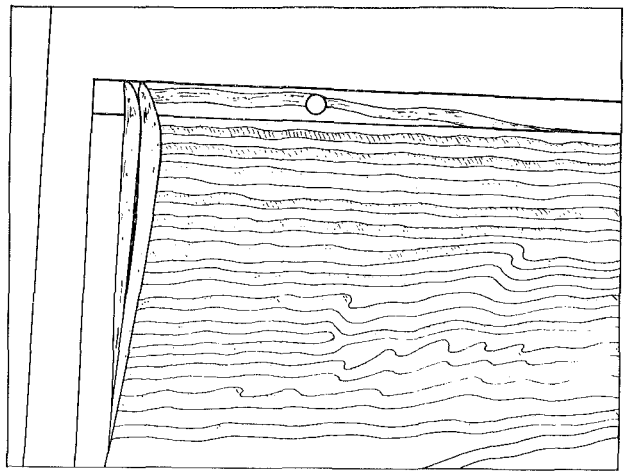

Fig. 11 Sketch of colored photographs of streaklines of phenolphtalein along the top cover plate

midheight. Thereafter the maximum decreases slowly, and a small region of downflow with a maximum velocity of only 0.3 mm/s occurs at a distance of about 8 mm from the hot wall, owing to the temperature difference between the cold upflow and the warmer stagnant core. Except near the top and bottom plates, the velocity normal to the wall is negligible. The velocity profile in the boundary layer agrees closely with that of an unconfined laminar boundary layer on a vertical plate near the wall at low elevations, but falls increasingly below at greater distances from the wall and at increasing elevations.

When the boundary layer flows upward along the hot wall and approaches the top plate, it turns toward the cold wall, creating a horizontal flow in the form of vortices with a thickness slowly increasing from 30 to 50 mm. The maximum horizontal velocity is about 0.5 mm/s.

The same boundary layer and vortex flows occur down the cold wall and along the bottom plate, respectively. The central core is essentially stagnant, as first observed by Martini and Churchill [9] for the fluid confined by a horizontal cylinder and heated and cooled on the vertical halves, and recently explained theoretically by Ostrach and Hantman [15].

The numerical values reported herein are only valid for the particular Rayleigh number (1.5×10^8), Prandtl number (9.1) and width-to-height ratio (1.85) of this work. However, similar behavior would be expected for related conditions. Also the same experimental technique is applicable for other conditions, at least for water.

Acknowledgment

We are sincerely grateful for the advice provided by Profs. Tetsu Fujii and Motoo Fujii of Kyushu University on the measurements and error corrections.

References

1 Ostrach, S., "Natural Convection in Enclosures," *Advances in Heat Transfer*, Vol. 8, Academic Press, New York, 1972, pp. 161-227.

2 Catton, I., "Natural Convection in Enclosures," *Proc. 6th Int. Heat Transf. Conf.*, Toronto, Vol. 6, Hemisphere, Washington, D.C., 1978, pp. 13-31.

3 Schmidt, E., and Beckmann, W., "Das Temperature- und Geschwindigkeitsfeld von einer wärmeabgebenden senkrechten Platte bei naturlicher Konvection," *Techn. Mech. and Thermodyn.*, Vol. 1, No. 10, 1930, pp. 341-349; and No. 11, 1930, pp. 391-406.

4 Cheesewright, R., "Turbulent Natural Convection from a Vertical Plane Surface," ASME JOURNAL OF HEAT TRANSFER, Vol. 90, 1968, pp. 1-8.

5 Steinberner, U., and Reineke, H. -H., "Turbulent Buoyancy Convection Heat Transfer with Internal Sources," *Proc. 6th Int. Heat Transf. Conf.*, Toronto, Vol. 2, Hemisphere, Washington, D.C., 1978, pp. 305-310.

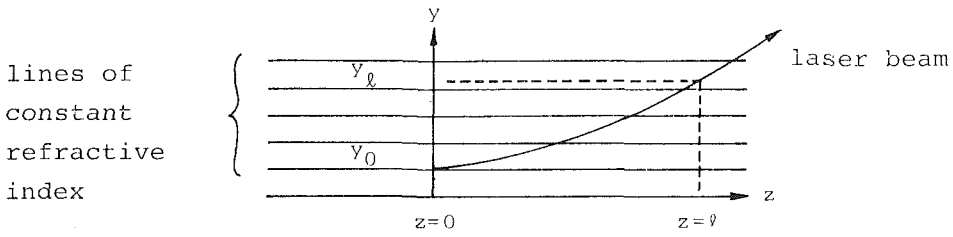

Fig. 12

6 Ostrach, S., "An Analysis of Laminar Free Convection Flow and Heat Transfer about a Flat Plate Parallel to the Direction of the Generating Force," NACA TN 2635, Washington, D.C., 1952.

7 Plumb, O. A., and C. A. Kennedy, "Application of a κ-ϵ Turbulence Model to Natural Convection from a Vertical Isothermal Surface," ASME JOURNAL OF HEAT TRANSFER, Vol. 99, 1977, pp. 79–85.

8 Lin, S. J., and Churchill, S. W., "Turbulent Free Convection from a Vertical Isothermal Plate," *Numerical Heat Transfer*, Vol. 1, 1978, pp. 129–145.

9 Martini, W. R., and Churchill, S. W., "Natural Convection Inside a Horizontal Cylinder," *AIChE Journal*, Vol. 6, 1960, pp. 251–257.

10 Schinkel, W. M. M., and Hoogendoorn, C. J., "An Interferometric Study of the Local Heat Transfer by Natural Convection in Inclined Airfilled Enclosures," *Proc. 6th Int. Heat Transf. Conf.*, Toronto, Vol. 2, Hemisphere, Washington, D.C., 1978, pp. 287–292.

11 Oertel, H., Jr., and Kirchartz, K. R., "Laser-Anemointerferometer for Simultaneous Measurements of Velocity and Density," *Appl. Optics*, Vol. 17, 1978, pp. 3535–3538.

12 DISA Instrument Manual for Mark-I LDV Anemometer.

13 Elder, J. W., "Laminar Convection in a Vertical Slot," *J. Fluid Mech.*, Vol. 23, 1965, pp. 77–98.

14 Pellow, A., and Southwell, R. V., "On Maintained Convective Motion in a Fluid Heated from Below," *Proc. Roy. Soc.*, London, Ser. A., Vol. 176, 1940, pp. 312–343.

15 Ostrach, S., and Hantman, R. G., "Natural Convection Inside a Horizontal Cylinder," *Chem. Eng. Commun.* Vol. 9, 1981, pp. 213–243.

16 Chao, P., Ozoe, H., and Churchill, S. W., "The Effect of a Non-Uniform Surface Temperature on Laminar Natural Convection in a Rectangular Enclosure," *Chem. Eng. Commun.* Vol. 9, 1981, pp. 245–254.

17 Hauf, W., and Grigull, U., "Optical Methods in Heat Transfer," *Advances in Heat Transfer*, Vol. 6, Academic Press, New York, 1970.

APPENDIX

The Effect of Nonuniformity in the Wall Temperature

The effect of experimental observed nonuniformity in the wall temperature on the flow can be bounded by using the theoretical solution for a laminar boundary layer on an unconfined vertical wall. If the entire wall were at the minimum hot-wall temperature of 14.4°C at $x=15$ mm instead of at the average value of 14.84°C, the fractional change in the velocities would be

$$\frac{\Delta u}{u}=1-\left(\frac{14.4-11.32}{14.84-11.32}\right)^{1/2}=0.0645$$

Similarly, for the maximum hot-wall temperature of 15.05°C at $x=145$ mm

$$\frac{\Delta u}{u}=1-\left(\frac{15.05-11.32}{14.84-11.32}\right)^{1/2}=-0.0294$$

The error due to the local variations about the mean would obviously be far less.

The effect of small nonuniformities in the surface temperature in an enclosure does not appear to have been studied experimentally or theoretically. Chao et al. [16] computed the effect of sawtooth variations in the surface temperature, with an amplitude of ± 20 percent of the mean temperature difference, for convection in an inclined 2 × 1 × 1 enclosure. Significant differences in the circulation pattern and overall rate of heat transfer were observed for heating from below but not for heating and cooling at the sides as in this work.

Effects of the Temperature Gradient on the Velocity Measurements

According to Hauf and Grigull [17], the deflection of a light beam in a one-dimensional refractive-index field $n(y)$ is

$$y_l-y_0=\frac{l^2}{2n_0}\frac{dn}{dy} \tag{A1}$$

for the field shown in Fig. 12. Usually, the temperature field is unknown and is the objective of the optical measurement. However, we measured the temperature separately, permitting estimation of the temperature gradient. The corresponding deflection of the laser beam was estimated as follows. The refractive index of water at 20°C for a wavelength of 632.8 mm is 1.33176, and the temperature coefficient is $-8\times10^{-5}\ \mathrm{K}^{-1}$. Thus at 14.4°C, $n=1.33176+8\times5.6\times10^{-5}=1.33221$. Then

$$\frac{dn}{dy}=\frac{dn}{dT}\frac{dT}{dy}=(-8\times10^{-5})\frac{dT}{dy}$$

For example, at $x=15$ mm

$$\left.\frac{dT}{dy}\right|_{y=0}=\frac{14.4-9.4}{0-2.5}=-2\mathrm{K/mm}$$

Then for $l=80$ mm

$$y_l-y_0=\frac{(-8\times10^{-5})(-2)(80)^2}{(2)(1.33221)}=0.384\ \mathrm{mm}$$

This means that when the laser beam is parallel to the hot wall, the deflection of the beam is 0.384 mm in a distance of 80 mm.

The laser beam was not quite parallel to the hot wall, but that is a good approximation. Prior to the measurement, the cross-point of the laser beams was moved to the hot plate, and the distance y was measured from that point. The deflection of the beam is toward the denser region, i.e., to a greater value of y. The temperature gradient is nearly constant near the hot wall but eventually decreases to zero with increasing distance. The local temperature gradient was estimated from the measured temperature profile and this local value was used to estimate the refractive index gradient as above. The distance from the wall was corrected in this way before plotting the measured velocities versus y at all elevations.

The location of the cross-point in the case of the horizontal velocity measurement was also corrected, presuming that the beam which was almost parallel to the hot wall (0.05 rad.) was deflected as previously shown, and that the other one reflected very little due to its incoming angle of 0.459 rad with the hot plate. The correction in y for this case was found to be almost the same as for measurements of the vertical velocity.

Analysis of Turbulent Thermal Convection Between Horizontal Plates

M. Kaviany
Department of Mechanical Engineering,
University of Wisconsin—Milwaukee,
Milwaukee, Wis. 53201
Mem. ASME

R. Seban
Department of Mechanical Engineering,
University of California—Berkeley,
Berkeley, Calif. 94720
Fellow ASME

The one-equation model of turbulence is applied to the turbulent thermal convection between horizontal plates maintained at constant temperatures. A pseudo-three-layer model is used consisting of a conduction sublayer adjacent to the plates, a turbulent region within which the mixing length increases linearly, and a turbulent core within which the mixing length is a constant. It is assumed that the Nusselt number varies with the Rayleigh number to the one-third power. As a result, the steady-state distributions of the turbulent kinetic energy and the mean temperature are obtrained and presented in closed forms. These results include the effects of Prandtl number. The predictions are compared with the available experimental results for different Prandtl and Rayleigh numbers. Also included are the predictions of Kraichnan, which are based on a less exact analysis. The results of the one-equation model are in fair agreement with the experimental results for the distribution of the turbulent kinetic energy and the mean temperature distribution. The predictions of Kraichnan are in better agreement with the experimental results for the mean temperature distribution.

Introduction

The problem of turbulent thermal convection between two horizontal plates maintained at constant temperatures has been studied both experimentally and theoretically. Deardorff and Willis [1] measured the horizontally averaged values of mean and fluctuating components of velocity and temperature. The fluid studied was air, and a range of Rayleigh numbers from 6.3×10^5 to 10^7 was examined. In the experiment of Somerscales and Gazda [2], liquids with Prandtl numbers ranging from 6 to 17.1 were used. Tanaka and Miyata [3] measured the mean and fluctuating components of temperature in an experiment with water for Rayleigh numbers of up to 4×10^9.

For a situation where the ratio of the distance between the plates to the width of the chamber is small, the mean temperature field is nearly one-dimensional. The mechanism for mixing is apparently due to the departure of blobs of fluid from near the rigid boundaries toward the central region between the plates. Sparrow et al. [4] observed these blobs in an experiment with water using an electrochemical technique for visualization. Chang [5] and Howard [6] have predicted the frequency of the release of these blobs. For the central region between the plates, Tanaka and Miyata [3] and Kraichnan [7] have suggested that in the central region between the plates the length scale of mixing has a magnitude comparable to the distance between the plates.

Examination of the experimentally obtained mean temperature distributions [1–3] indicates that the length scale associated with the mixing process is not uniform throughout the domain between the plates. Furthermore, observation of the departing blobs of fluid (thermals) [4] indicates that at a given location from the plate there is more than one scale associated with the mixing, i.e., the thermals constitute the larger scales and the distance between the thermals is made up of mixing processes with smaller length scales.

Kraichnan [7] considered a three-layer model and applied the Prandtl mixing length theory and a similarity theory. Through an order-of-magnitude analysis, he obtained an approximate solution to the distributions of the mean and fluctuating components of temperature and fluctuating components of velocity, as well as the Nusselt number. He obtained two sets of solutions, one for Prandtl numbers larger than 0.1 and one for Prandtl numbers less than 0.1.

In this study a pseudo-three-layer model is adapted and the one-equation model of turbulence is solved analytically. Due to experimentally observed symmetry about the midplane of the system, only the domain between the upper plate and the midplane is considered in the analysis that follows.

Analysis

A rectangular coordinate system is chosen with the z-axis in the direction of gravity and the origin at the upper plate (cold plate). The steady-state thermal energy equation in a situation with no mean motion is given by

$$\frac{d}{dz}\left(K\frac{dT}{dz}-\rho c_p\overline{w'T'}\right)=0 \tag{1}$$

Here the turbulent heat flux, $\overline{w'T'}$, is to be specified in terms of the turbulent kinetic energy and a prescribed mixing length. The boundary conditions for equation (1) are

$$(i)\quad T=T_C \text{ at } z=0$$

$$(ii)\quad \frac{dT}{dz}=0 \text{ at } z=\frac{L}{2}$$

The second boundary condition is based on the available experimental data [1–3].

The conservation equation for the turbulent kinetic energy, $k=\frac{1}{2}\overline{u_i'^2}$ is specified for steady state, with no mean motion and with P and D as the rates of production and dissipation of turbuelnt kinetic energy, as

$$\frac{d}{dz}(\nu+\epsilon_k)\frac{dk}{dz}+P-D=0 \tag{2a}$$

For situations where the molecular transport of turbulent kinetic energy is negligible, equation (2a) becomes

$$\frac{d}{dz}\epsilon_k\frac{dk}{dz}+P-D=0 \tag{2b}$$

where the production of turbulent kinetic energy arises from the interaction of the temperature and velocity fluctuations. This is

Contributed by the Heat Transfer Division for publication in the JOURNAL OF HEAT TRANSFER. Manuscript received by the Heat Transfer Division May 17, 1983.

$$P = -\beta g \overline{\overline{w'T'}} = \beta g \, \epsilon_h \frac{dT}{dz} \tag{3a}$$

The isotropic dissipation rate is defined in terms of the kinetic energy of the turbulence and a mixing length.

$$D = c_2 \frac{k^{3/2}}{l} \tag{4}$$

The magnitude of ϵ_h is defined as

$$\epsilon_h = c_1 k^{1/2} l \tag{5}$$

The boundary conditions for equation (2*b*) are

$$(i) \quad k = 0 \text{ at } z = 0$$

$$(ii) \quad \frac{dk}{dz} = 0 \text{ at } z = \frac{L}{2}$$

The second boundary condition, which is dictated by the symmetry of the system and is also observed experimentally [1], requires that at $z = L/2$ the production and dissipation be equal.

Upon applying equations (3*a*–5) to this equilibrium condition and solving for k, one obtains

$$k = \frac{c_1}{c_2} g\beta l^2 \frac{dT}{dt}$$

Then, by substituting this equation into equation (5), the following emerges

$$\epsilon_h = \left(\frac{c_1^3}{c_2}\right)^{1/2} (\beta g)^{1/2} l^2 \left(\left|\frac{dT}{dz}\right|\right)^{1/2}$$

Furthermore, we note that while equation (3*a*) shows that the buoyant production of the kinetic energy is proportional to $\beta g\,(dT/dz)$, the shear-production of this quantity is conventionally proportional to $(\partial w/\partial z)^2$. Therefore, by analogy, one can suggest that the Prandtl's eddy diffusivity for the buoyancy driven flow considered here is

$$\epsilon_h = (\beta g)^{1/2} l^2 \left(\left|\frac{dT}{dz}\right|\right)^{1/2}$$

Now, by comparing the last two equations, it becomes necessary that $c_2 = c_1^3$.

Conventionally, when there exists a momentum diffusivity, the turbulent and kientic energy Prandtl numbers are defined such that

$$\epsilon_k = \frac{\epsilon_m}{\mathrm{Pr}_k} = \frac{\epsilon_h \mathrm{Pr}_h}{\mathrm{Pr}_k} \tag{6}$$

This much specification, together with a definition of the necessary constants and a prescription about the magnitude of the mxing length, enables the solution of the problem.

Description of the Three Layers. The three-layer model adapted by Kraichnan, for $\mathrm{Pr} > 0.1$, consists of:

(*a*) A sublayer within which molecular transport of heat and momentum dominate the turbulent transport
(*b*) A buffer layer within which the dominant means of transport are molecular for momentum and turbulent for heat
(*c*) A turbulent core within which the molecular transport is neglected

These specifications were altered slightly for the case of $\mathrm{Pr} < 0.1$. The mathematical specifications for these three layers, with the arguments of the derivatives being either the turbulent kinetic energy or the temperature, are:

(*i*) Sublayer:

$$0 < z < z_\alpha \quad , \quad \epsilon_h = 0,$$

(*ii*) Buffer:

$$z_\alpha < z < z_\nu \quad , \quad \nu \frac{d}{dz} \neq 0, \alpha \frac{d}{dz} = 0, \epsilon_h \frac{d}{dz} \neq 0$$

(*iii*) Turbulent Core:

$$z_\nu < z < \frac{L}{2} \quad , \quad \nu \frac{d}{dz} = \alpha \frac{d}{dz} = 0, \epsilon_h \frac{d}{dz} \neq 0 \tag{7a}$$

Nomenclature

A = constant given in equation (8)
a_1, a_2, b_1, b_2 = coefficients defined in equations (2*g*) and (2*i*)
c_1, c_2 = constant defined in equation (4, 5)
c_p = specific heat at constant pressure
D = dissipation rate of turbulent kinetic energy
D_1, D_2 = defined in equations (9*a*)
g = gravitational acceleration
k = turbulent kinetic energy
K = thermal conductivity
l = mixing length
L = distance between the plates
Nu_L = Nusselt number $= \dfrac{q_o L}{\Delta T K}$
P = production rate of turbulent kinetic energy
P_1, P_2 = defined in equations (9*a*)
Pr = Prandtl number
q_o = heat flux
Ra_L = Rayleigh number $= \dfrac{g\beta\Delta T L^3}{\nu\alpha}$
Ra_δ = Rayleigh number based on δ
T = temperature
ΔT = $T_H - T_C$
$\bar{T}$ = $\dfrac{T - T_C}{T_H - T_C}$
w = the vertical component of velocity
z = distance from the cold plate
$\tilde{z}_c$ = distance to the turbulent core
z_α, z_ν = thermal and viscous sublayer thickness as defined by Kraichnan [7] and given by equations (7*a*)

Greek Symbols

α = thermal diffusivity
β = thermal expansion coefficient
γ = constant given in equation (8)
δ = thickness of the conduction sublayer
ϵ = eddy diffusivity
ν = kinematic viscosity
ρ = density
ϕ = $= \bar{k}^{3/2}$
ϕ_1 = defined by equation (17)

Subscript

C = cold plate
h = heat
H = hot plate
k = turbulent kinetic energy
$L/2$ = evaluated at $\dfrac{L}{2}$

Superscript

$'$ = fluctuating component
$-$ = dimensionless, defined in equations (9)
$=$ = time averaged

where

$$z_\alpha = \frac{L}{2\mathrm{Nu}_L}, \quad z_\nu = 3.2\,\mathrm{Pr}^{1/2} z_\alpha$$

The three-layer model adapted in this study is made of:

(*a*) A conduction sublayer within which only molecular transport takes place

(*b*) A turbulent region within which molecular transport is allowed for heat but not for turbulent kinetic energy, turbulent transport is significant, and the mixing length varies linearly with the distance from the plate

(*c*) A turbulent core within which only turbulent transport takes place and the mixing length is a constant

The mathematical specifications for these three layers, with the arguments of the derivatives being either the turbulent kinetic energy or the temperature, are:

(*i*) Sublayer:

$$0<z<\delta \quad , \quad \epsilon_h = 0, l = 0,$$

(*ii*) Turbulent Region:

$$\delta<z<z_c \quad , \quad \nu\frac{d}{dz}=0, \alpha\frac{d}{dz}\neq 0, \epsilon_h\frac{d}{dz}\neq 0, \; l=z-\delta$$

(*iii*) Turbulent Core:

$$z_c<z<\frac{L}{2} \quad \nu\frac{d}{dz}=\alpha\frac{d}{dz}=0, \epsilon_h\frac{d}{dz}\neq 0, \; l=z_c-\delta \tag{7b}$$

Chang [5] has suggested that the thickness of the conduction sublayer be taken such that $g\beta\Delta T\delta^3/\nu\alpha = 64.8$. In this study both z_c and δ are determined from the available experimental data.

Kraichnan has recommended the value of unity for the constant of proportionality in relating l to z, instead of the value of 0.4 used for forced convection. This recommended value is the one used for the turbulent region.

The assumption of negligible molecular transport of turbulent kinetic energy is rather arbitrary and is made here so that closed form solutions for the turbulent kinetic energy and for the temperature can be obtained.

Turbulent Kinetic Energy. In the turbulent region and the turbulent core, as defined above, equation (2*b*) describes the distribution of turbulent kinetic energy. In determining the production of the turbulent kinetic energy, it is assumed that turbulent heat flux, $\overline{w'T'}$ accounts for the entire heat flux. Therefore,

$$P = \beta g \epsilon_h \frac{dT}{dz} = \beta g \frac{q_o}{\rho c_p} = \beta g \frac{\Delta T\, K}{L\rho c_p}\mathrm{Nu}_L \tag{3b}$$

which does not vary with z. This assumption is not valid near the edge of the defined sublayer and is only marginally correct in the adjacent first turbulent region. However, it makes it possible to decouple the equation for turbulent kinetic energy from the thermal energy equation.

The value of the Nusselt number recommended by Deardorff and Willis is

$$\mathrm{Nu}_L = A\ \mathrm{Ra}_L^{1/3}\mathrm{Pr}^{\gamma} \tag{8}$$

where $A = 0.069$ and $\gamma = 0.074$. This relationship does not predict all the available data correctly. However, it is a relatively good approximation for $\mathrm{Ra}_L > 10^7$. The experimental results of Deardorff and Willis [1] for air and $\mathrm{Ra}_L = 6.3 \times 10^5$ are included in the comparison between the experimental results and those of the predictions, but the range of the applicability of the following analysis is expected to be for $\mathrm{Ra}_L > 10^7$.

Examination of the experimental results of Deardorff and Willis suggests that in the turbulent core, the value of turbulent kinetic energy is proportional to the Rayleigh number, and the dissipation rate is proportional to the Rayleigh number to the four third power. In order to obtain a solution which is independent of the Rayleigh number and the Prandtl number, equation (2*b*) is nondimensionalized as follows

$$\tilde{z} = \frac{z-\delta}{L\mathrm{Ra}_L^{1/6}}, \tilde{l} = \frac{l}{L\mathrm{Ra}_L^{1/6}}, \tilde{k} = \frac{k}{\frac{\alpha^2}{L^2}\mathrm{Ra}_L\mathrm{Pr}^{2(1+\gamma)/3}}$$

$$\tilde{D} = \frac{D}{\frac{\alpha^3}{L^4}\mathrm{Ra}_L^{4/3}\mathrm{Pr}^{1+\gamma}}, \tilde{\epsilon}_k = \frac{\epsilon_k}{\alpha\mathrm{Ra}_L^{2/3}\mathrm{Pr}^{(1+\gamma)/3}} \tag{9a}$$

By applying equations (3*b*), (4), (5), (8) and the above definitions to equation (2*b*), one obtains

$$c_1\frac{\mathrm{Pr}_h}{\mathrm{Pr}_k}\frac{d}{d\tilde{z}}\tilde{k}^{1/2}\tilde{l}\frac{d\tilde{k}}{d\tilde{z}} + A - c_1^3\frac{\tilde{k}^{3/2}}{\tilde{l}} = 0 \tag{2c}$$

Upon making the substitution

$$\phi = \tilde{k}^{3/2}$$

equation (2*c*) can be written as

$$\tilde{l}\frac{d}{d\tilde{z}}\tilde{l}\frac{d\phi}{d\tilde{z}} + \frac{A\ \mathrm{Pr}_k\tilde{l}}{(2/3)c_1\mathrm{Pr}_h} - \frac{c_1^2\mathrm{Pr}_k\phi}{(2/3)\ \mathrm{Pr}_h} = 0, \tag{2d}$$

where the distribution of the mixing length, given by equation (7*b*), in the nondimensionalized form becomes

$$\tilde{l} = \tilde{z} \quad \text{for} \quad 0<\tilde{z}<\tilde{z}_c$$
$$\tilde{l} = \tilde{z}_c \quad \text{for} \quad \tilde{z}_c<\tilde{z}<\tilde{z}_{L/2} \tag{7c}$$

The boundary conditions for equation (2*d*) are

$$(i) \quad \phi = 0 \text{ at } \tilde{z} = 0$$
$$(ii) \quad \frac{d\phi}{d\tilde{z}} = 0 \text{ at } \tilde{z} = \tilde{z}_{L/2} \tag{10}$$

Equation (2*d*), with these distribution of the mixing length, takes the following forms for the two regions:

$$\tilde{z}\frac{d\phi}{d\tilde{z}} - \tilde{z}\frac{d\phi}{d\tilde{z}} + P_1\tilde{z} - D_1 = 0 \qquad 0<\tilde{z}<\tilde{z}_c \tag{2e}$$

$$\frac{d^2\phi}{d\tilde{z}^2} + P_2 - D_2 = 0 \qquad \tilde{z}_c<\tilde{z}<\tilde{z}_{L/2} \tag{2f}$$

where

$$P_1 = \frac{A\ \mathrm{Pr}_k}{(2/3)c_1\mathrm{Pr}_h}, D_1 = \frac{c_1^2\mathrm{Pr}_k}{(2/3)\mathrm{Pr}_h}, P_2 = \frac{P_1}{\tilde{z}_c}, D_2 = \frac{D_1}{\tilde{z}_c^2} \tag{9b}$$

The solution to equation (2*e*) must satisfy the first of the boundary conditions given in equation (10) and the solution to equation (2*f*) must satisfy the second boundary condition given in equation (10). In order to simplify equation (2*e*) a substitution of the form

$$\eta = -ln\ \tilde{z}$$

is made. Then equation (2*f*) becomes

$$\frac{d^2\phi}{d\eta^2} + P_1 e^{-\eta} - D_1\phi = 0 \tag{2g}$$

The complete solution for (2*g*) is

$$\phi = a_1\sinh D_1^{1/2}\eta + a_2\cosh D_1^{1/2}\eta + \frac{P_1}{D_1-1}e^{-\eta}$$

which upon satisfying the boundary condition of $\phi = 0$ at $\tilde{z} = 0$, i.e., $\eta\to\infty$, becomes

$$\phi = -a_1[\sinh(D_1^{1/2}ln\tilde{z})] + \cosh(D_1^{1/2}ln\tilde{z})] + \frac{P_1}{D_1-1}\tilde{z}, \quad 0<\tilde{z}<\tilde{z}_c \tag{2h}$$

The complete solution to equation (2*f*) is

$$\phi = b_1 \sinh D_2^{1/2}\tilde{z} + b_2 \cosh D_2^{1/2}\tilde{z} + \frac{P_2}{D_2} \tag{2i}$$

Upon satisfying, $d\phi/d\tilde{z} = 0$, at $\tilde{z} = \tilde{z}_{L/2}$ and taking advantage of

$$\coth (D_2^{1/2}\tilde{z}_{L/2}) \approx 1.0 \text{ for } D_2^{1/2}\tilde{z}_{L/2} > 2 \tag{2j}$$

which will be shown to be a reasonable assumption, equation (2*i*) becomes

$$\phi = b_1[\sinh (D_2^{1/2}\tilde{z}) - \cosh (D_2^{1/2}\tilde{z})] + \frac{P_2}{D_2} \quad \tilde{z}_c < \tilde{z} < \tilde{z}_{L/2} \tag{2k}$$

The solutions given by equations (2*h*) and (2*k*) must also have the same magnitude and the same first derivative at $\tilde{z} = \tilde{z}_c$. After matching the solutions at $\tilde{z}_c$ and simplifying, one obtains

$$\phi = -\frac{\tilde{z}_c}{2}\left[\frac{P_1}{D_1 - 1}\left(1 + \frac{1}{D_1^{1/2}}\right) - \frac{P_1}{D_1}\right]\left(\frac{\tilde{z}}{\tilde{z}_c}\right)^{D_1^{1/2}} + \frac{P_1}{D_1 - 1}\tilde{z} \quad 0 < \tilde{z} < \tilde{z}_c \tag{11a}$$

$$\phi = -\frac{\tilde{z}_c}{2}\left[\frac{P_1}{D_1 - 1}\left(1 - \frac{1}{D_1^{1/2}}\right) - \frac{P_1}{D_1}\right] e^{D_1^{1/2}(1 - \tilde{z}/\tilde{z}_c)} + \frac{P_1}{D_1}\tilde{z}_c \quad z_c < z < z_{L/2} \tag{11b}$$

The dimensional turbulent kinetic energy is related to ϕ as

$$k = \frac{\alpha^2}{L^2}\mathrm{Ra}_L \mathrm{Pr}^{2(1+\gamma)/3}\phi^{2/3} \tag{12}$$

The dimensional eddy diffusivity is related to ϕ as

$$\epsilon_h = \alpha \mathrm{Ra}_L^{2/3}\mathrm{Pr}^{\frac{1+\gamma}{3}} c_1 \phi^{1/3}\bar{l} \tag{13}$$

Mean Temperature. In the conduction sublayer, due to the absence of any turbulent transport, the thermal energy equation when integrated becomes

$$K\frac{dT}{dz} = q_0 \text{ or } \frac{d\bar{T}}{d(z/L)} = \mathrm{Nu}_L \text{ for } 0 < \frac{z}{L} < \frac{\delta}{L} \tag{14}$$

In the region outside of the laminar region, the temperature gradient is

$$\frac{d\bar{T}}{d(z/L)} = \frac{\mathrm{Nu}_L}{1 + \frac{\epsilon_h}{\alpha}} \text{ for } \frac{\delta}{L} < \frac{z}{L} < \frac{1}{2} \tag{15}$$

Thus, the temperature distribution between the cold plate and the center line is

$$\int d\bar{T} = \mathrm{Nu}_L \int_0^{\delta/L} d(z/l) + \mathrm{Nu}_L \int_{\delta/L}^{0.5} \frac{d(z/L)}{1 + \frac{\epsilon_h}{\alpha}} \tag{16a}$$

Upon inserting equations (9*a*) and (13) in equation (16*a*), one obtains

$$\int d\bar{T} = \mathrm{Nu}_L(\delta/L) + \mathrm{Nu}_L \int_0^{\tilde{z}_c} \frac{d\tilde{z}\ \mathrm{Ra}_L^{1/6}}{1 + c_1\phi^{1/3}\mathrm{Ra}_L^{2/3}\mathrm{Pr}^{(1+\gamma)/3}\bar{l}} + \mathrm{Nu}_L \int_{\tilde{z}_c}^{\tilde{z}_{L/2}} \frac{d\tilde{z}\ \mathrm{Ra}_L^{1/6}}{1 + c_1\phi^{1/3}\mathrm{Ra}_L^{2/3}\mathrm{Pr}^{(1+\gamma)/3}\tilde{z}_c} \tag{16b}$$

conduction sublayer — turbulent region — turbulent core

If the temperature drops in all three layers are predicted properly, then the total temperature drop must be 0.5.

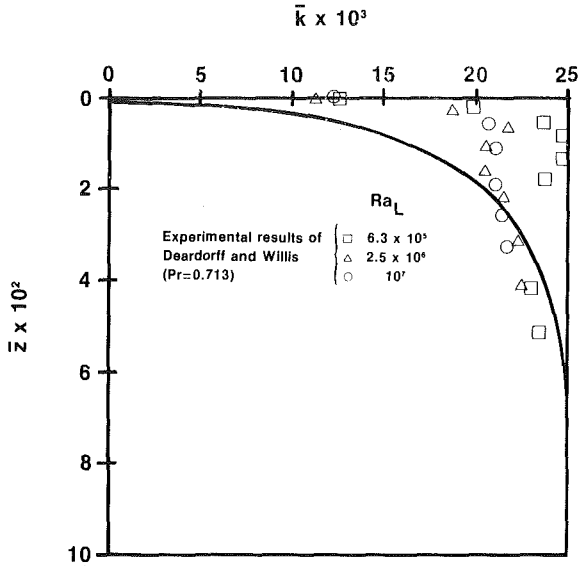

Fig. 1 Distribution of turbulent kinetic energy. The solid curve represents the results of the one-equation model, and the symbols represent the experimental results of Deardorff and Willis.

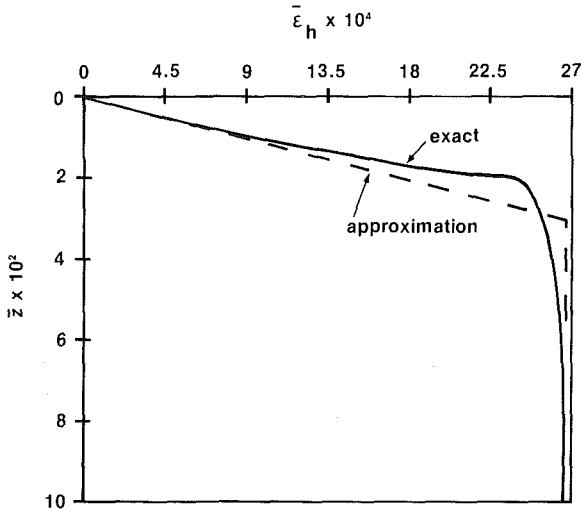

Fig. 2 Distribution of eddy diffusivity for heat. The solid curve shows the results of the one-equation model, and the dashed line represents an approximation to these results.

Results and Discussion

In order to complete the solution of the turbulent kinetic energy distribution, the constants that have been introduced must be specified. The constants used in this study are

c_1	Pr_h	Pr_k	$\tilde{z}_c$
0.39	0.59	1.0	0.022

The values for $\mathrm{Pr}_h = 0.59$ and $\mathrm{Pr}_k = 1.0$ are those that have been used with relative success, for the prediction of transient cooling of a pool of water [8]. The values of c_1 and $\tilde{z}_c$ were chosen such that the production and dissipation are equal at the midplane between the plates. Since the production term in equation (2*b*) is a constant throughout the spatial domain, then

$$\tilde{D}_{L/2} = c_1\left(\frac{k^{3/2}}{\tilde{z}_c}\right)_{L/2}, \tilde{D}_{L/2} = \tilde{P}_{L/2} = A$$

where $\bar{l} = \tilde{z}_c$ for $\tilde{z} \geq \tilde{z}_c$. Therefore,

$$\tilde{k}_{L/2}^{3/2} = A\ c_1\tilde{z}_c$$

So the value of $\tilde{z}_c$ also affects the magnitude of the turbulent

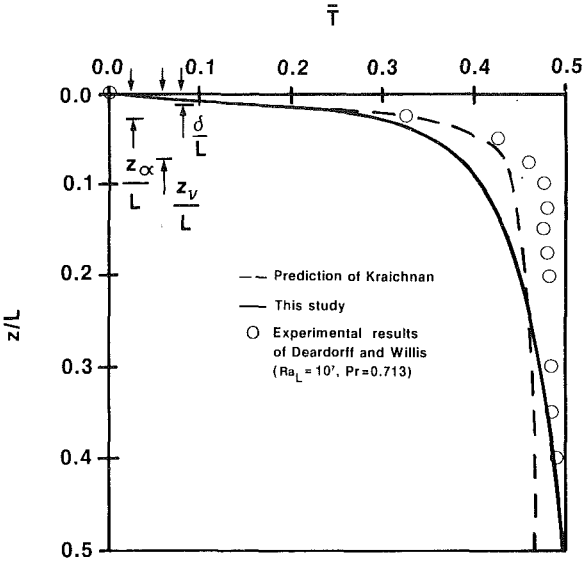

Fig. 3 Distribution of the mean temperature for $Ra_L = 10^7$, Pr = 0.71. The solid curve shows the results of the one-equation model, the dashed curve represents the predictions of Kraichnan, and the symbols represent the experimental results of Deardorff and Willis.

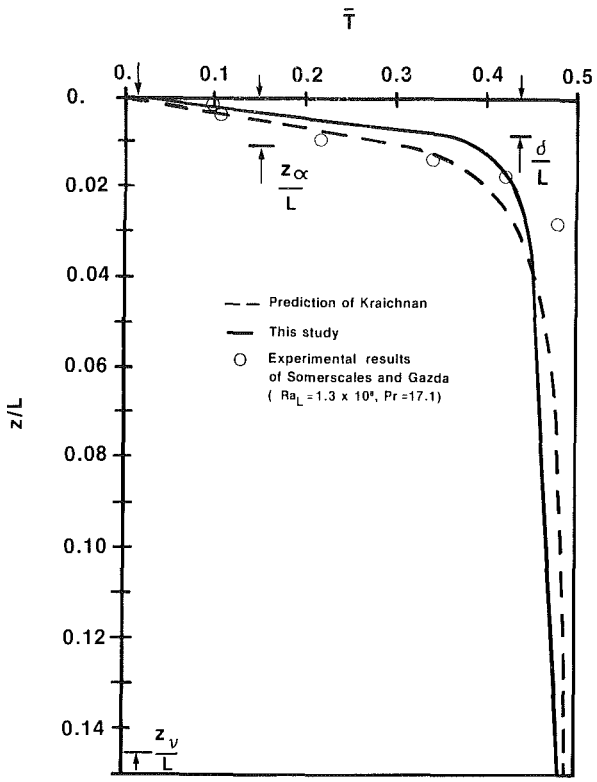

Fig. 4 Distribution of the mean temperature for $Ra_L = 1.3 \times 10^8$, Pr = 17.1. The solid curve shows the results of the one-equation model, the dashed curve represents the predictions of Kraichnan, and the symbols represent the experimental results of Somerscales and Gazda.

kinetic energy at $z = L/2$. Therefore, it was chosen such that, as much as possible, the numerical results would correspond to the experimental data.

With the values of c_1 and z_c specified, the requirement for validity of the assumption given by equation (2*j*) can be obtained. By neglecting the thickness of the conduction sublayer compared to the half distance between the two plates, the nondimensionalized half distance is approximated as

$$\bar{z}_{L/2} = \frac{0.5}{\mathrm{Ra}_L^{1/2}} - \frac{\delta}{L}\frac{1}{\mathrm{Ra}_L^{1/6}} \approx \frac{0.5}{\mathrm{Ra}_L^{1/6}}$$

By applying equation (9*a*), one obtains

$$D_2^{1/2}\bar{z}_{L/2} = \frac{50.3 \times 0.5}{\mathrm{Ra}_L^{1/6}} > 2$$

This requires that $\mathrm{Ra}_L < 4 \times 10^6$. However, due to the relatively small contribution that the turbulent core makes to the value of turbulent kinetic energy at $\bar{z}_{L/2}$, this assumption does not affect the results significantly. Furthermore, it will be shown that for $\mathrm{Ra}_L > 2 \times 10^7$, the turbulent core does not exist.

Turbulent Kinetic Energy. Figure 1 shows the distribution of the nondimensionalized turbulent kinetic energy. The solid curve shows the results obtained here, and the symbols show the experimental results of Deardorff and Willis for air at Rayleigh numbers of 6.3×10^5, 2.5×10^6, and 10^7. The spatial domain is from the edge of the laminar sublayer to the middistance between the two plates. This follows the definition of nondimensional spatial coordinate given in equation (9). The thickness of the sublayer must therefore be prescribed in order to plot the experimental data with the nondimensionalized spatial coordinate. The value of the sublayer thickness is that recommended by Chang [5]. The predicted values of $\bar{k}$ are much lower than the experimental results for $\bar{z} < 0.02$. This is due to the large eddy diffusivity predicted by the one-equation model. The results imply that the prescribed mixing length is too large near the edge of the conduction sublayer.

Eddy Diffusivity. Figure 2 shows the results of the one-equation model for the nondimesionalized eddy diffusivity for heat. The solid curve shows the results of the one-equation model and the dashed curve shows a linear approximation made to these results. As a result of this approximation, the eddy diffusivity can be expressed as

$$\epsilon_h = \begin{cases} c_1\phi_1^{1/3}\mathrm{Ra}_L^{2/3}\mathrm{Pr}^{\frac{1+\gamma}{3}}\bar{z} & 0<\bar{z}<0.03 \\ c_1\phi_1^{1/3}\mathrm{Ra}_L^{2/3}\mathrm{Pr}^{\frac{1+\gamma}{3}}(0.03) & 0.03<\bar{z}<\bar{z}_{L/2} \end{cases} \tag{17}$$

where ϕ_1 is chosen such that $\bar{\epsilon}_h = k^{1/2}\,\bar{l} = 0.0026$ for $\bar{z} = 0.03$. This results in $\phi_1 = 0.0109$. This approximation causes a small increase in the value of eddy diffusivity just outside the laminar sublayer, which makes it a little disadvantageous. The choice of the linear approximation enables an analytical integration for the temperature distribution, as will be shown in the next section.

With $\bar{z}_c = 0.03$, since $\bar{z}_{L/2} = (1/2)\,\mathrm{Ra}_L^{1/6}$, $\bar{z}_c = \bar{z}_{L/2}$ at $\mathrm{Ra}_L = 2.1 \times 10^7$ and the turbulent core no longer exists for larger Rayleigh numbers.

Mean Temperature. Figure 3 shows with the solid curve the mean temperature distribution for the approximate eddy diffusivity distribution given by equation (18). The Prandtl number is 0.71, and the Rayleigh number is 10^7. This corresponds to one of the experimental conditions of Deardorff and Willis [1]. Their experimental data are given by symbols. Also shown, with the dashed curve, is the prediction of Kraichnan [7]. The value of δ was chosen such that at $z/L = 1/2$, equation (16*b*) results in $\bar{T} = 0.5$. This was done by applying equation (17) to equation (16*a*), i.e.,

$$\int d\bar{T} = \mathrm{Nu}\frac{\delta}{L} + \frac{\mathrm{Nu}_L ln[(c_1\phi_1^{1/3}\mathrm{Ra}_L^{2/3}\mathrm{Pr}^{(1+\gamma)/3}(0.03)+1]}{c_1\phi_1^{1/3}\mathrm{Ra}_L^{1/2}\mathrm{Pr}^{(1+\gamma)/3}} + \frac{\mathrm{Nu}_L\mathrm{Ra}_L^{1/6}(\bar{z}_{L/2}-0.03)}{c_1\phi_1^{1/3}\mathrm{Ra}_L^{2/3}\mathrm{Pr}^{(1+\gamma)/3}(0.03)+1} \tag{16c}$$

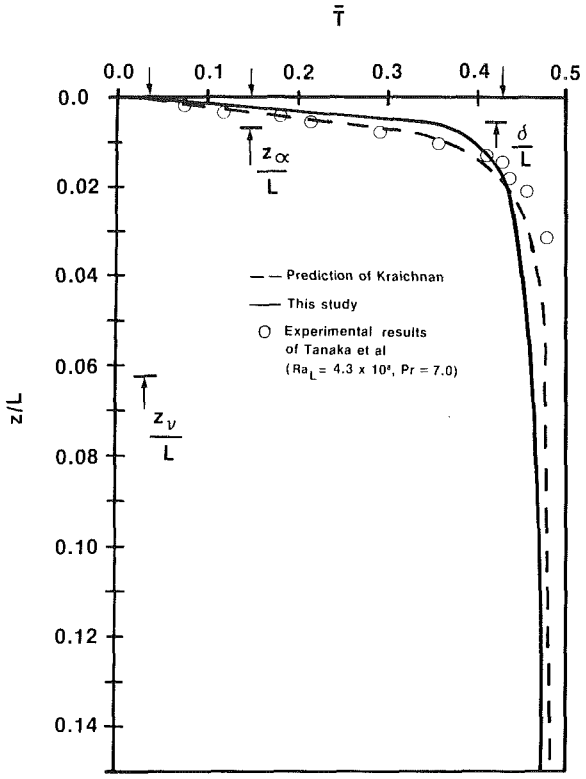

Fig. 5 Distribution of the mean temperature for $Ra_L = 4.3 \times 10^8$, Pr = 7.0. The solid curve shows the results of the one-equation model, the dashed curve represents the predictions of Kraichnan, and the symbols represent the experimental results of Tanaka and Miyata.

For Pr = 0.71 and $Ra_L = 10^7$, $\delta = 0.0127L$. The corresponding values recommended by Chang [5] and Kraichnan [7] are 0.0186 and 0.0345, respectively.

The prediction of the one-equation model is in fair agreement with the experimental results for z/L outside the range $0.05 < z/L < 0.3$. However, inside this range the predicted result is lower than the experimental results. This is due to the relatively large eddy diffusivity near the conduction sublayer. The prediction of Kraichnan [7] is in good agreement with the experimental results in the thermal sublayer. It should be noted that in general one expects for a Prandtl number of less than unity that the thermal sublayer be thicker than the viscous sublayer. However, this is not the case for the prediction made by Kraichnan.

Figure 4 shows the temperature distribution for the Prandtl number of 17.1 and the Rayleigh number of 1.3×10^8. The experimental results of Somerscales and Gazda [2] for these conditions are shown with symobls. The results are given for $0 < z/L < 0.15$ in order to show the temperature distribution near the surface more clearly. The results of the one-equation model seem to be in fair agreement with the experimental results. The prediction of Kraichnan is in better agreement with the experimental results. The value of the conduction sublayer thickness calculated using equation (16*c*) is 0.00863 L. Note that, although the thickness of the sublayer decreases with the Rayleigh number, its influence on the mean temperature increases substantially with increases in the Rayleigh number.

Figure 5 shows the temperature distribution for the Prandtl number of 7.0 and the Rayleigh number of 4.3×10^8. The experimental results of Tanaka and Miyata [3] for these conditions are shown with symbols. The format is similar to that of Fig. 4. The results imply that the eddy diffusivity predicted by the one-equation model is too small for $z/L > 0.02$. However, overall the prediction made by the one-equation model is in fair agreement with the experimental results. The prediction of Kraichnan is in better agreement with the experimental results. The thickness of the conduction sublayer calcualted from equation (16*c*) is 0.00596 L.

By examining the sublayer thicknesses obtained for the above mentioned conditions, it is clear that the previous recommendations made in [5-7, 9], which did not include Prandtl number dependency, should be reconsidered. For the cases considered here, the following expression predicts the conduction sublayer thickness to within 11 percent.

$$\frac{\delta}{L} = \left(\frac{17}{Ra_L}\right)^{1/3} Pr^{0.22}$$

Summary

The assumption of a turbulent region in which the mixing length varies linearly with distance near the wall and is constant in the central region enables an analytical integration of the turbulent kinetic energy equation. A suitable nondimensionalization, incorporating parameters defined by an empirical specification of the Nusselt number specifies a simple distribution of a nondimensionalized turbulent kinetic energy as a function of a nondimensionalized distance from the wall, and in turn, there is specified a simple nondimensionalized eddy diffusivity as a function of this distance from the wall.

A linear approximation for this nondimensional diffusivity is required to permit an analytical integration of the energy equation to specify the temperature distribution. To make this distribution agree with the empirically specified Nusselt number there must be specified the thickness of a laminar sublayer, and such a thickness is specified by these results. The temperature distributions so specified are in fair agreement with experimental results.

References

1 Deardorff, J. W., and Willis, G. E., "Investigation of Turbulent Thermal Convection Between Horizontal Plates," *Journal of Fluid Mechanics*, Vol. 28, 1967, pp. 675-704.

2 Somerscales, E. F. C., and Gazda, I. W., "Thermal Convection in High Prandtl Number Liquids at High Rayleigh Numbers," *International Journal of Heat and Mass Transfer*, Vol. 12, 1969, pp. 1491-1511.

3 Tanaka, H., and Miyata, H., "Turbulent Natural Convection in a Horizontal Water Layer Heated From Below," *International Journal of Heat and Mass Transfer*, Vol. 23, 1980, pp. 1273-1281.

4 Sparrow, E. M., Husar, R. B., and Goldstein, R. J., "Observations and Other Characteristics of Thermal," *Journal of Fluid Mechanics*, Vol. 41, pt. 4, 1970, pp. 793-800.

5 Chang, Y. P., "A Theoretical Analysis of Heat Transfer in Natural Convection and in Boiling," ASME *Transactions*, 1957, pp. 1501-1513.

6 Howard, L. W., "Convection at High Rayleigh Number," *Proceedings 11th Annual Meeting, International Congress of Applied Mechanics*, 1964, pp. 1109-1115.

7 Kraichnan, R. A., "Turbulent Thermal Convection at Arbitrary Prandtl Number," *The Physics of Fluids*, Vol. 15, No. 11, 1962, pp. 1374-1389.

8 Kaviany, M., and Seban, R. A., "Transient Turbulent Thermal Convection in a Pool of Water," *International Journal of Heat and Mass Transfer*, Vol. 24, No. 10, 1981, pp. 1742-1746.

9 Kaviany, M., "Turbulent Thermal Convection Between Horizontal Plates," *Natural Convection*, Vol. HTD-16, ASME, New York, 1981, pp. 75-80.

10 Chu, T. Y., and Goldstein, R. J., "Turbulent Convection in a Horizontal Layer of Water," *Journal of Fluid Mechanics*, Vol. 60, 1973, pp. 141-159.

11 Goldstein, R. J., and Chu, T. Y., "Thermal Convection in a Horizontal Layer of Air," *Progress in Heat and Mass Transfer*, Vol. 2, 1969, pp. 55-75.

12 Townsend, A. A., "Temperature Fluctuations Over a Heated Horizontal Surface," *Journal of Fluid Mechanics*, Vol. 5, 1956, pp. 209-241.

Natural Convection Experiments in a Liquid-Saturated Porous Medium Bounded by Vertical Coaxial Cylinders[1]

D. C. Reda
Member, Technical Staff,
Fluid and Thermal Sciences Department,
Sandia National Laboratories,
Albuquerque, N. M. 87185
Mem. ASME

An experimental effort is presently underway to investigate natural convection in liquid-saturated porous media utilizing a geometry and hydrodynamic/thermal boundary conditions relevant to the problem of nuclear-waste isolation in geologic repositories. During the first phase of this research program, detailed measurements were made of the steady-state thermal field throughout an annular test region bounded by a vertical, constant-heat-flux, inner cylinder and a concentrically placed, constant-temperature, outer cylinder. An overlying, constant-pressure fluid layer was utilized to supply a permeable upper surface boundary condition. Results showed the heater surface temperature to increase with increasing vertical distance due to the buoyantly driven upflow. The measured temperature difference (ΔT) between the average heater surface temperature and the constant outer-surface temperature was found to be progressively below the straight-line/conduction-only solution for ΔT versus power input, as the latter was systematically increased. Comparisons between measured results and numerical predictions obtained using the finite element code MARIAH showed very good agreement, thereby contributing to the qualification of this code for repository-design applications.

Introduction

Experimental and analytical studies of natural convection in liquid-saturated porous media have been motivated by such diverse engineering problems as geothermal energy extraction, pollutant dispersion in aquifers, and post-accident heat removal from nuclear reactor rubble beds. Recent review articles by Cheng [1] and Combarnous [2, 3] serve well to summarize the state-of-the-art through 1978.

More recent motivation for study in this area has come from efforts to identify a geologic repository for the storage of canisters containing high-level nuclear-waste material. Geologic media under investigation include deep-ocean seabed sediments and deep-earth rock layers, which are either fully saturated or partially saturated with liquid water. Water motion throughout such media, induced by radioactive-decay/ heat-release mechanisms, must be understood if one is to accurately predict canister/medium thermal response. The potential extent of radionuclide transport is also strongly dependent upon this thermally-induced velocity field.

Canisters are expected to be long, slender cylinders, emplaced in the geologic medium parallel to the gravity vector. Constant lateral spacings between adjacent canisters, and between parallel rows of canisters, will be maintained based on total projected heat loads. Due to these considerations, the "single-canister" problem can then be reduced to the study of natural convection in a liquid-saturated porous medium bounded by vertical, coaxial cylinders.

The boundary conditions of interest to this problem are stated as follows. A spatially-uniform heat flux exists along the surface of the "inner cylinder" (i.e., the canister), the absolute value of this heat flux decaying exponentially with time over a long time period. Symmetry dictates an "impermeable"/adiabatic boundary condition at the outer radius if the canisters are spaced close enough together to allow for thermal interaction; for "infinite" spacing (no thermal interaction), the outer boundary condition would become "impermeable"/constant temperature. The upper surface hydrodynamic boundary condition is generally accepted to be a constant-pressure/permeable surface, i.e., the interface between the seabed sediment and the ocean bottom, or the interface between the rock layer and the emplacement mine drift. The corresponding thermal boundary condition at such a permeable surface would be isothermal, or near-isothermal, due to the overlying fluid layer, or the environment maintained in the drift. The bottom boundary conditions would, of course, be site-specific; conditions chosen for the present study are impermeable/adiabatic.

In order to numerically model such complex problems, Gartling and Hickox developed the computer code MARIAH [4, 5]. This code is a general purpose, finite element, numerical simulator designed for the solution of two-dimensional problems involving fluid flow and heat transfer in fully-saturated porous media. It can treat isothermal, free-convection, mixed-convection, and forced-convection flows, for planar and axisymmetric geometries, in both transient and steady-state modes. This code has been used extensively to predict the thermal response of, and induced velocity field within, those seabed sediments under investigation as potential repositories for nuclear waste canisters [6, 7]. Similar fluid/thermal response calculations have also been conducted with this code to address the feasibility of land-based nuclear waste isolation [8].

Licensing procedures require that all such predictive tools used in repository design be "qualified" in order to demonstrate that they, in fact, simulate the physical situation of interest. This requirement can be met, in part, by conducting carefully controlled laboratory experiments, using the geometry and hydrodynamic/thermal boundary conditions of interest, then comparing the measured and predicted results.

A review of the recent experimental literature was conducted in order to ascertain the extent of the existing data base relevant to the problem at hand. The recent work can be categorized primarily by the geometry and boundary con-

[1]This work performed at Sandia National Laboratories and supported by the U.S. Department of Energy under Contract Number DE-AC04-76DP00789.

Contributed by the Heat Transfer Division and presented at the 1983 Joint ASME/JSME Thermal Engineering Conference. Manuscript received by the Heat Transfer Division December 17, 1982.

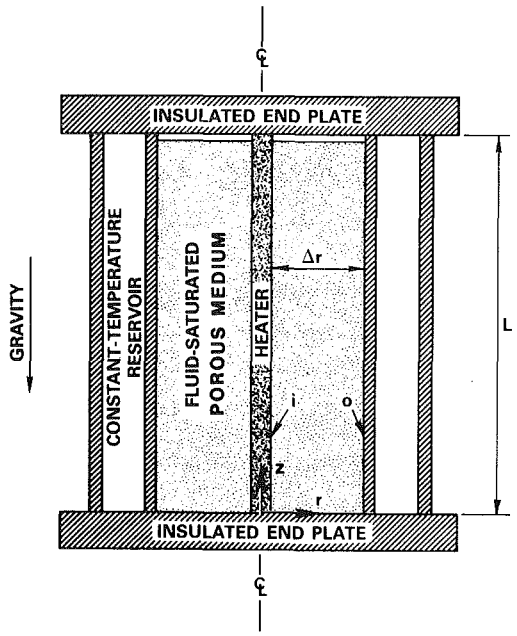

Fig. 1 Schematic of convection chamber

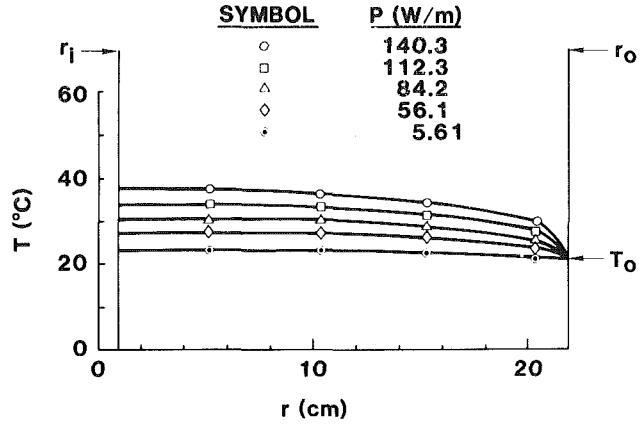

Fig. 2 Fluid-layer temperature distribution

ditions utilized. Rectangular enclosures were found to be the predominant geometry, with both bottom-heated [9, 10, 11] and side-heated [9, 11, 12, 13] isothermal walls being utilized as the convection-inducing mechanism. Vertical cylinders heated from below were studied in [14, 15] and concentric spheres were utilized in [16]. Non-Darcy (high-Rayleigh-number) effects were investigated in [17, 18].

Wooding [19] investigated flow in a porous medium bounded by vertical coaxial cylinders. However, the hydrodynamic and thermal boundary conditions applied in [19] were not in accordance with present interests; that is, the inner cylinder was maintained at a constant *temperature*, while all four bounding surfaces were restricted to be *impermeable*. The objectives of the present effort were, therefore, to generate the required data base, using the stated geometry and boundary conditions of interest, and to utilize these data for code-qualification purposes.

Experimental Approach

Figure 1 shows a schematic of the axisymmetric geometry utilized in the present experiment. A cylindrical heater of 1.90 cm o.d. was placed on the centerline of a cylindrical tube of 43.82 cm i.d., thereby forming an annular test region (containing the liquid-saturated porous medium under study) of gap width $\Delta r = 20.96$ cm. The overall height, L, of the test region was 89.08 cm, defining an aspect ratio for the apparatus, $L/\Delta r$, of 4.25.

Boundary conditions were established and maintained constant in the following manner. A second cylindrical tube was concentrically placed around the test chamber in order to form an annular fluid reservoir; water was continually circulated from a constant-temperature bath through this reservoir, then returned to the bath in a closed loop. Temperature along the entire outer circumferential surface of the test region was thereby maintained constant at 21.1°C ± 0.1°C for the present experiments. The two ends of the test region were bounded by 5.08-cm-thick plates of low conductivity material, effectively insulating these two boundaries from heat loss. A thin fluid layer (1 cm in depth) existed between the top of the porous medium and the inside of the upper end plate, thereby defining a constant-pressure/permeable-surface boundary condition at $Z = L$. All other surfaces were impermeable.

As a result of this experimental arrangement, the fluid layer assumed a near-isothermal condition at steady state, with its absolute temperature level being dictated by the power level input to the experiment (see Fig. 2). The measured $T(r)$ distribution at $Z = L$ was then used to supply the code with the required upper-surface thermal boundary condition for each power level tested. The final required thermal boundary condition was dictated by the total electrical power uniformly

Nomenclature

C_p = specific heat at constant pressure (kJ/kg − °C)
d = particle diameter (μm)
$\bar{d}$ = average particle diameter (μm)
g = gravitational constant (9.792 m/s^2)
K = thermal conductivity (W/m − °C)
K_e = effective thermal conductivity of the liquid-bead mixture (W/m − °C)
k = permeability (m^2)
L = test region height (m)
Nu = Nusselt number; see equation (6)
P = heater power per unit length (W/m)
Ra = Rayleigh number; see equation (7)
r = radial coordinate, measured from centerline (m)
Δr = annular gap width ($r_o - r_i$) [m]
T = temperature (°C)
$\bar{T}_i$ = average heater surface temperature (°C); see equation (4)
ΔT = average temperature drop across Δr (°C); see equation (5)
$\bar{T}$ = average temperature for property evaluation (°C); see equation (9)
t = time (min)
Z = vertical coordinate, measured from bottom of test region (m)
α_e = effective thermal diffusivity (m^2/s); see equation (8)
β = volumetric expansion coefficient (1/°C)
μ = viscosity (kg/m − s)
ρ = density (kg/m^3)
σ = standard deviation
ϕ = porosity

Subscripts

f = of fluid phase
i = at the innermost radial location (r_i) of the annular test region
m = of matrix (solid) phase
o = at the outermost radial location (r_o) of the annular test region
0.50 = fifty percentile value

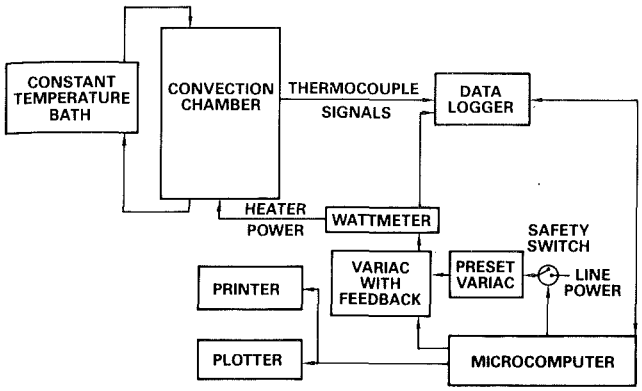

Fig. 3 Schematic of overall experimental arrangement

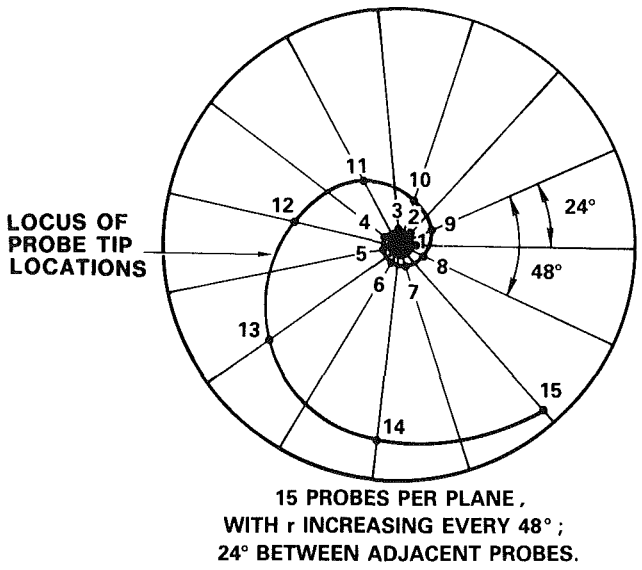

Fig. 4 Probe placement schematic

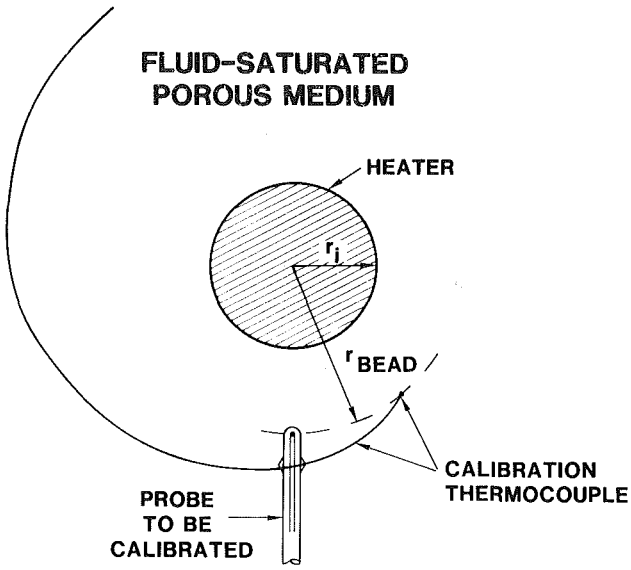

Fig. 5 Probe calibration schematic

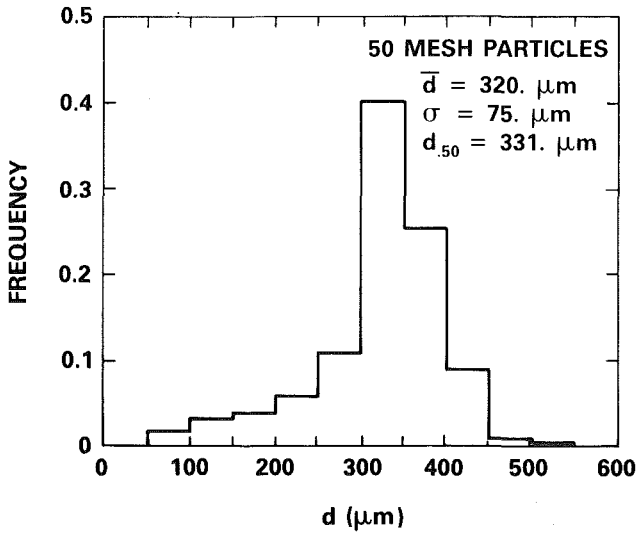

Fig. 6 50 mesh particle-size distribution

dissipated within the resistance heater. For each experiment, a preprogrammed power level was input to the heater, measured by an electronic wattmeter, and held constant (within ±1 percent) through a feedback loop incorporating a microcomputer and a stepping-motor-controlled variac (see Fig. 3).

Temperatures along the upper, lower, and outer boundaries were measured with 24 thermocouples. Temperatures throughout the annular test region were measured by 90 thermocouple probes, 15 placed on each of six measurement planes, located at $Z/\Delta r$ values of 1, 2, 3, 3.5, 3.75, and 4. The ratio of the total volume of all probes located inside the test region, to the volume of the test region itself, was 0.00084. All probes entered the test region radially, one every 24 deg in circumferential angle; probe tip radial distance, measured from the heater centerline, was increased every 48 deg, causing the locus of probe tip locations to form a spiral of ever-increasing radius (see Fig. 4). Measured $T(r)$ distributions obtained from such probe arrays were found to be "smooth and continuous," thereby demonstrating the attainment of axisymmetric conditions.

Probes utilized in the present study were 0.318-cm-o.d. Chromel-Alumel, sheathed, ungrounded thermocouples. The sheath was a thin-walled stainless-steel jacket, itself filled with a low-conductivity powder (magnesium oxide) which completely surrounded both the thermocouple junction and the lead wires. This probe design served to eliminate any potential electrical interference between the heater a-c power signal and the d-c thermocouple signal, while at the same time tending to minimize the effective thermal conductivity of the probe itself. The thermocouple junction was located one probe-tip radius (1.6 mm) away from the physical end of the probe (as determined by X-ray photography), and all measured temperatures were assigned the radial location of the junction itself.

Probe calibration tests were conducted both insitu, as well as in a separate/geometrically-similar apparatus. Flexible sheathed thermocouples of 0.05-cm (0.020 in.) and 0.10-cm (0.040 in.) diameter were used as the "references" (see schematic of Fig. 5). Power input, probe radial location, and matrix particle size were all varied. Results of these tests indicated that for $r_i \le r \le 2$ cm, probe error ranged from ≈ -2 to ≈ -1°C, and for 2 cm $\le r < r_o$, probe error was ≈ -1°C. All data presented here have been corrected accordingly.

Data acquisition was accomplished using the microcomputer (recall Fig. 3). All 114 thermocouple channels, plus the power channel, were monitored through a multichannel data logger upon commands from the computer. Transient temperatures were printed every hour, while steady-state values

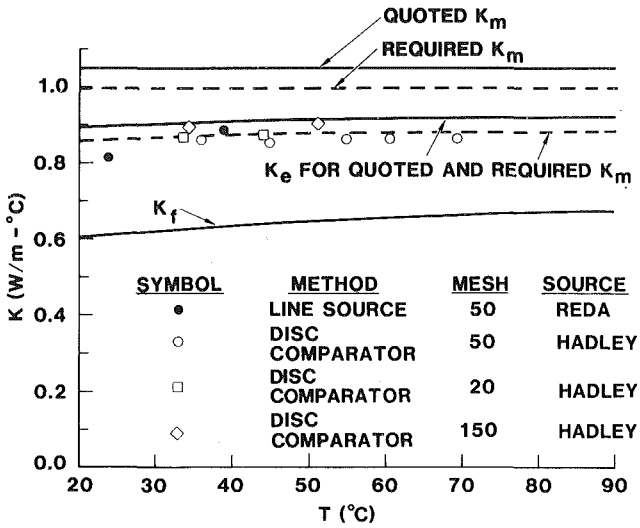

Fig. 7 Thermal conductivities

were both printed and stored on a disk file. Steady state was "achieved" when all temperatures on the $Z/\Delta r = 2$ plane agreed, within ± 0.2°C, with their corresponding values taken over a six-hour period. For each constant power level, approximately 24 hrs was required to reach steady state.

The porous medium used in the present study was comprised of glass beads, essentially spherical, possessing a size distribution as shown by Fig. 6. The average particle size, $\bar{d}$, was noted to be 0.32 mm. The thermal conductivity of the glass, as quoted by the manufacturer, was 1.047 W/m − °C, with no temperature dependence given. Porosity of the medium was measured to be 0.34. Distilled, de-aerated water was used as the working fluid.

The apparatus shown in Fig. 1 was designed so that water could be forced vertically through the porous medium, in situ, and the resultant pressure drop measured. Results so generated defined a medium permeability of 122 Darcies.

Since the heater length-to-diameter ratio was large (≈ 50), it could also be used as a line-source probe [20] in order to measure the effective thermal conductivity (K_e) of the liquid-bead mixture, in situ. For this technique, a low power level was input to the heater (5 W), and the heater "surface" temperature versus time history was recorded (via a thermocouple probe whose tip was in direct physical contact with the heater surface, but whose junction was 1.6 mm radially removed from the heater surface, as described above). The value for K_e was then defined from

$$K_e = \frac{P}{4\pi\left[\frac{dT_i}{d\ln t}\right]} \tag{1}$$

for P = 5.61 W/m. Two such tests were run, yielding an average value for K_e of 0.85 W/m − °C, ± ≈4 percent. Comparisons were made between these results and the mixture model for K_e used in [4, 5], given by

$$K_e = \phi K_f + (1-\phi)K_m \tag{2}$$

For the quoted matrix conductivity of 1.047 W/m − °C, equation (2) was found to overestimate these measured K_e values by ≈ 5 percent. Present data were found, however, to be in good agreement with the previously unpublished data of Hadley [21], for the same glass bead/water mixtures, obtained via the disk-comparator method (see Fig. 7). One may conclude, therefore, that either the quoted matrix conductivity is approximately 5 percent above its true value, or that the mixture model of equation (2) overpredicts K_e by ≈ 5 percent. In either case, to eliminate this thermophysical property uncertainty from the present code qualification exercise, agreement between equation (2) and measured K_e data was forced by redefining $K_m = 0.992$ W/m − °C.

Finally, since the line-source, thermal-conductivity tests were conducted at low power levels, and hence in the absence of any significant convective heat transfer effects, they provided an opportunity to experimentally verify heater output uniformity, in situ. For these conditions, steady-state heater surface temperatures were found to be essentially constant along the length of the heater, thereby indicating a spatially-uniform heat flux.

Numerical Approach

This section presents a brief review of the numerical approach. For complete details, see the reports of [4, 5], available, upon request, from their authors.

The computer code of [4, 5] utilizes Darcy's law as the momentum equation. The porous matrix is assumed to be rigid and in thermal equilibrium with the fluid. Density changes are allowed to occur in the fluid solely in response to changes in temperature. In accordance with the traditional Boussinesq approximation, the effects of such density changes are accounted for in the buoyancy term in the equations of motion and are neglected elsewhere. The fluid is treated as Newtonian, and the effects of viscous dissipation of energy are neglected.

In the present mathematical formulation, the classic no-slip boundary condition at solid surfaces cannot be applied. Flow channeling effects, due to porosity variations (increases) which occur near solid surfaces can be modeled indirectly by specifying a spatially-dependent permeability, e.g., a permeability which increases from its base-line (far-field) value to any prescribed value as a solid surface is approached. Thermal dispersion effects are modeled based on the works of [22, 23].

For purposes of numerical computation, the continuity equation is combined with Darcy's law to provide a Poisson equation for the pressure. A Galerkin form of the finite element method is used to discretize the pressure and energy equations; Darcy's law is similarly discretized to allow the velocity components to be recovered when needed. Within each element, the pressure and temperature are represented by biquadratic basis functions; the velocity components are approximated using bilinear functions. The code allows a choice of isoparametric (curved-sided) or subparametric (straight-sided) quadrilateral (8 node), or triangular (6 node) elements to be used in meshing any particular problem. The coupled set of nonlinear algebraic equations generated by the finite element procedure are solved using a Picard iteration scheme. Reduction of the matrix problem is carried out by a special form of Gauss elimination (frontal solution method).

Experimental Results in Comparison With Numerical Predictions

Measurements of the steady-state thermal field were obtained throughout the porous medium at each of five separate power levels (P = 5.61, 56.1, 84.2, 112.3, and 140.3 W/m). For $P \leq 56.1$ W/m, heat transfer was conduction dominated; at the highest power level of 140.3 W/m, heat transfer was significantly influenced by natural convection.

In order to compare these measurements with numerical predictions, the annular test region ($r_i \leq r \leq r_o$) was modeled by an 8 × 68 finite-element mesh. To allow for heater axial-conduction effects, the cylindrical heater ($0 \leq r \leq r_i$) was modeled by a 1 × 68, finite element mesh with an internal heat generation rate (W/m^3) dictated by the power input level. The resultant total number of elements in the problem

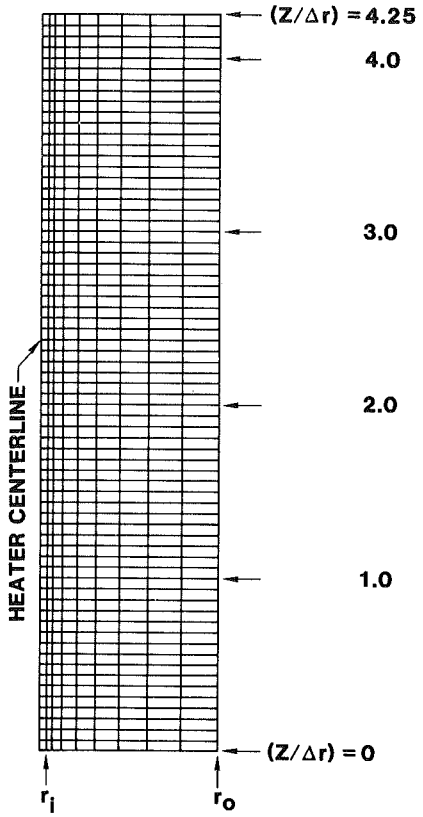

Fig. 8 Finite element mesh

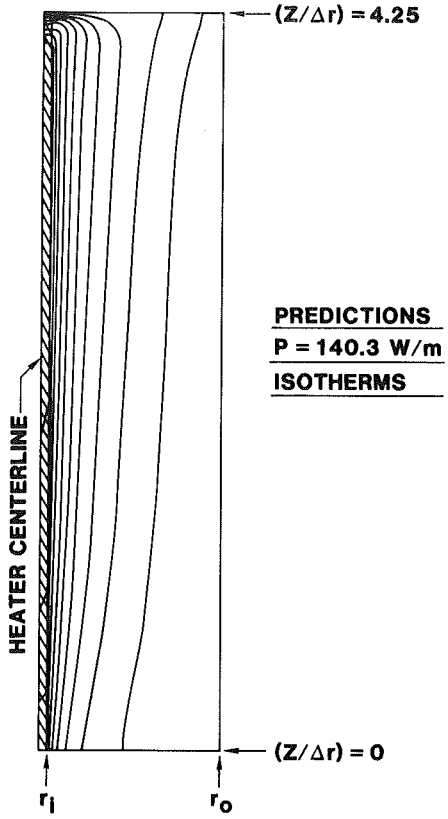

Fig. 10 Predicted isotherms

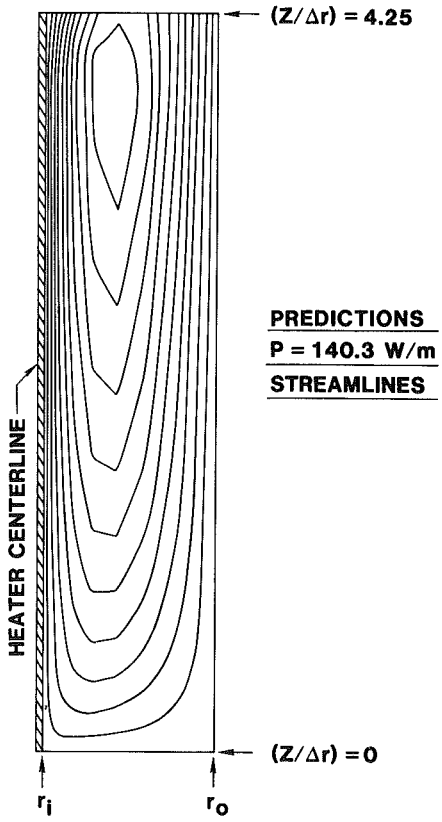

Fig. 9 Predicted streamlines

was 612 (see Fig. 8). Element radial dimensions within the annular test region were continually compressed as r decreased from r_o toward r_i in order to more accurately compute the steeper temperature gradients which occur in the immediate vicinity of the heater. Measured boundary conditions, physical properties for pure water (including viscosity, thermal conductivity, and volumetric expansion coefficient as functions of temperature), and physical properties of the matrix material (including measured values for porosity and permeability) were input to the code of [4, 5] for each power level tested. Computations were done on a CRAY-1 computer, each case taking $\approx$130 s to complete. Predicted streamlines and isotherms for one such case (P = 140.3 W/m) are shown in Figs. 9 and 10, respectively.

As a result of the constant-pressure/permeable-surface boundary condition imposed across the upper surface, essentially all of the streamlines were predicted to be U-shaped, i.e., fluid exited from the porous medium near the heater in a region of buoyantly-driven upflow, while an equal mass flux of fluid entered the porous medium near the outer boundary in a region of downflow. Resultant isotherms were predicted to be relatively parallel throughout the entire porous medium except in the immediate vicinity of the upper surface. Here, temperatures within the fluid/bead mixture were thermally accommodated to match conditions which existed within the near-isothermal fluid layer.

In the limit of a strictly isothermal fluid layer, for infinitely-small element sizes, one would expect the streamlines of Fig. 9 to be perpendicular to the constant-pressure interface for all r values. However, for a near-isothermal fluid layer, with element sizes selected so that predicted temperature distributions throughout the annular space became insensitive to further reductions in element size, plotted streamlines did show small departures from vertical at the interface. These departures occurred at intermediate r values, in the region of flow reversal (from upflow at small r to downflow at large r), where predicted vertical velocity components became exceedingly small. Such streamline plots are obtained by numerically integrating the predicted velocity

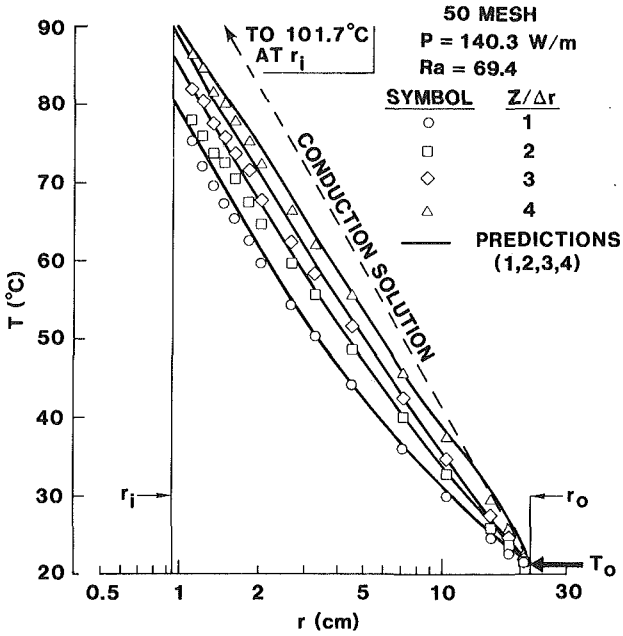

Fig. 11 Data versus predictions, $P = 140.3$ W/m

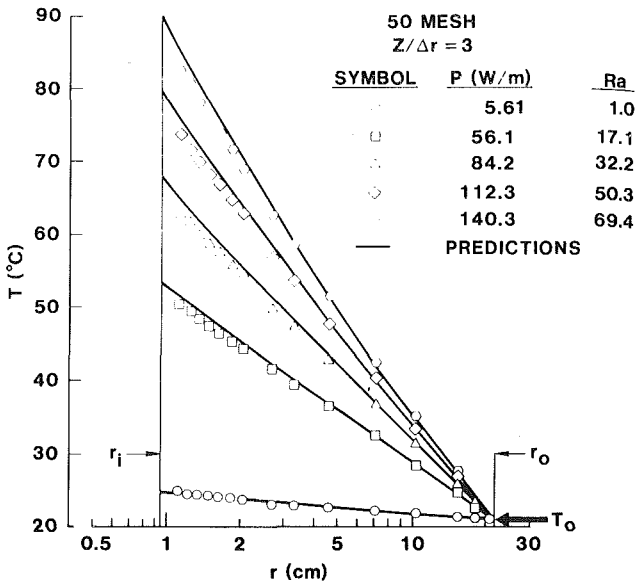

Fig. 13 Data versus predictions, $Z/\Delta r = 3$

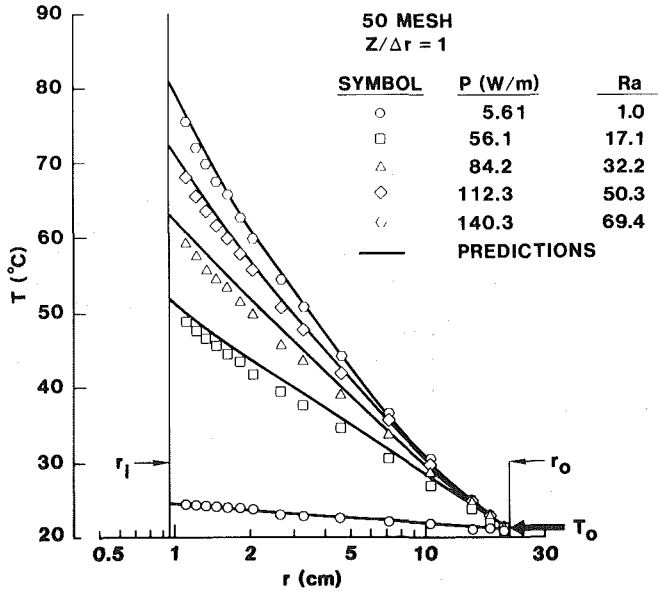

Fig. 12 Data versus predictions, $Z/\Delta r = 1$

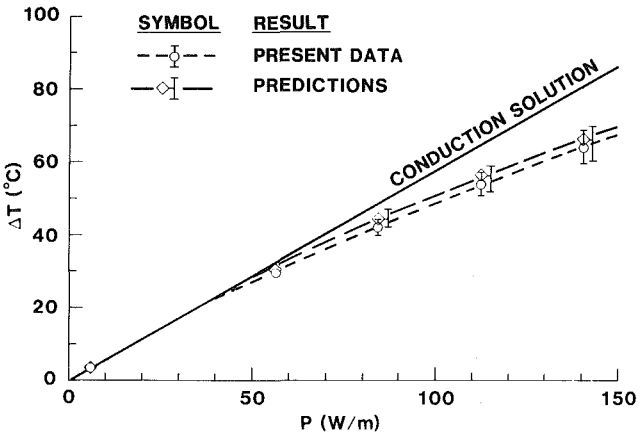

Fig. 14 Average temperature drop versus power input

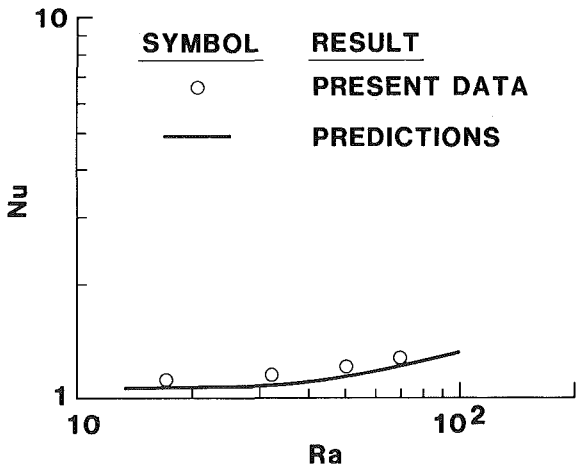

Fig. 15 Nusselt number versus Rayleigh number

field, using linear interpolation between velocities computed at the element corners, and thus supply the analyst solely with a "visual overview" of the predicted flowfield. Predictions of the thermal field within the porous medium were used as the quantitative basis for comparison herein.

Figure 11 shows a comparison of measured and predicted temperature distributions, on four equally spaced $Z/\Delta r$ planes, for a power input of 140.3 W/m. Temperatures measured in the immediate vicinity of the heater surface were seen to increase with increasing vertical distance along the heater, and all measured distributions were noted to be well below the conduction-only solution, providing direct physical evidence of convective-energy transport. Predicted $T(r)$ distributions were found to be in very good agreement with the data.

Figures 12 and 13 show similar comparisons, each for a constant $Z/\Delta r$ plane, with power input as the parameter. For all power levels tested, predicted and measured temperature distributions consistently exhibited the same functional dependence on r and were in very good agreement. Small differences were noted in the innermost portions of the annular test region, primarily on the $Z/\Delta r = 2$ and 3 planes,

where measured temperatures were ≈2 to 3°C below predicted values.

All predictions shown in Figs. 11 through 15 were made assuming no flow-channeling effects at solid surfaces and no thermal dispersion. In order to numerically demonstrate the sensitivity of predicted thermal fields to these effects, additional calculations were made for the highest-power-level case, wherein these separate and combined influences were modeled (recall discussions in the Numerical Approach section). To account for flow channeling, permeability was specified to linearly increase from its measured value to a value twice as large as r decreased towards r_i over a distance of the order of 20 $\bar{d}$. Predicted T_i values were seen to decrease by 0.9°C at $Z/\Delta r = 1$, by 0.8°C at $Z/\Delta r = 2$, by 0.7°C at $Z/\Delta r = 3$, and to remain essentially unchanged at $Z/\Delta r = 4$. Hence, a portion of the minor differences between predicted and measured temperatures can potentially be explained by such a phenomenon. Obviously, more work needs to be done in this area in order to quantify effective permeability increases near solid surfaces. Thermal dispersion effects were found to be unimportant at the low-Rayleigh-number/low-particle-size conditions encountered herein.

Figure 14 presents a plot of temperature difference across the porous medium as a function of power per unit length input to the medium. The solid line represents the conduction-only solution, given by

$$\Delta T = (T_i - T_o) = \frac{P}{2\pi K_e} \ln\left(\frac{r_o}{r_i}\right) \tag{3}$$

where T_i possesses a *single* value for each power level, other quantities held constant.

In the presence of convection, both the measurements and the predictions showed that T_i increases with Z due to the buoyantly-driven upflow along the heater surface. Hence, in order to represent such cases in the present plot, an "average" value was introduced

$$\bar{T}_i \equiv \frac{\sum_{j=1}^{4} T_{i(Z/\Delta r)=j}}{4} \tag{4}$$

where individual T_i values for the data were obtained by extrapolation of the measured T(r) distributions, over a 1.6-mm radial distance, to the heater surface (see again Figs. 11 through 13). ΔT was then defined by

$$\Delta T \equiv (\bar{T}_i - T_o) \tag{5}$$

Measured and predicted ΔT values were plotted as symbols, with "bars" above and below them to represent minimum and maximum T_i values for $1 \leq (Z/\Delta r) \leq 4$. A curve was then faired through the symbols for each case.

As can be seen in Figure 14, the measured and predicted curves for temperature difference ΔT, as a function of power input P, were found to be in very good agreement. Both curves showed an initial departure from the conduction-only solution near $P = 50$ W/m, followed by a steadily-increasing departure as P was increased from ≈50 to ≈150 W/m. Measured results were within ≈2°C of predicted results over this entire range.

Two interpretations of Fig. 14 are possible. Under stated test conditions, power input at r_i was maintained constant, not T_i. Hence, there was no augmentation of the heat transfer rate at r_i due to the presence of convection. Rather, for P = constant, the combined influences of convection and conduction allowed this specified heat flux to be removed at a *lower* ΔT than would have resulted under conduction-only conditions. Thus, one interpretation of Fig. 14 would be to quantify the relative influences of conduction versus convection, for any constant P condition, by the *vertical departure* of the data, and/or the predictions, from the conduction-only solution.

Alternatively, one can view these results in the classic Nusselt number/Rayleigh number framework by defining the dependent variable (i.e., the Nusselt number) as the ratio of the actual power transfered away from the heater to the power which would be transfered away by conduction only *at the measured* ΔT

$$\mathrm{Nu} \equiv \frac{P}{\left[\frac{2\pi K_e \Delta T}{\ln(r_o/r_i)}\right]} \tag{6}$$

In this context, the relative influences of convection versus conduction, for any constant ΔT condition, are quantified by the *horizontal departure* of the data, and/or the predictions, from the conduction-only solution.

The independent variable in this correlating approach is the Rayleigh number, defined here by

$$\mathrm{Ra} \equiv \left[\frac{\rho_f g \beta_f \Delta T k \Delta r}{\mu_f \alpha_e}\right] \tag{7}$$

where

$$\alpha_e = \left[\frac{K_e}{\rho_f C_{p,f}}\right] \tag{8}$$

Results of this correlating approach are shown in Fig. 15, where all fluid properties were evaluated at an average temperature, $\bar{T}$, given by

$$\bar{T} = \left[\frac{\bar{T}_i + T_o}{2}\right] \tag{9}$$

Once again, agreement between experiment and predictions was seen to be quite good, with Nu increasing from ≈1.1 at Ra ≈ 17 to ≈1.25 at Ra ≈ 70.

Therefore, these detailed comparisons of measured and predicted results tend to confirm the code of [4, 5] as a valid predictive tool for problems involving natural convection in a fluid-saturated porous medium. Further experiments, utilizing (*i*) a *finite-length heat source* buried in a uniform porous medium, and (*ii*) the "full-length" heater of the present effort buried in a "*layered*" *porous medium*, are planned in order to further assess the validity and utility of this code.

Conclusions

Based on present measurements, and on comparisons of these measured results with numerically generated predictions, the following observations were made:

(*i*) For a constant-heat-flux thermal boundary condition at the surface of the inner cylinder, heater surface temperature was found to increase with increasing vertical distance due to the presence of a buoyantly-driven upflow.

(*ii*) The measured temperature difference (ΔT) between the average heater surface temperature and the constant outer-surface temperature was found to be progressively below the straight-line/conduction-only solution for ΔT versus power input, as the latter was systematically increased.

(*iii*) Comparisons between measured and numerically predicted results, generated with a finite element code called MARIAH [4, 5], showed very good agreement, thereby contributing to the qualification of this code for repository-design applications.

References

1 Cheng, P., "Heat Transfer in Geothermal Systems," *Advances in Heat Transfer*, Vol. 14, 1978, pp. 1-105.

2 Combarnous, M. A., and Bories, S. A., "Hydrothermal Convection in Saturated Porous Media," *Advances in HydroScience*, Vol. 10, 1975, pp. 231-307.

3 Combarnous, M. A., "Natural Convection in Porous Media and

Geothermal Systems," *Proceedings of the 6th International Heat Transfer Conference*, Vol. 6, Aug. 1978, pp. 45-59.

4 Gartling, D. K., and Hickox, C. E., "MARIAH—A Finite Element Computer Program for Incompressible Porous Flow Problems, Part I—Theoretical Background," Sandia National Laboratories, Technical Report SAND79-1622, 1982.

5 Gartling, D. K., and Hickox, C. E., "MARIAH—A Finite Element Computer Program for Incompressible Porous Flow Problems," Sandia National Laboratories, Technical Report SAND79-1623, August 1980.

6 Gartling, D. K., "Finite Element Analysis of Thermal Convection in Deep Ocean Sediments," *Proceedings of the 3rd International Conference on Finite Elements in Water Resources*, University of Mississippi, 1980, pp. 7.30-7.44.

7 Hickox, C. E., Gartling, D. K., McVey, D. F., and Russo, A. J., "Analysis of Heat and Mass Transfer in Subseabed Disposal of Nuclear Waste," *Proceedings of the Annual Meeting, Marine Technology Society*, Washington, D.C., Oct. 1980, pp. 557-566.

8 Eaton, R. R., and Reda, D. C., "The Influence of Convective Energy Transfer on Calculated Temperature Distributions in Proposed Hard-Rock Nuclear Waste Repositories," *Radioactive Waste Management Journal*, Vol. 2, June 1982, pp. 343-361.

9 Schneider, K. J., "Investigation of the Influence of Free Thermal Convection on Heat Transfer Through a Granular Material," *Proceedings of the 11th International Congress of Refrigeration*, Munich, W. Germany, 1963, pp. 247-254.

10 Buretta, R. J., and Berman, A. S., "Convective Heat Transfer in a Liquid Saturated Porous Layer," ASME *Journal of Applied Mechanics*, Vol. 98, June 1976, pp. 249-253.

11 Bories, S. A., and Combarnous, M. A., "Natural Convection in a Sloping Porous Layer," *Journal of Fluid Mechanics*, Vol. 57, 1973, pp. 63-79.

12 Seki, N., Fukusako, S., and Inaba, H., "Heat Transfer in a Confined Rectangular Cavity Packed with Porous Media," *International Journal of Heat and Mass Transfer*, Vol. 21, July 1978, pp. 985-989.

13 Acasio, U. A., "An Experimental Study of Natural Convection Heat Transfer in Vertical Porous Media," Ph.D. thesis, Dept. of Grain Science and Industry, Kansas State University, 1979.

14 Elder, J. W., "Steady Free Convection in a Porous Medium Heated from Below," *Journal of Fluid Mechanics*, Vol. 27, 1967, pp. 29-48.

15 Bau, H. H., and Torrance, K. E., "Low Rayleigh Number Thermal Convection in a Vertical Cylinder Filled with Porous Materials and Heated from Below," JOURNAL OF HEAT TRANSFER, Vol. 104, February 1982, pp. 166-172.

16 Masuoka, T., Ishizaka, K., and Katsuhara, T., "Heat Transfer by Natural Convection in Porous Media Between Two Concentric Spheres," *Natural Convection in Enclosures*, HTD-Vol. 8, ASME 19th National Heat Transfer Conference, Orlando, Fla., July 1980, pp. 115-120.

17 Cheng, P., and Ali, C. L., "An Experimental Investigation of Free Convection About a Heated Inclined Surface in a Porous Medium," ASME Paper No. 81-HT-85, 20th Joint ASME/AIChE National Heat Transfer Conference, Milwaukee, Wis. Aug. 1981.

18 Huenefeld, J. C., and Plumb, O. A., "A Study of Non-Darcy Natural Convection From a Vertical Heated Surface in a Saturated Porous Medium," ASME Paper No. 81-HT-45, 20th Joint ASME/AIChE National Heat Transfer Conference, Milwaukee, Wis., Aug. 1981.

19 Wooding, R. A., "An Experiment on Free Thermal Convection of Water in Saturated Permeable Material," *Journal of Fluid Mechanics*, Vol. 3, 1958, pp. 582-600.

20 Tanaka, S., and Miyazawa, M., "The Measurement of Thermal Conductivity of Porous Media by a Needle Probe Method," *Energy Developments in Japan*, Vol. 2, 1979, pp. 375-391.

21 Hadley, G. R., personal communication, Sandia National Laboratories, Albuquerque, N.M., June 1982.

22 Kvernvold, O., and Tyvand, P. A., "Dispersion Effects on Thermal Convection in Porous Media," *Journal of Fluid Mechanics*, Vol. 99, 1980, pp. 673-686.

23 Saffman, P. G., "Dispersion Due to Molecular Diffusion and Macroscopic Mixing in Flow Through a Network of Capillaries," *Journal of Fluid Mechanics*, Vol. 7, 1959, pp. 194-208.

Natural Convection in a Rectangular Porous Cavity With One Permeable Endwall

M. Haajizadeh
Graduate Research Assistant.

C. L. Tien
Professor.
Fellow ASME

Department of Mechanical Engineering,
University of California,
Berkeley, Calif. 94720

This paper describes a theoretical and experimental study of two-dimensional, buoyancy-driven flow in a rectangular porous cavity with one permeable endwall. Connected to a constant temperature tank, the permeable end allows for natural recharge and discharge of the saturating fluid. The other vertical endwall is impermeable and maintained at a constant but higher temperature, thus inducing a buoyancy-driven flow. The theoretical study includes an asymptotic analysis developed for a shallow cavity with one permeable endwall and the numerical solutions of the power-law difference representation of the full governing equations. The experimental system consists of water-saturated glass beads packed in a rectangular cavity with a length-to-height aspect ratio of 3.17, for which the Rayleigh number can vary up to 120. Measurements were made of the steady-state temperature distribution in the cavity and the heat transfer rate from the impermeable endwall. It is shown that the constant pressure and temperature assumptions at the permeable wall, as employed in the theoretical analysis, satisfactorily predict the experimental data. Results are also compared with those existing in the literature.

Introduction

Owing to its numerous and wide-ranging applications natural convection in porous media has been the subject of many recent studies. For example, this phenomenon is encountered in the underground spreading of chemical wastes, water movement in geothermal systems, and porous insulations. Most of the previous studies have been theoretical, including natural convection in confined enclosures driven by horizontal temperature gradients [1–3], natural convection boundary layers [4], and convective flows in horizontal porous layers heated from below [5]. However, consideration of the permeable boundary effects on the heat transfer rate and the temperature distribution is rather limited [6–8]. Recently, Bejan and Tien [9] developed an approximate analytical solution of the flow and heat transfer in a shallow porous cavity with vertical permeable walls subjected to an end-to-end temperature difference. The validity of this approximate model, particularly concerning its treatment of permeable boundaries needs further examination.

In the present work, the asymptotic solutions for a shallow cavity along with the numerical and experimental results are presented for the problem originally considered by Bejan and Tien [9], for an aspect ratio of 3.17 and Rayleigh numbers up to 120. The physical model, Fig. 1, consists of a two-dimensional cavity filled with a saturated porous medium. One vertical side of the cavity is maintained at a constant temperature, T_h, while the other end is open to a fluid tank at a constant but lower temperature T_c ($T_c < T_h$); the horizontal walls are assumed to be insulated. Of specific interest in this investigation are the temperature distribution in the cavity and the heat transfer from the hot side to the tank.

Formulation of the Mathematical Problem

The model configuration and the coordinate system (x,y) are shown in Fig. 1. The flow is assumed to be steady and two-dimensional. The horizontal walls of length, l, are insulated. The impermeable endwall is held at a fixed temperature, T_h, while the other end of the porous cavity is connected to a constant temperature tank. The cavity height is h, and the tank temperature is kept at T_c ($T_c < T_h$). The impermeable walls allow no mass flux through the boundaries, while the permeable wall is assumed to be maintained at hydrostatic pressure. The dimensionless form of the governing equations are

$$\partial u/\partial x + \partial v/\partial y = 0 \tag{1}$$

$$u = -\partial p/\partial x \tag{2}$$

$$v = -\partial p/\partial y + \mathrm{R}T \tag{3}$$

$$u\frac{\partial T}{\partial x} + v\frac{\partial T}{\partial y} = \frac{\partial^2 T}{\partial x^2} + \frac{\partial^2 T}{\partial y^2} \tag{4}$$

$$u = \partial\psi/\partial y \quad v = -\partial\psi/\partial x \tag{5}$$

with the conditions

$$p = 0, \quad T = 0 \quad \text{on} \quad x = 0 \tag{6a}$$

$$u = 0, \quad T = 1 \quad \text{on} \quad x = L \tag{6b}$$

$$v = 0, \quad \partial T/\partial y = 0 \quad \text{on} \quad y = 0,1 \tag{6c}$$

Here, u and v are the dimensionless horizontal and vertical components of the Darcy's velocity vector, ψ is the steam function, $T = (T' - T_c)/(T_h - T_c)$, where T' is the dimensional temperature, $p = [p' - p_c + \rho_c hg(y - 1/2)]/(\mu\alpha/\kappa)$ where p' is the dimensional pressure, and p_c is the mean pressure of the open side of the cavity, $\mathrm{R} = (g\beta h\kappa\Delta T)/\nu\alpha$ is the Rayleigh number based on permeability,

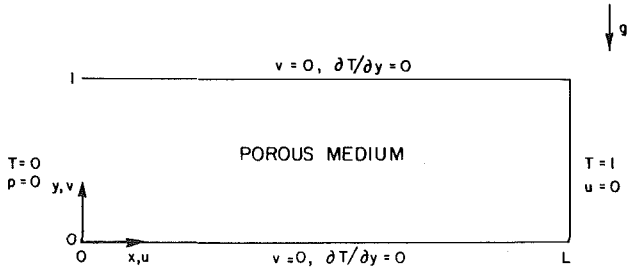

Fig. 1 Schematic of two-dimensional horizontal cavity

Contributed by the Heat Transfer Division for publication in the JOURNAL OF HEAT TRANSFER. Manuscript received by the Heat Transfer Division November 5, 1982.

and $L = l/h$ is the length-to-height aspect ratio. Lengths have been scaled by h, velocities by α/h, ν is the fluid kinematic viscosity, κ the permeability, β the coefficient of volume expansion, g the gravitational acceleration, α the effective thermal diffusivity and $\Delta T = T_h - T_c$. Darcy's law and the Boussinesq approximation have been invoked. The dimensionless heat transfer is characterized by the Nusselt number defined by

$$N = L\int_0^1 (\partial T/\partial x - uT)\,dy \tag{7}$$

Asymptotic Solution for $L \to \infty$

For a long cavity with fixed R, the problem can be solved by matched asymptotic expansions, and a treatment similar to that used by Walker and Homsy [2] can be employed. As the length of the cavity increases for a fixed R the resistance forces in the core become more important for establishing the flow structure. In this limit the core flow is driven mainly by the horizontal temperature gradient, the streamlines in the core are parallel to the horizontal walls, and the temperature profiles in the core are self-similar. By setting $v = 0$ in equations (1) to (4), the core solution can be obtained as [2, 9]

$$v_o = 0 \tag{8}$$

$$u_o = CR(1/2 - y)/L \tag{9}$$

$$p_o = CR(y - 1/2)x/L + C^2R(y^3/12 - y^4/24)/L^2 + Dy + E \tag{10}$$

$$T_o = Cx/L + D + C^2R(y^2/4 - y^3/6)/L^2 \tag{11}$$

The constant E can be eliminated in favor of C and D, by noting that

$$\int_0^1 p\,dy = 0:$$

$$E = -D/2 - C^2R/80L^2 \tag{12}$$

Thus, the solutions in the core are given in terms of the two unknown constants of integration, C and D. From equation (11), it is clear that the constant C is the core temperature gradient. Substituting equations (9) and (11) into the Nusselt-number definition, equation (7), and integrating yields

$$N = C(1 + R^2C^2/120L^2) \tag{13}$$

Therefore, having the expression for C, the Nusselt number can be evaluated.

The core solutions (8–11) are not uniformly valid and they break down near the end walls where the flow should either turn or submit to the connected reservoir (tank) condition. The details of the end-region flows, together with the matching of them with the core flow, will determine the unknown constants, C and D.

The solution procedure for the impermeable end region is similar to that in [2]. However, due to the asymmetry of the flow, the condition $T(1/2, 1/2) = 1/2$ cannot be used, and matching with the solutions valid in the permeable end region must be considered. The treatment for the permeable end region is the same as that given by Haajizadeh [10]. Finding the end-region solutions and matching with the solution in the core, one can find C and D as follows:

$$C = 1 - 23SR^2/\pi^7L^3 + 0(1/L^4) \tag{14}$$

$$D = -R/24L^2 + 8SR^2/\pi^7L^3 + 0(1/L^4) \tag{15}$$

where S is formally obtained as

$$\sum_{n=0}^{\infty} (2n+1)^{-7},$$

but for all practical purposes, it can be taken as one.

Substituting for C into equation (13), an expression for the Nusselt number can be obtained as

$$N = 1 + \frac{R^2}{L^2}\left(\frac{1}{120} - \frac{23}{\pi^7 L}\right) + 0(1/L^4) \tag{16}$$

By comparing equation (16) with the results given in [2, 10], it is seen that to $0(1/L^3)$ as $L \to \infty$ with fixed R, each permeable end increases the Nusselt number by $7R^2/\pi^7L^3$.

Numerical Procedure

To obtain the numerical solution to the equations (1) to (16), a finite difference system was used. The numerical code used for solving the present problem was a modified version of the existing code used for solving the problem with pressure-specified boundary conditions. Eliminating the velocity components from equations (2) and (3), results in a Poisson equation for pressure as

$$\partial^2 p/\partial x^2 + \partial^2 p/\partial y^2 = R\partial T/\partial y \tag{17}$$

The finite difference form of the foregoing equation, along with the energy equation and the boundary conditions, were solved by successive-relaxation method. The computation was achieved by a CDC-7600 computer. The power-law difference

Nomenclature

C = horizontal temperature gradient
D,E = constants
g = gravitational acceleration
h = height
k = effective thermal conductivity
l = length
L = aspect ratio, $L \equiv l/h$
n = dummy index
N = Nusselt number
p = dimensionless pressure
p_c = cold-side mean pressure
q = axial heat transfer rate
R = Rayleigh number, $R = g\beta h\kappa\Delta T/\nu\alpha$
S = constant
T = dimensionless temperature, $T = (T' - T_c)/(T_h - T_c)$
T_c = cold-side temperature
T_h = hot-side temperature
T_m = mean temperature, $T_m = (T_h + T_c)/2$
u,v = dimensionless horizontal and vertical velocities
w = width in z-direction
x,y = horizontal and vertical distances
α = effective thermal diffusivity
β = thermal expansion coefficient of the fluid
ΔT = temperature difference, $\Delta T = T_h - T_c$
ϵ = criterion for numerical convergence
θ = dimensionless temperature, equation (20)
κ = permeability
μ = absolute viscosity
ν = kinematic viscosity
ρ = fluid density
ρ_c = fluid density at T_c
σ = criterion for numerical convergence
ϕ = any dimensionless variable, u, v, p, or T
ψ = dimensionless stream function, $\psi = \int_0^y u\,dy$

Subscripts

c = pertaining to the cold side
h = pertaining to the hot side
m = mean
max = maximum
o = pertaining to the core region

Superscripts

$'$ = dimensional quantities

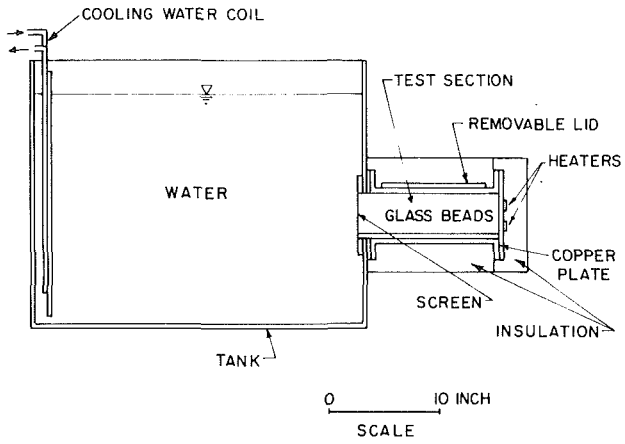

Fig. 2 Schematic of experimental apparatus

scheme [11] was incorporated along with a variable grid size. Although somewhat slower than the scheme with the stream function as the dependent variable, the present scheme has proved to be satisfactory.

The T, p, u, v fields were advanced iteratively one at a time until final convergence. The convergence criteria for all field variables were

$$|\phi_{new} - \phi_{old}|_{max} \leq E$$
$$|N_{new} - N_{old}| \leq \sigma \tag{18}$$

where ϕ stands for any of the field variables and max denotes the maximum value over all the grid points. The values for ϵ and σ were taken to be 10^{-4} and 10^{-4}. A check was also made of the overall energy for mass balances for the cavity; for all runs these balances were satisfied within 2 percent. Stream function values were calculated from the converged field. The accuracy of the scheme was also checked by decreasing the grid spacing and observing the change in the value of the Nusselt number.

For faster convergence, the energy equation was overrelaxed while the pressure equation was underrelaxed. The relaxation parameters for T and p were taken to be 1.1 and 0.9, respectively. Moreover, after each iteration the pressures are corrected in order to satisfy the zero net pressure condition,

$$\int_0^1 p dy = 0.$$

For all runs, a nonuniform grid of 41 × 21 points yielded sufficiently accurate results.

Since the pressure derivatives were prescribed on three boundaries, the convergence was slow and a run with R = 64 and a nonuniform grid of 81 × 51 points took 4000 iterations to converge and 200 computing seconds on CDC-7600 computer.

It should be noted that, although the power-law scheme is stable for a single equation like equation (4), the overall numerical iteration may not converge due to the coupling existing between the different equations.

Experimental Apparatus

The experimental setup constructed for this study, Fig. 2, consisted of a cavity, a tank, a heated copper plate, a cooling coil, a power supply system, and a temperature measurement system. The rectangular cavity is 9.53-cm deep, 30.16-cm long, and 30.48-cm wide. It was made of 1.27-cm-thick plexiglass sheet, and the heated surface was mounted on one of the vertical sides of the cavity. The top of the cavity was made of removable lid for inserting the glass beads inside the cavity. The saturating fluid was filtered tap water; the porous matrix which filled the cavity was composed of glass beads of approximately spherical shape (80 percent round by roundometer) and an average diameter of 2 mm (2.36–1.7 mm sieve opening) manufactured from lead-free, soda-lime silica glass. The permeability of the beads was experimentally determined to be 1.165×10^{-9} m^2 ± 5 percent. This was determined by running water at known constant rates through a packed bed of glass beads and measuring the corresponding steady-state pressure drops across the bed. The stagnant thermal conductivity of the glass beads saturated with water was measured to be k = 0.95 W/mK ± 7 percent. The same porosity was used in the experiment and the above measurements; therefore, the experimental permeability and the effective thermal conductivity used in calculations should be close to the measured values. To prevent falling of the glass beads into the tank a 30-mesh (0.3-mm wire) screen was mounted at the open side of the cavity. The heating plate, 40.64-cm long and 20.32-cm wide, was made of 1.27-cm-thick copper. There were five thermocouples located at 0.79 mm from the heating surface in contact with the glass beads. The copper plate was heated by two independent 175W mica strip heaters 0.48-cm thick, 30.48-cm long, and 2.54-cm wide. To ensure isothermal condition of the copper plate, power inputs to the heaters were controlled separately and the input power to each heater was measured by ammeter and voltmeter. Thus a uniform temperature surface was produced to ± 0.3°C for all of the reported experimental results. The rectangular tank is 60.96-cm deep, 76.2-cm long, and 60.96-cm wide and was made of 1.27-cm-thick plexiglass sheet. In order to attain a steady-state condition, a copper tube heat exchanger was placed inside the tank.

The experimental temperature profiles inside the porous cavity were found by using over one hundred thermocouples made of 0.254-mm (0.01-in.) copper-constantan wire. The thermocouple network was arranged in a cartridge form consisting of two 1.27-cm-thick parallel vertical walls connected by a 0.64-cm-thick plexiglass sheet. The thermocouples were mounted horizontally through holes drilled into the two opposing cartridge walls so they were placed horizontally inside the glass beads in parallel with the heated surface. The cartridge was then placed inside the cavity. All the thermocouple wires had Teflon coating for electrical insulations. To check the two-dimensionality of the flow field, six thermocouples were used in the lateral direction. Experimental results show that the temperature in the lateral direction is uniform to ± 0.3°C. A digital thermometer was used to read the temperature directly from the voltage outputs of the thermocouples.

After steady-state conditions had been achieved and the temperature of the copper plate had become constant with ± 0.5°C, the power inputs to the heaters and the outputs of the thermocouples were recorded. To check the consistency of the measurements a few data points were repeated.

Results and Discussion

In this section, the experimental results are presented and compared with those predicted by the theoretical model based on constant properties. The Rayleigh number is defined based on the maximum temperature difference encountered in the cavity ($T_h - T_c$) where T_h is the copper plate temperature and T_c is the temperature measured at the starting corner ($x = 0, y = 0$) where the flow enters the cavity. The properties of the medium were evaluated at the mean temperature $T_m = (T_h + T_c)/2$.

Typical temperature data plotted in terms of dimensionless temperature T versus dimensionless distance x at different depths are shown on Fig. 3, for R = 30 and 64; the solid lines are the numerically predicted results. These figures show that in the central part of the cavity the temperature distribution at

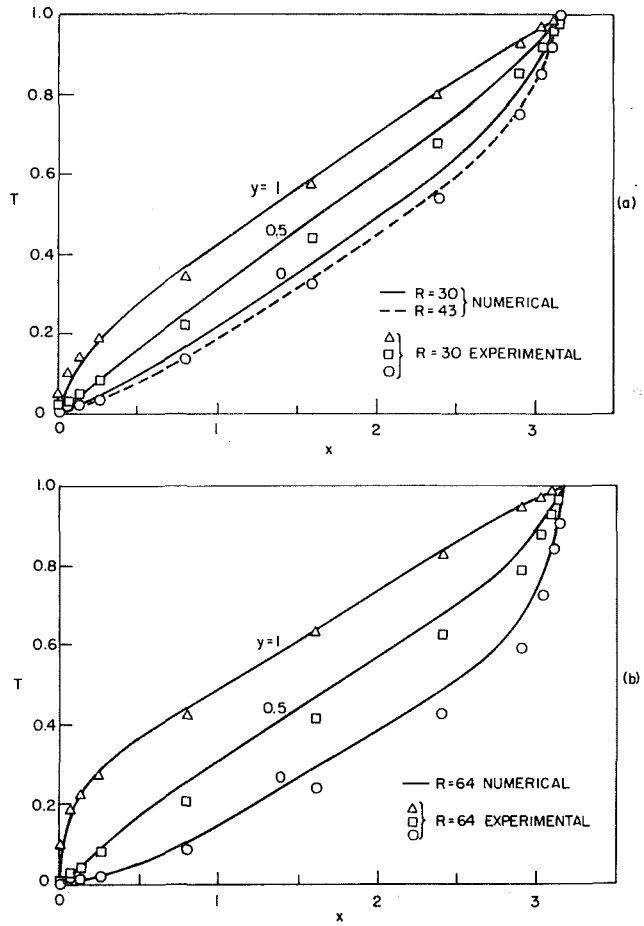

Fig. 3 Horizontal temperature profiles at different depths: (*a*) R = 30 and (*b*) R = 64

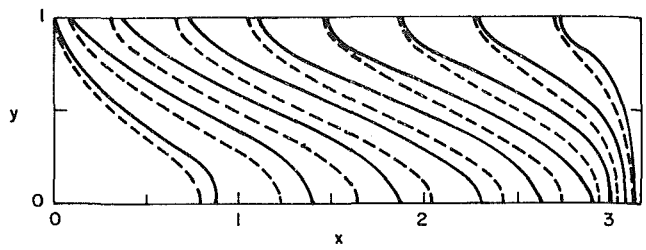

Fig. 4 Plot of isotherms for R = 64; —— experimental; · · · numerical. Isotherms are equally spaced between zero on the left and one on the right boundary.

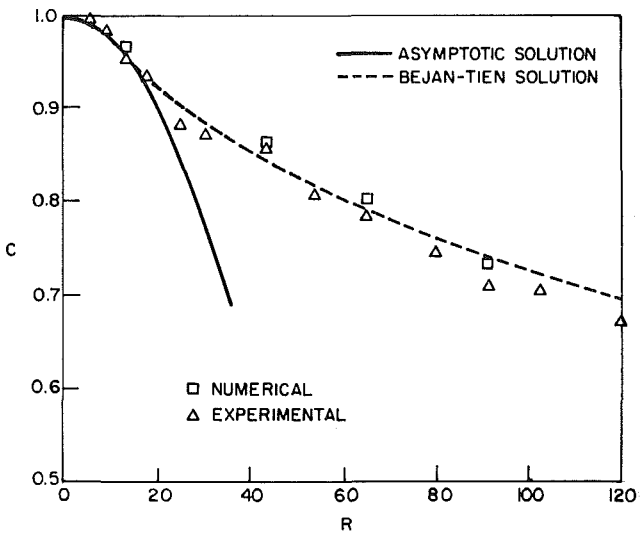

Fig. 5 Nondimensional average core temperature gradient versus the Rayleigh number

different depths are linear and parallel in agreement with the theoretical results, with deviation from this structure near the vertical boundaries where the flow should turn (hot wall) or submit to the reservoir condition. The deviation of the measured from the numerically predicted values is within 8 percent. Although the dependence of viscosity and other fluid properties on temperature and uncertainties with regard to the exact values of the thermal conductivity and permeability are partly responsible for this deviation, the major contributing factor is the thermal conductivity dependence on temperature, since the main driving mechanism for the flow is the initial conduction profile. The thermal conductivity of glass decreases with increasing temperature; therefore, the temperature gradient in the hot-end region becomes higher to maintain the total heat transfer constant. This sharper gradient causes the flow to move faster and consequently the apparent Rayleigh number for the flow entering the hot-end region is higher than the defined Rayleigh number based on constant properties. The dashed line in Fig. 3(*a*) is the numerically predicted temperature distribution at $y = 0$ for R = 43. As it can be seen, this prediction based on the higher Rayleigh number agrees better with the experimental results for R = 30, based on the mean temperature. This fact is also clear from Fig. 4 which shows the isotherms for R = 64. The solid lines are the experimental results, while the dashed lines are numerically predicted isotherms. Because the initial conduction profile is nonlinear and has steeper gradient near the hot wall, all the experimental isotherms shift towards the hot wall. On the other hand, nonuniform shifting of the isotherms may be attributed to the dependence of other properties (besides k) on temperature and the uncertainty with regard to the experimental value of the Rayleigh number. In the central region of the cavity, however, the isotherms are almost parallel and uniformly spaced, in concordance with the theoretical results. The agreement between the numerically predicted isotherms and those experimentally measured is better for the hot stream which flows along the negative horizontal direction.

Comparing Figs. 3(*a*) and 3(*b*), it can be seen that increasing the Rayleigh number results in lower temperature gradients in the core region indicating the relative importance of the convective heat transfer compared to the heat transfer by conduction.

The temperature at the open end of the cavity is fairly constant, except for the very top where the flow leaves the cavity at relatively higher velocities. (The vertical conduction through the screen helps to make the open-end temperature distribution uniform; however, the experimental data indicate that the screen does not disturb the cavity temperature distribution significantly.) In this region, due to the higher convective rates, the tank condition cannot effectively diffuse into the cavity; consequently, the flow does not submit to the tank temperature. However, the discharged flow from the cavity rise like a plume inside the tank and creates a thin boundary layer across which the temperature drops from the temperature of the discharged flow at the opening to that of the tank. Thus, for the theoretical solutions of this type of problems constant temperature (and hydrostatic pressure) at the open boundaries yields reasonable results, although in principle the tank and the cavity flows are coupled.

For cross sections where the temperature lines were parallel, value of the core temperature gradient, C, was determined by averaging all the nine gradients involved. Figure 5 shows the plot of the average core temperature gradient found from experimental data by the foregoing method, along with the

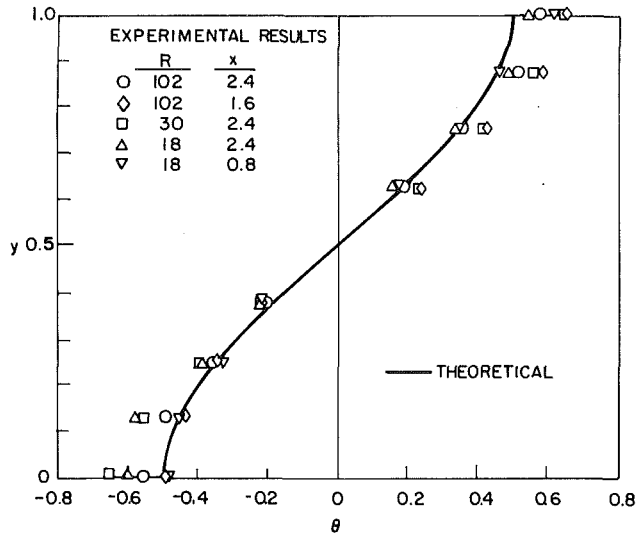

Fig. 6 Nondimensional temperature versus vertical distance at different stations, for different values of the Rayleigh number

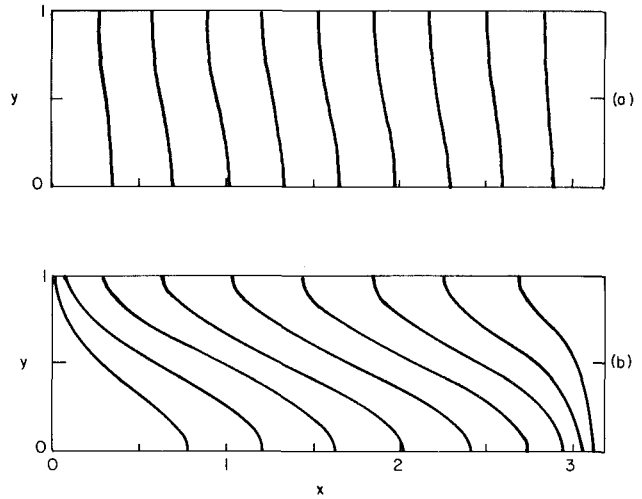

Fig. 7 Numerically predicted isotherms. Isotherms are equally spaced between zero on the left and one on the right boundary: (*a*) R = 5 and (*b*) R = 64.

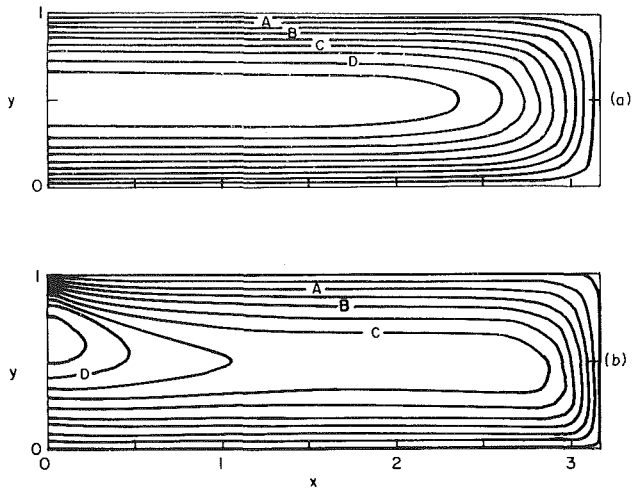

Fig. 8 Numerically predicted steamlines: (*a*) R = 5; *A* = 0.04, *B* = 0.08, *C* = 0.12, *D* = 0.16, and (*b*) R = 64; *A* = 0.63, *B* = 1.26, *C* = 1.87, *D* = 2.49

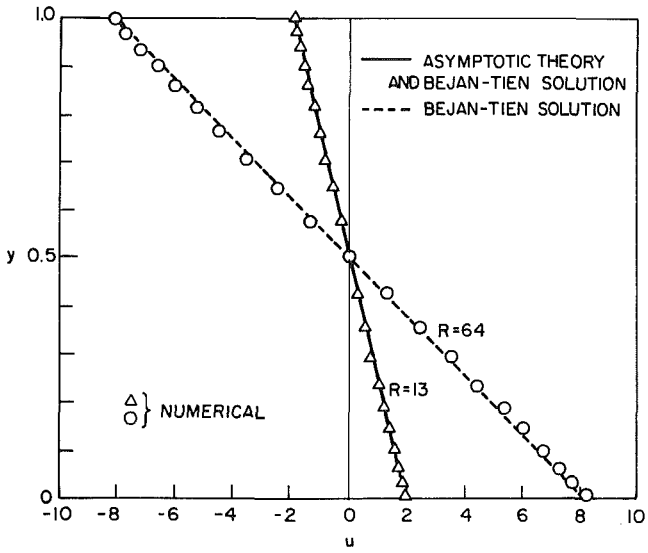

Fig. 9 Comparison of numerical and analytical predictions for horizontal velocity distribution on the vertical midplane

asymptotic (solid line) and numerical results; the dashed line in the figure shows the reported approximate analytical solution [9]. From the preceding asymptotic solution, it is clear that for a shallow cavity the core temperature gradient plays an important role. Having the core temperature gradient, one can find the total heat transfer through the cavity and the velocity and the temperature distribution in the core. Figure 5 indicates that even for this small aspect ratio (L = 3.17) the asymptotic theory result for R $\lesssim$ 20 is in good agreement with the numerical and experimental results. The Bejan-Tien results [9] concur with the experimental results in the range considered here. Increasing the Rayleigh number results in lower temperature gradients in the core region, and as the Rayleigh number tends towards infinity the core temperature gradient approaches zero. In this limit the heat transfer between the plate and the tank is dominated by convection while the conduction heat transfer is confined in thin regions near the vertical boundaries.

Equation (11) can be rewritten as

$$\theta = 3y^2 - 2y^3 - 1/2 \tag{19}$$

where

$$\theta = (12L^2/C^2\mathrm{R})[T(x,y) - T(x,1/2)] \tag{20}$$

Figure 6 shows the plots of the quantity θ for different Rayleigh numbers at different horizontal locations. The experimental points were obtained by inserting the experimental data in the right-hand side of equation (20); equation (19) is indicated by the solid line. The experimental results agree fairly well with the theoretical curve. The numerical solutions based on the average core temperature gradient lie on the solid line for the range considered, i.e., up to R = 64. It is conjectured that the deviation is partly due to the variable properties of the medium, conduction through the walls, and the experimental errors (the accuracy in experimental R being within 12 percent).

Figures 7 and 8 present numerically calculated isotherms and streamlines for two different values of the Rayleigh number R = 5 and 64. For R = 5, the dependence of the vertical temperature profiles on the vertical position, y, is insignificant. The constant temperature gradient induces a parallel flow in the core region with a weak intensity, which almost does not disturb the conduction temperature distribution. Consequently, the parallel counterflow in the core extends all the way to the open end of the cavity and flow recirculates only near the impermeable wall. On the other hand, for R = 64, due to the higher driving force (higher R)

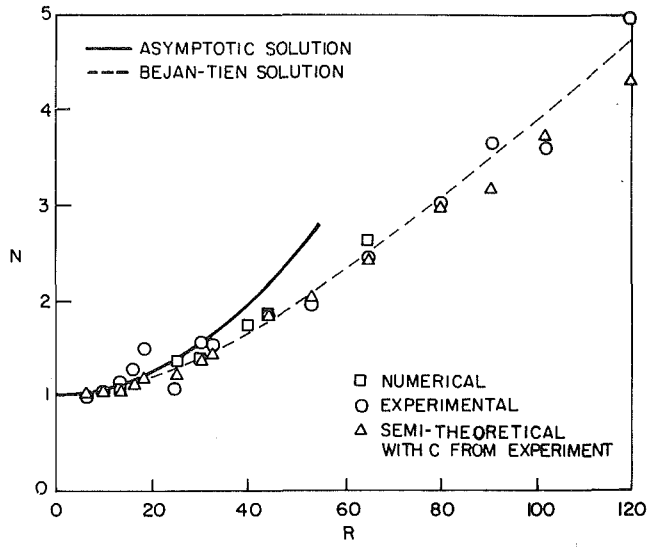

Fig. 10 Variation of the Nusselt number with the Rayleigh number

the induced flow has higher intensity and perturbs the conduction temperature distribution remarkably, Fig. 7(*b*). In this case, due to the compression of isotherms in the discharge area of the cavity, the outgoing flow accelerates and creates a reverse flow at the open end region. As the Rayleigh number increases, the reverse flow penetrates further into the central part of the cavity, while the recirculation at the hot wall is confined in a smaller region near the hotwall. Figure 8(*b*) shows that for R = 64, three-tenths of the flow streamlines reverse and do not penetrate significantly into the cavity; while for R = 5, all of the recharged flow streamlines recirculate only in the hot-end region.

In Fig. 9, numerically calculated and analytically predicted horizontal velcoity distributions at the vertical centerline of the cavity are compared. For R = 13, the asymptotic theory (solid line) agrees well with the numerical results; the Bejan-Tien results [9] also lie on the solid line. For R = 64, the numerically predicted velocity profile validates the approximate solutions indicated by the dashed line [9].

Heat Transfer Results. The net heat transfer between the hot wall and the tank through the horizontal cavity is presented in Fig. 10. The Nusselt number in terms of the overall heat transfer is

$$N = \frac{q}{khw(\Delta T/l)} \tag{21}$$

where q is the net heat transfer rate and w is the cavity width. The net heat transfer rate, q, is equal to the power input into the heaters minus a correction attributed to the heat loss. To quantify this correction, a separate experiment was conducted. For this experiment, the water was drained, so the inside of the cavity was insulated by the glass beads-air mixture; therefore, the heat input to the heaters was almost totally lost to the ambient. The heat input was then correlated with the copper plate-ambient temperature difference. Thus, an estimate of the heat loss by approximating the heat loss encountered during the main experiments with the correlation obtained from the auxiliary ones was acquired, and the Nusselt number was evaluated by using equation (21).

The figure shows the experimental heat transfer results along with the theoretical predictions. From the experimental average core temperature gradient, C, and equation (13), one can also estimate the Nusselt number; the values evaluated by this method are also shown in Fig. 10.

The asymptotic results predict the heat transfer for R $\lesssim$ 20. For higher values of R, however, higher order corrections become important and equation (16) becomes less accurate, while in the range covered in the present study, the numerical predictions and the approximate analytical results [9] are in accord with the experimental data. The small discrepancies between the two aforementioned experimental Nusselt numbers for higher values of R may be attributed partly to the deviation from the parallel flow structure in the core region. Moreover, the hump in the experimental data in the vicinity of R ~ 20 is due to the possible fluctuations of the ambient temperature for these data points.

Mention is made here also of the theoretical work of Bejan [12] in which the lateral penetration of natural convection into a horizontal porous layer was studied. However, the boundary conditions and the driving mechanism in [12] is totally different from those in the present work. For example, in that paper the axial conduction was neglected (R >> 1), while here it is the main driving mechanism for the flow.

Conclusions

The following conclusions can be drawn from the results obtained in the present study:

1 The asymptotic results for $L = 3.17$, calculated up to $0(1/L^3)$, are valid for R $\lesssim$ 20; at higher Rayleigh numbers, higher order corrections become important.

2 The numerical heat transfer results confirm the validity of the approximate solutions of Bejan and Tien [9]. The numerical solutions do indicate, however, that a reverse flow appears at the permeable end region and penetrates further into the cavity as the Rayleigh number increases, a phenomenon not accounted for in the approximate theory.

3 The numerical temperature distributions based on the constant properties agree well with the experimental data, indicating the suitability of the constant temperature and hydrostatic pressure assumptions at the permeable endwall, in spite of the coupling existing between the cavity flow and the flow inside the tank.

References

1 Burns, P. J., Chow, L. C., and Tien, C. L., "Convection in a Vertical Slot Filled with Porous Insulation," *International Journal of Heat and Mass Transfer*, Vol. 20, 1977, pp. 919-926.

2 Walker, K. L., and Homsy, G. M., "Convection in a Porous Cavity," *Journal of Fluid Mechanics*, Vol. 87, 1978, pp. 449-474.

3 Hickox, C. E., and Gartling, D. K., "A Numerical Study of Natural Convection in a Horizontal Porous Layer Subjected to an End-to-End Temperature Difference," ASME JOURNAL OF HEAT TRANSFER, Vol. 103, 1981, pp. 797-802.

4 Nilson, R. H., "Natural Convective Boundary-Layer on Two-Dimensional and Axisymmetric Surfaces in High-Pr Fluids or in Fluid-Saturated Porous Media," ASME JOURNAL OF HEAT TRANSFER, Vol. 103, 1981, pp. 803-807.

5 Chan, Y. T., and Banerjee, S., "Analysis of Transient Three-Dimensional Natural Convection in Porous Media," ASME JOURNAL OF HEAT TRANSFER, Vol. 103, 1981, pp. 242-248.

6 Elder, J. W., "Steady Free Convection in a Porous Medium Heated From Below," *Journal of Fluid Mechanics*, Vol. 27, 1967, pp. 29-48.

7 Ribando, R. J., and Torrance, K. E., "Natural Convection in a Porous Medium: Effects of Confinement, Variable Permeability, and Thermal Boundary Conditions," ASME JOURNAL OF HEAT TRANSFER, Vol. 98, 1976, pp. 42-48.

8 Lau, K. H., and Cheng, P., "The Effect of Dike Intrusion on Free Convection in Conduction-Dominated Geothermal Reservoirs," *International Journal of Heat and Mass Transfer*, Vol. 20, 1977, pp. 1205-1210.

9 Bejan, A., and Tien, C. L., "Natural Convection in a Horizontal Porous Medium Subjected to an End-to-End Temperature Difference," ASME JOURNAL OF HEAT TRANSFER, Vol. 100, 1978, pp. 191-198.

10 Haajizadeh, M., "Convection in Horizontal Porous Media with Different End Temperatures," Ph.D. thesis, University of California, Berkeley, California, 1982.

11 Patankar, S., *Numerical Heat Transfer and Fluid Flow*, McGraw-Hill, New York, 1980.

12 Bejan, A., "Lateral Intrusion of Natural Convection into a Horizontal Porous Structure," ASME JOURNAL OF HEAT TRANSFER, Vol. 103, 1981, pp. 237-241.

Experimental Comparison of Heat Transfer Data With Flow Visualization on a Flat Surface in an Air Fluidized Bed

B. Rubinsky
Assoc. Mem. ASME

G. L. Starnes

Department of Mechanical Engineering,
University of California,
Berkeley, Calif. 94720

A new experimental technique is introduced which facilitates visualization of the fluid flow phenomena occurring on a small surface immersed in an air fluidized bed. The flow visualization was correlated qualitatively with heat transfer data from the surface. Heat transfer coefficients versus air velocity curves were obtained and found to be strongly dependent on the angle of inclination of the surface relative to the air flow direction. Flow visualization has facilitated the identification of three mechanisms of heat transfer to a surface as a function of the angle of inclination and the air flow velocity. These include, conduction through a stationary layer of particles, convection through a flow of solid particles, and heat transfer by sequential contact with voids and a well mixed conglomerate of solid particles.

Introduction

A gas-solid fluidized bed contains a bed of particulate matter through which a gas (air) is passed. The vigorous mixing of particles in a fluidized bed yields good heat transfer [1, 2]. This has promoted the use of fluidized beds in heat exchanger technology. In heat exchangers, energy is transferred via surfaces (tubes, finnes). An understanding of the heat transfer mechanism between a surface immersed in the fluidized bed and the fluidized bed is of interest for the proper design of a heat exchanger.

Numerous analytical and experimental studies have been carried out to determine the heat transfer to a surface immersed in a fluidized bed [1–13]. Extensive experimental data have been gathered for the variation of heat transfer with respect to air flow velocity. The data have been obtained for surfaces that are parallel to the direction of the inlet air flow. Typical curves for heat transfer versus air flow velocity have been developed [1, 2]. It has been shown that the heat transfer is different in the four different fluidization regimes, i.e., fixed bed, incipient fluidization, bubbling bed, and slugging flow. The region of low air velocity corresponding to the fixed bed regime is characterized by low heat transfer coefficients. The incipient fluidization regime is characterized by a gradual increase in the heat transfer coefficients with maximal heat transfer occurring in the bubbling regime. Empirical correlations for the "maximal" heat transfer coefficient on surfaces that are parallel to the direction of the air flow are listed [6, 12]. The slugging regime is accompanied by a decrease in the heat transfer coefficient.

Measurements for the heat transfer to or from a tube immersed in a fluidized bed were reported in [14–17]. The observed variation of the local heat transfer coefficients along the circumference of the tube surface as well as the observed variation of the overall heat transfer coefficient from a tube as a function of the orientation with respect to the direction of the air flow is of specific interest to this work [14, 17]. A study on the variation of heat transfer with respect to the orientation of a flat plate immersed in a fluidized bed could promote the understanding of the basic heat transfer mechanisms which occur along the circumference of tubes, in tubes at different orientations and in finned tubes.

Contributed by the Heat Transfer Division for publication in the JOURNAL OF HEAT TRANSFER. Manuscript received by the Heat Transfer Division August 30, 1982.

However, only limited studies have been performed for such a configuration. For example, Fillipovsky and Baskakov [18] have measured the heat transfer from a large flat plate immersed in a fluidized bed as a function of the orientation of the plate relative to the direction of the bulk air flow. The plate used in their experiment is very large and is effectively the exterior wall of a fluidized bed. They report a large variation of the heat transfer coefficient as a function of orientation and indicate that the maximal heat transfer coefficient was observed for a plate at an angle of inclination toward the flow and not for surfaces parallel to the flow. Similar results were reported in a recent work by Kellogg, Rubinsky, and Greif [19], for a small flat plate immersed in a fluidized bed.

Various models have been proposed for the mechanism of heat transfer to a surface in a fluidized bed. These include the "packet model" first proposed by Mickley and Fairbanks [20]. This assumes that energy is carried from a surface to the bulk of the bed by means of "packet elements" consisting of groups of particles with interstitial gas. In another model, the "particle model," it is assumed that the energy is transferred from the surface to the bed by means of individual particles. The "particle model" was developed first by Gabor [21, 22] and Botterill and Williams [2].

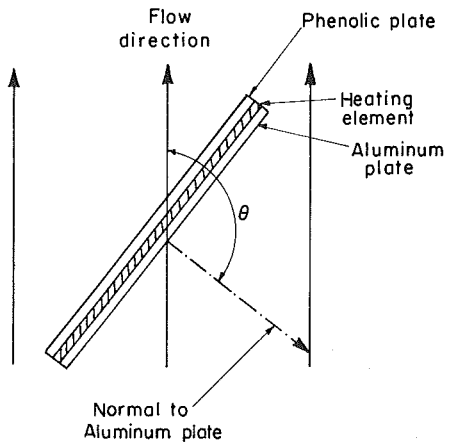

Fig. 1 Schematic of the heat transfer probe

A difficult task in the study of the heat transfer from an immersed surface is establishing a model for the transfer mechanism. The various models previously cited and the experimental data illustrate the need for a better understanding of the complex fluid flow phenomena near the immersed surface.

The purpose of this work is to introduce an experimental technique which facilitates observation of the phenomena occurring near an immersed surface and to investigate by means of this method the effect of the inclination angle of a surface immersed in a fluidized bed on the heat transfer. The results of this study should be useful to the qualitative understanding of the heat transfer mechanism and for future model development studies.

The experimental work employs a flow visualization technique which has been reported previously to visualize bubbles in a fluidized bed [2]. The application of this technique to observe phenomena near a surface immersed in a fluidized bed has not been reported previously.

Experimental System

The experimental apparatus consisted of a plexiglas chamber of rectangular cross section, 3.5 cm × 22.9 cm that was 83.2-cm high. Since the fluidized bed was constructed of transparent plexiglas, it was possible to observe the bubbling action, bulk particle motion, and the expansion of the fluidized bed. At the bottom of the chamber, a 40-μm pore dia stainless steel plate was used as the air distributor. Below the plate was a rectangular shaped air phenum of the same cross section as the fluidized bed chamber through which air was introduced in the fluidized bed. This plenum was filled with steel wool to ensure even air distribution. The fluidization gas used was compressed air available from a central compressor at 100 psia. The air was filtered by water and oil filters.

A schematic diagram of the heat transfer probe is shown in Fig. 1. The probe was constructed by mounting a flat "Minco" electrical resistance "thermo-foil" heater (165 ohms) between a thin aluminum plate (0.17 cm × 3.5 cm × 6.6 cm), and a layer of phenolic laminate (0.33 cm × 3.5 × 6.6 cm). The effective heat transfer areas were the 3.5 cm × 6.6 cm surfaces on both aluminum and phenolic laminate sides. The thermal resistances of the aluminum and phenolic were 6.5×10^{-6} m^2 K/W, and 0.021 m^2 K/W, respectively. The aluminum plate provided a uniform surface temperature. The temperature was shown to be uniform by two 0.25 mil, copper-constantan thermocouples. The thermocouples were positioned along the long axis of symmetry of the heat transfer surface (6.6 cm) each at a distance of 1 cm above and below the center of the surface. The lead wires were internal between the plates, and high thermal conductivity epoxy was used to assemble the plates.

The probe was positioned in the fluidized bed by two 1-mm dia pins which protruded from the long (20.3 cm × 83.2 cm) wall of the chamber and served as the axis of rotation for the probe. The flat heat transfer surface of the probe (3.5 cm × 6.5 cm) was perpendicular to the long 20.3 cm × 83.2 cm walls of the fluidized bed chamber. Thin rubber strips were glued to the narrow side of the probe. The probe assembly was compressed between the long side walls of the fluidized bed to prevent particles from flowing between the narrow side of the probe and the wall. The probe was positioned in the center of the fluidized bed, its axis of rotation at a height of 15.5 cm from the porous plate.

The particles used in the fluidized bed were Ottawa fine white sand, which is composed primarily of quartz. This sand had a solid density of 2720 kg/m^3. The particle sizes ranged between 0.09 mm and 0.28 mm. An average particle diameter of 0.182 mm was calculated by the following formula recommended by Botterill [5]

$$\bar{d}_p = [\Sigma_i (x/d_p)_i]^{-1} \quad (1)$$

The particle size is typical of Geldart Group "B" size powders [6, 12]. For this particle size the particle convective component is presumably the dominant mode of heat transfer [2].

Experimental Procedure

Experiments were conducted to determine the heat transfer coefficients from the flat surface immersed in the fluidized bed and to visualize the flow modes near the immersed surface. The probe angle, air flow rate, and probe heat flux were varied throughout the experiment. The heat flux was not varied consistently throughout the experiment, but only to maintain the probe temperature between 50°C to 70°C. The bulk bed temperature was 20°C. For this temperature range the radiative heat transfer component is presumably negligible [2].

Throughout the experiment the unfluidized height of the sand particles and the height of the probe axis were held constant at 30 cm and 15.5 cm, respectively. Since the heat transfer coefficients were expected to vary greatly with angle, measurements were made on surfaces at an angle, θ, of 0, 30, 60, 75, 82.5, 90, 97.5, 105, 120, 150, and 180 deg. The reason for concentrating in the region of 60–120 deg is that the maximal heat transfer was shown to occur in this region by Baskakov and Fillipovski [18] and Kellogg et al. [19]. The angle, θ, is defined to be the angle between the air flow direction and the normal to the surface (see Fig. 1). An angle of 0 deg corresponds to the surface facing up, and an angle of 180 deg corresponds to the surface facing down. It should be noted that for a surface facing the flow, the angle is always greater than 90 deg; for a surface away from the flow the angle is less than 90 deg.

At each probe angle, five constant air flow rates were used. The flow velocities were 0.0705, 0.1046, 0.1389, 0.1816, and 0.2244 m/s. The lower velocities correspond to incipient fluidization, while the higher velocities correspond to bub-

Nomenclature

c = heat capacity, J/kgK
d_p = particle diameter, m
f_o = fraction of the total time a surface is covered with bubbles
h = heat transfer coefficient, W/m^{2}K
h_o = heat transfer coefficient when surface is in contact with a bubble
k = thermal conductivity, W/mk
R = thermal resistance, m^{2}K/W
t_e = average "packet" residence time, s
T = temperature, K
x = weight fraction of sieved particles
ρ = density, kg/m^3
θ_1, θ_2 = supplementary probe angles, deg[$\theta_2 = 180$ deg $- \theta_1$]

Superscript

$-$ = mean

Subscript

Al = aluminum
b = steady state bulk bed
L = phenolic laminate
e = effective
S = steady-state probe surface

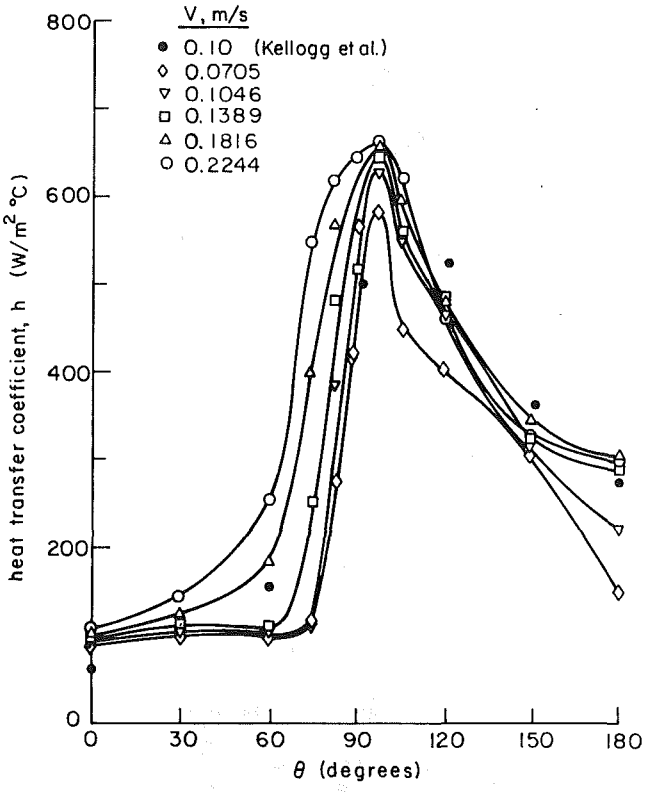

Fig. 2 Heat transfer coefficients versus probe angle

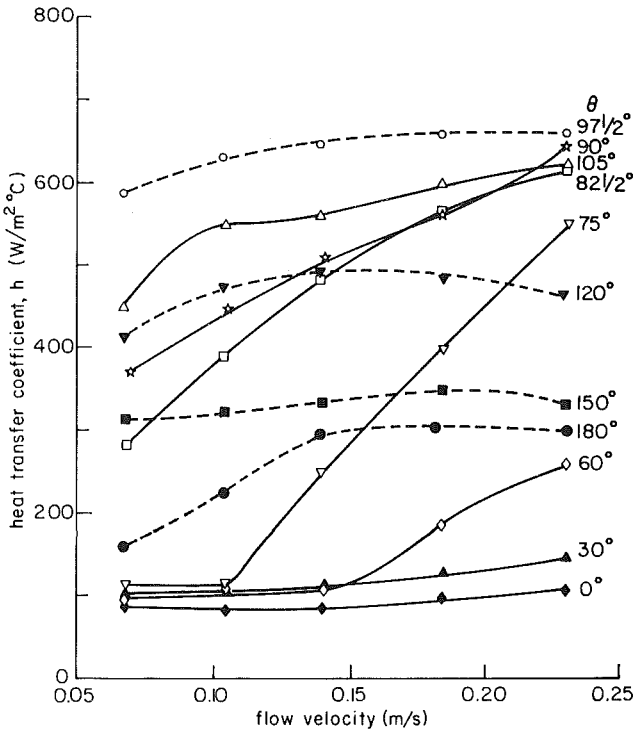

Fig. 3 Heat transfer coefficients versus air flow velocity

bling fluidization as evaluated using empirical correlations for the sand particle size in this experiment [2].

The thermocouple on the probe, in the absence of heating, provided the temperature in the fluidized bed, T_b. A predetermined heat flux, q, was applied to the heating element, and the thermocouple output for the aluminum plate at the angles θ_1 and $\theta_2 = \pi - \theta_1$ was recorded. Each heating experiment lasted only several minutes, and the temperature of the fluidized bed was measured before and after the heating to confirm that the bulk temperature of the fluidized bed was not changed.

Since the probe has an asymmetric construction with respect to the Minco heating element, an energy balance at each of the two supplementary angles yields the set of simultaneous equations (2) and (3).

$$\dot{q}_{\theta 1} = \frac{T_{s1} - T_{b1}}{1/h_{\theta 1} + R_L} + \frac{T_{s1} - T_{b1}}{1/h_{\theta 2} + R_{\mathrm{AL}}} \tag{2}$$

$$\dot{q}_{\theta 2} = \frac{T_{s2} - T_{b2}}{1/h_{\theta 2} + R_L} + \frac{T_{s2} - T_{b2}}{1/h_{\theta 1} + R_{\mathrm{AL}}} \tag{3}$$

The solutions to equations (2) and (3) yield the heat transfer coefficients at the angles θ_1 and θ_2. This method has the advantage that it does not require the insulation of one side of the probe while making heat transfer measurements from the other. It is important to realize that the heat flux from both sides of the plate (the phenolic laminate side and the aluminum side) are considered in equations (2) and (3). Therefore, an uninsulated thin probe can be used in these measurements to minimize the disturbing effects of the probe thickness on the flow.

Throughout the experiment, photographs were taken of the bubble formations surrounding the probe. A 3200 K photographic strobe was placed behind the large rear wall of the fluidized bed. The camera was placed facing the large front wall of the fluidized bed. Therefore, the narrow edges of the probe faced the camera lens and the strobe. Still photographs were taken with a Nikon F2 35 mm single lens reflex camera, equipped with a f/3.5, 135 mm lens, at an aperture setting of f/4.0 and a shutter speed of 1/60 s. A Nikon auto-winder was used, allowing pictures to be taken at a rate of approximately three per second. Kodak Tri-X black and white film was used at a speed of 400 ASA. The strobe was synchronized with the camera shutter and was the only source of light.

During normal fluidized bed operation, typical pictures (Figs. 4–7) were taken at random, so as not to bias the results. When the bed was unfluidized, the photographic strobe was set off, and it was observed that no light could pass through the test section. Consequently, when the fluidized bed was in operation, light could pass through the regions of lower particle density ("bubbles," voids) and be observed from the front of the fluidized bed. Typical pictures show bright regions surrounded by darker regions. The bright areas represent "bubbles" or voids; the dark areas represent fluidized particles, and the thin black line represents an edge view of the heat transfer probe.

Experimental Results and Discussion

Heat transfer measurements were made at several different probe angles and five different air flow velocities. Photographs were taken at each probe angle and air velocity to aid in flow visualization. The photographs are used to explain and clarify the results presented graphically.

In Fig. 2, the heat transfer coefficient is given as a function of the angle for five different air velocities. The angles have been identified in the schematic drawing of the probe in Fig. 1. The values presented are a time-average over a period of 10 min. At least three runs were performed at each condition. The experimental error based on instrument uncertainties was calculated to be 8 percent of the measured value.

The results indicate that the maximal heat transfer occurs at an angle of 97.5 deg. This is in good agreement with the maximum value at 100 deg that was reported by Fillipovskii and Baskakow [18]. Experimental data from [19] for a probe

at an elevation of 15 cm in a much larger fluidized bed with a cross section of 20.3 cm × 20.3 cm is also shown on Fig. 2. The comparison indicates good agreement between the results obtained in a wide bed [19] and the narrow bed used in this work. It should, nevertheless, be emphasized that in [19] the data was obtained for a fluidized bed which was 20-cm high, whereas here the fluidized bed height is 30 cm.

In general, the curves exhibit low values of the heat transfer coefficient at small angles (between 0 and 30 deg). This is followed by an increase in the heat transfer coefficient to a peak at 97.5 deg and then an almost linear decrease with the increase in angle to 180 deg. Figure 2 indicates that the heat transfer versus angle curve is strongly dependent on the air flow velocity at certain angles, whereas at other angles it is practically independent on the air velocity. This effect of the air velocity has not been investigated in [19].

In Fig. 3, the heat transfer coefficients are shown as a function of velocity for different angles. As indicated previously the velocities employed in this experiment range between the incipient fluidization velocities to bubbling fluidization velocities. According to the technical literature [1, 2, 6], and as discussed in the introduction, the heat transfer coefficients should increase dramatically in this velocity range between the low values at incipient fluidization to the maximal values in the bubbling regime. The results shown in Fig. 3 indicate that the dependence of the heat transfer coefficients on air flow velocities described in the literature [1, 2] is by no means universal but rather a function of the surface angle of inclination.

For a surface at an angle between 0 to 30 deg, the heat transfer coefficient is virtually independent on air flow even in the bubbling fluidized bed regime. The air flow velocities, at which an increase in the heat transfer coefficient with the velocity is observed, decrease for larger angles. Thus, for a surface at an angle of 60 deg, the heat transfer coefficients start to increase with velocity at an air velocity of 0.14 m/s, while at an angle of 75 deg, the heat transfer coefficient starts to increase at an air velocity of 0.1 m/s. The heat transfer versus velocity curve resembles the classical curve described in [2, 5, 6] for surfaces at angles between 82.5 and 90 deg. For angles larger than 90 deg, the heat transfer is a weaker function of velocity. In general, the heat transfer decreases with an increase in angle for angles larger than 97.5 deg.

Photographs which will be employed to present a tentative explanation for the results of Figs. 2 and 3 are shown in Figs. 4 to 7. We start by introducing two sets of three pictures taken at an interval of 0.37 s between each picture with an air velocity of 0.2244 m/s (the highest air velocity used in these experiments). Figures 4(*a*), 4(*b*), and 4(*c*) show the probe at an angle θ (as defined by Fig. 1) of 30 deg. (The surfaces of the probe are at angles of 30 and 150 deg, respectively.) Figures 5(*a*), 5(*b*), and 5(*c*) show surfaces at angles of 75 deg (105 deg). The direction of the air flow is up from the bottom of the photographs.

Note that the surface facing the air flow is almost always exposed to a bubble whereas the surface facing away from the air stream is usually never exposed to bubbles.

The interaction between bubbles rising in the bed and the probe surface is of interest. The sequences shown here illustrate that as a bubble rises and interacts with the immersed probe, it slides upward along the immersed surface facing the air stream. The bubble leaves and the bed particles then return and again come in contact with the surface. Note that the surface at 150 deg is almost always surrounded by bubbles, whereas the surface at 105 deg (whose projection on a plane perpendicular to the flow direction at 105 deg (whose projection on a plane perpendicular to the flow direction is much smaller than the 150 deg angle) is exposed much less to the bubbles, therefore more to the bed particles. Figures 6(*a*), 6(*b*), and 6(*c*) show a surface immersed in a fluidized bed at

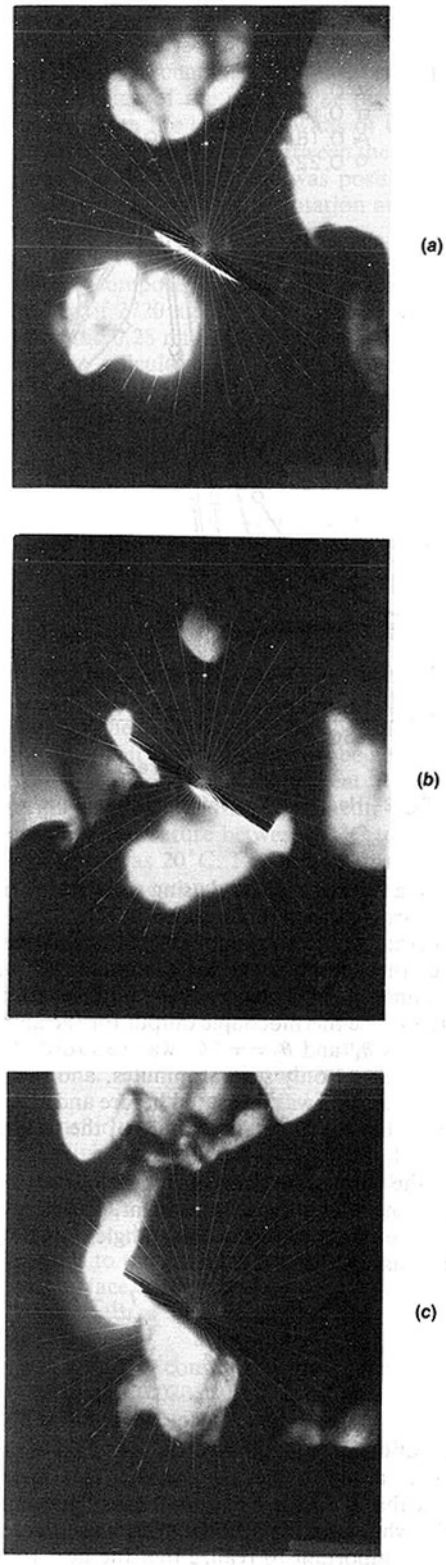

Fig. 4 Sequence of photographs for a surface at 30 deg (150 deg)

angles of 0, 60, 90 deg (and their supplementary angles), when the air velocity is 0.2244 m/s, the same air velocity as that for Figs. 4 and 5. Specific to this high air velocity and the bubbling fluidization regime is the appearance of bubbles throughout the whole fluidized bed. It is noticed that even at this high air flow rate there are no visible bubbles on surfaces at angles between 0 and 87.5 deg. It should be emphasized that the surface, at angles larger than 90 deg, are exposed to

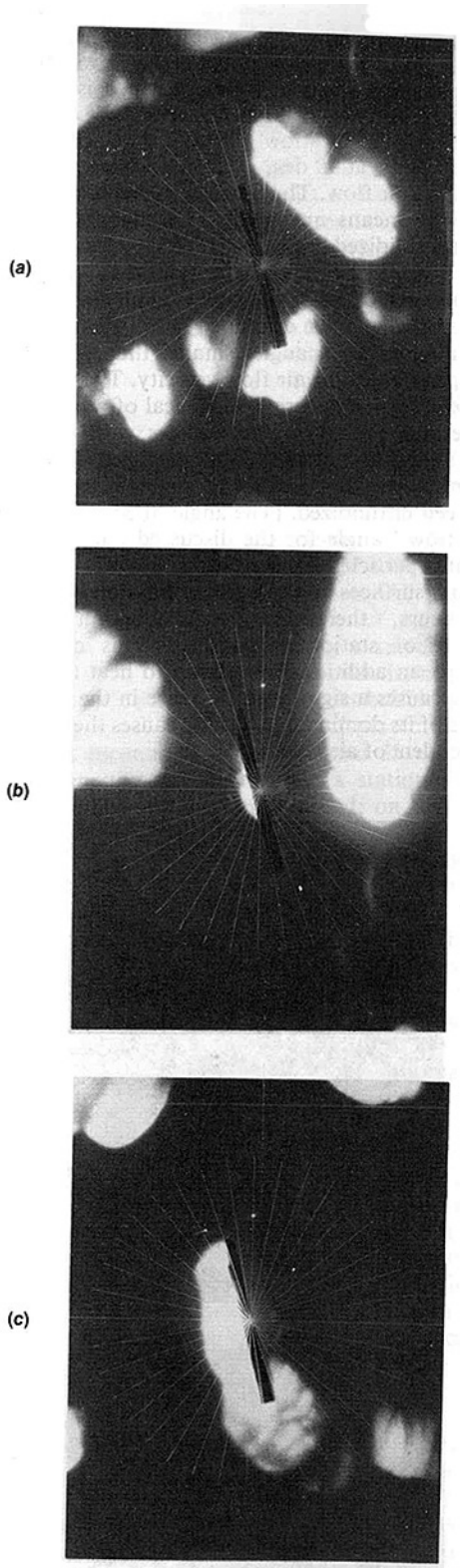

Fig. 5 Sequence of photographs for a surface at 75 deg (115 deg)

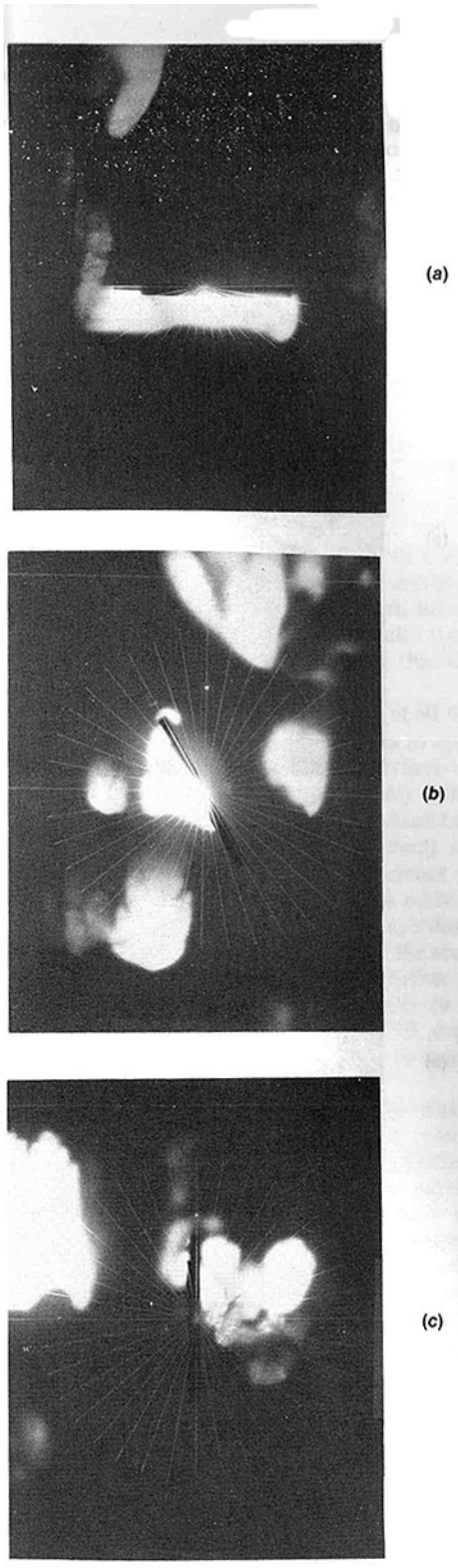

Fig. 6 Photographs of surfaces at 0 deg (180 deg), 60 deg (120 deg) and 90 deg

intermediate interaction with bubbles and the dense region of particles. The frequency of the interaction with bubbles, as well as the time a bubble resides near a surface increased with the increase in angle for angles larger than 90 deg. Thus, the situation depicted by Fig. 6(*a*), in which a bubble completely surrounds the surface at 180 deg, is very common, whereas the situation depicted by Fig. 6(*c*), in which a bubble rises in the vicinity of a surface at 90 deg, does occur less frequently.

Figures 7(*a*), 7(*b*), 7(*c*), 7(*d*) and 7(*e*) show a surface immersed in a fluidized bed at angles of 0, 30, 60, 75, 90 deg (and their supplementary angles), when the air velocity is 0.0705 m/s. This velocity is the lowest velocity used in our experimental work and is typical to incipient fluidization. Very few bubbles ar visible under these experimental conditions inside the fluidized bed. The lack of bubbles is

especially significant when compared to the bubbling regime shown in Figs. 4–6. No bubbles are observed on surfaces larger than 90 deg. Despite the lack of bubbles in the bulk of the fluidized bed, bubbles were always evident on surfaces facing the flow. The size of the bubble, as well as the period of time a surface was surrounded by the bubble increased with an increase in angle. Large voids were almost always visible on the surface at 180 deg as shown by Fig. 7(*a*).

The results of this study as shown by Figs. 2 and 3 and the photographs 4 to 7 indicate that the heat transfer process from a surface immersed in a fluidized bed is governed by three different mechanisms as a function of the orientation of the surface and the air flow velocity. A singular behavior occurs for surfaces at 90 deg, i.e., on surfaces parallel to the direction of the air flow. The heat transfer mechanism at that angle is by no means universally characteristic to surfaces immersed in a fluidized bed.

One mechanism of heat transfer typical to surfaces at inclinations between 0 and 35 deg occurs at all air velocities (the choice of the angle will be explained later). Figure 3 indicates that the heat transfer at angles smaller than 30 deg is practically independent of the air flow velocity. The values for the heat transfer coefficients are low, typical of a packed bed. A recent experiment done by the authors with the same experimental system but using colored particles, shows that the particles on the top of a surface at angles between 0 and 35 deg are indeed unfluidized. (The angle of 35 deg is known as the "solid flow" angle for the discussed particles, i.e., the angle at which particles will flow under gravitation.) The heat transfer from surfaces at angles of inclination between 0 and 35 deg occurs, therefore, by conduction through a conglomerate of stationary particles. This conglomerate, which acts as an additional resistance to heat transfer from the surface, causes a significant decrease in the heat transfer and because of its dominant low value causes the heat transfer to be independent of air velocity.

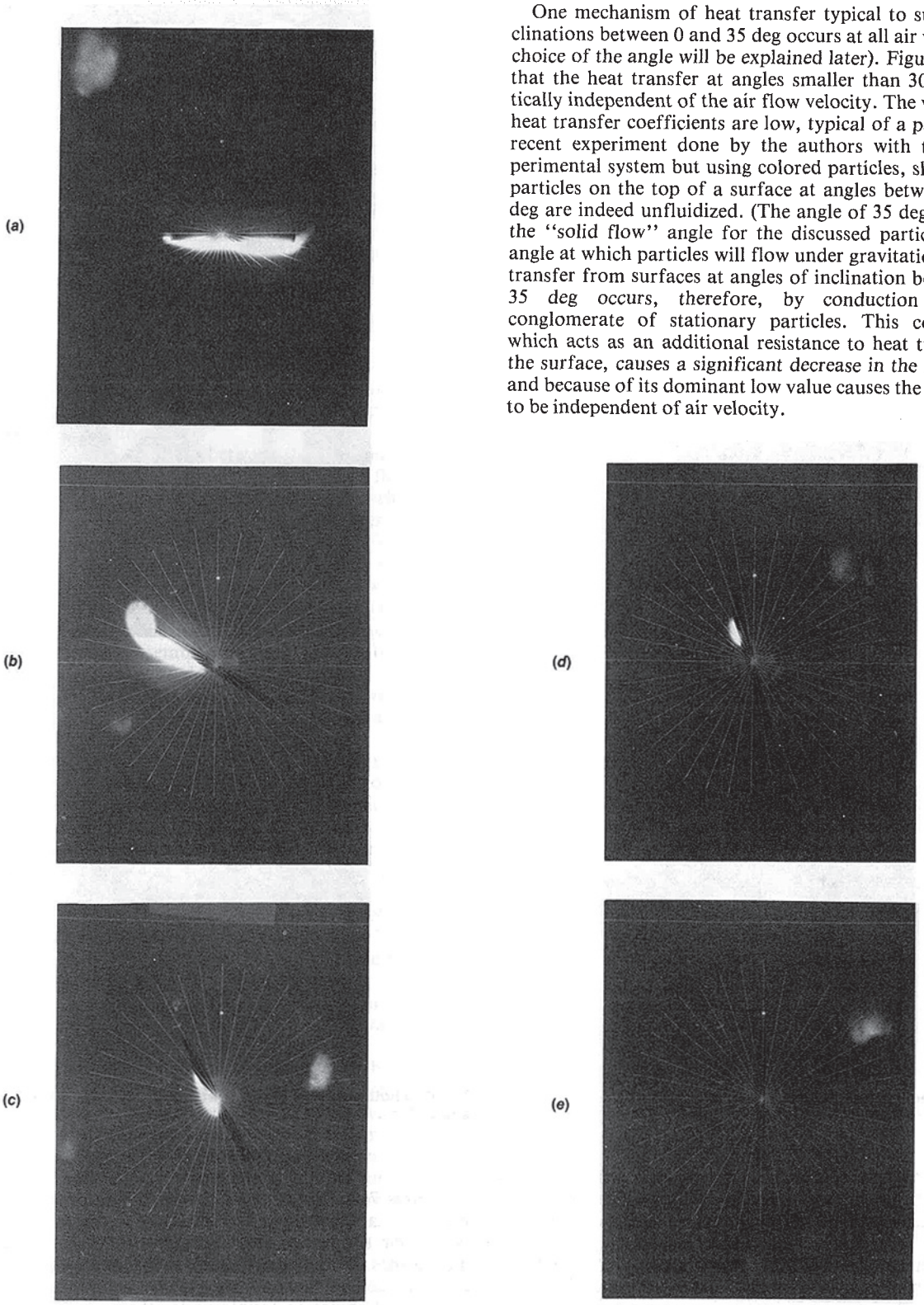

Fig. 7 Photographs of surfaces at various angles

The second mechanism of the heat transfer is typical to angles between 35 and 90 deg. Photographs 4–7 indicate that surfaces at angles between 35 and 90 deg are practically never surrounded by bubbles. (We would like to emphasize again that these pictures were taken at random.) Experimental results show that even when a bubble interacts with the probe as shown in Figs. 5(*a*), 5(*c*), it splits in two parts with the larger part of the bubble rising preferentially on the surface facing the flow while the smaller part rises parallel to the direction of the flow. There is always a layer of dense particles between the surface at angles ranging from 35 to 90 deg and the bubble which rises parallel to the direction of the air flow. From the discussion above, it is evident that for surfaces at angles between 35 and 90 deg the only possible heat transfer is through the surrounding dense phase. It is well known that a fluidized bed in the "bubbling regime" is composed of two regions, a region of dense "floating particles" with the density of the fluidized bed in the "incipient fluidization regime" and regions of lower density referred to as bubbles [2]. Zenz [7] suggested that a mechanism by which bubbles rise to the surface of a fluidized bed is by solid flow into the bubble space from surrounding particles. The passage of a bubble causes, therefore, displacement of particles in its vicinity. The dense phase surrounding a surface at angles between 35 and 90 deg has probably the density of a fluidized bed in an "incipient fluidized regime." As bubbles rise near a surface, the particles in its vicinity are displaced. Thus, while on surfaces at inclination between 0 and 35 deg, the heat transfer is from the surface through a stationary layer of particles to the bulk of the fluidized bed; on surfaces at an inclination between 35 and 90 deg, the heat transfer is through a flowing dense phase of granular particles to the bulk of the fluidized bed. Figure 3 shows that the heat transfer in "bubbling" fluidized beds (air flow velocities of 0.2244 m/s, 0.1816 m/s) rises dramatically at higher angles although it is independent on air flow velocity at angles between 0 and 30 deg. Since photographs 4–7 indicate that the immersed surface is always surrounded by a dense conglomerate of particles, the enhancement in heat transfer is probably caused by convection through the flowing granular particles as bubbles rise in the vicinity of the surface.

At low air flow velocities typical to the incipient fluidization regime the heat transfer is low for surfaces at inclinations of up to 75 deg. These results shown in Figs. 2 and 3 indicate that the heat transfer is to a media which is effectively stationary. Photographs 7(*a*)–7(*e*) confirm this observation by showing that very few voids are visible in the fluidized bed at air velocities of 0.0705 m/s. The increase in heat transfer occurring at larger angles is caused probably by the particle displacement due to bubbles passing occassionally in the vicinity of the surface.

The third mechanism of heat transfer observed in this work occurs near surfaces at an inclination between 90 deg (inclusive) and 180 deg. Photographs 4–7 indicate that at these angles the surfaces are surrounded most of the time by bubbles. It is remarkable that there is almost always a bubble near the surface even when very few bubbles are visible in the bulk of the fluidized bed. Bubbles that rise from the bottom and interact with the probe will slide preferentially on the surfaces facing the air flow. Also, surfaces at angles between 90 and 180 deg seem to generate or attract the bubbles. The size of bubbles increases with an increase in angle of inclination and air flow rate. At large angles, i.e., close to 180 deg the surface is surrounded by bubbles for a larger period in time than surfaces at smaller angles, i.e., 90 deg.

Figures 4–7, along with the results of Fig. 3, suggest the following. Bubbles rising near an immersed surface have the effect of mixing the bed particles. Thus, they enhance the energy transfer from particles near the surface to the bulk of the fluidized bed. However, the heat transfer from a surface is probably reduced in the presence of bubbles. The heat transfer from the immersed surface occurs primarily when the bed particles are in contact with the surface. Thus, the heat transfer from the surface to the bulk of the fluidized bed may be envisioned as a two-step mechanism: (*a*) from the surface to the adjacent solid particles; and (*b*) by mixing to the bulk of the fluidized bed. The mechanism described here has some similarity with the "packed particle model" prevalent in the fluidized bed heat transfer literature [2, 5, 6].

For example, an expression for the mean heat transfer coefficient was obtained in [23] from the "packed model" by considering the packet component and the bubble component of heat transfer

$$\bar{h} = (1 - f_0)\frac{2}{\sqrt{\pi}}\sqrt{k_e \rho_e c_e}\,\frac{1}{\sqrt{t_e'}} + f_o h_o \tag{4}$$

where

$$t_e' = [\Sigma t_e / \Sigma \sqrt{t_e}]^2 \tag{5}$$

According to this model the heat transfer will increase with a decrease in the mean packet residence time and a decrease in the fraction of total time a surface is covered with bubbles. This expression agrees qualitatively with the results for the heat transfer coefficients shown in Fig. 2 and the visual observation presented in photographs 4–7.

The maximal heat transfer coefficient observed at 97.5 deg is probably caused by the observed trend of bubbles to appear on surfaces facing the flow. Thus, while a surface at a singular point (angle) of 90 deg will encounter only bubbles generated at the bottom of the fluidized bed, a surface facing the air flow at 97.5 deg seems to generate (attract) more bubbles. This will reduce the average packet residence time for a surface at 97.5 deg as compared to that for a surface at 90 deg increase the mixing of the particles, and according to equation (4), increase the heat transfer. In view of the studies in [14], [15], and in this work, it is not certain whether 97.5 deg is the actual angle for a maximal heat transfer or it is sufficient to have any slight derivation from 90 deg to generate voids around an immersed surface and thus enhance the heat transfer.

It is, however, evident from this work that the classical curves for heat transfer coefficients versus air flow velocities appearing in many texts [1, 2] are merely the description of the correlation for a surface at a specific inclination and by no means universal curves for all surfaces immersed in a fluidized bed. Furthermore, the results indicate the existence of several different mechanisms of heat transfer to an immersed surface. The strong effect of the inclination on the heat transfer versus air velocity curve also indicates that different tolerances in the inclination of an experimental surface taken to be parallel to the air flow could affect significantly the experimental results.

Conclusions

A new experimental technique has been applied to observe the phenomena occurring on a small surface immersed in a fluidized bed and to determine the heat transfer from that surface. Measurements were made at various angles of the surface relative to the direction of the air flow and at various air flow velocities. The observations indicate that the heat transfer from the immersed surface is governed by three different mechanisms as a function of the surface angle and air flow velocities. The heat transfer from surfaces at angles between 0 and 35 deg is by conduction through a stationary conglomerate of particles to the bulk of the fluidized bed. Minimal heat transfer coefficients were obtained at these angles.

Heat transfer from surfaces at angles between 35 and 90 deg occurs by convection through a dense phase of particles which

flow across the surface and are at all times in contact with the surface.

At angles between 90 (inclusive) and 180 deg, the surface is experiencing a discontinuous contact with air voids and the well-mixed, dense-phase region of particles. The heat transfer is enhanced by this phenomena. It was observed that bubbles slide preferentially on a surface inclined toward the flow. Maximal heat transfer was recorded on surfaces at an angle of 97.5 deg.

References

1 Zabrodsky, S. S., *Hydrodynamics and Heat Transfer in Fluidized Beds*, MIT Press, 1966.

2 Botterill, J. S. M., *Fluidized Bed Heat Transfer*, Academic Press, 1975.

3 Kunii, D., and Levenspiel, O., *Fluidization Engineering*, J. Wiley & Sons 1969.

4 Rowe, P. N., *Fluidization*, edited by Davidson and Harrison, Academic Press, London, 1971, pp. 121–191.

5 Leva, M., *Fluidization*, McGraw-Hill, New York, 1959.

6 Hetsroni, G., ed., *Handbook of Multiphase Systems*, Hemisphere Publishing Corporation, McGraw-Hill Book Company.

7 Zenz, F. A., *Fluid Bed Reactors, Design Scale-Up, Problem Areas*, AIChE, Today Series, 1979.

8 *Fluidization*, edited by J. F. Davidson and Harrison, Academic Press, London, 1971.

9 Davidson, J. F., and Keairns, D. L., *Fluidization*, Cambridge University Press, 1978.

10 Mathur, K. B., and Epstein, N., *Spouted Beds*, Academic Press, 1979.

11 *Proceedings of the 1st, 2nd, 3rd International Conference Fluidized Bed Combustion*, sponsored by EPA, Hueston Woods, Oxford, Ohio, 1968, 1969, 1972.

12 Botterill, J. S. M., Teoman, Y., and Yuregir, K. R., "Temperature Effects on the Heat Transfer Behaviour of Gas Fluidized Beds," *AIChE Symposium Series*, 208, Vol. 77, 1981, pp. 330–340.

13 Adams, R. L., and Welty, J. R., "A Gas Convection Model of Heat Transfer in Large Particle Fluidized Beds," *AIChE Journal*, Vol. 25, No. 3, 1979, pp. 395–405.

14 Chandran, R., Chen, J. C., and Staub, F. W., "Local Heat Transfer Coefficients Around Horizontal Tubes in Fluidized Beds," ASME *Journal of Heat Transfer*, Vol. 102, 1980, pp. 152–157.

15 Saxena, S. C., Grewal, N. S., Gabor, J. D., Zabrodsky, S. S., and Galershtein, D. M., "Heat Transfer Between a Gas Fluidized Bed and Immersed Tubes," Vol. 14, *Advances in Heat Transfer*, edited by T. F. Irvine, Jr., and J. P. Hartnett, Academic Press, New York 1979.

16 Cretu, J., Yang, L. and Saxena, S. C., "Heat Transfer to a Single Smooth Vertical Tube Immersed in Air Fluidized Bed," *Lett. Heat Mass Transfer*, Vol. 8, 1981, pp. 465–474.

17 Genetti, W. E., Schmall, R. A., and Grimmett, E. S., "The Effect of Tube Orientation on Heat Transfer With Bare and Finned Tubes in a Fluidized Bed," *AIChE Symposium Series* 67 116, 1971, pp. 90–96.

18 Fillippovskii, N. F., and Baskakov, A. P., "Investigation of the Temperature Field in a Fluidized Bed Close to a Heated Plate and of Heat Transfer Between Them," *International Chemical Engineering*, Vol. 13, No. 1, 1973, pp. 5–9.

19 Kellogg, K., Rubinsky, B., Greif, R., "The Effect of Orientation on the Heat Transfer From a Flat Surface in an Air Fluidized Bed," *International Journal of Heat and Mass Transfer*, Vol. 26, No. 1, 1983, pp. 151–153.

20 Mickley, M. S., and Fairbanks, D. F., "Mechanism of Heat Transfer to Fluidized Beds," *AIChE Journal*, Vol. 1, 1955, pp. 374–384.

21 Gabor, J. D., "Wall to Bed Heat Transfer in Fluidized and Packed Beds," *Chem. Eng. Progr. Symp. Series*, Vol. 66, 1970, p. 76.

22 Gabor, J. D., "Wall to Bed Heat Transfer in Fluidized Beds," *AIChE Journal*, Vol. 18, 1972, p. 249.

23 Krause, W. B., and Peters, A. R., "Bubble and Emulsion Residence Time Study in an Air-Fluidized Bed," *Multiphase Transport*, edited by T. N. Veziroglu, Hemisphere Publishing Co., 1980, pp. 2151–2184.

G. S. Wang

F. P. Incropera
Mem. ASME

R. Viskanta
Fellow ASME

Heat Transfer Laboratory,
School of Mechanical Engineering,
Purdue University,
West Lafayette, Ind. 47907

Mixed Convection Heat Transfer in a Horizontal Open-Channel Flow With Uniform Bottom Heat Flux

Flow visualization studies and heat transfer measurements have been made for water flow in an open channel which is uniformly heated from below. In addition, a two-dimensional boundary layer model, which includes a buoyancy term in the momentum equation and accounts for the effect of buoyancy on turbulence, has been used to predict the heat transfer measurements. Thermal boundary layer development involves an inlet region for which buoyancy effects are negligible, a transition region characterized by mixed convection, and a downstream region which is dominated by turbulent free convection. The regions are delineated in terms of the mixed convection parameter $Gr_x/Re_x^{3/2}$, and heat transfer measurements are compared with existing forced, free, and mixed convection correlations.

Introduction

There is considerable interest in the effect which heating from below can have on hydrodynamic and thermal conditions in laminar, horizontal flows. The resulting buoyancy forces induce longitudinal vortex rolls, which constitute the first stage of transition to turbulence [1, 2]. The vortices are known to significantly enhance heat transfer in a mixed convection region, which separates the upstream laminar and downstream turbulent flows [3, 4]. Criteria for determining the onset of vortex instabilities have been established in terms of the mixed convection parameter $Gr_x/Re_x^{3/2}$, with estimates of the critical value ranging from 0.434 to 200 [2, 5–8]. This wide range of theoretical and experimental results may be attributed to the fact that instabilities must grow to a certain size before they can be detected. Buoyancy effects on heat transfer are negligible upstream of the onset point, where the Pohlhausen relation is known to apply [3, 4], and are dominant in a downstream region for which $Gr_x/Re_x^{3/2} > 300$ and conditions are fully turbulent [3]. Correlations have been obtained for the extent of the mixed convection region and for the associated heat transfer [4].

Attempts to predict the effects of buoyancy on hydrodynamic and thermal conditions in external, horizontal flows have been limited to the use of laminar, two-dimensional models [9–13]. Enhancement of heat transfer and wall shear by buoyancy, as well as criteria for determining when buoyancy can be neglected, have been determined as a function of Prandtl number and the mixed convection parameter $Gr_x/Re_x^{5/2}$. However, no attempt has been made to account for the effect of buoyancy induced turbulence or to compare predictions with available data.

The purpose of the present work is to investigate the effect of thermal instabilities on hydrodynamic and thermal conditions for water flow in an open channel which is uniformly heated from below. Experiments are performed in which hydrodynamic conditions are obtained from the shadowgraph and hydrogen bubble methods, and thermal conditions are determined from traversing thermocouple probes. Experimental results for the streamwise variation in the convection coefficient are compared with predictions based on two-dimensional, laminar and turbulent models of the flow.

Contributed by the Heat Transfer Division for publication in the JOURNAL OF HEAT TRANSFER. Manuscript received by the Heat Transfer Division March 16, 1982.

Experimental Procedures

A schematic of the water channel, which is 305-mm wide and 150-mm high, is shown in Fig. 1. Emerging from the flow straightener with a uniform velocity profile, the flow develops hydrodynamically in an unheated region, before entering a 0.99-m long heated test section. The water layer height is adjusted by lowering or raising the tailgate, and the water flow rate is adjusted by means of the valve arrangement. All sections of the channel were constructed from 12.7-mm plexiglass, except the bottom surface of the test section, which was made from 9.5-mm aluminum plate. Nineteen thermocouples, spot welded to the sides of slots machined on the top surface of the plate, were used to obtain longitudinal and transverse distributions of the surface temperature. The slots were filled with aluminum epoxy, and the surface was sanded to a smooth finish. Three electrofilm patch heaters, which provided a maximum output of 31.6 kW, were joined to the bottom surface of the plate, and a 140-mm thick layer of fiberglass insulation was installed below the heaters. Heat losses were estimated to be less than 1 percent of the heat input.

Vertical temperature distributions within the water were obtained by using six thermocouple probes, spaced at 111 mm intervals in the longitudinal direction. The probes were attached to a support, which could be traversed vertically at a rate of 0.38 mm/s. The vertical position of the probes was determined from the output of a potentiometer and, along with probe and plate temperatures, was recorded on a data logger at 5 s intervals. To obtain an indication of temperature fluctuations, vertical temperature profiles were also measured by traversing a single thermocouple probe and monitoring its output on an x-y recorder.

For uniform bottom heating, the convection coefficient may be determined from the expression

$$h = \frac{P/A}{(T_s - T_m)} \tag{1}$$

where the mean temperature of the water is defined as

$$T_m(x) = \frac{1}{H}\int_0^H T(y)\,dy \tag{2}$$

The coefficient is determined at nine longitudinal stations for which the surface temperature and the water vertical temperature distribution are measured. Results may be considered in terms of local Nusselt, Reynolds, and Grashof numbers (Nu_x, Re_x, Gr_x) or in terms of parameters based on

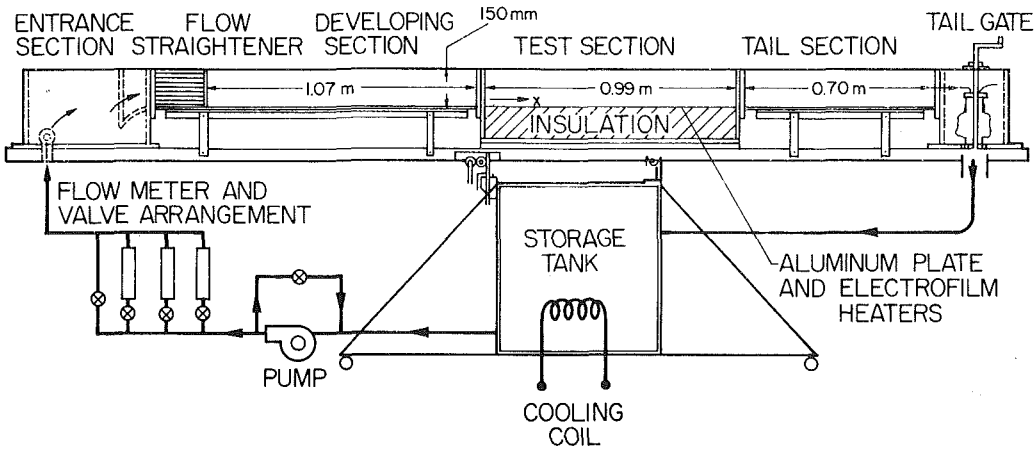

Fig. 1 Schematic of water channel facility

the water layer height (Nu_H, Re_H, Gr_H). Properties appearing in the parameters are evaulated at the temperature $(T_s + T_m)/2$. Heat transfer measurements were performed for the range of conditions 20.7 mm/s $\leq u_m \leq$ 124.2 mm/s, 1325 W/m^2 $\leq q \leq$ 7950 W/m^2, and 40 mm $\leq H \leq$ 80 mm, which correspond to 985 $\leq Re_H \leq$ 5850 and 0.70 $\leq (Gr_{q,H}/Re_H^2) \leq$ 320.

The hydrogen bubble technique was used for velocity measurements upstream of the test section and for flow visualization in the test section. Hydrogen bubbles were generated from a horizontal wire to determine spanwise nonuniformities in the flow and from a vertical wire to determine the vertical distribution of the longitudinal velocity and to infer the extent of vertical mixing. Flow visualization was also achieved by using the shadowgraph method. Collimated light from a Fresnel lens was directed normal to a channel sidewall, and the transmitted light was collected on a sheet of opal glass adjacent to the opposite sidewall. The resulting shadowgraph provided an indication of spanwise averaged flow conditions within the water.

Theoretical Procedures

Assuming incompressible, two-dimensional, constant property, steady flow, the conservation equations for a liquid layer of uniform height, H, may be expressed as

$$\frac{\partial \bar{u}}{\partial x} + \frac{\partial \bar{v}}{\partial y} = 0 \tag{3}$$

$$\bar{u}\frac{\partial \bar{u}}{\partial x} + \bar{v}\frac{\partial \bar{u}}{\partial y} = -\frac{1}{\rho}\frac{\partial \bar{p}}{\partial x} + g\beta\frac{\partial}{\partial x}\left[\int_y^H (\bar{T}-T_o)\,dy\right] + \frac{1}{\rho}\frac{\partial}{\partial y}\left(\mu_{\text{eff}}\frac{\partial \bar{u}}{\partial y}\right) \tag{4}$$

$$\bar{u}\frac{\partial \bar{T}}{\partial x} + \bar{v}\frac{\partial \bar{T}}{\partial y} = \frac{1}{\rho c_p}\frac{\partial}{\partial y}\left(k_{\text{eff}}\frac{\partial \bar{T}}{\partial y}\right) \tag{5}$$

The Boussinesq approximation has been used to evaluate the buoyancy force in the y-momentum equation, which has been integrated and combined with the x-momentum equation to

Nomenclature

A = surface area of heater plate
A^+ = Van Driest damping constant, $A^+ = 25$
c_p = specific heat
$Gr_{q,h}$ = Grashof number based on heat flux, $g\beta qH^4/k\nu^2$
Gr_x = local Grashof number, $g\beta(T_s - T_m)x^3/\nu^2$
g = gravitational acceleration
H = water layer height
h = local heat transfer coefficient
k = molecular thermal conductivity
k_{eff} = effective thermal conductivity, $k_{\text{eff}} = k + k_t$
k_t = turbulent thermal conductivity
l_m = Prandtl mixing length
Nu_H = Nusselt number, hH/k
Nu_x = Nusselt number, hx/k
P = heater power
p = pressure
Pe_t = turbulent Peclet number, $\epsilon_{mo}\text{Pr}/\nu$
Pr = Prandtl number
Pr_t = turbulent Prandtl number, $\epsilon_{mo}/\epsilon_{Ho}$
q = surface heat flux
Re_H = Reynolds number, $u_m H/\nu$
Re_x = Reynolds number, $u_m x/\nu$
Ri = Richardson number, $g\beta(\partial\bar{T}/\partial y)/(\partial\bar{u}/\partial y)^2$
T, T_m, T_s = local, mean, and surface temperatures
u, v = horizontal and vertical velocity components
u_m = mean velocity
u_* = friction velocity, $(\tau_w/\rho)^{1/2}$
x = distance from leading edge of heater surface
x_c = distance corresponding to onset of longitudinal vortices
x_1, x_2, x_3 = locations associated with buoyancy induced changes in boundary layer conditions
y = vertical coordinate measured from heater surface
y^+ = dimensionless vertical coordinate, yu_*/ν
β = thermal expansion coefficient
ϵ_H = turbulent diffusivity for heat transfer
ϵ_m = turbulent diffusivity for momentum transfer
κ = von Karman constant
μ = molecular viscosity
μ_{eff} = effective viscosity, $\mu_{\text{eff}} = \mu + \mu_t$
μ_t = turbulent viscosity
ν = kinematic viscosity
ρ = mass density
τ_w = wall shear stress

Subscripts

i = inlet conditions
o = reference conditions at $y = H$; without buoyancy
t = turbulent flow

Superscripts

$\overline{\quad}$ = time average quantity

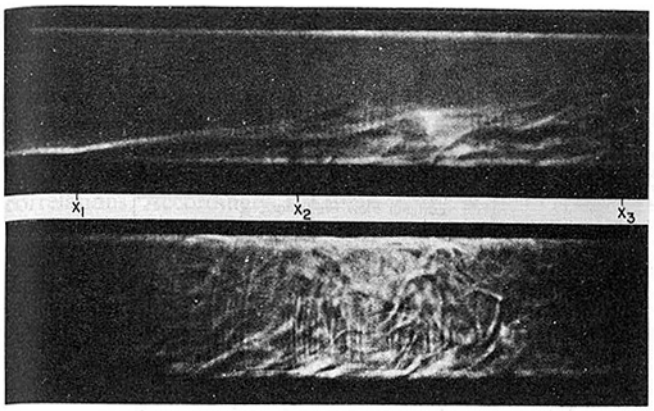

Fig. 2 Shadowgraph of thermal boundary layer development for H = 40 mm, u_m = 20.7 mm/s, and q = 5300 W/m^2 ($Gr_{q,H}$ = 9.6 × 10^7, Re_H = 1060)

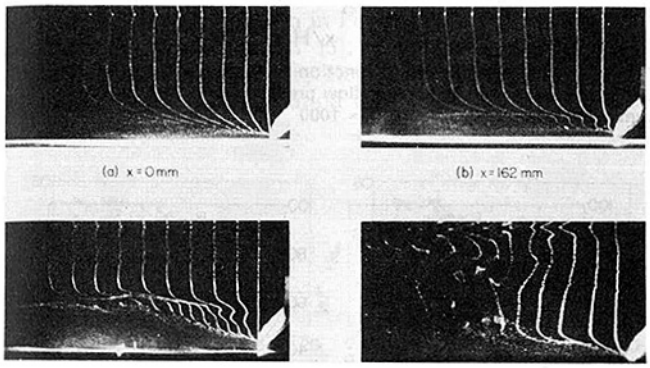

Fig. 3 Hydrogen bubble flow visualization results for H = 40 mm, u_m = 41.4 mm/s, and q = 2650 W/m^2 ($Gr_{q,H}$ = 4.0 × 10^7), Re_H = 1920)

obtain equation (4). The turbulent viscosity is determined from the Prandtl mixing length model

$$\mu_t = \rho\epsilon_{mo} = \rho l_m^2 \left|\partial\bar{u}/\partial y\right| \tag{6}$$

where, neglecting the effect of buoyancy on turbulence, the mixing length is evaluated from the Van Driest hypothesis [14]

$$l_m = \kappa y[1 - \exp(-y^+/A^+)] \tag{7}$$

for the wall layer and from a correlation suggested for open channel flows [15]

$$l_m = \kappa y\left(1 - \frac{y}{H}\right)^{1/2} \tag{8}$$

outside the wall layer. The eddy diffusivity for heat transfer is determined from a correlation for the turbulent Prandtl number [14]

$$\mathrm{Pr}_t = [0.58 + 0.22\mathrm{Pe}_t - (0.2\mathrm{Pe}_t)^2[1 - \exp(-5.39/\mathrm{Pe}_t)]]^{-1} \tag{9}$$

The effect of buoyancy on turbulence generation is treated by using eddy diffusivity correlations developed from experiments performed for thermally destabliized, open-channel flows [16]. The momentum diffusivity is correlated by

$$\epsilon_m = \epsilon_{mo}(1 - 25\mathrm{Ri})^{1/3} \tag{10}$$

where the diffusivity corresponding to no buoyancy, ϵ_{mo}, is determined from equation (6). The diffusivity for heat transfer is obtained from an expression due to Ellison [17].

$$\epsilon_H/\epsilon_m = 1.2\,\frac{1 - 10\mathrm{Ri}(\epsilon_H/\epsilon_m)}{[1 - \mathrm{Ri}(\epsilon_H/\epsilon_m)]^2} \tag{11}$$

The conservation equations are solved subject to no-slip, $u(x,0) = 0$, and uniform heat flux, $-k(\partial\bar{T}/\partial y)_{y=0} = q$, conditions at the bottom surface and zero shear, $\partial\bar{u}/\partial y)_{y=H} = 0$, and adiabatic, $\partial\bar{T}/\partial y)_{y=H} = 0$, conditions at the free surface. The heat flux at the free surface is estimated to be less than 1 percent of the bottom flux, justifying the assumption of an adiabatic surface. Entrance conditions of the form $\bar{u}(0,y) = \bar{u}_i(y)$ and $\bar{T}(0,y) = \bar{T}_i(y)$ are imposed, where the velocity profile is computed by solving the hydrodynamic equations for the unheated starting length. The equations are solved using the numerical procedure of Crawford and Kays [18], which was modified by adding the buoyancy term to the momentum equation and by adding the option of including the effects of buoyancy in the turbulence model. The solution could also be applied to laminar flow by setting μ_t and k_t equal to zero.

Results

Flow and Thermal Conditions. Shadowgraphs were obtained for a range of flow conditions, and representative results are shown in Fig. 2. Since the method is sensitive to variations in the density gradient normal to the flow direction, the shadows are indicative of vertical changes in the temperature field. For the inlet region corresponding to $x \le x_1 \approx$ 10 mm, the bright band is associated with a thin fluid layer adjacent to the heated plate and is indicative of a laminar thermal boundary layer for which the effects of buoyancy are negligible. For $x > x_1$, the boundary layer is influenced by the penetration of thermals rising from the bottom plate. In the region $x_1 < x \le x_2 \approx 80$ mm, this penetration significantly increases the boundary layer thickness, although conditions appear to remain ordered, as thermals are swept downstream with the mainflow. For $x > x_2$, boundary layer conditions become irregular, as thermal plumes emerge from the bottom plate along a steeper (more vertical) trajectory and begin to disintegrate. For $x > x_3 \approx 160$ mm, thermals have penetrated to the top of the water layer and mixing is evident throughout the layer. The foregoing trends were observed for a range of operating conditions, and the distance from the leading edge at which the flow changes occurred was found to decrease with increasing heat flux and decreasing velocity.

The progression from a stable, laminar flow to a thermally destabilized turbulent flow is similar to behavior observed by others [2, 3] for a uniform entrance velocity profile and is associated with the growth of longitudinal vortices, which subsequently break apart. The location, x_c, corresponding to the onset of vortex instability has been correlated by an expression of the form $\mathrm{Gr}_{x_c}/\mathrm{Re}_{x_c}^{3/2} = C$, where estimates of C range from 0.434 to approximately 200. Although conditions of this study are associated with a nonuniform entrance profile, correlation of the first transition point, x_1, by an equation of the same form provides results in the range $10 \lesssim \mathrm{Gr}_{x,1}/\mathrm{Re}_{x,1}^{3/2} \lesssim 85$. The fact that the results are within the range associated with a uniform entrance velocity profile suggests that the profile form has, at best, a small effect on the instability.

Representative results obtained from the hydrogen bubble method are shown in Fig. 3, where the direction of flow is from right to left. The distortion of bubble lines which occurs for $x > 0$, cases (*b*) and (*c*), is due to the penetration of thermals, and the effect becomes more pronounced with increasing x. At distances well removed from the leading edge, case (*d*), thermals have penetrated throughout the layer and there is complete mixing. Similar results obtained for other operating conditions revealed enhanced penetration with increasing heat flux and decreasing velocity.

Thermal penetration effects may also be inferred from vertical thermocouple scans, and results obtained for the instantaneous temperature (Fig. 4) are consistent with those

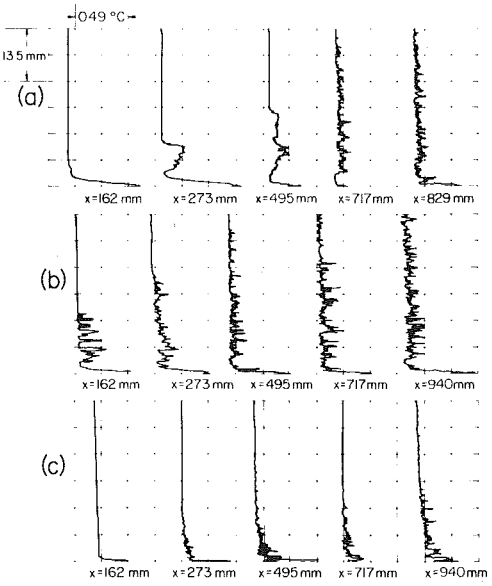

Fig. 4 Longitudinal variation of thermal penetration and mixing effects for different heat fluxes and mean velocities (H = 40 mm): (*a*) u_m = 41.4 mm/s, q = 1325 W/m^2, Re_H = 1920, $Gr_{q,H}$ = 1.5 × 10^7; (*b*) u_m = 41.4 mm/s, q = 2650 W/m^2, Re_H = 1920, $Gr_{q,H}$ = 4.0 × 10^7; (*c*) u_m = 124 mm/s, q = 2650 W/m^2, Re_H = 5430, $Gr_{q,H}$ = 3.2 × 10^7

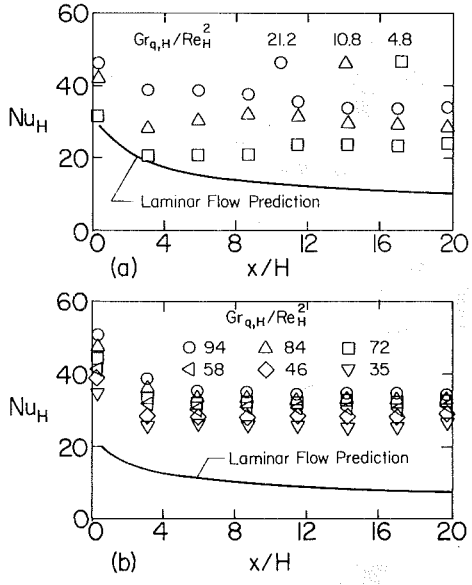

Fig. 5 Nusselt number as a function of distance along the heated section: comparison of laminar flow predictions with data for H = 40 mm and (*a*) $Re_H \approx 1900$, (*b*) $Re_H \approx 1000$

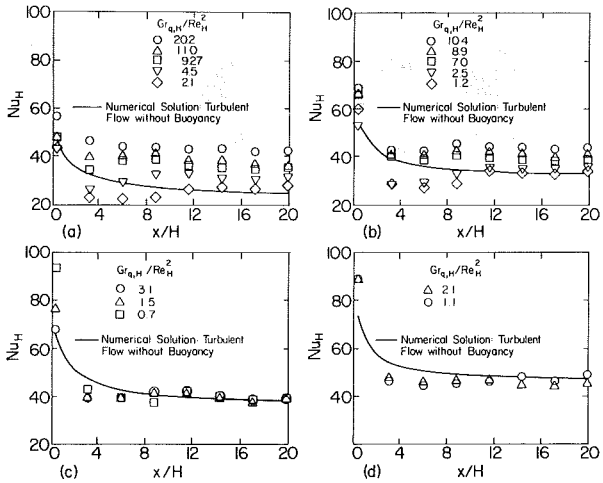

Fig. 6 Nusselt number as a function of distance along the heated section: comparison of turbulent flow predictions with data for $H \approx 40$ mm and (*a*) $Re_H \approx 3100$, (*b*) $Re_H \approx 4100$, (*c*) $Re_H \approx 4600$, (*d*) $Re_H \approx 5700$

inferred from the flow visualization. From Fig. 4(*a*), it is evident that, at x = 162 mm, the temperature profile is smooth and the effects of buoyancy are negligible. With increasing x, the effects of thermal plume penetration become evident, as profile disturbances develop in regions close to the bottom, temperature fluctuations become discernible, and the vertical extent of the mixed region increases. For $x \gtrsim 720$ mm, thermal effects have penetrated throughout the water and, with the exception of a thin sublayer adjoining the wall, mixing is complete. With increasing bottom heat flux (Fig. 4(*b*)), mixing is intensified and, for a particular location, the penetration of thermal disturbances is enhanced. Contrasting Figs. 4(*b*) and 4(*c*), the opposite is seen to be true for increasing velocity. Concerning the effect of velocity, it should also be noted that dye injection and hydrogen bubble measurements performed upstream of the heated section revealed intermittent signs of hydrodynamic instability for $Re_H \gtrsim 2500$. In no case, however, was there any indication of turbulence in the upstream region.

Comparisons of Heat Transfer Results. Representative low Reynolds number results for the longitudinal distribution of the Nusselt number are shown in Fig. 5, along with predictions based on the laminar version of equations (3–5). The entrance velocity profile used for the predictions was obtained by solving equations (3) and (4) for the unheated starting length. Agreement is poor and worsens with increasing x/H and $Gr_{q,H}/Re_H^2$. Moreover, the data reveal the existence of fully developed conditions for $x/H \gtrsim 5$, while the predictions suggest that such conditions are not reached until $x/H > 20$. Although buoyancy is neglected in the predictions, little improvement is gained by accounting for its effect. Calculations performed with and without the buoyancy term in the momentum equation indicate that its effect is to enhance heat transfer by less than 5 percent over the range $0 \leq Gr_{q,H}/Re_H^2 \leq 100$. Accordingly, with or without a buoyancy term in the momentum equation, a two-dimensional, laminar flow model is unable to predict the significant effect of buoyancy on heat transfer.

Experimental results for $Re_H > 2500$ are shown in Fig. 6, along with predictions based on a turbulent model which neglects the effects of buoyancy. The data reveal that, with decreasing $Gr_{q,H}/Re_H^2$, buoyancy effects become less significant and that, for $Gr_{q,H}/Re_H^2 \lesssim 3$, the effects are negligible. For $Gr_{q,H}/Re_H^2 \lesssim 3$, the data are well predicted, particularly for $x/H \gtrsim 10$. Overprediction of this data for $x/H \lesssim 10$ is more pronounced for the lower Reynolds numbers (Cases (*a*) and (*b*)), suggesting that the boundary layer may actually be laminar or transitional in this region. Transitional conditions are also suggested by the Case (*a*) and (*b*) data corresponding to $Gr_{q,H}/Re_H^2 \lesssim 5$, which are characterized by a minimum just downstream of the entrance.

Predictions based on turbulent models with and without buoyancy are compared with data in Fig. 7. In the region $x/H > 10$, the buoyancy model slightly overpredicts the data for small values of $Gr_{q,H}/Re_H^2 \lesssim 3$ (Case (*a*)), provides good agreement for intermediate values in the range $3 \lesssim Gr_{q,H}/Re_H^2 \lesssim 15$ (Cases (*b*) and (*c*)), and underpredicts the data for large values of $Gr_{q,H}/Re_H^2 \gtrsim 15$ (Case (*d*)). This underprediction may be due to the fact that, for large values of the mixed convection parameter, conditions are dominated by turbulent free convection [2, 3], while the turbulence

model of this study presumes the existence of mixed convection.

Despite the existence of an unheated starting length, all attempts to correlate data in terms of parameters based on distance measured from the beginning of the unheated starting section were unsuccessful, irrespective of whether starting length correction terms were applied to the correlations. Accordingly, the decision was made to compute parameters on the basis of distance measured from the beginning of the heated section and to contrast the data of this study with results obtained for the simultaneous development of velocity and thermal boundary layers [3, 4]. From these results, it is known that, in a region close to the inlet, the flow is laminar and, for constant wall temperature, heat transfer is well correlated by the Pohlhausen relation, $Nu_x = 0.332\ Re_x^{1/2}\ Pr^{1/3}$. In regions well removed from the inlet, however, conditions are dominated by turbulent free convection, and heat transfer is correlated by an expression due to Fujii and Imura [19], $Nu_x = 0.13\ (Gr_x Pr)^{1/3}$.

The extent to which the results of this study comply with the foregoing behavior is shown in Fig. 8, where, in the manner suggested by Imura et al. [3], the data are plotted as $(Nu_x/Re_x^{1/2}Pr^{1/3})$ versus $(Gr_x/Re_x^{3/2})$. Overprediction of the data by the Pohlhausen relation for $Gr_x/Re_x^{3/2} < 5$ may be attributed to the existence of a nonuniform velocity profile at $x = 0$. From comparative calculations performed using the two-dimensional model, results obtained for the uniform profile were found to exceed those obtained for the developed profile by more than 50 percent at the first measurement station ($x = 12.7$ mm), with the difference diminishing to less than 15 percent at the second station. Overprediction of the data by the laminar forced convection correlation is more pronounced, and extends to $Gr_x/Re_x^{3/2} \approx 10$, if the expression corresponding to constant wall heat flux [14], $Nu_x/Re_x^{1/2}Pr^{1/3} = 0.453$, is used in lieu of the Pohlhausen relation. Although this expression would seem to be more appropriate for the conditions of this study, it should be noted that the laminar flow data of Wang [4], which were also obtained for constant wall flux, were well correlated by the Pohlhausen expression. It should also be noted that, in this study, the wall temperature was characterized by a nearly constant value beyond the first measurement station.

For $Gr_x/Re_x^{3/2} > 400$ the data of this study are well correlated by the Fujii and Imura relation for turbulent free convection. For the mixed convection region, $10 < Gr_x/Re_x^{3/2} < 400$, the data are correlated to within 25 percent by the expression due to Wang [4]

$$Nu_x = 2.7(Gr_x/Re_x^{2.2})^{1/3}(3.379 + 0.0285Re_x^{4/5})Pr^{1/3} \qquad (12)$$

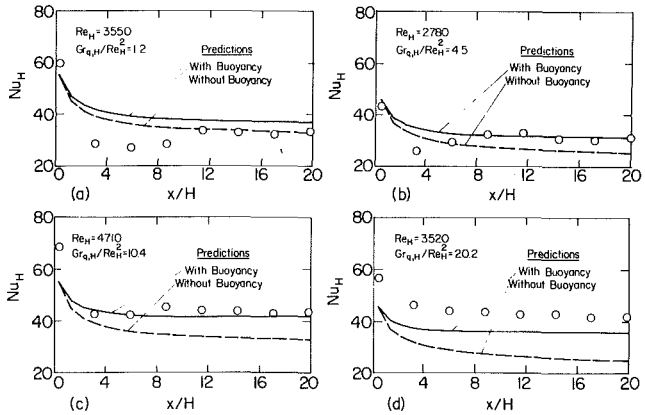

Fig. 7 Nusselt number as a function of distance along the heated section: comparison of turbulent flow predictions with data for $H = 40$ mm

Conclusions

Experiments have been performed to determine hydrodynamic and thermal conditions for water flow in an open channel which is uniformly heated from below, and a two-dimensional, boundary layer model has been used to predict the results. The principal conclusions are as follows:

1 Thermal boundary layer development on the heated surface is characterized by several regions which are influenced to varying degree by buoyancy. Buoyancy effects are negligible to a distance x_1 from the leading edge, after which the boundary layer thickness is significantly increased due to thermal plumes which are swept downstream with the main flow. Further downstream, the plumes begin to break up and the boundary layer is characterized by turbulent mixing. Eventually, thermal effects penetrate to the top of the water layer and turbulent mixing exists throughout the layer. With increasing heat flux and decreasing velocity, the location x_1 at which buoyancy effects are discernible decreases, and the

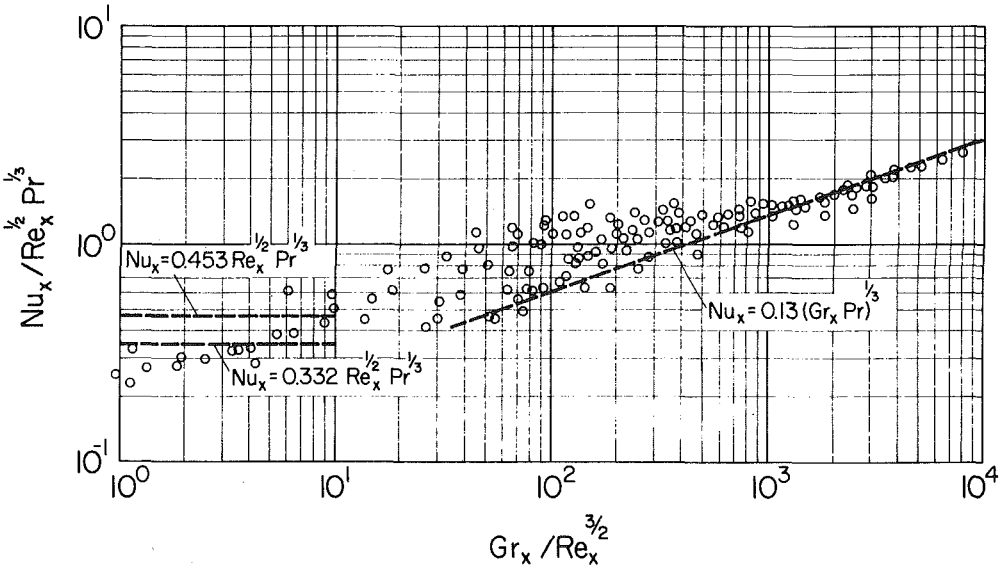

Fig. 8 Representation of heat transfer data in terms of the parameters $(Nu_x/Re_x^{1/2}\ Pr^{1/3})$ and $(Gr_x/Re_x^{3/2})$

penetration of thermal disturbances is enhanced. The onset of buoyancy induced disturbances is associated with the range $10 \lesssim \mathrm{Gr}_{x_1}/\mathrm{Re}_{x_1}^{3/2} \lesssim 85$.

2 Heat transfer is characterized by laminar forced convection in an inlet region, $\mathrm{Gr}_x/\mathrm{Re}_x^{3/2} \lesssim 10$, mixed convection in a transition region, $10 \lesssim \mathrm{Gr}_x/\mathrm{Re}_x^{3/2} \lesssim 400$, and turbulent free convection in the downstream region, $\mathrm{Gr}_x/\mathrm{Re}_x^{3/2} \gtrsim 400$. Due to the effect of the entrance velocity profile, the inlet region data are overpredicted by standard laminar, forced convection correlations. Data for the mixed convection and turbulent regions are correlated, respectively, by expressions proposed by Wang [4] and Fujii and Imura [19].

3 Heat transfer data are significantly underpredicted by a two-dimensional, laminar model which includes the effect of buoyancy in the momentum equation. In the fully developed region, data corresponding to $\mathrm{Gr}_{q,H}/\mathrm{Re}_H^2 \lesssim 3$ are well predicted by a turbulent model which ignores buoyancy, while data corresponding to $3 \lesssim \mathrm{Gr}_{q,H}/\mathrm{Re}_H^2 \lesssim 15$ are well predicted by a model which includes the effects of buoyancy on the turbulence.

Acknowledgment

This work was supported by the National Science Foundation under Grant MEA-8009034.

References

1 Akiyama, M., Hwang, C. J., and Cheng, K. C., "Experiments on the Onset of Longitudinal Vortices in Laminar Forced Convection Between Horizontal Plates," ASME JOURNAL OF HEAT TRANSFER, Vol. 93, 1971, pp. 335–341.

2 Gilpin, R. R., Imura, H., and Cheng, K. C., "Experiments on the Onset of Longitudinal Vortices in Horizontal Blasius Flow Heated from Below," ASME JOURNAL OF HEAT TRANSFER, Vol. 100, 1978, pp. 71–77.

3 Imura, H., Gilpin, R. R., and Cheng, K. C., "An Experimental Investigation of Heat Transfer and Buoyancy Induced Transition from Laminar Forced Convection to Turbulent Free Convection on a Horizontal, Isothermally Heated Plate," ASME JOURNAL OF HEAT TRANSFER, Vol. 100, 1978, pp. 429–434.

4 Wang, X. A., "An Experimental Study of Mixed, Forced, and Free Convection Heat Transfer From a Horizontal Flat Plate to Air" ASME JOURNAL OF HEAT TRANSFER, Vol. 104, 1982, pp. 139–144.

5 Moutsoglou, A., Chen, T. S., and Cheng, K. C., "Vortex Instability of Mixed Convection Flow Over a Horizontal Flat Plate," ASME JOURNAL OF HEAT TRANSFER, Vol. 103, 1981, pp. 257–261.

6 Matsuda, O., Hayashi, Y., and Takimoto, A., "Thermal Instability of Blasius Flow Over a Horizontal Flat Plate, II: Theoretical Study," Japan Society of Mechanical Engineers, *Proceedings of 29th Tokai Branch Conference*, 1980, pp. 97–99.

7 Hayashi, Y., Takimoto, A., and Matsuda, O., "Thermal Instability of Blasius Flow Over a Horizontal Flat Plate, I: Experimental Study," Japan Society of Mechanical Engineers, *Proceedings of 29th Tokai Branch Conference*, 1980, pp. 94–96.

8 Wu, R.-S., and Cheng, K. C., "Thermal Instability of Blasius Flow Along Horizontal Plates," *International Journal of Heat and Mass Transfer*, Vol. 19, 1976, pp. 907–913.

9 Mori, Y., "Buoyancy Effects on Forced Laminar Convection Flow Over a Horizontal Flat Plate," ASME JOURNAL OF HEAT TRANSFER, Vol. 83, 1961, pp. 479–482.

10 Sparrow, E. M., and Minkowycz, W. J., "Buoyancy Effects on Horizontal Boundary Layer Flow and Heat Transfer," *International Journal of Heat and Mass Transfer*, Vol. 5, 1962, pp. 505–511.

11 Hieber, C. A., "Mixed Convection Above a Heated Horizontal Surface," *International Journal of Heat and Mass Transfer*, Vol. 16, 1973, pp. 769–785.

12 Chen, T. S., Sparrow, E. M., and Mucoglu, A., "Mixed Convection in Boundary Layer Flow on a Horizontal Plate," ASME JOURNAL OF HEAT TRANSFER, Vol. 99, 1977, pp. 66–71.

13 Ramachandran, N., Armaly, B. F., and Chen, T. S., "Mixed Convection over a Horizontal Heated Flat Plate," ASME Paper 82-HT-75, 1982.

14 Kays, W. M., and Crawford, M. E., *Convective Heat and Mass Transfer*, McGraw-Hill, New York, 1980.

15 Reynolds, A. J., *Turbulence Flows in Engineering*, John Wiley and Sons, London, 1974.

16 Mizushina, T., Ogino, F., Ueda, H., and Komori, S., "Buoyancy Effect on Eddy Diffusivities in Thermally Stratified Flow in Open Channel," *Proceedings of Sixth International Heat Transfer Conference*, Vol. 1, 1978, pp. 91–96.

17 Ellison, T. H., "Turbulent Transport of Heat and Momentum from an Infinite Rough Plate," *Journal of Fluid Mechanics*, Vol. 2, 1957, pp. 456–466.

18 Crawford, M. E., and Kays, W. M., "STAN5-A Program for Numerical Computation of Two-Dimensional Internal/External Boundary Layer Flow," Rep. HMT-23, Stanford University, 1975.

19 Fujii, T., and Imura, H., "Natural Convection Heat Transfer from a Plate With Arbitrary Inclination," *International Journal of Heat and Mass Transfer*, Vol. 15, 1972, pp. 755–767.

An Experimental Study of Laminar Heat Transfer Downstream of Backsteps

W. Aung
Heat Transfer Program,
National Science Foundation
and Adjunct Professor,
Mechanical Engineering Department,
Howard University,
Washington, D. C. 20550
Fellow ASME

Results of a study of heat transfer in the vicinity of a backward-facing step of a uniform temperature are presented. Temperature distribution are measured using a Mach-Zehnder interferometer. The heat transfer upstream of the step is shown to be strongly enhanced by streamline curvature. Downstream of the step the heat transfer increases monotonically in the streamwise direction but is always less than the flat-plate value. For the largest step investigated, the average heat transfer in the reverse flow region is reduced to 56 percent of the flat-plate results, in agreement with an existing theory for laminar separated flow originally developed for a cavity. The heat transfer is systematically smaller for smaller steps. For all steps, the average heat transfer is described by the equation, $\overline{St} = 0.787(Re_s)^{-0.55}(s/x_s)^{0.72}$.

Introduction

Among the many separated forced convection situations that have been studied, the backward-facing step or backstep has received perhaps more attention than any other single flow situation. The majority of the existing studies for this case, which is depicted in Fig. 1(*a*), deal with turbulent flow though, and increasingly, laminar flow is also of concern. The recent studies in the laminar category include those by Mueller and O'Leary [1], Goldstein, Eriksen, Olson, and Eckert [2], Durst, Melling, and Whitelaw [3], Armaly and Durst [4], and Sinha, Gupta, and Oberai [5]. The existing data suggest that in the laminar range the reattachment length of the shear layer increases with the flow velocity with the reattachment varying almost linearly with the velocity. The maximum value of L/s obtained is 21, which is attained at $Re_s = 820$ [5]. At a larger value of the Reynolds number, transition occurs in the shear layer and the reattachment length abruptly decreases.

Though a number of investigations on the flow field have been reported, there appears to be no published study concerning the corresponding heat transfer problem. The purpose of the present paper is to present the results of a comprehensive experimental study on heat transfer in laminar flow of air past a heated backstep. The boundary layer flow approaching the step is laminar and the flow remains laminar through separation, reattachment, and redevelopment. The step walls are all maintained at a uniform temperature. In a previous companion paper [6], heat transfer data for laminar flow past a rectangular cavity have been reported. It is indicated there that the average Nusselt number in the cavity floor varies with the Reynolds number raised to a power that is very nearly equal to 1/2. Experiments aimed at obtaining the corresponding relationship for the backstep are described in the present paper.

Experimental Techniques and Apparatus

The present experiments are conducted in a low speed wind tunnel having a contraction ratio of 12.5: 1 and a test section of 20 cm height, 15 cm width, and 61 cm length. Step heights of 1.27 cm, 0.64 cm, and 0.38 cm are employed, giving channel expansion ratios of 1.06, 1.03, and 1.02, respectively. The top wall of the test section is composed of two aluminum blocks, the downstream block being adjustable to form the step models. The inverted step models are chosen in order to reduce free convection effects. Each block contains machined channels for heated water from a constant temperature bath that maintains each block at very nearly the same temperature that is monitored by thermocouples. Windows of optical quality are provided on the side walls of the test section which are fabricated of clear plexiglas. Air flow is induced by a squirrel-cage-type suction fan. The air velocity is varied by changing the speed of the fan through a voltage transformer.

Temperature distributions are obtained by means of a Mach-Zehnder interferometer located at the University of Minnesota, Department of Mechanical Engineering. This interferometer has a field of view that permits the observation of 9 cm in the main flow direction, including approximately

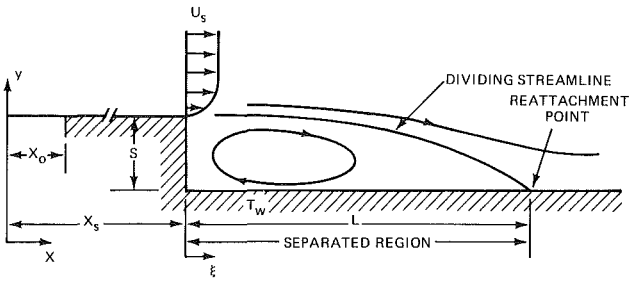

(a) TWO-DIMENSIONAL BACKSTEP

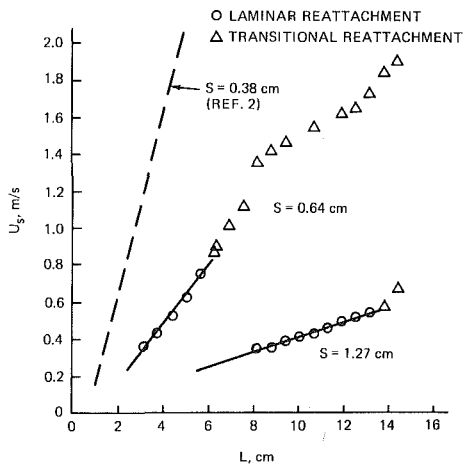

(b) REATTACHMENT DISTANCES

Fig. 1 Two-dimensional backstep and reattachment distances

Contributed by the Heat Transfer Division and presented at the 21st ASME/AIChE National Heat Transfer Conference, Seattle, Washington, July 24-28, 1983. Manuscript received by the Heat Transfer Division September 28, 1982.

Table 1 Summary of heat transfer results for laminar reattachment

Run No.		s [m]	U_s $\left[\frac{m}{s}\right]$	L [m]	$\bar{h}$ $\left[\frac{W}{m^2-C}\right]$	$\overline{St}$	Re_{x_r}	Re_s	Re_θ
11-78		.0127	0.20	.049	0.922	.00397	6205	156	49.7
11-79		.0127	0.23	.057	0.950	.00355	7243	179	53.3
11-59		.0127	0.27	.067	0.965	.00308	8632	209	57.6
11-2	11-114	.0127	0.31	.076	1.055	.00298	9771	233	60.8
11-3	11-92	.0127	0.42	.103	1.262	.00263	13905	315	70.7
11-4	11-94	.0127	0.56	.137	1.381	.00216	19671	420	81.7
12-72	12-29	.0064	0.24	.025	0.862	.00315	6836	91	53.5
12-73	12-30	.0064	0.34	.031	0.958	.00247	9817	129	63.7
12-74	12-31	.0064	0.47	.039	1.068	.00199	13793	178	74.8
12-75	12-32	.0064	0.54	.044	1.140	.00185	15994	204	80.2
12-76	12-33	.0064	0.63	.050	1.240	.00172	18883	238	86.6
12-77	12-34	.0064	0.72	.056	1.443	.00176	21849	272	92.6
13-2		.0038	0.28	.012	0.812	.00254	7751	63	57.7
13-3		.0038	0.41	.015	0.975	.00208	11415	92	69.8
13-4		.0038	0.49	.016	1.118	.00200	13699	110	76.4
13-5		.0038	0.59	.019	1.145	.00170	16587	132	83.8
13-6		.0038	0.66	.020	1.200	.00159	18608	148	88.6
13-7		.0038	0.72	.022	1.325	.00161	20354	162	92.6
13-8		.0038	0.80	.023	1.350	.00148	22678	179	97.6
13-9		.0038	0.90	.026	1.467	.00143	25664	202	103.5

1.2 cm upstream of the step. For the larger step heights investigated in this study, where the separated regions are correspondingly longer, the field of view is inadequate to cover the entire reverse flow, and a small shift in the position of the interferometer is necessary in a repeat run.

The free-stream velocity in the tunnel is measured with an impact tube via a U-tube manometer later replaced by a "Baratron" pressure transducer. The emf's of thermocouples are recorded by a Honeywell self-balancing, multipoint voltage indicator. The shear layer is investigated for any evidence of transition to turbulence by means of a TSI hot-wire system. The probe contains a 0.0001-cm dia platinum wire of 0.11 cm length. The signals from the hot wire are recorded on an oscillograph. The transition of the shear layer is determined by comparing the hot wire signal as the probe is made to traverse across the shear layer from the free stream towards the wall. If the signal indicates that the turbulence intensity in the shear layer is not noticeably larger than that at the free stream then that particular location of the shear layer is considered to be laminar; otherwise, it is taken to be transitional. The reattachment location of the shear layer is determined by smoke injection through a specially designed but simple downstream plate constructed of plexiglas and provided with 0.15-cm dia holes at 0.64 cm centers.

The hot wire anemometer is also used to probe the development of the velocity profile along the test plates with the step height set equal to zero thus forming a flat plate. These measurements suggest that the effective origin of the boundary layer flow along the plate lies 45.5 cm upstream of the location of the step, giving $x_s = 45.5$ cm, and $x_o = 15$ cm, since the heated upstream plate is of 30.5 cm length.

Further details on the experimental techniques and apparatus may be obtained from [6, 7]. It is estimated that the present method of using the interferometric technique to measure temperature gives results that are accurate to ± 7 percent. A summary of the present results for laminar reattachment is presented in Table 1. In this Table, Re_{x_r} is based on x_r, which is equal to $(45.5 + L)$ cm; Re_θ is computed using the following conventional relation for a flat plate at zero incidence

$$Re_\theta = 0.664\sqrt{Re_{x_s}}$$

The above equation is applicable here because of the large height (20 cm) of the channel compared with the displacement thickness, which is less than 1 cm at the step for practically all the experiments in the present study. As shown in [7], the heat transfer results for $s = 0$ clearly shows the applicability of the flat-plate theory.

Reattachment Length

Experiental data have been obtained for step heights of 1.27

Nomenclature

c_p = heat capacity
d = characteristic length
h = local heat transfer coefficient: $-k\left(\frac{\partial T}{\partial y}\right)_w / (T_w - T_\infty)$
$\bar{h}$ = average heat transfer coefficient in separated region
k = thermal conductivity
L = reattachment length
$\overline{Nu}$ = average Nusselt number: $\bar{h}s/k$
Pr = Prandtl number
Re_d = Reynolds number defined with d: $U_s d/\nu$
Re_θ = Reynolds number defined with the momentum thickness at the step
s = step height
$\overline{St}$ = average Stanton number in the separated region
T = temperature
U_s = free-stream velocity
x,y = coordinate directions, see Fig. 1(*a*)
x_o = unheated starting length

Greek Letters

δ_t = thermal boundary layer thickness: $\int_0^\infty \frac{T - T_\infty}{T_w - T_\infty} dy$
ν = kinematic viscosity
ρ = density
ξ = distance downstream of step

Subscripts

d = value defined with d
fp = value on flat plate
w = wall value
r = value at reattachment
x = value at location x
s = value at step or defined with s
∞ = free-stream value

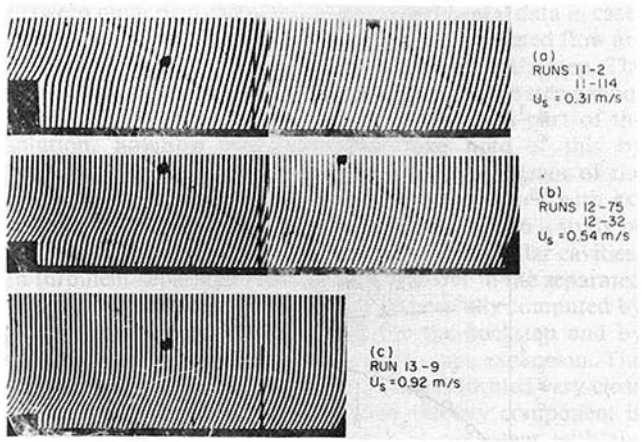

Fig. 2 Typical interferograms: (*a*) for $s = 1.27$ cm; (*b*) for $s = 0.64$ cm; (*c*) for $s = 0.38$ cm

cm, 0.64 cm, and 0.38 cm. Reattachment distances are plotted versus the free-stream velocities in Fig. 1(*b*). The data shown include those obtained in this study for $s = 1.27$ cm and $s = 0.64$ cm, and those given in [2] for $s = 0.38$ cm using a very similar apparatus. In the laminar range, the present data generally confirm the nearly linear dependence of the reattachment length on the free-stream velocity. The change in the slope following transition in the shear layer indicates an abrupt drop in the rate of increase of the reattachment length with velocity, a phenomenon also noticed by a number of other investigators. Contrary to the data reported by Sinha et al. [5], the present data show a maximum reattachment distance of $L/s \approx 10$ only. The difference may be the use in this study of a more stringent transition criterion made possible by the use of hot wire anemometry. In addition to providing information on L, which is interpolated from the figure when U_s is known in any given heat transfer run, Fig. 1(*b*) also serves to indicate the upper limit of the velocity to be used for each step height in the present experiments on laminar separated forced convection. For the three steps investigated here, the upper limits, when expressed in terms of the Reynolds number defined using the momentum thickness of the boundary layer at the step, are:

for $s = 0.0127$ m: $\mathrm{Re}_\theta = 81.7$
$s = 0.0064$ m: $\mathrm{Re}_\theta = 92.6$
$s = 0.0038$ m: $\mathrm{Re}_\theta = 103.5$

The continued increase of L, even after transition sets in, is not surprising. Turbulence causes a more rapid spread of the shear layer, and hence, a tendency for the reattachment length to shorten. However, during the early stages of transition, the effect is confined to a small region at the end of the free shear layer; hence, the shear layer continues to lengthen as the velocity increases. The rate of increase of the reattachment distance is reduced as compared with the fully laminar regime, as shown by the change in the slope in each of the two data sets in Fig. 1(*b*). Eventually, as transition occurs further and further upstream along the free shear layer with the continued increase in the velocity, turbulence mixing in the shear layer begins to have an impact in bringing the reattachment location back towards the step. This continues until the shear layer is fully turbulent, at which stage the reattachment length becomes roughly independent of the velocity [10].

Temperature Profiles and Heat Transfer Coefficients

Typical interferograms are shown in Fig. 2 for the three step heights investigated and representative temperature profiles are plotted in Fig. 3. It is evident from these figures that the boundary layer thicknesses at the step in these studies are of the order of the step height. Compared with profiles in

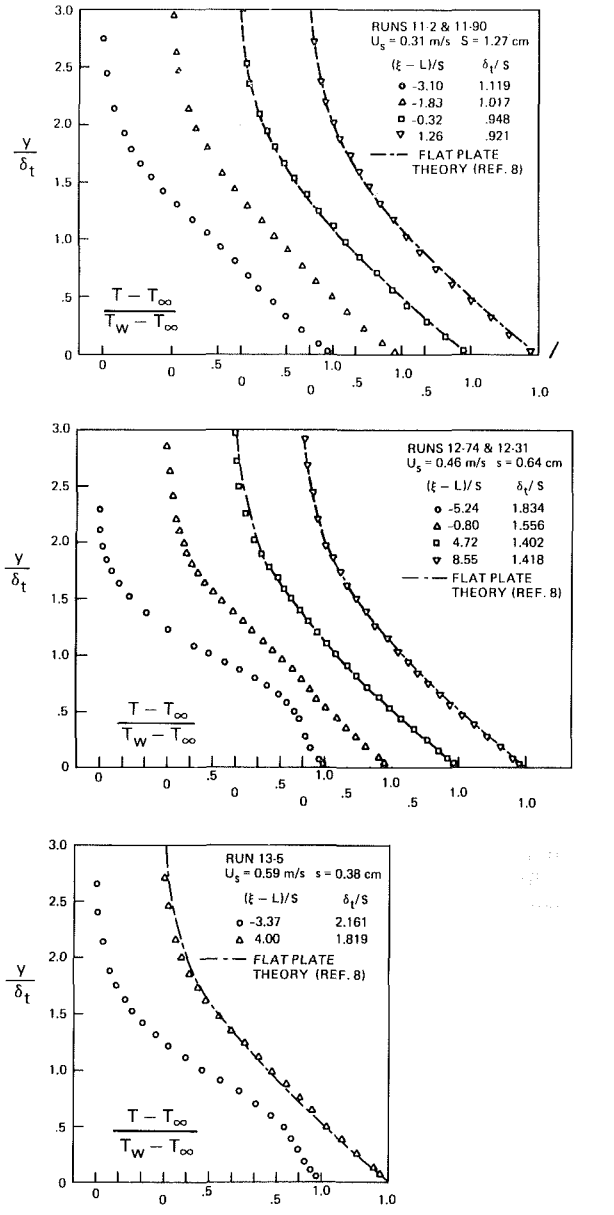

Fig. 3 Temperature distributions downstream of step and comparison with flat-plate theory

transitional and turbuent flow reported by Aung and Goldstein [9, 10], the laminar profiles have the tendency to more quickly develop into shapes that are reminiscent of attached laminar boundary layer flow along a heated flat plate at zero incidence. However, the present profiles fail to completely merge into the conventional flat-plate profile even at a distance 4 step heights downstream of the reattachment point. At 8.55 step heights the measured profile finally becomes almost indistingishable from that given by the flat-plate theory. Thus, though boundary layer theory for a flat plate at zero incidence is inadequate for the description of the heat transfer process in a relatively large region following rettachment, the flow does redevelop into a simple boundary layerlike situation after about 9 step heights beyond reattachment. The continued decrease of the thermal boundary layer thickness beyond the reattachment point indicates that the local heat transfer continues to increase. This is confirmed by the distributions of the local heat transfer coefficients shown in Fig. 4, where the reattachment locations are also indicated. The broken lines represent the heat transfer that

would occur if the step height were set to zero, and are calculated from the following conventional equation for Pr = 0.72 [11]

$$h_{fp,x} = 0.298\,(\mathrm{Re}_x)^{1/2}\,(k/x)\,[1-(x_o/x)^{3/4}]^{-1/3} \qquad (1)$$

where x_o = 15 cm for the present study. Figure 4 shows that in all cases the heat transfer downstream of the step is smaller than the zero step height, flat plate or attached flow value. By contrast when the boundary layer is turbulent prior to separation, the heat transfer is always somewhat larger than the attached flow results [10]. For the transitional shear layer prior to reattachment the heat transfer at the reattachment point may be as high as 6 or 7 times the attached (laminar) flow value [9]. In laminar flow, the maximum heat transfer occurs downstream of the reattachment point. The increase of the heat transfer following reattachment is proportionately larger for the smaller step. Nevertheless, the ratio $h_r/h_{fp,r}$ is relatively constant for each individual step as indicated in Fig. 5.

Heat Transfer Coefficients Upstream of the Step

Immediately downstream of the step, the pressure attains relatively low values [12] causing the normal component of velocity to decrease. This means that streamlines will tend towards the wall. This effect will normally propagate upstream of the step (in subsonic flow) and streamline curvature should be felt upstream of the step. Flow visualization studies conducted using the infinite fringe setting of the Mach-Zehnder interferometer seem to confirm this, as do the smoke injection studies carried out by Goldstein et al. [2]. However, the streamline curvature, though unmistakable, is slight and the implication from both flow visualization studies is that the streamline curvature effect causes the streamlines upstream of the step to become essentially parallel to the wall (instead of turning away from it as in the normal growth of an attached boundary layer). They continue in the same direction for a significantly distance downstream of the step before dramatically bending to the wall for reattachment. The curvature effect upstream of the step, however, is to enhance the heat transfer there. This effect is shown in Fig. 6 for s = 1.27 cm. The local heat transfer at the step is more than 30 percent higher than the flat-plate value at the lowest Reynolds number investigated. When the velocity is increased, the reattachment distance increases, the curvature at the step is lessened, and the overvalue of the heat transfer at the step decreases. This trend continues until the maximum velocity for laminar reattachment is attained. Here the heat transfer at the step is still about 10 percent higher than the flat-plate value. A further increase in the velocity causes transition to occur in the shear layer. Turbulence causes a larger spread of the shear layer, giving it the tendency to reattach sooner, except that in the initial stages of transition the effect is confined to the downstream region of the shear layer so that there is only a small net impact on the reattachment length. The reattachment distance therefore continues to increase with velocity, and the overvalue of the heat transfer at the step continues to decrease as the velocity increases. Since the location of transition moves upstream along the shear layer as the velocity is increased, a point is reached where a further increase in the velocity causes the reattachment location to move upstream and the heat transfer overvalue to increase once more. Figure 6 shows that for s = 1.27 cm this point occurs at a Reynolds number of approximately 2×10^4. When the shear layer is fully turbulent existing data indicate that the reattachment distance becomes independent of the velocity. Presumably, the overvalue in the heat transfer also reaches a constant, though this has not been investigated.

The phenomenon described above appears not to have been studied before but its existence could lead to disagreements

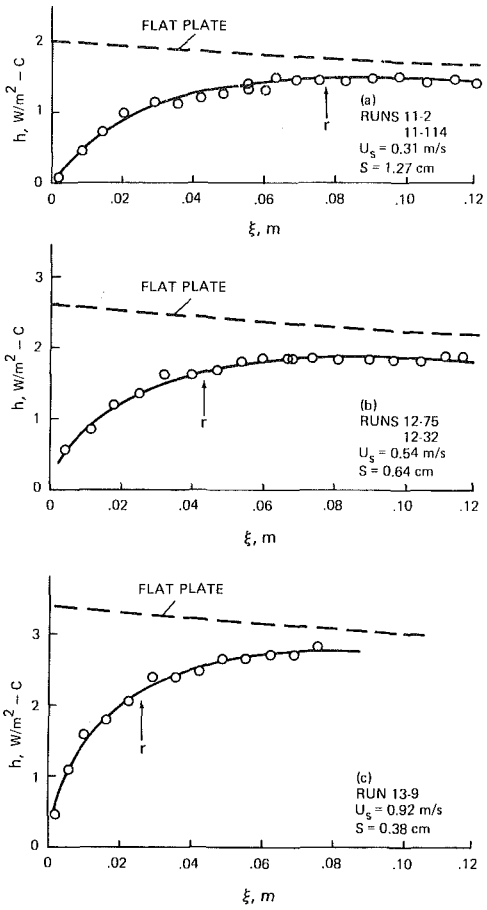

Fig. 4 Typical axial variation of local heat transfer coefficient

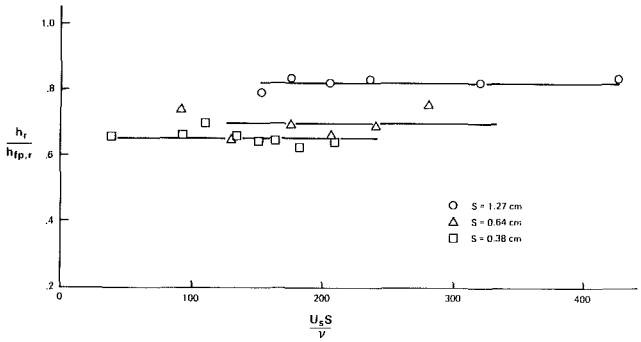

Fig. 5 Heat transfer coefficient at the reattachment point

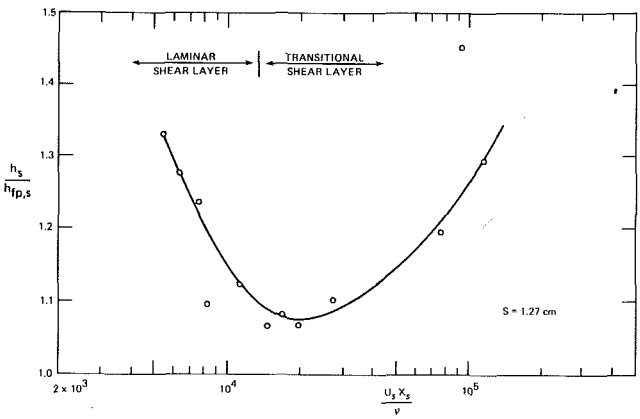

Fig. 6 Heat transfer upstream of step

between numerical calculations and experimental data in cases where numerical computations for laminar separated flow are carried out by specifying boundary conditions at the step. The data in Fig. 6 would suggest that conditions at the step cannot be specified *a priori*, but must be calculated as part of the solution. Solution procedures that take note of this by beginning the calculation at some distance upstream of the point of separation have been shown to agree well with experiments as illustrated by Bhatti and Aung [13] in a study of laminar separated forced convection past rectangular cavities. In turbulent separated flow the heat transfer in the separated and redevelopment region has been successfully computed by Gooray, Watkins, and Aung [14] for the backstep and by Chieng and Launder [15] for the sudden pipe expansion. The inflow boundary in each of these studies is located very close to the step but the inflow transverse velocity component is specified to be zero. This approach is consistent with the experimental evidence that steamlines are approximately parallel to the wall just upstream of the step.

Correlation of Transfer Coefficients in the Separated Region

The heat transfer between the step and the reattachment point is governed by the interaction between the reattaching shear layer and the recirculating flow. As such, the transport mechanism is different from that downstream of reattachment where as shown previously the heat transfer process is eventually controlled by a boundary layerlike transfer mechanism. It is therefore customary to isolate the heat transfer in the separated region, i.e., between the step and the reattachment point, for the purpose of discussion and correlation. In Fig. 7, all the data obtained in the present lamiar flow study are plotted in terms of Stanton number and Reynolds number. The data for transitional reattachment with the 0.64 cm step [9], which are correlated by the equation

$$\overline{\mathrm{St}} = 0.188 \times 10^{-5}\ \mathrm{Re}_{x_r}{}^{0.6} \tag{2}$$

are also indicated for comparison. The Stanton number is defined as

$$\overline{\mathrm{St}} = \frac{\bar{h}}{\rho U_s c_p} = \frac{\overline{\mathrm{Nu}}_d}{\mathrm{PrRe}_d}$$

Note the opposing trends for the Stanton number in the two flow situations. Extension of the line representing the turbulent flow data of Seban, Emergy, and Levy [16] for s = 0.64 cm is also plotted to complete this heat transfer regime map. Note also that the data from Aung and Goldstein [10] are not included in the plot, since in that study, the turbulent boundary layer is generated by a trip, and hence a meaningful Reynolds number cannot be determined easily. The line representing laminar flat plate theory is obtained by noting in Fig. 4 that in the region of interest the attached flow is given by nearly straight lines. Hence, we have

$$\bar{h}_{fp} = 0.5\,(h_{fp,x_s} + h_{fp,x_r}) \tag{3}$$

where h_{fp,x_s} and h_{fp,x_r} are given by equation (1)

The laminar separated flow theory shown in Fig. 7 is derived using Chapman's classical results [17] for open cavities. The latter situation is somewhat different from the flow past backsteps. The more significant difference lies in the reattachment distances which are fixed for open cavities and are equal to their widths. As discussed in [6], the external flow tends to skim over the cavity. For the backstep, it may be inferred from previous remarks in connection with Fig. 6 that the dividing streamline remains relatively straight along the axial direction for a significant portion of the separated region. In this respect, the flow past a backstep resembles the

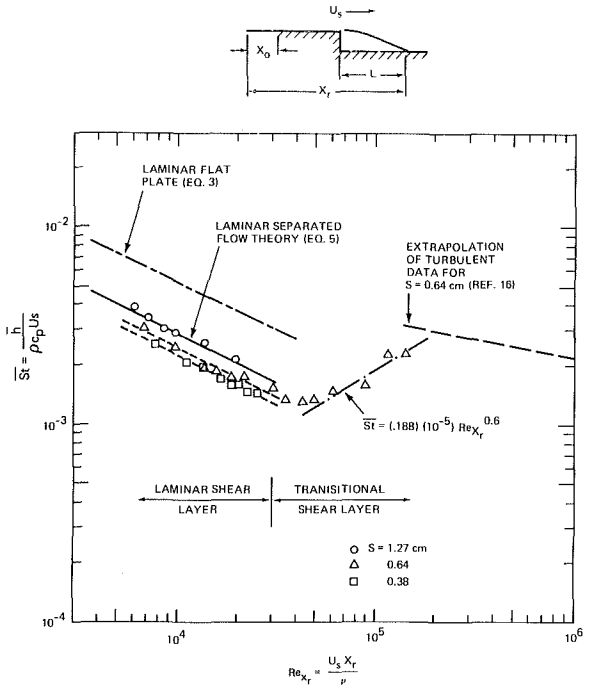

Fig. 7 Average Stanton number versus Reynolds number

flow past a cavity. One may also conclude from the work of Chapman et al. for the backstep [12] and of Nicoll for the cavity [18] that the flow structures in the two geometries are also similar to the extent that in either case the pressure distribution remains constant for some distance downstream of the point of separation. The above similarities provide a rationale for applying Chapman's theory to the backstep problem. Rephrasing Chapmans' theory, we can write

$$\frac{\bar{h}}{\bar{h}_{fp}} = 0.56 \tag{4}$$

Combining equations (3) and (4), we have

$$\bar{h} = 0.28\,(h_{fp,x_s} + h_{fp,x_r})$$

With this expression, the theoretical average Stanton number in the separated region may be calculated. The result, when plotted as a function of Re_{x_r}, can be represented by the following equation

$$\overline{\mathrm{St}} = 0.293\,(\mathrm{Re}_{x_r})^{-0.50} \tag{5}$$

This is the laminar separated flow theory indicated in Fig. 7. Nearly perfect agreement is seen with the present data for s = 1.27 cm, but the data for the smaller steps are systematically lower. Remarkably, the variation of the Stanton number with Reynolds number is close to that predicted by the theory.

The poorer agreement with Chapman's theory as obtained by the data for the two smaller steps can be explained by the comparatively short shear layer lengths at the same velocities when the step sizes are small. When the shear layer length is short, the thickness of the initial shear layer cannot be ignored. Since Chapman's theory is based on a shear layer of vanishing initial thickness, the theory cannot be expected to accurately predict the heat transfer in the separated regions of small steps. The present exprimental evidence would suggest that the theory should be valid for steps with $s \geq 1.27$ cm, but this conclusion must be regarded as tentative.

For general application, it is desirable to rephrase the present data using as an independent parameter the Reynolds number based on step height. From graphs of $\overline{\mathrm{St}}$ versus Re_s, the following correlations may be obtained

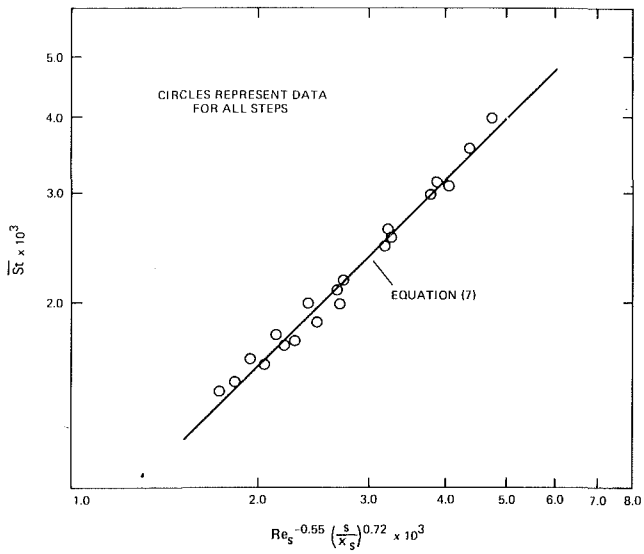

Fig. 8 Correlations of average Stanton number for all steps

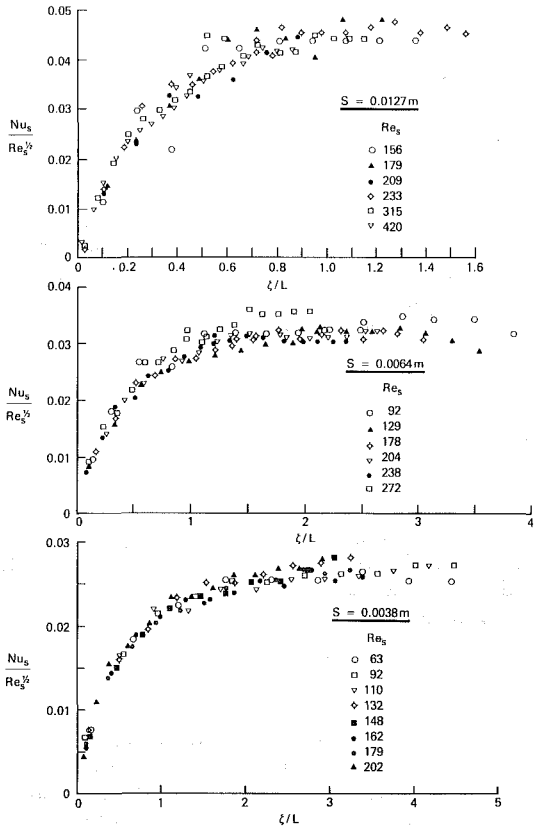

Fig. 9 Dimensionless local heat transfer downstream of the step (note differences in scales)

$$\overline{St} = c\,(Re_s)^{-0.55} \tag{6}$$

where $c = 0.061$ for $s = 1.27$ cm
$c = 0.037$ for $s = 0.64$ cm
$c = 0.026$ for $s = 0.38$ cm

Upon normalizing s by x_s, the coefficient, c, may be obtained as a function of s/x_s by cross-plotting the above data. This leads to the following overall correlation that is valid for all steps

$$\overline{St} = 0.787\,(Re_s)^{-0.55}\,(s/x_s)^{0.72} \tag{7}$$

This equation is compared in Fig. 8 with all the laminar data obtained in this study. The equation predicts the measurement to ± 5 percent in the range of the present data which is $63 \leq Re_s \leq 420$ and $0.0084 \leq s/x_s \leq 0.0279$.

Note that equation (6) implies that $Nu \propto Re_s^{0.45}$ or $\bar{h} \propto U_s^{0.45}$. The cavity data by Aung [6] show the index to be 0.55 for the square cavity and 0.47 for the cavity with width to depth ratio equal to 4. All these indices are quite close to the value of 0.5 given by Chapman's theory [cf. Eq. (5)]. In Fig. 9, the local Nusselt number downstream of the step is divided by the factor $(Re_s)^{0.5}$ and plotted against the distance from the step normalized by the reattachment length. For each step the data for all velocities (i.e, Reynolds numbers) appear to collapse into a single curve and the parameter $Nu_s/Re_s^{0.5}$ approaches an asymptote that is proportional to the step size. The asymptotes are approximately 0.045, 0.032, and 0.027 for the step sizes of 1.27 cm, 0.64 cm, and 0.38 cm, respectively.

Conclusion

A number of interesting aspects of laminar separated forced convection have emerged from the present experimental study. The effect of streamline curvature has been shown to significantly enhance the heat transfer upstream of the step. The flow and heat transfer conditions at the step therefore deviate from those given by boundary layer theories on a flat plate. Where these theories are utilized to specify upstream conditions in separated flow calculations, the specification should be made at some distance upstream of the step. The local heat transfer has been shown to increase monotonically across the reattachment point, and quantitatively, it is less than the flat-plate value. The separated region, in which the heat transfer is governed by a vortex flow mechanism, and the redevelopment zone, controlled by a conventional boundary layerlike heat transfer mechanism, are demarcated by a reattachment point without any distinctive heat transfer property, except that it is situated upstream of the location of maximum heat transfer. The interaction of the above two heat transfer mechanisms near the reattachment point, and the subsequent redevelopment process further downstream are not sufficiently well understood to allow for the prediction of the associated heat transfer. However, the present evidence suggests that the boundary layer profile may have evolved into a conventional flat-plate profile at about 8–9 step heights downstream of reattachment. The degree of agreement of the present data with the separated flow heat transfer theory of Chapman, initially developed for a cavity, is not surprising in view of the similarities in the basic flow structures for the backstep and the cavity.

Acknowledgment

The experiments discussed in this paper were performed in the Department of Mechanical Engineering, University of Minnesota. The author is pleased to record this appreciation to Professor Richard J. Goldstein for a number of critical comments and suggestions.

References

1 Mueller, T. J., and O'Leary, R. A., "Physical and Numerical Experiments in Laminar Incompressible Separating and Reattaching Flow," AIAA Paper No. 70-763, July 1970.

2 Goldstein, R. J., Eriksen, V. L., Olson, R. M., and Eckert, E. R. G., "Laminar Separation, Reattachment and Transition of Flow Over a Downstream Facing Step," ASME *Journal of Basic Engineering*, Vol. 92, Dec. 1970, pp. 732-741.

3 Durst, F., Melling, A., and Whitelaw, J. H., "Low Reynolds Number

Flow Over a Plane Symmetric Sudden Expansion," *Journal of Fluid Mechanics*, Vol. 64, June 1974, pp. 111–128.

4 Armaly, B. F., and Durst, F., "Reattachment Length and Circulation Regions Downstream of a Two-Dimensional Single Backward Facing Step," *Momentum and Heat Transfer Processes in Recirculating Flows, Proceedings of ASME*, HTD Vol. 13, Winter Annual Meeting, Chicago, Ill., Nov. 16–21, 1980.

5 Sinha, S. N., Gupta, A. K., and Oberai, M. M., "Laminar Separating Flow Over Backsteps and Cavities Part I: Backsteps," *AIAA Journal*, Vol. 19, Dec. 1981, pp. 1527–1530.

6 Aung, W., "An Interferometric Investigation of Separated Forced Convection in Laminar Flow Past Cavities," ASME JOURNAL OF HEAT TRANSFER, Vol. 105, No. 3, pp. 505–512, 1983.

7 Aung, W., "Heat Transfer in the Separated Region Beyond a Rearward-Facing Step," Ph.D. thesis, Department of Mechanical Engineering, University of Minnesota, 1969.

8 Eckert, E., "Die Berechnung des Warmeubegangs in der laminaren Grenzschicht," *VDI - Forschungsheft* 416, 1942.

9 Aung, W., and Goldstein, R. J., "Temperature Distribution and Heat Transfer in a Transitional Separated Shear Layer," *Heat Transfer, Proceedings of Fourth International Heat Transfer Conference*, Paper No. FC 1.5, Versailles, France, 1970.

10 Aung, W., and Goldstein, R. J., "Heat Transfer in Turbulent Separated Flow Downstream of a Rearward-Facing Step," *Israel Journal of Technology*, Vol. 10, No. 1-2, 1972, pp. 35–41.

11 Eckert, E. R. G., and Drake, R. M., *Heat and Mass Transfer*, McGraw-Hill Book Co., 2nd ed., 1959, p. 176.

12 Chapman, D. R., Kuehn, D., and Larson, H., "Investigation of Separated Flow in Supersonic and Subsonic Streams with Emphasis on the Effect of Transition," NACA Report 1356, 1958.

13 Bhatti, A., and Aung, W., "Finite Difference Analysis of Laminar Separated Forced Convection in Cavities," to appear in ASME JOURNAL OF HEAT TRANSFER.

14 Gooray, A., Watkins, C. B., and Aung, W., "Numerical Calculations of Turbulent Heat Transfer Downstream of a Rearward-Facing Step," *Numerical Methods in Laminar And Turbulent Flow: Proceedings of the Second International Conference*, Venice, Italy, July 13–16, 1981, edited by C. Taylor and B. A. Schrefler, Pineridge Press, Swansea, U.K., pp. 639–651.

15 Chieng, C. C. and Launder, B. E., "On the Calculation of Turbulent Heat Transport Downstream from an Abrupt Pipe Expansion," *Numerical Heat Transfer*, Vol. 3, 1980, pp. 189–207.

16 Seban, R. A., Emery, A. F., and Levy, A., "Heat Transfer to Separated and Reattached Subsonic Turbulent Flows Obtained Downstream of a Surface Step," *Journal of Aerospace Sciences*, Vol. 26, 1959, pp. 809–814.

17 Chapman, D. R., "A Theoretical Analysis of Heat Transfer in Regions of Separated Flow," NACA TN 3792, 1956.

18 Nicoll, K. M., "A Study of Laminar Hypersonic Cavity Flows," *AIAA Journal*, Vol. 2, No. 9, 1964, pp. 1535–1541.

On the Cooling of Fibers

A. Moutsoglou
Department of Mechanical Engineering, Virginia Polytechnic Institute and State University, Blacksburg, Va. 24061
Mem. ASME

The effects of the stretching of filaments on the cooling of fibers during the melt-spinning process are studied numerically. The filament is modeled as a continuous, cylindrical cone that moves steadily through an otherwise quiescent environment, with its diameter attenuating exponentially. Radiative cooling from the fiber surface is also accounted for in the analysis. The buoyancy-affected laminar and turbulent boundary layer equations are solved by a finite difference scheme, to determine the axial temperature variation of the filament. It is found that the reduction of the fiber diameter and the subsequent increase in the local speed of the filament enhances greatly the cooling from the filament surface, whereas the increase of the cooling due to radiative losses is not significant for all the flow cases considered.

Introduction

In the melt-spinning process the high-viscosity molten polymer is extruded at a temperature in the range of 200–300°C, from an array of small holes (about 0.01 ~ 0.1 mm in diameter) in the spinneret. The filaments formed, lose heat to the cooler surroundings by both convection and radiation mechanisms, while they attenuate in diameter due to the spinning stretch until they solidify, and are then wound up on a rotating bobbin. Copley and Chamberlain [1] and Barnett [2] independently attempted to predict the heat losses and, subsequently, the axial temperature distribution of a spinning isolated monofilament. However, their heat transfer estimates were based on empirical relations mostly derived for stationary constant-diameter cylinders. Recently, the cooling of a constant diameter fiber has been studied in [3, 4]. In both studies, however, the filament attenuation and the radiation losses were neglected. A systematic numerical model in simulating the cooling of a spinning fiber is presented in this paper in order to predict more accurately the axial temperature variation of the filament.

Analysis

The filament is modeled as a cylindrical cone of initial radius, r_i, the spinnaret hole radius, and final radius, r_f, the desired fiber radius as shown in Fig. 1. By adjusting the take-up speed of the bobbin, one can attain any desired final fiber diameter. However, one should note that the decrease in filament diameter and the heat loss from the fiber are coupled with each other. This is because the loss of heat is the main reason of the increase in polymer viscosity, which ultimately stops attenuation and therefore the increase of the local velocity of the filament, as the mass flow of the extruded polymer is constant. The decrease in filament diameter and increase of local speed in turn, affect the convective and radiative losses from the fiber. Copley and Chamberlain [1] experimentally found that the attenuation of the filaments they spun followed an exponential decay of the form

$$r_o(x) = r_f + (r_i - r_f)e^{-x/K} \tag{1}$$

where the constant, K, is the distance from the spinneret at which the filament has attenuated 63.2 percent of the way toward its final diameter; at $x = 3K$ this attenuation is 95 percent, and at $x = 5K$ it has reached 99.3 percent.

The melt-spinning of fibers possesses the characteristics of moving surfaces where the boundary layers grow in the direction of motion of the surface. The modeled monofilament is assumed to be extruded under steady-state conditions at a constant extrusion temperature T_i, with a given wind-up speed of the bobbin, u_f, and with the properties of the polymer taken to be constant and averaged at some mean temperature. The quiescent ambient fluid is at a constant temperature, T_∞, and the properties of the fluid are assumed to be constant and that of air, where the density variations due to temperature gradients in the fluid induce buoyancy forces according to the Boussinesq approximation. In the analysis, however, the buoyancy force component perpendicular to the surface is neglected in order to make the boundary layer axisymmetric and reduce the analysis to two-dimensional. The stationary coordinate frame has its origin located at the center of the spinneret hole, with the x-axis extending along the centerline of the cylindrical cone in the direction of motion of the filament, while the r-axis is measured from the centerline of the cone in the radial direction as shown in Fig. 1.

The governing two-dimensional steady turbulent boundary layer equations are given as

$$\frac{\partial u}{\partial r} + \frac{1}{r}\frac{\partial}{\partial r}(rv) = 0 \tag{2}$$

$$u\frac{\partial u}{\partial x} + v\frac{\partial u}{\partial r} = \frac{1}{r}\frac{\partial}{\partial r}\left[(\nu + \nu_t)r\frac{\partial u}{\partial r}\right] \pm g\beta\cos\gamma(T - T_\infty) \tag{3}$$

$$u\frac{\partial T}{\partial x} + v\frac{\partial T}{\partial r} = \frac{1}{r}\frac{\partial}{\partial r}\left[(\alpha + \alpha_t)r\frac{\partial T}{\partial r}\right] \tag{4}$$

where the conventional symbols have been used, γ is the acute angle of inclination of the filament measured from the vertical, and the plus and minus signs of the streamwise buoyancy force component term refer to upward or downward motion of the fiber, respectively.

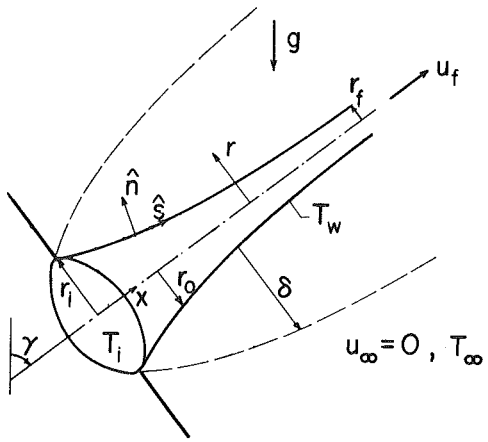

Fig. 1 Schematic and coordinate system

Contributed by the Heat Transfer Division for publication in the JOURNAL OF HEAT TRANSFER. Manuscript received by the Heat Transfer Division October 4, 1982.

The corresponding boundary conditions for equations (2–4) are

$$u=u_o(x),\quad v=0,\quad T=T_w(x)\ \text{at}\ r=r_o(x)$$
$$u=0,\quad T=T_\infty\ \text{as}\ r\to\infty \tag{5}$$

In equations (5), $u_o(x)$ is the local average speed of any cross section of the fiber and can be evaluated from the constant mass-flux of the polymer as

$$u_o(x)=u_f\left[\frac{r_f}{r_o(x)}\right]^2 \tag{6}$$

where the variation of the density of the polymer is neglected, and $r_o(x)$ is estimated from equation (1).

The surface temperature of the filament, $T_w(x)$, is evaluated from an energy balance on the filament, approximated as

$$\frac{1}{2}\frac{\rho_s C_s}{k}u_f\frac{r_f^2}{r_o(x)}\frac{1}{(ds/dx)}\frac{dT_w}{dx}=\frac{1}{(ds/dx)}\frac{\partial T}{\partial r}\bigg|_{r=r_o(x)}-\frac{\epsilon\sigma}{k}(T_w^4-T_\infty^4) \tag{7}$$

$$T_w(x)=T_i\ \text{at}\ x=0 \tag{8}$$

where n and s are the normal and tangential coordinates on the fiber surface, as shown in Fig. 1, and

$$\hat{n}=\frac{\hat{r}-(dr_o/dx)\hat{x}}{(ds/dx)},\quad \frac{ds}{dx}=\left[1+\left(\frac{dr_o}{dx}\right)^2\right]^{1/2} \tag{9}$$

In equation (7), it is assumed that the temperature of the fiber at any axial location, $T_w(x)$, is uniform across the cross section of the filament. In [2], it was found that the maximum difference in temperature between the center of the filament and its surface was always under 7°C for all cases considered. In [3], the Biot numbers calculated were always found to be 0.1 or smaller for all flow configurations considered, thus assuring an error of 5 percent or less regarding the assumption of the radial uniformity of the fiber temperature. With Peclet numbers for the fiber, $\mathrm{Pe}_s=u_f r_i/\alpha_s$ of the order of 136 Re, where the properties are evaluated at a film temperature of 123°C, the axial conduction term has been neglected in equation (7). The mean film temperature of 123°C is based on the mean surface temperature of 228°C (the mean of the spinning temperature and melting point of the polymer), and the mean air temperature of 18°C. In evaluating the convective loss from the tapered surface, in equation (7), the heat flux in the x-direction is neglected when compared to that in the r-direction, since $|(\partial T/\partial r)_{r=r_o}|>|(\partial T/\partial x)_{r=r_o}|$ and $|(dr_o/dx)|<<1$ for all cases considered in the analysis. Opaque, gray, diffuse surface behavior is assumed in estimating the radiation loss from the fiber in equation (7). As mentioned in [1], for Nylon 6, the latent heat of solidification is about 15 cal/g, and its effect would be to decrease the temperature gradient in the regions of the filament where it is being evolved. Since in the present study the phase change of the fiber is not taken into account, it was deemed appropriate to neglect the latent heat of solidification.

A mixing length model is used to approximate the turbulent diffusivities for momentum and heat that appear in equations (3) and (4). An extension of the Van Driest model accomodating Rao's law of the wall to account for the curvature of the boundary layer is employed in describing ν_t in the inner region. The eddy diffusivity for momentum in the outer region is based on the kinematic displacement thickness. A constant turbulent Prandtl number of 0.9 is utilized in evaluating the eddy diffusivity for heat α_t. The details of the model are given in equations (8–14) of [4] with r_o and u_o now denoting the local radius and local speed of the cylindrical cone, respectively.

The governing system of equations is nondimensionalized using the following transformation

$$\xi(x)=x/r_i,\quad \eta=(r^2-r_o^2)(u_f/\nu x)^{1/2}/4r_0$$
$$f(\xi,\eta)=\psi(x,r)/r_i(\nu u_f x)^{1/2},\quad \theta(\xi,\eta)=(T-T_\infty)/(T_i-T_\infty) \tag{10}$$

where $u=(\partial\psi/\partial r)/r$ and $v=-(\partial\psi/\partial x)/r$. The resulting dimensionless form of the differential equations, equations (2–4) and (7), is

$$\left[(1+\nu_t^+)\left(\frac{r_o}{r_i}+4\eta\frac{\xi^{1/2}}{\mathrm{Re}^{1/2}}\right)f''\right]\quad +ff''$$

Nomenclature

A = r_i/r_f, dimensionless geometry parameter
B = r_i/K, dimensionless spinning parameter
C = specific heat of fluid
C_s = specific heat of fiber
f = reduced stream function, equation (10)
g = gravitational acceleration
Gr = Grashof number, equation (17)
h = $q_w/(T_w-T_\infty)$, local heat transfer coefficient
k = thermal conductivity of fluid
K = distance constant
M = dimensionless radiation parameter, equation (18)
n = normal coordinate, Fig. 1
Nu_x = hx/k, local Nusselt number
Pe_s = $u_f r_i/\alpha_s$, Peclet number of fiber
Pr = Prandtl number
Pr_t = turbulent Prandtl number
q_w = $-k(\partial T/\partial n)_{r=r_o}$, local surface heat transfer flux
r = radial coordinate, Fig. 1
r_i = spinnaret hole radius, Fig. 1
r_f = final fiber radius, Fig. 1
r_o = local fiber radius, Fig. 1
Re = Reynolds number, equation (17)
R_{δ_i} = kinematic momentum Reynolds number, equation (21)
s = tangential coordinate, Fig. 1
T = fluid temperature
T_i = temperature of fiber at point of issuance ($x=0$)
T_w = local fiber temperature
T_∞ = free-stream temperature
u,v = velocity components in x- and r-directions
u_o = local fiber velocity
u_f = final fiber velocity
x = axial coordinate
α = thermal diffusivity of fluid
α_s = thermal diffusivity of fiber
α_t = turbulent thermal diffusivity of fluid
β = volumetric coefficient of thermal expansion
γ = angle of inclination from vertical
δ = boundary layer thickness, Fig. 1
ϵ = emissivity of fiber
η = pseudo-similarity variable, equation (10)
η_δ = $[(r_o+\delta)^2-r_o^2]\sqrt{u_o/\nu x}/4r_o$, dimensionless boundary layer thickness
θ = dimensionless temperature, equation (10)
θ_w = $(T_w-T_\infty)/(T_i-T_\infty)$, dimensionless filament temperature
ν = kinematic viscosity of fluid
ξ = dimensionless axial coordinate, equation (10)
ρ = density of fluid
ρ_s = density of fiber
σ = Stefan-Boltzmann constant
ϕ_i = T_i/T_∞, dimensionless temperature parameter
ψ = stream function
Ω = buoyancy force parameter, equation (16)

$$+2\xi\frac{dr_o/dx}{r_o/r_i}(f')^2 \pm 8\Omega\frac{r_o}{r_i}\xi\theta = 2\xi\left(f'\frac{\partial f'}{\partial\xi} - f''\frac{\partial f}{\partial\xi}\right) \quad (11)$$

$$\left[\left(\frac{1}{\mathrm{Pr}}+\alpha_l^+\right)\left(\frac{r_o}{r_i}+4\eta\frac{\xi^{1/2}}{\mathrm{Re}^{1/2}}\right)\theta'\right]' + f\theta' = 2\xi\left(f'\frac{\partial\theta}{\partial\xi} - \theta'\frac{\partial f}{\partial\xi}\right) \quad (12)$$

$$\frac{1}{A^2(r_o/r_i)}\frac{\rho_s C_s}{\rho C}\mathrm{Pr}\,\mathrm{Re}^{1/2}\xi^{1/2}\frac{d\theta_w}{d\xi} = \theta'(\xi,0) - 2M\left[1+\left(\frac{dr_o}{dx}\right)^2\right]^{1/2}\frac{\xi^{1/2}}{\mathrm{Re}^{1/2}}[4\theta_w + 6(\phi_i-1)\theta_w^2 + 4(\phi_i-1)^2\theta_w^3 + (\phi_i-1)^3\theta_w^4] \quad (13)$$

The boundary conditions, equations (5) and (8), have the dimensionless form

$$f(\xi,0) + 2\xi\frac{\partial f}{\partial\xi}(\xi,0) = \frac{dr_o}{dx}\mathrm{Re}^{1/2}\xi^{1/2}f'(\xi,0)$$

$$f'(\xi,0) = \frac{2}{A^2(r_o/r_i)}, \quad f'(\xi,\infty) = 0 \quad (14)$$

$$\theta(\xi,0) = \theta_w(\xi), \quad \theta(\xi,\infty) = 0, \quad \theta_w(0) = 1$$

where with the aid of equation (1), one has

$$\frac{r_o}{r_i} = \frac{1+(A-1)e^{-B\xi}}{A}, \quad \frac{dr_o}{dx} = -\frac{(A-1)\mathrm{Be}^{-B\xi}}{A} \quad (15)$$

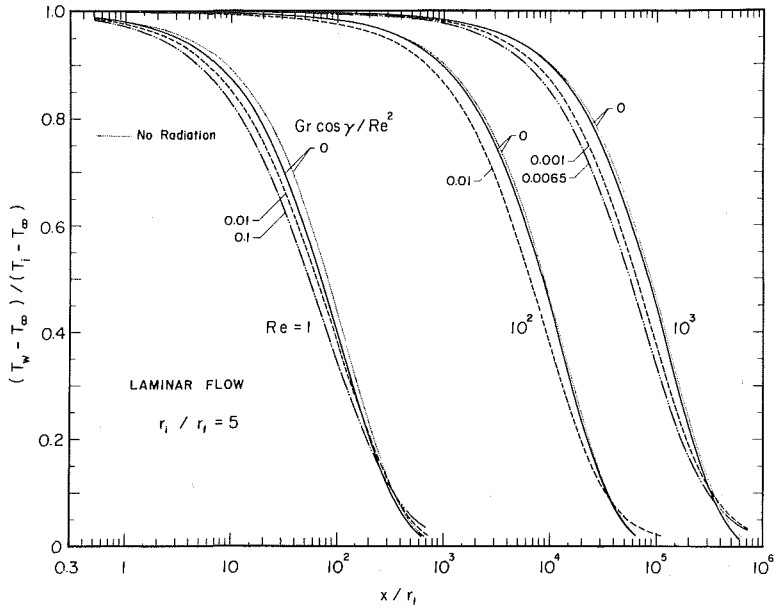

Fig. 2 Filament temperature variation for laminar regime, $r_i/K = 0.02$, $T_i/T_\infty = 2$, $\epsilon\sigma T_\infty{}^3 r_i/k = 0.005$, Pr = 0.7

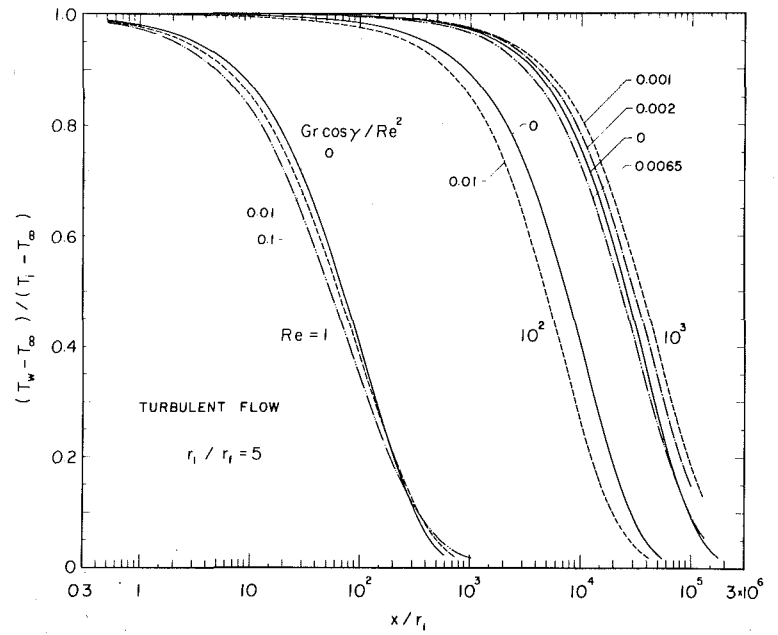

Fig. 3 Filament temperature variation for turbulent regime, $r_i/K = 0.02$, $T_i/T_\infty = 2$, $\epsilon\sigma T_\infty{}^3 r_i/k = 0.005$, Pr = 0.7

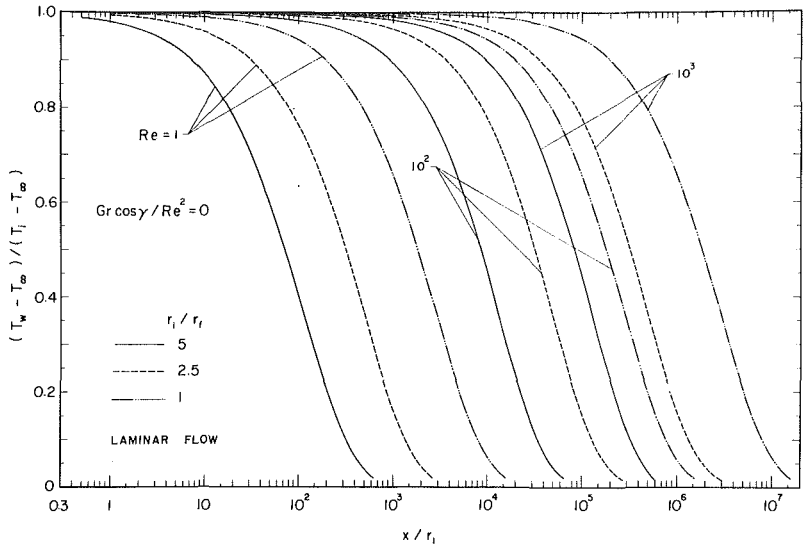

Fig. 4 Effect of fiber attenuation on filament temperature, r_i/K = 0.02, $T_i/T_\infty = 2$, $\epsilon\sigma T_\infty^3 r_i/k = 0.005$, Pr = 0.7

In the foregoing equations, the primes stand for partial differentiation with respect to η, $\theta_w(\xi) = [T_w(x) - T_\infty]/(T_i - T_\infty)$ is the dimensionless filament temperature, and Ω is the buoyancy force parameter given as

$$\Omega = |\mathrm{Gr}|\cos\gamma/\mathrm{Re}^2 \tag{16}$$

where the Grashof and Reynolds numbers are given by

$$\mathrm{Gr} = g\beta(T_i - T_\infty)r_i^3/\nu^2, \quad \mathrm{Re} = u_f r_i/\nu \tag{17}$$

The dimensionless constants appearing in equations (11–15) defined as

$$A \equiv r_i/r_f, \quad B \equiv r_i/K, \quad \phi_i \equiv T_i/T_\infty, \quad M \equiv \epsilon\sigma T_\infty^3 r_i/k \tag{18}$$

and the property ratio, $\rho_s C_s/\rho C$, are all assigned parameters for the problem. The plus and minus signs associated with the buoyancy force term in equation (11), pertain to buoyancy assisting and opposing flow situations, respectively.

The dimensionless turbulent diffusivities for momentum and heat, defined as $\nu_t^+ = \nu_t/\nu$ and $\alpha_t^+ = \alpha_t/\nu$, respectively, have the form

$$\nu_t^+ = \begin{cases} \nu_{t_i}^+ = 0.01\ \mathrm{Re}^{3/2}\xi^{-1/2}\dfrac{r_o}{r_i}\left(\dfrac{r}{r_o}\right)^2\left[ln\left(\dfrac{r}{r_o}\right)^2\right]^2 \\ \left\{1 - \exp\left[-\dfrac{\mathrm{Re}^{3/4}}{104}\xi^{-1/4}\left(\dfrac{r_o}{r_i}\right)^{1/2}|f''(\xi,0)|^{1/2} ln\left(\dfrac{r}{r_o}\right)\right]\right\}^2 \\ \quad |f''(\xi,\eta)| \text{ for } \nu_{t_i}^+ \le \nu_{t_o}^+ \\ \nu_{t_o}^+ = \bar{\kappa}\dfrac{\mathrm{Re}^{1/2}\xi^{1/2}}{(r_o/r_i)}\displaystyle\int_0^\infty \frac{f'(\xi,\eta)}{r/r_o}\,d\eta\left\{1\right. \\ \quad \left. + \left[5.5\dfrac{(r/r_o)-1}{\delta/r_o}\right]^6\right\}^{-1} \text{ for } \nu_{t_o}^+ < \nu_{t_i}^+ \end{cases} \tag{19}$$

$$\alpha_t^+ = \frac{\nu_t^+}{\mathrm{Pr}_t} \tag{20}$$

where $\bar{\kappa}$ is defined in equation (10) of [4], with the kinematic momentum Reynolds number given now as

$$R_{\delta_i} = \frac{1}{2}\frac{\mathrm{Re}^{1/2}\xi^{1/2}}{(r_o/r_i)^2}\int_0^\infty \frac{[f'(\xi,\eta)]^2}{r/r_o}\,d\eta \tag{21}$$

and

$$\frac{r}{r_o} = \left[1 + \frac{4\eta\xi^{1/2}}{\mathrm{Re}^{1/2}(r_o/r_i)}\right]^{1/2},$$

$$\frac{\delta}{r_o} = \left[1 + \frac{4\eta_\delta\xi^{1/2}}{\mathrm{Re}^{1/2}(r_o/r_i)}\right]^{1/2} - 1 \tag{22}$$

The system of equations described above was solved by a marching finite difference scheme, the box method, which is well documented in the literature. Solutions were carried out for both laminar and turbulent flows, where in the latter case the boundary layer was assumed to be turbulent from the start ($\xi = 0$).

Results and Discussion

Numerical results for the cooling of a fiber were obtained for several Reynolds number and buoyancy force parameter combinations, for air with a Prandtl number of 0.7, for the buoyancy assisting flow situation (the cooling of an upward or heating of a downward moving filament). The dimensionless property ratio of $\rho_s C_s/\rho C$ was taken as 2×10^3, a value characteristic of the spinning of various polymers at an average film temperature of 123°C. The remaining assigned dimensionless parameters defined in equation (18), were chosen as $A = 1$, 2.5, and 5, $B = 0.02$, $\phi_i = 2$ and $M = 0.005$, the values of which are characteristic of the spinning of nylon 6 filaments as reported in [1].

The dimensionless filament temperature variation, θ_w, with axial distance is plotted in Figs. 2 and 3 for laminar and turbulent regimes, respectively, for the case $r_i/r_f = 5$. The trends observed are similar to those in [3, 4]. Thus, for laminar boundary layers, the effect of the assisting buoyancy force is to enhance the heat transfer from the filament as seen from Fig. 2, thus resulting in lower temperature ratios. For turbulent boundary layers on the other hand, as the buoyancy force increases from 0, it first decreases the heat transfer of the surface below its corresponding value for zero buoyancy force. At larger assisting buoyancy forces, eventually this trend is reversed, and further increases in the Grashof number result in the enhancement of the surface heat transfer, as seen from Fig. 3 for $\mathrm{Re} = 10^3$. A detailed discussion of these trends is given in [4]. An inspection of Figs. 2 and 3 reveals that the heat transfer rate is higher for turbulent boundary layers than the corresponding laminar ones. This reduction of the dimensionless temperature ratio due to turbulent nature of the

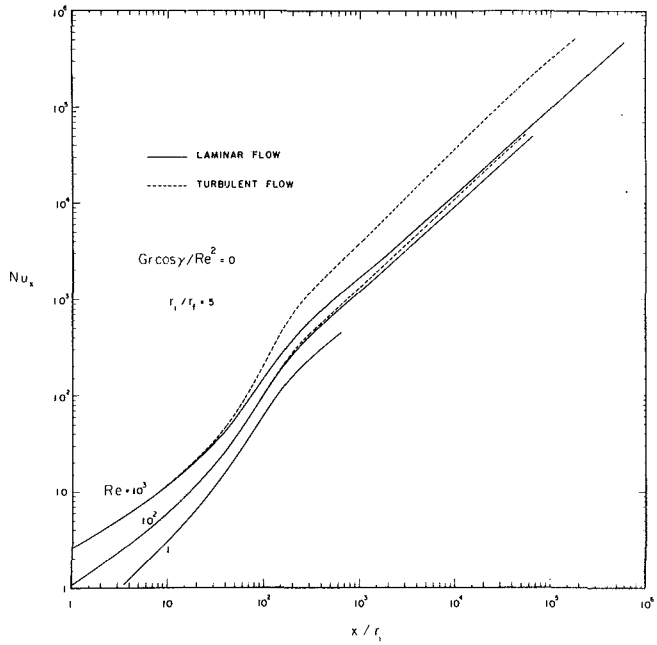

Fig. 5 Local Nusselt number results, $r_i/K = 0.02$, $T_i/T_\infty = 2$, $\epsilon\sigma T_\infty{}^3 r_f/k = 0.005$, Pr = 0.7

boundary layer is approximately 0, 8, and 75 percent, respectively, for Re = 1, 10^2, 10^3, and $\Omega = 0$, when compared at axial locations where the laminar temperature ratio is about 0.5.

In order to evaluate the effect of the radiation loss on the cooling of the filament, the filament temperature ratio obtained without accounting for radiation from the surface is plotted as dotted lines in Fig. 2, for the three Reynolds numbers and zero buoyancy force for the laminar regime. The increase of the temperature ratio due to the neglect of the radiation loss is about 8 percent for Re = 1 and less than 2.5 percent for Re = 10^2 and 10^3.

The magnitude of the effect of the attenuation of the filament diameter on the surface heat transfer rate is depicted in Fig. 4, where the dimensionless temperature for three different radii ratios, $A = r_i/r_f$ of 1, 2.5, and 5, are plotted for the laminar regime and zero buoyancy force. As seen from the figure, the reduction of local radius of the fiber and thus the increase in local speed of the polymer results in the tremendous enhancement of the cooling of the filament.

The local Nusselt number, $\mathrm{Nu}_x = hx/k$ can be expressed as

$$\mathrm{Nu}_x = -\frac{1}{2}\frac{\mathrm{Re}^{1/2}\xi^{1/2}}{[1+(dr_o/dx)^2]^{1/2}}\frac{\theta'(\xi,0)}{\theta(\xi,0)} \tag{23}$$

Representative Nusselt number results for zero buoyancy force and $r_i/r_f = 5$ are plotted in Fig. 5 for both laminar and turbulent flow regimes. The local Nusselt numbers at a given axial location are found to increase with increasing Re, and decrease as the filament is tilted from the vertical. As seen from the figure, at a low Reynolds number, Re = 1, the laminar and turbulent Nusselt numbers are indistinguishable, while for the larger Reynolds numbers considered in the analysis their difference is of significance only at axial locations away from the spinneret. This may serve as an indication of the relative unimportance of the transition point in this study, which is assumed to occur at the point of issuance of the filament (i.e., $x = 0$).

Acknowledgement

This study was supported in part by a grant from the National Science Foundation (NSF CME 80-05682).

References

1 Copley, M., and Chamberlain, N. H., "Filament Attenuation in Melt Spinning and Its Effect on Axial Temperature Gradient," *Applied Polymer Symposia*, No. 6, 1967, pp. 27-50.

2 Barnett, T. R., "Calculation of the Temperature of Filaments in Melt Spinning," *Applied Polymer Symposia*, No. 6, 1967, pp. 51-65.

3 Bhattacharya, A. K., and Moutsoglou, A., "Laminar Boundary Layers on Moving, Nonisothermal Continuous Cylinders," ASME Paper No. 82-HT-74, 1982.

4 Moutsoglou, A., and Bhattacharya, A. K., "Turbulent Boundary Layers on Moving, Nonisothermal Continuous Cylinders," *Proceedings, Seventh International Heat Transfer Conference*, Vol. 3, FC34, 1982, pp. 189-194.

Turbulent Boundary Layer Heat Transfer Experiments: A Separate Effects Study on a Convexly Curved Wall

T. W. Simon
Department of Mechanical Engineering,
University of Minnesota,
Minneapolis, Minn. 55455
Mem. ASME

R. J. Moffat
Department of Mechanical Engineering,
Stanford University,
Stanford, Calif.
Mem. ASME

Measured heat transfer rates through turbulent and transitional boundary layers on an isothermal, convexly curved wall show Stanton numbers 20–50 percent below flat wall values. Recovery is slow on a flat wall downstream of the curve; after 60 cm, Stanton numbers were 15–20 percent below flat wall values. Five secondary effects were studied: (i) initial boundary layer thickness, (ii) free-stream velocity, (iii) free-stream acceleration, (iv) unheated starting length, and (v) transition. Regardless of the initial state, curvature without acceleration eventually forced the boundary layer into an asymptotic condition: $St \alpha Re_{\Delta_2}{}^{-1}$. Strong acceleration with curvature brought the exponent on Re_{Δ_2} to -2.

Introduction

Experimental work on the effects of curvature dates back to 1930. Wilcken [1], a student of Ludwig Prandtl, concluded that curvature significantly affected the "free path length" (mixing length) and that "boundary layer events on curved surfaces should be ascribed more importance than has generally been the case." A comprehensive survey of the literature on curvature effects, prior to 1972, was given by Bradshaw [2]. He stated that by simply incorporating the extra rate of strain, $\partial V/\partial s$, the effect of curvature is about ten times as strong as one would predict from a thin shear layer, eddy-viscosity model. A bibliography of recent curved boundary layer studies can be found in [3].

In 1955, Kreith [4] showed that heat transfer from a concave wall was more than from a convex wall. In 1968, Thomann [5] made local heat transfer measurements on straight, convex, and concave surfaces in a flow with a free-stream Mach number of 2.5. Curvature caused an increase in convective heat flux of about 20 percent for the concave case and a decrease of about 15 percent for the convex case relative to the flat-wall case. Mayle, Blair, and Kopper [6] measured local heat transfer rates in curved boundary layer at low-to-moderate velocities (M about 0.06) and with δ/R about 0.01. Wall heat flux decreased about 20 percent on the convex wall and increased about 33 percent on the concave wall relative to the flat-wall values.

Weakly convex-curved ($\delta/R \approx 0.01$) heated boundary layer data, including local Stanton numbers and profiles of mean velocity and temperature by Gibson, Verriopoulos, and Nagano [7] showed that the depression of heat flux was larger than that of skin friction.

As a consequence of the works cited above, it is clear that convex curvature decreases the Stanton number (up to 20–30 percent has been observed) and concave curvature raises it, (20–30 percent has been observed). It is generally agreed that δ/R is a measure of the "strength of curvature."

The objective of this work was to investigate the interaction between convex curvature and several other factors: boundary layer thickness, free-stream velocity, free-stream acceleration, and variable wall temperature. One or more of these factors are frequently found in combination with curvature.

Previous heat transfer studies have dealt only with the curved region; none have reported results from the recovery region. The present investigation includes both the introduction of and recovery from curvature. With gas turbine blade cooling or many other applications where curvature effects on heat transfer are significant, strong curvature in the leading edge region is followed by regions of weak or no curvature. The recovery region may be as important to the overall problem as the curved region.

The present heat transfer results are from a program which covered both the heat transfer and the fluid mechanics of a convexly curved flow. Detailed results of the accompanying isothermal hydrodynamic study have been reported by Gillis and Johnston [8, 9].

Previous hydrodynamic studies have shown a significant drop in surface shear stress in the convex region. So and Mellor [10] measured the distribution of shear stress within the convex wall boundary layer and showed lower levels of Reynolds stress throughout, but particularly in the outer region. Gillis and Johnston's work [9] confirmed these observations and extended the study to include the recovery region. They described the curved wall boundary layer as having two layers: an inner layer of thickness, δ_{s1}, with shear stress and turbulence, and an outer layer having turbulence but no shear stress. We will use this concept of shear layer thickness, δ_{s1}, in later discussions of the heat transfer response. Their data can be used to document the hydrodynamic field of the baseline case of the present heat transfer studies.

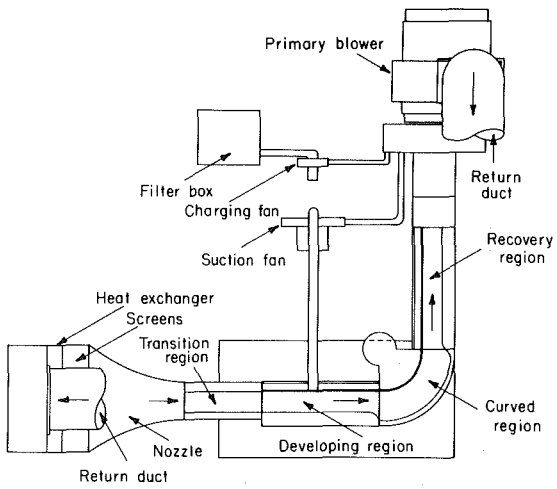

Fig. 1 Plan view of the facility

Contributed by the Heat Transfer Division for publication in the JOURNAL OF HEAT TRANSFER. Manuscript received by the Heat Transfer Division February 16, 1982. Paper No. 81-HT-78.

The Present Experiment. The objective of the present work was to determine the effect on surface heat transfer of convex curvature in combination with other effects (i.e., acceleration, transition, variable wall temperature, and variable boundary layer thickness).

The heat transfer tests were run on the same rig and during the same calendar period as the Gillis and Johnston work on the hydrodynamics. The heat transfer program consisted of a baseline case which was thoroughly studied and a set of separate effects tests on the following subjects: (*a*) initial boundary layer thickness, (*b*) free-stream velocity, (*c*) free-stream acceleration, (*d*) location of the beginning of heating, (*e*) maturity of the momentum boundary layer. The present paper presents only the "separate effects study," the details of the baseline case were reported by Simon and Moffat [11].

The Experimental Apparatus

The test rig, shown in Fig. 1, consisted of a closed-loop wind tunnel having a 90 deg bend in the middle of the test section. The test section included an approach region (200-cm long), the curved section (45-cm radius with 90 deg of turning), and the recovery region (125-cm long). The tunnel cross section was 56-cm wide and 16.5-cm high. The static pressure was uniform everywhere along the surface of the test plate, including the curved region, within 2 percent of the dynamic head. Wall static pressure was controlled by a combination of wall shape and boundary layer bleed. The developing region was equipped with boundary layer suction for control of the boundary layer thickness. Secondary flow convergence angles were measured in the curved region and controlled by a combination of suction on the side walls and boundary layer fences on the test surface and in the recovery region.

The test surface was made of copper, segmented in the streamwise direction. The segments in the preplate and in the recovery plate were heated with circulating hot water and were instrumented with built-in heat flux sensors. Each segment in the curved section was electrically heated and instrumented so heat transfer rates could be measured by energy balance means.

Wall temperatures and boundary layer temperature profiles were measured with thermocouples. Instruments and experimental procedures were designed in accordance with recommendations in the literature [12, 13, 14]. Details of the test can be found in [3].

Qualification Tests

Upstream of the curved region, the potential core was uniform within 0.15 percent in mean velocity, and 0.05° C in temperature, with turbulence intensity less than 0.5 percent. Temperature and velocity could be maintained constant as long as desired.

Spanwise variation of the momentum and enthalpy thicknesses were typically less than ±5 percent at the beginning of the curved region. Some secondary flow became noticeable at about 60 deg around the curve, but streamline convergence within the boundary layers did not exceed 2 deg within the central span of 13 cm, or 5 deg over a 25-cm span, anywhere. Most of the convergence was in the outer regions of the boundary layer and is not believed to have significantly influenced the surface heat transfer. Some nonuniformity of heat transfer was found within 2 cm of the edges of the test plate by special tests using surface-mounted heat flux gages, but an analysis of the conduction problem in the plates showed that this disturbance would not measurably affect the data taken in the center span.

Energy balances were made, comparing integrations of the boundary layer traverses with integrations of the surface heat transfer data. Results agreed within 7 percent. This supports the view that the flow was substantially two-dimensional. Most of the 7 percent disagreement arose downstream of the curved region.

Baseline data sets showed the preplate Stanton numbers to be within 5 percent of the expected correlation for flat plates (Figs. 2 and 3). Stanton numbers deduced from the temperature profiles agreed with those measured on the plates within 5 percent for all of the profiles, except the one farthest downstream, which was within 9 percent.

Measurement of mean velocity in a curved flow field is complicated by the gradient of static pressure. In the present work the static pressure was measured at the test wall, and its distribution through the boundary layer was calculated assuming potential flow.

Results and Discussion

The Baseline Case. The baseline case is a fully turbulent boundary layer responding to the introduction and then withdrawal of convex curvature, subject to uniform wall static pressure and temperature. The ratio of initial boundary layer thickness to radius of curvature, δ/R, was 0.10. The wall to free-stream temperature difference, nominally 17°C, was uniform to within ±0.6°C. The momentum thickness Reynolds number was 4173, and the shape factor was 1.41 at the beginning of curvature, indicating a mature turbulent boundary layer. The Nth-order uncertainty in the Stanton number data was 3.5 percent in the developing and recovery regions and 4.8 percent in the curved region. The difference reflects different data reduction methods in the two regions.

The effect of curvature on the Stanton number is quite dramatic (Fig. 2). The Stanton number decreases ~15 percent when the curvature is introduced and continues to decrease within the bend to ~35–40 percent below the value that would be expected on a flat wall (dashed line) for the same

Nomenclature

c_p = specific heat
K = acceleration parameter, $\nu/U_{pw}^2(dU_{pw}/ds)$
M = Mach number
n = distance normal to the test wall
Pr = Prandtl number
$\dot{q}''$ = heat flux
R = radius of curvature
Re_{δ_2} = momentum thickness Reynolds number, $U_{pw}\delta_2/\nu$
Re_{Δ_2} = enthalpy thickness Reynolds number, $U_{pw}\Delta_2/\nu$
s = streamwise distance referenced to start of curvature
St = Stanton number, $\dot{q}''/\rho c_p U_{pw}(T_w - T_\infty)$
T = temperature
U_{pw} = the velocity that would exist at the test wall were there no boundary layer
V = mean velocity normal to the test wall
δ = thickness of boundary layer, where mean velocity is 99 percent of the potential flow mean velocity
δ_2 = momentum thickness
δ_{s1} = shear layer thickness, distance from wall where Reynolds shear stress profile extrapolates to zero
Δ_2 = enthalpy thickness
ρ = density
θ = angular distance around bend
ν = kinematic viscosity

Subscripts

pw = of the potential flow at the wall
w = at the wall
∞ = in the free-stream

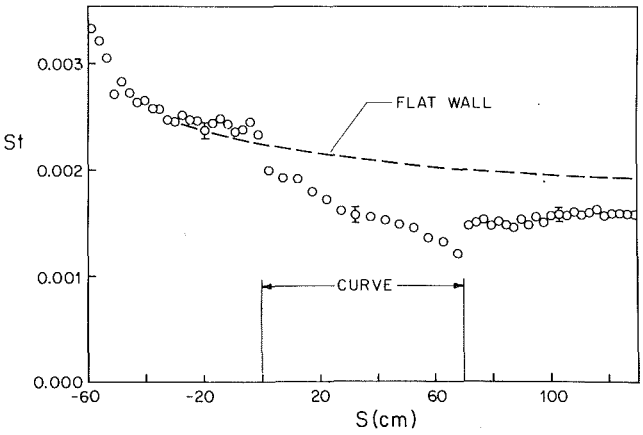

Fig. 2 The effect of streamwise convex curvature on turbulent boundary layer heat transfer – the baseline case (070280); $\delta/R(\theta=0)=0.10$, $U_{pw}=14.8$ m/s, K = 0.0

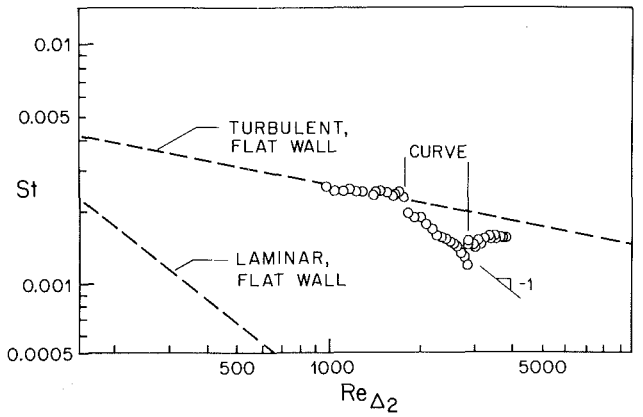

Fig. 3 The effect of streamwise convex curvature on turbulent boundary layer heat transfer – the baseline case (070280); $\delta/R(\theta=0)=0.10$, $U_{pw}=14.8$ m/s, $K=0.0$

streamwise distance. The recovery on the downstream flat wall is extremely slow. After 60 cm of recovery, the Stanton number is still ~15 percent below the flat-plate value. This is similar to the behavior of the skin friction, as noted by So and Mellor [10] and by Gillis and Johnston [8].

Removal of curvature seems to cause an abrupt, but small drop in Stanton number. This drop, which can be observed in each data set presented rests on more than the one data point involved; tests with surface-mounted heat flux meters support the finding.

The data of Fig. 2 can be recast into enthalpy thickness Reynolds number coordinates, employing the two-dimensional energy integral equation to calculate the growth in enthalpy thickness from the Stanton number data; velocity and temperature profiles at an upstream location were used to start the integration. These coordinates present data in a form which is less dependent on prior history of the boundary layer than the x-Reynolds number coordinates. The turbulent boundary layer flat isothermal wall correlation in these coordinates is [15]

$$St = 0.0125\,Pr^{-0.5}Re_{\Delta_2}^{-0.25}$$

The preplate data join this correlation as the effect of the unheated starting length disappears. When curvature is introduced, the data begin to drop below the correlation. Shown also is the equivalent correlation for a laminar boundary layer [15]

$$St = 0.220\,Pr^{-1.33}Re_{\Delta_2}^{-1.00}$$

The present curved wall data have a slope of $-1{,}0$, in these coordinates, suggesting "relaminarization." This same response was observed in strongly accelerated turbulent boundary layers [16]. The boundary layer, however, is not laminar. Turbulence measurements by Gillis and Johnston [8], for example, show that the curved boundary layer is still an active turbulent layer, but one in which the production of turbulence is contained within a thin region near the wall. The outer region still contains turbulent flow but has near-zero Reynolds stresses.

After a sufficient distance downstream of the curve, the curvature effect should become distant history and the data should once again be on the flat wall correlation. The recovery is very slow, however, and at the end of the present recovery section, the Stanton number is still about 20 percent low.

The Effect of the Initial Boundary Layer Thickness. The parameter δ/R, "strength of curvature," has been found useful, when its magnitude is small. It appears, however, that beyond some critical value, δ/R is of little further significance. Three cases were used in this study with $\delta/R=0.10$, 0.05, and 0.02 (each evaluated at the beginning of curvature). In enthalpy thickness coordinates, the data for $\delta/R=0.10$ and 0.05 display the -1 sloped line almost from the start of curvature. Because of this behavior these cases are considered "strong curvature" cases.

Gillis and Johnston [9] found the inner layer thickness, δ_{sl}, to be equal to 0.03 R for both $\delta/R=0.10$ and 0.05. One could surmise that, if no other parameter but δ/R were changed, cases with $\delta/R>0.03$ would have their region of active turbulence compressed to 0.03 R, whereas cases with $\delta/R<0.03$ might grow until $\delta/R=0.03$.

The data of the $\delta/R=0.02$ case are quite different from the "strong" curvature cases. The asymptotic state is approached much more slowly and only the last two data points suggest that the boundary layer may be approaching the asymptotic state. This is presumably because the boundary layer thickness was initially less than the asymptotic shear layer thickness and must grow. In spite of the "weak curvature" there is still an immediate decrease in Stanton number at the onset of curvature, similar to that seen for the strong curvature cases. The minimum Stanton numbers for the three cases are 30–40 percent below the flat-wall correlation.

Within the 60-cm recovery length, the Stanton data for each case return to within 10–15 percent of the Re_{Δ_2} correlation values. The rate of return of the Stanton number to the flat-wall turbulent boundary layer correlation seems to be proportional to the difference between the local Stanton number and the flat plate Stanton number for the same Re_{Δ_2}.

The Effect of U_{pw}. The value of U_{pw} has little effect on the variation of Stanton number within the curved region, considering the data in Re_{Δ_2} coordinates. The principal effect of U_{pw} is to change the shape of the St versus Re_{Δ_2} curve in the very early curvature region without changing its eventual -1 slope. The data within the curved region, for the three cases of differing U_{pw} eventually follow a -1 relationship with Re_{Δ_2}. The low-velocity data approach a -1 slope only after 30–40 percent of the curve has been completed. The midvelocity data quickly reach the -1 correlation, and the highest-velocity case data drop below the -1 correlation, then return to it within the first 20–30 deg of curvature. In the recovery region, the rate of recovery is approximately proportional to the distance from the flat-wall correlation for all three cases.

Effect of Free-stream Acceleration. The curved boundary layer responds more vigorously to acceleration than does the flat-wall boundary layer. For this study streamwise curvature and constant K acceleration were combined within the curved region. There was no acceleration in the preplate and recovery regions. In their discussion of the accelerating boundary

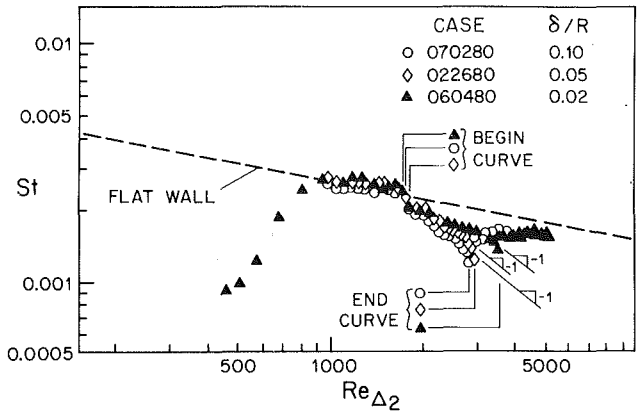

Fig. 4 The effect of initial boundary layer thickness on convex-curved turbulent boundary layer heat transfer

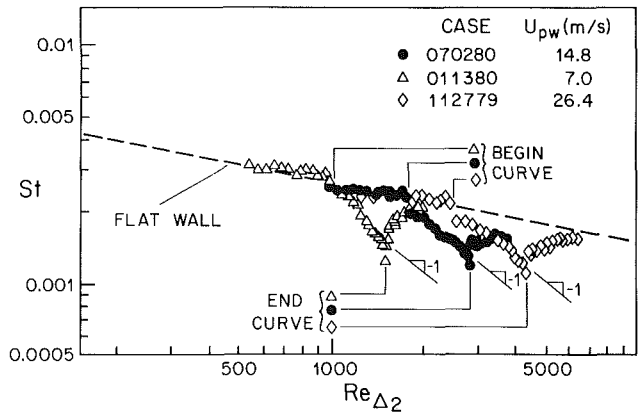

Fig. 5 The effect of free-stream velocity on convex-curved turbulent boundary layer heat transfer

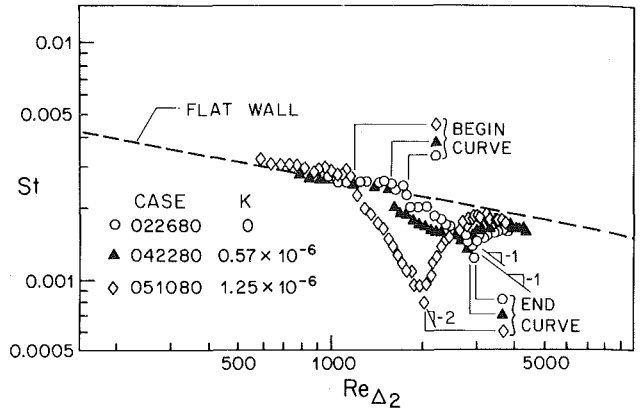

Fig. 6 The effect of free-stream acceleration on convex-curved turbulent boundary layer heat transfer

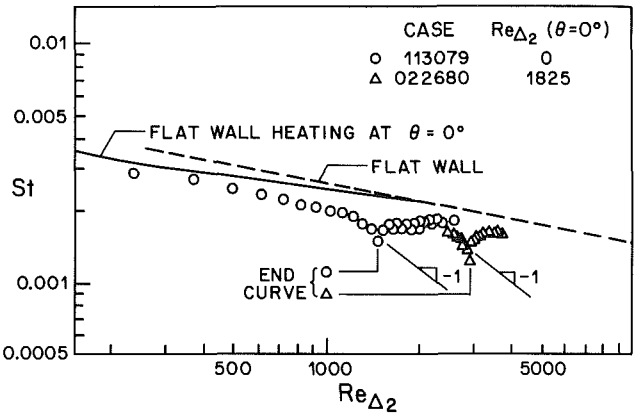

Fig. 7 The effect of unheated starting length on convex-curved turbulent boundary layer heat transfer – heating begins at the start of curvature

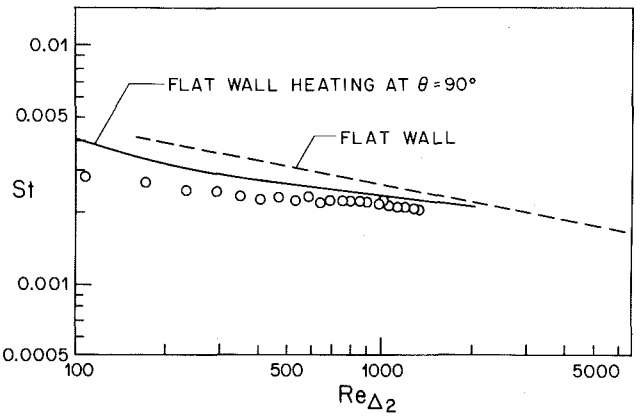

Fig. 8 The effect of unheated starting length on convex-curved turbulent boundary layer heat transfer – heating begins at the end of curvature

layer, Kays and Moffat [16] point out that, for the asymptotic-accelerated boundary layer, Re_{δ_2} is constant while Re_{Δ_2} continues to increase. In the present study, Re_{δ_2} at the start of curvature was set to within 10 percent of the flat-plate asymptotic value corresponding to the value of K.

Three cases with $\delta/R = 0.05$ were compared for the study: $K = 0.0$, 0.57×10^{-6}, and 1.25×10^{-6}. The $K = 1.25 \times 10^{-6}$ case shows a different Stanton number trace within the curved region than seen in the preceding figures or in the case of milder acceleration. There apparently is an acceleration effect which is as important as the curvature effect.

In the prior work on accelerating boundary layers on flat walls (e.g. [16]), it has been found that acceleration with $K = 0.57 \times 10^{-6}$ does not significantly influence heat transfer rates. Acceleration with $K = 1.45 \times 10^{-6}$ results in a -0.5 slope in Stanton number versus Re_{Δ_2} coordinates and $K = 2.5 \times 10^{-6}$ would be required to have a -1.0 slope in these coordinates.

Curvature increases the sensitivity to acceleration. With both curvature and strong acceleration ($K = 1.25 \times 10^{-6}$) the slope of Stanton number versus Re_{Δ_2} is approximately -2.0. The case of $K = 0.57 \times 10^{-6}$ with curvature approaches an eventual -1 slope at the end of the curved region, but there appears to be an effect of even this small acceleration at the beginning of curvature.

Effect of Unheated Starting Length. In this study a thermal boundary layer grows within a mature turbulent momentum boundary layer. Its growth is initiated with a 15°C step in test wall temperature downstream of an unheated length. After the step, the wall is isothermal. Two cases are discussed. In the first (Fig. 7) the step is at the start of curvature, and in the second (Fig. 8) the step is at the end of the curved section (the beginning of the recovery section). Curvature effects are observed by comparing the data to the flat-wall unheated starting length prediction. Unheated starting length effects are seen by comparing the flat-wall correlation and the unheated starting length prediction.

In the case where the wall temperature steps at the start of the curved section (Fig. 7), the heat transfer data eventually become similar to data of cases discussed in previous sections which had no unheated starting length effect. There is a small influence of curvature initially, but farther downstream, curvature becomes more influential. After 70 deg of turning, Stanton numbers begin to drop rapidly and eventually assume the -1 sloped trajectory observed in previous cases. Data

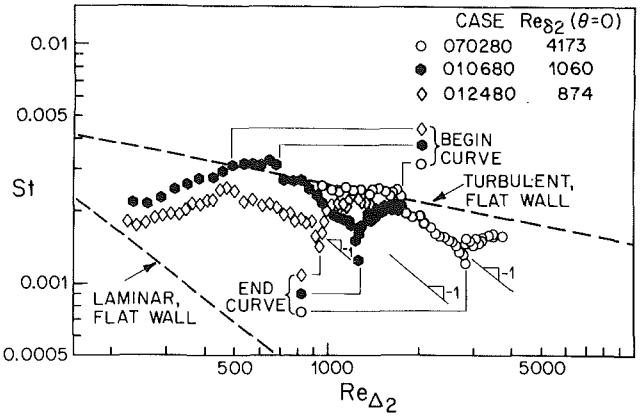

Fig. 9 The effect of initial momentum thickness Reynolds number on convex-curved turbulent boundary layer heat transfer

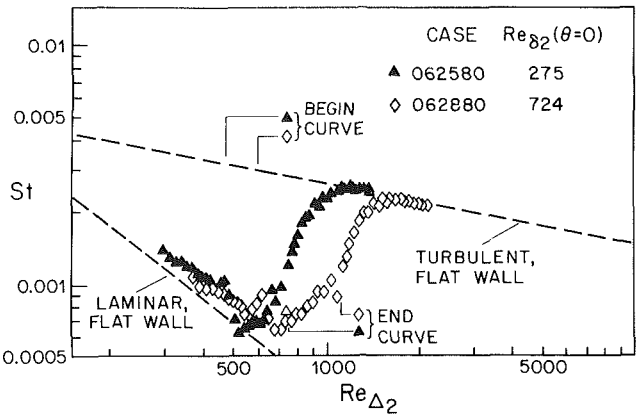

Fig. 10 The effect of streamwise convex curvature on transitional boundary layer heat transfer

showing recovery from curvature are also similar to those observed for cases without unheated starting length effects (a partial data set for such a case is shown).

In the second unheated starting length case where the wall temperature is stepped at the end of the curved section (Fig. 8), the effect of curvature and the effect of the unheated starting length are nearly equally prominent. Recovery from the two effects progresses at nearly the same rate. By the end of the recovery section, the reduction of Stanton number attributable to each effect is 7–8 percent.

Observations from this study are consistent with the "shear layer" model discussed previously. In the case where the thermal boundary layer begins growing at the start of curvature (Fig. 7), the thermal boundary layer is initially too thin to be influenced greatly by curvature (predominantly an outer region effect). Farther downstream, the shear length, which is also the region of active turbulent transport of thermal energy, begins to fill with heated fluid and the curvature constraint becomes more prominent. When the shear layer has been heated to its full thickness, heat transfer rates begin to drop with a -1 slope. Calculated temperature profiles from the flat wall unheated starting length prediction show that at $Re_{\Delta_7} \approx 1200$, where the St data of Fig. 7 begin the -1 slope, the thermal boundary layer thickness is approximately 3 percent of the radius of curvature. This supports the earlier hypothesis that the shear layer (also the layer of active transport) is constrained to 0.03R by strong convex curvature.

When heating is initiated at the start of recovery from curvature (Fig. 8), the thermal boundary layer grows inside the shear layer which, in turn, is growing inside the velocity boundary layer. Gillis and Johnston [9] have shown that the shear layer recovers from curvature slowly. It is felt that the Stanton number data for this unheated starting length case are slightly below the flat-wall unheated starting length prediction values because slow recovery from curvature (slow regrowth of δ_{s1} is restraining growth of the thermal boundary layer).

The Effect of Transition and the Maturity of the Momentum Boundary Layer. Convex curvature delays the onset of and retards the completion of transition. Transitional boundary layers recover quickly, after curvature ends, compared with more mature boundary layers. The descriptor Re_{δ_2} at the start of curvature was used to identify the maturity of the momentum boundary layer, which for this study varied from 275 (laminar-to-early transitional) to the baseline case of 4173 (a fully turbulent boundary layer).

In Fig. 9, the data with $Re_{\delta_2} = 874$ at the beginning of curvature do not demonstrate the existence of the -1 slope although such a region may have been developing near the end of curvature. For both cases with $Re_{\delta_2} > 1000$, the -1 slope is apparent almost from the onset of curvature. The response of low Reynolds number boundary layers is entirely different (Fig. 10). A plausible hypothesis concerning this difference can be based on the previously discussed "shear layer" model. If the boundary layer is sufficiently mature, the layer which will become the "shear layer" (the inner region, of about 0.03R) is already occupied by fluid with well-established turbulence properties. When curvature is introduced, the inner region turbulence structures are quickly rescaled (to be consistent with the "shear layer" thickness) while the outer region becomes uncorrelated. If the boundary layer is laminar or early transitional (Fig. 10), a turbulent "shear layer" region must be developed before the -1 sloped trajectory can be displayed.

Laminar and early transitional flows recover more quickly because they do not have the outer layer of decaying turbulence found in the turbulent and late transitional cases.

Curvature retards transition (Fig. 10). When curvature is released, the boundary layer rapidly completes its transition on the recovery plate, reaching turbulent flat-wall behavior. Figure 10 shows two cases in which the boundary layers are just beginning transition at the onset of curvature as indicated by a rise in Stanton number above the laminar correlation. They show that curvature affected but did not prevent transition. At the onset of curvature, the Stanton number data immediately fall nearly to the laminar correlation but immediately began to rise again – almost as though transition had restarted.

Interaction Between Variables. In making separate effects studies, there were instances in which the characteristics of the apparatus made it impossible to change only one factor at a time.

In the study concerning the effects of boundary layer thickness, it was not possible to create three fully mature boundary layers (i.e., $Re_{\delta_2} \geq 1000$) with different values of δ/R while, at the same time keeping the free-stream velocity constant at 14 m/s. One test case, $\delta/R = 0.02$, was run with $U_{pw} = 24$ m/s (Table 1). The effect of the difference in U_{pw} (from 14 to 24 m/s) was judged to be insignificant, relying on the evidence in Fig. 5: the effect of U_{pw} on heat transfer. Those data showed that U_{pw} had little or no effect if the heat transfer was described in local coordinates.

Similarly, tests investigating free-stream velocity at constant boundary layer thickness was slightly "contaminated" by changes in boundary layer thickness. Once again, the evidence developed from large, intentional changes in boundary layer thickness (Fig. 4) showed that the unavoidable changes occurring on Fig. 5 could be ignored. Similar arguments were relied upon in the study of transition and acceleration effects.

Another possible source of contamination is the unheated starting length effect in cases where this effect was not desired. Thicker boundary layers were created by moving the

Table 1 Case descriptors

Case#	U_{pw}(m/s) (ref.)	Re_{δ_2} ($\theta=0$)	δ/R ($\theta=0$)	T.B.L. Virtual Origin (cm)	Re_{Δ_2} $\theta=0$	Re_{Δ_2} $\theta=90°$
070280	14.8	4173	0.10	−214	1775	2845
022680	14.5	2563	0.05	−119	1825	2892
060480	24.2	1724	0.02	−39	1755	3572
112779	26.4	4795	0.06	−142	2476	4368
011380	7.0	1696	0.08	−147	998	1496
113079	14.5	2563	0.05	−119	0	1498
030280	14.5	2563	0.05	−119	0	0
010680	7.0	1060	0.05	−81	697	1270
012480	5.2	874	0.06	−86	480	953
062880	12.4	724	0.02	−30	600	1109
062580	7.0	275	0.02	−15	472	746
042280	13.3	2313	0.05	−113	1560	2869
051080	9.0	1349	0.05	−85	1181	2038

boundary layer trip upstream, making the trips thicker and using multiple trips. The location of the beginning of heating was fixed, however. Therefore, thicker boundary layer cases had longer effective unheated starting lengths. The most severe case is the base case with $\delta/R=0.10$ (Fig. 3). It is felt that even in this most severe case, unheated starting length effects are not significant because the data lie on the turbulent flat wall correlation far upstream of the beginning of curvature, indicating a complete recovery from the far upstream adiabatic length (see Fig. 3). All other cases, except those in the unheated starting length study, would have even smaller effects.

Conclusions and Recommendations

Surface heat transfer rates have been measured for several different flows on an isothermal, convexly curved surface. Free stream velocity, boundary layer thickness, acceleration, and unheated starting length were varied systematically to produce a broad data base. Both turbulent and transitional boundary layers were studied.

The principal conclusions are:

1 The present work confirms that the effect of convex curvature on heat transfer rates is significant with Stanton numbers reduced 20–50 percent below flat wall values. There is an immediate drop in Stanton number at the beginning of curvature and a continued decline throughout the curved region.

2 Recovery from curvature on a downstream flat wall is extremely slow; after 60 cm (15–20 boundary layer thicknesses), Stanton numbers were still 15–20 percent below flat wall values for the same Re_{Δ_2}.

3 The Stanton number behavior of the boundary layers tested in this program suggest the existence of an asymptotic convex curvature condition characterized by $St \propto Re_{\Delta_2}^{-1}$.

4 Boundary layer thickness, free-stream velocity, unheated starting length, and boundary layer maturity do not alter the eventual asymptotic state characterized by the -1 slope. There are some small effects visible on the initial response to the introduction of curvature and the rate at which the asymptotic state is approached.

5 Convex curvature increases the boundary layer's sensitivity to acceleration.

6 Convex curvature delays and retards transition.

Availability of Data

Reference [3] contains tabulated data for all the cases presented herein. This data includes streamwise variation of St, Re_{Δ_2}, Re_x, T_w, and U_{pw} and starting profiles of mean temperature and velocity 35 cm upstream of the beginning of curvature. Also, profiles of mean temperature and velocity at seven streamwise locations are presented for cases 070280 and 022680.

Acknowledgments

This study was supported by NASA-Lewis Laboratories under the grants, NSG-3124 and NAG-3-3. Dr. Raymond Gaugler was the project officer.

Significant contributions were made by Dr. J. C. Gillis, Professor J. P. Johnston and Dean W. M. Kays at Stanford University. The authors appreciate their support.

References

1 Wilcken, H., "Effect of Curved Surfaces on Turbulent Boundary Layers," NASA-TT-F-11421, 1968, (original paper dated 1930).

2 Bradshaw, P., "Effects of Streamline Curvature on Turbulent Flow," AGARDograph No. 169, 1972.

3 Simon, T. W., Moffat, R. J., Johnston, J. P., and Kays, W. M., "Turbulent Boundary Layer Heat Transfer Experiments: Convex Curvature Effects, Including Introduction and Recovery," NASA-CR-3510, 1982.

4 Kreith, F., "The Influence of Curvature on Heat Transfer to Incompressible Fluids," ASME Transactions, 1955, pp. 1147–1256.

5 Thomann, H., "Effect of Streamwise Wall Curvature on Heat Transfer in a Turbulent Boundary Layer," *Journal of Fluid Mechanics*, Vol. 33, Pt. 2, 1968, pp. 282–292.

6 Mayle, R. E., Blair, M. F., and Kopper, F. C., "Turbulent Boundary Layer Heat Transfer on Curved Surface," ASME JOURNAL OF HEAT TRANSFER, Vol. 101, No. 3, 1979, pp. 521–525.

7 Gibson, M. M., Verriopoulos, C. A., and Nagano, Y., "Measurements in the Heated Turbulent Boundary Layer on a Mildly Curved Convex Surface," *Proceedings of the Third Symposium on Turbulent Shear Flows*, 1981, pp. 4.7–4.11.

8 Gillis, J. C., and Johnston, J. P., "Experiments on the Turbulent Boundary Layer over Convex Walls and its Recovery to Flat-Wall Conditions," *Turbulent Shear Flows*, 1980, pp. 116–120.

9 Gillis, J. C., Johnston, J. P., Moffat, R. J., and Kays, W. M., "Experimental Data and Model for the Turbulent Boundary Layer on a Convex, Curved Surface," NASA-CR-3391, 1981.

10 So, R. M. C., and Mellor, G. L., "Experiment on Convex Curvature Effects in Turbulent Boundary Layers," *Journal of Fluid Mechanics*, Vol. 60, Pt. 1, 1973, pp. 43–62.

11 Simon, T. W., and Moffat, R. J., "Convex Curvature Effects on the Heated Turbulent Boundary Layers," *Proceedings of the VIIth Int. Heat Trans. Conf.*, Vol. 3, 1982, pp. 295–301.

12 Moffat, R. J., "Temperature Measurement in Solids," ISA Paper 68-514, 1968.

13 Blackwell, B. F., and Moffat, R. J., "Design and Construction of a Low-Velocity Boundary Layer Temperature Probe," ASME JOURNAL OF HEAT TRANSFER, Vol. 97, No. 2, 1975, pp. 313–315.

14 Moffat, R. J., "Gas Temperature Measurement," *Temperature—Its Measurement and Control in Science and Industry*, Vol. 3, Pt. 2, Reinhold Publishing Corp., New York, 1962, pp. 553–571.

15 Kays, W. M., and Crawford, M. E., *Convective Heat and Mass Transfer*, McGraw-Hill Publishing Co., 1980.

16 Kays, W. M., and Moffat, R. J., "The Behavior of Transpired Turbulent Boundary Layers," HMT-20, Thermoscience Division, Department of Mechanical Engineering, Stanford University, 1975.

17 Crawford, M. E., and Kays, W. M., "STAN5—A Program for Numerical Computation of Two-Dimensional Internal and External Boundary Layer Flows," NASA CR-2742, 1976.

The Response of a Turbulent Boundary Layer to a Double Step-Change in a Wall Heat Flux

J. Andreopoulos
Sonderforschungsbereich 80,
University of Karlsruhe,
West Germany

Extensive measurements were made of the response of a turbulent boundary layer to a double step change of wall heat flux. The measurements include mean temperature and velocity as well as temperature-velocity correlations up to third order occurring in the $\overline{\vartheta^2}$ and $\overline{v\vartheta}$ transport equations together with the skewness and flatness of temperature fluctuations. Two thermal layers start to develop within the primary boundary layer due to the change in heat flux at boundary. These layers are characterized with different growth rates which depend on the wall heat flux. Most of the changes in the downstream stations take place inside the second thermal layer.

1 Introduction

The problem of scalar transport by turbulence is of great importance in engineering studies. If the Reynolds analogy between heat and momentum was valid for any flow situation one could expect that the predictions of such flows would be simple. In fact, this analogy is not always valid, and the various prediction methods need accurate velocity-temperature (or concentration) correlation measurements. The Reynolds analogy could be valid if both thermal and hydrodynamic fields had the same boundary conditions.

The flow immediately after a simple step change in surface heat flux (unheated to heated wall) has a relaxation distance of 100 boundary layer thicknesses where the flow has almost established to fully developed heated boundary layer [2].

In the present flow a zero pressure gradient boundary layer over a smooth wall is subjected to a wall heat flux "impulse," i.e., the developing thermal field after the first step change in surface temperature has to readjust again after the second and sudden change in wall heat flux. The experiment is shown schematically in Fig. 1. A fully developed boundary layer has formed on the upstream surface with zero heat flux, Q_w. At $x=0$, the wall heat flux abruptly changes to a significant value and after $1_T \simeq 3\delta_o$ changes again to the value of zero.

The aim of the present experiment is twofold. First, it is a more severe test of calculation methods as the second step change at $1_T = 150$ mm (Fig. 1) occurs before the flow has fully adjusted to the new heated surface. Second, the response of a boundary layer to a double surface temperature changes in a very short distance, gives further indication of the transport of heat by turbulence. The origin for the momentum and thermal layers are not coincident. In fact, the thermal layers are developing inside the initial boundary layer. Andreopoulos and Wood [3] investigated the response of a high Re number boundary layer to a short length of surface roughness. In both cases, sudden changes on boundary conditions show some similarity in the development of the internal layers and in the transportation of the disturbance caused by these changes towards the outer layer but similarities in transport of momentum and heat were not expected.

2 Experimental Techniques

The measurements were made in the closed circuit wind tunnel of the Sonderforschungsbereich 80 which has a 6-m-long by 1.5-m i.d. octagonally shaped working section. A flat plate was installed at about 0.28 m from the tunnels's floor (see Fig. 2). The heated wall part had a length of 150 mm ($\simeq 3\delta_o$). It was located at 2.95 m from the leading edge, and it was made from a thin brass plate, a heating element, and two thick layers of asbestos. The material of the rest of the plate was formica. Mean temperature was measured with Phillips Chromel-Alumel thermocouple type T1. The wall at $x>0$ (including the downstream unheated part) was fitted with the same type of thermocouples 0.25 mm in diameter. The thermocouple e.m.f. was measured with a PRIMA 5060 voltmeter with a resolution of 0.1 μV. The experiments were made at three different values of heating: 1007 w, 310 w, and 105 w, corresponding roughly to $T_w - T_e = 100°C$, 50°C, 10°C, respectively. Fully described details of the experimental arrangement and data tabulations of the mean temperature and velocity fields can be found in the work by Triantafyllou [6]. Quoting from there, the estimates of heat losses by radiation are of the order of 0.2 percent for the worst case of $Q_w = 1007$ w, while a balance between the transported heat and the heat input show an out of balance term in percent of the heat input as follows: 4 percent for $Q_w = 105$ w, 12 percent for $Q_w = 310$ w, and 14 percent for $Q_w = 1007$ w. This can be attributed to heat losses, experimental error, and/or numerical error in the integration of the mean heat-flux profiles. The isothermal flow conditions at $x = 0$ are shown in Table 1.

Turbulence measurements were measured with DISA 55M01 C.T.A. and DISA miniature crosswire probes with 3-

Table 1

U_e	δ_o	c_f	$R_e = U_e \delta^{xx}/\nu$
14.9 m/s	50 mm	0.00285	5200

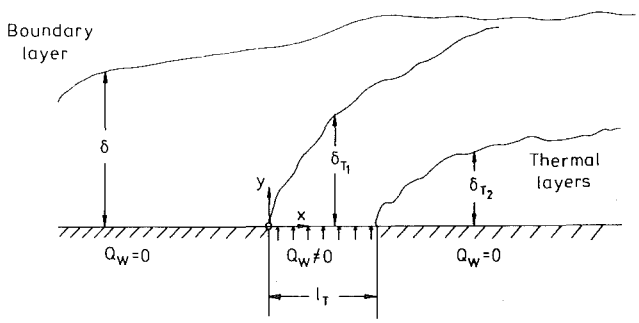

Fig. 1 Flow configuration

Contributed by the Heat Transfer Division for publication in the JOURNAL OF HEAT TRANSFER. Manuscript received by the Heat Transfer Division October 14, 1982.

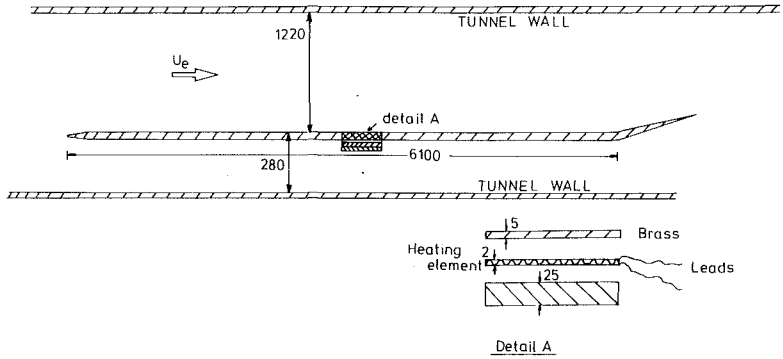

Fig. 2 Experimental arrangement (dimensions in mm)

μm home-made wire. Temperature fluctuations were measured by a 0.6-μm "cold" wire (resistance thermometer) mounted in a probe clamped to the side of the crosswire. The technique is similar to that described by Andreopoulos and Bradshaw [1]. The cold wire was operated with a heating current of 0.29 mA to avoid undesirable velocity fluctuations on the temperature wire. Its output voltage was compensated for thermal inertia by a conventional operational amplifier network. The time constant is a function of the instantaneous velocity normal to the wire. Therefore, the compensator must be set at each point because of the velocity variation across the boundary layer. However, Smits [7] estimated that a variation of 10 percent in the mean velocity will cause an error of only 3 percent in the sensitivity at high frequencies, and the error in the broad band temperature fluctuations will be much less than this. It is also pointed out in [13] that for wire-length to wire-diameter ratios above 1000, the time constant is reduced and the system is less sensitive to compensation errors. Therefore, the time constant was adjusted once only in the region where the intermittency was bout 0.5, so that the signal was falling to the T_e level as sharply as possible but without any overshoot. The instantaneous x-wire velocity signals were corrected for temperature contamination according to the method of Dean and Bradshaw [8], which is based on the value of the instantaneous temperature. If no corrections were applied, the expected error for the case of $Q_w = 105$ w where turbulence measurements have been made could be of the order of 10–15 percent on turbulence intensities. The ratio of the velocity sensitivity to temperature sensitivity of the temperature wire found to be of the order of $3.2\ 10^{-3}$ °C/m/s by using Wyngaard's formula from [14]. This value results in a typical error of 1–2 percent on ϑ-rms. A check on the noise level of the temperature wire in the absence of heating at $y+ \simeq 60$, which is the closest to the wall measuring point with roughly 15 percent turbulence intensity, gave a signal to noise ratio of 9 to 1. This noise level includes possible velocity fluctuations, electronic noise, or background temperature fluctuations. Finally the errors in the turbulence measurements are estimated to be of the order of 7 percent on $\overline{\vartheta^2}$, 8–12 percent on mixed temperature-velocity correlations and 15–18 percent on the third-order correlations. Approximately 40 min of operating time were required for the flow field to reach a steady state. All signals were digitized at 5 kHz per channel on the HP-Fourier Analyzer and recorded on magnetic tapes for later data reduction. Full description of the data acquisition processing system is given in [9].

The temperature and the velocity fields were found to be uniform in the spanwise direction, and the flux Richardson number which characterizes the ratio of the buoyant production to the shear production of turbulent kinetic energy was found to be very small (of the order of 0.0022). Generally the dynamic effects of the weak heating were found to be negligible and thus the temperature served merely as a passive contaminant, although some weak stratification effects may be present in the viscous sublayer in the high heating case only, but it is believed to be restricted only in the very near to the wall region, (the ratio Gr/Re^2 was of the order of 0.0069).

The results include velocity-temperature correlations up to third order, together with the flatness and skewness.

3 Results and Discussion

The present flow shows some similarities with the flow described in [3]. Both flows adjust themselves to the new wall conditions by forming two internal layers which denote the outward extent of the influence of abrupt changes of wall conditions. The first thermal layer is formed by the first step change in wall temperature (case of cold to hot change) and the second is a result of a second step change in wall temperature (case of hold to cold). The second internal layer

Nomenclature

c_f = skin friction coefficient $\tau_w(/0{\cdot}5)\ U_e^2\rho$
c_p = specific heat at constant pressure
F_ϑ = flatness of temperature fluctuations
Q = heat transfer per unit area per unit time
l_T = length of heated surface
Pr_t = $(-\overline{uv}/d\bar{U}/dy)/(-\overline{v\vartheta}/d\bar{T}/dy)$, turbulent Prandtl number
S_ϑ = skewness of temperature fluctuations
S_t = $Q_w/\rho c_p U_e(T_w - T_e)$, Stanton number
$\bar{T}$ = mean temperature
ϑ = fluctuating temperature
θ_τ = $Q_w/\rho c_p u_\tau$
u,v,w = fluctuating velocity components in x-, y-, z-directions
u_τ = friction velocity
y^+ = $u_\tau y/\nu$
δ = boundary layer thickness
δ^{xx} = momentum thickness
δ_{T1}, δ_{T2} = height (thickness) of the first and second thermal internal layer, respectively
δ_H = $\int_0^\infty \bar{U}/U_e(\bar{T}-T_e)/(T_w - T_e)\,dy$ enthalpy thickness
ρ = density
ν = kinematic viscosity
τ = shear stress

Subscripts

e = value at the boundary layer edge
w = value at surface
o = value at the origin

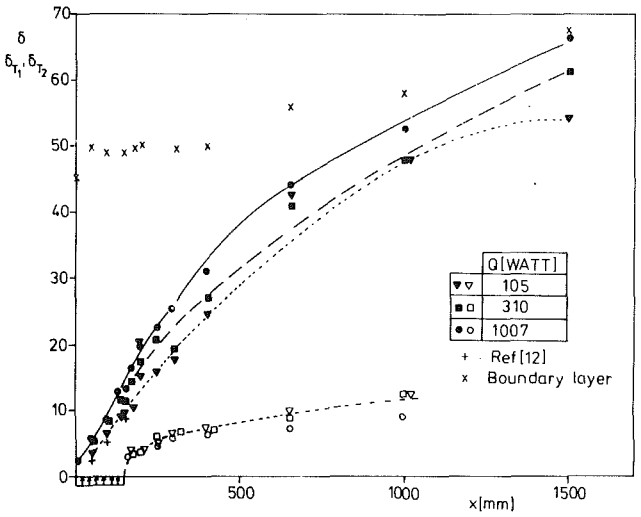

Fig. 3 Internal layers growth: filled symbols, δ_{T1}; open symbols, δ_{T2}; x, hydrodynamic boundary layer thickness

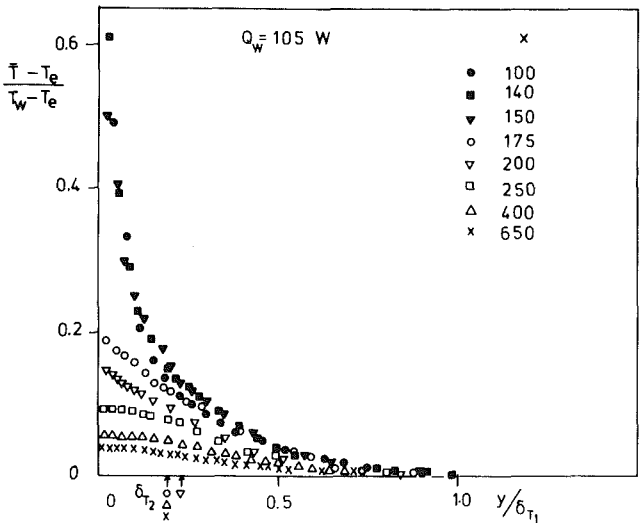

Fig. 4 Mean temperature distribution arrows show the edge of the second internal layer (x in mm)

grows inside the first, whose height is not expected to be affected by the presence of the second. The height of both internal layers, which indicates the rate of propagation of the thermal disturbance, was found as the points at which successive mean or temperature fluctuation profiles merged. More precisely, mean longitudinal temperature gradients $\partial\bar{T}/\partial x$ were compared to $\epsilon(T_w - T_e)/\delta$ where T_w and T_e are the heated wall and free-stream temperature, respectively, δ is the thickness of the boundary layer, and ϵ some suitable small number. The height of the internal layer is defined as the distance, y, where

$$\frac{\partial \bar{T}}{\partial x} \leq \frac{\epsilon(T_w - T_e)}{\delta} \tag{1}$$

The value ϵ depends on the available accuracy of mean temperature measurements and the uncertainities involved in deducing the longitudinal gradients.

The growth of the thermal layers is shown in Fig. 3, for the three different heating cases together with the outer boundary layer growth. It is clear that the higher the heat flux, the higher the edge of the thermal layer and the smaller the edge of the second layer. This means that the "plume" from the heated wall strip has a faster spreading rate at higher heat fluxes. In all cases the growth rates of the first thermal layer is very high in its early stage of development and then gradually

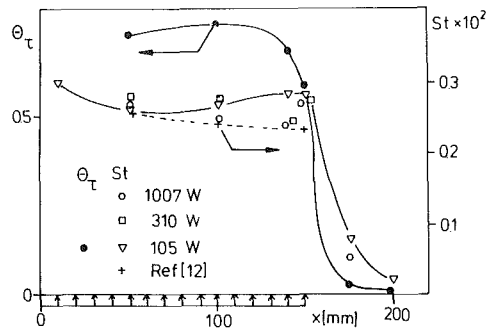

Fig. 5 Friction temperature and Stanton number distributions

reduces to smaller values up to the position where the thermal layer edge meets that of the momentum boundary layer. At this point the growth rate of both seems to match each other, and the two layers have started to interact between each other in an unknown way. There the viscous superlayer is expected to play a predominant role. If the thermal field was fully developed and because the turbulent Pr_t for air is roughly equal to one, the edges of these layers should coincide. However, this is not the case here, because the thermal one is still developing even at the distance of 30 δ downstream of its origin.

The growth rate of the second thermal layer seems to be very high at the beginning but very soon drops down to much smaller values. This is an essential difference from the first layer, which seems to affect the second rather than to be affected by that.

Figure 4 shows the mean temperature distribution above the free-stream temperature at various downstream positions. They have been nondimensionalised by $T_w - T_e$. The profiles downstream the trailing edge of the heated wall, i.e., for $x \geqq 150$ mm, have been nondimensionalised by $T_w - T_e$ at $x = 150$ mm, since further downstream $T_w - T_e$ is small, practically zero. As scale for the distances from the wall the thickness δ_{T1} of the first (outer) thermal layer has been used. It can be seen that the use of these two scales to present the results make the data to collapse, only in the region above the heated wall. At the first downstrean station, $x = 175$ mm mean temperatures fall to about 20 percent of $T_w - T_e$ and the resulting very high but negative longitudinal gradient $\partial\bar{T}/\partial x$ is expected to contribute significantly in the production of $\overline{\vartheta^2}$ or $\overline{v\vartheta}$. Further downstream, mean temperature distribution continues to drop, and at $x = 650$ mm (the last measuring station, which corresponds to about 13 initial boundary layer thicknesses), the maximum temperature difference has a value of 0.03 of $T_w - T_e$. The edge of the second internal layer is also shown in Fig. 4. Inside this layer the temperatures are not zero. This is an important feature of the flow which does not allow us to call the heated present flow a rising plume, because outside the plume the mean temperature is zero.

The longitudinal variation of the friction temperature θ_τ and Stanton number St is shown in Fig. 5. The wall heat flux Q_w has been obtained from the mean temperature gradient very close to the wall (first measuring point at $y^+ = 10$) and accounts for about 93 percent of the electrical heat inputs. It was found to be fairly constant above the heated part of the plate except probably at $x = 150$ mm where some "end effects" are present. In fact, Q_w has the same distribution as θ_τ since u_τ decreases very slowly with x. The friction temperature changes abruptly at $x = 150$. At the first downstream station it has a rather small value, although above a nominally adiabatic wall must be zero. This is reflected on the St number distribution as well, but since $Q_w/T_w - T_e$ goes slower to zero than Q_w, St does not change so suddenly with x, as θ_τ does. There are some weak evidences that the St number is smaller

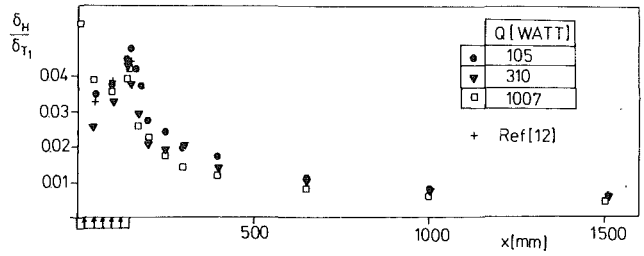

Fig. 6 Enthalpy thickness along the plate

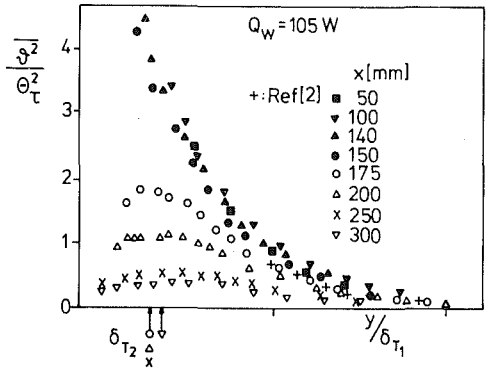

Fig. 7 $\overline{\vartheta^2}$ distribution

at higher heating rates not only above the heated strip where it reduces slowly with x but even at the immediately downstream stations.

Figure 6 shows the longitudinal variation of the enthalpy, thickness δ_H. Around the trailing edge, δ_H reaches its maximum value of 5 percent of the total boundary layer thickness. Exactly after that point, it drops, suddenly at the beginning and slowly later and about $x=1500$ ($\simeq 30\delta$) seems to reach an asymptotic value of 0.8 percent of local boundary layer thickness. Again, in the relaxation region some heating power effects are present: the higher the heat flux, the smaller the enthalpy thickness. The results of the integral analysis of Kays [12] to predict δ_{T1}, θ_τ and δ_H have also been incorporated in Figs. 3, 5, 6, respectively. A comparison with the measurements shows a rather good agreement although for predictions of the details of the temperature profiles, a more sophisticated analysis is needed.

Figure 7 shows the temperature fluctuation, $\overline{\vartheta^2}$, distribution at various downstream stations. The results are normalized by θ_τ and δ_{T1}, except for $x \geqq 150$ mm where the value of θ_τ at $x=150$ has been used. It is rather difficult to say that the profiles above the heated plate region collapse as the data of Antonia et al. [2] surprisingly do, since near-similarity assumes thermal equilibrium of the flow in the near wall region. Generally, agreement with those data for the case of $C \rightarrow H$ (cold to hot change) is not to be expected since Antonia et al. have taken measurments at longer distances from the first step than the present and probably only their first profile may compare with the last profile, at $x=150$ of the present data, which have been obtained very close to the step.

In the heated near wall region, temperature fluctuations are high, indicating that partially heated flat-plate fluid alternates with nonheated turbulent fluid from the oncoming boundary layer, while in the outer region most of the fluid is cold. In the downstream wall region, however, the temperature fluctuations reduce, particularly inside the second internal layer were the gradient $\partial\overline{\vartheta^2}/\partial y$ is positive over a great part of the layer.

Figures 8 and 9 shows the velocity-temperature correlations at various positions downstream. Both are involved in the mean enthalpy equation

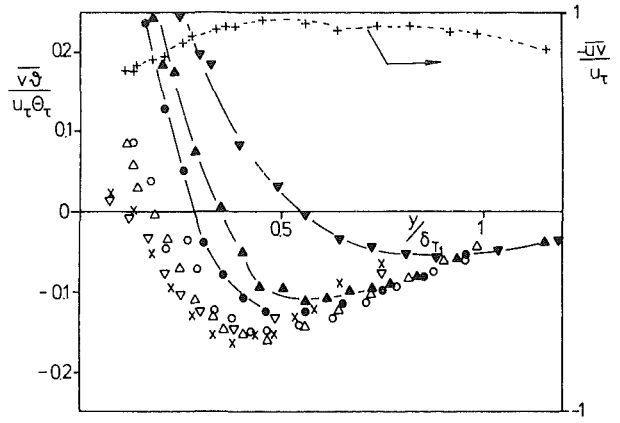

Fig. 8 $\overline{v\vartheta}$: symbols as in Fig. 7., + shear stress at $x = 150$ mm

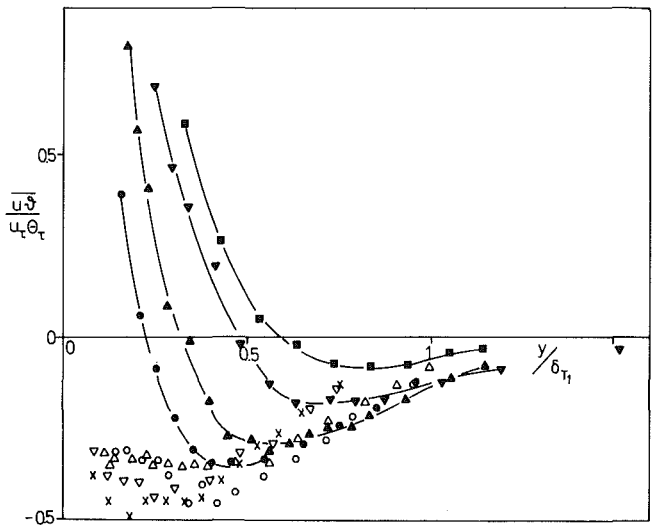

Fig. 9 $\overline{u\vartheta}$ distribution symbols as in Fig. 7

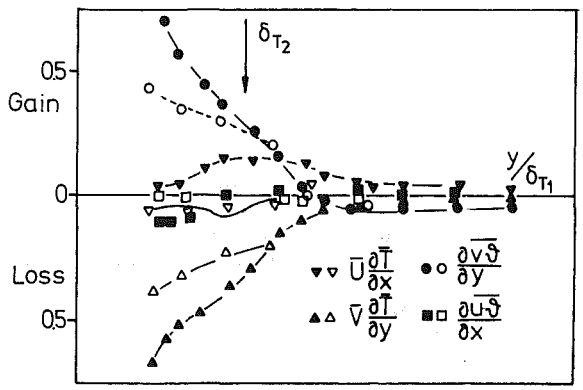

Fig. 10 Balance of terms in mean enthalpy equation. All terms are normalized with $\delta_{T1}/\theta_\tau u_\tau$. Filled symbols, $x = 150$ mm; open symbols, $x = 175$ mm. Solid line ____, out of balance term at $x = 150$ mm.

$$\bar{U}\frac{\partial \bar{T}}{\partial x} + \bar{V}\frac{\partial \bar{T}}{\partial y} + \frac{\partial \overline{v\vartheta}}{\partial y} + \frac{\partial \overline{u\vartheta}}{\partial x} = 0 \quad (2) \qquad (2)$$

Since the flow is developing, longitudinal gradients like $\partial\bar{T}/\partial x$ and $\partial\overline{u\vartheta}/\partial x$ are not negligible and particularly the last one, which is usually very small in two-dimensional thin shear layers, has significant values. It is very interesting to see how $\overline{v\vartheta}$ profiles develop at downstream stations. They start with some negative values at the near wall region and gradually become positive at higher x as it is in the usually fully heated

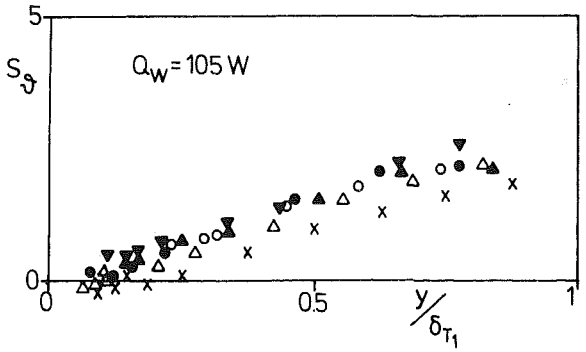

Fig. 11 Skewness profiles (symbols as in Fig. 7)

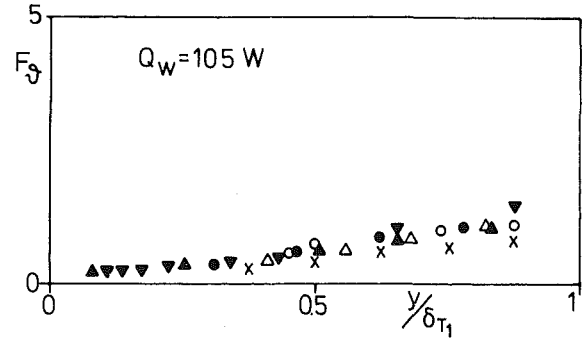

Fig. 12 Flatness profiles (symbols as in Fig. 7)

boundary layer. It is worth noting that in the outer part of all profiles $\overline{v\vartheta}$ is positive with negative gradient $\partial\overline{v\vartheta}/\partial y$. This rather surprising behavior of $\overline{v\vartheta}$ implies changes in the other terms of (2), which are shown in Fig. 10 where balances of all terms included in (2) are plotted, for $x=150$ mm and 175 mm. Somewhere around the middle of the thermal layer $\partial\overline{v\vartheta}/\partial y$ changes sign and becomes negative. Roughly at the same position the longitudinal gradient of $\overline{u\vartheta}$ becomes positive, although it has smaller values that $\partial\overline{v\vartheta}/\partial y$. In the outer part of the flow, the term $\bar{U}\partial\bar{T}/\partial x$ counterbalances the negative $\partial\overline{v\vartheta}/\partial y$ and $\bar{V}\,\partial\bar{T}/\partial y$. In the wall region, i.e., $y \leqq 0.5\delta_{T1}$, and above the heated part of the plate (case of $x=150$) $\partial\overline{v\vartheta}/\partial y$ is positive as is $\bar{U}\partial\bar{T}/\partial x$; there are counterbalanced mainly by $\bar{V}\partial\bar{T}/\partial y$. Closer to the wall, i.e., at $y\simeq 0.2\,\delta_{T1}$, the term $\partial\overline{u\vartheta}/\partial x$ reaches significant negative values while the longitudinal gradient $\partial\bar{T}/\partial x$ is small. At the downstream station, $x=175$ mm, however; $\partial\overline{u\vartheta}/\partial x$ is rather small, and the $\bar{U}\partial\bar{T}/\partial x$ is negative, with the rest of the terms having the same behavior as at $x=150$ mm.

It is remarkable to say that $\overline{v\vartheta}$ crosses zero and reaches negative values exactly at the point where the shear stress start to decrease at the beginning of the logarithmic region around $y/\delta\simeq 0.04$ ($y^+\simeq 80$) (or $y/\delta_{T1}\simeq 0.4$). The thermal layer at $y/\delta_{T1}\geqq 0.4$ is in the constant shear stress region, i.e., in the logarithmic law region of the momentum boundary layer, where the produced turbulent kinetic energy is directly dissipated. However, the equivalent feature in the thermal field is not valid because there is no thermal equilibrium in rapidly developing flows very close to step changes in wall heat flux.

The eddy diffusivity concept which relates the heat flux, $-\overline{v\vartheta}$, with the mean temperature gradient, $\partial\bar{T}/\partial y$, is not expected to be valid at least in regions over the heated strip, for obvious reasons. For similar reasons the turbulent Prandtl number does not behave well. Only in the outer region does it have a value close to one. Figure 11 and 12 show the distributions of skewness and flatness of temperature fluctuations. In the outer part of the flow, i.e., near the edge of the first thermal layer, both quantities reach very high values indicating appreciable deviations from a Gaussian distribution. The main reason for this behavior seems to be the highly intermittent character of the flow, i.e., the "time-sharing" effect between the heated and nonheated eddies of the flow. The values of S_ϑ and F_ϑ decrease slightly at downstream stations. In fact, downstream of the heatd part of the plate and close to the wall region, S_ϑ starts to have negative values, which is in agreement with the measurements of [5] or the fully heated boundary layer of Chen and Blackwelder [10] or Zaric [11].

Conclusions

The foregoing measurements are believed to give a good picture of the temperature-velocity correlations in the flow field over a short heated part of the wall. The flow consists of two step changes in wall heat flux: one, cold (unheated) to hot which takes place at the leading edge of the heated strip; and another, hot to cold which takes place within a short distance after the first. However, the present case can be considered as a simple superposition of these simpler flows, like those described in [2] and [5]. Both step changes are associated with the appearance of two internal layers having quite different growth rates. In fact, the second one which starts to develop later in time, has smaller growth rates and seems to be affected by the first one considerably. In addition, both growth rates seem to depend on the amount of the wall heat flux at least at their early stages of development. At the downstream stations, changes start to happen first – inside the second layer then they propagate outwards. In this region, mean temperature and fluctuations are decreased considerably while the turbulent heat flux, $\overline{v\vartheta}$, has negative values and some conductivity effects may be present. This limits the possibility of using the eddy diffusivity concept to calculate the flow.

Acknowledgment

The author wishes to acknowledge the financial support provided by the Deutsche Forschungsgemeinschaft as part of the project A 33. Fruitful discussions with Dr. D. H. Wood are also acknowledged.

References

1 Andreopoulos, J., and Bradshaw, P., "The Thermal Boundary Layer far Downstream of a Spanwise Line Source of Heat," ASME JOURNAL OF HEAT TRANSFER, Vol. 102, 1980, pp. 755-760.

2 Antonia, R. A., Danh, H. Q., and Prabhu, A., *Journal of Fluid Mechanics*, Vol. 80, 1977, pp. 153-177.

3 Andreopoulos, J., and Wood, D. H., "The Response of a Boundary Layer to a Short Length of Surface Roughness," *Journal of Fluid Mechanics*, Vol. 118, 1982, pp. 143-164.

4 Bradshaw, P., and Ferris, D. H., NPL Report No. 1271, 1968.

5 Subramanian, C. S., and Antonia, R. A., "Study of Turbulent Boundary Layer Downstream of Sudden Decrease in Wall Heat-Flux," *7th Australasian Hydraulics and Fluid Mech.* Conference, Brisbane, Australia, 1980.

6 Triantafyllou, E., "Das Verhalten der turbulenten Wandgrenzschicht bei Strömungen uber einen beheizten Streifen," *Diplomarbeit*, SFB 80 Universitat Karlsruhe, 1982.

7 Smits, A., "Further Development of Hot-Wire and LASER Methods in Fluid Mechanics," PhD thesis, University of Melbourne, 1974.

8 Dean, R. B., and Bradshaw, P., "Measurements of Interacting Shear Layers in a Duct," *Journal of Fluid Mechanics*, Vol. 78, 1976, pp. 641-678.

9 Andreopoulos, J., "Digital Techniques and Computer Programs for Hot-Wire Data Processing," Report SFB 80/ME/181, 1980.

10 Chen, C. P., and Blackwelder, R. F., "Large-Scale Motion in a Turbulent Boundary Layer: A Study Using Temperature Contamination," *Journal of Fluid Mechanics*, 89, 1, 1978.

11 Zaric, Z., "Contribution a l'étude statisique de la turbulence partiale," These doctorat d' étude et sciences physiques, Universite Paris VI, 1974.

12 Kays, W. M., *Convective Heat and Mass Transfer*, McGraw-Hill, 1966, p. 244.

13 Smits A. J., Perry A. E., and Hoffmann, *J. Physics E: Sci. Instrum*, Vol. 11, 1978, pp. 909-914.

14 Wyngaard, J. C., The Effect of Velocity Sensitivity on the Temperature Derivatives Statistics in Isotropic Turbulence," *Journal of Fluid Mechanics*, Vol. 48, 1971, pp. 763-769.

Influence of Forced Flow on the He II-He I Transition in the Presence of Heat Flow

S. Caspi
Lawrence Berkeley Laboratory,
University of California,
Berkeley, Calif. 94720

T. H. K. Frederking
University of California,
Los Angeles, Calif. 90024

The influence of forced flow on the He I-He II, two-phase flow has been studied during heat transfer to superfluid He II in a U-shaped tube, at pressures from 2.4 bar to 10 bar, bath temperatures from 1.6 K to 2.1 K, and flow velocities from zero internally applied speed ("zero net mass flow") to the order of 0.1 cm/s. Within this range of conditions, forced flow (i) did not influence heat transfer prior to phase transitions more than 10 percent; (ii) reduced temperature excursions at lambda phase transitions by a factor of 2 at most with respect to zero net mass flow; (iii) did not influence the limiting heat flux density at initiation of the lambda transition in the supercritical pressure range covered.

1 Introduction

Superconducting magnets are refrigerated nearly exclusively by liquid He I using pool boiling or forced flow. Technology improvements recently have created interest in magnet operation at 1.8 K in superfluid He II [1]. It boosts critical magnetic fields and accomplishes excellent thermostatic bath stability. For optimum conductor stabilization, appropriate choices of the He II states and modes of operation are required.

First attempts to obtain the desirable state have focused on operation from 1 bar to supercritical pressures ($P > P_c$; $P_c = 2.3$ bar). Data obtained showed three regimes of operation along isobars: (*i*) He II-dominated heat transfer; (*ii*) transition from He II to He I (lambda transition); (*iii*) He I-He II, two-phase motion due to formation of wall-adjacent He I domains. The latter cause large thermal impedances. The present paper has as its purpose the study of the influence of small forced convection speeds on these phenomena. A simple, two-phase model is summarized to elucidate important flow phenomena (section 2). The experiments are described in section 3 and discussed in section 4. Conclusions are given in section 5. Early results have been outlined elsewhere [2, 3].

2 Theoretical Discussion

The discussion below is a summary of physical assessment detailed in [4]. An assessment of the entrance length is considered because of the short heated section. He I, being a classical Newtonian fluid, requires an entrance length of about 10 cm to achieve a fully developed flow (velocity 0.1 cm/s, radius 0.2 cm). Since Pr is of the order of unity, the thermal entrance length is of the same order. In He II, this type of assessment is difficult since the liquid is non-Newtonian. However, in the Gorter-Mellink regime [4, 5], an order-of-magnitude approach in terms of the apparent thermal diffusivity is permitted. This estimate of a thermal entrance length of 10^{-6} cm indicates that He II is reminiscent of the behavior of low Pr-number fluids, e.g. liquid metals. It is therefore concluded that the He II flow may be considered developed in the present experiment.

Two-Phase Flow. After the lambda transition has been initiated due to heat supply from the duct walls, a "hot" He I layer is formed in the He I-He II, two-phase flow regime. In view of the entrance conditions discussed so far, He II constitutes a heat sink with a very large thermal conductance, i.e., a reservoir in the thermodynamic sense. Consequently, there is a large ΔT_I in He I, and a small ΔT_{II} in He II during the two-phase flow. He II is assumed to cause a negligible momentum transfer at the He II-He I interface where the latent heat of phase change is absent. This set of thermodynamic conditions appears to permit unimpeded motion of He II in the hydrodynamic sense.

The thermal conductivity of the He I layer is of the order 10^{-4} to 10^{-3} $\mathrm{Wcm^{-1}\,K^{-1}}$, i.e., up to five orders below the He II values. This causes the major thermal resistance to reside in the He I layer. This suggests the use of a simple flow model whose limited cases are discussed below.

Flow Model. The flow configuration is a He I film in the entrance region of a duct (Fig. 1). According to the classical boundary conditions [6], He I is sticking to the wall. There is zero shear at the He I-He II interface. The walls are presumed isothermal, and constant properties are introduced. For recognition of salient flow features two extreme cases of predominant gravitational motion and governing forced convection are considered. We shall then superpose the two effects and take their ratio with respect to the gravitational buoyancy case (zero net mass flow). Subsequently, the resulting flow equation will be compared with experimental results.

Using a simplified version of the equations of motion and energy, the ratio of velocities is characterized by $[\tan \epsilon] = v_\perp / v_\parallel$. This ratio is proportional to the heat flux density ratio, $q_\perp / q_\parallel$, of convection. The rate, q, is the product of v and the thermal energy density convected. For $\Delta T_I > 1$ K, gravitational buoyancy turns out to be dominant, and ϵ is greater than $(\pi/3)$ as long as $v_\parallel$ does not exceed 1 cm/s. At low ΔT_I, forced flow dominates. Therefore, in the present range of parameters covered, both heat transport modes, in the axial and in the transverse direction, should be considered.

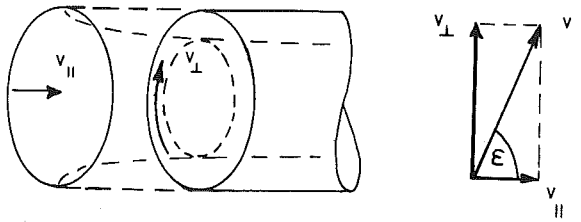

Fig. 1 Two-phase flow model with angle between velocity components

Contributed by the Heat Transfer Division for publication in the JOURNAL OF HEAT TRANSFER. Manuscript received by the Heat Transfer Division September 29, 1981.

The forced flow Nusselt number [7] based on the heated length, L, is

$$\mathrm{Nu}_1 = (2/3)\mathrm{Re}^{1/2};\ \mathrm{Pr} \sim 1 \tag{1}$$

The Nusselt number for the other extreme case of gravitational buoyancy at zero net mass flow [6,7] is

$$\mathrm{Nu}_{0,1} = C\,\mathrm{Ra}^{1/4} \tag{2}$$

where C is a constant of the order of 0.7 for two-phase motion.

Nonlinear superposition of equations (1) and (2) leads to an interpolation equation which contains the two extreme cases as asymptotes. Normalizing in terms of h_0 for gravitational buoyancy, we arrive at an h-ratio of the interpolation function (Appendix A)

$$h/h_0 = \{1 + 0.9[g^{-1} v_\parallel^2 D L^{-2} (\Delta\rho/\rho)^{-1} \mathrm{Pr}^{-1}]^{1/2}\}^{1/2} \tag{3}$$

The insert of Fig. 3 is an illustration of the present flow model. It shows the ratio (h/h_0) for $D = L = 1$ cm and for $v_\parallel = 1$ cm/s as a function of ΔT_I, properties evaluated at the arithmetic mean temperature of the He I film. There are two limiting cases of low and high ΔT_I. For very small ΔT_I, when $T_\mathrm{I} \to T_\lambda$, the local He I state approaches zero expansivity $(\Delta\rho \to 0)$. As a result, h/h_0 increases to high values. At very large ΔT_I, gravitational buoyancy is the relevant driving force, and the h-ratio approaches unity. However, in this limit turbulence is established in general, and equation (3) becomes a lower bound to data.

In between there is a *local* crossing of the transposed critical curve (TCC). At the TCC, $\Delta\rho \to \infty$, and the Pr number approaches very high values. Again, h/h_0 approaches unity. Because of the property assumption introduced, the ΔT_I at the TCC anomaly is larger than the distance between T_λ and the TCC. The effect is small, and the use of a smooth function in the insert (Fig. 3) causes an error of less than 2 percent.

Thus, on the basis of the present simple, two-phase model, we do not expect a significant increase in heat transfer rates due to forced convection, i.e., more than 10 percent for laminar He I film flow. As will be shown subsequently, the real world is much less conservative.

3 Experiments

Experiments of $P > P_c$ have been conducted with a modified version (Fig. 2) of the U-shaped system described previously [2]. The insert of Fig. 2 is a schematic of the vacuum can, containing the horizontal Cu-tube, which serves as test section (OFHC copper, 2.54-cm long, 0.635-cm o.d., 0.335-cm i.d.). The residual resistivity ratio of the Cu is 41 ± 1 at 4.2 K with a corresponding thermal conductivity of $k = 2.6$ W cm^{-1} K^{-1}. The two vertical tubes made from stainless steel alloy 304 have a length of 11.8 cm, an o.d. of 0.5 cm, and a wall thickness of 0.0254 cm. Brass elbow pieces are used between the Cu-tube and the vertical stainless steel sections. The resulting distance from center to center of the vertical legs is 4.0 cm. The mass flow direction is indicated by arrows. Three thermometer locations (1 to 3) are shown downstream of the heater, and a thermometer 4 is mounted on the heater. Two additional thermometers record temperatures upstream.

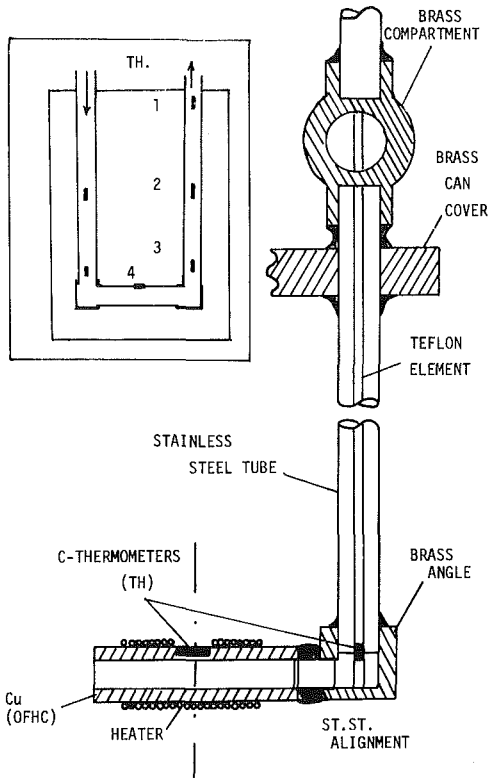

Fig. 2 Experimental apparatus (schematically) with carbon thermometers

The constantan heater wire (0.0075-cm dia, teflon insulation) has a resistance of 135 Ohms at liquid helium temperatures. Two sections of these windings surround the central thermometer 4. The carbon thermometers have a nominal resistance of 39 Ohms at room temperature (Allen-Bradley-Ohmite with a rating of 1/8 W). Special brass compartments are located on top of the vacuum can. They connect upstream to the heat exchanger, and to a flow meter on the downstream side.

Nomenclature

A_i = area (i = cu, GM)
C = constant
D = diameter
g = gravitational acceleration
h = heat transfer coefficient; (h_o values for $v_\parallel = 0$)
k = thermal conductivity
L = length
m = mass flow rate
Nu_i = Nusselt number
P = pressure
Pr = Prandtl number
q = heat flux density; q_i for $i = \perp, \parallel$
Re = Reynolds number $L\rho v_\parallel/\eta$
Ra = Rayleigh number, $D^3 g(\Delta\rho/\rho)\rho^2 \mathrm{Pr}/\eta^2$
T = temperature
$\Delta T = T - T_\infty$
$\Delta T_\mathrm{I} = T - T_\lambda$
$\Delta T_\mathrm{II} = T_\lambda - T_\infty$
v_i = velocity ($i = \perp, \parallel$)
δ = boundary layer thickness
ϵ = angle between velocity components
η = shear viscosity
ρ = density

Subscripts

1 = Nu number for heated area, hL/k
I = He I
II = He II
c = critical
GM = Gorter Mellink
L = limiting value
o = zero net mass flow
∞ = bulk fluid (He II)
$\perp$ = gravitational flow (transverse)
$\parallel$ = axial flow
λ = lambda transition

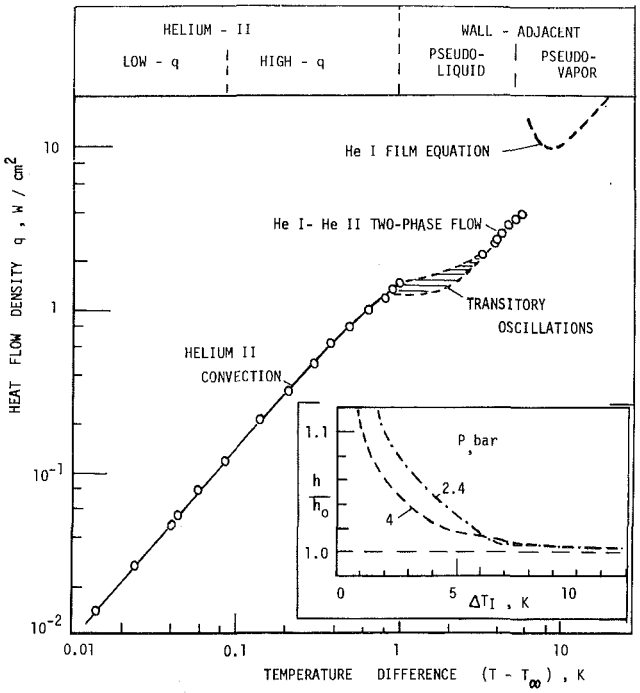

Fig. 3 Lambda transition record of thermometer 4: bath temperature $T_\infty = 1.95$ K, $P = 2.4$ bar, $\dot{m} = 1.4$ g/min (Insert: Ratio h/h_0 of model equation (3) for $v_{11} = 1$ cm/s)

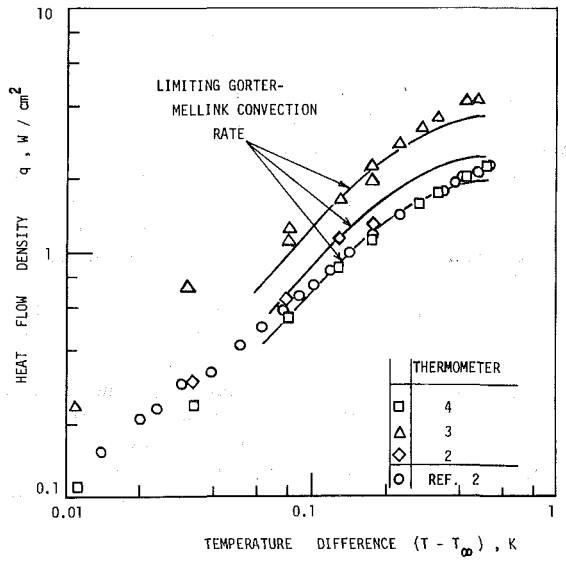

Fig. 4 Comparison of predicted GM results with experimental data for the limiting q-value ($q = q_L$) prior to onset of two-phase flow; $P = 4$ bar; full curve: GM equation [4]

Prior to a run, the system is cooled down and the outer vessel is filled with liquid He^4 (He I at NBP). Subsequently, the outer bath temperature is brought in steps below the lambda temperature by reducing its vapor pressure. At various selected temperatures thermometers are calibrated. During a run the bath temperature is kept constant using a vapor pressure controller. Below T_λ, the test section is pressurized to $P > P_c$, and a mass flow is switched on. This gas is admitted via a system of heat exchangers located upstream of the U-shaped test section. Finally the fluid is brought back to room temperature where the flow rate is measured.

The heater is energized using a current source in conjunction with a programmer which provides a linear rate of change of the heater current. For quasi-steady operation a slow rate of the order 1 mA/s is established. X-Y plots of the thermometer signal as a function of the heater current are then recorded. The power is related to the cross sections of the heater section and the GM-duct, respectively. These q-values are a monotonically increasing function of the difference ($T - T_\infty$) between the heater temperature and the bath temperature ($T_\infty = T_{II}$). Further details of the experiments are described elsewhere [8].

4 Data Discussion

There are three major regimes visible in the records (e.g., Fig. 3): first, the low-q regime with a negligible effect of v on the Kapitza resistance and He II convection, respectively; second, a transition from low-q convection of He II to He II-He I, two-phase transport; third, two-phase flow involving wall-adjacent He I and bulk He II. The phase transition curve, Fig. 3, has been recorded by thermometer 4 at a pressure, slightly above the thermodynamic critical pressure, $P = 2.4$ bar. The heat flow rate per duct cross sectional area is plotted versus the difference ($T_4 - T_\infty$), i.e., the reference area, A_{cu}, is replaced by the duct cross section A_{GM}.

Low-q Regime. The $q(\Delta T)$-functions appear to be quite similar to results for zero net mass flow [9]. The wall temperature of the heating section is controlled by the Kapitza resistance of the Cu in conjunction with convection of the He II in the tube system. This transport is a modified form of Gorter-Mellink (GM) convection [4, 5] at zero net mass flow. The GM results obtained are in drastic contrast to the high-speed flow of He II covered by Johnson et al. [10]. The low-q regime extends to a Kapitza ΔT of about 1 K and the limiting q_L. At q_L a macroscopic, He I phase domain is formed, which is separated by a "lambda transition layer" from the He II.

The limit, q_L, is compared with theory [4] in Fig. 4. Various q_L-values observed with thermometers 2, 3, and 4 are position-dependent in agreement with the GM theory [4]. In contrast, the influence of the flow velocity, $v_\parallel$, on the Kapitza conductance $h = q/\Delta T$ at the Cu surface is insignificant in the data range covered. Similar results are observed in the runs depicted in Figs. 5 to 7. Further details are in [8] and [11].

Transition Regime. The excursion from $\Delta T_L(q_L)$ toward a higher ΔT is accompanied by temperature oscillations that are similar to fluctuations at zero net mass flow [9]. At larger ΔT, upon termination of the transition, a lower overall h-value is reached because of the He I layer at the Cu-wall. Upon power reversal, another oscillation pattern characterizes the recovery from two-phase transport to He II convection. Finally, the low-q regime is recovered.

It is noted that the transition, in principle, may involve two phase transitions: first, the present λ-crossing along an isobar into the He I pseudo-liquid region of the He^4 phase diagram; and second, a subsequent transition from pseudo-liquid across the transposed critical curve (TCC) into the pseudo-vapor region. Indeed, a transition across the TCC has been reported recently [12]. Obviously, for the present geometry, the He II-He I transition is most dominant such that the TCC transition is masked by the first phase change.

He I-He II Two Phase Regime. In the two-phase regime the influence of the velocity, $v_\parallel$, is no longer negligible. Data obtained with thermometer 4 (Figs. 5 and 6) indicate that initially $v_\parallel$ raises q significantly, at a specified ΔT, when $v_\parallel$ is increased from zero to finite values. As $v_\parallel$ is raised even more, however, the enhancement of q by $v_\parallel$ tends to get weaker. The mean velocity of the flow is listed in the inset of Fig. 6 for the lambda point vicinity.

Figure 7 presents the ratio h/h_0 versus $\Delta T/\Delta T_{II}$. Sub-

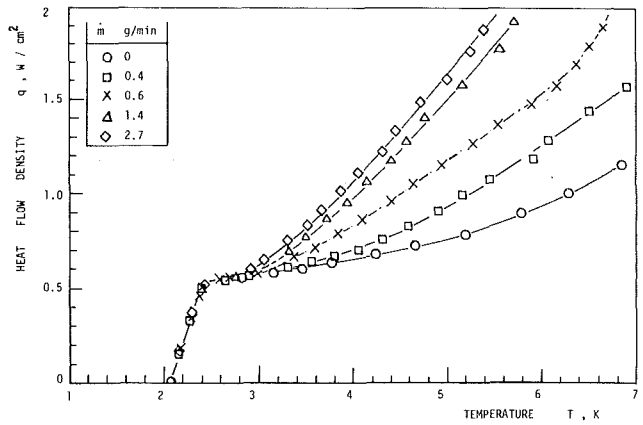

Fig. 5 Two-phase flow He II-He I: $P = 4.0$ bar; bulk bath temperature, $T_\infty = 2.05$ K

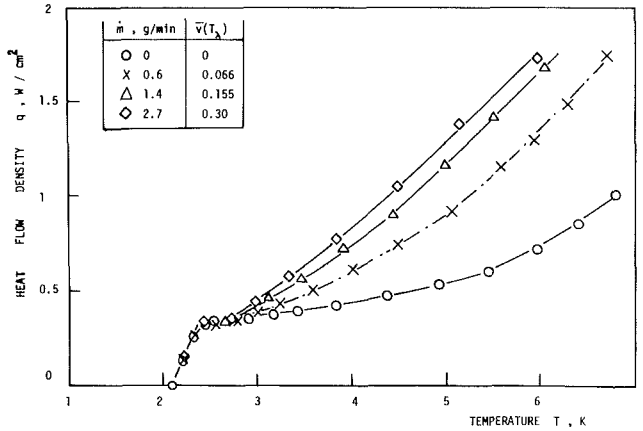

Fig. 6 Two-phase flow He II-He I; $P = 2.4$ bar; bulk bath temperature, $T_\infty = 2.1$ K

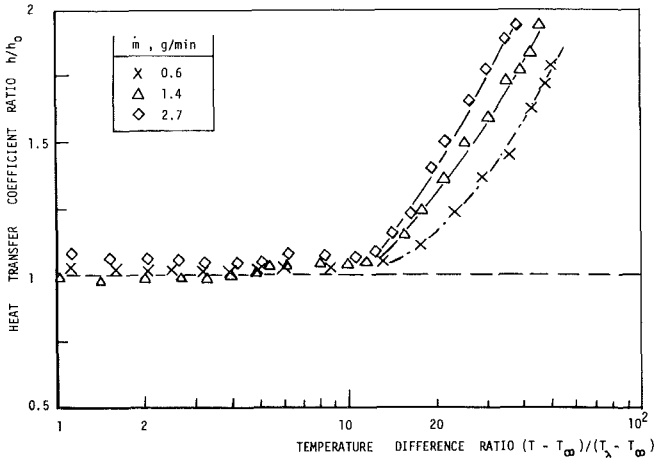

Fig. 7 Normalized heat transfer coefficient; $P = 2.4$ bar, bulk bath temperature, $T_\infty = 2.05$ K

sequent to the low-q regime with negligible influence of $v_\parallel$ (within data scatter), the ratio h/h_0 is seen to rise rapidly. Values of the ratio of up to 2 are obtained in the upper range of the experiments. Quantitatively, this rise in the ratio is much larger than the model prediction.

The order of magnitude of the data is compared with prediction based on the present interpolation equation (3) (Fig. 3). Instead of the reference area of the heater (A_{cu}), the GM duct cross-sectional area is used requiring a renormalization of equation (3). For the limit of dominant gravitational buoyancy, for instance, equation (2) is rewritten, ($A_{cu}/A_{GM} = 2.67/0.88 = 30.3$), as

$$\mathrm{Nu_{GM}} = \mathrm{C}(A_{cu}/A_{GM})\mathrm{Ra}^{1/4} \tag{4}$$

In the two phase regime at pseudo-vapor temperatures, there appears to be good order of magnitude agreement between the data and equation (3). Upon initiation of the two-phase pattern, however, there are departures of the experimentally obtained mean values of $q/\Delta T$ from equation (3). Because of the strong He II-He I transition, the *local* high-q excursion is not visible in the mean h-values. Another possible reason is the support of turbulence initiation by the U-system geometry. The Reynolds number, at $v \sim 1$ cm/s, expressed as ($D\ v\ \rho/\eta_n$) reaches the order 10^3. In addition, the U-system favors oscillations [9]. Thus, turbulence is likely to exert a partial influence on the present transition pattern.

Another possible reason for discrepancies between model and data is the change in the He II order parameter. According to the results of Johnson [10], this effect may be significant. For the present system, the separation of He II effects from Newtonian fluid effects of He I is not available at present. At high speed, superfluidity is nearly eliminated hydrodynamically [10]. In contrast to [10], the present h-data show a significant increase by application of only moderate forced flow. Despite the complicated set of influential variables, the present model equation appears to be quite a useful lower bound in the T-range of the pseudo-vapor regime ($T > \mathrm{TCC}$).

5 Conclusions

It is concluded that three features characterize the present studies: (*i*) at $P = P_c$, two-phase flow (He I-He II) is established during the lambda transition despite a lack of latent heat of phase change; (*ii*) there is a large influence of the small forced flow speeds on heat transfer in the two-phase region; (*iii*) the effect of forced flow is underestimated by the present laminar He I-He II flow model, which provides a lower bound to the mean heat transfer rates.

The model is of limited utility in the range affected by the two higher-order phase transitions of He^4 (transition at T_λ [He II-He I] and at the TCC). The He II-He I transition is quite dominant. This causes a large rise in T, along an isobar, in the transition regime all the way up to the vicinity of the TCC (for $dq > 0$). The oscillatory motion of the U-system partially explains the discrepancy between data and model prediction in the pseudo-liquid regime [11, 12]. This motion interacts with the flow favoring the transition to localized cellular motion and turbulence, respectively. Thus, the model serves as a meaningful lower bound in the pseudo-vapor regime [12].

The present findings point out favorable properties of magnet operation, which has to rely on He II forced flow. There is the benefit of a smaller "jump" in T during the forced flow lambda transition, and a substantial increase in heat transfer after two-phase flow has been established.

Acknowledgment

This work has been supported in part by the National Science Foundation.

References

1 Caspi, S., Gilbert, W. S., and Rechen, J. B., "The Ramp Rate Sensitivities of Several Superconducting Dipole Magnets Operated in He I and Superfluid He II," Paper No. LH-16, Appl. Superconductivity Conf., Knoxville, Tenn., 1982.

2 Caspi, S., Lee, J. Y., and Frederking, T. H. K., "Lambda Transition (He II-He I) During Heat Flow at Supercritical Pressures," ASME JOURNAL OF HEAT TRANSFER, Vol. 99, 1977, pp. 479–482.

3 Caspi, S., and Frederking, T. H. K., "Thermophysical Properties of the Lambda Transition in Helium-4," Paper No. 94b, 72nd Annual Meeting, Am. Inst. Chem. Engrs., San Francisco, Calif., 1979.

4 Soloski, S. C., and Frederking, T. H. K., "Dimensional Analysis and Equations for Axial Heat Flow of Gorter-Mellink Convection (He II)," *International Journal of Heat and Mass Transfer*, Vol. 23, 1980, pp. 437–441.

5 Van Sciver, S. W., "Transient Heat Transport in He II," *Cryogenics*, Vol. 19, 1979, pp. 385–392.

6 Schlichting, H., *Boundary Layer Theory*, 4th ed., McGraw-Hill, New York, 1960.

7 Incropera, F. P., and De Witt, D. P., *Fundamentals of Heat Transfer*, Wiley, New York, 1981.

8 Caspi, S., Ph.D. thesis, University of California, Los Angeles, 1978.

9 Caspi, S., Lee, J. Y., and Frederking, T. H. K., "Oscillations and Hysteresis of Helium During Lambda Transition Above the Thermodynamic Critical Pressure in the Presence of Heat Flow," *Adv. Cryog. Eng.*, Vol. 23, 1978, pp. 349–357.

10 Johnson, W. W., and Jones, M. C., "Measurements of Axial Heat Transport in Helium II with Forced Convection," *Adv. Cryog. Eng.*, Vol. 23, 1979, pp. 363–370.

11 Chuang, C., et al., Report UCLA-ENG 8225, 1982, pp. 285–301.

12 Kim, Y. I., Kamioka, Y., and Frederking, T. H. K., "Dynamic Quench of NbTi in Pressurized He^4: Single Transition During Temperature Excursion Across the Transposed Critical Curve," *Cryogenics*, Vol. 22, 1982, pp. 523–526; see also [11], pp. 262–281.

APPENDIX A

Interpolation Equation of Laminar Film Model of He I-He II Two-Phase Flow

Consider the He I film moving along the walls of the heat emitting surface with constraints imposed as stated in section 2. An interpolation is desired between the two extreme Nu numbers of dominant gravitational buoyancy ($Nu = Nu_0$) and dominant, forced, two-phase flow ($Nu = Nu_1$). In many flow cases it has been found that a linear superposition is not appropriate. Therefore, nonlinear superposition for h is introduced with resulting Nu number expressions

$$Dh/k = Nu = [Nu_0^2 + (D/L)^2 Nu_1^2]^{1/2} \tag{A1}$$

The geometry ratio (D/L) is needed because of different reference lengths used in Nu. The ratio of the Nu numbers is

$$Nu/Nu_0 = h/h_0 = \{1 + (Nu_1/Nu_0)^2 (D/L)^2\}^{1/2} \tag{A2}$$

This ratio may be rewritten in terms of physical parameters using the Nu_i-numbers of section 2.

$$h/h_0 = \{1 + 0.9(D/L)^2 Re/Ra^{1/2}\}^{1/2} \tag{A3}$$

Enhanced Heat Transfer in a Flat Rectangular Duct With Streamwise-Periodic Disturbances at One Principal Wall

E. M. Sparrow
Fellow ASME

W. Q. Tao

Department of Mechanical Engineering,
University of Minnesota,
Minneapolis, Minn. 55455

Experiments were performed in a flat rectangular duct to determine the heat transfer and pressure drop response to periodic, rod-type disturbance elements situated adjacent to one principal wall and oriented transverse to the flow direction. In a portion of the experiments, heat transfer occurred only at the rodded wall, while in the remainder, heat was transferred at both principal walls of the duct. Highly detailed axial distributions of the local heat transfer coefficient were obtained. These distributions revealed the rapid establishment of a periodic (i.e., cyclic) fully developed regime as well as recurring local maxima and minima. Cycle-average, fully developed heat transfer coefficients were evaluated and were found to be much larger than those for a smooth-walled duct. Linear pressure distributions were measured between periodically positioned stations in the fully developed region, and the corresponding friction factors were several times greater than the smooth-duct values. The heat transfer and friction data were very well correlated using parameters that take account of the effective surface roughness associated with the disturbance rods.

Introduction

In the pursuit of heat transfer enhancement in turbulent duct flows, considerable attention has been given to the use of surface protuberances to disturb the laminar sublayer. An example of the implementation of this technique is the use of a succession of ringlike ribs implanted periodically along the wall of a circular tube and oriented transverse to the flow. The corresponding configuration for a parallel-plate channel is a set of rods, also placed transverse to the flow, which are positioned adjacent to either or both principal walls such as to form a streamwise-periodic array.

Despite the experimental work that has been performed for systems such as the aforementioned, the periodic nature of the flow appears neither to have been fully recognized nor taken into account in the execution of the experiments. The presence of periodic, two-dimensional disturbance elements will give rise to a periodic fully developed fluid flow at sufficient distances from the duct inlet. In such a flow, the pressure decreases linearly between successive axial stations which are separated by a distance equal to the pitch of the disturbance elements. If pressures were to be measured at axial stations with separation distances different from the pitch (or from a multiple of it), the data points would not lie in a straight line but would appear to scatter. A straight line forced through such data points may not yield the true pressure gradient for the system.

Similarly, for certain thermal boundary conditions such as uniform wall temperature and uniform wall heat flux, a periodic, thermally developed regime will be established downstream of the duct inlet. One of the characteristics of this regime is that if the average heat transfer coefficient is calculated for a streamwise length equal to the pitch (hereafter called a cycle), then the coefficient takes on the same value for all cycles. On the other hand, an average coefficient evaluated over a streamwise length different from the pitch (or from a multiple of it) will depend on the averaging length, unless the length is very large.

Contributed by the Heat Transfer Division for publication in the JOURNAL OF HEAT TRANSFER. Manuscript received by the Heat Transfer Division November 13, 1982.

The foregoing discussion sets the stage for the present investigation, where heat transfer and pressure drop experiments were performed for periodically disturbed turbulent airflow in large-aspect-ratio rectangular ducts. Heat transfer measurements were made at 160 axial stations, permitting a detailed determination of the variation of the local heat transfer coefficient and yielding a definitive picture of the periodic nature of the heat transfer process. This highly localized information was used for the proper evaluation of cycle-average heat transfer coefficients. Pressure distributions were also measured, with the taps positioned in accordance with the periodic nature of the flow.

Two distinct but closely related physical situations were investigated. In both cases, the periodic disturbances were created by a succession of small-diameter cylindrical rods positioned adjacent to one of the principal walls of the duct and oriented transverse to the airflow. For one case, heat transfer occurred only at the duct wall along which the disturbance elements were situated, with the other walls being adiabatic. In the other case, heat transfer occurred at both of the principal walls.

All told, four parameters were varied during the course of the investigation. One is the aforementioned one-sided versus two-sided heating. The second is the pitch-to-height ratio of the disturbance elements, which spanned the range from 9.15 to 36.6. The third parameter, the ratio of the disturbance height to the duct height, had values of 0.082 and 0.164. For all combinations of the heating and geometrical parameters, data runs were made at five values of the duct Reynolds number between about 10,000 and 45,000.

For each data run, the aforementioned detailed distribution of the local heat transfer coefficient was measured on each of the walls that participated in the heat transfer process. Representative distributions will be presented in the paper to illustrate the role of each of the four independent parameters. These distributions show the heat transfer response to the participating fluid flow phenomena and how the responses differ at the rodded and smooth walls of the duct. Cycle-average, fully developed heat transfer coefficients, evaluated

for each of the thermally participating walls, are plotted as a function of the Reynolds number for the various geometric and thermal parameters, with two-wall average values also given when both principal walls participate.

Friction factors were evaluated from the slopes of the pressure distributions, which were linear because of the periodic placement of the pressure taps. These friction factors are presented in their own right and are also used as the basis of a correlation involving the so-called roughness parameters. A correlation of the cycle-average heat transfer results in terms of the roughness parameters is also presented.

To supplement the heat transfer and friction measurements, flow visualization was performed using the oil-lampblack technique. As a prelude to the main body of experiments, heat transfer coefficients and friction factors were measured in a smooth-walled version of the test section and compared with available correlations.

There is a broad literature on protuberance-enhanced, duct-flow heat transfer but, for the sake of brevity, only the most relevant work will be cited here. In [1], a channel having one heated wall with rods periodically positioned adjacent to it was studied, but the results are of uncertain accuracy because of the nature of the test setup and the experimental technique. Cycle-average results were not evaluated, and the local results are presented as a ratio but without values given for the denominator. An electrochemical technique was used in [2] to determine average transfer coefficients in a square duct with one wall having periodic disturbance elements of a highly specific shape. In [3], disturbance elements were positioned adjacent to both principal walls of a channel, and average heat transfer coefficients were determined. The test setup may have been underinstrumented because no mention is made of periodic variations in the measured temperatures of the electrically heated walls.

For checking the results of the present smooth-wall experiments, heat transfer coefficients and friction factors were respectively taken from the correlations of Petukhov-Popov [4] and of Jones [5].

Experimental Apparatus and Procedure

By direct heat transfer measurements, it is well-nigh impossible to achieve the desired highly localized spatial resolution, high level of accuracy, well-defined boundary conditions, and absence of extraneous losses. These objectives can, however, be achieved with the naphthalene technique, and it will be used here.

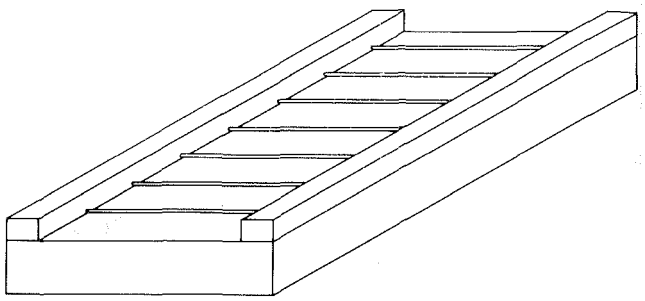

Fig. 1 Pictorial view of the test section with the upper wall removed

Test Section. The description of the experimental apparatus is facilitated by referring to Fig. 1. This figure is a pictorial view of the test section with the upper wall removed to reveal its interior. When fully assembled, the test section includes the two principal walls (i.e., the upper and lower walls), the two side walls which act as spacers between the principal walls, and an array of small-diameter cylindrical rods situated adjacent to the lower wall.

The surface of the lower wall is of naphthalene, freshly cast for each data run and with a surface finish comparable in quality to the highly polished stainless steel plate against which it was cast. The napthalene surface is framed by the exposed edges of an aluminum block within which it is housed, and the side walls of the duct rest on the lateral edges of the frame. That part of the frame, which bounds the upstream end of the naphthalene surface, was made very narrow to avoid significant differences in the starting points of the hydrodynamic and mass transfer boundary layers. The dimensions of the naphthalene surface are 19 cm by 8.13 cm, respectively, in the streamwise and transverse directions.

Either of two upper walls were used, depending on the desired boundary conditions. One of the upper walls is identical to the lower wall, and it was employed in experiments where mass transfer was desired at both principal

Nomenclature

A_{cyc} = per cycle surface area
AR = aspect ratio, W/H
C = constant in equation (15)
D_h = hydraulic diameter
$\mathfrak{D}$ = diffusion coefficient
e = roughness height (diameter)
e^+ = roughness Reynolds number, equation (19)
f = friction factor
H = duct height
H_e^+ = heat (mass) transfer function, equation (22)
$K_i(X)$ = local mass transfer coefficient at wall i
$K_{i,cyc}$ = cycle-average mass transfer coefficient at wall i
$\bar{K}_{cyc}$ = two-wall, cycle-average mass transfer coefficient
$\dot{M}_{i,cyc}$ = per cycle mass transfer rate at wall i
$\dot{m}_i(X)$ = local mass transfer rate per unit area at wall i
n = exponent in equation (15)
P = pressure
P_{atm} = ambient pressure
p = center-to-center inter-rod pitch
$\dot{Q}$ = volume flow rate
R^+ = modified roughness function, equation (18)
R_e^+ = roughness function, equation (17)
Re = Reynolds number
Sc = Schmidt number
$Sh_i(X)$ = local Sherwood number at wall i
Sh_{cyc} = cycle-average Sherwood number
$Sh_{i,cyc}$ = cycle-average Sherwood number at wall i
$\overline{Sh}_{cyc}$ = two-wall, cycle-average Sherwood number
St = Stanton number
V = mean velocity
W = duct width
$\dot{w}$ = mass flow rate
X = axial coordinate

Greek Symbols

$\delta_i(X)$ = local change in elevation at wall i
μ = viscosity
ν = kinematic viscosity
ρ = air density
ρ_{nb} = bulk density of naphthalene vapor
ρ_{nw} = wall density of naphthalene vapor
$\Delta\rho_{cyc}$ = per-cycle difference between ρ_{nw} and ρ_{nb}
ρ_{sol} = density of solid naphthalene
τ = duration of data run

Subscripts

r = rodded
s = smooth wall

walls. The other upper wall is a solid aluminum block which is impervious to naphthalene vapor and, therefore, does not participate in the mass transfer process.

At this point, it is relevant to relate the mass transfer boundary conditions of the present experiments to those for heat transfer in an analogous rectangular duct. At the naphthalene surface, the partial density (i.e., the concentration) of naphthalene vapor is uniform, and this corresponds to uniform wall temperature for the analogous heat transfer surface. Furthermore, a surface that is impervious to naphthalene vapor corresponds to an adiabatic surface. Thus, the present experiments in which both principal walls are of naphthalene are analogous to heat transfer in a rectangular duct in which both principal walls are at the same uniform temperature. Moreover, the present case in which one of the principal walls is of naphthalene and the other is metallic corresponds to a heat transfer situation where the principal walls are respectively isothermal and adiabatic. The metallic side walls of the present experiments correspond to adiabatic side walls.

The side walls were made from aluminum bar stock. Two sidewall heights were employed, 0.636 cm and 1.275 cm, respectively. The resulting aspect ratios of the flow cross section (AR = duct width/duct height) for the respective side walls are 12.8 and 6.4.

The disturbance elements were cut from lengths of 1.051-mm dia drill rod stock. Drill rod was chosen because of its highly uniform diameter. As seen in Fig. 1, the rods spanned the width of the duct. To ensure their precise and secure positioning, the rods were seated in holes drilled along the lower edge of each side wall. By this seating arrangement, the rods were maintained in contact with the naphthalene surface (essentially point contact).

To achieve a periodic flow pattern, the positioning holes were spaced at equal intervals along the length of the respective side walls. The streamwise center-to-center distance between successive rods corresponds to the pitch. Three different pitches were employed during the course of the experiments, respectively, 0.952, 1.905, and 3.811 cm.

From a consideration of the preceding paragraphs, it is evident that six configurations were employed during the experiments. The characteristics of these configurations, expressed in dimensionless terms, are presented in Table 1. In the table, the height of the disturbance element (i.e., the rod diameter) is denoted by e, in accordance with contemporary practice (e.g., [3, 6]); H denotes the duct height, and p the pitch. The quantities D_h and AR are, respectively, the hydraulic diameter and cross-sectional aspect ratio of the duct.

As was mentioned in the Introduction, fluid flow experiments encompassing pressure measurements and flow visualization were performed to supplement the mass (heat) transfer work. The naphthalene-surfaced principal walls were not employed in the fluid-flow test section. Rather, one of the walls was an aluminum plate equipped with pressure taps deployed along the spanwise centerline of the duct. The streamwise center-to-center distance between successive taps was 1.905 cm, which is, respectively, twice, equal, and half the three disturbance-element pitches. These relationships between the intertap spacing and the disturbance pitches enabled the measurement of truly linear pressure distributions in the periodic fully developed regime. The other principal wall was made of plexiglass to facilitate visual observations during the flow visualization experiments.

Other Apparatus Components and Instrumentation. The upstream end of the test section was seated in a rectangular aperture in a large vertical baffle plate and was positioned so that its upstream edges were flush with the upstream face of the baffle. This arrangement simulates the duct inlet being built into the downstream wall of a large plenum chamber. At its downstream end, the test section mated with a rectangular-to-circular transition piece which connected it to the air-handling system.

Table 1 Characteristics of the investigated configurations

Case	e/H	e/D_h	AR	p/e
1	0.082	0.0472	6.4	9.15
2				18.3
3				36.6
4	0.164	0.0883	12.8	9.15
5				18.3
6				36.6

The experimental apparatus was operated in the suction mode, with air being drawn into the duct inlet from the temperature-controlled, naphthalene-free laboratory room. After its passage through the test section and the transition piece, the air was metered by a calibrated rotameter, from which it passed through a control valve to the blower. The blower was situated outside the laboratory to ensure that its compression-heated, naphthalene-laden discharge was not recycled through the apparatus.

The key feature of the mass transfer experiments was the instrumentation employed to determine the detailed distribution of the mass transfer on the naphthalene surface. This was accomplished by measuring the contour of the surface both before and after a data run. For the contour measurements, the naphthalene surface and its surrounding aluminum frame were placed on a horizontal coordinate table which could be traversed in two perpendicular horizontal directions (x and y) with an accuracy of about 0.0025 cm. The table was equipped with fixtures for positioning and clamping the frame, and a torque wrench was used to apply the same reproducible force when tightening the clamping bolts. This ensures consistent positioning of the naphthalene surface with respect to the coordinate table.

Surface contours were measured by an electronic depth gage suspended from a fixed strut which overhung the coordinate table. The measurement system consisted of a stylus, a linear variable differential transformer, signal conditioning electronics, and a printer-equipped digital voltmeter. The system output was strictly linear and yielded 0.01 V per 0.001 in. of vertical displacement of the stylus, with the last digit of the printout corresponding to 10^{-5} in.

The pressure distributions were measured with the aid of a Baratron capacitance-type, solid-state pressure meter which has a resolving power of 10^{-3} or 10^{-4} Torr, respectively, for a 10 Torr sensing head or a 1 Torr sensing head. Pressures were fed to the meter from a selector switch into which all of the pressure taps were tied by plastic tubing.

The temperature of the naphthalene surface was sensed by copper-constantan thermocouples that were installed during the casting process, with the junctions positioned flush with the surface. Two thermocouples were employed for each of the naphthalene test surfaces, with the deviations between the thermocouples being no greater than 0.05-0.1°C. The thermocouples had been calibrated prior to their use.

Experimental Procedure. Each naphthalene casting, tightly wrapped to prevent extraneous sublimation, was placed in the laboratory at least 8 hrs prior to a data run to enable it to attain thermal equilibrium. Immediately preceding the run, a set of surface contour measurements were made. Then, the test section was assembled and the airflow initiated. During the run, periodic readings were taken of the test section temperatures, the rotameter float position and static pressure, and the barometer. Immediately after the run, another set of surface contour measurements were made.

With regard to the contour measurements, streamwise traverses were made along three parallel lines aligned with the

flow direction. One of the lines was situated midway between the side walls. Each of the other measurement lines was halfway between the midline and the side wall, one to either side of the midline. Along each line, elevations were recorded at 160 equally spaced points.

Both the pressure drop and flow visualization runs were performed with the modified test section that was described earlier. The flow visualization studies utilized the oil-lampblack technique, whereby a fluid mixture of lampblack powder and oil is applied to a surface to determine the pattern of the adjacent airflow. When the airflow is initiated, the mixture may move along the surface, following the paths of the fluid particles. The method is not very effective on vertical, inclined, or downfacing surfaces because the mixture tends to sag.

In the present study, the oil-lampblack mixture was applied to the lower wall of the test section, which was covered with white contact paper to provide high contrast. In a portion of the visualization runs, the disturbance rods were positioned adjacent to the lower wall, while in other runs the rods were positioned adjacent to the upper wall. It was found most effective to apply the mixture either as individual drops or as discrete lines, in contrast to a total coverage of the surface. The observations from the visualization studies will be interspersed among the mass transfer results.

Data Reduction

The methods used to evaluate local and cycle-average mass transfer coefficients, Reynolds numbers, and friction factors will not be described. In the determination of both the local and cycle-average mass transfer coefficients, separate consideration will be given to the wall along which the disturbance rods are positioned (i.e., the rodded wall) and to the wall without disturbance rods (i.e., the smooth wall). Subscripts r and s will be respectively employed to identify the two walls. Average coefficients encompassing both walls will also be evaluated for the fully developed regime. In those cases where there was no mass transfer at the smooth wall, all s-subscripted quantities should be deleted from the forthcoming analysis.

The local mass transfer coefficient, $K_i(X)$, for wall, i ($i = r,s$), at an axial station, X, may be evaluated from the defining equation

$$K_i(X) = \dot{m}_i(X) / (\rho_{nw} - \rho_{nb}(X)), \quad i = r,s \tag{1}$$

In this equation, $\dot{m}_i(X)$ denotes the rate of mass transfer per unit area at station, X, for wall, i. The denominator is the local difference in naphthalene vapor density that drives the mass transfer, with ρ_{nw} and ρ_{nb} respectively representing the wall and bulk values. When both of the principal walls were of naphthalene, they both had the same spatially uniform value of ρ_{nw}. The bulk vapor density $\rho_{nb}(X)$ is common to both $K_r(X)$ and $K_s(X)$.

In determining $\dot{m}_i(X)$, the first step is to difference the before-run and after-run elevation measurements at X for surface i, and the difference is denoted by $\delta_i(X)$. As noted earlier, surface contour measurements were made along three parallel lines oriented with the flow diretion, so that at each X there are three values of $\delta_i(X)$. These values were averaged and, henceforth, $\delta_i(X)$ will denote the average. Then, if ρ_{sol} is the density of solid naphthalene (equal to 1.146), and τ is the duration time of the data run

$$\dot{m}_i(X) = \rho_{sol}\delta_i(X)/\tau, \quad i = r,s \tag{2}$$

Attention is next turned to the denominator of equation (1). The vapor density at the wall, ρ_{nw}, was determined by the successive use of the Sogin vapor pressure/temperature relation [7] and the perfect gas law, with the measured surface temperature being used as input. To find $\rho_{nb}(X)$, the first step is to write a mass balance between the cross sections at X and at $(X + dX)$. If $d\rho_{nb}$ is the increase in the bulk density, and $d\dot{M}$ is the rate at which naphthalene sublimes from the surface into the airstream, then the mass balance yields

$$\dot{Q}d\rho_{nb} = d\dot{M} \tag{3}$$

Furthermore

$$d\dot{M} = \dot{m}_r(X)\,W dX + \dot{m}_s(X)\,W dX \tag{4}$$

so that upon combining equations (2–4) and integrating from $X = 0$ to $X = X$, there follows

$$\rho_{nb}(X) = (\rho_{sol}W/\tau\dot{Q})\int_0^X \{\delta_r(X) + \delta_s(X)\}dX \tag{5}$$

where the condition that $\rho_{nb} = 0$ at $X = 0$ was used. The volume flow, $\dot{Q}$, was taken as the mean value for the test section. The indicated integration in equation (5) was carried out numerically.

With the $K_i(X)$ thus determined, a dimensionless form may be attained via the local Sherwood number

$$\mathrm{Sh}_i(X) = K_i(X)D_h/\mathfrak{D} = (K_i(X)D_h/\nu)\mathrm{Sc}, \quad i = r,s \tag{6}$$

in which Sc is the Schmidt number, the value of which is 2.5 [7] for naphthalene diffusion into air. The hydraulic diameter, D_h, is the conventional one for rectangular ducts, $4HW/(2H + 2W)$.

The cycle-average mass transfer coefficients and Sherwood numbers will now be evaluated from the definitions

$$K_{i,\mathrm{cyc}} = (\dot{M}_i/A\Delta\rho)_{\mathrm{cyc}}, \quad \mathrm{Sh}_{i,\mathrm{cyc}} = (K_{i,\mathrm{cyc}}D_h/\nu)\mathrm{Sc} \tag{7}$$

in which

$$\dot{M}_{i,\mathrm{cyc}} = \int_x^{x+p} \dot{m}_i(X)\,W dX \tag{8}$$

and

$$A_{\mathrm{cyc}} = Wp \tag{9}$$

where p is the pitch of the periodic disturbance. The quantity $\Delta\rho_{\mathrm{cyc}}$ is the mean difference between ρ_{nw} and ρ_{nb} for the cycle. Three methods of evaluating $\Delta\rho_{\mathrm{cyc}}$ were explored. These included the log mean, the arithmetic mean, and the integrated mean of $(\rho_{nw} - \rho_{nb}(X))$. The results from the three methods of evaluating $\Delta\rho_{\mathrm{cyc}}$ were virtually coincident.

The cycle-average mass transfer coefficient encompassing both principal walls may also be evaluated. To begin

$$\bar{K}_{\mathrm{cyc}} = \{(\dot{M}_r + \dot{M}_s)/2A\Delta\rho\}_{\mathrm{cyc}} \tag{10}$$

Since $\Delta\rho$ is common to both the r and s walls, it follows from equations (7) and (10)that

$$\bar{K}_{\mathrm{cyc}} = \tfrac{1}{2}(K_{r,\mathrm{cyc}} + K_{s,\mathrm{cyc}}) \tag{11}$$

$$\overline{\mathrm{Sh}}_{\mathrm{cyc}} = \tfrac{1}{2}(\mathrm{Sh}_{r,\mathrm{cyc}} + \mathrm{Sh}_{s,\mathrm{cyc}}) \tag{12}$$

The periodic, fully developed regime is characterized by values of $\mathrm{Sh}_{i,\mathrm{cyc}}$ and $\overline{\mathrm{Sh}}_{\mathrm{cyc}}$ that are constant from cycle to cycle, aside from slight experimental scatter. The scatter was averaged out, and it is the average values that will be reported.

Dimensionless groups which pertain to the fluid flow will now be evaluated. The first of these is the duct Reynolds number, which is given by

$$\mathrm{Re} = 4\dot{w}/\mu(\mathrm{Per}), \quad \mathrm{Per} = (2H + 2W) \tag{13}$$

in which $\dot{w}$ is the rate of mass flow through the test section. The other dimensionless quantity is the friction factor, f

$$f = (-dP/dX)D_h/\tfrac{1}{2}\rho V^2 \tag{14}$$

where $\rho V^2 = (\dot{w}/HW)^2/\rho$, and ρ is the mean density in the test section. Particular attention will be given to the evaluation of f in the periodic fully developed regime.

For a flow configuration of the type considered here, a plot of P versus X will not be linear, neither in the entrance region

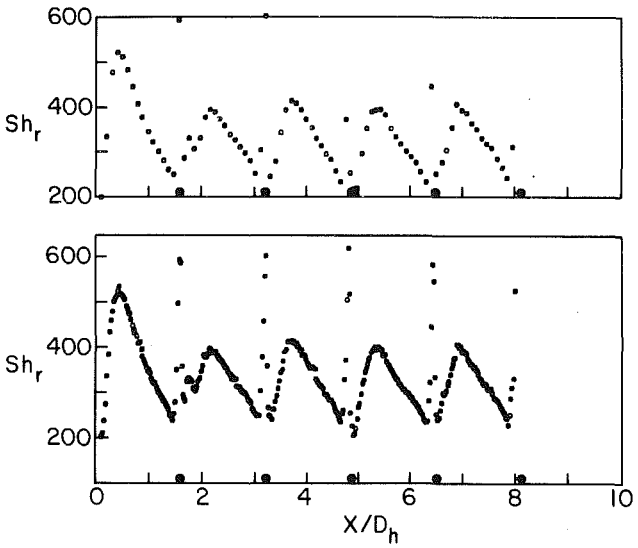

Fig. 2 Degree of resolution of the local Sherwood number distribution by different numbers of data points (Case 5, Re ≈ 43,770, mass transfer only at the rodded wall)

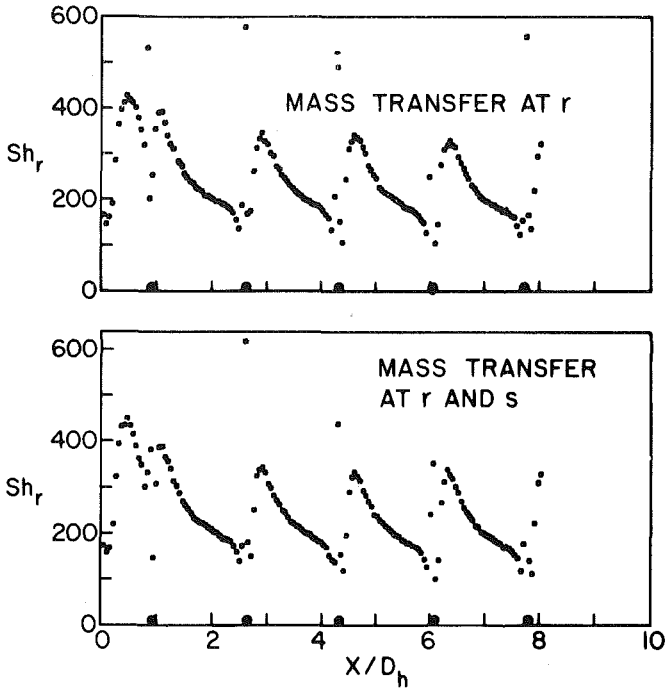

Fig. 3 Comparison of Sh_r distributions when there is mass transfer either at one principal wall or at both principal walls (Case 3, Re ≈ 28,500)

nor in the periodic fully developed region. However, in the periodic regime, the pressure differences between stations X and $(X + p)$, $(X + p)$ and $(X + 2p)$, $(X + 2p)$ and $(X + 3p)$, etc., are identical. Thus, if the pressures at X, $(X + p)$, $(X + 2p)$, . . . are plotted, they will fall on a straight line, and the slope of such a straight line yields dP/dX for equation (14). The linear behavior of the pressure will be illustrated later.

Local Mass Transfer Results

For each of the more than one hundred data runs which were executed, the local Sherwood number distributions were evaluated and plotted. From among these, a representative sample will be presented here in order to display the main features of the results.

The first issue to be addressed is the degree of resolution that is provided by the 160-point axial traverse that was standard in the experiments. To explore this issue, a few special runs were made in which the axial traverse contained 640 points. These data were processed in two ways. In the first, all 640 points were retained, while in the second every fourth point was retained which, in effect, corresponds to a 160-point traverse. The fully developed Sherwood numbers for the two ways of processing the data agreed to within 2 percent, which is altogether satisfactory.

The local Sherwood number distributions corresponding to the two ways of processing the data for a given run are presented in Fig. 2, where the lower graph shows all points while the upper graph shows every fourth point. The geometric configuration is that of Case 5 of Table 1, with Re = 43,770 and with mass transfer only at the rodded wall (so that Sh_r is plotted in the figure). Only the data for the first half of the wall are shown, thereby enabling the data points to be spread axially for easier examination. Also, to assist in interpreting the results, the axial positions of the disturbance rods are indicated by the black circles distributed along the abscissa axis.

Before comparing the upper and lower graphs, it is useful to discuss the main features of the Sh_r distribution, since these are common to subsequent figures as well as to Fig. 2. The portion of the distribution upstream of the first rod (i.e., the rise in Sh_r, the attainment of a maximum, and the subsequent decrease) reflects the separation of the flow at the sharp-edged inlet of the duct and its subsequent reattachment. The remainder of the distribution is controlled by the presence of the disturbance rods, and it is remarkable that a periodic pattern is established so rapidly, indicating a very short entrance region.

To help understand the nature of the periodic pattern, it should be noted that the flow separates from the wall when it encounters a rod and then reattaches to the wall in the interrod space. The flow visualization studies confirmed that the interrod maximum in the Sh_r distribution coincides with the point of reattachment. After reattachment, the flow tends to redevelop, with a consequent decrease in Sh_r that is arrested when the next rod is encountered.

In the lower graph of Fig. 2, and to a lesser extent in the upper graph, there are data points in the neighborhood of each rod which do not lie on the main undulating distribution, but rather, lie above it in a narrow vertical column. As shown by the flow visualization, these points reflect the presence of intense but compact vortices situated immediately fore and aft of the rod. Because they are so compact, their presence may go undetected by the 160-point scan, but they are well resolved by the 640-point scan. This is the main difference between the upper and lower graphs of Fig. 2.

The next issue to be considered concerns the sensitivity of the rodded-wall Sherwood number, Sh_r, to the presence or absence of mass transfer at the smooth principal wall of the duct, and Fig. 3 has been prepared in this regard. The lower graph of the figure is for the situation where mass transfer occurs at both the rodded and smooth (r and s) walls, while the upper graph corresponds to transfer only at the r wall. The results shown in the figure are for Case 3 and Re ≈ 28,500.

Examination of the figure reveals that the Sh_r distributions in the two graphs are virtually coincident. Furthermore, within the slight scatter of the data, this finding holds for all of the investigated geometries and Reynolds numbers, as will be evident later by the nearly identical values of $Sh_{r,cyc}$ corresponding to mass transfer either at r alone or at both r and s.

Consideration will next be given to the response of the Sh_r

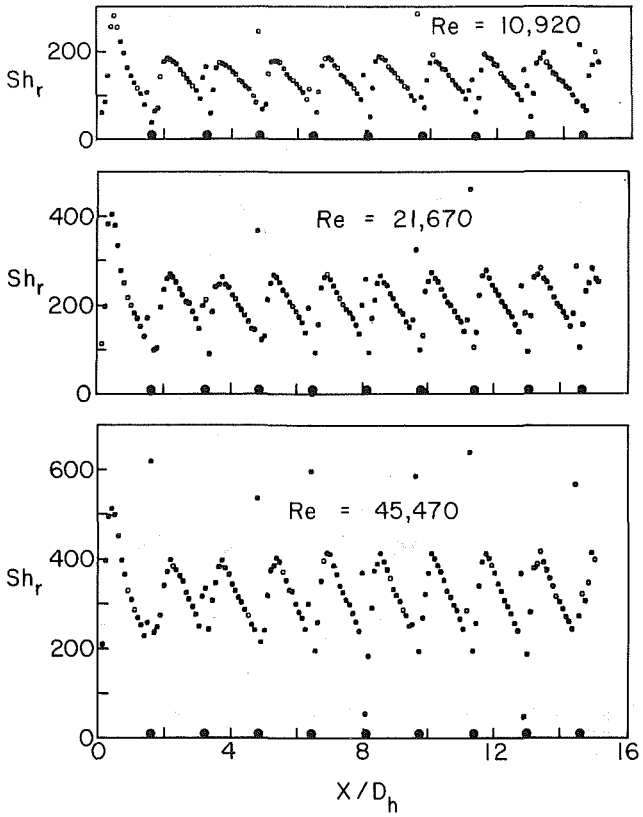

Fig. 4(*a*) Response of Sh_r to the Reynolds number (Case 5)

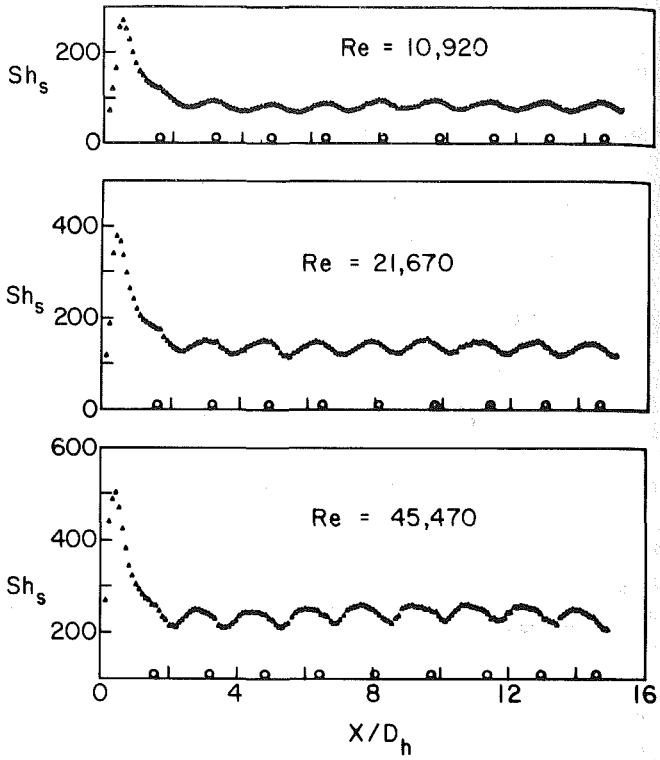

Fig. 4(*b*) Response of Sh_s to the Reynolds number (Case 5)

and Sh_s distributions to variations in the Reynolds number, as is respectively illustrated in Figs. 4(*a*) and 4(*b*). These results are for Case 5 and for simultaneous mass transfer at the *r* and *s* walls. In each figure, there are three graphs with respective Reynolds numbers of 10,920, 21,670, and 45,470.

The Sh_r distributions plotted in Fig. 4(*a*) for the various Reynolds numbers are generally of the same form and display the same pattern as those of Figs. 2 and 3. The level of the Sherwood number increases with increasing Reynolds number, and the maximum becomes somewhat more peaked.

The Sh_s distributions of Fig. 4(*b*) indicate that the mass transfer at the smooth wall is influenced by the periodic disturbances at the rodded wall. The axial positions of the rods are indicated by the open circles deployed along the abscissa of Fig. 4(*b*). From the figure, it is seen that the Sh_s distributions rapidly attain the periodic fully developed regime, in common with Sh_r. At the lowest Reynolds number, the upper and lower lobes of the undulating distribution are nearly symmetric, while at the highest Reynolds number there is a relatively flat maximum and a somewhat peaked minimum. Of particular interest is the fact that for the latter Re, Sh_s starts to descend at about the same point in the cycle where Sh_r starts to rise and that, furthermore, the minimum in Sh_s coincides with the location of the maximum of Sh_r. On the other hand, at the lowest Reynolds number, the dropoff of Sh_s and its minimum occur later than the rise and the maximum of Sh_r.

The next factor to be examined is the effect of the pitch, *p*, of the disturbance elements on the Sh_r and Sh_s distributions, and Figs. 5(*a*) and 5(*b*) convey information in this regard. These figures are for Re $\simeq$ 32,600, and the three graphs in each figure respectively correspond to p/e = 9.15, 18.3, and 36.6 (fixed *e*, variable *p*).

The Sh_r distributions of Fig. 5(*a*) show that for all three of the investigated pitches, flow reattachment occurs in the interrod space, as witnessed by the interrod maxima. The reattachment distance is relatively unaffected by the change in pitch, but the redevelopment region downstream of the reattachment point is substantially lengthened as the pitch increases. In the longer redevelopment region, the Sh_r distribution tends to flatten. The value of Sh_r at the successive periodic maxima remains about the same when p/e decreases from 36.6 to 18.3, but a further decrease to 9.15 yields a slightly lower value of the maximum Sh_r.

The shape of the smooth-wall Sherwood number distribution Sh_s is significantly affected by the pitch. When the pitch is small, Sh_s is seen to be almost uniform beyond the entrance region. For an intermediate pitch, Sh_s displays a regular, rounded undulation, while for a large pitch, the distribution consists of rather long, slowly varying segments punctuated by relatively rapid changes just downstream of the axial positions of the disturbances. The Sh_s values for the large-pitch case appear to be slightly lower than those for the other cases.

The last issue to be addressed is the effect of the duct height, *H* (i.e., the interwall spacing) on the distributions of Sh_r and Sh_s. On a dimensionless basis, *H* will be expressed via the ratio, e/H, where *e* is a constant, with values e/H = 0.082 and 0.164. The Sh_r and Sh_s distributions are respectively presented in Figs. 6(*a*) and 6(*b*). The shapes of the Sh_r distributions for the two duct heights are identical and, if not for the different abscissa ranges (corresponding to the different D_h values), the two distributions would be virtually coincident. On the other hand, the Sh_s distributions display duct-height-related differences. With increasing duct height, Sh_s is less affected by the presence of the disturbance rods. The distribution becomes smooth and the magnitude of Sh_s decreases somewhat.

Fully Developed Mass Transfer Results

The first order of business will be to report on auxiliary experiments that were performed without the disturbance rods in the test section, and Fig. 7 has been prepared for this

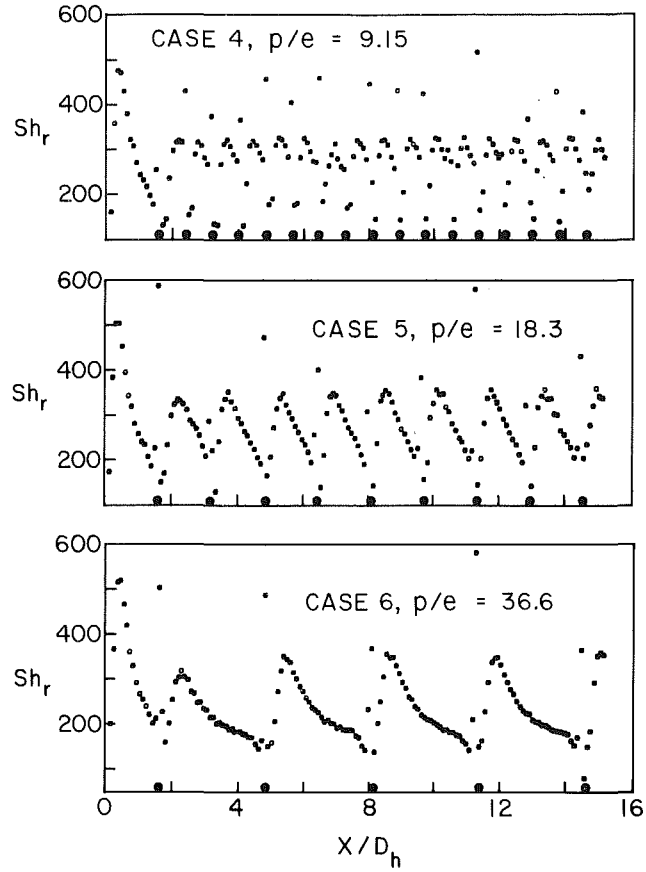

Fig. 5(*a*) Response of Sh_r to the pitch of the disturbance elements (Re ≃ 32,600)

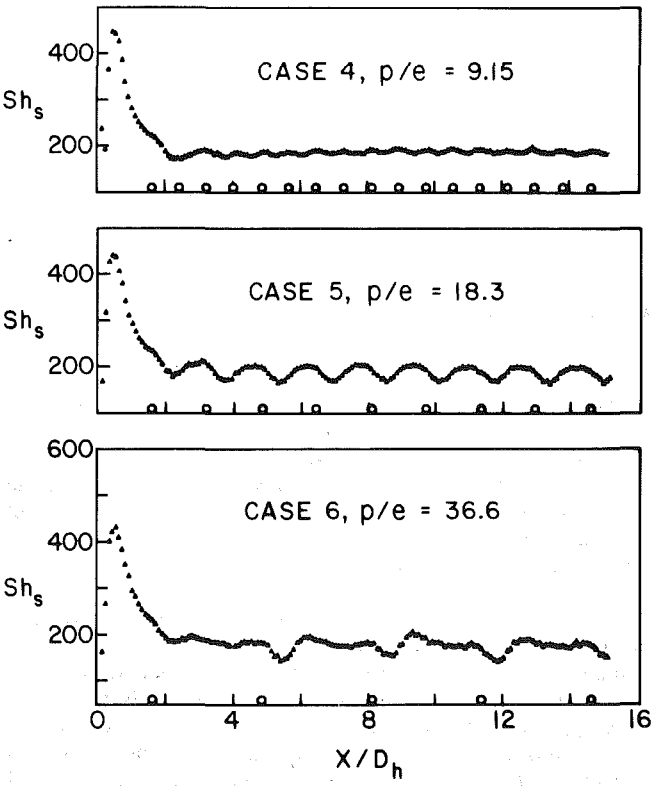

Fig. 5(*b*) Response of Sh_s to the pitch of the disturbance elements (Re ≃ 32,600)

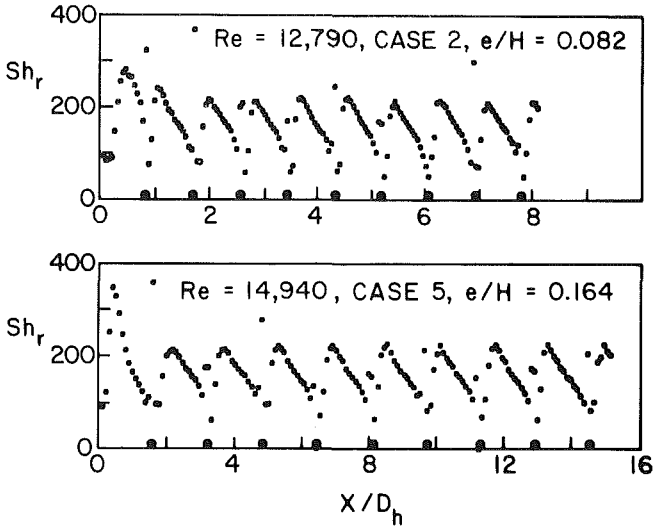

Fig. 6(*a*) Response of Sh_r to the duct height

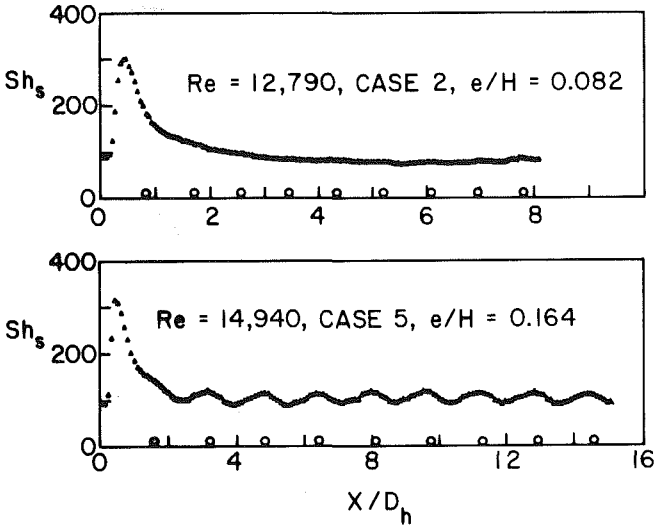

Fig. 6(*b*) Response of Sh_s to the duct height

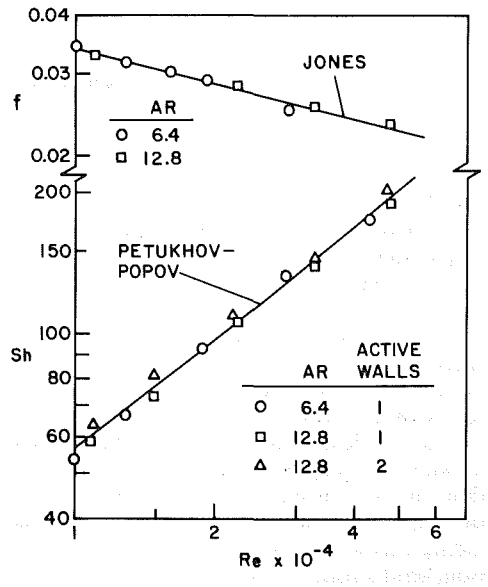

Fig. 7 Sherwood numbers and friction factors in a smooth-walled duct

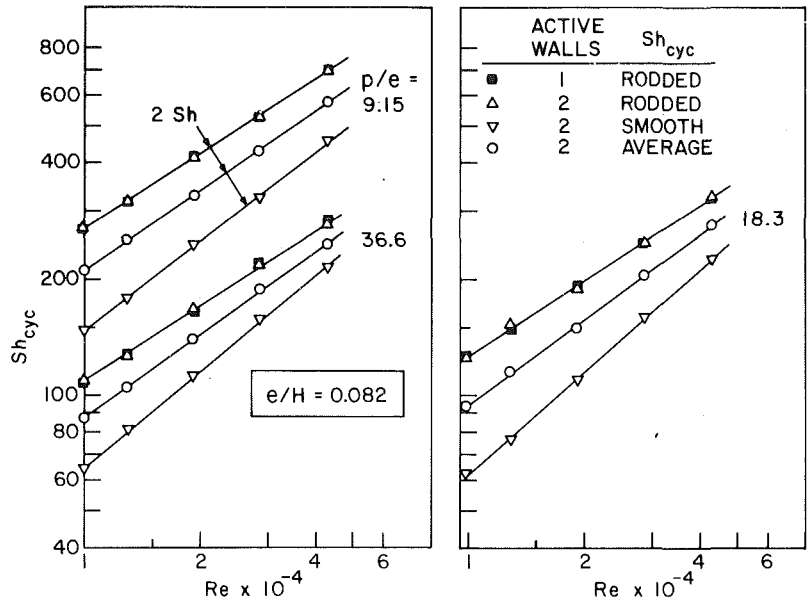

Fig. 8 Cycle-average, fully developed Sherwood numbers for e/H = 0.082

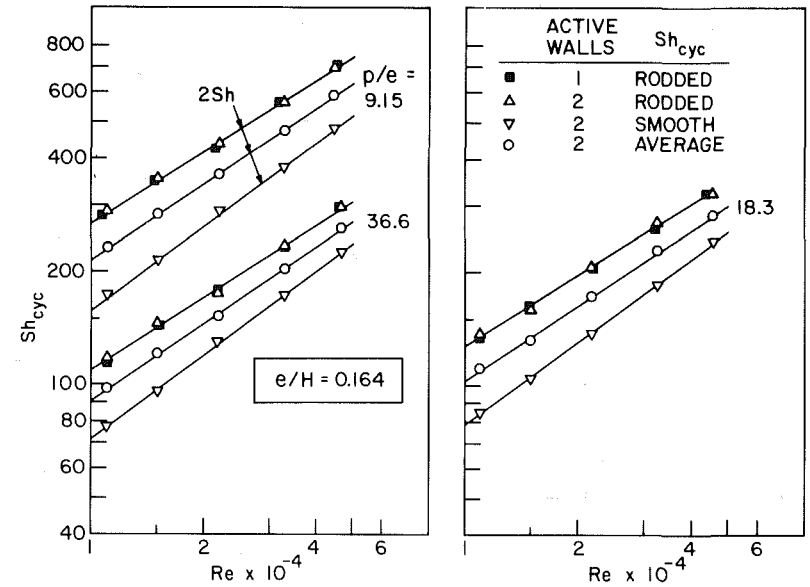

Fig. 9 Cycle-average, fully developed Sherwood numbers for e/H = 0.164

purpose. The measured fully developed friction factors are plotted in the upper part of the figure, while the fully developed Sherwood number data are plotted in the lower part. Comparison of the friction data is made with a recent correlation by Jones [5] for rectangular ducts of various aspect ratios, and excellent agreement is found to prevail.

The Sherwood number experiments were performed for mass transfer either at one or both of the principal walls. In the former case, two aspect ratios (AR = 6.4 and 12.8) were employed—with excellent agreement of the data. The data for two active walls typically fall about 5 percent above those for one active wall, which agrees well with literature information. In addition, the present data are well within the ±6 percent band that is specified for the Petukhov-Popov equation [4]. These findings, as well as the aforementioned friction factor comparison, lend strong support to the present experimental method.

The cycle-average fully developed Sherwood numbers for the enhanced duct configuration (i.e., rods adjacent to one principal wall) will now be presented in Figs. 8–10. Figures 8 and 9 are companion figures which convey basic data for the two duct heights respectively characterized by $e/H = 0.082$ and 0.164 (e = constant), while Fig. 10 shows comparisons among the data and with the literature.

In Figs. 8 and 9, data are plotted for the individual wall Sherwood numbers $\mathrm{Sh}_{r,\mathrm{cyc}}$ and $\mathrm{Sh}_{s,\mathrm{cyc}}$ and for the two-wall average Sherwood number $\overline{\mathrm{Sh}}_{\mathrm{cyc}}$. The data for the case in which mass transfer occurs only at the rodded wall are depicted by blackened symbols that pertain only to $\mathrm{Sh}_{r,\mathrm{cyc}}$. The open symbols represent data for the case in which there is mass transfer at both principal walls, and these symbols pertain to $\mathrm{Sh}_{r,\mathrm{cyc}}$, $\mathrm{Sh}_{s,\mathrm{cyc}}$, and $\overline{\mathrm{Sh}}_{\mathrm{cyc}}$. There are three sets of data in each figure, respectively corresponding to the three investigated pitches p/e = 9.15, 18.3, and 36.6.

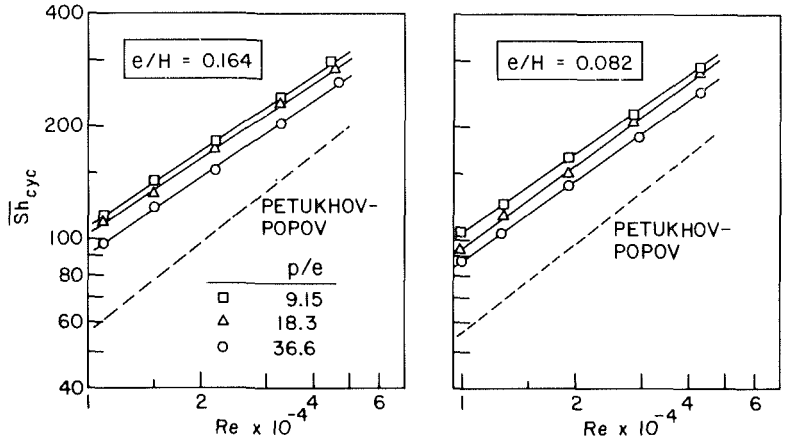

Fig. 10 Cycle-average, fully developed Sherwood numbers encompassing both principal walls

Table 2 Values of C and n in $\overline{Sh}_{cyc}$ correlations

	$Sh_{r,cyc}$		$Sh_{s,cyc}$		$\overline{Sh}_{cyc}$	
Case	C	n	C	n	C	n
1	0.366	0.643	0.0632	0.767	0.184	0.689
2	0.322	0.649	0.0175	0.888	0.107	0.737
3	0.276	0.649	0.0337	0.822	0.116	0.719
4	0.394	0.634	0.0898	0.737	0.216	0.674
5	0.392	0.628	0.0855	0.740	0.208	0.673
6	0.298	0.642	0.0754	0.745	0.166	0.684

The straight lines which interconnect the various families of data in Figs. 8 and 9 were obtained from least-squares fits of the power law

$$\mathrm{Sh} = C\mathrm{Re}^n \tag{15}$$

where the numerical values of C and n are listed in Table 2. Examination of the figures shows that the data are very well represented by the power law (15) and that there is very little scatter about the respective correlating lines.

It is especially interesting to note that whereas the correlating lines for $Sh_{r,cyc}$ were based on the open data symbols, the black data symbols appear to be equally well represented by the same correlating lines. It thus follows that the Sherwood numbers at the rodded wall are independent of whether or not mass transfer occurs at the smooth principal wall.

The exponents, n, for the rodded wall all lie within a narrow range, with an average value of 0.64. This is very close to the exponent $n = 2/3$ that typifies separated flows, thereby underscoring the important role of flow separation in the enhancement process. The exponents for the smooth wall results are higher, as is expected since that wall is not directly washed by a separated flow.

Not only is there a tendency for $Sh_{r,cyc}$ and $Sh_{s,cyc}$ to converge with increasing Reynolds number, but there is also a tendency for the spread between the curves to diminish as the pitch increases. This trend is reasonable because in the limit as $p \to \infty$, $Sh_{r,cyc}$, and $Sh_{s,cyc}$ should coincide.

Figure 10 has been prepared to facilitate a comparison between the results for the various pitches and with the smooth-wall duct. The left- and right-hand graphs of Fig. 10 respectively pertain to the two investigated duct heights, and in each graph the $\overline{Sh}_{cyc}$ values for $p/e = 9.15$, 18.3, and 36.6 are plotted as a function of Re. Also plotted is the Petukhov-Popov equation which provides an excellent representation of the present data for a smooth-wall duct (Fig. 7).

It is seen from Fig. 10 that the disturbance rods give rise to substantial enhancements relative to the smooth-wall duct, ranging from 40 to 90 percent. The extent of the enhancement is largest at the lower Reynolds numbers. Also, as expected, more closely spaced rods (i.e., smaller pitches) yield higher enhancements, but to an extent which is modest compared with the pressure drop penalty to be displayed shortly. The enhancement appears to be little affected by the duct height, despite the higher pressure drop penalty associated with the lesser height.

The aforementioned enhancements pertain to $\overline{Sh}_{cyc}$. Even large enhancements, in the range from 60 to 140 percent, are encountered for $Sh_{r,cyc}$.

Pressure Drop and Friction Factor

Typical pressure distributions are presented in Fig. 11 to illustrate the linearity encountered when properly positioned pressure taps are employed. In each graph, the pressure difference between the ambient and an axial station, X, is plotted versus X. For the $p/e = 9.15$ case, the successive taps are separated by a distance $2p$. In accordance with the principles discussed in the final paragraph of the Data Reduction section, this tap placement should yield a linear distribution in the periodic fully developed regime—and it does.

When $p/e = 36.6$, the separation between taps is $\frac{1}{2}p$, so that there are two taps in each cycle. Consequently, the pressures from consecutive taps do not fall on a straight line. However, since the distance between every other tap is p, a straight line is obtained by interconnecting the pressures from every other tap. There are two such sets of taps, and the straight lines for the two sets should be parallel—and they are.

The linearity in evidence in Fig. 11 is indicative of the establishment of the fully developed region, which is very rapid. Note should also be taken of the substantially higher pressure drop for $e/H = 0.164$ compared with that for $e/H = 0.082$.

Fully developed friction factors were evaluated from equation (14) and are plotted in Fig. 12, respectively for $e/H = 0.082$ and 0.164 in the right- and left-hand graphs. Each graph conveys data for the three investigated p/e values. Also shown is the smooth-duct friction factor representation of Jones, which also represents the present smooth-duct results (Fig. 7).

The experimental data are well correlated by the power law

$$f = C_1 \mathrm{Re}^{-m} \tag{16}$$

with least-squares values (C_1, m) of (2.04, 0.297), (1.51, 0.291), (0.945, 0.273), (1.26, 0.204), (0.938, 0.199), and (0.330, 0.132), respectively, for Cases 1–6.

The friction factors for the rodded duct are seen to be many times greater than those for the smooth-walled duct. Also, as

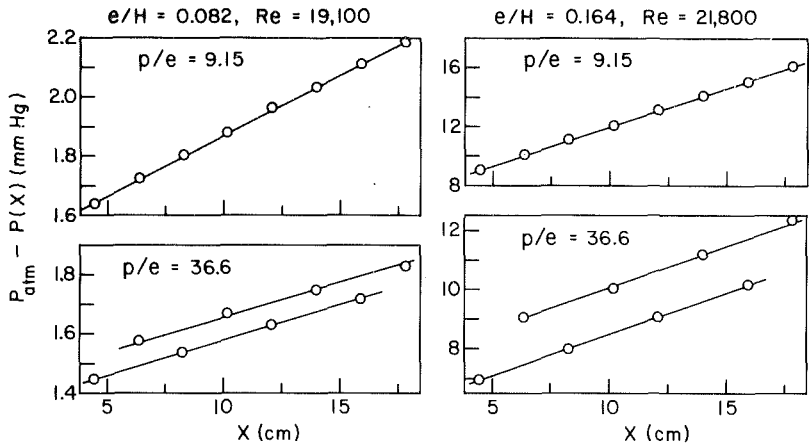

Fig. 11 Typical axial pressure distributions

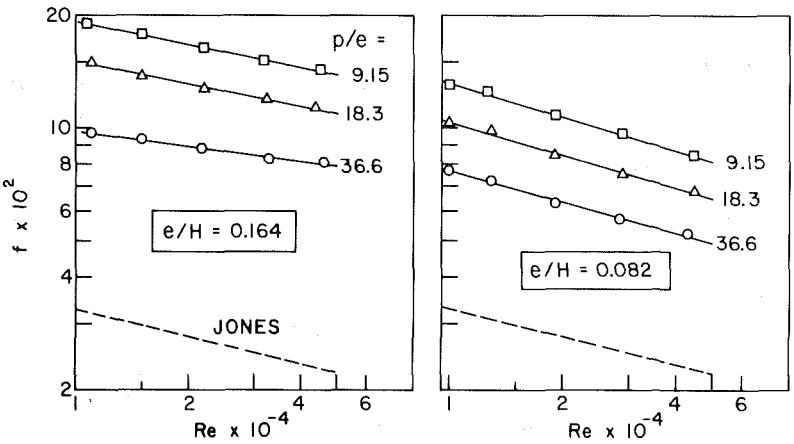

Fig. 12 Fully developed friction factors

expected, there is a marked increase of the friction factor as the pitch decreases. In addition, the greater the value of e/H (which may be regarded as an index of an effective roughness), the larger is f and the flatter are the f versus Re curves.

In general, the increase in the friction factor due to rodding is much greater than the increase of the Sherwood number, and f is more sensitive to the geometrical parameters than is Sh.

Correlations Based on Roughness Parameters

Friction factor data for ducts with sand-grain roughness were well correlated by Nikuradse using a roughness function. In more recent years, several investigators (e.g., [3, 6, 8]) concerned with using surface protuberances to enhance heat transfer have extended Nikuradse's work. The present mass transfer and friction factor data will be correlated by employing (and modifying) roughness parameters from the literature.

The first step is to write the roughness function R_e^+ in a form suitable for a high aspect ratio rectangular duct

$$R_e^+ = \sqrt{8/f} + 2.5 ln(2e/D_h) + 4.23 \tag{17}$$

The constant 4.23 is specific to a rectangular duct[1]. To specialize to the present "roughness" configuration, a modified roughness function is defined as

$$R^+ = \{(e/D_h)/(p/e)\}^{1/4} R_e^+ \tag{18}$$

[1] In [3], the circular-tube value of 3.75 was used.

The Reynolds number is embedded in another roughness parameter, the roughness Reynolds number, e^+, defined as

$$e^+ = \sqrt{f/8}(e/D_h)\,\mathrm{Re} \tag{19}$$

With the use of R^+ and e^+, the friction factor data have been plotted in Fig. 13. By comparing Figs. 12 and 13, the success of the R^+, e^+ variables in collapsing the friction factor data is clearly evident. Equations were fit to the data of Fig. 13 as follows

$$R^+ = 0.685(e^+)^{0.218}, \quad e^+ \le 120 \tag{20}$$

$$R^+ = 1.18(e^+)^{0.105}, \quad e^+ \ge 120 \tag{21}$$

Of the 30 points plotted in Fig. 13, 28 are within 3 percent of the correlating lines.

A heat (mass) transfer function H_e^+ is next introduced as

$$H_e^+ = \{(f/8\mathrm{St}) - 1\}/\sqrt{f/8} + R_e^+ \tag{22}$$

where St is the Stanton number (= Sh/ReSc). The cycle-average, fully developed Sherwood numbers were used to evaluate equation (22), and the results are shown in Fig. 14.

The figure contains two sets of results, that in the upper part corresponding to the case where there is mass transfer at the rodded wall only, while that in the lower part is for mass transfer at both walls. To separate the two sets, the former is plotted as H_e^+, while the latter is plotted as $0.5H_e^+$. The respective least-squares correlations are

$$H_e^+ = 6.47(e^+)^{0.297} \tag{23}$$

$$H_e^+ = 9.84(e^+)^{0.253} \tag{24}$$

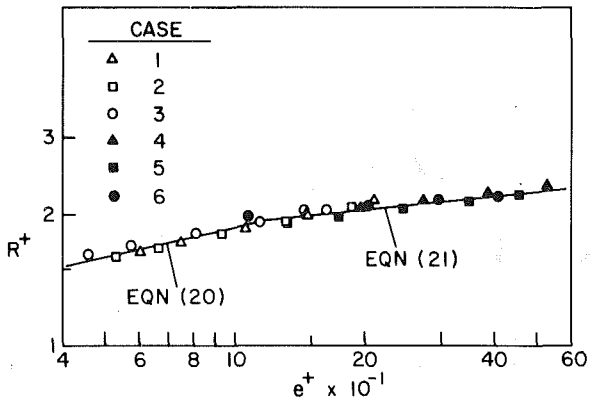

Fig. 13 Correlation of the friction factor results

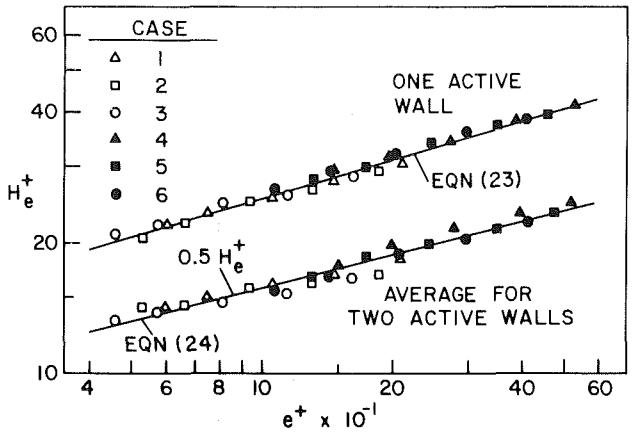

Fig. 14 Correlation of the cycle-average, fully developed Sherwood numbers

The correlations are seen to be very good, although there is some moderate data scatter. On the basis of findings encountered earlier in the paper, equation (23) can also be employed to represent the Sherwood number of the rodded wall when there is mass transfer at both principal walls.

Concluding Remarks

The experiments reported here have provided definitive information on the mass (heat) transfer and pressure drop response to periodic disturbances caused by cylindrical rods situated adjacent to one of the principal walls of a flat rectangular duct. The experiments were performed for mass transfer boundary conditions which, in thermal terms, are: (*a*) uniform temperature at the rodded wall; no heat transfer at the non-rodded (i.e., smooth) wall, and (*b*) the same uniform temperature at both walls.

Highly detailed axial distributions of the local Sherwood number were obtained, and these revealed the rapid establishment of a periodic fully developed regime. Cycle-average, fully developed Sherwood numbers displayed substantial enhancement compared with the smooth-wall duct. For the average Sherwood number for mass transfer at both principal walls, enhancements as large as 90 percent were encountered. At the rodded wall, enhancements of up to 140 percent occurred for either one-wall or two-wall transfer.

Linear pressure distributions were measured between periodically deployed stations in the fully developed regime. The corresponding friction factors were several times larger than those for the smooth-wall case.

The Sherwood number and friction factor data were very well correlated using parameters that took account of the effective surface roughness created by the presence of the disturbance elements.

References

1 Edwards, F. J., and Sheriff, N., "The Heat Transfer and Friction Characteristics for Forced Convection Air Flow Over a Particular Type of Rough Surface," *Proceedings, 1961 International Heat Transfer Conference*, pt. II, ASME, New York, 1961, pp. 415–425.

2 Dawson, D. A., and Trass, O., "Mass Transfer at Rough Surfaces," *International Journal of Heat and Mass Transfer*, Vol. 15, 1972, pp. 1317–1336.

3 Han, J. C., Glicksman, L. R., and Rohsenow, W. M., "An Investigation of Heat Transfer and Friction for Rib-Roughened Surfaces," *International Journal of Heat and Mass Transfer*, Vol. 21, 1978, pp. 1143–1156.

4 Karlekar, B. V., and Desmond, R. M., *Heat Transfer*, 2nd ed., West Publishing, St. Paul, 1982, pp. 497–498.

5 Jones, O. C., Jr., "An Improvement in the Calculation of Turbulent Friction in Rectangular Ducts," *Journal of Fluids Engineering*, Vol. 98, 1976, pp. 173–181.

6 Webb, R. L., Eckert, E. R. G., and Goldstein, R. J., "Heat Transfer and Friction in Tubes with Repeated-Rib Roughness," *International Journal of Heat and Mass Transfer*, Vol. 14, 1971, pp. 587–600.

7 Sogin, H. H., "Sublimation from Disks to Air Streams Flowing Normal to Their Surfaces," ASME *Transactions*, Vol. 80, 1958, pp. 61–71.

8 Dipprey, D. F., and Sabersky, R. H., "Heat and Momentum Transfer in Smooth and Rough Tubes at Various Prandtl Numbers," *International Journal of Heat and Mass Transfer*, Vol. 6, 1963, pp. 329–353.

R. S. Amano
Assistant Professor.
Mem. ASME

M. K. Jensen
Assistant Professor.
Mem. ASME

P. Goel
Graduate Student.

Department of Mechanical Engineering,
University of Wisconsin—Milwaukee,
Milwaukee, Wis. 53201

A Numerical and Experimental Investigation of Turbulent Heat Transport Downstream From an Abrupt Pipe Expansion

An experimental and numerical study is reported on heat transfer in the separated flow region created by an abrupt circular pipe expansion. Heat transfer coefficients were measured along the pipe wall downstream from an expansion for three different expansion ratios of $d/D = 0.195$, 0.391, and 0.586 for Reynolds numbers ranging from 10^4 to 1.5×10^5. The results are compared with the numerical solutions obtained with the $k \sim \epsilon$ turbulence model. In this computation a new finite difference scheme is developed which shows several advantages over the ordinary hybrid scheme. The study also covers the derivation of a new wall function model. Generally good agreement between the measured and the computed results is shown.

Introduction

Many real flows of engineering interest contain regions of highly turbulent flow which exhibit instantaneous reversals of flow direction, even though the flow field is nominally steady overall. Examples include the turbulent separated flow region downstream from an abrupt expansion in a pipe and a simulated flow in an aircraft gas turbine combustor. Experimental studies, e.g., [1-3], have investigated this phenomenon by examining both heat and mass transfer coefficients downstream from the expansion. They found that in such flows, on the downstream side after the separation, the heat/mass transfer coefficients are several times greater than those for fully developed turbulent pipe flow at the same Reynolds number. This heat/mass transfer augmentation may be attributed to increases in the level of the stream's turbulent kinetic energy due to an increase in energy generation rate after the separation of the flow.

Numerical studies on this type of separated and recirculating flow have been reported by several researchers: Chieng and Launder [4], Syed and Sturgess [5], Rastogi et al. [6], and Amano [7]. Chieng and Launder developed a near-wall model in which the turbulent kinetic energy, the energy dissipation rate, and the turbulent shear stress varies within the viscous sublayer and formulated the mean rates of generation and dissipation of the k-equation. Their results showed generally better agreement when the near-wall model was adopted than when the normal procedure was used, in which the variations of these turbulence variables are neglected. However, Rastogi et al. [6] showed, by using the same model as Chieng and Launder [4], that their near-wall model displayed little difference in the predicted Sherwood number compared with the results obtained by the simple normal procedure in which the variations of turbulence variables are neglected when applied to very high Schmidt numbers (Sc = 1670). Amano [7] further extended the wall function treatment for the evaluation of mean generation and destruction rates of the ϵ-equation and obtained better results in the prediction of Sherwood number for high Schmidt number flows than by the treatment of [4]. Although everyone employed the $k \sim \epsilon$ turbulence model, which allows the turbulent length scale variation throughout the flow to be predicted, the solution method everyone used was a hybrid scheme which generally underestimates the diffusion rate of the governing equations. Consequently, the refinement of the turbulence model has not always improved the computed results.

In this paper an extensive experimental and numerical investigation of the flow downstream from an abrupt circular pipe expansion is presented with regard to heat transfer characteristics. In the experimental study, the local heat transfer coefficients downstream from an abrupt pipe expansion were measured by using liquid R-113 as the working fluid for pipe expansion ratios (d/D) of 0.195, 0.391, and 0.586 and for a wide range of Reynolds numbers ($10^4 - 1.5 \times 10^5$). In the numerical study, computations of heat transfer coefficients have been carried out by solving the elliptic equations of the momentum and the $k \sim \epsilon$ turbulence model. The heat transfer coefficients are obtained by employing the analogy between momentum and heat fluxes. The numerical method adopted in the present study is a fourth-order finite difference scheme which was developed by expanding the exponential finite difference scheme. For the near-wall region, a more refined model of the wall function is developed in which the turbulent boundary layer is divided into three regions: a viscous sublayer, a buffer zone, and a fully turbulent zone. These formulations are given in the section of Mathematical Formulation and Physical Model.

Experimental Apparatus and Procedure

To determine the heat transfer characteristics downstream from a circular abrupt expansion, three test sections were tested over a wide range of Reynolds numbers.

A test section, placed vertically in a flow loop, was constructed from a 12.2 mm i.d., 457-mm long stainless steel tube. A uniform wall heat flux was obtained by passing a d-c current through the tube. A thick layer of insulation reduced heat losses to a negligible level. Thirty thermocouples were spaced along the outside tube wall, including three on the inlet bus bar to help evaluate the effect of the axial conduction. The first 19 thermocouples were spaced 4.76 mm apart; the next four were spaced 12.7 mm apart; and the final seven were spaced 25.4 mm apart. The shorter thermocouple spacing just

Contributed by the Heat Transfer Division for publication in the JOURNAL OF HEAT TRANSFER. Manuscript received by the Heat Transfer Division September 23, 1982.

downstream of the expansion was necessary since relatively large variations over short distances in the heat transfer coefficients were anticipated in this area. The thermocouple voltages as well as the test section voltage drop and shunt voltage drop (from which test section current was obtained) were measured with a digital voltmeter with an accuracy of 1μv.

The nozzles were machined from a hard plastic ("Delrin"). Nozzle diameters of 2.38 mm, 4.76 mm, and 7.15 mm were used which resulted in expansion ratios (d/D) of 0.195, 0.391, and 0.586, respectively. The nozzle exit was perpendicular and concentric to the stainless steel tube. Total nozzle length was about $L_N/d \simeq 50$ for all three cases so that a fully developed turbulent flow would be ensured at the nozzle exit. The entrance to the nozzle was contoured so that there was a relatively smooth transition from the 25.4 mm supply piping to the nozzle.

Before any data were taken, the flow rate and inlet fluid temperature were adjusted to give a specified Reynolds number based on the tube diameter downstream from the abrupt expansion. The test section power was then adjusted so that a maximum temperature difference between the wall and the fluid never exceeded approximately 35 K. At the location of the maximum heat transfer coefficient, these power settings resulted in a minimum temperature difference ranging from about 2 K at $\mathrm{Re} \simeq 1 \times 10^4$ to 10 K at $\mathrm{Re} \simeq 1.5 \times 10^5$. The temperature rise of the fluid ranged from about 3 to 5 K. After steady-state conditions were attained, the data were taken.

The inside wall temperatures were obtained using the measured outside wall temperature and the electrical power dissipation rate. The steady-state heat conduction equation with internal heat generation in cylindrical coordinates was solved by assuming one-dimensional radial conduction with constant thermophysical properties. Because of the thin tube wall, low thermal conductivity, and relatively high heat transfer coefficients, axial conduction was assumed to be small. Thus, the heat flux was calculated by dividing the total power dissipation by the inside wall area of the heated tube. (Error due to longitudinal conduction is estimated to be less than 2 percent.) The heat transfer coefficients were then calculated by dividing the heat flux by the local temperature difference ($T_w - T_f$) at any location along the test section.

A total of 13 tests were run. (Tabulated data are available upon request.) The three diameter ratios were tested at five Reynolds numbers, $\mathrm{Re} \simeq 1.5 \times 10^5$, 8×10^4, 5×10^4, 2×10^4, and 1×10^4, except that at the smallest d/D ratio, the two highest Reynolds numbers could not be tested because of equipment limitations. Heat balances comparing electrical dissipation with enthalpy rise of the fluid generally were within ± 5 percent; 85 percent of the data were within ± 5.6 percent and all data were within ± 10 percent. A propagation-of-error analysis suggests that the uncertainty in the heat transfer coefficients at the point of the maximum heat transfer coefficient range from about ± 4.7 percent for the largest d/D ratio and highest Reynolds number to about ± 9.5 percent for the smallest d/D ratio and lowest Reynolds number. Uncertainties at other locations in the tube are smaller than these. The uncertainty in the Reynolds number is estimated to be ± 2 percent.

Mathematical Formulation and Physical Model

Governing Equations. The present work is based on the numerical solution of the axisymmetic two-dimensional form of the time-averaged continuity, Navier-Stokes, and the high

Nomenclature

C_μ, C_1, C_2, C_l = coefficients in turbulence model
C_P = specific heat at constant pressure
D = diameter of pipe downstream of expansion
d = diameter of pipe upstream of expansion
E = empirical constant in logarithmic law
H = step height (equal to $(D-d)/2$)
k = turbulent kinetic energy (equal to $\overline{u_i^2}/2$)
L_N = nozzle length
Nu = Nusselt number based on diameter of pipe downstream of expansion
P_f = P-function
p = pressure
$\dot{q}_w''$ = wall heat flux
R = numerical cell Reynolds number
Re_D = Reynolds number based on diameter of pipe downstream of expansion
R_v = viscous sublayer Reynolds number (equal to $k_v^{1/2} y_v/\nu$) given in Table 1)
r = radial coordinate
T = temperature
T_f = fluid temperature
U = mean velocity in x-direction
U_τ = friction velocity (equal to $\sqrt{\tau_w/\rho}$)
U^+ = dimensionless velocity (equal to U/U_τ)
u = turbulent fluctuating velocity
V = mean velocity in r-direction
x = coordinate parallel to pipe axis
y = distance from pipe wall
y^+ = dimensionless distance from wall (equal to yU_τ/ν)
Γ_ϕ = diffusivity of variable ϕ
ϵ = dissipation rate of turbulence energy $\left(\text{equal to } \nu\left(\overline{\frac{\partial u_i}{\partial x_j}}\right)^2\right)$
κ = von Karman constant
μ_t = turbulent dynamic viscosity
ν = kinematic viscosity
ρ = density
σ = Prandtl number
$\sigma_k, \sigma_\epsilon, \sigma_T$ = turbulent Prandtl numbers for diffusion of k, ϵ, and temperature
τ = turbulent shear stress

Subscripts

B = values at the edge of buffer layer
E,N,S,W, = values at east, north, south and west node points
e,n,s,w = values at east, north, south and west edge of the cells
i, j = tensor subscript notation
k,ϵ = values pertaining to kinetic energy and dissipation rate, respectively
P = values of node point P
v = values at the edge of viscous sublayer
w = wall values

Table 1 Near-wall three zone model

Generation rate in k-equation $\bar{P}$

$$\frac{\tau_w(U_n-U_B)}{y_n}+\frac{\tau_B}{4{y_B}^3 y_n}({y_B}^4-{y_v}^4)\left(\frac{\partial U}{\partial y}\right)_B$$
$$+\frac{\tau_w(\tau_n-\tau_w)}{\rho\kappa^* {k_B}^{1/2} y_n}\left(1-\frac{y_B}{y_n}\right)$$
$$+\left[\tau_w\left(1-\frac{y_B}{y_n}\right)+\frac{\tau_n-\tau_w}{2}\left\{1-\left(\frac{y_B}{y_n}\right)^2\right\}\right]\frac{\partial V}{\partial x}$$

Dissipation rate in k-equation $\bar{\epsilon}$

$$\frac{2{k_v}^{3/2}}{y_n R_v}+\frac{1}{y_n C_l}\left[\frac{2}{3}{k_B}^{3/2}\left\{1-\left(\frac{y_v}{y_B}\right)^{3/2}\right\}+\frac{2}{3}({k_n}^{3/2}-{k_B}^{3/2})\right.$$
$$\left.+2a({k_n}^{1/2}-{k_B}^{1/2})+a^2\lambda\right]$$

Generation rate in ϵ-equation ($C_1\overline{P\epsilon/k}$)

$$\frac{2}{7}\frac{C_1\tau_B}{C_l y_n}{k_B}^{1/2}\left\{1-\left(\frac{y_v}{y_B}\right)^{7/2}\right\}\left(\frac{\partial U}{\partial y}\right)B$$
$$+\frac{\tau_w}{\rho}\frac{C_1}{{k_B}^{1/2}\kappa^* C_l y_n}\left[\tau_w\left(\frac{{k_B}^{1/2}}{y_B}-\frac{{k_n}^{1/2}}{y_n}+\frac{b}{2}\lambda\right)\right.$$
$$\left.+\frac{\tau_n-\tau_w}{y_n}\{2({k_n}^{1/2}-{k_B}^{1/2})+a\lambda\}\right]$$
$$+\frac{C_1}{C_l y_n}\left[\tau_w\{2({k_n}^{1/2}-{k_B}^{1/2})+a\lambda\}\right.$$
$$\left.+\frac{2}{3}\frac{\tau_n-\tau_w}{y_n}\frac{1}{b}({k_n}^{3/2}-{k_B}^{3/2})\right]\frac{\partial V}{\partial x}$$

Destruction ($C_2\overline{\epsilon^2/k}$)

$$C_2\left[\frac{12}{y_n y_v}\left(\frac{k_v}{\mathrm{R}v}\right)^2+\left(\frac{k_B}{C_l}\right)^2+\frac{1}{y_B y_n}\left(1-\frac{y_v}{y_B}\right)\right.$$
$$\left.+\frac{1-y_B/y_n}{{C_l}^2}\left(\frac{a^2}{y_B y_n}+\frac{2ab}{y_n-y_B}\log\frac{y_n}{y_B}+b^2\right)\right]$$

$$\lambda=\begin{cases}\dfrac{1}{a^{1/2}}\log\left[\dfrac{({k_n}^{1/2}-a^{1/2})({k_B}^{1/2}+a^{1/2})}{({k_B}^{1/2}-a^{1/2})({k_n}^{1/2}+a^{1/2})}\right] & (a>0)\\[2ex] \dfrac{2}{(-a)^{1/2}}\left[\tan^{-1}\left(\dfrac{k_n}{-a}\right)^{1/2}-\tan^{-1}\left(\dfrac{k_n}{-a}\right)^{1/2}\right] & (a<0)\end{cases}$$

$$a=k_P-\frac{k_P-k_N}{y_P-y_N}y_P;\quad b=\frac{k_n-k_B}{y_n-y_B}$$

Reynolds number version of $k\sim\epsilon$ turbulence equations [4]. The equations following this approach for the present flow configuration can be written in the following general form

$$\frac{1}{r}\left[\frac{\partial}{\partial x}(r\rho U\phi)+\frac{\partial}{\partial r}(r\rho V\phi)\right]$$
$$=\frac{1}{r}\left[\frac{\partial}{\partial x}\left(r\Gamma_\phi\frac{\partial\phi}{\partial x}\right)+\frac{\partial}{\partial r}\left(r\Gamma_\phi\frac{\partial\phi}{\partial r}\right)\right]+S_\phi \qquad (1)$$

where ϕ stands for different dependent variables (U, V, k, and ϵ) for which the equations are to be solved, and S_ϕ stands for a source term. The diffusion coefficient Γ_ϕ may be specified in each equation by way of

$$\mu_t=C_\mu\rho k^2/\epsilon$$
$$\Gamma_\phi=\mu_t/\sigma_\phi$$

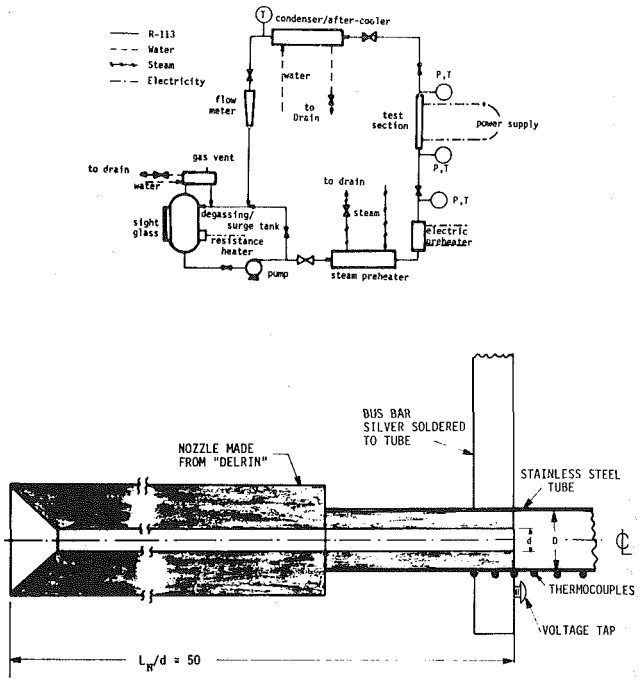

Fig. 1 Experimental set-up

where σ_ϕ stands for turbulent Prandtl numbers (σ_k and σ_ϵ). The present model has been used in a wide variety of turbulent flow situations and good predictive capability has been achieved [4–7].

Numerical Solution Procedure. The control volume approach was adopted for solving equation (1) by using the finite difference scheme. The grid system used in this program is a so-called staggered grid system in which the value of each scalar quantity is associated with every grid node (i.e., the points where the grid lines intersect), although the vector quantities (velocity components) are displaced in space relative to the scalar quantities. This grid system has advantages in solving the velocity field since the pressure gradients are easy to evaluate and velocities are conveniently located for the calculation of convective fluxes.

The finite difference scheme used in this paper is a method derived by expanding the exponential finite difference scheme of Spalding [8]. This scheme can be shown in the following form if equation (1) is written in a finite difference form.

$$A_P\phi_P=A_E\phi_E+A_W\phi_W+A_N\phi_N+A_S\phi_S+b \qquad (2)$$

where

$$A_E=D_e f(|\mathrm{R_e}|)+[-F_e,0]$$
$$A_W=D_w f(|\mathrm{R_w}|)+[F_w,0]$$
$$A_N=D_n f(|\mathrm{R_n}|)+[-F_n,0]$$
$$A_S=D_s f(|\mathrm{R_s}|)+[F_s,0]$$
$$A_P=A_E+A_W+A_N+A_S$$
$$b=S_\phi\delta Vol$$
$$D=\Gamma_{\mathrm{eff}}/\delta x$$
$$F=\rho U$$
$$\mathrm{R}=F/D$$

and where

$$f(|\mathrm{R}|)=\left[0,\left(1-\frac{1}{2}|\mathrm{R}|+\frac{1}{12}|\mathrm{R}|^2-\frac{1}{720}|\mathrm{R}|^4\right)\right] \qquad (3)$$

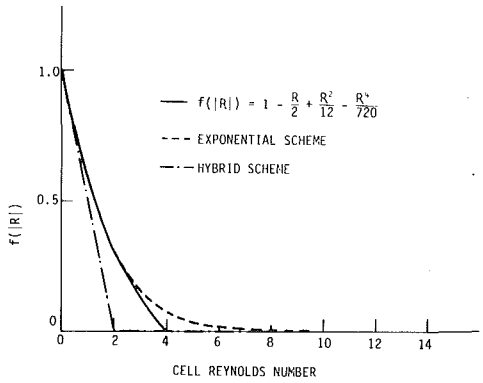

Fig. 2 The function of $f(|R|)$ for various schemes

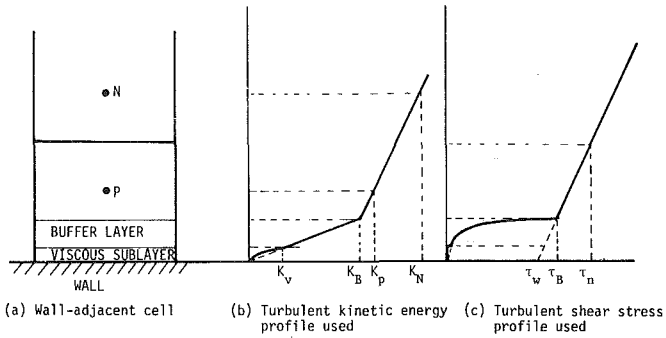

Fig. 3 Near-wall, three-zone model

where [ ] shows the symbol which stands for the largest of the quantities contained within it.

The function $f(|R|)$ shows the curve as in Fig. 2 in which the hybrid and the exponential schemes are compared with the present scheme. The nature of the hybrid scheme is such that it is identical with the central difference scheme for the cell Reynolds number range $-2 \le R \le 2$, and outside this range it reduces to the upwind difference scheme in which diffusion has been set equal to zero. However, as can be seen in Fig. 2, the departure of the hybrid scheme from the exact solution (exponential scheme) is rather large at $R = \pm 2$; also, it seems rather premature to set the diffusion effects equal to zero as soon as $|R|$ exceeds 2. Considering the shortcomings of the exponential scheme, i.e., exponentials are expensive to compute and the scheme is not exact for two- or three-dimensional situations, the above expression of $f(|R|)$ in equation (3) is obtained by expanding the exponential expression to the fourth-order term. This scheme is not particularly expensive to compute compared to the exponential scheme; and, noting that this scheme reduces to the upwind differencing for $|R|$ greater than 4, it is relatively simple. Furthermore, the accuracy has been improved in the range $1 < |R| < 4$.

Near-Wall Model. The viscous-affected zone, no matter how small it is, normally gives significant effects over the whole flow field since the major change in the velocity from the wall to the free stream occurs in this near-wall region. This model was originally developed by Chieng and Launder [4] for the evaluation of the mean generation and dissipation rates in the k-equation and it was further extended by Amano [7] for the evaluation of the mean generation and destruction rates in the ϵ-equation. In the above analyses the near-wall region is divided into two parts: a viscous-affected region and a fully turbulent region.

By using a nondimensional distance, y^+, based on distance y from the wall and the friction velocity, U_τ, the near-wall region is divided into two regions at the midpoint of the buffer zone ($y^+ = 11.0$) where the linear velocity profile in the viscous sublayer meets the logarithmic velocity profile. However, most of the experimental data show ([9] and [10], for example) that both the linear and logarithmic profiles deviate from the experimental data in the buffer zone. Therefore, in the pesent study, a three-zone, near-wall model is proposed which is comprised of a viscous sublayer ($0 < y^+ < 5$) adjacent to the wall, a buffer zone ($5 < y^+ < 30$), and a fully turbulent zone ($30 < y^+ < 400$).

Figure 3 shows a computational node, P, whose associated control volume is bounded on the south side by a wall. In this figure, the three zones are shown such that the node point P lies outside the buffer zone assuming the near-wall cell is large enough. A mathematical relationship describing the behavior of the turbulent kinetic energy, k, and the turbulent shear stress, τ, needs to be developed especially in the viscous sublayer and the buffer zone. Backwell and Lumley [11] reported that the streamwise fluctuating velocity increases linearly with distance from the wall, y, within the viscous sublayer, and then it increases with y^n in the outer region of the viscous sublayer. A close examination of Klebanoff's data [12] indicates that the power of n shows nearly 0.5 in the range of buffer zone ($5 < y^+ < 30$). Therefore, it is easily approximated that k varies parabolically in the viscous sublayer, after which it varies linearly with distance from the wall. Within the fully turbulent region, however, the variation of k is controlled by the methodology of finite difference, and the linear variation between node P and its northern neighbor is considered to extrapolate to the edge of the buffer layer (see Fig. 3(*b*)).

Unlike the variation of k, the turbulent shear stress, τ, has a different dependence on y. If the streamwise velocity has a relation $U \sim y$ near the wall, then, from the continuity equation, it is deduced that $V \sim y^2$, and the convective acceleration is proportional to y^2. Hence, we have

$$\frac{\partial}{\partial y}\left(\mu_t \frac{\partial U}{\partial y}\right) \sim y^2$$

or

$$\tau \sim y^3$$

This cubic profile generally yields very small values of τ within the viscous sublayer, which thus permits τ to be treated as negligible in this viscous sublayer. While in the buffer zone, the shear stress τ is assumed to vary with a cubic profile and undergoes a relatively sharp increase at the edge of the buffer layer and varies linearly over the remainder of the cell. The precise form of this linear variation is fixed by connecting the turbulent shear stress at the outer edge of the cell, τ_n, with the wall stress, τ_w (see Fig. 3(*c*)).

By adopting the normal procedure of ϵ evaluation by Amano [7], the variation of k, ϵ, and τ can be expressed in the following form in the three zones.

(*i*) Viscous Sublayer

$$k = k_v\left(\frac{y}{y_v}\right)^2 ; \epsilon = 2\nu\left(\frac{\partial k^{1/2}}{\partial y}\right)^2 ; \tau = 0 \tag{4}$$

(*ii*) Buffer layer

$$k = k_B \frac{y}{y_B} ; \epsilon = k^{3/2}/C_l y ; \tau = \tau_B\left(\frac{y}{y_B}\right)^3 \tag{5}$$

(*iii*) Fully Turbulent Region

$$k = \frac{k_n - k_B}{y_n - y_B} y + \left(k_P - \frac{k_P - k_N}{y_P - y_N} y_P\right) = by + a$$

$$\epsilon = k^{3/2}/C_l y ; \tau = \tau_w + (\tau_n - \tau_w)\frac{y}{y_n} \tag{6}$$

where

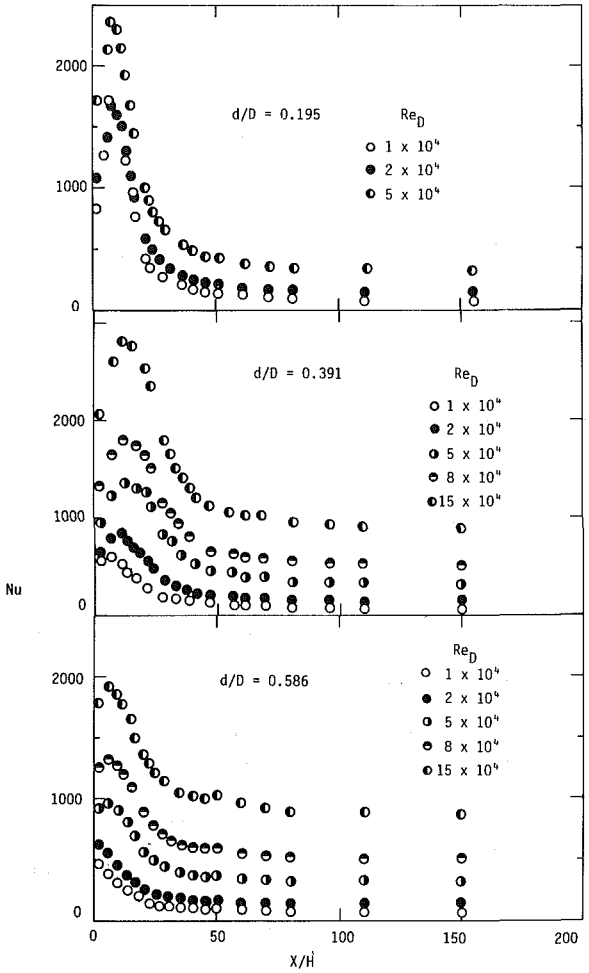

Fig. 4 Measured Nusselt number distribution for different pipe Reynolds numbers

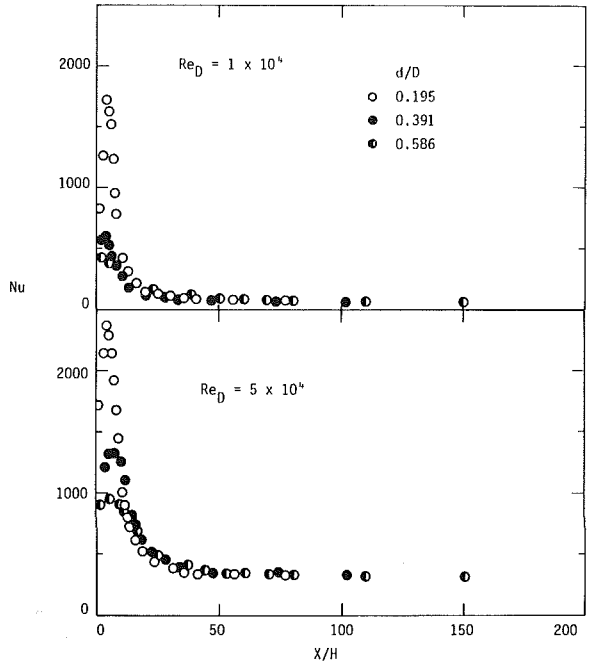

Fig. 5 Measured Nusselt number distribution for different pipe expansion ratios

$$a = k_P - \frac{k_P - k_N}{y_P - y_N} y_P;\ b = \frac{k_n - k_B}{y_n - y_B}.$$

In equations (4–6) the notations in Fig. 3 are used.

The terms in equation (1) represent a ϕ-balance involving convection, diffusion, generation, and destruction. The convection and diffusion terms, which are generally of minor influence near the wall, are handled in such a way that all fluid leaving the cell next to the wall is assumed to have the energy at node P as is employed for the evaluation over the remainder of the flow. Noting the expression of equation (4), both k and ϵ have zero gradient at the wall. This fact corresponds to no diffusion of k and ϵ toward the wall.

The mean values of generation and destruction rates for both k and ϵ equations are obtained by integrating the local variables of generation (P and $C_1 P\epsilon/k$) and destruction (ϵ and $C_2\epsilon^2/k$) over the computational cell after inserting the relations in equations (4–6) and then dividing by the volume of the cell. The results are summarized in Table 1. In this expression the streamwise velocity in the fully turbulent region can be given the following form which was attained from the logarithmic law of the wall.

$$\frac{U k_B^{1/2}}{\tau_w/\rho} = \frac{1}{\kappa^*} \ln(E^* y_B k^{1/2}/\nu) \tag{7}$$

where $E^* = EC_\mu^{1/4}$ and $\kappa^* = \kappa C_\mu^{1/4}$ which are the limiting values obtained by imposing the local equilibrium of turbulence at the boundary of buffer zone and fully turbulent zone.

The Nusselt number is obtained by using the interlinkage between the near-wall variation and the local wall fluxes as

$$\frac{\rho C_p (T - T_w) U_\tau}{q_w''} = (U^+ + P_f) \tag{8}$$

where P_f is the P-function given by Jayatilleke [13] as

$$P_f = 9.24[(\sigma/\sigma_T)^{0.75} - 1][1 + 0.28\exp(-0.007\sigma/\sigma_T)], \tag{9}$$

where σ_T is the turbulent Prandtl number and equal to 0.9.

Results

Experiment. The experimental results are shown in Figs. 4 and 5. Figure 4 represents the variation of Nusselt number for different pipe Reynolds numbers and Fig. 5 represents the variation of Nusselt number for different ratios.

For any particular test (see Figs. 4 and 5), the heat transfer coefficients start at a low level, increase as one moves away from the expansion section, reach a peak 6 to 8 step heights from the expansion section and then decrease, eventually reaching the fully developed condition in 30 to 40 pipe diameters. The peak heat transfer coefficient occurs about 6 to 8 step heights downstream of the expansion section in all cases. The dependency of Nusselt number on Reynolds number seems to be reasonable for $d/D = 0.391$ and 0.586; the levels of Nusselt number increase with increasing Reynolds number. However, the data for $d/D = 0.195$ do not show the same trend; for example, the maximum Nusselt number of $\mathrm{Re}_D = 1\times10^4$ is about the same as that of $\mathrm{Re}_D = 2\times10^4$. This feature is discussed in the last part of the next section.

Computation. To test the validity of the grid system the computations were performed for two different grid systems. One is a 22 × 22 grid system in which the grid size contracts in the radial direction and expands in the axial direction so that a finer grid spacing is formed near the large pipe wall and the vertical wall at the expansion. The other run was made with a 22 × 30 grid system wherein extra nodes were inserted midway between each node except for the column adjacent to the wall boundary. For both cases, the nondimensional near-

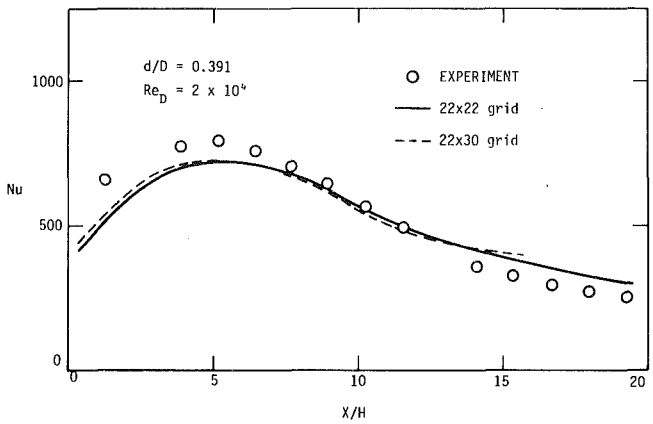

Fig. 6 Nusselt number distribution

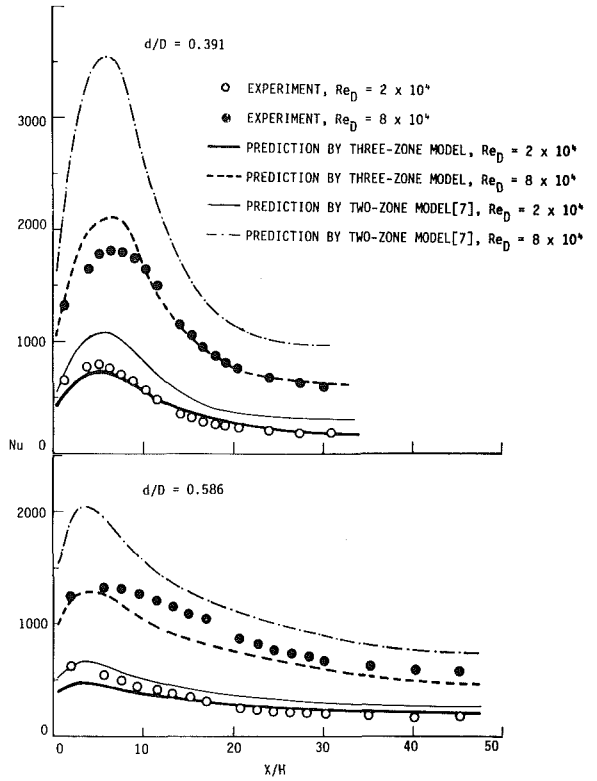

Fig. 7 Nusselt number distribution

wall distance y_P^+ was found to vary between 40 and 80 along the wall.

Differences in predicted heat transfer rates between these two node systems did not exceed 4 percent as seen in Fig. 6, and considering the large computing time with a 22 × 30 grid, the 22 × 22 grid system was adopted for the rest of the computations. This also shows that the present computational scheme is sufficiently insensitive to the cell size.

Average central processor time on a UNIVAC 1100 computer was about 8-1/2 min to convergence, which was typically achieved after 300 iterations.

Figure 6 also compares the computed results with the experimental data for the expansion ratio $d/D = 0.391$ and $\mathrm{Re}_D = 2 \times 10^4$. Agreement between experiment and computation is very good (within 10 percent discrepancy).

Figure 7 displays a comparison of the numerical results obtained employing two different wall functions (near-wall models) with the experimental data for $d/D = 0.391$ and 0.586. The rest of the computations were performed with the three-zone, near-wall model only and are compared with the experimental data for three pipe expansion ratios and for different pipe Reynolds numbers and are shown in Fig. 8.

Discussion

From Fig. 7, it is easily seen that the computational results obtained by employing the present three-zone wall function model show surprisingly better results than those obtained with the two-zone wall function model of [7]. Note also that the maximum Nusselt numbers predicted by the two-zone model display 5–20 percent higher values than the experimental data for $\mathrm{Re}_D = 2 \times 10^4$, while the predictions are 50–100 percent higher than the experimental values at $\mathrm{Re}_D = 8 \times 10^4$. On the other hand, the predictions of the maximum Nusselt number using the three-zone model show differences of −20 percent at $\mathrm{Re}_D = 2 \times 10^4$ and +13 percent at $\mathrm{Re}_D = 8 \times 10^4$.

It is noticed that the prediction by the two-zone model agrees better with the experimental data for lower Reynolds numbers than for higher Reynolds numbers, while the prediction made by using the three-zone model agrees relatively well with the experimental data for a wide range of Reynolds numbers. Why the present three-zone model shows much better prediction at higher Reynolds numbers compared to the two-zone model may be explained from the way in which these models are set up in the wall proximity region. In the two-zone model the determination of the length scale in this region is not appropriate enough since a linear length scale starts from $y^+ = 11$ (at the midpoint of the buffer zone), while a linear length scale starts from $y^+ = 5$ in the three-zone model, which corresponds to the actual situation. Also, for higher Reynolds number flows, the higher values of k_v result in a thinner viscous sublayer. These effects combine to produce a much lower thermal resistance in the near-wall layer which results in very high Nusselt numbers if the two-zone model is employed. However, the error in the approximation of the two-zone model will be negligibly small for relatively lower Reynolds number flows. Thus, the difference appearing in the predictions between the two-zone and the three-zone models is small in lower Reynolds number flows.

Unlike the difference in the predicted levels of Nusselt number, the location of the predicted maximum Nusselt number does not vary with the different wall function models. Therefore, it may be concluded that none of the various aspects of the wall function models used and/or developed in this paper has any significant effect on the axial location of the maximum Nusselt number but that the position of the maximum Nusselt number is controlled by the turbulence model per se. It is also concluded that the wall function treatment is not very important for relatively low Reynolds number flows ($\mathrm{Re}_D < 5 \times 10^4$) but is significant for higher Reynolds number flows. The rest of the computations were performed with the three-zone wall function model.

Figure 8 compares the measured and calculated distribution of Nusselt number at different Reynolds numbers for three different expansion ratios. There is generally close similarity in both measured and calculated distributions for $d/D = 0.195$ and 0.391, i.e., the maximum heat transfer coefficient is reached at about 5 step heights for $d/D = 0.195$ and at about 7 step heights for $d/D = 0.391$. However, for $d/D = 0.586$ the maximum calculated Nusselt numbers do not coincide with the maximum measured Nusselt numbers but occur about 2–3 step heights upstream from the measured peak. Since the step height for this relatively small expansion (large d/D) is the smallest of the expansion ratios used in this study, a small error in the axial distance is amplified when expressed in terms of the step heights. Hence, the positions of the maximum measured and calculated Nusselt numbers are

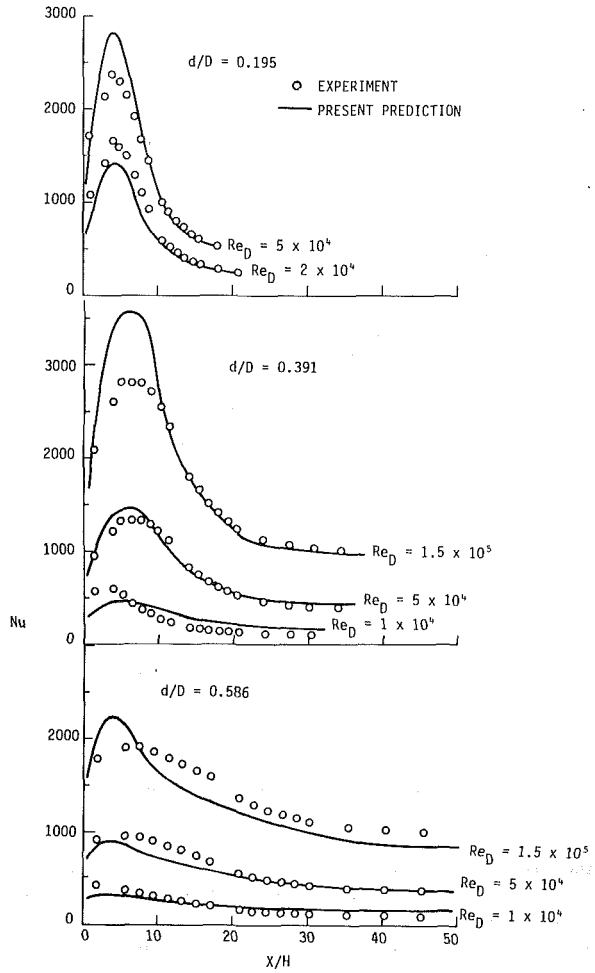

Fig. 8 Nusselt number distribution

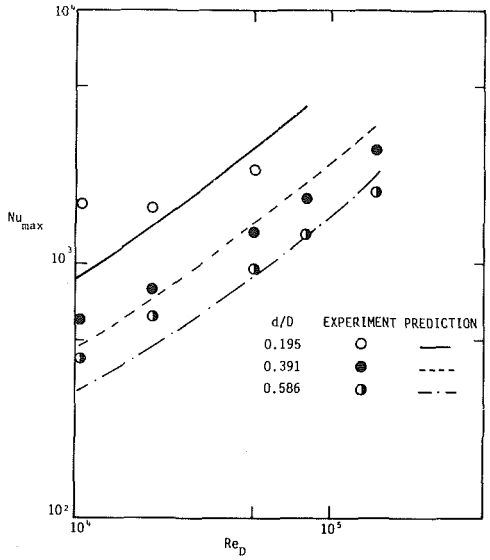

Fig. 9 Variation of maximum Nusselt number with Reynolds number

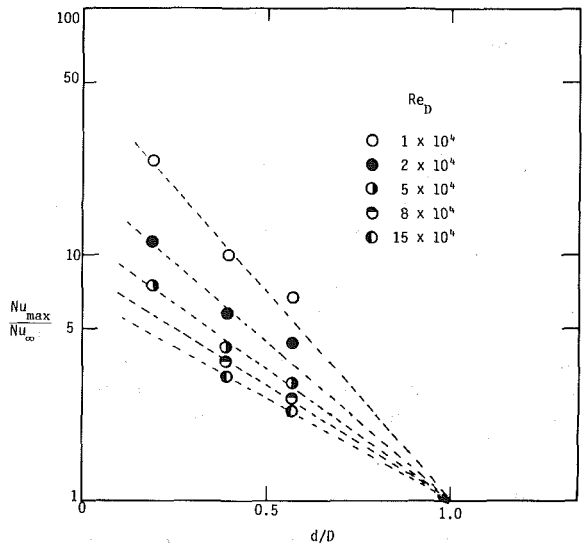

Fig. 10 Ratio of maximum and fully developed Nusselt numbers as a function of pipe expansion ratio

sufficiently close such that it would be rather difficult to say whether or not this difference in the axial location is significant for this large d/D. Note also that the locations of the maximum Nusselt numbers obtained by both experiment and computation are consistent for all the expansion and Reynolds number cases. For example, for $d/D = 0.391$ the computed location of Nu_{max} varies from 4.7 to 6.2 step heights as Re_D increases from 1×10^4 to 1.5×10^5, while those of measured values vary from 4.1 to 6.6 step heights downstream from the expansion section.

The percentage difference between the calculated and measured values of Nu_{max} ranges from -15 percent at $Re_D = 2 \times 10^4$ to $+17$ percent at $Re_D = 5 \times 10^4$ for $d/D = 0.195$. Those differences for the other two expansion ratios show a similar trend, i.e., the computation underpredicts at lower Reynolds numbers and overpredicts at higher Reynolds numbers. The variations of the maximum Nusselt number shown in Fig. 9 suggest that the calculated behavior exhibits a slightly greater sensitivity to Reynolds number than do the measured results for both $d/D = 0.391$ and 0.586. However, the experimental data for $d/D = 0.195$ display very small dependence on the Reynolds number. Furthermore, the experimental data show a decrease in Reynolds number dependency as the expansion ratio d/D decreases, while the calculated results show the same dependence on Reynolds number of approximately 0.75–0.78. It is generally seen that the measured and calculated curves agree with each other for $Re_D > 5 \times 10^4$. When the level of turbulence is strong enough to penetrate the flow field for the large step height case (small d/D), the performance of heat transfer rates at the wall shows similar behavior to the cases of $d/D = 0.391$ and 0.586. However, for lower Reynolds number the turbulence intensity promoted at the nozzle exit propagates in the axial and radial direction, and the condition of the nozzle exit is affected more by the recirculating flow than the cases of higher Reynolds number or larger d/D.

Figure 10 shows the experimental results of the ratio of the maximum Nusselt number to the Nusselt number at fully developed flow as a function of the expansion ratio d/D for different Reynolds numbers. This figure indicates that for the higher Reynolds number flows the experimental data converge to the limit where $Nu_{max}/Nu_\infty = 1.0$ at $d/D = 1.0$ although those for lower Reynolds number do not. At low Reynolds numbers the data for $d/D = 0.195$ agree with the convergence line better than for $d/D = 0.586$. This is probably because the data shown in Fig. 10 are normalized by the fully developed Nusselt number. Any disturbance or systematic error is also influencing the measurements of both Nu_{max} and Nu_∞ at the same rate. Although the power law of the measured data for $d/D = 0.195$ displayed in Fig. 9 is unrealistic, the data shown in Fig. 10 are quite reasonable.

Conclusion

The main conclusions from the study of the flow downstream of an abrupt pipe expansion are summarized as follows:

1 The development of the three-zone wall function model improved the predicted heat transfer results, especially for higher Reynolds number flows. This fact indicates that the variations of turbulent quantities in the buffer zone produce a significant effect on the heat transfer fluxes at the wall for higher Reynolds number flows but not too much for lower Reynolds number flows.

2 The maximum heat transfer rate is predicted to occur at about the same position as do the experimental data.

3 The maximum Nusselt number is predicted to increase with Reynolds number at effectively the same rate as that for fully developed pipe flow. This pattern has been shown to agree to some extent with the experimental data for larger expansion ratios d/D, but not for smaller expansion ratios.

4 The experimental data show less dependence of Nusselt number on Reynolds number for small pipe expansion ratio ($d/D = 0.195$), while the numerical results show the same dependence as for the large expansion ratios.

Finally, it should be emphasized that the simple $k \sim \epsilon$ turbulence model gives relatively good agreement with experiments by modifying the wall function treatment. This improvement should be performed prior to extending the turbulence model to a multi-equation model in which all the stress components must be computed in their own transport equations. Furthermore, the improvement of the finite difference scheme as well as the near-wall treatment is important.

Acknowledgments

This work was conducted at the University of Wisconsin-Milwaukee through the sponsorship of the NASA-Ames Research Center under contracts NAG 2-160.

References

1 Zemanick, P. P., and Dougall, R. S., "Local Heat Transfer Downstream of Abrupt Circular Channel Expansion," ASME JOURNAL OF HEAT TRANSFER, Vol. 92, 1970, pp. 53–60.

2 Krall, K. M., and Sparrow, E. M., "Turbulent Heat Transfer in the Separated Reattached and Redevelopment Regions of a Circular Tube," ASME JOURNAL OF HEAT TRANSFER, Vol. 83C, 1961, p. 131.

3 Runchal, A. K., "Mass Transfer Investigation in Turbulent Flow Downstream of Sudden Enlargement of a Circular Pipe for Very High Schmidt Numbers," *International Journal of Heat and Mass Transfer*, Vol. 14, 1971, pp. 781–792.

4 Chieng, C. C., and Launder, B. E., "On the Calculation of Turbulent Heat Transport Downstream From an Abrupt Pipe Expansion," *Numerical Heat Transfer*, Vol. 3, 1980, pp. 189–207.

5 Syed, S. A., and Sturgess, G. J., "Validation Studies of Turbulence and Combustion Models for Aircraft Gas Turbine Combustors," ASME HTD-Vol. 13, ASME, New York, 1980, pp. 71–89.

6 Rastogi, A. K., Kvernold, O., and Sontvedt, T., "Flow and Mass Transfer in a Perturbed Turbulent Pipe Flow," ASME HTD-Vol. 13, ASME, New York, 1980, pp. 91–96.

7 Amano, R. S., "On the Calculation of Turbulent Heat and Mass Transport Downstream from an Abrupt Pipe Expansion," AIAA/SAE/ASME 18th Joint Propulsion Conference, June 1982, AIAA-82-1269.

8 Spalding, D. B., "A Novel Finite-Difference Formulation for Differential Expressions Involving Both First and Second Derivatives," *International Journal for Numerical Methods in Engineering*, Vol. 4, 1972, pp. 551–559.

9 Laufer, J., NACA Report No. 1174, 1954.

10 Lindgren, E. R., Oklahoma State University, Civil Engineering Department Report 1AD621071, 1965.

11 Bakewell, H. P., and Lumley, J. L., "Viscous Sublayer and Adjacent Wall Region in Turbulent Pipe Flow," *Physics of Fluids*, Vol. 10, 1967, p. 1880.

12 Klebanoff, P. S., *NACA TN* No. 3178, 1954.

13 Jayatilleke, C. L., "The Influence of Prandtl Number and Surface Roughness on the Resistance of the Laminar Sub-Layer to Momentum and Heat Transfer," *Progress in Heat and Mass Transfer*, Vol. 1., 1969, pp. 193–329.

In-Tube Heat Transfer for Skewed Inlet Flow Caused by Competition Among Tubes Fed by the Same Plenum

M. Molki

E. M. Sparrow
Fellow ASME

Department of Mechanical Engineering,
University of Minnesota,
Minneapolis, Minn. 55455

Measurements were made of the axial and circumferential distributions of the heat transfer coefficient in a tube in which the entering airflow is highly skewed. The skewness was caused by competition between the test section tube and a parallel tube which draws air from the same plenum chamber. For each of several fixed Reynolds numbers in the test section tube, the flow imbalance between the competing tubes was varied parametrically (up to a factor of eighteen), as was the center-to-center separation distance between the tubes (separation = 1.5, 3, and 4.5 times the tube diameter). Measurements were also made of the pressure drop, and a visualization technique was employed to examine the pattern of fluid flow. Practically significant effects of the flow imbalance on the axial distribution of the heat transfer coefficient were encountered only at the smallest of the investigated inter-tube spacings. Even for that case, the effects were moderate; for example, the imbalance-related changes for an imbalance ratio of two did not exceed 7 percent. The experiments involved naphthalene sublimation, and a new technique was developed for coating the inside surface of a tube with naphthalene.

Introduction

It is a common occurrence in heat exchange devices that a number of tubes draw fluid from the same header or plenum so that, in effect, the tubes are competing for the available fluid. This occurs, for example, in a shell and tube heat exchanger where the tube inlets, built into a tube sheet, face upstream into a plenum chamber from which all tubes draw their fluid. The inherent competition among the tubes plays a decisive role in shaping the velocity distribution in the fluid entering any given tube. Indeed, even in the simplest configurations, the tube inlet velocity will differ significantly from the classical cases (e.g., either uniform or fully developed profiles) which are used in both experimental and analytical studies of in-tube heat transfer.

As a case in point, consider a very large plenum supplied with fluid at its upstream end and bounded at its downstream end by a tube sheet in which the tubes are arranged on equilateral triangular centers. If the rate of fluid flow drawn into each tube is the same, then, owing to symmetry, each inlet is fed by a stream tube of hexagonal cross section which extends from the face of the tube sheet back into the plenum. Thus, the velocity profile at inlet corresponds to that for an abrupt contraction from the hexagonal stream tube to the circular inlet aperture in the tube sheet and is, clearly, more complex than those of the standard pipe-flow literature.

The next stage of inlet profile complexity—that which is the focus of the present investigation—is the presence of a high degree of skewness in the profile. The skewness may result from a number of factors. One of these, the one involved in the present experiments, is differences in the rate of fluid flow passing through the various tubes which draw from the plenum. Thus, for example, a tube inlet situated next to one which draws a relatively high rate of flow from the plenum will experience an entering velocity distribution that is skewed in the direction of the high-inflow tube. Furthermore, the extent of the skewness will be accentuated as the degree of the tube-to-tube flow imbalance increases.

Contributed by the Heat Transfer Division for publication in the JOURNAL OF HEAT TRANSFER. Manuscript received by the Heat Transfer Division November 12, 1982.

Skewed inlet profiles may also result from the geometry of the plenum or from the manner in which fluid is supplied to the plenum. In a narrow plenum, the fluid particles must move on highly curved trajectories in order to reach the various inlet apertures in the tube sheet. Similarly, fluid supplied to the plenum via a port in the side of the plenum will also move along trajectories that are highly curved.

In the presence of a skewed inlet velocity distribution, the separation of the flow (which occurs at any sharp-edged inlet) will also be skewed, as will the subsequent reattachment. Moreover, the nonaxisymmetric turning of the flow as it enters the tube should also give rise to a secondary (i.e., circumferential) flow superposed on the mainflow. These features are not encountered in conventional, axisymmetric, single-tube flows from which heat transfer results are customarily obtained for subsequent use in heat exchanger design.

The focus of this investigation is the determination of turbulent pipe-flow heat transfer coefficients in the presence of skewed inlet velocity distributions. The approach taken here is to look at the generic problem rather than to be concerned with the large number of specific physical situations where skewness occurs. To this end, an experimental setup was employed which enabled the skewness to be varied in a systematic manner and which was capable of yielding skewnesses even more exaggerated than those encountered in normal practice.

A schematic view of the experimental arrangement is shown in the upper diagram of Fig. 1. As seen there, two parallel tubes are set into a large circular plate (hereafter called the baffle plate) and draw from the open space upstream of the plate. Each tube was equipped with a downstream-positioned blower, control valve, and flowmeter (not shown), so that the rate of airflow passing through each could be controlled independently.

The experiments were conducted at several fixed Reynolds numbers (i.e., flow rates) in the test section tube 1 covering the range from 5000 to 44,000. At each fixed Re_1, the Reynolds number Re_2 of the second tube was varied from

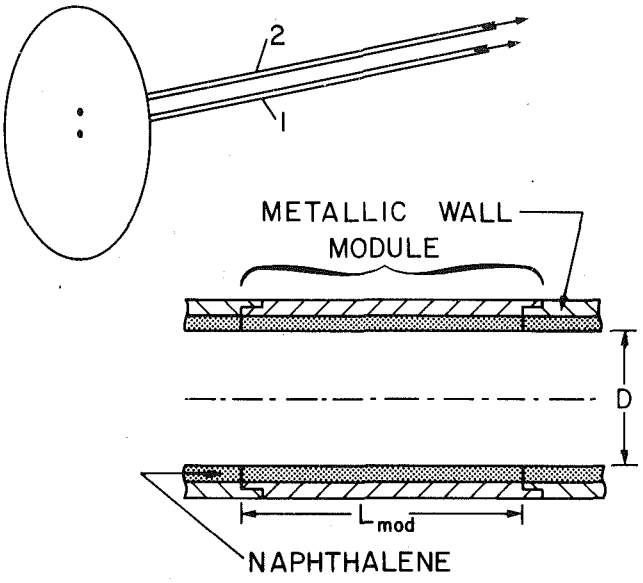

Fig. 1 Upper diagram: two tube and baffle plate arrangement; lower diagram: typical module

zero to as large a value of Re_2/Re_1 as was permitted by the capabilities of the apparatus (up to $Re_2/Re_1 = 18$). The variation of Re_2/Re_1 at a fixed value of Re_1 served to vary the degree of skewness of the velocity distribution at the inlet of tube 1. Correspondingly, the measured Nusselt numbers for tube 1 revealed the response of a fixed Reynolds number pipe flow to the degree of flow imbalance and inlet-profile skewness.

Another parameter varied during the course of the investigation was the proximity of the tubes. If S denotes the center-to-center separation distance and D is the internal diameter of the tubes, then the proximity may be defined by the S/D ratio. The investigated values of S/D included 1.5, 3, and 4.5.

Two types of heat transfer coefficients were measured. For each data run, circumferential-average coefficients were obtained at 21 to 24 axial stations along the length of the test section tube. For selected runs and at a specific axial station, circumferential variations of the coefficient were also measured.

In actuality, the heat transfer coefficients were determined indirectly via the analogy between heat and mass transfer by employing the naphthalene sublimation technique. In this regard, a new procedure was developed for applying on the inside of a tube a naphthalene coating of precise dimensions and having a hydrodynamically smooth surface finish.

Two types of fluid flow measurements were made to supplement the heat transfer experiments. The oil-lampblack flow visualization method was employed to examine the pattern of fluid flow adjacent to the tube wall, especially in the region where the separated flow reattaches to the wall. Axial pressure distributions were also measured to identify the effect of the skewed inlet velocity on the pressure drop.

To the knowledge of the authors, the work described here is the first research involving multiple-tube competing flows. A variety of inlet conditions for single tubes has been investigated, as reported in [1–3].

Experimental Apparatus

As noted earlier, the experiments were conducted utilizing a pair of parallel tubes whose upstream ends mated with a large baffle plate and which drew air competitively from the space upstream of the baffle. Whereas the two tubes experienced strong hydrodynamic interactions, no mass transfer interactions can occur (note that extraneous, difficult-to-control, thermal interactions would have occurred had heat transfer experiments been performed). Therefore, only one of the two tubes (i.e., tube 1) need participate in the mass transfer process, while the other tube (tube 2) functions only as a fluid flow device. Correspondingly, tube 1 was internally coated with naphthalene and tube 2 was metallic (aluminum), without naphthalene. Both tubes had approximately the same internal diameter.

Each of the tubes was part of an independent flow circuit which, along the path of the airflow, included the tube itself, a flowmeter (one of three calibrated rotameters), a control valve, and a blower. The blowers were situated in a service corridor outside the laboratory room, which enabled their discharge, heated by blower compression and laden with naphthalene vapor, to be vented away from the laboratory. As a result of this arrangement, the air in the laboratory was free of naphthalene vapor and at a nearly uniform temperature (about 20°C), maintained by a control system.

Mass Transfer Test Sections. Two distinct mass transfer test sections were employed during the experiments—one to determine the axial distribution of the mass transfer coefficient and the other for the circumferential distribution. The axial distribution was, by far, the major focus of the work, and the test section used in its determination will be described first and in greater detail, with that for the circumferential distribution to follow.

The test section used for the axial distribution was of modular design, and a typical module, flanked by portions of the adjacent upstream and downstream modules, is pictured schematically in the lower diagram of Fig. 1. As seen there, the module consists of an outer metallic shell and an inner annular layer of solid naphthalene that was implanted by a casting process to be described shortly. The metallic shell is a

Nomenclature

A = mass transfer surface area
D = tube inner diameter
$\mathfrak{D}$ = diffusion coefficient
f = friction factor, $(-dp/dX)D/\frac{1}{2}\rho V^2$
K = mass transfer coefficient, equation (1)
K_p = incremental pressure loss coefficient
L_{mod} = axial length of naphthalene surface per module
ΔM = mass sublimed during data run
$\dot{Q}$ = volumetric flow rate
p = pressure at X
p_∞ = pressure in plenum
Re = Reynolds number, $4\dot{w}/\mu\pi D$
Re_1 = Reynolds number of test section tube
Re_2 = Reynolds number of competing tube
S = center-to-center separation
Sc = Schmidt number
Sh = Sherwood number, $KD/\mathfrak{D}$
$Sh_{fd,0}$ = fully developed Sherwood number for single tube
V = mean velocity
$\dot{w}$ = airflow rate
X = axial coordinate
θ = angular coordinate
μ = viscosity
ν = kinematic viscosity
ρ = density
ρ_{nb} = naphthalene vapor density in bulk
ρ_{nw} = naphthalene vapor density at wall
τ = duration of run

Subscripts

1 = test section tube
2 = competing tube

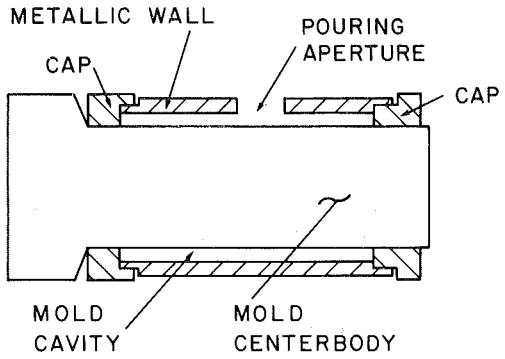

Fig. 2 Setup for forming a naphthalene coating on the inside of a circular tube

segment of aluminum tube (i.d. = 4.064 cm, o.d. = 4.826 cm). At one end of the segment, an internal recess, 0.508-cm long, was formed by cutting away half the wall thickness. A similar recess was cut into the external surface at the other end of the module. As can be seen in the diagram, the test section was assembled by mating the internal recess of one module with the external recess of the adjacent module, with pressure-sensitive tape used to seal the joint against leaks.

The internal diameter, D, of the cast naphthalene layer was 3.272 cm, while the axial length, L_{mod}, of the naphthalene that was exposed to the airflow varied with the selected module. For the modules of the type pictured in Fig. 1, three different lengths, L_{mod}, were employed, respectively, $L_{mod}/D = 0.388$, 0.766, and 1.553. In the assembly of the test section, the shortest modules were positioned nearest the inlet, followed by the intermediate modules and then the longest modules. The specific positions of the respective modules will be apparent from the forthcoming presentation of results.

The most upstream module was, necessarily, somewhat different from the others. The external surface of the metallic wall of the module was machined so that it fit snugly in an aperture in the baffle plate, and the upstream faces of the module and the baffle plate were aligned flush. Moreover, the module design was such that its upstream face was metallic, so that naphthalene sublimation occurred only along the bore of the module. The L_{mod}/D ratio for this special module was 0.466.

All told, as many as 24 modules were assembled to form the test section. Fixtures and supports were provided to ensure the straightness of the assembled test section tube.

The technique which was developed for forming a naphthalene coating on the inside surface of a circular tube will now be described. As a first step, the naphthalene coating from the preceding data run was removed from each module by melting and evaporation. Then, a mold was assembled as shown in Fig. 2. The components of the mold included the metallic wall of the module, end caps which mated with the recesses at the respective ends of the metallic wall, and a shaft (diameter = 3.272 cm) which passed through apertures in the end caps and served as the centerbody of the mold. The surface of the shaft had been polished to a mirrorlike finish with a succession of lapping compounds.

Molten naphthalene was poured into the annular cavity between the metallic wall and the centerbody through an aperture in the wall. Once the naphthalene had solidified, the shaft and end caps were removed. The resulting surface quality of the cast naphthalene was comparable to that of the polished shaft. As a final step, the pouring aperture was sealed with tape to prevent extraneous sublimation. In certain modules (a total of four), thermocouples were cast into the naphthalene layer, flush with its interior surface.

Attention is now turned to the test section used for the measurement of the circumferential distribution of the heat transfer coefficient. In this regard, it may be noted that the scope of this phase of the investigation was more limited than that for determining the axial distribution. In particular, the circumferential measurements were confined to the axial zone $0.472 \leq X/D \leq 0.848$, which corresponds to the axial range of the second module of the primary test section that was described earlier. This is the range in which the maximum heat transfer coefficients were encountered, and it was, therefore, chosen as the site for the circumferential studies.

In essence, the test secction was an aluminum tube with a circular patch of naphthalene built into its wall. The tube was fabricated from solid aluminum rod stock whose external surface was first turned down to the desired outside diameter (to fit snugly into the aperture in the baffle plate). Then, a hole, 1.232 cm in diameter, was drilled radially into the rod at a distance of 2.159 cm from one end. Finally, the rod was bored axially, resulting in a circular tube with an i.d. of 3.272 cm (matching the i.d. of the test section described earlier).

The naphthalene patch was cast by employing the polished shaft that was used in the casting process for the modules. The shaft was inserted into the bore of the just-described fabricated tube, thereby blocking off the base of the radial hole. Molten naphthalene was poured into the open end of the radial hole, into which a thermocouple was also implanted. After solidification was completed, the polished shaft was removed, leaving a patch of naphthalene which now formed part of the surface which bounded the bore of the tube.

The circumferential position of the patch was varied by rotation of the tube, thereby enabling the detection of the circumferential variation of the transfer coefficient.

The patch was the only naphthalene surface in its test section at which mass transfer occurred. Therefore, the measured circumferential variations of the mass transfer coefficient reflect circumferential nonuniformities of the velocity field but do not reflect mass transfer events at upstream locations. Since the role of the velocity is expected to be dominant, the measured coefficients should give a true accounting of the circumferential variations.

Other Apparatus Components and Instrumentation. As already noted, the second of the two parallel tubes served a hydrodynamic function in that it controlled the skewness of the velocity distribution at the inlet of the test section tube. The second tube was of seamless aluminum, with internal and external diameters of 3.239 cm and 4.227 cm, respectively, and a length of 88.9 cm. The tube fit snugly into an aperture in the baffle plate, and the upstream face of the tube wall was flush with the upstream face of the baffle. Fourteen taps deployed along the length of the tube were used for the pressure drop measurements described later.

The baffle was also of aluminum, 91.44 cm in diameter and 1.23-cm thick. An aperture was bored through the plate at its center to accommodate the test section tube. In addition, four other apertures were machined into the baffle, to be used one at a time to accommodate the second tube. The three apertures not in use were closed by aluminum disks, with the joints filled with body putty. The entire upstream face of the plate was sanded with 600-grit wet or dry paper, with special attention given to ensure a hydrodynamically smooth surface adjacent to the sealed apertures. The apertures were deployed along a radial line, with the respective centers at $1.5D$, $3D$, $4.5D$, and $6D$ from the center of the test section tube (D = internal diameter of test section tube).

With regard to instrumentation, the four thermocouples implanted in the test section have already been mentioned. A fifth thermocouple measured the inlet air temperature. All thermocouples were precalibrated and were read with a programmable, 1 μV datalogger. Airflow rates were measured with calibrated rotameters.

Perhaps the most critical measurement was the deter-

mination of the masses of the individual modules. The amount of naphthalene sublimed during a data run was determined by differencing the masses of the respective modules measured before and after the run. For this purpose, a Sartorius ultra-precision, electronic analytical balance was employed. This balance has a resolving power of 10^{-5} g and a capacity of 166 g. Typical changes of mass during a run were in the 0.05 g range.

Pressure measurements were made with a Baratron capacitance-type, solid-state pressure meter able to detect differences of 10^{-3} mm Hg.

Flow Visualization

Flow visualization studies were undertaken to gain insights into the effects of the skewed inlet velocity on the pattern of fluid flow in the initial portion of the test section tube. These studies were performed utilizing the oil-lampblack technique, whereby a mixture of oil and lampblack powder is brushed on the surface which bounds the airflow. Ideally, under the action of the forces exerted by the flow, the mixture will move along the surface, following the paths of the fluid particles which pass adjacent to the surface. In regions of low velocity (e.g., stagnation zones, reattachment zones), the mixture will remain stationary, so that such regions show themselves as black, streak-free zones on the surface.

The technique works best at high Reynolds numbers owing to the relatively high stresses that exist. At low Reynolds numbers, experience with a variety of flows has demonstrated that very little can be seen, even if a mixture of high fluidity is used (low viscosity oil and low particle loading). Furthermore, for vertical or downfacing surfaces, relatively stiff mixtures have to be utilized to prevent sagging and runoff, and such stiff mixtures preclude successful visualizations at low Reynolds numbers. Since the test section tube was horizontal in the present experiments, the employed mixture had to be stiff enough to avoid sagging along a considerable portion of the tube circumference. These realities restricted the visualization work to the high Reynolds number range (> 35,000).

To obtain a record of the visualized flow pattern, the inside surface of the test section tube was covered at its upstream end with white, plasticized contact paper. Once the oil-lampblack visualization pattern had been formed, the contact paper was carefully separated from the tube wall and laid flat on a sheet of cardboard for photography.

A photograph of a typical visualization pattern, shown in the aforementioned laid-out format, is presented in the upper portion of Fig. 3. This photograph corresponds to a test-section Reynolds number $Re_1 = 70{,}000$, to the modest flow imbalance $Re_2/Re_1 = 1.26$, and to a separation distance $S/D = 1.5$. The right- and left-hand edges of the photo are parallel to the tube axis, and these edges are in contact with each other during the visualization experiment. The lower edge corresponds to the inlet edge of the test section, while the upper edge corresponds to an axial station that is about $2\frac{1}{2}D$ from the inlet. To aid in the interpretation of the pattern, the lower part of Fig. 3 shows both the inlets of the test section tube and the competing tube and defines angular positions around the circumference of the test section tube.

Prior to the start of the visualization experiment, the entire surface of the contact paper was covered by a uniformly black film of the oil-lampblack mixture, so what is seen in the photograph represents a substantial rearrangement. Four distinct zones are in evidence. There is a relatively straight black band adjacent to the lower edge (i.e., the tube inlet) and a curved black band somewhat downstream. Zones containing streak lines are situated between the two bands and downstream of the second band.

The visualization pattern indicates that the flow separates

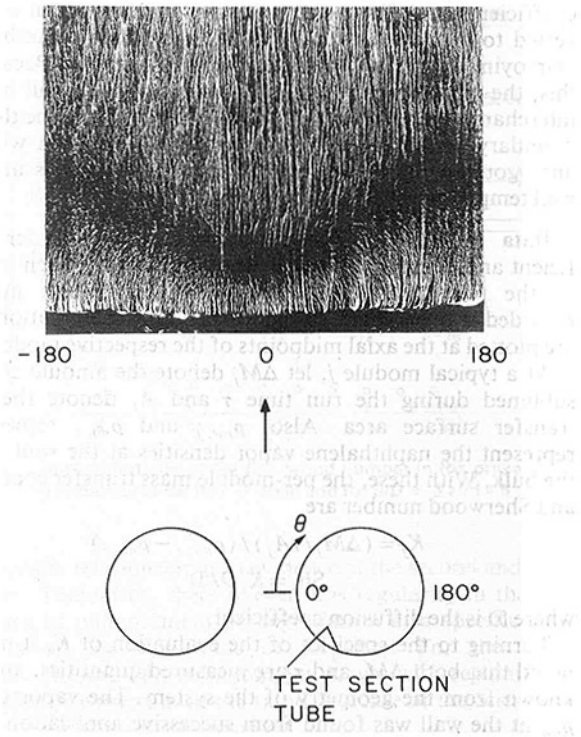

Fig. 3 Upper part: typical flow visualization pattern ($Re_1 = 70{,}000$, $Re_2/Re_1 = 1.26$, $S/D = 1.5$); lower part: diagram showing definition of angular positions in the test section tube

at the sharp-edged inlet of the tube and reattaches to the tube wall along the wavy black band. The angular variation of the reattachment is a direct consequence of the skewed inlet velocity resulting from the flow imbalance. In view of the modest imbalance ($Re_2/Re_1 = 1.26$), the extent of the circumferential variation is remarkable. The most forward point of the reattachment is at $\theta = 0$ deg, i.e., at the position of nearest proximity of the tubes, while the most downstream reattachment occurs at $\theta = \pm 180$ deg (i.e., on the side of the test section away from the competing tube). These results are consistent with the skewing of the test-section inlet flow in the direction of the competing tube.

The streak lines upstream of reattachment indicate a wall-adjacent backflow—a flow directed upstream. This backflow is one leg of the recirculating flow which occupies the separation bubble. The backflow carries the oil-lampblack mixture toward the tube inlet and deposits it there, giving rise to the inlet-adjacent black band. The backflow streaks are not parallel to the tube axis. Their curvature is indicative of the presence of a circumferential velocity, probably a secondary flow caused by the nonaxisymmetric turning of the fluid as it enters the tube.

The streak lines downstream of reattachment suggest the absence of circumferential (secondary) flow except, perhaps, in the neighborhood of $\theta = 180$ deg. However, at greater flow imbalances, it is quite likely that secondary motions would persist to greater downstream distances.

With regard to the forthcoming mass transfer results, perhaps the most significant finding of the flow visualization is that the flow imbalance (i.e., the initial skewing) shifts the reattachment upstream at $\theta = 0$ deg and downstream at $\theta = 180$ deg. Observations of numerous visualization patterns indicate that this behavior is accentuated with increasing imbalance.

Mass (Heat) Transfer Results

The experiments performed here provide mass transfer

coefficients and Sherwood numbers, and these can be converted to heat transfer coefficients and Nusselt numbers by employing the analogy between the two processes. Because of this, the phrases heat transfer and mass transfer will be used interchangeably in the forthcoming presentation. The thermal boundary condition for the heat transfer problem which is analogous to the present mass transfer problem is uniform wall temperature.

Data Reduction. The per-module mass transfer coefficient and Sherwood number were evaluated at each module of the primary test section. These coefficients may be regarded as quasi-local. In the forthcoming presentation, they are plotted at the axial midpoints of the respective modules.

At a typical module j, let ΔM_j denote the amount of mass sublimed during the run time τ and A_j denote the mass transfer surface area. Also, $\rho_{nw,j}$ and $\rho_{nb,j}$ respectively represent the naphthalene vapor densities at the wall and in the bulk. With these, the per-module mass transfer coefficient and Sherwood number are

$$K_j = (\Delta M_j/\tau A_j)/(\rho_{nw,j} - \rho_{nb,j}) \quad (1)$$

$$\mathrm{Sh}_j = K_j D/\mathfrak{D} \quad (2)$$

where $\mathfrak{D}$ is the diffusion coefficient.

Turning to the specifics of the evaluation of K, it may be noted that both ΔM_j and τ are measured quantities, and A is known from the geometry of the system. The vapor density ρ_{nw} at the wall was found from successive application of the Sogin vapor pressure-temperature relation [4] and the perfect gas law. The measured wall temperatures were uniform along the test section, so that ρ_{nw} was the same at all modules for a given data run.

To find the bulk vapor density, ρ_{nb}, at module, j, it may first be noted that the increase in ρ_{nb} between the inlet and outlet sections of any module, m, is

$$(\Delta\rho_{nb})_m = (\Delta M_m/\tau)/\dot{Q} \quad (3)$$

where $\dot{Q}$ is the volumetric flow rate passing through the module. Then, it follows that

$$\rho_{nb,j} = \rho_{nb,o} + \sum_{m=1}^{j-1} (\Delta\rho_{nb})_m + \tfrac{1}{2}(\Delta\rho_{nb})_j \quad (4)$$

The quantity $\rho_{nb,o}$ is the naphthalene bulk density at the inlet of the test section tube, which is zero for the present experiments. Also, $\dot{Q}$ is virtually constant along the test section (typical variation ~0.04 percent).

For the Sherwood number evaluation, it is convenient to eliminate the diffusion coefficient by using the definition of the Schmidt number, Sc, which gives

$$\mathrm{Sh}_j = (K_j D/\nu)\mathrm{Sc} \quad (5)$$

For naphthalene diffusion in air, Sc = 2.5 [4]. The kinematic viscosity, ν, was evaluated as that for pure air—consistent with the minute concentrations of the naphthalene vapor.

The evaluation of K and Sh for the circumferentially orientable test section follows the same pattern as that for each module. The area, A, that appears in equation (1) now represents the surface area of the naphthalene patch, while ρ_{nb} = 0 since no mass transfer occurs upstream of the patch.

The Sherwood number results will be parameterized by the Reynolds number, Re, defined in the conventional manner as

$$\mathrm{Re} = 4\dot{w}/\mu\pi D \quad (6)$$

in which $\dot{w}$ is the mass flow rate of the air.

Axial Distributions of the Transfer Coefficient. As a prelude to the presentation of the axial distributions, the measured fully developed Sherwood numbers for single-tube operation will be compared with the literature. For these experiments, the second tube's aperture in the baffle plate was sealed. Comparisons were made over the range from Re = 5000 to 88,000 with the Petukhov-Popov equation (equations (8-23) and (8-24) of [5]) and its low Reynolds number extension due to Gnielinski [6]. Agreement to 5 percent or better was encountered over the entire range, lending strong support to the present experimental technique.

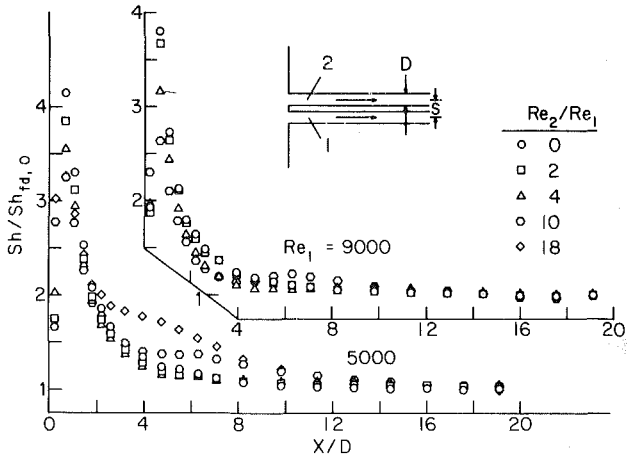

Fig. 4 Axial distributions of the Sherwood number in the presence of various flow imbalances for Re_1 = 5000 and 9000 and for S/D = 1.5

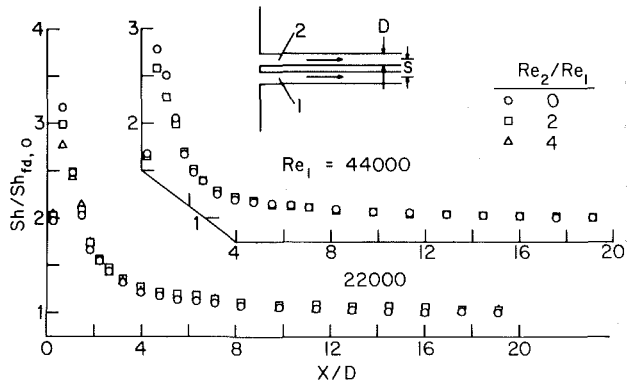

Fig. 5 Axial distributions of the Sherwood number in the presence of various flow imbalances for Re_1 = 22,000 and 44,000 and for S/D = 1.5

Axial distributions of the Sherwood number along the test section tube are presented in Figs. 4 and 5. These results correspond to two-tube operation (with the single tube as a special case) and to the smallest of the investigated center-to-center separation distances, S/D = 1.5. Figure 4 conveys results for two fixed values of the test section Reynolds number, Re_1 = 5000 and 9000, while Fig. 5 presents the corresponding information for Re_1 = 22,000 and 44,000.

At each fixed value of Re_1, data are plotted for various flow imbalance ratios Re_2/Re_1 = 0 (single-tube operation), 2, 4, ... Since the maximum attainable value of Re_2 was approximately 88,000, the largest imbalance ratio, ~18, was achieved at the smallest Re_1 (=5000). As Re_1 increased, the range of the imbalance ratio decreased, so that at Re_1 = 44,000, the largest imbalance ratio was about two. Correspondingly, the successive graphs, starting with Re_1 = 5000 and proceeding toward larger Re_1, include fewer data points.

The local Sherwood numbers for all operating conditions at a fixed value of Re_1 have been normalized by the measured fully developed Sherwood number corresponding to single tube operation at that Re_1. This quantity is designated as $Sh_{fd,0}$, and the ordinates of the graphs are $Sh/Sh_{fd,0}$.

An overall view of Figs. 4 and 5 indicates a common pattern for all the Sherwood number distributions. Starting with a moderate value adjacent to the tube inlet, the Sherwood

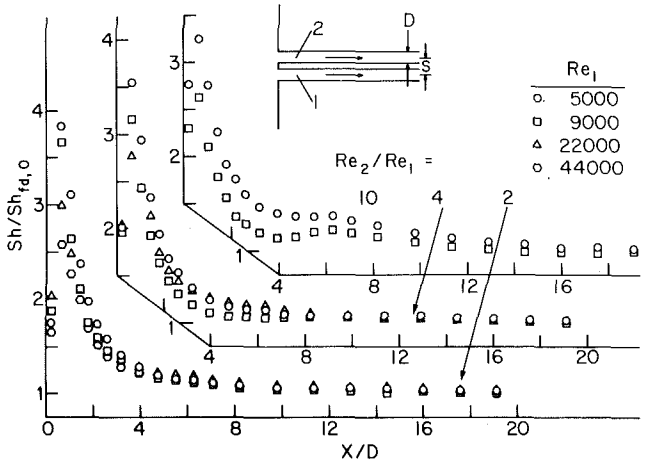

Fig. 6 Axial distributions of the Sherwood number for flow imbalances Re_2/Re_1 = 2, 4, and 10 for various test section Reynolds numbers Re_1 and for S/D = 1.5

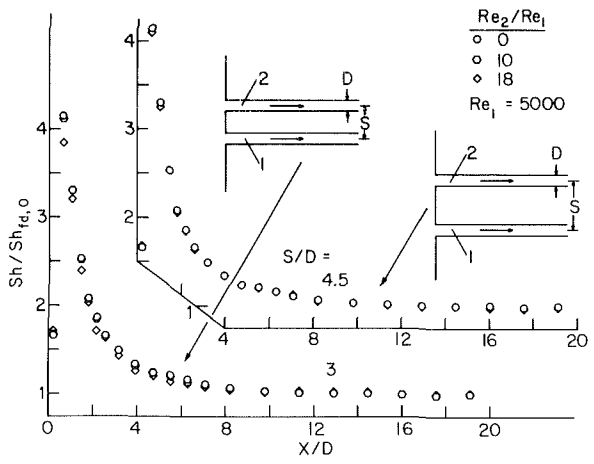

Fig. 7 Axial distributions of the Sherwood number in the presence of various flow imbalances for Re_1 = 5000 and for S/D = 3 and 4.5

number increases sharply to a maximum, whereupon it decreases, rapidly at first, and more gradually thereafter, finally approaching the fully developed value. For all cases, the maximum occurs at the second module, which is centered at $X/D = 0.660$.

The aforementioned distribution is characteristic of tube flow with a sharp-edged inlet, which gives rise to inlet-adjacent separation. The reattachment of the flow at the tube wall is responsible for the sharp peak in the transfer coefficient, and the subsequent dropoff of the coefficient is a consequence of the post-reattachment redevelopment of the flow. Despite the frequent occurrence of the sharp-edged inlet, analytical predictions for this configuration have not appeared in the literature.

In assessing the effects of flow imbalance (i.e., the skewing of the inlet flow), it is useful to regard the single-tube data (i.e., $Re_2/Re_1 = 0$, open circles) as a reference. Relative to that reference, an overview of Figs. 4 and 5 shows that the imbalance can cause substantial changes in the Sherwood number. However, a closer inspection reveals that if very large imbalances such as $Re_2/Re_1 = 10$ and 18 are momentarily excluded from the discussion, then the effects of the imbalance are moderate. For instance, for $Re_2/Re_1 = 2$ and $Re_1 = 9000$, there is no axial station at which the imbalance-related change in Sh exceeds 5 percent, while for $Re_1 = 22{,}000$ and 44,000, 5 percent (or slightly greater) changes occur at only a few discrete points. Even for $Re_1 = 5000$ and $Re_2/Re_1 = 2$, the largest imbalance-related change is 7 percent. In this regard, it may be noted that a factor-of-two flow imbalance is by no means small when viewed from the standpoint of practice.

Large flow imbalances such as $Re_2/Re_1 = 10$ and 18 significantly affect the Sherwood number distribution, both in the immediate neighborhood of the inlet and downstream of the sharp dropoff which follows reattachment. For example, at $Re_1 = 5000$, deviations of 10 percent between the large-imbalance distributions and that for the single tube persist to $X/D = 12$. However, with increasing Re_1, the effect of the imbalance appears to lessen, as suggested by a comparison of the $Re_2/Re_1 = 10$ distributions for $Re_1 = 5000$ and 9000. This trend is not unexpected, since low Reynolds number flows are generally more susceptible to disturbances than high Reynolds number flows.

Another interesting characteristic of the results is that the presence of the imbalance does not have a universally enhancing or degrading effect on the Sherwood number. At the first measurement station, the imbalanced flows yield larger Sherwood numbers than that for the single tube, while the opposite relationship is in evidence at the second and third stations. Thereafter, there is even less regularity in that the existence of enhancement or degradation at a specific X/D depends on the magnitude of Re_2/Re_1. For the larger Re_2/Re_1 (10 and 18), enhancement occurs with regularity in the region downstream of the rapid decrease of the Sherwood number that follows reattachment.

Certain of the trends noted in the preceding paragraph can be rationalized by taking cognizance of the shifting of the reattachment line which accompanies an increase in the flow imbalance ratio, as indicated by the visualization study. Another factor which may explain the downstream enhancement in evidence at large values of the ratio is the presence of a secondary flow (i.e., a swirl) induced when the fluid turns to enter the tube (in a manner similar to a pipe bend).

The data of Figs. 4 and 5 have been brought together in an alternate presentation in Fig. 6 in order to address the question of whether the imbalance-related effects can be correlated solely as a function of the imbalance ratio, Re_2/Re_1. The figure contains three graphs, respectively, for $Re_2/Re_1 = 2$, 4, and 10 (lower to upper), and in each graph $Sh/Sh_{fd,0}$ data are plotted for various Reynolds numbers. It is evident from the figure that $Sh/Sh_{fd,0}$ depends on Re_1 as well as on Re_2/Re_1. Overall, at a fixed Re_2/Re_1, there is a tendency for $Sh/Sh_{fd,0}$ to increase with decreasing Re_1, which is consistent with the expectation that lower Reynolds number flows are more sensitive to disturbing influences.

Thus far, the presentation of results has been focused on the closest of the investigated center-to-center distances, i.e., $S/D = 1.5$. Attention is now turned to the effect of increases in S/D. Since the lowest Reynolds number case, $Re_1 = 5000$, is the most sensitive to the flow imbalance, it will be considered first.

In Fig. 7, $Sh/Sh_{fd,0}$ distributions for $Re_1 = 5000$ are plotted for $S/D = 3$ and 4.5, respectively, in the lower and upper graphs. If Fig. 4 is kept in mind, then Fig. 7 indicates a great decrease in the effects of the flow imbalance with increasing S/D. At $S/D = 3$, there is no detectable effect of the $Re_2/Re_1 = 10$ flow imbalance, and even for $Re_2/Re_1 = 18$ the deviations of the Sherwood numbers from the single-tube values are, for the most part, negligible. If the spacing is increased to $S/D = 4.5$, then the results for $Re_2/Re_1 = 18$ are coincident with those for $Re_2/Re_1 = 0$.

The S/D effect is addressed for larger values of Re_1 in Fig. 8, where results for $Re_1 = 9000$ and 22,000 are plotted for $S/D = 3$. Here again, the data for the $Re_2/Re_1 > 0$ cases are indistinguishable from those for $Re_2/Re_1 = 0$.

Figures 7 and 8 indicate that even enormous flow imbalances are not felt when the tubes are moderately far apart.

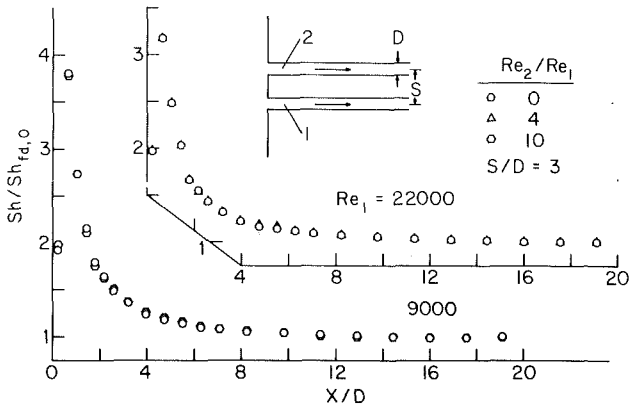

Fig. 8 Axial distributions of the Sherwood number in the presence of various flow imbalances for Re_1 = 9000 and 22,000 and for S/D = 3

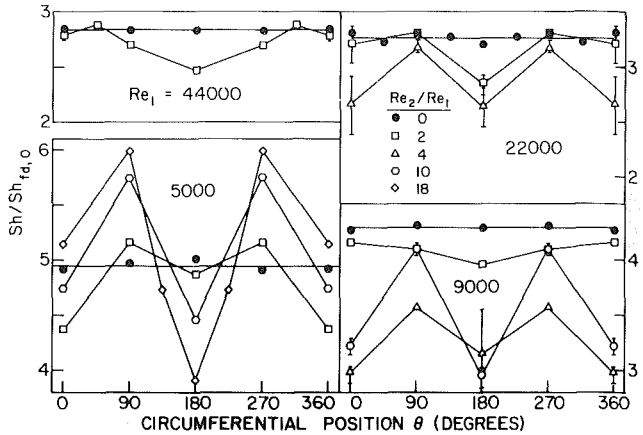

Fig. 9 Circumferential distributions of the Sherwood number at X/D = 0.660 for various flow imbalances and test section Reynolds numbers and for S/D = 1.5

By the same token, if the tubes were to be positioned much closer together than the S/D = 1.5 separation investigated here, there could well be a large magnification of the effects of the flow imbalance.

Efforts made to correlate the results are reported in [7]. Specific consideration was given to the use of Re_2/Re_1 as a correlating parameter, but the $Sh/Sh_{fd,0}$ results corresponding to a given value of Re_2/Re_1 are not independent of Re_1 (Fig. 6). Neither was it possible to correlate the results with S/D since there were virtually no imbalance-related effects for any S/D other than 1.5.

Circumferential Distributions of the Transfer Coefficient. The circumferential distributions of the Sherwood number, measured by a naphthalene surface patch centered at X/D = 0.660, are plotted in Fig. 9. The figure consists of four graphs, respectively, for Re_1 = 5000, 9000, 22,000, and 44,000. In each graph, data for $Sh/Sh_{fd,0}$ are plotted as a function of the circumferential position, θ, where θ is defined in the diagram below the photograph of Fig. 3. The data are parameterized by the flow imbalance ratio Re_2/Re_1, with the single tube (Re_2/Re_1 = 0) included for reference purposes. All the data are for S/D = 1.5.

In appraising the results, it is helpful to recall that θ = 0 deg corresponds to the position of closest proximity of the two tubes, while θ = 180 deg is the position farthest from the competing tube. It may be noted that uncertainty bars have been affixed to various of the data points. These bars reflect the range of the data from multiple repeated runs; in those cases where there are no bars, the repeated runs gave virtually identical results.

As seen in the figure, the Sherwood number, starting from its value at θ = 0 deg, increases to a maximum, whereafter it declines and attains a minimum at θ = 180 deg. Owing to symmetry, the pattern repeats for 180 deg $\leq \theta \leq$ 360 deg. Since the number of circumferential measurement sites was limited, the actual maxima of the respective distributions may not be quite coincident with the plotted maxima. It is believed, however, that the true minimum occurs at θ = 180 deg.

At high values of the flow imbalance ratio Re_2/Re_1, the maximum and minimum of the circumferential distribution are widely separated. As Re_2/Re_1 decreases, the extrema tend to come together, and when Re_2/Re_1 = 0, the distribution is circumferentially uniform (within the scatter of the data).

The development of the circumferential variation with increasing Re_2/Re_1 can be traced to the related shifting of the flow reattachment—in the upstream direction at θ = 0 deg and in the downstream direction at θ = 180 deg. Thus, for sufficiently large Re_2/Re_1, the reattachment at θ = 0 deg lies upstream of the patch location, while for θ = 180 deg the reattachment occurs downstream of the patch. At these angles, the patch is respectively situated in the (post-reattachment) redevelopment region and in the (pre-reattachment) separated region. The curved reattachment line (Fig. 3) passes through the patch site at an angular position somewhere between θ = 0 and 180 deg, causing the maximum in the distribution curve.

Pressure Drop Results

For the pressure drop measurements, the tap-equipped metallic tube was positioned in the baffle aperture otherwise occupied by the mass transfer test section. Another metallic tube was employed to establish the flow imbalance.

In all cases, the linearity of the pressure distribution was established for $X/D \geq 10$. In the linear region, the local pressure $p(X)$ can be related to the pressure, p_∞, in the upstream plenum via the expression

$$(p_\infty - p(X))/\tfrac{1}{2}\rho V^2 = (X/D)f + K_p \qquad (7)$$

where f is the friction factor. The quantity, K_p, is the incremental pressure loss coefficient. It takes account of the losses associated both with the entry of the flow into the tube and with the hydrodynamic development which occurs within the tube.

Values of K_p were determined for both single-tube and imbalanced two-tube operation. For the single tube, the measured K_p values were 1.66, 1.58, 1.53, 1.52, and 1.52, respectively, for Re = 5, 9, 22, 44, and 88 thousand. Flow imbalance was found to increase K_p but to a remarkably small extent. For example, for Re_2/Re_1 = 4, Re_1 = 22,000, and S/D = 1.5, the K_p value was only 3.7 percent larger than that for the single tube. The maximum imbalance effect on K_p among all of the investigated cases was about 10 percent.

Concluding Remarks

The present work appears to be the first investigation of turbulent tube-flow heat transfer and pressure drop in the presence of inlet flow skewness caused by flow imbalances between tubes which draw fluid from a common plenum. The investigated imbalances far exceeded those that may be expected in practice (even those which might occur due to a narrow plenum).

In the experiments, the test section Reynolds number was fixed at one of several preassigned values, while the flow imbalance was varied parametrically. The effect of the center-to-center distance, S, between the two competing tubes was also investigated, with S/D being varied from 1.5 to 3 to 4.5.

The heat transfer results were determined indirectly by mass transfer measurements utilizing the naphthalene sublimation

technique. In this regard, a new coating procedure was developed which enabled naphthalene to be cast on the inside of a circular tube. The pattern of fluid flow in the test section tube, just downstream of the inlet, was visualized with the oil-lampblack technique. Axial pressure distributions were measured to determine the additional losses due to the flow imbalance.

Practically significant effects of the flow imbalance on the axial distribution of the Sherwood number were encountered only at the smallest of the investigated intertube spacings, i.e., $S/D = 1.5$. Even for that case, the effects were moderate except at very large imbalances. For example, for a flow imbalance ratio of two, which is by no means small from the standpoint of practice, the largest imbalance-related changes did not exceed 7 percent.

The pressure drop information was presented in terms of a coefficient, which reflects the losses associated with the entry of the flow into the tube and with its hydrodynamic development. For all of the investigated cases, the imbalance-related changes in the loss coefficient were less than 10 percent.

The issues of pressure drop balancing and the consequent flow redistribution among the tubes of a multitube array are beyond the scope of the paper.

Acknowledgment

The research reported here was performed under the auspices of the Office of Naval Research.

References

1 Boelter, L. M. K., Young, G., and Iversen, H. W., "An Investigation of Aircraft Heaters, XXVII—Distribution of Heat Transfer Rate in the Entrance Section of a Circular Tube," NACA Technical Note, No. 1451, 1948.

2 Mills, A. F., "Experimental Investigation of Turbulent Heat Transfer in the Entrance Region of a Circular Conduit," *Journal of Mechanical Engineering Science*, Vol. 4, 1962, pp. 63-77.

3 Lau, S. C., Sparrow, E. M., and Ramsey, J. W., "Effect of Plenum Length and Diameter on Turbulent Heat Transfer in a Downstream Tube and on Plenum-Related Pressure Losses," ASME JOURNAL OF HEAT TRANSFER, Vol. 103, 1981, pp. 415-422.

4 Sogin, H. H., "Sublimation from Disks to Air Streams Flowing Normal to Their Surfaces," ASME *Transactions*, Vol. 80, 1958, pp. 61-71.

5 Karlekar, B. V., and Desmond, R. M., *Heat Transfer*, 2d ed., West Publishing, St. Paul, Minn., 1982.

6 Gnielinski, V., "New Equations for Heat and Mass Transfer in Turbulent Pipe and Channel Flow," *International Chemical Engineering*, Vol. 16, 1976, pp. 359-368.

7 Molki, M., "Turbulent Tube-Flow Heat Transfer Coefficients in the Presence of Flow Imbalance in the Tubes of a Parallel Array," Ph.D. thesis, Department of Mechanical Engineering, University of Minnesota, Minneapolis, Minn., 1982.

A. Haji-Sheikh
Mem. ASME

M. Mashena

M. J. Haji-Sheikh

Mechanical Engineering Department,
The University of Texas at Arlington,
Arlington, Tex. 76019

Heat Transfer Coefficient in Ducts With Constant Wall Temperature

An analytical method for the numerical calculation of the heat transfer coefficient in arbitrarily shaped ducts with constant wall temperature at the boundary is presented. The flow is considered to be laminar and fully developed, both thermally and hydrodynamically. The method presented herein makes use of Galerkin-type functions for computation of the Nusselt number. This method is applied to circular pipes and ducts with rectangular, isosceles triangular, and right triangular cross sections. A three-term or even a two-term solution yields accurate solutions for circular ducts. The situation is similar for right triangular ducts with two equal sides. However, for narrower ducts, a larger number of terms must be used.

Introduction

Analytical calculation of the friction factor and the heat transfer coefficient has received considerable attention in the literature. A recent book by Shah and London [1] provides a valuable collection of the available information on this subject. This reference preempts the need for an exhaustive literature survey on the subject. Only references directly affecting the development of the present method are mentioned here.

Information on the heat transfer coefficient for hydrodynamically and thermally fully developed laminar flow in ducts are given under the condition of locally constant wall heat flux, axially constant wall heat flux with circumferentially constant wall temperature, and constant wall temperature. The computation of the heat transfer coefficient for both constant wall heat flux and the friction factor requires solution of Poisson-type partial differential equations. In problems of this type, especially for arbitrarily shaped ducts, the use of orthogonal functions introduced by Sparrow and Haji-Sheikh [2] and a similar method using a standard least squares method [3] has been successful and has received considerable attention. Other successful solution methods are based on the finite difference technique [4] and the Ritz variational procedure [5]. The computations leading to evaluation of the heat transfer coefficient under the condition of constant wall heat flux are plentiful. However, the heat transfer coefficients, under the constant wall temperature condition designated by the symbol Ⓣ in [1], are not readily available for ducts of nonelementary shape.

A simplified procedure is described for calculation of the heat transfer coefficient in thermally fully developed laminar flow in arbitrarily shaped ducts when the wall temperature is maintained constant. This procedure leads to an eigenvalue problem for determination of the average Nusselt number. The Galerkin method is used in order to complete numerical computations. The numerical values of the Nusselt number for a circular pipe was initially prepared to ascertain the feasibility of this solution method. Then the right triangular ducts, for which similar information has not been cited in the literature, are studied. Also, the data provided for isosceles triangular ducts in this study are more accurate than those available in the literature.

Analysis

The thermally fully developed condition refers to a flow condition when the temperature profile can be expressed by similar functions. Accordingly, the temperature distribution can be expressed as

$$T(X,Y,Z) = T^* + \frac{BF(X,Y)}{k}\frac{dH_b}{dZ} \tag{1}$$

in which $T^* = T_w$ is a quasi-steady-state solution, k is the thermal conductivity of the fluid, and H_b is the bulk enthalpy. The function $F(X,Y)$ is an auxiliary function which must satisfy homogeneous boundary conditions. For the problem under investigation $F(X,Y)$ equals zero along the contour of the duct. In addition, the quasi-steady-state solution, T^*, must satisfy the condition

$$\oint_s \frac{\partial T^*}{\partial n}\,ds = 0 \tag{2}$$

where n is selected along the outer normal and s is along the contour of the duct. A detailed discussion concerning this method is presented in [6].

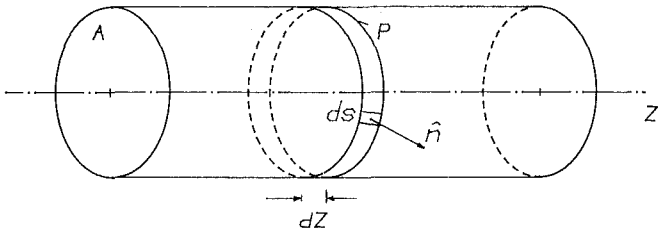

Fig. 1 Schematic of a duct, surface element, and volume element

The constant B can be evaluated if consideration is given to energy balance on a fluid element as depicted in Fig. 1.

$$\frac{dH_b}{dZ} = \oint_s k\frac{\partial T}{\partial n}\,ds \tag{3}$$

$$= \oint_s k\left[\frac{\partial T_w}{\partial n} + \frac{B}{k}\frac{dH_b}{dZ}\frac{\partial F}{\partial n}\right]ds$$

The first term in the square bracket vanishes in accordance with equation (2). Then the value of B can be expressed as

$$B = 1/\oint_s \frac{\partial F}{\partial n}\,ds \tag{4}$$

According to the definition of the bulk enthalpy for most of the liquids and ideal gases

$$H_b = \int_A \rho C_p u T dA \tag{5}$$

The value of T from equation (1) can be substituted in equation (5), then

$$H_b = \int_A \rho C_p u T_w dA + \frac{B}{k}\frac{dH_b}{dZ}\int_A \rho C_p u F dA \tag{6}$$

Contributed by the Heat Transfer Division for publication in the JOURNAL OF HEAT TRANSFER. Manuscript received by the Heat Transfer Division October 21, 1982.

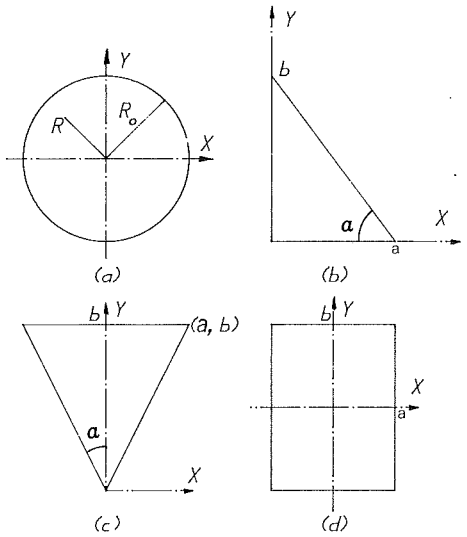

Fig. 2 Configuration of circular, right triangular, isosceles triangular, and rectangular ducts

Cognizance may be taken that $H_b = \rho C_p \bar{u} T_b A$ and $dH_b/dZ = q_w P$, where T_b is the bulk temperature, $\bar{u}$ is the average velocity, q_w is the average heat flux along the circumference, and P is the perimeter. The substitutions of the appropriate quantities for B, H_b, and dH_b/dZ in equation (6) result in the following equation

$$\rho C_p \bar{u} A (T_b - T_w) = \frac{q_w p}{k} \frac{\int_A \rho C_p u F dA}{\oint_s \left(\frac{\partial F}{\partial n}\right) ds} \tag{7}$$

The heat transfer coefficient is derived in the customary manner, that is

$$q_w = \bar{h}(T_w - T_b)$$

Equation (7), following application of the divergence theorem

$$\oint_s (\partial F/\partial n)\, ds = \int_A \nabla^2 F dA$$

and the definition of $\bar{\text{Nu}} = \bar{h} D_e/k$ reduces to

$$\int_A \left(\nabla_1^2 F + \frac{4\bar{\text{Nu}}}{\bar{D}_e^2} \frac{u}{\bar{u}} F\right) dA = 0 \tag{8}$$

where $\bar{D}_e$ is the dimensionless hydraulic diameter, that is, the ratio of D_e to an appropriate characteristic length and the coordinates in the Laplace operator are also dimensionless using the same characteristic length. The characteristic length for each geometry studied is defined later.

This is an eigenvalue problem and the Nusselt number properly appears in the eigenvalue. The computation of $\bar{\text{Nu}}$ requires the knowledge of velocity distribution. The function F can be any function which is finite, continuous and single-valued in the region representing the cross section of the duct. The first and second derivatives of F must satisfy similar conditions. Moreover, the function F must vanish on the contour of the duct. A Galerkin-type function satisfies all the conditions just mentioned and is ideally suited for this application. An additional reason for selecting a Galerkin-type function is to investigate the usefulness of the Galerkin method and its convergence behavior.

According to the Galerkin procedure [7], function $\phi = 0$ on the contour. Then the function F, selected as

$$\begin{aligned} F &= \phi[C_1 + C_2 x + C_3 y + C_4 x^2 + C_5 xy + C_6 y^2 + \ldots] \\ &= C_1 f_1 + C_2 f_2 + C_3 f_3 + \ldots \\ &= \sum_{j=1}^{M} C_j f_j \end{aligned} \tag{9}$$

unconditionally satisfies the boundary condition $F = 0$ on the contour of the duct. The functions F, ϕ, x, and y are dimensionless using a suitable characteristic length. The substitution of equation (9) in equation (8) and following the standard Galerkin procedure results in

$$\mathbf{A} + \frac{4\bar{\text{Nu}}}{D_e^2} \mathbf{B} = 0 \tag{10}$$

The elements of the matrices **A** and **B** are

Nomenclature

a,b = dimensions, Fig. 2
a_{ij}, b_{ij} = elements of matrices **A** and **B**
A = flow area of the duct
A,B = matrices
B = a constant in equations (1) and (4)
C_p = specific heat
C_j = coefficients
C_f = friction factor
d_j = elements of the array **D**
D = array of coefficients d_j, equation (14)
D_e = hydraulic diameter, $4A/P$
$\bar{D}_e$ = D_e/R_o or D_e/a
f_j = solution functions, dimensionless
F = auxiliary function, equation (1) and (9)
$\bar{h}$ = average heat transfer coefficient
H_b = bulk enthalpy
i,j = indices
k = thermal conductivity
M = number of terms
n = elemental distance along the unit normal
$\bar{\text{Nu}}$ = Nusselt number, $\bar{h}\text{De}/k$
p = pressure
P = perimenter of the duct
q_w = wall heat flux
r = cylindrical coordinate, dimensionless
R = cylindrical coordinate
R_o = radius of circular duct
Re = duct Reynolds number, $\bar{u} D_e/\nu$
s = area element on the contour of the duct
T = local temperature
T^* = quasi-steady state temperature
T_b = bulk temperature
T_w = wall temperature of the duct
u = local velocity
$\bar{u}$ = average velocity
u^* = dimensionless local velocity, $u/\left(-\frac{a^2}{\mu}\frac{\partial p}{\partial Z}\right)$
$\bar{u}^*$ = average dimensionless velocity, equation (18)
x,y,z = Cartesian coordinates, dimensionless
X,Y,Z = Cartesian coordinates
α = angle
μ = viscosity coefficient
ν = kinematic viscosity
ρ = density
ϕ = Galerkin function, dimensionless
ψ_j = elements of the array $\boldsymbol{\Psi}$
$\boldsymbol{\Psi}$ = array with elements ψ_j, equation (16)
ν = kinematic viscosity
∇ = Laplace operator, $\partial/\partial Y + \partial/\partial Z$
∇_1 = Laplace operator, $\partial/\partial y + \partial/\partial z$

$$a_{ij} = \frac{1}{A}\int_A f_i \nabla_1^2 f_j dA \tag{11a}$$

and

$$b_{ij} = \frac{1}{A}\int_A \left(\frac{u}{\bar{u}}\right) f_i f_j dA \tag{11b}$$

which can be computed numerically when a duct has an arbitrary cross section.

Results

Several examples are presented to qualify and illustrate the application of the proposed method. Further details are available in the Appendix.

Circular Duct. The first example is appropriately devoted to the well-known Graetz solution [8] for the thermally fully developed portion of the flow in a pipe, Fig. 2(*a*). The value of $u/\bar{u} = 2(1-r^2)$, $\phi = 1-r^2$, $F = \Sigma\, C_j \phi r^{2(j-1)}$, $f_j = \phi r^{2(j-1)}$, and $r = R/R_o$ is the dimensionless radius and the characteristic length is the physical radius of the pipe, R_o. Accordingly, the elements of the matrices **A** and **B** are computed using equations (11*a*) and (11*b*) as

$$a_{ij} = -(8i-4)\left(\frac{1}{i+j-1} - \frac{1}{i+j}\right) + 4(i-1)^2\left(\frac{1}{i+j-2} - \frac{2}{i+j-1} + \frac{1}{i+j}\right) \tag{12a}$$

and

$$b_{ij} = 2\left(\frac{1}{i+j-1} - \frac{3}{i+j} + \frac{3}{i+j+1} - \frac{1}{i+j+2}\right) \tag{12b}$$

It is apparent that the matrix **B** is symmetric. It can be shown that the matrix **A** is also symmetric if equation (11*a*) is integrated by parts one time and the appropriate boundary condition is used. The first eigenvalue of equation (10) now can be computed following the substitution of matrices (12*a*) and (12*b*) in equation (10). When $M=1$, the value of $\bar{Nu} = 3$ is obtained. Whereas, when M is increased to 2, the value of $\bar{Nu} = 20(1-\sqrt{2/3}) = 3.6701$ exhibits a remarkable accuracy. An excellent accuracy is achieved by selecting $M = 3$. The resulting Nusselt number is $\bar{Nu} = 3.6570$, which compares with the exact value of 3.6568.

The aforementioned example indicates that a sufficient accuracy may be obtained by using this Galerkin-type solution with a few terms. However, the next example illustrates that this is not true when the duct has a narrow profile.

Right Triangular Duct. In order to investigate the accuracy of this method as applied to a geometry which does not accept an exact analytical solution, a duct with a right triangular configuration is selected. The values of the friction factor, entrance region pressure drop, and heat transfer coefficient for axially constant heat flux for that geometry are reported by Sparrow and Haji-Sheikh [4], using the finite difference technique. Similar results, utilizing a variational method, are reported by Iqbal et al. [9]. The constant wall heat flux problem is studied in [5]. However, the value of the heat transfer coefficient for the constant wall temperature boundary condition is not reported in the literature. This value, for an isosceles right triangle, is given by Schmidt and Newell [10]. Other limited information may be deduced from [1].

For this geometry, the exact value of the velocity distribution, $u/\bar{u}$, for computation of the Nusselt number, $\bar{Nu}$, is not readily available. Preliminary to computation of the Nusselt number, the value of $u/\bar{u}$ must be determined for substitution in equation (11*b*). As a by-product of the computation of $\bar{Nu}$, the value of $u/\bar{u}$ is calculated using Galerkin's method. The right triangular duct selected for this study is depicted in Fig. 2(*b*). One side of the triangle, adjacent to the right angle, has a length designated by "*a*." This value is selected as the characteristic length for subsequent calculations.

The velocity distribution is computed using equation

$$\nabla_1^2 u^* + 1 = 0 \tag{13}$$

where $u^* = u/(-a^2/\mu\ \partial p/\partial Z)$ and u^* vanishes on the boundary of the duct. According to the standard Galerkin procedure, the value of u^* is selected as

$$u^* = \phi(d_1 + d_2 x + d_3 y + d_4 x^2 + d_5 xy + d_6 y^2 + \ldots) \tag{14}$$

Table 1 Coefficients d_j[a] for calculation of velocity distribution in right triangular ducts[b]

α	d_1	d_2	d_3	d_4	d_5	d_6	d_7	d_8
85	.222694(1)	-.183914(0)	-.133101(1)	.141166(0)	.117256(0)	.335958(0)	.144412(-1)	-.763844(-1)
80	.743024(1)	-.250532(1)	-.757888(1)	.200711(1)	.309878(1)	.347064(1)	-.180546(0)	-.197539(1)
75	.144578(2)	-.939714(1)	-.185468(2)	.794731(1)	.165814(2)	.112769(2)	-.184210(1)	-.107812(2)
70	.236608(2)	-.225868(2)	-.350061(2)	.209249(2)	.499133(2)	.256858(2)	-.765189(1)	-.350626(2)
65	.358013(2)	-.442298(2)	-.593522(2)	.455429(2)	.114171(3)	.512440(2)	-.216195(2)	-.900754(2)
60	.519319(2)	-.778601(2)	-.948419(2)	.887176(2)	.225638(3)	.951007(2)	-.495926(2)	-.202195(3)
55	.736831(2)	-.129333(3)	-.146188(3)	.161233(3)	.411016(3)	.167745(3)	-.101168(3)	-.415358(3)
50	.103686(3)	-.208444(3)	-.220978(3)	.281233(3)	.715161(3)	.286138(3)	-.193495(3)	-.804128(3)
45	.146321(3)	-.332278(3)	-.331954(3)	.481294(3)	.121547(4)	.480192(3)	-.358015(3)	-.150316(4)

α	d_9	d_{10}	d_{11}	d_{12}	d_{13}	d_{14}	d_{15}
85	-.218138(-1)	-.372955(-1)	-.250013(-2)	-.329326(-2)	.916796(-2)	.119753(-2)	.149828(-2)
80	-.113382(1)	-.721552(0)	.555101(-1)	.661708(-1)	.440507(0)	.124111(0)	.553170(-1)
75	-.885115(1)	-.320552(1)	.464907(0)	.111953(1)	.336129(1)	.143844(1)	.341923(0)
70	-.341187(2)	-.899544(1)	.174646(1)	.644736(1)	.135025(2)	.723136(1)	.119145(1)
65	-.928636(2)	-.215894(2)	.471889(1)	.230528(2)	.406276(2)	.237906(2)	.346545(1)
60	-.209119(3)	-.476685(2)	.109650(2)	.628177(2)	.104605(3)	.617315(2)	.919708(1)
55	-.423698(3)	-.980578(2)	.238066(2)	.145306(3)	.243563(3)	.140245(3)	.222021(2)
50	-.809861(3)	-.190527(3)	.498478(2)	.305495(3)	.527247(3)	.297368(3)	.489870(2)
45	-.150119(4)	-.357090(3)	.101282(3)	.612826(3)	.108241(4)	.611293(3)	.101216(3)

[a] $d_j = d_j C_f \mathrm{Re}/2\bar{D}_e^2$

[b] Each entry in the table is multiplied by 10^n, where n is the number in parentheses.

Table 2 Computed values of C_fRe for right triangular duct using the Galerkin method

	C_fRe							
α	M = 1	M = 3	M = 6	M = 10	M = 15	M = 21	M = 28	Available Data [1]
5	73.73	57.33	52.53	50.55	49.69	49.35	49.12	49.08
10	68.69	54.63	51.04	50.24	49.98	49.93	49.90	49.96
15	64.65	53.14	51.07	50.71	50.65	50.65	50.638	50.72
20	61.47	52.50	51.40	51.28	51.26	51.26	51.253	51.32
25	59.00	52.37	51.83	51.77	51.75	51.75	51.748	51.76
30	57.16	52.50	52.20	52.15	52.13	52.13	52.129	52.14
35	55.89	52.71	52.46	52.41	52.40	52.40	52.398	52.36
40	55.15	52.88	52.61	52.57	52.56	52.56	52.558	52.52
45	54.90	52.94	52.66	52.62	52.61	52.61	52.612	52.62

Table 3 Computed value of $\bar{N}u$ for right triangular duct using Galerkin functions

	$\bar{N}u$						
α	M = 3	M = 6	M = 10	M = 15	M = 21	M = 28	Available Data [1]
5	2.22	1.69	1.50	1.46	1.46	1.46	
10	2.16	1.78	1.74	1.73	1.71	1.70	
15	2.179	1.965	1.963	1.913	1.893	1.896	
20	2.249	2.154	2.099	2.051	2.048	2.048	
25	2.356	2.291	2.191	2.169	2.165	2.164	
30	2.480	2.366	2.268	2.258	2.250	2.250	
35	2.598	2.399	2.328	2.317	2.310	2.309	
40	2.684	2.411	2.368	2.351	2.346	2.345	
45	2.715	2.414	2.382	2.361	2.358	2.357	2.34

in which $\phi = xy[b/a - (b/a)x - y]$, $x = X/a$, and $y = Y/a$. The coefficients $d_1, d_2, \circ\circ\circ, d_M$ must now be determined by solving the following system of M equations,

$$\mathbf{A} \circ \mathbf{D} = \mathbf{\Psi} \tag{15}$$

where $\mathbf{D}$ is the vector of coefficients, and vector $\mathbf{\Psi}$ has elements

$$\psi_j = -\frac{1}{A}\int_A f_j dA \tag{16}$$

and f_j is dimensionless. The solution of equation (15) results in the evaluation of coefficients, d_j. In the subsequent analysis, the matrix $\mathbf{A}$ is used for computation of the Nusselt number. Once the value of d_j is in hand, the value of the friction factor, C_f, and a relation for $u/\bar{u}$ can be defined. That is

$$C_f \mathrm{Re} = 2\bar{D}_e^2/\bar{u}^* \tag{17}$$

where

$$\bar{u}^* = \frac{1}{A}\int_A u^* dA = -\sum_{j=1}^{M} d_j \psi_j \tag{18}$$

Moreover

$$u/\bar{u} = u^*/\bar{u}^* = \frac{C_f \mathrm{Re}}{2\bar{D}_e{}^2}\sum_{j=1}^{M} d_j f_j \tag{19}$$

The function of f_j is dimensionless and is an algebraic product of the Galerkin function, ϕ, and appropriate terms of the two-dimensional Taylor series, equation (14).

The coefficients $d_1, d_2, \ldots, d_{15}$, for $M = 15$, computed at various angles α, with 5 deg increments, between 45 and 85 deg, are presented in Table 1. Then, equation (17) is utilized for computation of the friction factor C_f. The values of C_fRe, using the same angular increments, are tabulated in Table 2. In order to investigate the convergence behavior of the Galerkin method as applied to problems of this type, different values of M are selected, and the corresponding values of C_fRe are computed. The calculation of C_fRe is a by-product of this investigation and is not the essential goal of this research, which is the development of a simple solution method for computation of the Nusselt numbers for ducts with arbitrary cross section having constant wall temperature boundary condition. However, the accuracy in the value of C_fRe influences the value of $u/\bar{u}$, equation (19), which is in turn used for calculation of the Nusselt number. As observed, the values of C_fRe, when $M=1$, obtained from equation $C_f\mathrm{Re} = 320\,[1 + (b/a)^2] \,/\, [1 + b/a + (1 + (b/a)^2)^{1/2}]^2$ are at best crude. When $M = 3$, a reasonable accuracy is obtained for angles near 45 deg. As the size of the angle α reduces, larger values of M are needed for an acceptable accuracy. When $\alpha = 5$ and 10 deg, $M > 15$, a double precision computer code is used for the entries in Table 2. Inasmuch as the available data are also approximate, the agreement between the present result and those of [1] is remarkably good. For angles $\alpha > 15$ deg and $M = 15$, the single precision code and double precision code produced identical values and are presented in Tables 2 and 3.

From this point, the computation follows the procedure described earlier in this paper; that is, to utilize equation (10) for calculation of the Nusselt number. Equation (11*b*) is employed for determination of the elements of Matrix $\mathbf{B}$. The elements of matrix $\mathbf{A}$ are computed for calculation of $u/\bar{u}$, stored in the computer memory and reused for calculation of the Nusselt number. The surface integrals are computed by numerical quadrature. The behavior of the determinant of the matrix $\mathbf{A} + (4\bar{N}u/\bar{D}_e^2)\mathbf{B} = 0$ is of special interest for computation of the eigenvalue. When angle α is small and/or M is large, special care is necessary. The matrix had to be scaled upward so that the absolute value of the aforementioned determinant does not become small beyond the capability of the available digital computer. The need for a double precision computer code is necessary when $M > 15$. The values of the Nusselt number computed by this procedure are tabulated in Table 3. The only reliable data observed in the literature also appears in the same table. At $\alpha = 45$ deg, the present results for $M > 3$ are in good agreement with the available data. As the angle α decreases, the value of the Nusselt number asymptotically approaches that of an isosceles triangle with its apex angle equal to α. When $\alpha = 0$, it is 1/8 of $\bar{N}u = 7.5407$ for a parallel plate duct.

Isosceles Triangular Ducts. The computation of the Nusselt number follows the same procedure as described for right triangular ducts except for $\phi = (y^2 - b^2x^2)(y - b)$ which vanishes on the boundary of this duct. Due to symmetry, Fig. 2(*c*), the terms with odd exponent on "x" are neglected. Therefore, a solution using, for example, 12 terms is comparable in accuracy to a solution obtained for right triangular ducts using 21 terms. The value of the Nusselt number when the number of terms $M = 16$ and 25 are computed and presented in Table 4. The data presented in this table for $M = 25$ are considerably more accurate than those reported in the literature [1]. Further discussion on the accuracy of the results appears in a later section.

Rectangular Ducts. The rectangular ducts at various aspect ratios are selected mainly to investigate the accuracy of this method as the ducts assume narrow profiles. Accurate exact values of the friction factor and the Nusselt number at various aspect ratios are well documented in the literature [1]. Some approximate methods are often incapable of dealing with geometries which have sharp corners. However, the Galerkin functions selected for this study vanish at the exact boundary of the duct. It is anticipated that, for ducts with narrow configurations, the velocity and temperature profile at the central portion of the duct in the direction of the larger dimension are somewhat flat. Therefore, a polynomial of a higher order is required to approximate the variation of velocity and temperature in the direction of the longer

Table 4 Computed values of C_fRe and $\bar{N}u$ for isosceles triangular ducts using Galerkin functions

α	M = 16		M = 25		Reference (1)	
	C_fRe	$\bar{N}u$	C_fRe	$\bar{N}u$	C_fRe	$\bar{N}u$
2.5	49.123	1.453	49.063	1.468		
5	49.903	1.715	49.900	1.702	49.896	1.61
7.5	50.652	1.899	50.651	1.900		
10	51.289	2.055	51.289	2.053	51.288	2.00
12.5	51.823	2.177	51.822	2.175		
15	52.262	2.272	52.262	2.272	52.260	2.26
20	52.889	2.405	52.889	2.405	52.888	2.39
25	53.229	2.475	53.229	2.475	53.228	2.45
30	53.333	2.496	53.333	2.495	53.332	2.47
35	53.242	2.478	53.242	2.479	53.244	2.45
40	52.991	2.430	52.991	2.430	52.992	2.40
45	52.611	2.357	52.610	2.357	52.612	2.34
50	52.130	2.264	52.198	2.256		
55	51.574	2.155	51.579	2.152		
60	50.971	2.032	50.981	2.027	50.976	2.00
65	50.350	1.902	50.361	1.892		
70	49.743	1.77	49.756	1.74		
75	49.189	1.64	49.214	1.60	48.904	1.50
80	48.73	1.56	48.75	1.48		
85	48.43	1.48	48.44	1.39		

Table 5 Computed values of C_fRe and $\bar{N}u$ for rectangular ducts using Galerkin functions

b/a	M = 10		M = 15		Reference (1)	
	C_fRe	$\bar{N}u$	C_fRe	$\bar{N}u$	C_fRe	$\bar{N}u$
1	56.910	2.977	56.909	2.977	56.908	2.976
2	62.195	3.392	62.193	3.392	62.192	3.391
3	68.360	3.957	68.360	3.958	68.359	3.956
5	76.294	4.288	76.285	4.828	76.282	
8	82.368	5.591	82.346	5.593	82.339	5.597
10	84.734	5.903	84.687	5.907	84.676	
20	90.289	7.039	90.012	7.084	89.908	

dimension of a duct. Despite the aforementioned undesirable situation, the polynomials are selected because they yield to simpler algebraic manipulations and exact integrations. Accordingly, all integrations for isosceles triangular and rectangular ducts are performed analytically. The computation procedure is identical to the method discussed for triangular geometries except $\phi = (x^2-1)(y^2-b^2/a^2)$ and only the terms of the polynomial having even exponents are retained. The characteristic length selected for this geometry is "a." The values of the friction factor and the Nusselt number using $M = 10$ and 15 terms are computed and presented in Table 5. The exact solution also appears in the same table.

Discussion and Remarks

A simple Galerkin-type solution is introduced for calculation of the Nusselt number for laminar fully developed flow in the duct with arbitrary cross sections. The Galerkin functions are used because they are highly suitable for the solution method presented in this paper. The Galerkin-type solution described herein provides accurate solutions for the Nusselt number, with a few terms, only for compact geometries. The required number of terms, M, will be large for geometries with narrow profiles.

The value of $M = 15$ is satisfactory for calculation of C_fRe, Table 2, especially when $\alpha > 10$ deg. The calculations for the values of the Nusselt number, when $M = 28$, Table 3, are estimated to be accurate within 0.1 percent for $\alpha > 15$ deg and the error gradually decreases as the value of α increases. When $\alpha = 5$ deg, the error is within 1 percent. This estimation of the error is based on the difference between the results obtained when $M \leq 28$. However, a comparison with the result obtained for rectangular ducts, see Table 5, indicate that this estimation is conservative and that only the last digit of the entries in Table 3 are somewhat larger than the actual values. The results for rectangular ducts are also used in order to study the accuracy of the solutions obtained for isosceles triangular geometries. The accuracy of the Nusselt number computed for rectangular ducts using 15 terms is comparable to that for isosceles triangular ducts with 25 terms with comparable aspect ratios. However, the solution for a right triangular duct with 28 terms has an accuracy similar to a solution obtained for a rectangular duct using 10 terms and having similar aspect ratios. Therefore, the data presented for isosceles triangular geometry when $M = 25$ are accurate to all digits except possibly for narrow profiles which may have small errors in the last digit. The data in Table 4 for $\alpha = 2.5$ and 5 deg can be used for right triangular ducts when $\alpha = 5$ and 10 deg with error less than .003. The value of the Nusselt number in most cases decreases as M increases except in some narrow ducts.

The IBM 4341 digital computer is used in this study for calculation of the friction factor and the Nusselt number in the right triangular ducts. All remaining computations are carried out on a HP-85 minicomputer.

References

1 Shah, R. K., and London, A. L., *Laminar Flow Forced Convection in Ducts*, Supplement 1 to *Advances in Heat Transfer*, Academic Press, Inc., New York, 1978.

2 Sparrow, E. M., and Haji-Sheikh, A., "Flow and Heat Transfer in Ducts of Arbitrary Shape With Arbitrary Thermal Boundary Conditions," ASME JOURNAL OF HEAT TRANSFER, Vol. 88, 1966, pp. 351-358.

3 Shah, R. K., "Laminar Flow Friction and Forced Convection Heat Transfer in Ducts of Arbitrary Geometry," *International Journal of Heat and Mass Transfer*, Vol. 18, 1975, pp. 849-862.

4 Sparrow, E. M., and Haji-Sheikh, A., "Laminar Heat Transfer and Pressure Drop in Isosceles Triangular, Right Triangular and Circular Sector Ducts," ASME JOURNAL OF HEAT TRANSFER, Vol. 87, 1965, pp. 426-427,

5 Iqbal, M., Aggarwala, B. D., and Fowler, A. G., "Laminar Combined Free and Forced Convection in Vertical Non-Circular Ducts Under Uniform Heat Flux," *International Journal of Heat and Mass Transfer*, Vol. 12, 1969, pp. 1123-1139.

6 Mashena, M., "An Integral Solution of the Moving Boundary Problems," Ph.D. thesis, University of Texas at Arlington, in progress.

7 Kantorovich, L. V., and Krylov, V. I., *Approximate Methods of Higher Analysis*, John Wiley, New York, 1964.

8 Brown, G. M., "Heat or Mass Transfer in a Fluid in Laminar Flow in a Circular or Flat Conduit," *AIChE Journal*, Vol. 6, 1960, pp. 179-183.

9 Iqbal, M., Khatry, A. K., and Aggarwala, B. D., "On the Second Fundamental Problems of Combined Free and Forced Convection Through Noncircular Ducts," *Applied Scientific Research*, Vol. 26, 1972, pp. 183-208.

10 Schmidt, F. W., and Newell, M. E., "Heat Transfer in Fully Developed Laminar Flow Through Rectangular and Isosceles Triangular Ducts," *International Journal of Heat and Mass Transfer*, Vol. 10, 1967, pp. 1121-1123.

APPENDIX

Nomenclature of Indices

i,j,k,m,n	indices
l	$m_i+n_i+m_j+n_j$
μ_1	$m_i+m_j+m_k$
ν_1	$n_i+n_j+n_k$
ν	$\mu_1+\nu_1$

Description

The elements of the matrices **A** and **B** for triangular geometries are provided. The elements of the matrix **A** are also useful for computation of the Nusselt number under the condition of constant heat flux using the Galerkin method. The relation

$$\frac{1}{A}\int_A f_i \nabla_1{}^2 f_j = -\frac{1}{A}\int_A \nabla_1 f_i . \nabla_1 f_j$$

simplifies the integration process. When $f_i = x^{m_i}y^{n_i}\phi$ and $f_j = x^{m_j}y^{n_j}\phi$, the elements of the matrices **A** and **B** for triangular ducts studied are defined.

Right Triangular Ducts. For the following calculations Fig. 3 is used.

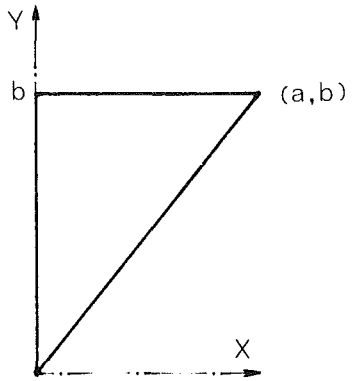

Fig. 3 Coordinates of the right triangular duct

$$a_{ij} = -2\left(\frac{b}{a}\right)^{n_i+n_j+4}\left[\frac{(m_i+1)(m_j+1)}{m_i+m_j+1} - \frac{2m_im_j+3(m_i+m_j)+4}{m_i+m_j+2} + \frac{(m_i+2)(m_j+2)}{m_i+m_j+3}\right]\left(\frac{1}{l+6} - \frac{2}{l+5} + \frac{1}{l+4}\right) - 2\left(\frac{b}{a}\right)^{n_i+n_j+2}\left(\frac{G_1}{m_i+m_j+3} - \frac{G_2}{m_i+m_j+4} + \frac{G_3}{m_i+m_j+5}\right)$$

where

$$G_1 = \frac{n_in_j+2(n_i+n_j)+4}{l+6} - \frac{2n_in_j+3(n_i+n_j)+4}{l+5} + \frac{n_in_j+(n_i+n_j)+1}{l+4}$$

$$G_2 = \frac{2n_in_j+3(n_i+n_j)+4}{l+6} - \frac{4n_in_j+4(n_i+n_j)+2}{l+5} + \frac{2n_in_j+n_i+n_j}{l+4}$$

$$G_3 = \frac{n_in_j+n_i+n_j+1}{l+6} - \frac{2n_in_j+n_i+n_j}{l+5} + \frac{n_in_j}{l+4}$$

$$b_{ij} = 2\sum_{k=1}^{M} d_k\left(\frac{b}{a}\right)^{\nu_1+6}\left[\frac{1}{\mu_1+4} - \frac{3}{\mu_1+5} + \frac{3}{\mu_1+6} - \frac{1}{\mu_1+7}\right]\left[\frac{1}{\nu+11} - \frac{3}{\nu+10} + \frac{3}{\nu+9} - \frac{1}{\nu+8}\right]$$

$$\psi_j = 2\left(\frac{b}{a}\right)^{n_j+2} / (m_j+2)(m_j+3)(m_j+n_j+4)(m_j+n_j+5)$$

Isosceles Triangular Ducts. For the following calculations Fig. 2(*c*) is used.

$$a_{ij} = -2\left(\frac{b}{a}\right)^{n_i+n_j+6}\left[\frac{m_im_j}{m_i+m_j-1} - \frac{2(m_im_j+m_i+m_j)}{m_i+m_j+1} + \frac{(m_i+2)(m_j+2)}{m_i+m_j+3}\right]\left(\frac{1}{l+6} - \frac{2}{l+5} + \frac{1}{l+4}\right) - 2\left(\frac{b}{a}\right)^{n_i+n_j+4}\left(\frac{G_1}{m_i+m_j+1} - \frac{G_2}{m_i+m_j+3} + \frac{G_3}{m_i+m_j+5}\right)$$

where

$$G_1 = \frac{(n_i+3)(n_j+3)}{l+6} - \frac{(n_i+2)(n_j+3)+(n_i+3)(n_j+2)}{l+5} + \frac{(n_i+2)(n_j+2)}{l+4}$$

$$G_2 = 2\left[\frac{n_in_j+2(n_i+n_j)+3}{l+6} - \frac{2n_in_j+3(n_i+n_j)+2}{l+5} + \frac{n_in_j+n_i+n_j}{l+4}\right]$$

$$G_3 = \frac{n_in_j+n_i+n_j+1}{l+6} - \frac{2n_in_j+n_i+n_j}{l+5} + \frac{n_in_j}{l+4}$$

$$b_{ij} = 2\sum_{k=1}^{M} d_k\left(\frac{b}{a}\right)^{\nu_1+9}\left[\frac{1}{\mu_1+1} - \frac{3}{\mu_1+3} + \frac{3}{\mu_1+5} - \frac{1}{\mu_1+7}\right]\left[\frac{1}{\nu+11} - \frac{3}{\nu+10} + \frac{3}{\nu+9} - \frac{1}{\nu+8}\right]$$

$$\psi_j = 4\left(\frac{b}{a}\right)^{n_j+3} / (m_j+1)(m_j+3)(m_j+n_j+4)(m_j+n_j+5)$$

G. Klingenberg
Fraunhofer-Institut
für Kurzzeitdynamik,
Ernst-Mach-Institut (EMI-AFB),
7858 Weil an Rhein, West Germany

H. Mach
Deutsch-Französisches
Forschungsinstitut (ISL),
F-68301 Saint Louis, France

G. Smeets
Deutsch-Französisches
Forschungsinstitut (ISL),
F-68301 Saint Louis, France

Flow Field Measurements of an Unsteady Reacting Muzzle Exhaust Flow

The events associated with the discharge of a 20-mm caliber weapon have been examined in detail in order to identify and understand important features of the reacting gun muzzle flow field. The diagnostics applied involves shadowgraph and Schlieren photography, invasive pressure probes, spectroscopy for temperature measurements and Laser-Doppler velocimetry for velocity measurements. Emphasis has been on velocity measurements using two setups to determine both the axial and lateral velocity components throughout the muzzle flow field. The data clearly demonstrate the complexity of the processes involved in the unsteady flow expansion of the gun muzzle exhaust flow.

1 Introduction

The unsteady reacting muzzle flow field, produced by the compressed, hot, gas-particle mixture emptying from the gun tube, is a complex process [1, 2]. It encompasses aspects as precursor/propellant flow interactions [3, 4], the formation of an outer strong shock or blast wave interacting with the highly underexpanded supersonic jet flow commencing at the muzzle exit [4–8], turbulence [1, 4, 8], gas-particle interactions [9–12], radiation, exothermic pyrolytic reactions of the gases and/or of vaporized particles, and homogeneous gas-phase chemical reactions as well as possible heterogeneous chemical reactions causing the well-known phenomenon of muzzle flash [10–14]. The many complexities of the processes makes the gun muzzle exhaust flow a most formidable problem both theoretically and experimentally [2, 11, 15]. A detailed analysis is well beyond the present state of the art, and there is a dearth of experimental data for interpreting the complex events and for validation purposes [1, 2].

Since only some data have been taken in these reacting flow fields [14–18], this paper presents new measurements of flow properties in the muzzle exhaust flow of a 20-mm gun. The work is part of an extensive experimental program studying the flow using a variety of diagnostics [11, 19, 20]. A novel Laser-Doppler velocimeter, devised by Smeets and George [21, 22], permitted the evaluation of velocity vector projections throughout the flow field [23].

2 Experimental

Data were taken at the muzzle of a caliber 20-mm rifled gun firing normal 20 × 139, DM 1 A 1 ammunition. The propellant used was A 5020 composed of nitrocellulose with small amounts of chemical additives. The weapon has a barrel length of 1.836 m. The projectile has a weight of 120 g and a length of 91 mm. The muzzle launch velocity of the projectile was measured as 1040 ± 20 m/s. The initial exit conditions at the exit plane of the muzzle immediately after projectile launch were measured as gas pressure p = 40 MPa, gas temperature T = 1650 K, and gas velocity v = 1050 m/s.

The experimental techniques for flow and flame visualization, spectroscopic temperature and invasive pressure measurements are well established in the field of ballistics studies. They are thoroughly documented in [6, 8, 14, 16, 17]. No specific details will be given here except to mention that two different pressure probes consisting of stainless steel rods were used for invasive pressure measurements. The first needle-shaped probe connects the quartz with the flow by means of small orifices of 0.1-mm dia drilled normal to the surface thus permitting the measurements of static pressure-time histories. The second "open-end" probe of 8-mm dia is designed for Pitot-pressure measurements. The procedure for calibrating the probes using a quasi-steady, free-air jet of known pressure ratio, p_e/p_∞, is well described in [8]. Data were taken simultaneously using both probes. In order to reduce flow disturbances, the probes were symmetrically aligned to the flow direction, facing the muzzle exit, see Fig. 2. Pressure distributions were measured at several positions ranging from x = 5, y = 5 cm through x = 30, y = 10 cm, i.e., at angles of 8.5 to 65 deg [2, 11, 23]. Spectroscopic temperature measurements are based upon emission - absorption methods and Abel - inversion techniques used in-bore and upon line reversal in the erratic intermediate flash area as described in [6, 16, 17].

Since the Laser-Doppler velocimeter [21, 22] measures the velocity of flow-borne particles, the size distribution of these particles has been determined yielding a medium diameter of $\bar{D}$ = 0.9 ± 0.1 μm with a logarithmic geometrical standard deviation of σ = 0.7. Hence, particle lag was considered to be small. In order to record simultaneously both the axial and lateral velocity components v_x and v_y, the set-up shown in Fig. 1 was used. Data were taken at 45 local positions throughout the flow field using equal incident and scattering angles of θ = 45, 65, and 75 deg [20, 23]. The light scattered by the flow-borne particles was recorded by separating the imaged radiation through light pipes and feeding the signals to the two velocimeters "x" and "y" (see Fig. 1). The test

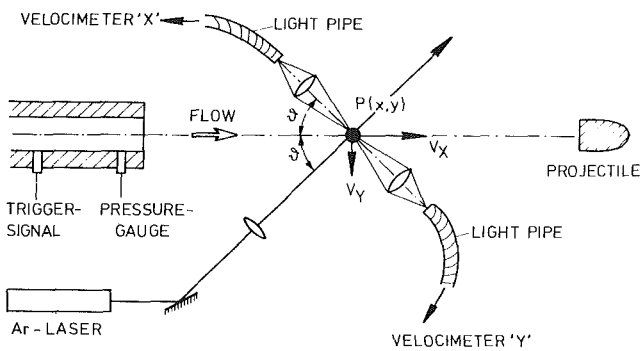

Fig. 1 Schematic of LDV-set-up for measurements of axial and lateral velocity components

Contributed by the Heat Transfer Division and presented at the AIAA/ASME Fluids Plasma Thermophysics and Heat Transfer Conference, St. Louis, Missouri, June 7–11, 1982. Manuscript received by the Heat Transfer Division September 9, 1982. Paper No. 82-HT-34.

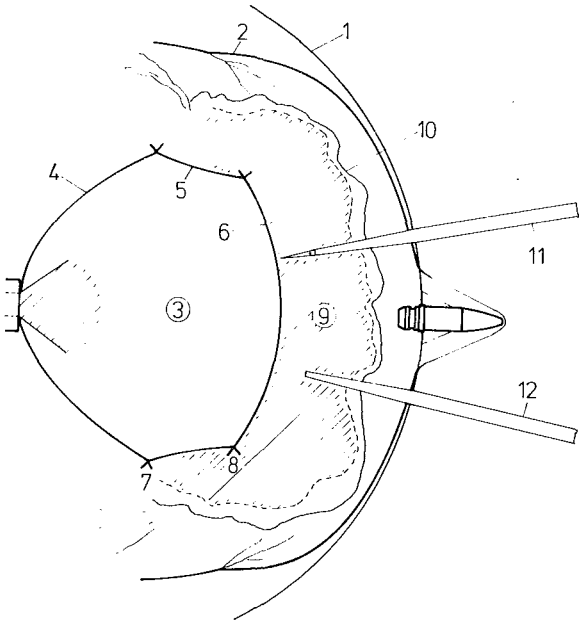

Fig. 2 Schematic of 20-mm gun muzzle blast field at $t = 400$ μs after projectile emergence:
1 Blast wave of precursor flow
2 Blast wave of propellant gas flow
3 Underexpanded supersonic flow area
4 Barrel shock
5 Inner shock front
6 Shock disk
7, 8 Triple points (Mach reflection)
9 Accumulated, restrained flow
10 Turbulent gas/air interface
11 Needle-shaped static pressure probe
12 "Open-end" Pitot pressure probe

volume along the incident laser beam was a cylinder of 8-mm length with a dia of 0.5 mm so that its x and y-projections were 4, and 6 mm, respectively. The overall time constant of these velocity recordings was 10 μs.

3 Results

3.1 Flow Development and Pressure Measurements. At the high launch velocity tested, $v_o = 1040 \pm 20$ m/s, typically two impulsive jet flows are formed about the muzzle of the 20-mm gun. The first, or precursor, is produced by the air and leaked propellant gases which are compressed and forced out of the gun tube ahead of the projectile during its in-bore travel. The second, propellant gas-particle efflux commences as the projectile separates from the muzzle. Since the energy in the propellant flow is much higher than that in the precursor, the initial flow is rapidly engulfed in the expanding propellant flow. Figure 2 presents a schematic of the 20-mm gun muzzle blast field. In addition, the immersed pressure probes are shown in Fig. 2. This drawing was deduced from a shadowgraph taken at $t = 400$ μs after projectile emergence (see also Fig. 10 for a schematic of the 20-mm gun muzzle blast field at $t = 200$ and 1000 μs).

In principle, these gun muzzle blast fields develop in a similar manner. The rapid gas release produces a strong blast wave which encapsulates the flow field. Due to the high muzzle exit pressure, an underexpanded supersonic flow region is established at the exit plane of the muzzle. This underexpanded flow area is terminated by time-varying inner shock fronts. For $t < 1.0$ ms the restraint by the outer blast wave causes the flow to coalesce in the barrel shocks, the inner shocks, and the shock disk. Also, the gas/particle flow is accumulated between the shock disk and the outer blast wave (Fig. 2). For $t \geq 1.0$ ms, this restraint diminishes with the

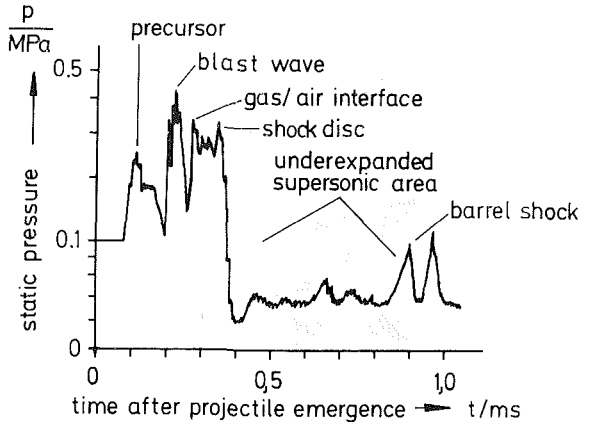

Fig. 3 Measured static pressure versus time: $x = 20$ cm; $y = 10$ cm

decay of the blast wave, permitting the flow to expand freely. The barrel shocks move toward the main flow axis, converging with the shock disk in a one-triple-point inner shock configuration (Fig. 10). Concurrently, for $t \leq 1.0$ ms the motion of the shock disk follows the trajectory of the blast wave attaining its maximum standoff from the muzzle at about 1.0 ms and is then reversed retracting upstream [11, 23].

The measured pressure histories reproduce the flow development. For example, Fig. 3 shows the static pressure versus time as recorded at position $x = 20$ cm, $y = 10$ cm.

First, the precursor flow and then the blast wave of the propellant gases arrive at the invasive pressure probe. Between the propellant blast wave and the gas-air interface the pressure decays continuously. A pressure jump in the static pressure is observed at arrival of the gas-air interface, indicating that the gas density increases. Between the gas-air interface and the shock disk, the static pressure first decreases and then shows an increase due to the arrival of the inner shock disk. The static pressure change in this flow area may be due to an reestablished expansion, which commences downstream at some distance from the shock disk. The pressure pulses in this area may be possibly due to the interaction with the intermediate flash. This would be in accordance with the earlier 7.62-mm gun firings [8]. Finally, it is noted that a rapid pressure decrease to subatmospheric pressure occurs within the underexpanded supersonic area of the propellant flow. Then the barrel shock arrives at this position. The second pressure jump arriving after the barrel shock is due to a second lateral front which was clearly seen on the shadowgraphs. This front is due to a distortion of both the barrel shock and the jet boundary and is most likely caused by the interaction with the outer turbulent flow.

3.2 Spectroscopic Temperature Measurements. The complexitity of the muzzle signature is further enhanced by the occurrence of muzzle flash producing considerable radiation in distinct areas of the muzzle blast field. Generally, there exist three main radiating flow areas [6, 14]. Due to the gas dynamics involved, these three luminous regions are separated in space and time. The first or primary flash is a low luminousity region commencing at the exit plane of the muzzle. Further from the muzzle, behind the underexpanded area of the flow, is a region of greater luminosity called the intermediate flash. Still further from the muzzle and adjacent to the intermediate flash is an extensive and very bright region called the secondary flash. However, in these particular 20-mm gun firings the secondary flash was completely suppressed by the alkali metal salts added to the propellants as chemical flash suppressants [11].

Spectroscopic temperature measurements have been made in this intermediate flash region. For example, Fig. 4 shows a time-resolved, drum-camera recording of the intermediate

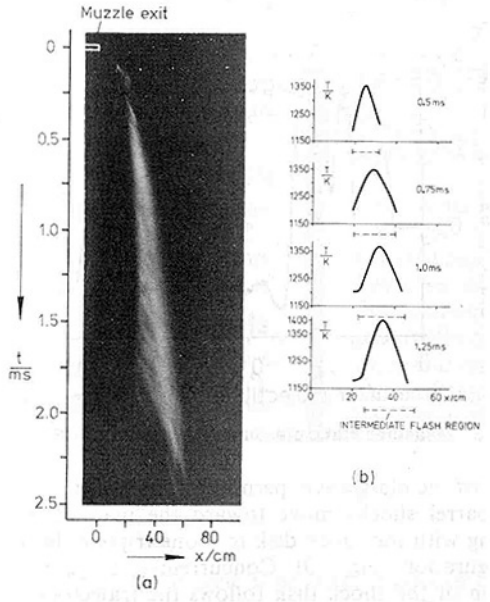

Fig. 4 (*a*) Time-resolved, drum-camera recording of the 20-mm intermediate flash (*b*) and corresponding spatial temperature distributions measured across this flash

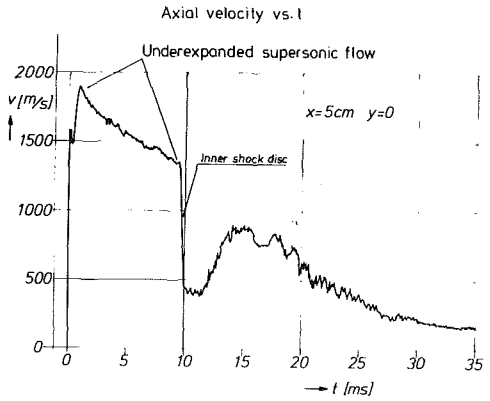

Fig. 5 Measured axial velocity versus time at $x = 5$ cm ($y = 0$)

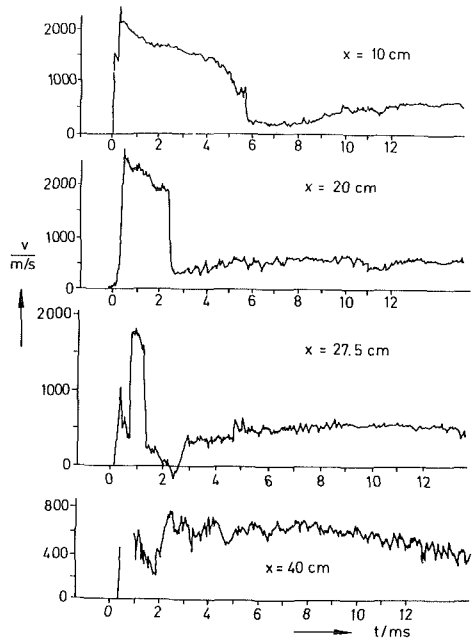

Fig. 6 Measured axial velocity versus time at $x = 10$, 20, 27.5, and 40 cm ($y = 0$)

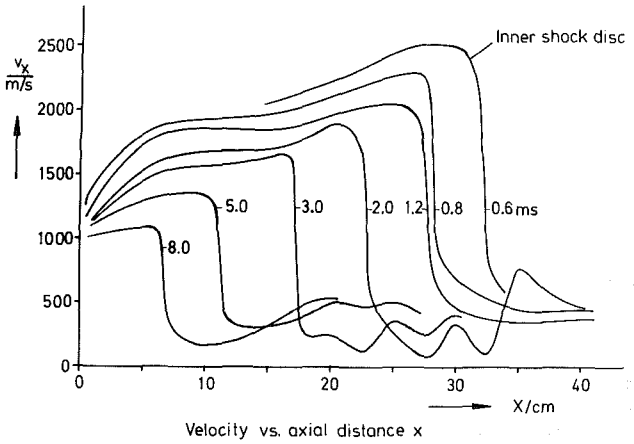

Fig. 7 Velocity versus axial distance, *x*

flash and the corresponding spatial temperature distribution, measured across this flash for $t = 0.5$, 0.75, 1.0, and 1.25 ms. These data show an increase of temperature downstream at some distance from the shock disk towards the center of the intermediate flash in accordance with earlier measurements with a 7.62-mm rifle [6]. Obviously, energy releasing processes are induced within the intermediate flash region [11, 12].

3.3 Velocity Measurements.

Data Taken in the Main Flow Axis. Axial velocity data were taken for 15 positions along the main flow axis commencing at $x = 12$ mm. For example, Fig. 5 shows the velocity versus time as recorded at $x = 5$ cm ($y = 0$) during the time interval $0 < t \leq 35$ ms, i.e., for the whole flow expansion. Due to the selected time resolution, the precursor flow and the propellant blast wave are not resolved. However, the motion of the inner shock disk and the flow behavior downstream behind this shock disk is clearly seen on Fig. 5. At early times, the gases attain high velocity of about 1950 m/s immediately after arrival of the inner shock disk. Upstream behind the retracting disk the velocity is about 1400 m/s at $t = 10$ ms. The gases are rapidly decelerated to less than 400 m/s downstream behind the shock disk. Apparently, the flow expansion is reestablished downstream at some distance from the shock disk attaining finally velocities of about 800 to 900 m/s at $t = 15$ ms. Later on the velocity decreases slowly.

A sequence of axial velocity versus time - curves is shown in Fig. 6 for positions $x = 10$, 20, 27.5, and 40 cm. These axial velocity recordings show the flow behavior along the main axis and correspond to the distribution of velocity shown in Fig. 5. Interestingly, the velocity within the underexpanded supersonic propellant flow area decays nonlinearly with time apart from the small fluctuations caused by the different particles of deviating diameters. Remarkable also is that for position $x = 27.5$ the reestablished flow expansion commencing downstream at some distance from the shock disk is disturbed. The velocity drops even below zero for $2 < t < 3$ ms, indicating a drastic change in the gas motion. As mentioned previously, this flow disturbance was also observed in 7.62-mm caliber firings [7, 8] and thought to be due to the complex energy releasing processes occuring in the intermediate flash area. The velocity decrease across the strong inner shock disk is not as steep as in the real shock front. This may be due to relaxation of flow-borne particles.

From these axial velocity profiles, the local distribution of gas velocity particularly within the underexpanded portion of the propellant flow was derived (Fig. 7). The nonlinear in-

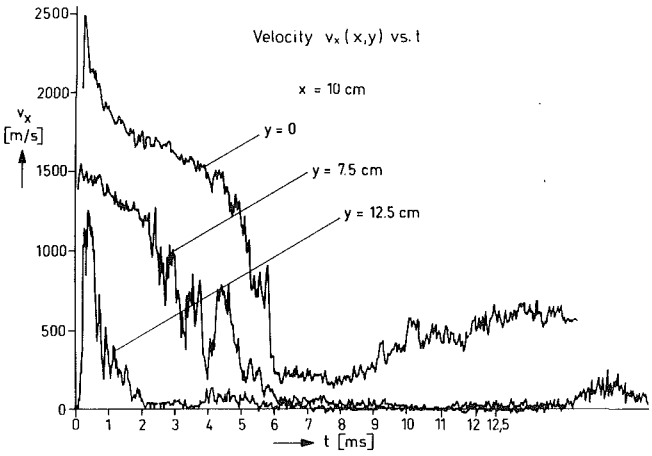

Fig. 8 Measured velocity, v_x (x, y), versus time

crease of velocity versus x up to the inner shock disk and the retarded decrease across this shock front reproduces the behavior of the axial v versus t curves.

Lateral Positions. The velocity (v_x (x, y) and v_y (x, y), versus time was recorded simultaneously at 30 lateral positions [20]. For example, Fig. 8 presents a sequence of three recordings v_x (x, y) taken at $x = 10$ cm, and $y = 0$, 7.5, and 12.5 cm. As the lateral distance to the main flow axis increases, the measuring point approaches the moving lateral shock boundaries and these inner shocks are finally passing the probe volume. These oblique shocks can be distorted by the outer turbulent gas flow. Therefore, velocity fluctuations are measured for $y \geq 7.5$ cm, Fig. 8.

The axial turbulence rate which amounts to $\sqrt{v_x'^2/\bar{v}_x} = 0.5$ was evaluated from these $v_x(x, y)$ versus time recordings and is shown in Fig. 9. However, no essential deviations for different times and locations, x, were obtained since the scatter of these data were too high.

Velocity Vector Projections. Simultaneously measurements of both the axial and lateral velocity components, v_x (x, y) and v_y (x, y), throughout the muzzle blast field in the x-as well as in the y-direction permitted the evaluation of velocity vector projections [11, 20]. In addition, the shadowgraphs taken at corresponding times were used to correlate the evaluated vector projections with the flow field development. For example, Fig. 10 shows three velocity vector projections with superimposed flow patterns, displaying three stages of the muzzle flow field development, i.e., for $t = 200$ μs, 400 μs, and 1000 μs after projectile emergence.

For $t = 200$ μs, the inner shock structure shows the initial restrained flow development due to the containment of the outer blast wave and the presence of the departing projectile. In the axial or downrange direction, the underexpanded zone of the flow is still terminated by a bow shock which forms behind the base of the departing projectile [11].

For $t = 400$ μs, the inner shock disk is fully developed; the barrel shock has moved towards the main flow axis, and the inner lateral shock between the two triple points converges. There is still the interaction with the outer blast wave restraining the flow and forcing it to coalesce in the lateral barrel shock and the inner shock front.

The schematic shown for $t = 1000$ μs displays the change of the inner shock structure to the on-triple-point, shock-barrel configuration known from free jet expansion processes, since the decaying blast wave decouples from the nearfield and the restraint of the outer strong shock ceases.

Generally, the axial velocity within the underexpanded supersonic flow area increases towards the inner shock disk.

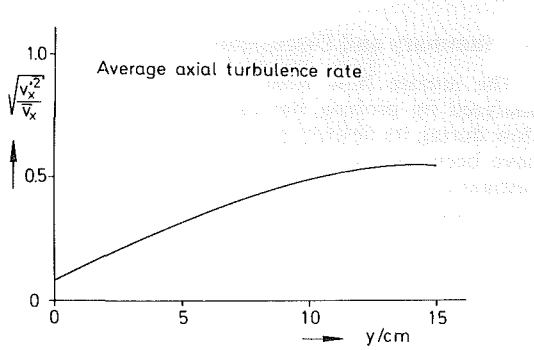

Fig. 9 Average turbulence rate versus y

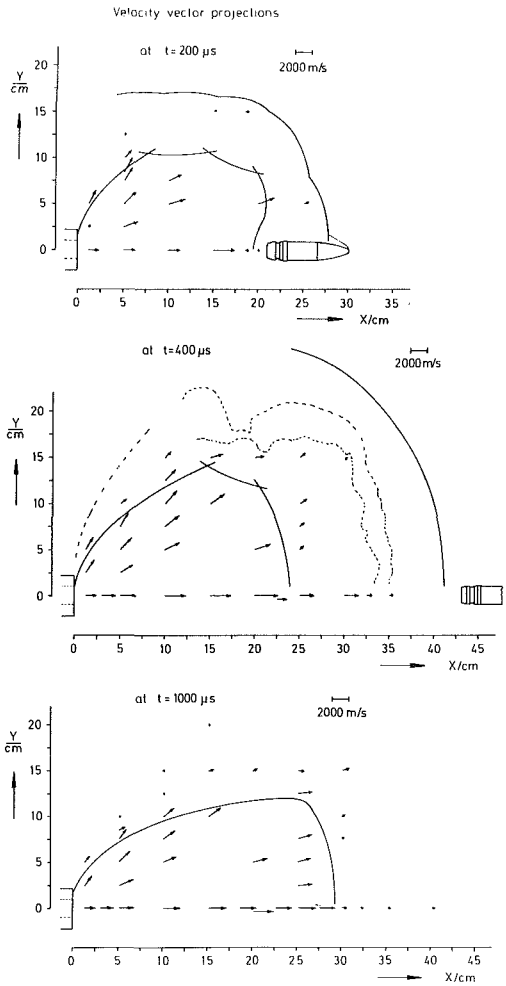

Fig. 10 Velocity vector projections at $t = 200$, 400, and 1000 μs after projectile emergence

The flow is rapidly decelerated behind this shock. The vector projections indicate the direction of the flow. Between the barrel shock and the jet boundary, the flow direction and the amount of the velocity vector changes accordingly. Also, in the downrange direction an increase of velocity between the inner shock and the gas-air interface is measured due to the reestablished flow expansion, in particular for times $t < 1$ ms. However, the velocity decreases rapidly in the proximity of the gas-air interface (see $t = 400$ μs), due to the restraint of the outer blast wave. Also, the flow disturbance in the intermediate flash region is apparent from Fig. 10 (See $t = 1000$ μs). The amount of the velocity vector decreases considerably in this radiating flow area.

4 Summary and Discussion

The muzzle flow field of the 20-mm caliber gun was analyzed by probing the expanding propellant gas-particle flow during its development for $0 < t \leq 12$ ms. The studies have been focussed on the main propellant flow areas investigating the underexpanded zone and the conditions between the inner shock disk and the outer blast wave. The results of this analysis confirm that analogy to quasi-steady free jet flow is inadequate, due to the basic unsteady nature of the propellant flow expansion. Time-varying shock contours determine the near field, controlled by the outer blast wave. Also, considerable interaction of flow and the processes involved in the intermediate flash occurs downstream behind the inner shock disk. A remarkable velocity decrease associated with an increase of gas temperature of about 250 to 300 K characterizes the flow behavior in the intermediate flash area. This may be due to shock-induced, exothermic, pyrolytic reactions of the propellant gases and/or of vaporized, flow-borne particles. The heat released by these reactions may cause the observed flow disturbances. However, more detailed information is required on the role of these particles and the interacting processes occurring within the reacting muzzle exhaust flow.

The results presented here show further the excellent potential of the novel Laser-Doppler velocimeter for determining velocity distributions in highly unsteady, two-phase flows containing large particle concentrations. The main advantage of this novel technique is the real-time recording of velocities. In the present case, a time resolution of 10 μs was selected. However, care must be taken to obtain sufficient scattered light [20].

References

1 Schmidt, E. M., "Survey of Muzzle Blast Research," *Proceedings of the 5th International Symposium on Ballistics*, Toulouse, France, April 16–18, 1981.

2 Klingenberg, G., and Banks, N. E., "Review on Interior and Transitional Ballistic Research: State of the Art of Computational and Experimental Efforts," EMI-AFB Rep. E 12/81, Weil am Rhein, Sept. 1981.

3 Klingenberg, G., "Analysis of Gun Muzzle Flash Phenomena," *Proceedings of 4th International Symposium on Ballistics*, Monterey, Calif. Oct. 26–29, 1978.

4 Schmidt, E. M., Gion, E. J., and Fansler, K. S., "Analysis of Weapon Parameters Controlling the Muzzle Blast Overpressure Field," *Proceedings of the 5th International Symposium on Ballistics*, Toulouse, France, Apr. 16–18, 1981.

5 Schmidt, E. M., and Shear, D. D., "Optical Measurements of Muzzle Blast," *AIAA Journal*, Vol. 13, No. 8, Aug. 1975.

6 Klingenberg, G., and Mach, H., "Investigation of Combustion Phenomena Associated With the Flow of Hot Propellant Gases . . . I: Spectroscopic Temperature Measurements Inside the Muzzle Flash of a Rifle," *Journal Combustion and Flame*, Vol. 27, 1976. pp. 163–176.

7 Klingenberg, G., and Schröder, G. A., " . . . II. Gas Velocity Measurements by Laser-Induced Gas Breakdown," *Journal Combustion and Flame*, Vol. 27, 1976, pp. 177–187.

8 Klingenberg, G., ". . .III: Experimental Survey of the Formation and Decay of Muzzle Flow Fields and of Pressure Measurements," *Journal Combustion and Flame*, Vol. 29, 1977, pp. 289–309.

9 Klingenberg, G., "Investigation of Multiphase Flows Encountered in Ballistics Application," EMI-AFB Rep. E 2/81, Weil am Rhein, Feb. 1981.

10 Trinks, H., and Klingenberg, G., "Gun Muzzle Blast Field Research: Multiphase Flow Aspects and Chemistry of Muzzle Flash Including Chemical Flash Suppression," *Proceedings of the 6th International Symposium on Ballistics*, Orlando, Fla., Oct. 26–29, 1981.

11 Klingenberg, G., and Heimerl, J. M., "Investigation of Gun Muzzle Exhaust Flow and Muzzle Flash," EMI-AFB Rep. 1/82, Weil am Rhein, Oct. 1982.

12 Mach, H., "Measurements of Two-Phase Exhaust Flow Parameters of a Small Caliber Gun Associated with Muzzle Flash Phenomena," *Proceedings of the 7th International Symposium on Ballistics*, The Hague, The Netherlands, Apr. 19–21, 1983.

13 Heimerl, J. M., and Klingenberg, G., "Gun Muzzle Flash and Its Suppression," Proceedings of the 7th International Symposium on Ballistics, The Hague, The Netherlands, Apr. 19–21, 1983.

14 Schmidt, E. M., "Gun Muzzle Flash and Associated Pressure," *Proceedings of the Symposium on the AIAA Thermophysics Conference* (16th), Palo Alto, Calif., June 23–25, 1981.

15 Klingenberg, G., and Banks, N. E., "Review on Interior Ballistic Research: State of the Art of Computational and Experimental Efforts," *Proceedings of the 6th International Symposium on Ballistics*, Orlando, Fla., Oct. 26–29, 1981.

16 Klingenberg, G., and Mach, H., "Experimental Study of Non-Steady Phenomena Associated With the Combustion of Solid Gun Propellants," *Proceedings of the 16th International Symposium on Combustion*, Cambridge, Mass., Aug. 15–20, 1976, The Combustion Institute, pp. 1193–1200.

17 Klingenberg, G., and Mach, H., "In-Bore Measurements of Gas Velocity and of Radial Gas Temperature Distributions," *Proceedings of the 4th International Symposium on Ballistics*, Monterey, Calif., Oct. 17–19, 1978.

18 Farmer, W. M. et al., "Laser Velocimeter Measurements of the Chronological Velocity at Selected Positions in the Muzzle Blast From a 20-mm Cannon," University of Tennessee, DAAK 40-77-C-0123, 1980.

19 Mach, H., Schafer, H. J., and Klingenberg, G., "Laser Anemometry Applied to Unsteady, Two-Phase Reacting Propellant Flow," ISL-Rep. CO 217/82, St. Louis, December 1982.

20 Mach, H., Werner, U., and Masur, H., "LDV-Measurements of the Velocity-Histories of the Muzzle Exhaust Gases of a 20 mm Gun at 45 Selected Positions," ISL Rep. R 128/81, St. Louis, Oct. 1981.

21 Smeets, G., and George, A., "Instantaneous Laser-Doppler Velocimeter Using a Fast Wavelength Tracking Michelson," *Journal Review Scientific Instrum.*, Vol. 49, 1977, p. 1589.

22 Smeets, G., and George A., "Michelson Spectrometer for Instantaneous Doppler Velocity Measurements," *Journal Phys. E: Sci. Instrum.*, Vol. 14, 1981, pp. 838–845.

23 Klingenberg, G., Mach, H., and Smeets, G., "Probing of the Unsteady Reacting Muzzle Exhaust Flow of 20 mm Gun," AIAA/ASME Third Joint Thermophysics, Fluids, Plasma and Heat Transfer Conference, St. Louis, Missouri, June, 7–11, 1982.

T. Yazaki
Research Associate,
Department of Physics,
Aichi University of Education,
Igaya-cho, Kariyashi,
448 Japan

A. Tominaga
Lecturer.

Y. Narahara
Professor.

Institute of Physics,
University of Tsukuba,
Sakuramura,
Niihari-gun,
Ibaraki-ken,
305 Japan

Large Heat Transport Due to Spontaneous Gas Oscillation Induced in a Tube With Steep Temperature Gradients

This paper describes experimental studies of heat transfer due to the oscillations of gas columns that are spontaneously induced in a tube with steep temperature gradients. The tube (~3 m in length) is closed at both ends and bent into U-shaped form at the midpoint. The temperature distribution along the tube is step-functional and symmetrical with respect to the midpoint. The warm part (closed-end sides) is maintained at room temperature and the cold one is immersed in liquid helium (4.2 K). The heat transported from the warm part to the cold is estimated from the evaporation rate of liquid helium. The heat flux by the oscillations is proportional to the square of the pressure amplitude, and the effective heat conductivity can be several orders of magnitude larger than the molecular heat conductivity of gas. The experimental results are compared with the theory of the second-order heat flux proposed by Rott and are found to be in satisfactory agreement with this.

Introduction

The oscillations of gas columns can be spontaneously generated in a long tube with steep temperature gradients leading to cryogenic systems: for example, in liquid helium transfer lines, pressure sensing lines, and vent lines. Their frequencies are normally of the order of 10 Hz (depending on the tube geometry and temperature distribution along the tube axis), and their pressure amplitudes can sometimes attain the order of 10^4Pa. The most remarkable phenomenon is the abnormal evaporation of liquid helium accompanied by the oscillations as earlier experimenters [1] sometimes experienced; there is a large amount of heat transport from the part of the tube at room temperature to the cold (4.2 K) portion. It is well known that the heat flux into a helium dewar due to the oscillations can be three orders of magnitude larger than that without oscillation. Thus, the studies of the instabilities accompanying the heat transport have recently acquired great importance for development of cryogenics. This type of oscillation, which is associated with thermally driven acoustic oscillations, has been observed not only in cryogenics [2, 3] but also in high-temperature systems [4].

The stability of the oscillation has been theoretically investigated by Kramers [5] and Rott [6, 7, 8, 9]. Rott has given the stability curves between oscillation and no oscillation, as well as frequency diagrams for helium gas taking account of a finite boundary layer thickness formed on the tube wall and using a discontinuous model for the temperature distribution. The stability curves consist of two branches; the boundary layer is thin for one branch and thick for the other.

Comparisons between theory and experiments for helium gas have been performed by von Hoffmann et al. [10] and Yazaki et al. [11, 12]. The agreement was satisfactory, and it was concluded that the boundary layer thickness on the tube wall plays an important role in characterizing the stability of the oscillation.

The heat exchange between the oscillating gas and the tube wall is related to the theory of second-order heat flux by Merkli and Thomann [13] and Rott [14]. Merkli and Thomann have investigated the thermal effects produced by standing acoustic waves using a tube closed at one end with a rigid barrier and at the other end by a harmonically vibrating piston for an initially uniform temperature distribution. They have numerically given the distribution of the local time-averaged, second-order heat flux penetrating into the tube wall. It was found that not only heating occurs near the closed end where the velocity node exists, but also that cooling occurs near the midpoint (at the pressure node). Merkli and Thomann have experimentally verified these thermal effects. More general theory, which is closely related to our experiments, has been given by Rott [14]. His theory shows that large axial heat transport occurs in the vicinity of steep temperature gradients in the gas oscillating tube.

Relatively little experimental work has been reported on the abnormal heat transport due to spontaneous oscillations. Banister [15] measured the heat flux into a helium dewar during oscillations. However, due to unknown parameters, e.g., the temperature distribution and boundary layer thickness at the tube wall, the experimental results were not compared with the theory.

In order to take these parameters into account, a tube closed at both ends which is bent into a U-shaped form at the midpoint was used in our experiments. A step function and symmetrical temperature distribution with respect to the midpoint is established by external means as shown in Fig. 1. The warm part ($L \gtrsim |x| \gtrsim l$) is maintained at room temperature and the cold ($|x| \lesssim l$) is immersed in liquid helium (4.2 K). For proper conditions, the gas column (helium gas) spontaneously oscillates with considerable amplitude and liquid helium begins to evaporate. The effective heat conductivity proposed by Rott is estimated from measurements of the evaporation rate of helium. The pressure amplitude-dependence of the evaporation rate (heat transport) due to the oscillations was experimentally determined and order-of-magnitude comparisons are made between experimental and theoretical values of the effective heat conductivities.

Experimental Apparatus and Procedure

Figure 2 shows the experimental apparatus. The warm parts

Contributed by the Heat Transfer Division for publication in the JOURNAL OF HEAT TRANSFER. Manuscript received by the Heat Transfer Division June 1, 1982.

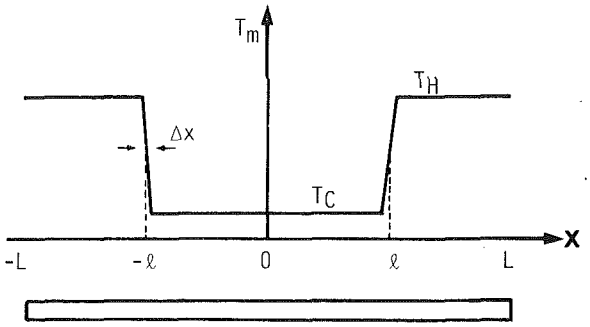

Fig. 1 Temperature distribution along the tube closed at both ends

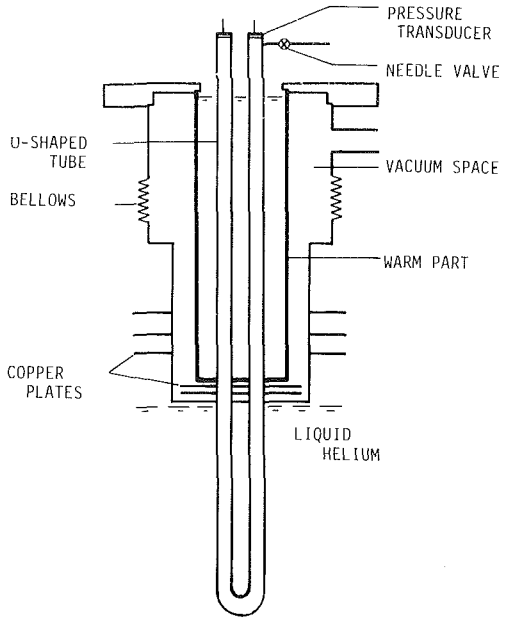

Fig. 2 A schematic drawing of the experimental apparatus

of the tube are immersed in vacuum pump oil which is kept at room temperature by several heaters wound around the copper jacket. The jacket is vacuum-insulated from the liquid helium reservoir. The cold part of the tube, which is smoothly joined by a U-shaped brass attachment at $x = 0$, is immersed in liquid helium. The length, Δx, with a steep temperature gradient at $x = l$, is 70 mm. The apparatus in Fig. 2 is inserted into a double pirex glass dewar subcooled with liquid nitrogen. Thus, we could establish a nearly step function temperature distribution as shown in Fig. 1. The top ends of the tube are closed by rigid and small semiconductor pressure transducers for measurements of the mean and acoustic pressures. The evaporation rates of liquid helium were measured using a flow meter made of a spiral copper tube. The following U-shaped tubes (stainless steel; 0.3 mm wall thickness) were used in our experiments

$$(a)\ r_0 = 1.2\ \text{mm},\ L - l = 1.0\ \text{m}$$

$$(b)\ r_0 = 2.2\ \text{mm},\ L - l = 1.0\ \text{m}$$

Experiments for $\xi (= (L-l)/l) = 2$ and 3 were performed for both tubes.

When helium gas is gradually poured into the tube through a needle valve (see Fig. 2), the gas columns become unstable above a critical value of P_m (mean pressure), and pressure oscillations with finite amplitudes are spontaneously generated. The wave forms of the pressure fluctuations with small amplitudes ($\sim 10^2$Pa) observed at the closed ends are normally sinusoidal,[1] as shown in Fig. 3. These correspond to the fundamental, which has a pressure node at $x = 0$. The critical values of P_m vary as the tube inner radius and ξ are changed. Rott [7] has introduced dimensionless variables, $|\eta_c|$ and α, in order to characterize the stability of the oscillation; $|\eta_c|$ is the ratio of the tube inner radius to the Stokes boundary layer thickness at the cold part, ($\sqrt{\nu_c/\omega}$,) and

[1] As reported by Yazaki et al. [16], for small ξ it is possible that higher harmonics are generated at left-hand branches of the stability curves so that the wave forms are a superposition of sinusoidal waves. Experiments presented here were performed in the regions where only the fundamental was excited.

Nomenclature

a = speed of sound
C_p = specific heat at constant pressure
d = reference location, see Fig. 5
E_2 = enthalpy increment
h = heat of vaporization
J_0, J_1 = the zeroth and the first-order Bessel functions
K_{eff} = effective heat conductivity
k = heat conductivity of gas
L = tube length
l = location of temperature jump, see Fig. 1
$\dot{m}$ = evaporation rate during oscillations
$\dot{m}_o$ = natural evaporation rate
P = pressure
Q_{ex} = heat flux into dewar, equation (1)
Q_2 = axial second-order enthalpy flux over the whole tube cross section
q_2 = second-order heat flux to the tube wall per unit area
r_0 = tube inner radius
r = radial coordiniate
S = particle displacement
t = time
T = temperature
T_H, T_C = mean temperature at warm, cold parts
T_1, T_2 = first- and second-order temperature
u_1 = the axial core velocity
u_1 = the axial velocity
x = axial coordinate, see Fig. 1
x' = axial coordinate, see Fig. 5
α = temperature ratio, T_H/T_C
β = constant value
γ = specific heat ratio
Δx = distance of temperature jump, see Fig. 1
δ = boundary layer thickness, $\sqrt{\nu/\omega}$
$|\eta|$ = the ratio of tube inner radius to boundary layer thickness, r_0/δ
λ = dimensionless frequency, $\omega l/a$
μ = viscosity coefficient
ν = kinematic viscosity
ξ = the ratio of warm length to cold length
ρ = density
ρ_0 = mean density at $T_0\left(=\dfrac{T_H+T_C}{2}\right)$, see Fig. 5
ρ_l = liquid density
ρ_v = vapor density
σ = Prandtl number
ω = angular frequency

Subscripts and Superscripts

C = cold part
H = warm part
m = mean value
1 = first-order
2 = second-order
$-$ = time average
$\langle\rangle$ = radial average
$\sim$ = complex conjugate
Re = real part
Im = imaginiary part

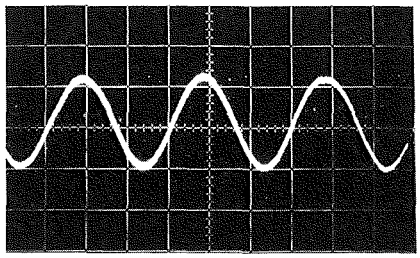

Fig. 3 Typical wave-forms of pressure fluctuations observed at the closed end of the tube

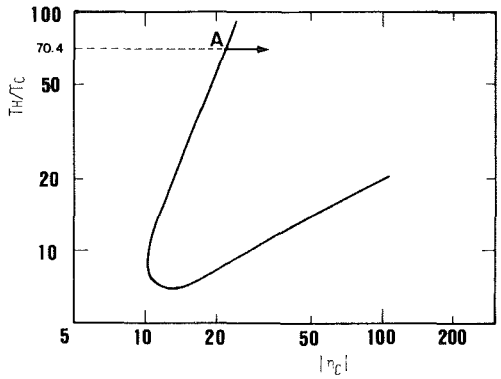

Fig. 4 Stability curve ($\xi = 2$) for helium gas calculated by Rott: temperature ratio, T_H/T_C, versus $|\eta_c| = r_0\sqrt{\omega/\nu_c}$. The critical value of $|\eta_c|$ at the point A obtained in experiments is 22.6.

α is the temperature ratio, T_H/T_C. Figure 4, for example, shows the numerical stability curve for $\xi = 2$ by Rott. The critical values of $|\eta_c|$, and the dimensionless frequency parameter λ_c ($= \omega l/a_c$) obtained in experiments for (*a*) and (*b*) are shown in Table 1 for pressure amplitudes in the range 27–100 Pa. We can obtain larger values of $|\eta_c|$ for a constant temperature ratio (α = 70.8) by decreasing the boundary layer thickness through the mean density. Pressure amplitudes abruptly increase for a slight variation of $|\eta_c|$ near the stability curves as shown in Table 2. Therefore, we are able to determine the pressure amplitude-dependence of the heat transport due to the oscillations.

Heat transfer into the helium dewar, due to oscillations, is determined by

$$Q_{ex} = h(\dot{n} - \dot{n}_o) \tag{1}$$

where h is the heat of vaporization of helium at 4.2 K (82 J/mol). The evaporation rate of helium during oscillations, $\dot{n}$(mol/s), included several other mechanisms of heat transfer besides the oscillations: for example, radiative heat transfer from the top flange (300 K), conductive heat transfer by the undisturbed gas and the tube wall. The effect of radiation was reduced by inserting copper plates as heat shields (see Fig. 2). The rate, $\dot{n}_o$, without oscillations, which is very small ($\sim 10^{-4}$mol/s) compared with that due to oscillations, is attributed to these mechanisms. Thus, Q_{ex} gives the heat flux accompanied by spontaneous oscillations only.

Table 1 Experimental data for critical values, $|\eta_c|$ and $\lambda_c = \omega l/a_c$

r_0 (mm)	L-ℓ (m)	ξ	$\lvert\eta_c\rvert$	λ_c
1.2	1	2	22.6	1.14
2.2	1	2	22.6	1.16
1.2	1	3	27.5	1.01
2.2	1	3	28.0	1.01

Table 2 Experimental data

ξ	r_0 (mm)	P_m (10^3Pa)	ω (s-1)	P_1 (Pa)	$\lvert\eta_c\rvert$	Q_{ex} (10^{-3}W)	K_{eff} (W·m^{-1}·K^{-1})
2	1.2	14.1	267	293	23.9	3.3	3.1 X 10^{-2}
2	1.2	14.7	265	378	24.3	5.1	5.4 X 10^{-2}
2	1.2	15.2	262	462	24.6	7.4	8.3 X 10^{-2}
2	1.2	15.5	261	510	24.7	8.6	1.0 X 10^{-1}
2	1.2	15.8	260	551	24.9	9.8	1.2 X 10^{-1}
2	1.2	16.3	258	637	25.3	12.7	1.6 X 10^{-1}
2	1.2	16.6	256	677	25.4	13.6	1.9 X 10^{-1}
2	1.2	17.3	254	801	25.8	19.9	2.7 X 10^{-1}
2	1.2	17.7	253	874	26.1	23.4	3.3 X 10^{-1}
2	1.2	18.3	251	979	26.4	28.0	4.4 X 10^{-1}
2	1.2	19.0	249	1069	26.7	34.1	5.3 X 10^{-1}
2	1.2	19.6	247	1216	27.1	42.7	7.1 X 10^{-1}
2	1.2	20.5	245	1430	27.6	58.3	1.0
2	1.2	21.0	244	1506	27.9	67.0	1.1
2	2.2	4.21	269	118	24.0	5.9	1.8 X 10^{-2}
2	2.2	4.44	268	162	24.6	10.4	3.6 X 10^{-2}
2	2.2	4.61	266	185	24.9	13.3	4.9 X 10^{-2}
2	2.2	4.75	264	213	25.3	17.3	6.6 X 10^{-2}
2	2.2	4.94	263	245	25.7	23.4	9.3 X 10^{-2}
2	2.2	5.12	260	282	26.0	29.4	1.2 X 10^{-1}
2	2.2	5.33	259	320	26.5	37.5	1.7 X 10^{-1}
2	2.2	5.50	256	350	26.7	43.2	2.0 X 10^{-1}
2	2.2	5.68	254	381	27.1	50.0	2.5 X 10^{-1}
2	2.2	5.85	251	414	27.3	57.2	2.9 X 10^{-1}
2	2.2	6.01	249	478	27.6	75.1	4.0 X 10^{-1}
2	2.2	6.18	247	530	27.9	95.8	5.0 X 10^{-1}
2	2.2	6.41	246	583	28.3	121.0	6.4 X 10^{-1}
2	2.2	6.53	246	609	28.6	136.2	7.2 X 10^{-1}
2	2.2	6.72	245	655	28.9	160.2	8.6 X 10^{-1}
2	2.2	6.86	244	677	29.2	180.8	9.4 X 10^{-1}
2	2.2	7.17	243	743	29.8	211.5	1.2
3	1.2	14.3	360	174	28.0	3.6	3.6 X 10^{-2}
3	1.2	14.6	358	213	28.2	5.0	5.3 X 10^{-2}
3	1.2	15.2	354	307	28.6	9.3	1.1 X 10^{-1}
3	1.2	15.5	352	350	28.7	10.9	1.5 X 10^{-1}
3	1.2	15.8	350	402	29.0	13.1	2.0 X 10^{-1}
3	1.2	16.1	350	444	29.2	15.5	2.4 X 10^{-1}
3	1.2	16.5	346	508	29.4	19.6	3.2 X 10^{-1}
3	1.2	16.8	343	557	29.6	23.1	3.9 X 10^{-1}
3	1.2	17.4	338	659	29.9	30.8	5.5 X 10^{-1}
3	1.2	17.8	335	722	30.1	35.9	6.6 X 10^{-1}
3	1.2	18.2	332	805	30.3	43.9	8.2 X 10^{-1}
3	1.2	18.5	329	881	30.4	52.9	9.7 X 10^{-1}
3	1.2	14.2	361	240	27.9	6.0	6.7 X 10^{-1}
3	1.2	15.1	355	361	28.5	12.6	1.5 X 10^{-1}
3	1.2	15.3	353	396	28.6	13.4	1.9 X 10^{-1}
3	1.2	16.5	345	602	29.4	26.0	4.5 X 10^{-1}
3	1.2	17.7	336	790	30.0	40.8	7.9 X 10^{-1}
3	1.2	18.2	331	858	30.2	45.5	9.2 X 10^{-1}
3	1.2	18.4	329	918	30.3	52.3	1.0
3	1.2	18.6	326	1009	30.4	62.5	1.2
3	2.2	4.42	360	109	28.5	9.4	4.9 X 10^{-2}
3	2.2	4.43	360	143	28.5	15.7	8.4 X 10^{-2}
3	2.2	4.52	358	166	28.7	20.8	1.1 X 10^{-1}
3	2.2	4.67	358	189	29.2	24.9	1.6 X 10^{-1}
3	2.2	4.83	351	234	29.4	39.3	2.3 X 10^{-1}
3	2.2	5.08	346	277	29.9	53.1	3.4 X 10^{-1}
3	2.2	5.45	339	338	30.7	73.6	5.3 X 10^{-1}
3	2.2	5.79	331	383	31.2	92.0	6.8 X 10^{-1}
3	2.2	5.93	327	415	31.4	108.2	8.0 X 10^{-1}
3	2.2	5.94	326	466	31.4	167.7	1.0
3	2.2	6.39	323	564	32.4	211.9	1.6
3	2.2	6.94	322	730	33.7	355.5	2.9

Results and Discussion

Before comparing experiments with the theory in more detail, we will briefly consider the heat transport due to the oscillations of gas columns. Let's assume that the mean temperature and density distributions along the tube axis in the transition region can be, as shown in Fig. 5, written as follows (making use of the fact that $T_m\rho_m$ is a constant everywhere)

$$\rho_m = \rho_0 + \beta x'$$

$$T_m = T_0\left(1 + \frac{\beta}{\rho_0}x'\right)^{-1}$$

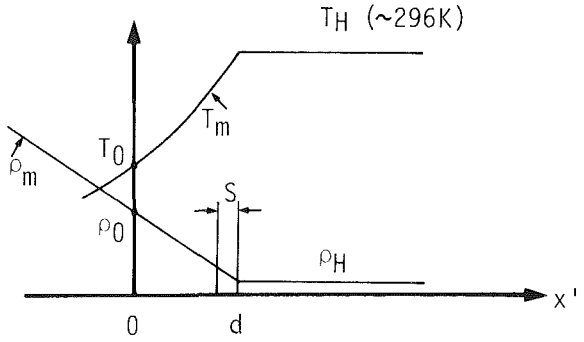

Fig. 5 Temperature and density distributions

where ρ_0 is the mean density at $T_0(=(T_H+T_C)/2)$, and β is a constant value. Consider the particles displacement with the amplitude S around $x'=d$. When the mass fraction contained between $x'=d-S$ and $x'=d$ moves to the warm part and takes the warm temperature, T_H, the increment of the enthalpy is given by

$$E_2=\pi r_0^2 C_p\int_{d-S}^{d}\rho_m(T_H-T_m)\,dx'=-\frac{1}{2}\beta\pi r_0^2 C_p T_H S^2$$

since the enthalpy of the ideal gas depends on the temperature only. Here, subscript 2 means the displacement, S, is the first order. With the help of the relation, $S=u_1/\omega$, (u_1 = axial velocity of the particle) after time-averaging, this equation is approximately transformed into the form

$$\bar{Q}_2(=\overline{E_2\omega})\sim\frac{1}{2}\pi r_0^2 C_p\rho_0\frac{|u_1|^2}{\omega}\left(\frac{dT_m}{dx'}\right)_{x'=0} \tag{2}$$

$$\equiv\pi r_0^2 K_{\text{eff}}(\text{grad}\,T_m)_{x'=0}$$

which is the enthalpy increment per unit time accompanied by the oscillations of gas column that should be transported to the cold part along the tube axis. Thus, the effective heat conductivity ($\propto|u_1|^2/\omega$) induced by the gas oscillation corresponds to the normal (molecular) heat conductivity of gas from kinetic theory; namely, the velocity, u_1, and the particle displacement, S, correspond to molecular velocity and the mean free path. The axial velocity in equation (2) is approximately estimated from a set of one dimensional hydrodynamic equations with acoustic variables, $P_1(x)$ as pressure, $u_1(x)$ as velocity, etc., whose time variation is assumed to be given by the factor $\exp(i\omega t)$. Thus, the following relationship between the acoustic pressure and the axial velocity is derived

$$P_1(x)=\frac{i\gamma P_m}{\omega}\frac{du_1(x)}{dx} \tag{3}$$

where γ is the specific heat ratio. The variation of the acoustic pressure amplitude between $x=L$ and $x=l$ is small, because the oscillation of the gas column is the fundamental in our case. Therefore, we can roughly estimate the axial velocity amplitude at $x=l$ from the pressure amplitudes measured at $x=L$; consequently integrating of equation (3) with respect to x from l to L after multiplication with dx we obtain, since the velocity is zero at the closed end,

$$|u_1(l)|^2=u_1(l)\,\tilde{u}_1(l)=\left(\frac{\omega}{\gamma P_m}\right)^2(L-l)^2P_1^2(L) \tag{4}$$

where $P_1(L)$ is the real pressure amplitude at the closed end. Thus, it is found that the effective heat conductivity is proportional to the square of pressure amplitude and is determined from the measurement of the pressure at the closed end.

Experimental results are shown in Fig. 6 where Q_{ex} presented in equation (1) is plotted as a function of $P_1^2(L)$. These results support the relationship of P_1^2-dependence of the effective heat conductivity over the wide range of the pressure amplitude with ξ as a parameter.

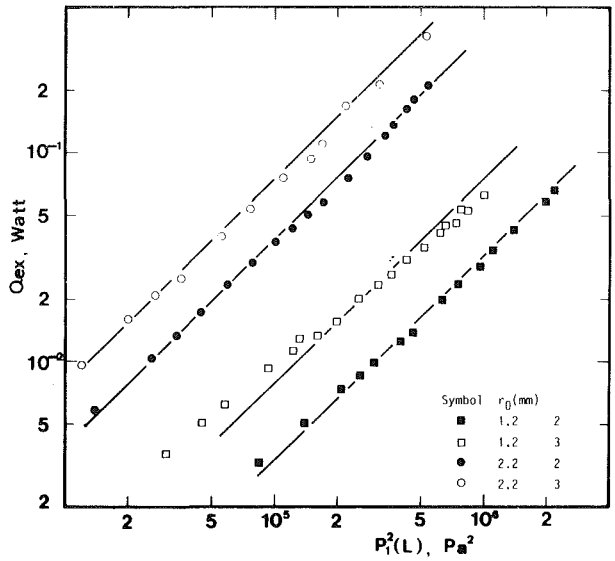

Fig. 6 Pressure dependence of heat flux, Q_{ex}, into the helium dewar accompanied by spontaneous oscillations. The solid line shows that Q_{ex} is proportional to $P_1^2(L)$, where $P_1(L)$ is the pressure amplitude at the closed end.

The earlier experiments by Banister [15] were performed using half-open tubes which were closed at the warm end and open at the cold. In this case the heat flux into helium dewar due to the spontaneous oscillation was proportional to the product of the pressure amplitude and the frequency. Equation (4) shows that the effective heat conductivity depends on the frequency and the mean pressure as well as the acoustic pressure. However, as shown in Table 2 the variations of ω and P_m near the stability curves are very small compared with those of $P_1^2(L)$ for present test conditions. Therefore, it is concluded that the heat flux by the oscillations is proportional to the square of the pressure amplitude for our experiments.

The foregoing is a qualitative analysis of the abnormal heat transport by the oscillations. The order of magnitude comparison between the experiments and the theory of the second-order heat flux proposed by Rott et al. is given as follows, where several parameters of the helium gas and the boundary layer thickness are taken into account.

Let's consider the heat exchange between the oscillating gas and the tube wall. The first-order terms in the energy equation vanish by time averaging; therefore, we consider only terms of the second-order. The time averaged axial enthalpy flux, $\bar{Q}_2$, over the whole cross section of the tube is given as follows: after expanding quantities such as $T=T_m+T_1+T_2+\ldots$ as temperature, velocity $u=u_1+u_2+\ldots$ and others

$$\bar{Q}_2(x)=\pi r_0^2 C_p\rho_m<\overline{T_1u_1}> \tag{5}$$

where bar and $<>$ mean the time and the radial averages, respectively, and T_1 and u_1 are acoustic variables taking account of the dissipative effects (viscosity and heat conduction of the gas) and a finite temperature gradient along the tube axis. The local variation $\Delta\bar{Q}_2(x)$ with x corresponds to the local second-order heat flux, $\bar{q}_2$, penetrating into the tube wall per unit area; therefore

$$-2\pi r_0\bar{q}_2=\frac{d\bar{Q}_2}{dx}$$

$$-\bar{q}_2\equiv k_m\left(\frac{\partial\overline{T_2}}{\partial r}\right)_{r=r_0}+\overline{k_1\left(\frac{\partial T_1}{\partial r}\right)_{r=r_0}}$$

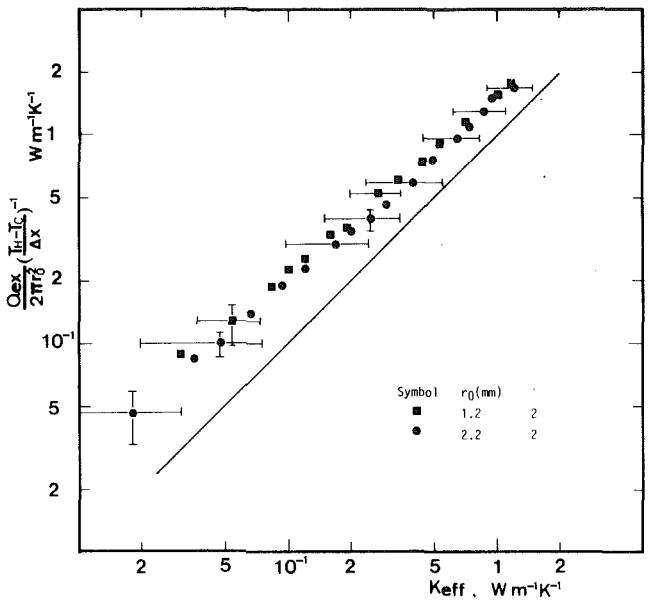

Fig. 7 The effective heat conductivity for $\xi = 2$ enhanced by spontaneous oscillations. The solid line is drawn based on equations (8) and (9).

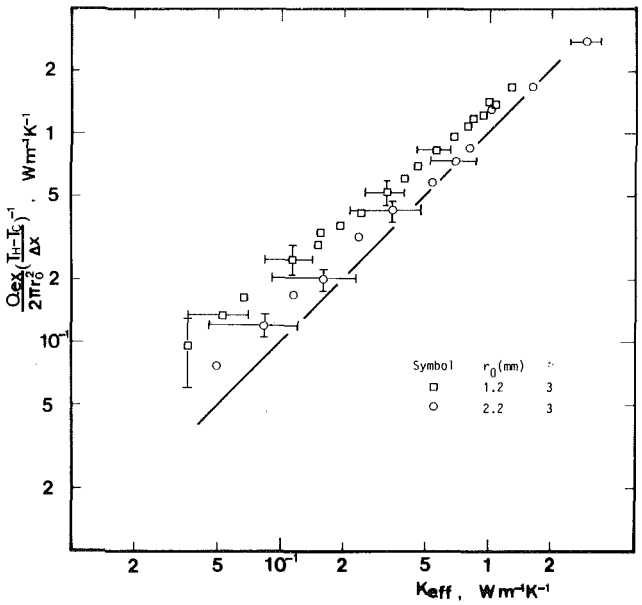

Fig. 8 The effective heat conductivity for $\xi = 3$

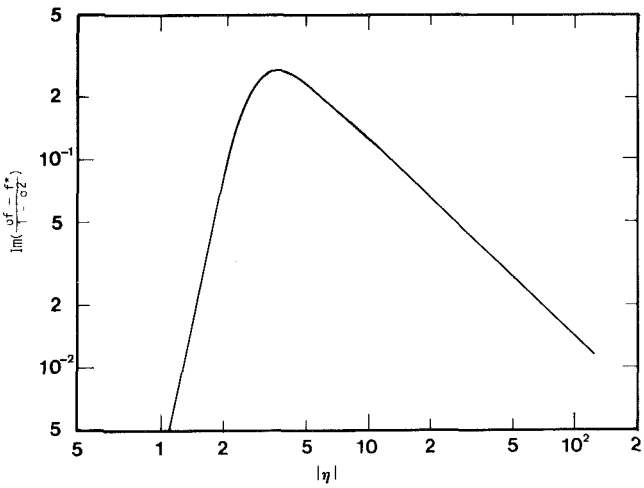

Fig. 9 The relationship between $Im\{(\sigma f - f^*)/(1-\sigma^2)\}$ and $|\eta| = r_0\sqrt{\omega/\nu}$ for helium gas ($\sigma = 2/3$)

These relations have been derived by Merkli and Thomann. Thus, heat flux, Q_{ex}, in equation (1) into the helium dewar, if we neglect terms higher than the fourth order, should be equal to

$$Q_{ex} = 2\pi r_0 \int_{\text{cold part}} \tilde{q}_2 dx = -\int_{\text{cold part}} d\tilde{Q}_2 \tag{6}$$

Rott [6] has calculated the acoustic variables T_1 and u_1, and the following results for $\tilde{Q}_2(x)$ in equation (5) have been derived

$$\tilde{Q}_2(x) = \pi r_0^2 \mathrm{Re}\left[\left\{\frac{1}{2}\mathrm{u}_1\tilde{P}_1 - i\frac{C_p\rho_m|\mathrm{u}_1|^2}{2\omega(1-\sigma)}\frac{dT_m}{dx}\right\}g\right] \tag{7}$$

where

$$g = 1 - \frac{\sigma}{1+\sigma}f(\eta) - \frac{1}{1+\sigma}\tilde{f}^*(\eta)$$

with

$$f(\eta) = \frac{2J_1(i\eta)}{i\eta J_0(i\eta)} \quad f^*(\eta) = f(\sqrt{\sigma}\eta) \quad \text{and} \quad \eta = r_0\sqrt{i\frac{\omega}{\nu}}$$

and u_1 is the core velocity given by $i/\omega\rho_m\, dP_1/dx$. For a steep temperature gradient, the first term in equation (7), which shows the local cooling and heating effects as experimentally verified by Merkli and Thomann, is neglected; therefore, we obtain the exact form as K_{eff} instead of equation (2)

$$\tilde{Q}_2 = -2\pi r_0^2 K_{\text{eff}}\frac{dT_m}{dx} \tag{8}$$

with

$$K_{\text{eff}} = \frac{|\mathrm{u}_1|^2}{2\omega}\rho_m C_p Im\left\{\frac{\sigma f - f^*}{1-\sigma^2}\right\} \tag{9}$$

where the factor 2 in equation (8) is due to contributions from $x = \pm l$. In equation (9), the effects of viscous and thermal boundary layer are taken into account in f and f^*, respectively.

In our experiments the heat flux near $x = \pm l$ mainly contributes to the integration in equation (6). Substituting Q_{ex} in equation (1) for $\tilde{Q}_2$ in equation (8), we can compare the experimental results with the second-order theory using equations (8) and (9). The temperature gradient and the square of the core velocity, $|\mathrm{u}_1|^2$, were replaced by the mean value, $(T_H - T_C)/\Delta x$, and the result found from equation (4), respectively. The values of ρ_m and μ_m at the mean temperature (~ 150 K) were used in equation (9). Experimental data shown in Fig. 6 were rearrangd based on above equations. The results are shown in Figs. 7 and 8 with ξ as a parameter, where the effective heat conductivity, experimentally determined from the evaporation rate of helium, is plotted as a function of K_{eff} from equation (9). The experimental data are correlated by equations (8) and (9) – independent of ξ. Experiments were performed several times and satisfactory reproducibility was obtained. The order-of-magnitude agreement of the experimental and the theoretical values provides strong evidence that the abnormal evaporation of helium under the oscillation is due to the second-order heat flux based on the heat exchange between the oscillating gas and the tube wall.

Strict comparison is difficult because the effective heat conductivity is determined by combination of several paramenters dependent on the temperature. For example, as shown in Fig. 9, $Im\{(\sigma f - f^*)/1-(\sigma^2)\}$ strongly depends on $|\eta|$ ($|\eta| \sim T_m^{-0.82}$), which varies from the order of 10^{-1} to 10

for the present temperature range. Although we employed the values at mean temperature as gas parameters in K_{eff}, the variation of K_{eff} along the tube axis in the transition region is not small for a steep temperature gradient. According to the theory, it is indicated that for a thin boundary layer, the variation of K_{eff} in equation (9) ($K_{\text{eff}} \sim T_m^{-0.17}$) is not very large. Therefore, experiments for such conditions should be also performed to verify the theory. But it is very difficult to perform the experiment, because at the right-hand branch of the stability curves (see Fig. 4) the critical value of $|\eta_c|$ at $\alpha \sim 70$ becomes large ($\sim 10^3$).

The approximation used in equation (4) to estimate the core velocity becomes better for smaller ξ, but the oscillations are complicated because of the appearance of higher harmonics at the left-hand branch as stated in the previous section.

If all the liquid helium evaporated contributes to the gas flow rate out of the system, equation (1) is correct. Actually, not all of the evaporating liquid helium contributes to the gas current, because vaporization of liquid causes decrease of volume of liquid, and the space occupied by liquid is taken up by the gas. Therefore, the correction factor, $(1-\rho_v/\rho_l)^{-1}$, for equation (1) is necessary as indicated by Wexler [17]. Since the ratio of the vapor density, ρ_v, to the liquid density, ρ_l, at 4.2 K for helium is about 0.1, the correction factor is not too small.

Although there are several difficulties in strict comparison with the theory, we think that the rough experiments presented in this paper support the second-order theory.

As stated in the Introduction, experimenters sometimes observed vigorous oscillations with considerable amplitudes ($\sim 10^4$Pa). The extrapolated lines in Fig. 6 suggest that the effective heat conductivity can be on the order of 10^2 $\text{Wm}^{-1}\text{K}^{-1}$ for such large amplitudes, which is several orders of magnitude larger than the normal heat conductivity of the gas, and equivalent to that of metals. Such high heat conductivity is in agreement with our experience. Thus, we may be able to apply the enhanced heat conductivity by oscillating gas columns to precooling in large cryogenic instruments in the future.

Summary

Abnormal heat transport due to the spontaneous oscillations of gas (helium) columns induced by steep temperature gradients was experimentally studied in a cryogenic system. U-shaped tubes closed at both ends were employed in our experiments. The temperature distribution along the tube axis was of a step-function symmetrical with respect to the midpoint. The warm part (closed end side) was maintained at room temperature while the cold side was immersed in liquid helium (4.2 K). Experiments were performed near the left-hand branches of the stability curves predicted by Rott for ξ = 2 and 3. The evaporation rate of liquid helium for various pressure amplitudes was measured in order to estimate the heat transport due to the oscillations. The experimental results show that the effective heat conductivity is proportional to the square of pressure amplitude and can be several orders of magnitude larger than the normal heat conductivity of the gas. These findings are in agreement with the theory of the second-order heat flux proposed by Merkli and Thomann, and Rott.

Acknowledgments

The authors would like to thank Professor K. Sawada and Dr. K. Shibata for their valuable advice and discussion, and thank Mr. K. Ichikawa and Miss. T. Toyama for their technical assistance. One of authors is indebted to Professors S. Hashizume and S. Naruse for their encouragement. This work was partially supported by the Grand-in-Aid for Developmental Scientific Research 5785001 of the Ministry of Education.

References

1 Keesom, W. H., *Helium*, Elsevier, Amsterdam, 1942, pp. 174–175.

2 Taconis, K. W., Beenakker, J. J. M., Nier, A. O. C., and Aldrich, L. T., "Measurements Concerning the Vapor Liquid Equilibrium of Solutions of He^3 in He^4 Below 2.19 K," *Physica*, Vol. 15, 1949, pp. 733–739 (see footnote on page 738).

3 Clement, J. R., and Gaffney, J., "Thermal Oscillations in Low Temperature Apparatus," *Advances in Cryogenic Engineering*, Vol. 1, 1953, pp. 302–306.

4 Rayleigh, J. W. S., Lord., *Theory of Sound*, 2d ed., Vol. 2, Dover Publications, Inc., pp. 230–231.

5 Kramers, H. A., "Vibration of a Gas Column," *Physica*, Vol. 15, 1949, pp. 971–984.

6 Rott, N., "Damped and Thermally Driven Acoustic Oscillations in Wide and Narrow Tubes," *Zeitschrift Angewandt Mathematik & Physik*, Vol. 20, 1969, pp. 230–243.

7 Rott, N., "Thermally Driven Acoustic Oscillations, Part II: Stability Limit for Helium," *Zeitschrift Angewandt Mathematik & Physik*, Vol. 24, 1973, pp. 54–72.

8 Rott, N., and Zouzoulas, G., "Thermally Driven Acoustic Oscillations, Part IV: Tubes with Variable Cross Section," *Zeitschrift Angewandt Mathematik & Physik*, Vol. 27, 1976, pp. 197–224.

9 Rott, N., "Thermoacoustics," *Advances in Applied Mechanics*, Vol. 20, 1980, pp. 135–175.

10 von Hoffmann, T., Lienert, U., and Quack, H., "Experiments on Thermally Driven Gas Oscillations," *Cryogenics*, Vol. 13, 1973, pp. 490–492.

11 Yazaki, T., Tominaga, A., and Narahara, Y., "Stability Limit for Thermally Driven Acoustic Oscillations," *Cryogenics*, Vol. 19, 1979, pp. 393–396.

12 Yazaki, T., Tominaga, A., and Narahara, Y., "Experiments on Thermally Driven Acoustic Oscillations of Gaseous Helium," *Journal of Low Temperature Physics*, Vol. 41, No. 1/2, 1980, pp. 45–60.

13 Merkli, P., and Thomann, H., "Thermoacoustic Effects in a Resonance Tube," *Journal of Fluid Mechanics*, Vol. 70, 1975, pp. 161–177.

14 Rott, N., "Thermally Driven Acoustic Oscillations, Part III: Second-Order Heat Flux," *Zeitschrift Angewandt Mathematik & Physik*, Vol. 26, 1975, pp. 43–49.

15 Bannister, J. D., "Spontaneous Pressure Oscillations in Tubes Connecting Liquid Helium Reservoirs to 300 K Environments," *Bull. Intern. Inst. Refrigeration*, Vol. 5, 1966, pp. 127–134.

16 Yazaki, T., Tominaga, A., and Narahara, Y., "Thermally Driven Acoustic Oscillations: Second-Harmonic," *Physics Letters A*, Vol. 79A, No. 5, 6, 1980, pp. 407–409.

17 Wexler, A., "Evaporation Rate of Liquid Helium.1," *Journal of Applied Physics*, Vol. 22, No. 12, 1951, pp. 1463–1470.

I. Tokura
Research Assistant.

H. Saito
Professor.

K. Kishinami
Associate Professor.

Department of Industrial Mechanical Engineering,
Muroran Institute of Technology,
Muroran 050, Japan

Study on Properties and Growth Rate of Frost Layers on Cold Surfaces

An experimental study was carried out on the properties and growth rate of the frost layer which developed on a cooled vertical plate in free convective flow. Dimensionless parameters introduced by dimensional analysis were found to be effective in predicting frost densities, its thermal conductivities and growth rates. It was also found that the frost formation process can be divided into two periods if the frost growth data are correlated with the dimensionless parameters presented.

1 Introduction

In the field of low-temperature engineering, it is very important to predict the thermal properties and the growth rate of a frost layer which grows on a surface with a temperature below the freezing point of water. Many papers have been published on frost formation which have dealt with the measurement of the frost growth rate and the density and thermal conductivity of frost layers [2–8].

Most literature dealing with frosting problems were recently reviewed in detail by Cremers and Mehra [1], so we will not repeat the history of the work in this field. Much attention and effort has been given to clarify the structure and thermal properties of frost layers; however, predictions of frost properties presented to date seems to be still insufficient to explain the growth rate of frost layer in connection with its structure. Few papers have been published on the prediction of the thermal properties of a frost layer which are very important in practical applications. On this point, Hayashi et al. [9] and Yamakawa et al. [10] proposed structural models of a frost layer in order to calculate its properties. Since both of their works were based on assumptions concerning the microscopic structure of a frost layer, some difficulties arise in actual application of their results. The main difficulty comes from the determination of the factors that represent the configurations of frost structure which are obtained by frosting experiments in specific conditions.

Recently, Cremers and Mehra [1] reported on the frost formation on a vertical cylinder in free convection, having performed experiments in a wide range of wall temperatures (145–258 K). They proposed an empirical formula, simple and easy to use, for predicting the growth rate of frost layers. Their formula is based on the temperature difference between the frost surface and the cooling wall; therefore, its applicability is limited to the conditions of high ambient humidity, as they mentioned in their paper. This is because the frost-surface temperature is far below the triple-point temperature of water and hard to predict particularly when the humidity and the cooling temperature are low.

In the present investigation, the authors clarify qualitatively, on the basis of visual observation of the frosting process, the transient behavior of frost-density which is inherent in a frost layer in its early period of formation. An attempt was made to propose a more practical method for predicting the density and growth rate of a frost layer by presenting the results of frosting experiments in natural convection and a dimensional analysis of frost formation. The present method is much easier to use and applicable in a wider range of humidity conditions.

2 The Experiment

The experiment was carried out to examine the thermal and physical properties of frost layers which grow on a vertical plate in natural convection. In this experiment, a cooling plate 270-mm by 340-mm high and 38-mm thick was prepared in a large air-conditioned room and cooled to deposit frost on both sides as shown in Fig. 1. The plate was cooled by coolant (ethylene glycol water solution) flowing through an inside channel and the edges were insulated by polyurethane-foam leaving only the surfaces for frost deposition exposed. The surface temperatures and the thickness of the frost layers were measured on one side of the plate and the amount of frost deposition was measured on the other side. The surface for frost deposition was constructed of 0.1-mm-thick stainless steel sheet bonded to a bakelite plate 5-mm thick.

The surface temperature was measured at five different points along the plate by thermocouples, (type T) 0.1 mm diameter, buried in grooves in the bakelite plate. Total heat

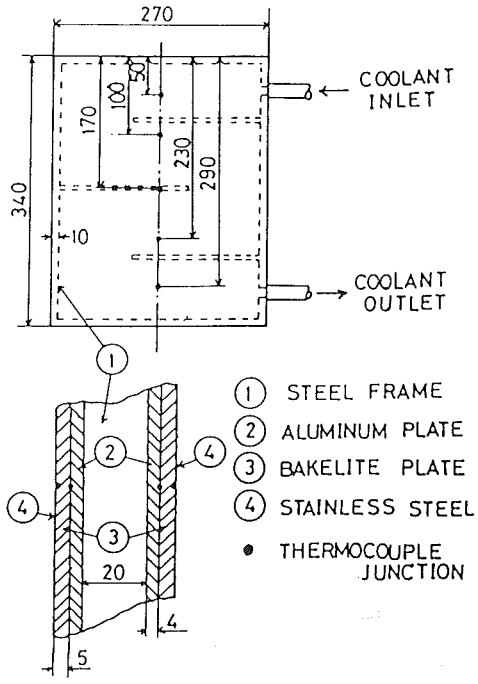

Fig. 1 Schematic view of test plate

Contributed by the Heat Transfer Division for publication in the JOURNAL OF HEAT TRANSFER. Manuscript received by the Heat Transfer Division July 28, 1982.

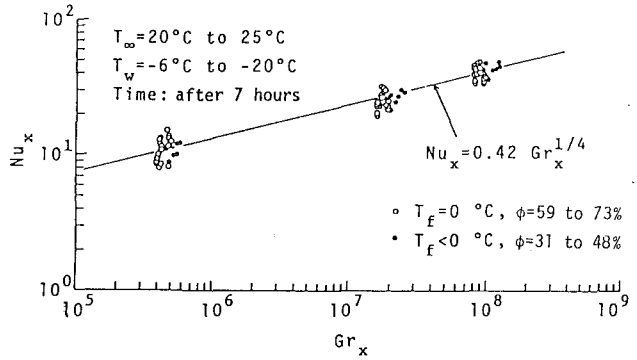

Fig. 2 Local Nusselt number as a function of Grashof number

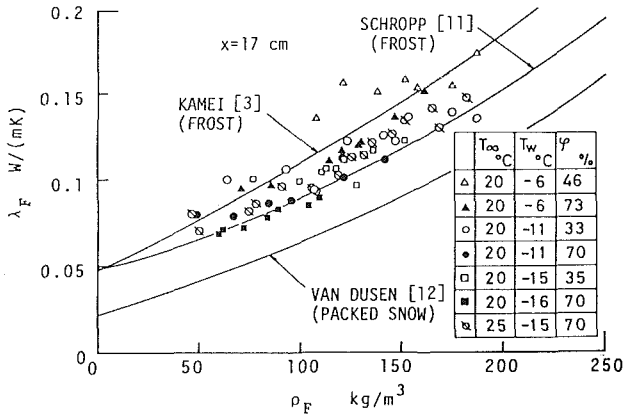

Fig. 3 Effective thermal conductivity of frost as a function of its density

transfer rates were estimated from the temperature difference between the sides of the bakelite plate and the thermal conductivity of the material. For measuring mass transfer rates, a small amount of frost was scraped off the plate and weighed by a precision balance. The surface of a frost layer is not flat because of the random accumulation of water vapor on the porous structure of frost. Therefore, the height of the frost surface may be measured differently by other observers. The authors examined several possible definitions of the surface of the layers and found that not one could be completely reproducible. In this work, the frost surface was defined as an average position of roughness of frost growth front observed laterally by a reading microscope. The thickness and surface temperatures of the frost layer were measured by using an arch-shaped thermocouple, (type K) 50 micron in diameter, which was traversed through the boundary layer and brought into contact with the frost surface by a micro-cathetometer.

The thickness and the mass of the frost were measured at three different points, i.e., 50, 170, and 290 mm from the top of the test plate. Before cooling the test plate, the surfaces prepared for frost deposition had been covered by thin polyethylane films so that no water vapor could condense on the surfaces of the test plate before starting the test. After the prescribed temperature was reached, the test was started by taking off the film.

Each experiment was conducted over 9 hrs, and the temperature and the frost growth were measured approximately every hour after starting the test. The ambient air temperature was kept at either 20°C or 25°C. The relative humidity of the air and the surface temperature of the plate were varied over the ranges of 30 to 70 percent and −6 to −20°C, respectively.

3 Heat and Mass Transfer Results

The total heat flux through a frost layer can be expressed as the sum of contributions by convection, phase change and radiation,

$$q_T = h(T_\infty - T_f) + \dot{m}_1 L + f_0 \sigma(T_\infty^4 - T_f^4) \quad (1)$$

and can be decided experimentally by the temperature difference between the sides and the thermal conductivity of the bakelite plate, as previously mentioned. The f_o in equation (1) is a factor that depends upon both (*a*) the emissivities of frost and room wall surfaces and (*b*) the geometrical factor between those surfaces. In this experiment, the value of f_o was found to be 0.80, which was obtained by using the mass transfer rates and convection heat transfer rates calculated directly from the measured temperature distributions in the thermal boundary layers on the frost surface of some experimental runs. Since the mass flux of water vapor transferring to the frost surface is obtained by the direct measurement of the mass transfer rate, the local mass transfer coefficient can be calculated from

$$\dot{m}_1 = h_D(\rho_{1\infty} - \rho_{1f}) \quad (2)$$

The relative humidity is taken to be 100 percent at the frost surface. The equations by Goff [15] were employed in calculating the saturation pressure of water vapor.

Figure 2 shows Nusselt number versus Grashof number at about 7 hrs after starting the test. The data represented by open circles were measured when the surface temperature of the frost was nearly equal to 0°C, and the other data were measured when the surface temperature of the frost was from 0°C to about −10°C. No appreciable difference can be found between both groups of data and the local heat transfer rate is correlated with the following equation.

$$\mathrm{Nu}_x = 0.42\mathrm{Gr}_x^{1/4} \quad (3)$$

The local mass transfer rate is also correlated with the following equation.

$$\mathrm{Sh}_x = 0.40\mathrm{Gr}_x^{1/4} \quad (4)$$

Nomenclature

D = diffusion coefficient, (m^2/h)
Gr_x = Grashof number, $gx^3(1-\rho_\infty/\rho_w)/\nu^2$
g = acceleration of gravity, (m/h^2)
H_F = thickness of frost layer, (m)
h = local heat transfer coefficient, (W/(m^{2}K))
h_D = local mass transfer coefficient, (m/h)
L = latent heat of sublimation, (J/kg)
$\dot{m}_1$ = mass flux of water vapor, (kg/(m^{2}h))
Nu_x = local Nusselt number, hx/λ_a
q_T = total heat flux, (W/m^2)
Sh_x = local Sherwood number, $h_D x/D$
T = temperature, (K)
x = length, (m)
λ_a = thermal conductivity of air, (W/(mK))
λ_F = thermal conductivity of frost, (W/(mK))
ν = kinematic viscosity of air, (m^2/h)
ρ = density of humid air, (kg/m^3)
ρ_F = density of frost, (kg/m^3)
ρ_{ice} = density of ice, (kg/m^3)
σ = Stefan-Boltzmann constant, (W/(m^{2}K^4))
τ = time, (h)
ϕ = relative humidity, (%)

Subscript

F = frost layer
f = frost surface
w = wall (cooling surface)
1 = water vapor
∞ = ambient

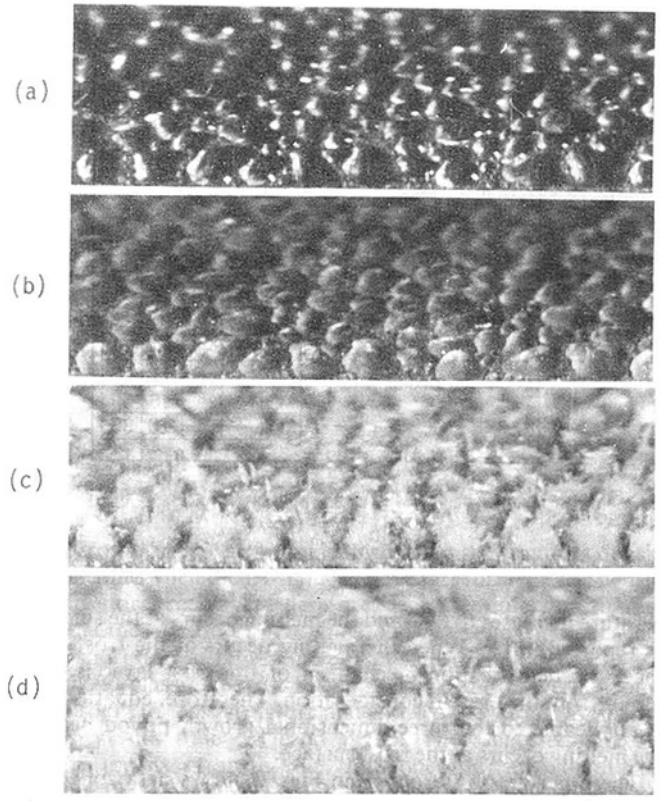

Fig. 4 Photographs of the frost formation in forced convection: $T_\infty = 21°C$, $T_w = -7.5°C$, $\phi = 73$ percent, Stream Velocity 1.6 m/s, X31

The effective thermal conductivity of frost can be defined as follows:

$$q_T = \lambda_F \frac{T_f - T_w}{H_F} \tag{5}$$

The experimental results of the thermal conductivity and the density of frost are cross-plotted in Fig. 3 together with the data from other investigations. This figure shows that the density of the frost layer is the main factor that affects its thermal conductivity when compared with other parameters, such as the temperature and water content of the ambient air and the wall-surface temperature. This means parameters affecting frost density are also the major factors in the thermal conductivity of a frost layer. In practical applications, therefore, information about the parameters that describe the frost density is also essential in estimating the thermal conductivity of a frost layer.

4 Dimensional Analysis of Frost Formation

As mentioned in the foregoing section, it is important to discuss how the density of a frost layer changes according to the frosting and ambient conditions. When the ambient humidity and temperature are constant, the frost density decreases with the decreasing wall-surface temperature, i.e., with increasing heat transfer. On the other hand when the ambient humidity is low, that is, the mass transfer rate is low, the frost density tends to be high even when the wall-surface temperature is low. Therefore, it can be considered that both the rate of the heat transfer and the rate of mass transfer affect the frost density not independently but in terms of a product of both conditions.

Figure 4 shows an example of the microscopic observation of the frost deposition on a cold wall. The process can be explained as follows: immediately after starting the test, water vapor condenses on the wall in the form of microscopic

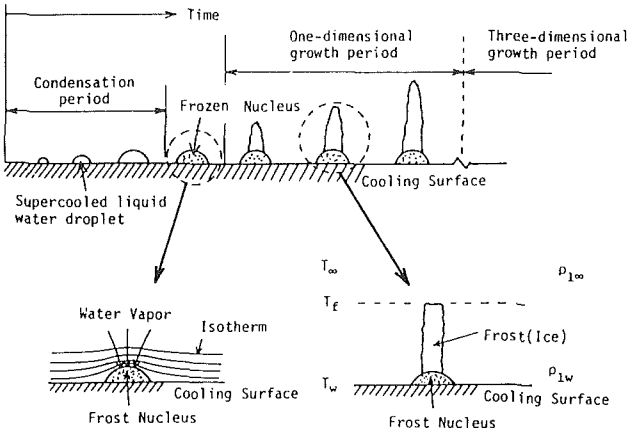

Fig. 5 Illustration of frost deposition in early stage of formation

droplets of supercooled liquid water (Fig. 4(*a*)). The liquid droplets freeze at a certain point (Fig. 4(*b*)), become nuclei from which micro-ice crystals originate, and grow up to become a visible frost layer as time progresses (Fig. 4(*c*,*d*)). In the early period of this process, water vapor sublimates mainly on the top of the nuclei and the crystals developed on them grow mainly in the direction normal to the wall. Therefore, we will call this period of frost formation the "one-dimensional growth period." In the succeeding period of time, the frost layer grows not only in the normal direction but also in the direction parallel to the wall. In this period, the frost grows more slowly than in the former period of frost formation since some portion of the water vapor transferred to the frost surface sublimates inside the frost layer. For convenience, we will call this period of frost deposition the "three-dimensional growth period." Figure 5 is an illustration of the frosting process in the early period of its formation.

In the one-dimensional growth period, frost density is determined more by the number of frost nuclei than by conditions at the frost growth front, such as the frost-surface temperature, etc. In other words, a frost layer will have a growth pattern in this period which is determined by the number of frost nuclei. Many factors contribute to the formation of frost nuclei; the properties of the surface on which frost is deposited (i.e., affinity with water), the heat transfer rate, the mass transfer rate, etc.

On the basis of the foregoing considerations about frost density, a dimensional analysis was carried out to find the dimensionless parameters which correlate the thermal conductivity of a frost layer. It can be considered that the formation of frost nuclei depends strongly upon the heat and mass transfer rates to the cold wall. Therefore, the fundamental physical quantities are basically the same as those in usual boundary layer problems, i.e., λ_F, h, $T_\infty - T_w$, h_D, $\rho_{1\infty} - \rho_{1w}$, L, X, τ, and λ_a. The result of the dimensional analysis is

$$\frac{\lambda_F}{\lambda_a} = F\left(\frac{h_D(\rho_{1\infty} - \rho_{1w})L}{h(T_\infty - T_w)}, \frac{h_D \tau}{x}, \frac{h\ x}{\lambda_a}\right) \tag{6}$$

where the first term in F( ) represents the ratio of latent heat of phase change to sensible heat transferred by convection. The meaning of the second term can be interpreted as follows.

$$h_D \tau / x = \frac{h_d x^2 (\rho_{1\infty} - \rho_{1w})\tau}{x^3(\rho_{1\infty} - \rho_{1w})}$$

$$= \frac{\left(\begin{array}{l}\text{mass of water vapor transferred to}\\ \text{surface } x^2 \text{ during } \tau\end{array}\right)}{\left(\begin{array}{l}\text{mass of water contained}\\ \text{in volume } x^3\end{array}\right)}$$

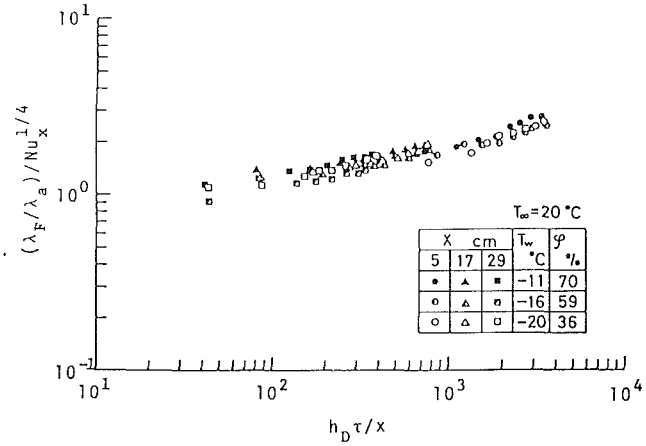

Fig. 6 Combined nondimensional parameter $(\lambda_F/\lambda_a)/Nu_x^{1/4}$ as a function of $h_D\tau/x$

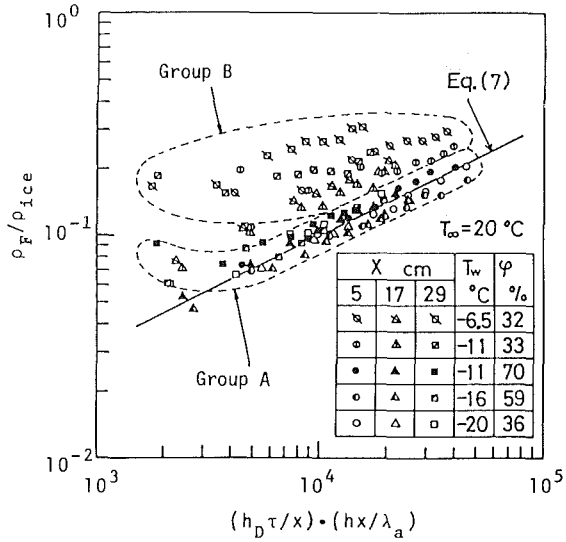

Fig. 7 Frost density as a function of $(h_D\tau/x)\cdot(hx/\lambda_a)$

The third is the Nusselt number. In the strict sense, T_f and ρ_{1f} should be employed as fundamental quantities instead of T_w and ρ_{1w}. However, the authors considered it important that the experimental data are correlated by using the quantities at the ambient and the wall. Therefore, since the quantities in F( ) do not vary with the growth of the frost, these parameters can be determined if only the conditions of frost formation, i.e., T_w, T_∞, ϕ, τ, and x are given. The values of h and h_D can be obtained from equation (3) and (4), respectively. It should be noted that no values associated with unknown frost-surface temperatures are required in estimating the parameters.

5 Nondimensional Correlation of Experimental Results

Since the combined nondimensional parameter $(\lambda_F/\lambda_a)/Nu_x^{1/4}$ increases proportionally to the one-fourth power of $h_D\tau/x$, except when the mass transfer rate is extremely low, the ratio λ_F/λ_a is considered to be a function of the nondimensional parameter $(h_D\tau/x)\cdot(hx/\lambda_a)$ (see Fig. 6). The frost densities, ρ_F/ρ_{ice}, at three different positions along the surface of the wall are shown in Fig. 7 as a function of the parameter above. The data in this figure can be divided into two groups.

One group of data (Group A in Fig. 7) was measured when the wall was at comparatively low temperature and in high ambient humidity (i.e., corresponds to the condition which causes relatively rapid growth of the frost layer), can be correlated by the following equation

$$\rho_F/\rho_{ice} = 0.001[(h_D\tau/x)\cdot(hx/\lambda_a)]^{1/2},$$
$$(h_D\tau/x)\cdot(hx/\lambda_a) > 5 \times 10^3 \quad (7)$$

Although it cannot be clearly seen in the figure, the frost density has a tendency to decrease slightly with the decreasing wall temperature. Consequently, the density can be regarded as a function primarily of the nondimensional parameter above, and then to a lesser degree, of the wall temperature. The equation satisfies the measured values with a maximum error of ±30 percent in the ranges of $\phi > 35$ percent and $T_w < -10°C$ at $T_\infty = 20°C$. The frost density increases with the square root of time since the mass of a frost layer increases linearly with time and the height of the frost layer increases in proportion to the square root of time after a certain period of time has elapsed as will be mentioned below. This correlation represented by equation (7), therefore, means that a frost layer grows three-dimensionally, i.e., the water vapor sublimates both on the frost surface and inside the frost layer at the same time. Another constraint will limit the applicability of the equation (7) when the frost surface temperature increases to 0°C and the melting occurs at the surface as reported in [2]. When the melting occurs at the frost surface, the densification mechanism of the frost layer is different from the present consideration. Therefore, equation (7) is applicable to the three-dimensional growth period before the melting occurs at the frost surface.

The other group (Group B in Fig. 7) shows data collected when the wall was at comparatively high temperature and in low ambient humidity, i.e., conditions when the mass transfer rate was low – indicating nearly constant frost density – but not as low as in the former group. Referring to Fig. 10, it can be understood that the group B data in Fig. 7 belong to the one-dimensional growth period of the frost formation. It is indicated in Fig. 10 that some portion of the group A data which overlaps with the group B data in the same figure belongs also to the one-dimensional growth period. Therefore, even though they are in the one-dimensional growth period, both groups are considerably different in frost density from each other, depending upon the frosting conditions (see Fig. 7). In both groups, the apparent density at the time when the frost nuclei have just formed is expected to be high since the nuclei are frozen droplets of supercooled liquid water which condensed on the wall.

Figure 8 shows schematically the present interpretation that the frost density in the one-dimensional growth period is determined by the relative relation between the apparent density at the time when the frost nuclei have just formed and the density of the frost (ice columns) which has grown up one-dimensionally on top of the nuclei. In the case of low mass transfer rates (Fig. 8(*b*)), the size of a frost nucleus has a tendency to be smaller than in the cases of high mass transfer rates, because a droplet which condenses on the wall cannot grow very large before freezing. The ice columns that grow are therefore quite close together and, because of the low humidity, grow very slowly and compactly. Therefore, at a low rate of mass transfer, the density of the frost (ice columns) that has grown up on top of the frost nuclei is not very different from the density immediately after the formation of the frost nuclei. Consequently, the density of the entire frost layer is high and nearly constant for a long period of time, as indicated by the line (*b*) in Fig. 8, since only a small amount of water vapor is being transferred to the frost surface.

In the case of high mass transfer (Fig. 8(*a*)), the frost nuclei are large, and therefore the columns are more widely spaced and also grow more quickly than in the case of a low mass transfer. Therefore, the density of frost (ice columns) which

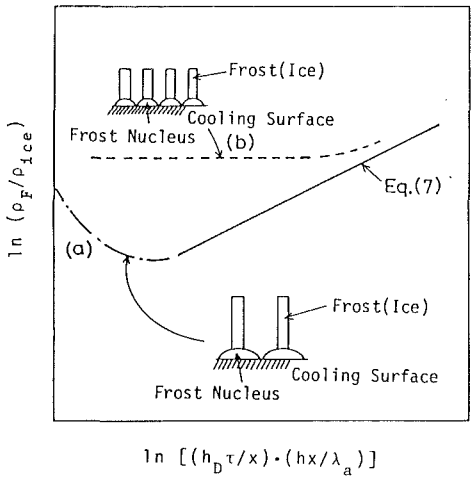

Fig. 8 Schematic explanation of frost density variation

has grown up on the nuclei is lower than the apparent density at the time when the frost nuclei have just formed. The density of an entire frost layer, therefore, decreases quickly with time, so that the situation where equation (7) is valid can be reached in a short time as represented by the line (*a*) in Fig. 8. Hayashi et al. [9] classified frost formation types into several groups according to frost structure and showed the variation of frost density with time for each group. They reported that the higher the mass transfer rate, the sooner the transition in frost formation process occurs and that the frost density does not change greatly with time when the mass transfer rate is low. Their results are in good agreement qualitatively with our experimental ones.

The mass of a frost layer per unit area of the wall is presented in Fig. 9 as a function of time. The experimental data are approximated by the solid lines in the figure. The time dependence of the mass of a frost layer, i.e., the exponent of time measured from the beginning of deposition, obtained in this experiment ranged from 0.90 to 1.00. Therefore, it can be considered that the mass of a frost layer increases almost linearly with time. This means that the driving force of mass transfer to a frost layer, i.e., the difference in water vapor concentrations between the ambient air and the frost layer, does not vary considerably with time. In other words, the increase in the surface temperature of a frost layer has little effect on the deposition rate in the course of its formation. This is one of the reasons why the authors excluded the frost surface temperature from the fundamental physical quantities in the foregoing dimensional analysis. Thus, the mass of a frost layer can be approximated by the following relation

$$m_F = \rho_F H_F \propto h_D(\rho_{1\infty} - \rho_{1w})\tau \tag{8}$$

Therefore, the thickness of a frost layer can be written in the form

$$\frac{hH_F}{\lambda_a} \propto \left(\frac{\rho_{1\infty} - \rho_{1w}}{\rho_F}\right)\left[\left(\frac{h_D\tau}{x}\right)\cdot\left(\frac{hx}{\lambda_a}\right)\right] \tag{9}$$

where the density of the layer is given by equation (7) in the case of the three-dimensional growth period. Consequently, the following relationship is obtained for the deposition thickness

$$\frac{hH_F}{\lambda_a} \propto \left(\frac{\rho_{1\infty} - \rho_{1w}}{\rho_{ice}}\right)\left[\left(\frac{h_D\tau}{x}\right)\cdot\left(\frac{hx}{\lambda_a}\right)\right]^{1/2} \tag{10}$$

The thickness of the layer, hH_F/λ_a, is presented in Fig. 10 as a function of the combined variable $[(\rho_{1\infty} - \rho_{1w})/\rho_\infty]^2[(h_D\tau/x)\cdot(hx/\lambda_a)]$. The relationship (10) well represents the experimental data for values of the variable greater than about 10^{-1}. The authors tried to compare our

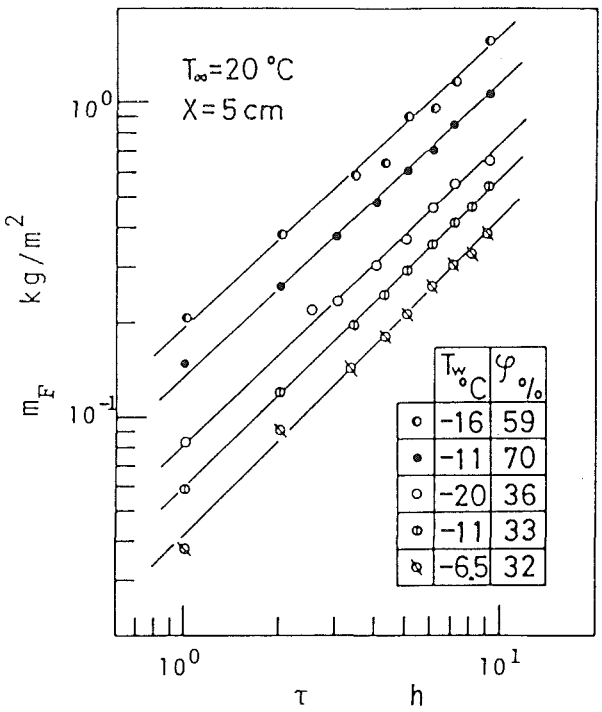

Fig. 9 Change in forst mass with time

results with those of other investigators in order to check the validity of the nondimensional correlation. However, in most cases it was found to be very difficult to cite others' data because of insufficient descriptions of the frosting conditions and apparatus from which the values of the dimensionless parameters should be determined. The results obtained by Kennedy and Goodman [13] are presented in Fig. 10 for comparison, based on the assumption that their data had been measured with the temperature of the cooling wall at $-17°C$. Their results were lower than ours as indicated in the figure. This might be caused by differences in experimental conditions but that point is not yet clear. However, it is clear that their results can also be correlated well with the present parameters.

Additional experiments were carried out using another test plate to find the detailed relationship between the frost thickness and the parameter $[(\rho_{1\infty} - \rho_{1w})/\rho_\infty]^2[(h_D\tau/x)\cdot(hx/\lambda_a)]$. In that case, each experiment continued for 3 hrs, and the frost thickness was measured every 5 or 10 min after starting the run. The results are approximated by the solid lines indicated in Fig. 11. It is clearly seen in the figure that the frost growing process can be divided into two regions, separated by a certain value of abscissa, i.e., about 10^{-1}. One is the region indicated by the line (*a*) in Fig. 11 in which the frost layer grow linearly with time, suggesting one-dimensional growth of the layer as seen in Fig. 5. The other region indicated by the line (*b*) in Fig. 11 represents the frost deposition process in which the frost layer develops in proportion to the square root of time, corresponding to the three-dimensional growth of the frost layer mentioned before. The measured values can be correlated by the following equations, respectively. One-dimensional growth period (line (*a*) in Fig. 11)

$$hH_F/\lambda_a = 3.23\,Z, \quad Z < 0.11 \tag{11}$$

Three-dimensional growth period line (*b*) in Fig. 11)

$$hH_F/\lambda_a = 1.08Z^{1/2}, \qquad Z > 0.11 \tag{12}$$

where

$$Z = [(\rho_{1\infty} - \rho_{1w})/\rho_\infty]^2[(h_D\tau/x)\cdot(hx/\lambda_a)]$$

The measured values in the one-dimensional growth period

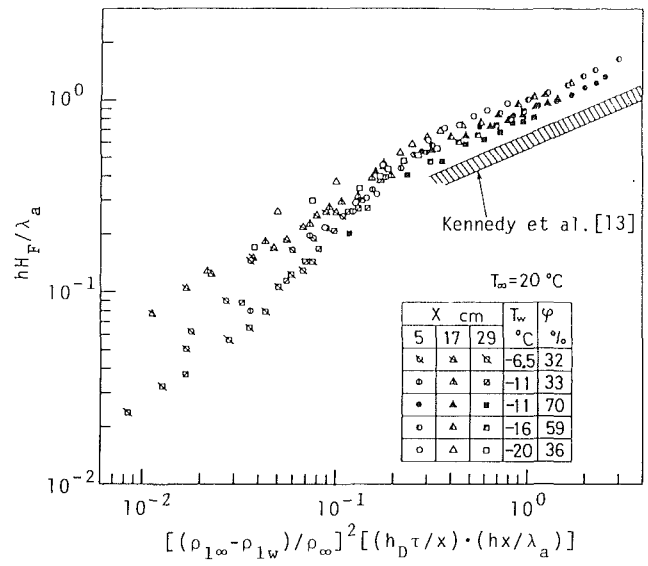

Fig. 10 Dimensionless frost thickness as a function of $[(\rho_{1\infty}-\rho_{1w})/\rho_\infty]^2\,[(h_D\tau/x)\cdot(hx/\lambda_a)]$

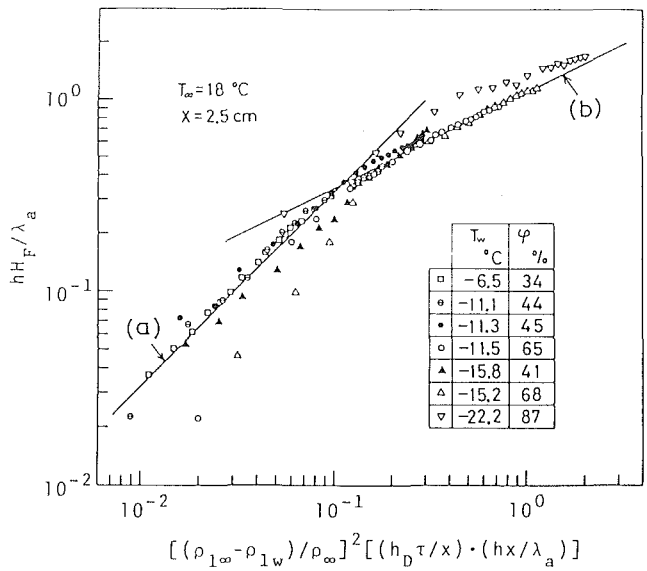

Fig. 11 Dimensionless frost thickness as a function of $[(\rho_{1\infty}-\rho_{1w})/\rho_\infty]^2\,[(h_D\tau/x)\cdot(hx/\lambda_a)]$

scattered because measurement was difficult due to the thinness of the frost layer and its relatively coarse structure (see Fig. 10 and Fig. 11). A square-root of time dependence for the thickness of frost has been reported by other investigators [1, 2, 14]. For example, White and Cremers [2] proposed similar functional relation to equation (12). However, their relation includes the frost surface temperature and the thermal conductivity of frost layer which are usually very difficult to predict for a given frosting condition. Therefore, the applicability of the relation in [2] is limited to the cases for $T_f=0°C$, which means frost formations in high ambient humidity. On the contrary, equation (12) is applicable to the wide range of the ambient humidity as indicated in Fig. 11.

The equation (12), which is valid in the three-dimensional growth period, can be rewritten as follows

$$H_F \propto (\rho_{1\infty}-\rho_{1w})(\tau h_D/h)^{1/2} \tag{13}$$

If an analogy exists between heat and mass transfer, the value of h_D/h should be equal to a constant. Therefore, the thickness of a frost layer is independent of the position along the plate and is determined by time and the difference in water vapor density between the ambient air and the wall. This result coincides with the facts, as observed by others [7, 14], that the thickness of a frost layer developed on a flat plate or on a circular cylinder is almost uniform around the surface. On this point, Schneider [14] reported that the frost thickness turns out to be independent of the variables commonly significant in mass transfer, such as Reynolds number and the vapor pressure difference between the air stream and the frost surface. Referring to the relationship (13), it can be understood that Reynolds number has little effect on the frost thickness in a forced convection condition. However, the present study shows that the difference in vapor density between ambient air and the cooling wall is an important factor that governs frost growth rate. These apparently opposite conclusions on frost thickness may come from the difference in experimental conditions. Schneider conducted frosting experiment in nearly saturated conditions so that the possibility of fog formation arises in his experiment. In that case, the mass flux of water vapor may be determined by the temperature distribution in the thermal boundary layer on the frost surface and therefore be independent of the vapor pressure difference between the air stream and the frost surface. As the frost layer becomes thick and dense so that the melting occurs at the frost surface, the frosting problem should be considered the coupling problem of the heat and mass transfer in the frost layer and those in the boundary layers over it. The present study dealt mainly with frost layer in relatively early periods of formation. Therefore, cases where melting occurs at the surface of the frost layer are excluded from the consideration.

6 Conclusions

The density and the growth rate of a frost layer were correlated by the dimensionless parameters obtained both by frosting experiments on a vertical plate in free convection and by dimensional analysis. These parameters do not include variables that vary with the growth of a frost layer, so their values are determined only by frosting conditions. For the use of these parameters in practical situations, the values of the local heat transfer coefficient must be known. The mass transfer coefficient can be obtained by using an analogy between heat and mass transfer. Compared with previous methods, the advantages of the present one are that the estimation of frost properties and growth rates are possible at any position along the wall and that frost-surface temperature predictions are not required. Frost densities are correlated by the relationship (7) which is valid in the three-dimensional growth period of frost formation under comparatively high mass transfer conditions. In contrast, the frost density shows higher, but nearly constant, values for a long period of time when the mass tranfer rate is low and, at the same time, the surface temperature of a wall is relatively high (up to around $-6°C$).

It can be clearly shown by the measurement of the thickness of a frost layer that the frost formation process is divided into two regions depending upon the dimensionless parameter, $[(\rho_{1\infty}-\rho_{1w})/\rho_\infty]^2[(h_D\tau/x)\cdot(hx/\lambda_a)]$. When the value of the parameter is less than around 10^{-1}, a frost layer grows linearly with time, while it grows proportionally with the square root of time when the value is greater. These regions correspond to the one-dimensional growth period and the three-dimensional growth period of frost formation, respectively.

The same consideration of frost density as mentioned in this study is also possible in the case of frost formation in forced convection. Therefore, it can be expected that the presented parameters will be effective in correlating the density and the thickness of a frost layer in that case as well.

Acknowledgment

The authors extend their heartfelt appreciation to Dr. N. Seki, professor at Hokkaido University, for his valuable discussion and also to Mr. K. Muramoto, research assistant at Muroran Institute of Technology, for his help in constructing experimental apparatus.

References

1 Cremers, C. J., and Mehra, V. K., "Frost Formation on Vertical Cylinders in Free Convection," ASME JOURNAL OF HEAT TRANSFER, Vol. 104, 1982, pp. 3-7.

2 White, J. E., and Cremers, C. J., "Prediction of Growth Parameters of Frost Deposits in Forced Convection," ASME JOURNAL OF HEAT TRANSFER, Vol. 103, 1981, pp. 3-6.

3 Kamei, S., Mizushina, T., Kifune, S. and Koto, T., "Research on Frost Formation in Low Temperature Dehumidifier," *Chemical Engineering*, Japan, Vol. 14, 1950, pp. 53-60.

4 Whitehurst, C. A., "Heat and Mass Transfer by Free Convection From Humid Air to a Metal Plate under Frosting Conditions," *ASHRAE Journal*, Vol. 4, 1962, pp. 58-69.

5 Trammell, G. J., Little, D. C., and Killgor, E. M., "A Study of Frost Formed on a Flat Plate Held at Sub-Freezing Temperature," *ASHRAE Journal*, Vol. 10, No. 7, 1968, pp. 42-47.

6 Brian, P. L. T., Reid, R. C., and Shah, Y. T., "Frost Deposits on Cold Surfaces," *Ind. Eng. Chem. Fundamentals*, Vol. 9, No. 3, pp. 375-380.

7 Biguria, G., and Wenzel, L. A., "Measurement and Correlation of Water Frost Thermal Conductivity and Density," *Ind Eng. and Chem. Fundamentals*, Vol. 9, No. 1, 1970, pp. 129-138.

8 Biguria, G., "The Moving Boundary Problem With Frost Deposition to a Flat Plate at Subfreezing Temperatures and Forced Convection Conditions: the measurement and Correlation of H_2O Frost Properties," Ph.D. thesis, Chemical Engineering Department, Lehigh University, 1968.

9 Hayashi, Y., Aoki, A., Adachi, S., and Hori, K., "Study of Frost Properties Correlating With Frost Formation Types," ASME JOURNAL OF HEAT TRANSFER, Vol. 99, 1977, pp. 239-345.

10 Yamakawa, N., and Ohtani, S., "Heat and Mass Transfer in Frost Layer," *Kagaku Kogaku*, Vol. 36, No. 2, 1972, pp. 197-203.

11 Schropp, K., "Investigations of Dew and Frost Formation on Cooling Tubes in Still Air and the Influence Upon the Heat Transfer," *Zeitshr. ges. Kälte. Ind.*, Vol. 42, 1935, pp. 81-85, 127-131, 151-154.

12 Van Dusen, M. S., *International Critical Tables*, Vol. 5, 1929, p. 216.

13 Kennedy, L. A., and Goodman, J., "Free Convection Heat and Mass under Conditions of Frost Deposition," *International Journal of Heat and Mass Transfer*, Vol. 17, 1974 pp. 477-484.

14 Schneider, H. W., "Equation of the Growth Rate of Frost Forming on Cold Surface," *International Journal of Heat and Mass Transfer*, Vol. 21, 1978, pp. 1019-1024.

15 Goff, J. A., Saturation Pressure of Water on the New Kelvin Scale, Humidity and Moisture, 3, Reinhold Publishing Corp., 1965.

Growth and Decay of a Thermal Pulse Predicted by the Hyperbolic Heat Conduction Equation

B. Vick
Mechanical Engineering Department,
Virginia Polytechnic Institute and
State University,
Blacksburg, Va. 24061

M. N. Özisik
Mechanical and Aerospace Engineering
Department,
North Carolina State University,
Raleigh, N.C. 27650
Mem. ASME

The wave nature of heat propagation in a semi-infinite medium containing volumetric energy sources is investigated by solving the hyperbolic heat conduction equation. Analytic expressions are developed for the temperature and heat flux distributions. The solutions reveal that the spontaneous release of a finite pulse of energy gives rise to a thermal wave front which travels through the medium at a finite velocity, decaying exponentially while dissipating its energy along its path. When a concentrated pulse of energy is released, the temperature and heat flux in the wave front become severe. For situations involving very short times or very low temperatures, the classical heat diffusion theory significantly underestimates the magnitude of the temperature and heat flux in this thermal front, since the classical theory leads to instantaneous heat diffusion at an infinite propagation velocity.

Introduction

According to classical heat conduction theory, heat flux is directly proportional to temperature gradient in the form

$$q = -k\frac{\partial T}{\partial x} \tag{1}$$

This heat flux law predicts that heat conduction is a diffusion phenomenon in which temperature disturbances will propagate at infinite velocities. Despite this physically unacceptable notion of instantaneous energy diffusion, equation (1) gives quite reliable results for most situations encountered in practice.

However, in situations dealing with transient heat flow for extremely short periods of time or at temperatures approaching absolute zero, the classical heat diffusion theory breaks down. In these situations, heat has been observed to travel as a wave with a finite propagation velocity. One of the earliest experiments detecting thermal waves was performed by Peshkov [1] in 1944 using superfluid liquid helium at a temperature near absolute zero. He referred to this phenomenon as "second sound," because of the similarity between the observed thermal waves and ordinary acoustic waves. Since then, the wave nature of heat propagation has been the subject of several investigations [2–13].

In order to accommodate the finite propagation speed and to account for the observed thermal waves, it appears that Vernotte [12] (1958 in the French literature) and Chester [3] (1963 in the English literature) used a heat flux law originally suggested by Maxwell [14] in the form

$$\tau\frac{\partial q}{\partial t} + q = -k\frac{\partial T}{\partial x} \tag{2}$$

Here, τ represents some relaxation or start-up time for the commencement of heat flow after a temperature gradient has been imposed. That is, the heat flow does not start instantaneously, but grows gradually with a relaxation time, τ, after applying a temperature gradient. Clearly, the case $\tau \to 0$, leads to an infinite propagation velocity and coincides with the classical heat diffusion theory given by equation (1).

When τ is relatively large, as in the case of temperatures near absolute zero, the thermal disturbances will appear to propagate as waves at finite speeds as observed in [1, 9]. The experimental observation of [9] is especially interesting. It shows an oscilloscope trace of a temperature pulse of finite height and width, propagating at finite speed in superfluid helium at about 1 degree Kelvin. The pulse appears to retain its shape while propagating with a constant speed through the sample medium in which the observation is made.

A numerical solution using the method of characteristics was applied by Wiggert [13] for the case of a step change in the heat flux at the boundary surface of a semi-infinite medium to illustrate the effects of finite heat propagation velocity. Theoretical predictions are available in the literature illustrating the wave front resulting from a step change in temperature at the boundary surface [7, 11]. However, no theoretical predictions appear to be available showing the more interesting case of a single heat pulse, propagating with a finite speed in a manner demonstrated experimentally in [9]. The objective of the present investigation is to examine theoretically the wave nature of heat flow in a semi-infinite medium containing distributed volumetric energy sources. The results of such a general analysis will then be utilized to study analytically the behavior of a single temperature pulse caused by the activation of a pulsed energy source of finite width.

Problem Formulation

The one-dimensional energy conservation equation in the rectangular coordinates is written as

$$-\frac{\partial q}{\partial x} + g(x,t) = \rho C_p\frac{\partial T}{\partial t} \tag{3}$$

where $g(x, t)$ represents the volumetric energy sources in the medium. The elimination of the heat flux, q, between equations (2) and (3) leads to the following hyperbolic heat conduction equation with energy sources in the medium

$$\frac{1}{C^2}\frac{\partial^2 T}{\partial t^2} + \frac{1}{\alpha}\frac{\partial T}{\partial t} = \frac{\partial^2 T}{\partial x^2} + \frac{1}{k}\left[g(x,t) + \frac{\alpha}{C^2}\frac{\partial g}{\partial t}\right] \tag{4}$$

Here, C is the wave propagation speed which is related to the relaxation time, τ, by

$$\tau = \frac{\alpha}{C^2} \tag{5}$$

For infinite propagation speed (i.e., $C \to \infty$), equation (4) reduces to the parabolic heat diffusion equation.

We note that the hyperbolic heat conduction equation with energy generation includes an additional term involving the

Contributed by the Heat Transfer Division for publication in the JOURNAL OF HEAT TRANSFER. Manuscript received by the Heat Transfer Division January 7, 1983.

time derivative of the energy generation. Such a term in the energy equation does not seem to be reported in the literature previously. It is caused by the presence of the relaxation time, and is obtained by the cross differentiation process in the manipulation of equations (2) and (3) in order to eliminate the heat flux term, q.

In the present investigation we are concerned with the solution of the hyperbolic heat conduction equation (4) for a semi-infinite medium, $0 \le x < \infty$, which is initially at a uniform temperature, T_o. For times $t > 0$, the boundary surface at $x = 0$ is considered insulated, while energy is generated in the medium at a rate of $g(x, t)$, W/m^3. We restrict the energy generation function to be of the form

$$g(x,t) \to 0 \quad \text{as} \quad x \to \infty$$

Then, the boundary conditions are taken as

$$\frac{\partial T}{\partial x} = 0 \quad , \quad \text{at } x = 0 \tag{6a}$$

$$T \to T_o \quad , \quad \text{as } x \to \infty \tag{6b}$$

and the initial conditions as

$$T = T_o \quad , \quad \text{for } t = 0 \tag{7a}$$

$$\frac{\partial T}{\partial t} = 0 \quad , \quad \text{for } t = 0 \tag{7b}$$

For convenience in the subsequent analysis, we now introduce the following dimensionless quantities

$$\eta = \frac{1}{2}\frac{Cx}{\alpha}, \text{ the dimensionless distance} \tag{8a}$$

$$\xi = \frac{1}{2}\frac{C^2 t}{\alpha}, \text{ the dimensionless time} \tag{8b}$$

$$\theta(\eta,\xi) = \frac{T(x,t) - T_o}{g_o C/k}, \text{ dimensionless temperature} \tag{8c}$$

$$G(\eta,\xi) = \frac{g(x,t)}{g_o C^3/4\alpha^2}, \text{ dimensionless energy generation} \tag{8d}$$

$$Q(\eta,\xi) = \frac{q(x,t)}{g_o C^2/\alpha}, \text{ dimensionless heat flux} \tag{8e}$$

Here, the reference quantity, g_o, is considered to be finite, and defined as

$$g_o = \int_{t=0}^{\infty}\int_{x=0}^{\infty} g(x,t)\,dx\,dt \tag{8f}$$

which represents the total energy generated per unit area normal to the x-axis over the region $0 \le x < \infty$ and over all times $0 \le t < \infty$.

The energy equation (4) and its boundary and initial conditions given by equations (6) and (7) are expressed in terms of the above dimensionless variables as

$$\frac{\partial^2\theta}{\partial\xi^2} + 2\frac{\partial\theta}{\partial\xi} = \frac{\partial^2\theta}{\partial\eta^2} + \left[G(\eta,\xi) + \frac{1}{2}\frac{\partial G}{\partial\xi}\right] \quad \text{in } \eta > 0,\ \xi > 0 \tag{9a}$$

$$\frac{\partial\theta}{\partial\eta} = 0, \quad \text{at } \eta = 0 \tag{9b}$$

$$\theta \to 0, \quad \text{as } \eta \to \infty \tag{9c}$$

$$\theta = 0, \quad \text{for } \xi = 0 \tag{9d}$$

$$\frac{\partial\theta}{\partial\xi} = 0, \quad \text{for } \xi = 0 \tag{9e}$$

The solution of this system is developed in the following section.

Analysis

The system defined by equations (9) can be solved by the application of the Fourier cosine transform in the space variable since the boundary condition at $\eta = 0$ is of the second kind.

The appropriate integral transform pair is taken as [15]

$$\text{Transform:} \quad \bar{\theta}(\omega,\xi) = \int_{\eta=0}^{\infty} \theta(\eta,\xi)\cos(\omega\eta)\,d\eta \tag{10a}$$

$$\text{Inversion:} \quad \theta(\eta,\xi) = \frac{2}{\pi}\int_{\omega=0}^{\infty} \bar{\theta}(\omega,\xi)\cos(\omega\eta)\,d\omega \tag{10b}$$

The integral transform of the system (9), by the application of the transform (10a) becomes

$$\frac{d^2\bar{\theta}}{d\xi^2} + 2\frac{d\bar{\theta}}{d\xi} + \omega^2\bar{\theta}(\omega,\xi) = \bar{G}(\omega,\xi) + \frac{1}{2}\frac{d\bar{G}}{d\xi}, \xi > 0 \tag{11a}$$

$$\bar{\theta} = 0 \quad , \quad \text{for } \xi = 0 \tag{11b}$$

$$\frac{d\bar{\theta}}{d\xi} = 0 \quad , \quad \text{for } \xi = 0 \tag{11c}$$

where

$$\bar{G}(\omega,\xi) = \int_{\eta=0}^{\infty} G(\eta,\xi)\cos(\omega\eta)\,d\eta \tag{12}$$

By a rather lengthy but straightforward series of manipulations, the solution of the transformed system (11) is determined as

$$\bar{\theta}(\omega,\xi) = \int_{\xi'=0}^{\xi}\left[\bar{G}(\omega,\xi') + \frac{1}{2}\frac{d\bar{G}}{d\xi'}\right]\frac{\sin[\sqrt{\omega^2-1}(\xi-\xi')]}{\sqrt{\omega^2-1}}e^{-(\xi-\xi')}\,d\xi' \tag{13}$$

Nomenclature

C = speed of propagation
C_p = constant pressure specific heat
$g(x,t)$ = heat generation per time per volume
g_o = total heat per unit area added by heat generation in the entire region over all time
$G(\eta,\xi)$ = dimensionless heat generation
$H(z)$ = step function of argument z
k = thermal conductivity
$q(x,t)$ = heat flux
$Q(\eta,\xi)$ = dimensionless heat flux
t = time variable
$T(x,t)$ = temperature
T_o = initial temperature
x = space variable
α = thermal diffusivity
$\delta(z)$ = delta function of argument z
$\eta = \frac{1}{2}\frac{Cx}{\alpha}$ = dimensionless space variable
$\theta(\eta,\xi)$ = dimensionless temperature
$\bar{\theta}(\omega,\xi)$ = transformed temperature
$\xi = \frac{1}{2}\frac{C^2 t}{\alpha}$ = dimensionless time variable
ρ = density
$\tau = \frac{\alpha}{C^2}$ = relaxation time
ω = transform variable

The formal solution for the temperature distribution $\theta(\eta, \xi)$ is immediately determined by inverting equation (13) using the inversion formula (10*b*) to obtain

$$\theta(\eta,\xi) = \frac{2}{\pi}\int_{\omega=0}^{\infty}\left\{\int_{\xi'=0}^{\xi}\left[\bar{G}(\omega,\xi') + \frac{1}{2}\frac{d\bar{G}}{d\xi'}\right]\cdot\frac{\sin[\sqrt{\omega^2-1}(\xi-\xi')]}{\sqrt{\omega^2-1}}e^{-(\xi-\xi')}d\xi'\right\}\cos(\omega\eta)\,d\omega \tag{14}$$

This result actually involves a triple integral, since $\bar{G}(\omega, \xi)$ is in the integral form as given by equation (12). Assuming that the order of integration is interchangeable, equation (14) is rewritten in the form

$$\theta(\eta,\xi) = \frac{2}{\pi}\int_{\xi'=0}^{\xi}\int_{\eta'=0}^{\infty}\left[G(\eta',\xi') + \frac{1}{2}\frac{dG}{d\xi'}\right]e^{-(\xi-\xi')}\cdot\left\{\int_{\omega=0}^{\infty}\frac{\sin[\sqrt{\omega^2-1}(\xi-\xi')]}{\sqrt{\omega^2-1}}\cos\omega\eta'\cos\omega\eta\,d\omega\right\}d\eta'\,d\xi' \tag{15}$$

The inner integral with respect to the variable ω can be performed by utilizing trigometric identities and carefully interpreting the integral given in [16]. We find

$$\int_{\omega=0}^{\infty}\frac{\sin[\sqrt{\omega^2-1}(\xi-\xi')]}{\sqrt{\omega^2-1}}\cos(\omega\eta')\cos(\omega\eta)\,d\omega = \frac{\pi}{4}I_o\left(\sqrt{(\xi-\xi')^2-(\eta-\eta')^2}\right)H[(\xi-\xi')-|\eta-\eta'|] + \frac{\pi}{4}I_o\left(\sqrt{(\xi-\xi')^2-(\eta+\eta')^2}\right)H[(\xi-\xi')-(\eta+\eta')] \tag{16}$$

where $H(z)$ is a step function defined as

$$H(z) = \begin{cases}1, & \text{for } z>0\\ 0, & \text{for } z<0\end{cases} \tag{17}$$

and $I_o(z)$ is the modified Bessel function of the first kind of order zero. Also, care should be exercised in regard to the absolute value sign appearing in the first $H[(\xi-\xi')-|\eta-\eta'|]$ function in equation (16).

Now, the integral (16) is introduced into equation (15) to obtain the solution for the temperature distribution $\theta(\eta, \xi)$ in the form

$$\theta(\eta,\xi) = \frac{1}{2}\int_{\xi'=0}^{\xi}\int_{\eta'=0}^{\infty}\left[G(\eta',\xi') + \frac{1}{2}\frac{dG}{d\xi'}\right]e^{-(\xi-\xi')}\cdot\left\{I_o\left(\sqrt{(\xi-\xi')^2-(\eta-\eta')^2}\right)H[(\xi-\xi')-|\eta-\eta'|] + I_o\left(\sqrt{(\xi-\xi')^2-(\eta+\eta')^2}\right)H[(\xi-\xi')-(\eta+\eta')]\right\}d\eta'\,d\xi' \tag{18}$$

Depending on the functional form of the energy source term $G(\eta, \xi)$, many special cases can be obtained from the solution given by equation (18). We consider a pulsed energy source as a special case, as described next.

Pulsed Energy Source of Finite Width

Consider a pulsed energy source, concentrated in an interval Δx adjacent to the boundary surface at $x = 0$. The total energy is released spontaneously at time $t = 0$. Let g_o be the total amount of energy released per unit area normal to the x-axis, over the region Δx.

Such an energy source can be expressed as

$$g(x,t) = \begin{cases}\dfrac{g_o\delta(t)}{\Delta x}, & \text{in } 0<x<\Delta x\\ 0, & \text{in } x>\Delta x\end{cases} \tag{19}$$

where $\delta(t)$ is the Dirac delta function. Strictly speaking, the delta function is regarded as the limit of a pulse-type function as the pulse becomes infinitely concentrated [17]. The corresponding dimensionless form of the energy generation function, (19), is

$$G(\eta,\xi) = \begin{cases}\dfrac{\delta(\xi)}{\Delta\eta}, & \text{in } 0<\eta<\Delta\eta\\ 0, & \text{in } \eta>\Delta\eta\end{cases} \tag{20}$$

The behavior of the delta function $\delta(\xi)$ and its derivative $d\delta(\xi)/d\xi$ under the integral sign is as follows

$$\int_{\xi=0}^{\infty}f(\xi)\delta(\xi)\,d\xi = f(0) \tag{21a}$$

$$\int_{\xi=0}^{\infty}f(\xi)\frac{d\delta(\xi)}{d\xi}\,d\xi = -f'(0) \tag{21b}$$

where $f(\xi)$ is an arbitrary function of ξ.

The energy generation function $G(\eta, \xi)$ as specified by equation (20) is introduced into the solution (18). As the generation function is now in the form of a delta function in the ξ variable, the integration of the delta function and its derivative is performed according to the integration rules as defined by equation (21). We immediately obtain

$$\theta(\eta,\xi) = \frac{e^{-\xi}}{4\Delta\eta}\left[\int_{\eta'=\eta-\Delta\eta}^{\eta}P(\xi,|\eta'|)\,d\eta' + \int_{\eta'=\eta}^{\eta+\Delta\eta}P(\xi,\eta')\,d\eta'\right] \tag{22}$$

where

$$P(\xi,\eta) = I_o\left(\sqrt{\xi^2-\eta^2}\right)\delta(\xi-\eta) + \left[I_o\left(\sqrt{\xi^2-\eta^2}\right) + \frac{\xi}{\sqrt{\xi^2-\eta^2}}I_1\left(\sqrt{\xi^2-\eta^2}\right)\right]H(\xi-\eta) \tag{23a}$$

or

$$P(\xi,\eta) = e^{-\xi}\frac{\partial}{\partial\xi}\left[e^{\xi}I_o\left(\sqrt{\xi^2-\eta^2}\right)H(\xi-\eta)\right] \tag{23b}$$

Once the solution for the temperature distribution is known, the heat flux can be determined by expressing equation (2) in dimensionless form

$$\frac{\partial Q}{\partial\xi} + 2\,Q(\eta,\xi) = -\frac{\partial\theta}{\partial\eta} \tag{24a}$$

and integrating to obtain

$$Q(\eta,\xi) = -e^{-2\xi}\int_{\xi'=0}^{\xi}e^{2\xi'}\frac{\partial\theta(\eta,\xi')}{\partial\eta}\,d\xi' \tag{24b}$$

We now introduce the temperature function equation (22), with $P(\xi, \eta)$ as given by equation (23*b*), into the heat flux relation given by equation (24*b*), and perform the indicated operations. The solution for the dimensionless heat flux becomes

$$Q(\eta,\xi) = \frac{e^{-\xi}}{4\Delta\eta}\left\{I_o\left(\sqrt{\xi^2-(\eta-\Delta\eta)^2}\right)H(\xi-|\eta-\Delta\eta|) - I_o\left(\sqrt{\xi^2-(\eta+\Delta\eta)^2}\right)H[\xi-(\eta+\Delta\eta)]\right\} \tag{25}$$

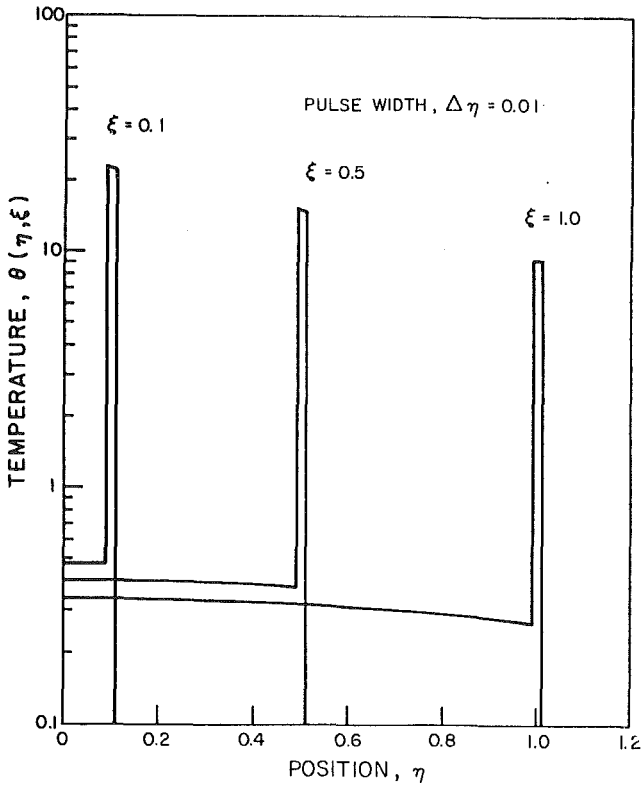

Fig. 1 Temperature solutions to the hyperbolic heat equation with a pulsed heat source

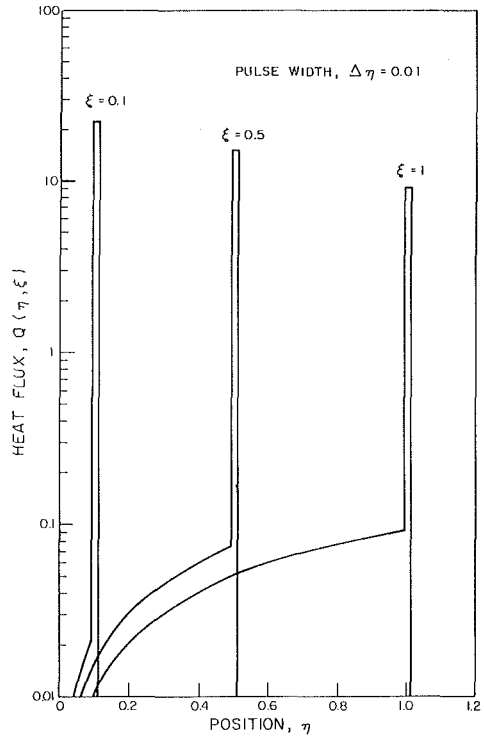

Fig. 2 Heat flux solutions to the hyperbolic heat equation with a pulse heat source

We note that the first $H(\xi - |\eta - \Delta\eta|)$ function involves an absolute value.

Equations (22) and (25), respectively, give the temperature and heat flux distributions resulting from the solution of the system (9) for a pulsed energy source of width $\Delta\eta$. We note that this energy source is located adjacent to the boundary surface at $\eta = 0$, has a concentration $1/\Delta\eta$, and releases its energy spontaneously at time $\xi = 0$.

Concentrated Energy Pulse ($\Delta\eta \to 0$)

It is interesting to examine the above pulse solution for the limiting case of a concentrated energy pulse, namely as $\Delta\eta \to 0$.

The temperature distribution is immediatedly obtained from equation (22) as

$$\lim_{\Delta\eta\to 0} \theta(\eta,\xi) = \frac{e^{-\xi}}{2}\left\{I_o\left(\sqrt{\xi^2-\eta^2}\right)\delta(\xi-\eta) + \left[I_o\left(\sqrt{\xi^2-\eta^2}\right) + \frac{\xi}{\sqrt{\xi^2-\eta^2}} I_1\left(\sqrt{\xi^2-\eta^2}\right)\right] H(\xi-\eta)\right\} \quad (26)$$

Similarly, the heat flux is determined from equation (25), by utilizing the fundamental definition of the derivative to deduce

$$\lim_{\Delta\eta\to 0} Q(\eta,\xi) = -\frac{e^{-\xi}}{2}\frac{\partial}{\partial\eta}\left[I_o\left(\sqrt{\xi^2-\eta^2}\right)H(\xi-\eta)\right]$$

$$= \frac{e^{-\xi}}{2}\left[I_o\left(\sqrt{\xi^2-\eta^2}\right)\delta(\xi-\eta) + \frac{\eta}{\sqrt{\xi^2-\eta^2}} I_1\left(\sqrt{\xi^2-\eta^2}\right)H(\xi-\eta)\right] \quad (27)$$

Alternately, these limiting forms can be determined by observing that in equation (20)

$$\lim_{\Delta\eta\to 0} G(\eta,\xi) = \delta(\eta) \quad \delta(\xi) \quad (28)$$

When the energy generation given by equation (28) is used directly in the general temperature solution (18), the limiting form given by equation (26) immediately follows. The heat flux again can be deduced by using equation (24*b*). The physical significance of the foregoing results are now illustrated.

Results and Discussions

Numerical computations were performed in order to examine the behavior of the temperature and heat flux distribution for the case of a pulsed energy source of finite width released spontaneously at a location adjacent to the insulated boundary. Equations (22) and (25) are utilized to compute the temperature and the heat flux, respectively.

Figure 1 shows a plot of temperature versus position at various times (i.e., $\xi = 0.1, 0.5, 1$), for a given pulse width, $\Delta\eta$. The striking feature of this graph is that an energy pulse gives rise to a thermal wave front which travels in the medium at a finite velocity and decays exponentially while dissipating its energy along its path. We note that the initial energy pulse of width, $\Delta\eta$, gives rise to a wave front of width, $2\,\Delta\eta$, due to the pulse being reflected from the insulated boundary. This wave front lies in the region, $\xi - \Delta\eta < \eta < \xi + \Delta\eta$. The temperature pulse in this figure has already passed the region $0 < \eta < \xi - \Delta\eta$ and has dissipated a portion of its energy in its wake, while the region $\eta > \xi + \Delta\eta$ remains undisturbed since the thermal wave has not reached here.

The experimental investigation of Bertman and Sandiford [9] shows an oscilloscope trace of a temperature pulse propagating in a sample of solid helium maintained at a temperature near absolute zero. Clearly, the present analytical solution predicts the existence of such a thermal pulse, propagating with a finite speed.

Figure 2 shows the behavior of the heat flux as a function of position at times $\xi = 0.1$, 0.5, and 1.0. This figure, also, distinctly illustrates the presence of a thermal pulse propagating through the medium at a finite speed, and

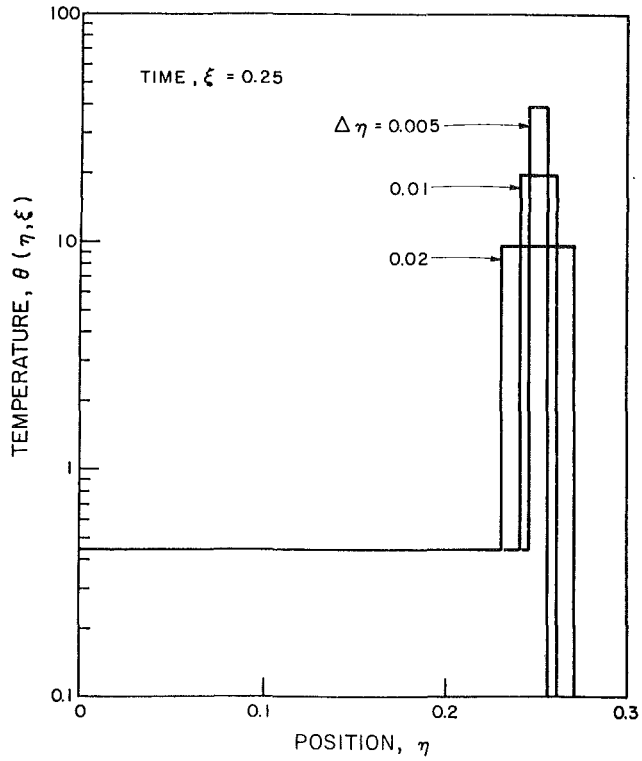

Fig. 3 Effect of pulse width on temperature solutions to the hyperbolic heat

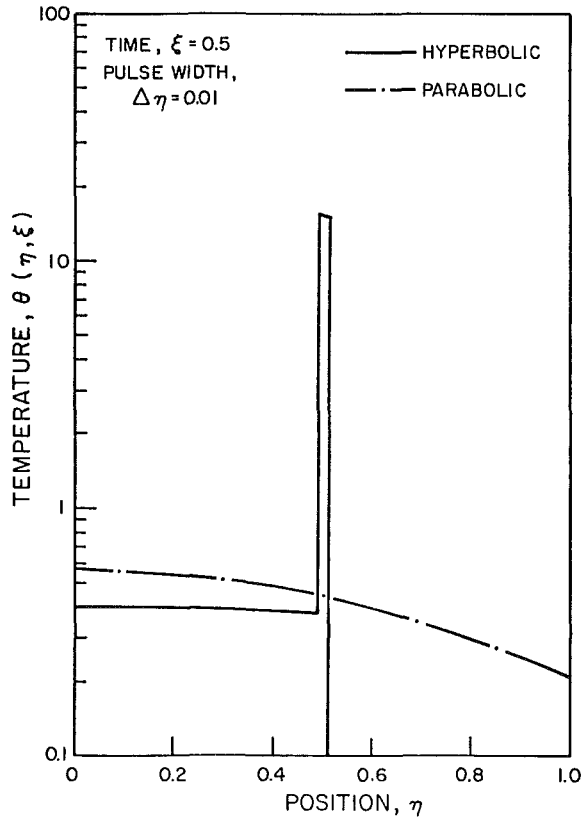

Fig. 4 Comparison of temperature solutions obtained with hyperbolic and parabolic equations

dissipating its energy along its path. There is no heat flux in the region beyond the wave front.

Figure 3 shows a temperature pulse at a given position for a specified time for different values of the pulse concentration. We note that reducing the pulse width increases the energy concentration. There is no detectable difference in the amount of energy deposited behind the pulse regardless of the concentration of energy in the wave front, since changing the energy concentration does not affect the total energy released. For a pulse containing a specified amount of energy, the theoretical limit of the pulse width approaching zero ($\Delta\eta \to 0$), gives rise to temperatures of infinite magnitude in the wave front because the energy concentration becomes infinite. This is the case associated with the delta function behavior of the pulse as described in equation (26). For such a case, the heat flux must also exhibit a delta function behavior, as can be seen from equation (27).

Figure 4 was prepared in order to illustrate the difference between temperature solutions predicted by the hyperbolic and parabolic heat equations for given values of pulse width and time. The graph shows that diffusion theory exhibits no wave nature due to infinite propagation speed and as a result greatly underestimates the severe temperatures in the wave front. Although the same total energy content is present in both cases, the distribution of this thermal energy is markedly different. The peak energy concentration occurring at the wave front in the hyperbolic case is distributed over the entire region in the parabolic case.

Figures 5(*a*) and 5(*b*) show a comparison of the hyperbolic and parabolic temperatures at the insulated surface ($\eta = 0$) as a function of time, ξ, for the shorter and longer time scales, respectively. The parabolic equation gives rise to an infinite slope at $\xi = 0$ and a smooth variation of temperature with time as a result of instantaneous heat diffusion. In contrast, the hyperbolic equation shows that a severe initial temperature is sustained at the insulated boundary for a period of time equal to the pulse width. This phenomenon of sustained temperature at the insulated surface might have significant practical implications in such fields as semiconductor processing or laser annealing [20, 21] where surface melting could occur due to application of a laser pulse. Figure 5(*a*) shows that after a period of time equal to the pulse width, the thermal front leaves the surface giving rise to a substantial drop in the surface temperature below that predicted by the diffusion theory. Eventually, as illustrated in Fig. 5(*b*), the predictions from both the hyperbolic and the parabolic theories merge as ξ approaches a value of about 6. The time required for the two solutions to merge is insentitive to the pulse width.

The results of the present investigation clearly show that the finite propagation speed gives rise to a severe thermal front following the release of an energy pulse of finite width. Such a behavior cannot be predicted by the classical linear or nonlinear diffusion theory, because it allows for the immediate diffusion of heat as soon as the energy is released, without a relaxation or start up time. The implications of the wave nature of heat propagation become important at very low temperatures approaching absolute zero and for extremely short times. For example, in exothermic catalytic reactions discussed in [10] in which extremely short times are involved, the hyperbolic heat conduction equation gives significantly different results from that predicted by the parabolic heat conduction equation.

Another possible physical system where the hyberpolic heat conduction equation involving a pulse type source term may come into play involves laser pulses of short duration incident upon absorbing media. Such systems are of current interest [18, 19] in the general field of semiconductor processing, where major efforts are currently being made to develop circuits having submicron feature sizes and to integrate them into circuits with greater functional packing density and performance [20].

Recently, several questions of basic scientific interest arose

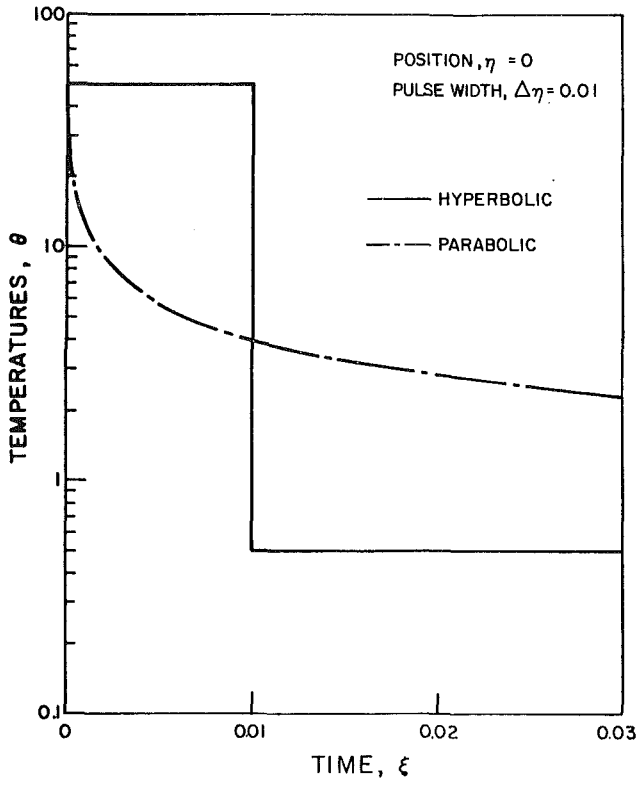

(a)

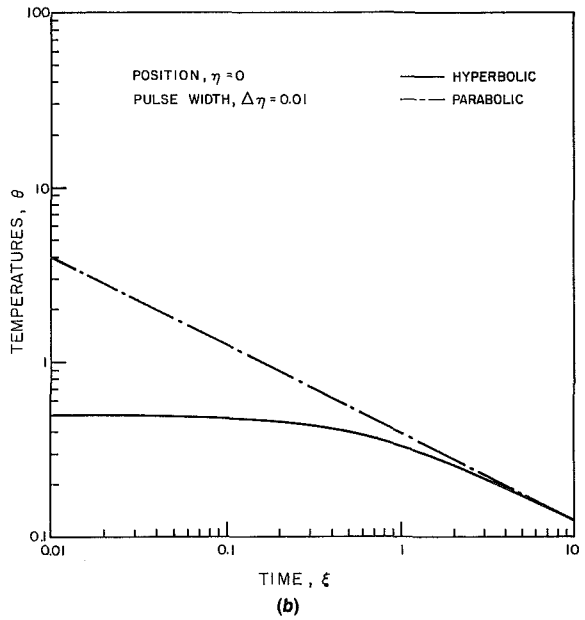

(b)

Fig. 5 Temperature at the boundary surface $\eta = 0$ predicted by the hyperbolic and parabolic heat conduction equations: (a) short tmes, (b) long times

in connection with the experiments involving laser pulses of nanosecond and picosecond duration in which the energy is absorbed within a distance of a minute fraction of a micron from the surface. Among these, the question of the energy transfer to the lattice and the resulting temperature attained by the lattice during such a period of time, over such a small region, is of fundamental importance and still a matter of controversial discussion [21]. Clearly, the classical heat diffusion theory is no longer applicable to predict the temperature distribution over such a short period of time since the wave nature of heat propagation, as predicted by the hyperbolic heat equation, becomes appropriate under such conditions.

Acknowledgment

This work was supported in part through the National Science Foundation Grant #MEA-8110 705.

References

1 Peshkov, V., " 'Second Sound' in Helium II," *Journal of Physics*, USSR, Vol. VIII, 1944, p. 381.

2 Goldstein, S., "On Diffusion by Discontinuous Movements, and on the Telegraph Equations," *Quarterly Journal of Mechanics and Applied Mathematics*, Vol. IV, pt. 2, 1951, pp. 129–156.

3 Chester, M., "Second Sound in Solids," *Physical Reveiw*, Vol. 131, No. 5, 1963, pp. 2013–2015.

4 Weymann, H. D., "Finite Speed of Propagation in Heat Conduction, Diffusion, and Viscous Shear Motion," *American Journal of Physics*, Vol. 36, No. 6, 1967, pp. 488–496.

5 Gurtin, M. E., and Pipkin, A. C., "A General Theory of Heat Conduction With Finite Wave Speeds," *Archive for Rational Mechanics and Analysis*, Vol. 31, 1968, pp. 113–126.

6 Chen, P. J., "On the Growth and Decay of Temperature Rate Waves of Arbitrary Form," *ZAMP*, Vol. 20, 1969, pp. 448–453.

7 Baumeister, K. J., and Hamil, T. D., "Hyperbolic Heat-Conduction Equation—A Solution for the Semi-Infinite Body Problem," ASME JOURNAL OF HEAT TRANSFER, Vol. 91, 1969, pp. 543–548.

8 Amos, D. E., and Chen, P. J., "Transient Heat Conduction With Finite Wave Speeds," ASME *Journal of Applied Mechanics*, Vol. 37, 1970, pp. 1145–1146.

9 Bertman, B., and Sandiford, D. J., " 'Second Sound' in Solid Helium," *Scientific American*, Vol. 222, No. 5, 1970, pp. 92–101.

10 Chan, S. H., Low, M. J. D., and Mueller, W. K., "Hyperbolic Heat Conduction in Catalytic Supported Crystallites," *AIChE Journal*, Vol. 17, No. 6, 1971, pp. 1499–1501.

11 Taitel, Y., "On the Parabolic, Hyperbolic, and Discrete Formulation of the Heat Conduction Equation," *International Journal of Heat and Mass Transfer*, Vol. 15, 1972, pp. 369–371.

12 Vernotte, M. P., "Les Paradoxes de la Théorie Continue de l'équation de la Chaleur," *Comptes Rendus*, Vol. 246, 1958, pp. 3154–3155.

13 Wiggert, D. C., "Analysis of Early-Time Transient Heat Conduction by Method of Characteristics," ASME JOURNAL OF HEAT TRANSFER, Vol. 99, 1977, pp. 35–40.

14 Maxwell, J. C., "On the Dynamical Theory of Gases," *Phil. Trans. Roy. Soc.*, Vol. 157, 1867, pp. 49–88.

15 Özişik, M. N., *Heat Conduction*, John Wiley and Sons, New York, 1980, p. 543.

16 Gradshteyn, I. S., and Ryzhik, I. M., *Table of Integrals*, Series, and Products, Corrected and Enlarged Edition, Academic Press, 3.876, #1, New York, 1980, p. 472.

17 Churchill, R. V., *Operational Mathematics*, 3rd ed., McGraw-Hill, New York, 1972, pp. 29–34.

18 Gibbons, J. F., Hess, L. D., and Sigman, T. W., eds., *Laser and Electron-Beam Solid Interactions and Material Processing*, Elsevier North Holland, Inc., New York, 1981.

19 Appleton, B. R., and Cellar, G. K., eds., *Laser and Electron-Beam Interactions with Solids*, Elsevier Science Publishing Co., Inc., New York, 1982.

20 Hess, L. D., Kokorowski, S. A., Olson, G. L., and Yaron, G., "Laser Processing of Silicon for Advanced Microelectronic Devices and Circuits," in [18], 1981, pp. 307–319.

21 Bloembergen, N., Kurz, H., Kiu, J. M., and Yen, R., "Fundamentals of Energy Transfer During Picosecond Irradiation of Silicon," in [19], 1982, pp. 3–10.

Journal of Heat Transfer

Technical Notes

This section contains shorter technical papers. These shorter papers will be subjected to the same review process as that for full papers.

Microstructure of Flow Inside Minute Drops Evaporating on a Surface

Ningli Zhang[1] and Wen-Jei Yang[2]

Introduction

Interfacial flow structures in small liquid drops evaporating on flat plates were investigated by the methods of laser shadowgraphy and direct photography cited in [1]. Three types of drop evaporation were identified: stable, substable, and unstable. The domains of each were defined in a plot of the dielectric constant, ϵ, versus the Marangoni number, Ma, which was defined as $d_e \Delta T(d\sigma/dT)/(M\alpha)$. Here, d_e denotes the equivalent diameter of a drop on the test plate at zero time; ΔT, temperature difference between the surface and the saturation temperature; σ, mean surface tension at air-liquid interface; T, liquid temperature; μ, absolute viscosity; and α, thermal diffusivity of the liquid. Since ϵ and Ma depend upon temperature, the stability types of a liquid may change with temperature. Their difference was exhibited in (*i*) the drop morphology and (*ii*) the drop volume-time history [1]. During the entire process of evaporation, the stable-type maintained a smooth interface which appeared as perfect concentric circles in the shadowgraphic image. In contrast to this, the unstable-type drop evaporation consisted of quiet, vigorous, and residual stages. The shadowgraphic image of the drop surface exhibited a form of irregular radiant stripes within a sawtoothlike circle. The substable-type drop had its shadowgraphic image distorted from a circular shape and spiked. The volume-time history of both the stable-and substable-type drop evaporation fell close to a single, monotonic curve. However, in the unstable evaporation case, each liquid was represented by a specific curve with three stages of distinct evaporation mechanisms.

This paper reveals the microstructure of flow inside liquid drops evaporating on a flat plate by means of aluminum suspension method. The Benard cells, well known in the case of an enclosed liquid layer heated from below, are observed for the first time in evaporating liquid drops. The main features that characterize three types of drop evaporation are summarized.

Experimental Apparatus

The apparatus for direct photography, shown in Fig. 1, was employed to observe the flow structure visualized by suspending fine aluminum powder in an evaporating drop. It consisted of a white light source, a glass plate coated with developed emulsion on one side, and a 16-mm, Bolex H16, EBM movie camera having a Nikon Nikkor, 300-mm, 1:4.5 lens. A Kalt, 72-mm, Close-Up Dioptor lens was mounted on top of the Nikon lens. The developed emulsion had a specific density such that the photographic density was approximately 1.7. Some drops were unheated, while others were slightly heated to enhance the strength of natural convection using a thermofoil heater that was placed on the exposed side of the developed emulsion. When the light source and the camera were situated at proper positions, the process of drop evaporation could be recorded clearly in photos with sharp contrast. Fine aluminum particles were carefully sprinkled over a liquid drop, which was placed on the glass plate by means of a 50 μl Monoject micro syringe. The addition of solid particles did not affect the total evaporation time of the drop.

Results and Discussion

In testing some liquid drops, the heater was turned on to raise the temperature of the glass plate by 2 to 3 °C. (in the absence of a drop). Thus, natural convection within the drop could be properly enhanced for a better visualization of cellular motion. However, a higher plate temperature would produce natural convection currents and destroy the cellular structure.

All three types of liquid drops were tested including (*i*) unstable type such as acetone, ethyl alcohol, and methanol, (*ii*) substable type like ethyl acetate, benzene, chloroform and

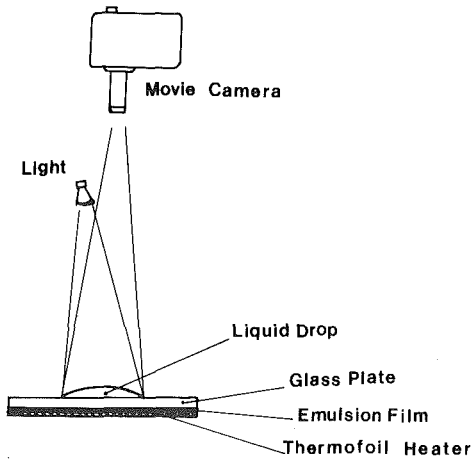

Fig. 1 A schematic of direct photography

[1] Visiting Scholar, Department of Mechanical Engineering and Applied Mechanics, University of Michigan, on leave from the Department of Thermal Engineering, Tsinghua University, Beijing, China

[2] Department of Mechanical Engineering and Applied Mechanics, University of Michigan, Ann Arbor, Mich. 48109. Mem ASME

Contributed by the Heat Transfer Division for publication in the JOURNAL OF HEAT TRANSFER. Manuscript received by the Heat Transfer Division October 12, 1982.

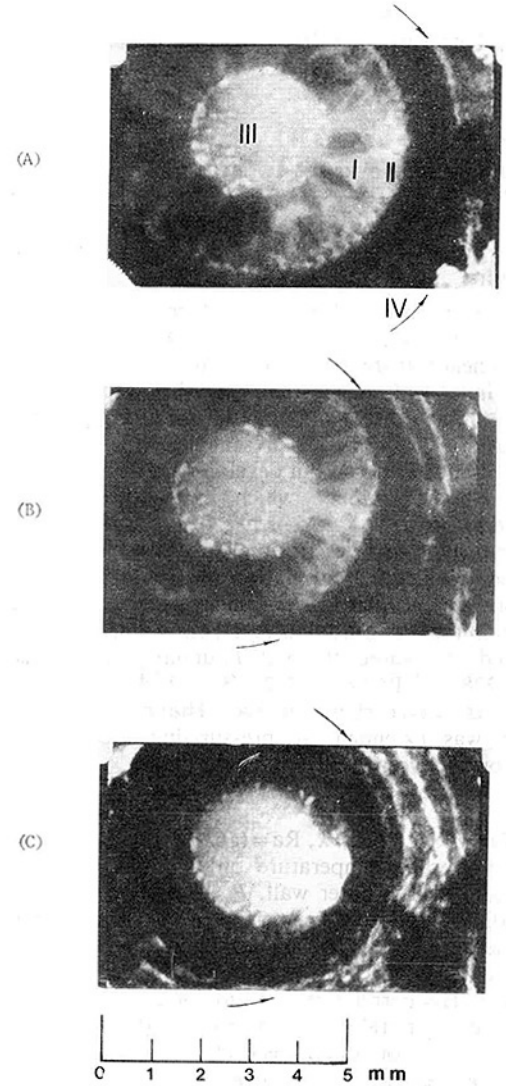

Fig. 2 Flow pattern in an evaporating chloroform drop at (*a*) early stage, (*b*) intermediate stage, and (*c*) final stage

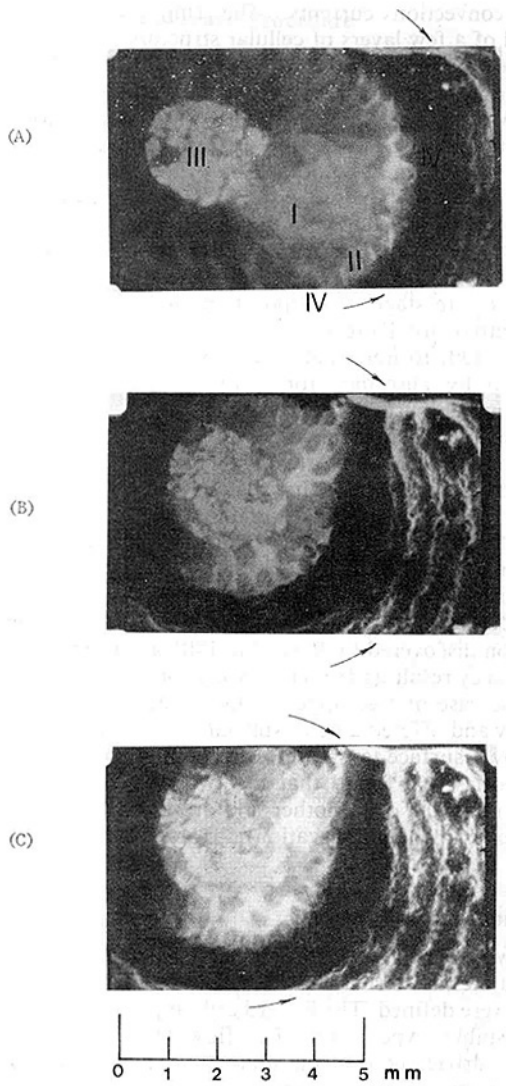

Fig. 3 Flow pattern in an evaporating methylene chloride drop at (*a*) early stage, (*b*) intermediate stage, and (*c*) final stage

methylene chloride, and (*iii*) stable type such as cyclohexane, carbon tetrachloride and ethyl ether.

The most interesting was the appearance of the Benard cells in both the stable- and substable- type drops, similar to the cellular motion in an enclosed fluid layer heated from below. The higher the Marangoni number of the evaporating drop, the better the clearness of cellular motion in the drop.

Figures 2 and 3 show the flow patterns in a chloroform drop and a methylene chloride drop, respectively. Chloroform exhibited largest Benard cells. The cellular shape in both chloroform and methylene chloride drops was somewhat hexagonal, while the Benard cells in other liquids of stable- and substable-type evaporation were either smaller or nonhexagonal. In each figure, photos (*a*), (*b*), and (*c*) correspond to three instants of a drop lifetime. The arrow sign indicates the location of the liquid-solid interface (edge of drop on the plate). The white stripes on the right are the traces of aluminum particles left behind after the drop edge receded leftward with evaporation. Different drops exhibited different cellular patterns. In the same drop, the cell size changed with time, smaller in the initial stage of evaporation but growing slightly thereafter. A scale was prepared to estimate the dimension. In the case of a chloroform drop, for example, the cells were hexagonal and looked somewhat like a honeycomb.

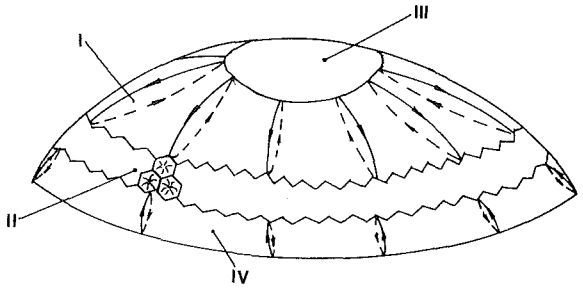

Fig. 4 A schematic diagram of flow patterns in a drop evaporating on an unheated horizontal plate

The side of the hexagon measured from 0.3 to 0.5 mm. It was observed through a 10x magnifying glass that the flow in the hexagonal cells was from the center to the sides. Evidently, warm fluid flowed toward the drop surface at each cell center, spreading over the surface, where it was cooled and then returned to the interior of the drop along the cell periphery. Figure 4 is a schematic illustration of the flow pattern that appeared in Figs. 2 and 3. The flow field may be divided in four regions, I through IV. Region I was the space of intense

natural convection currents. The ring-shaped region II consisted of a few layers of cellular structure. Located at the top of the drop like a cap was the stagnation region III. A very weakly circulating region existed at the bottom of the drop, region IV. The flow there was so weak that the motion of aluminum particles was barely visible by the naked eye but failed to appear in the photos. As evaporation proceeded, region I continued to lose ground, while the region II of cellular motion moved toward the stagnant region I, as seen in Figs. 2(*b*) and 3(*b*). Figures 2(*c*) and 3(*c*) show the direct contact between regions II and III in the absence of region I during the late stage of evaporation. Region II eventually merged into region III toward the end of evaporation process. It is important to note that while both regions I and II are dominated by buoyancy force, the flow in region IV is overwhelmingly surface-tension driven.

In case of the unstable-type drop evaporation, natural convection currents of vortex type prevailed in the major portion of the drop, including regions I and II. The current strength was so intense that aluminum particles moved in a random fashion. The stagnant region III still remained at the drop center, while the surface-tension-driven region IV practically disappeared.

Lord Rayleigh [2] considered the phenomena of cellular convection discovered by Benard in 1901 as instability due to the buoyancy resulting from the expansion of a heated liquid. Citing the case of free upper surface, Pearson [3] neglected buoyancy and offered a new explanation for the instability as caused by a surface-tension effect. Nield [4] combined these rival theories. He found that the two agencies causing instability reinforce one another and are tightly coupled. The present experimental observation supports Nield's viewpoint.

Conclusion

A flow visualization method using particle suspension has disclosed the flow structure in evaporating liquids. Four flow regimes were defined. The Benard cells appeared in the stable- and substable- type drops. The flow patterns induced by buoyancy-driven convection and those due to a surface-tension-driven instability were identified. Supplemented by the findings [1], it is concluded that the distinction among the stable- substable- and unstable- type drop evaporation can be identified by three features: (*i*) the morphology of drop image on the laser shadowgraphy, a circular and smooth periphery (outer rings) for the stable-type drop, and irregular radiant stipes within a sawtooth-like circle in the case of unstable-type drop [1]; (*ii*) the drop volume-time history, a monotonic curve for the stable-type evaporation, but a three-stage volume-time plot in the unstable-type case [1]; and (*iii*) the internal flow structure visualized by the surfae suspension of fine solid particles, a region of cellular motion (clearness increasing with the Marangoni number) in the stable-type drop, and natural convection currents in the bulk of an unstable-type drop. The substable-type drop evaporation possesses the characteristics transitional between the stable- and unstable-types.

Reference

1 Zhang, N., and Yang, Wen-Jei, "Natural Convection in Evaporating Minute Drops," ASME JOURNAL OF HEAT TRANSFER, Vol. 104, 1982, pp. 656-662.

2 Rayleigh, Lord, "On the Convection Currents in a Horizontal Layer of Fluid When the High Temperature is on the Upper Side," *Philosophical Magazine*, Vol. 32, 1916, pp. 529-46.

3 Pearson, J. R. A. "On Convection Cells Induced by Surface Tension," *Journal of Fluid Mechanics*, Vol. 4, 1958, pp. 489-500.

4 Nield, D. A., "Surface Tension and Buoyancy Effects in Cellular Convection," *Journal of Fluid Mechanics*, Vol. 19, 1964, pp. 341-352.

Correlations for Convective Heat Transfer in Vertical Annular Gas Layers With Constant Heat Flux on the Inner Wall

R. Bhushan[1], M. Keyhani[1], R. N. Christensen[1], and F. A. Kulacki[1,2]

Introduction

This note reports experiments which have extended the work of Keyhani, Kulacki, and Christensen [1], who measured heat transfer in a vertical annulus in air and helium with the inner wall at constant heat flux, the outer wall at constant temperature, a radius ratio, K, of 4.33, and height-to-gap ratio, H, of 27.6. The present experiments increase the range of K and H and permit development of correlations for average Nusselt number which explicitly include these parameters.

Before turning to a description of the present experiments, it may be noted that a correlation for the thermal boundary conditions and geometrical parameters treated here has not appeared in the literature. However, early work by Sheriff [2] considered the same thermal boundary conditions with $38 < H < 228$ and $1.03 < K < 1.23$. The working fluid in these experiments was carbon dioxide. The range of Rayleigh numbers was extended by pressurizing the system. His correlation for average Nusselt number is

$$\mathrm{Nu} = 0.25\mathrm{Ra}^{0.30} H^{-0.25} \tag{1}$$

where $\mathrm{Nu} = h_c\,(R_o - R_i)/k$, $\mathrm{Ra} = (g\beta/\alpha\nu)\,(R_o - R_i)^3\,(T_i - T_o)$, T_i is the average temperature on the inner wall, T_o the temperature on the outer wall, R_o the outer radius, R_i the inner radius, β the isobaric coefficient of thermal expansion, α the thermal diffusivity, ν the kinematic viscosity, k the thermal conductivity, and h_c the convective heat transfer coefficient. His correlation is valid for $\mathrm{Ra} > 10^5$. For a rectangular enclosure ($K = 1$), the work of Landis and Yanowitz [3] and MacGregor and Emery [4] seems to complete the literature on the subject. The working fluids in the Landis and Yanowitz experiments were air, silicone oil, and water. While glycerin, castor oil, water, and ethyl alcohol were used by MacGregor and Emery.

If both walls of the annulus are at constant temperature, more literature is available. Generally, three regimes of heat transfer have been identified (conduction, transition, and boundary layer regimes) with the structure of the flow field in each dependent on Ra [5, 6]. Heat transfer correlations for average Nusselt numbers developed by Thomas and de Vahl Davis were:

Conduction Regime:

$$\mathrm{Nu} = 0.595\ \mathrm{Ra}^{0.101}\mathrm{Pr}^{0.024} H^{-0.052} K^{0.505} \tag{2}$$

Transition Regime:

$$\mathrm{Nu} = 0.202\ \mathrm{Ra}^{0.294}\ \mathrm{Pr}^{0.097} H^{-0.264} K^{0.423} \tag{3}$$

Boundary Layer Regime:

$$\mathrm{Nu} = 0.286\ \mathrm{Ra}^{0.258}\ \mathrm{Pr}^{0.006} H^{-0.238} K^{0.442} \tag{4}$$

These correlations were developed for $1 \le K \le 10$, $1 \le H \le 33$, $0.5 \le \mathrm{Pr} \le 10^4$ and $\mathrm{Ra} \le 2 \times 10^5$, where all parameters are as defined for equation (1).

[1]Department of Mechanical Engineering, The Ohio State University, Columbus, Ohio 43210

[2]Present address: Department of Mechanical and Aerospace Engineering, University of Delaware, Newark, Del. 19711, Mem. ASME

Contributed by the Heat Transfer Division for publication in the JOURNAL OF HEAT TRANSFER. Manuscript received by the Heat Transfer Division December 13, 1982.

natural convection currents. The ring-shaped region II consisted of a few layers of cellular structure. Located at the top of the drop like a cap was the stagnation region III. A very weakly circulating region existed at the bottom of the drop, region IV. The flow there was so weak that the motion of aluminum particles was barely visible by the naked eye but failed to appear in the photos. As evaporation proceeded, region I continued to lose ground, while the region II of cellular motion moved toward the stagnant region I, as seen in Figs. 2(*b*) and 3(*b*). Figures 2(*c*) and 3(*c*) show the direct contact between regions II and III in the absence of region I during the late stage of evaporation. Region II eventually merged into region III toward the end of evaporation process. It is important to note that while both regions I and II are dominated by buoyancy force, the flow in region IV is overwhelmingly surface-tension driven.

In case of the unstable-type drop evaporation, natural convection currents of vortex type prevailed in the major portion of the drop, including regions I and II. The current strength was so intense that aluminum particles moved in a random fashion. The stagnant region III still remained at the drop center, while the surface-tension-driven region IV practically disappeared.

Lord Rayleigh [2] considered the phenomena of cellular convection discovered by Benard in 1901 as instability due to the buoyancy resulting from the expansion of a heated liquid. Citing the case of free upper surface, Pearson [3] neglected buoyancy and offered a new explanation for the instability as caused by a surface-tension effect. Nield [4] combined these rival theories. He found that the two agencies causing instability reinforce one another and are tightly coupled. The present experimental observation supports Nield's viewpoint.

Conclusion

A flow visualization method using particle suspension has disclosed the flow structure in evaporating liquids. Four flow regimes were defined. The Benard cells appeared in the stable- and substable- type drops. The flow patterns induced by buoyancy-driven convection and those due to a surface-tension-driven instability were identified. Supplemented by the findings [1], it is concluded that the distinction among the stable- substable- and unstable- type drop evaporation can be identified by three features: (*i*) the morphology of drop image on the laser shadowgraphy, a circular and smooth periphery (outer rings) for the stable-type drop, and irregular radiant stipes within a sawtooth-like circle in the case of unstable-type drop [1]; (*ii*) the drop volume-time history, a monotonic curve for the stable-type evaporation, but a three-stage volume-time plot in the unstable-type case [1]; and (*iii*) the internal flow structure visualized by the surfae suspension of fine solid particles, a region of cellular motion (clearness increasing with the Marangoni number) in the stable-type drop, and natural convection currents in the bulk of an unstable-type drop. The substable-type drop evaporation possesses the characteristics transitional between the stable- and unstable-types.

Reference

1 Zhang, N., and Yang, Wen-Jei, "Natural Convection in Evaporating Minute Drops," ASME JOURNAL OF HEAT TRANSFER, Vol. 104, 1982, pp. 656-662.

2 Rayleigh, Lord, "On the Convection Currents in a Horizontal Layer of Fluid When the High Temperature is on the Upper Side," *Philosophical Magazine*, Vol. 32, 1916, pp. 529-46.

3 Pearson, J. R. A. "On Convection Cells Induced by Surface Tension," *Journal of Fluid Mechanics*, Vol. 4, 1958, pp. 489-500.

4 Nield, D. A., "Surface Tension and Buoyancy Effects in Cellular Convection," *Journal of Fluid Mechanics*, Vol. 19, 1964, pp. 341-352.

Correlations for Convective Heat Transfer in Vertical Annular Gas Layers With Constant Heat Flux on the Inner Wall

R. Bhushan[1], M. Keyhani[1], R. N. Christensen[1], and F. A. Kulacki[1,2]

Introduction

This note reports experiments which have extended the work of Keyhani, Kulacki, and Christensen [1], who measured heat transfer in a vertical annulus in air and helium with the inner wall at constant heat flux, the outer wall at constant temperature, a radius ratio, K, of 4.33, and height-to-gap ratio, H, of 27.6. The present experiments increase the range of K and H and permit development of correlations for average Nusselt number which explicitly include these parameters.

Before turning to a description of the present experiments, it may be noted that a correlation for the thermal boundary conditions and geometrical parameters treated here has not appeared in the literature. However, early work by Sheriff [2] considered the same thermal boundary conditions with $38 < H < 228$ and $1.03 < K < 1.23$. The working fluid in these experiments was carbon dioxide. The range of Rayleigh numbers was extended by pressurizing the system. His correlation for average Nusselt number is

$$\mathrm{Nu} = 0.25\mathrm{Ra}^{0.30} H^{-0.25} \tag{1}$$

where $\mathrm{Nu} = h_c\,(R_o - R_i)/k$, $\mathrm{Ra} = (g\beta/\alpha\nu)\,(R_o - R_i)^3\,(T_i - T_o)$, T_i is the average temperature on the inner wall, T_o the temperature on the outer wall, R_o the outer radius, R_i the inner radius, β the isobaric coefficient of thermal expansion, α the thermal diffusivity, ν the kinematic viscosity, k the thermal conductivity, and h_c the convective heat transfer coefficient. His correlation is valid for $\mathrm{Ra} > 10^5$. For a rectangular enclosure ($K = 1$), the work of Landis and Yanowitz [3] and MacGregor and Emery [4] seems to complete the literature on the subject. The working fluids in the Landis and Yanowitz experiments were air, silicone oil, and water. While glycerin, castor oil, water, and ethyl alcohol were used by MacGregor and Emery.

If both walls of the annulus are at constant temperature, more literature is available. Generally, three regimes of heat transfer have been identified (conduction, transition, and boundary layer regimes) with the structure of the flow field in each dependent on Ra [5, 6]. Heat transfer correlations for average Nusselt numbers developed by Thomas and de Vahl Davis were:

Conduction Regime:

$$\mathrm{Nu} = 0.595\ \mathrm{Ra}^{0.101}\mathrm{Pr}^{0.024} H^{-0.052} K^{0.505} \tag{2}$$

Transition Regime:

$$\mathrm{Nu} = 0.202\ \mathrm{Ra}^{0.294}\ \mathrm{Pr}^{0.097} H^{-0.264} K^{0.423} \tag{3}$$

Boundary Layer Regime:

$$\mathrm{Nu} = 0.286\ \mathrm{Ra}^{0.258}\ \mathrm{Pr}^{0.006} H^{-0.238} K^{0.442} \tag{4}$$

These correlations were developed for $1 \le K \le 10$, $1 \le H \le 33$, $0.5 \le \mathrm{Pr} \le 10^4$ and $\mathrm{Ra} \le 2 \times 10^5$, where all parameters are as defined for equation (1).

[1]Department of Mechanical Engineering, The Ohio State University, Columbus, Ohio 43210

[2]Present address: Department of Mechanical and Aerospace Engineering, University of Delaware, Newark, Del. 19711, Mem. ASME

Contributed by the Heat Transfer Division for publication in the JOURNAL OF HEAT TRANSFER. Manuscript received by the Heat Transfer Division December 13, 1982.

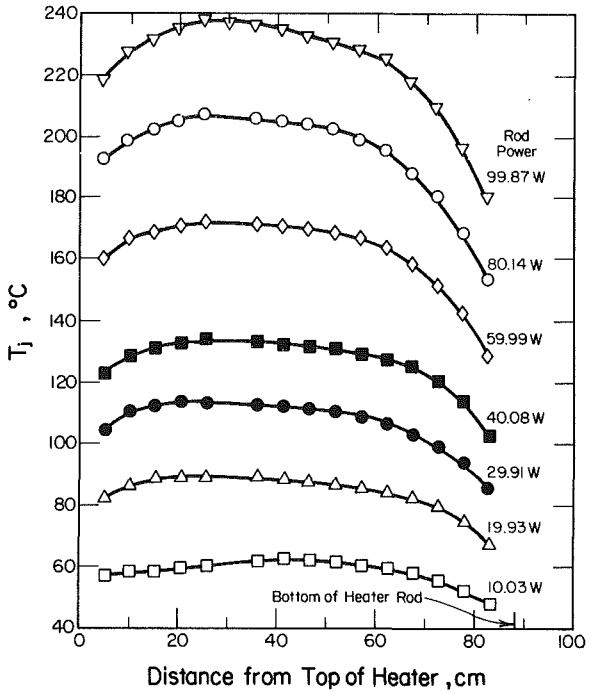

Fig. 1 Temperature distribution along the inner cylinder for air at 2.0 Atm

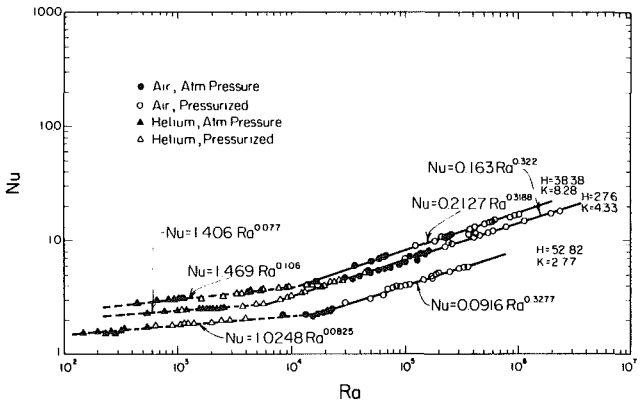

Fig. 2 Experimental Nusselt numbers versus Rayleigh numbers

Table 1 Ranges of parameters in correlations

H	K	Ra
52.82	2.77	82–3.47×10^5
38.38	8.28	423–10^6
27.6[a]	4.33	1000–2.33×10^6

[a] ref [1]

Experimental Apparatus and Procedure

The apparatus employed in the present study was similar to that in [1]. The inner cylinder was a uniformly wound electrical heater while the outer cylinder was 5.23-cm i.d. × 90.2-cm tall and was maintained at a constant temperature by a water jacket. The ends of the annulus were insulated. Sixteen equally spaced thermocouples were used to measure the temperatures along the inner cylinder and eight equally spaced thermocouples were used to measure temperatures along the outer cylinder.

Heat transfer measurements were made for air and helium at atmospheric and elevated pressures to extend the range of Ra. The overall heat transfer data were corrected as in [1] by evacuating the system and obtaining an adjusted applied power so that the mean temperature on the inner cylinder matched that for a given run at higher power. This power input (the radiation correction) was used to calculate heat transfer coefficient for radiation, which was subtracted from the total heat transfer coefficient (see [1] and Bhushan [7] for details).

In the calculation of Ra and Nu, fluid properties were evaluated at the film temperature, $(T_i + T_o)/2$. Experimental uncertainties in Ra and Nu were 4 to 5 percent and 10 to 11 percent, respectively. These uncertainties represent the maximum uncertainty based on the absolute value of individual uncertainties. End losses via conduction along the heated cylinder amounted to less than 10 percent of applied power.

Results

Figure 1 presents typical distributions of temperature on the inner wall as a function of rod power. The accuracy of the temperature measurements was ±1.5°C, which is reflected in the size of the data points. The temperature distribution exhibits an almost symmetrical distribution at low power, but at higher power, an asymmetrical distribution is observed. The temperature increases with distance from the bottom, indicating a thickening of a thermal boundary layer at the top of the annulus. Based on the data presented in [1] and the streamlines calculated by Thomas and de Vahl Davis [5], it appears that the flow field for $10^4 < Ra < 10^5$ is most probably unicellular, and for $Ra > 10^5$ is dominated by a well mixed core and thermal boundary layers on each wall. Numerical solutions for the flow field and flow visualization at a large Ra would be needed, however, to verify this conclusion.

Overall Nusselt numbers as a function of Ra are presented in Fig. 2. The present results permit the identification of only two regimes of heat transfer, a conduction regime and a boundary layer regime. Table 1 contains the values of Ra, H, and K for each set of data as indicated in Fig. 2.

When all of the data of the present study and Keyhani et al. [1] are combined, the following correlations are obtained by multiple regression analysis:

Table 2 Summary of the results of multiple regression analysis for equations (5) and (6)

	Leading coefficient		Rayleigh number coefficient		Height to gap ratio coefficient		Radius ratio coefficient	
	Estimate	3σ	Estimate	3σ	Estimate	3σ	Estimate	3σ
Conduction regime: equation (5))	0.845	0.047	0.092	0.002	−0.087	0.013	0.467	0.007
Boundary layer regime: equation (6))	0.281	0.015	0.322	0.003	−0.407	0.013	0.555	0.009

Table 3 Comparison of present results with those of other investigators

H	K	Ra*	Nu			
			Sheriff [2]	Landis and Yanowitz [3]	Keyhani et al. [1]	Present study, of equation (8)
38	1.23	10^6	4.15	------	3.91	3.97
		10^7	7.05	------	6.85	6.96
20	1.	10^4	----	1.44	1.35	1.44
		10^6	----	3.94	4.15	4.43
38.38	8.28	10^6	----	------	9.05	8.81
52.82	2.77	10^6	----	------	5.17	5.04

Conduction Regime:

$$\mathrm{Nu} = 0.845\ \mathrm{Ra}^{0.092} H^{-0.087} K^{0.467} \tag{5}$$

Boundary Layer Regime:

$$\mathrm{Nu} = 0.281\ \mathrm{Ra}^{0.322} H^{-0.407} K^{0.555} \tag{6}$$

In these correlations, the regression coefficients are both greater than 0.99, with a t-value for all parameters greater than 2.0. Table 2 presents a summary of the results of the multiple regression analysis.

Equations (5), (6) in terms of modified Rayleigh number, $\mathrm{Ra}^* = (g\beta/\alpha\nu)\ (q_c/k)\ (R_o - R_i)^4$, where q_c is the convective heat flux based on the surface of the inner cylinder, become:

Conduction Regime:

$$\mathrm{Nu} = 0.857\ \mathrm{Ra}^{*0.084} H^{-0.080} K^{0.428} \tag{7}$$

Boundary Layer Regime:

$$\mathrm{Nu} = 0.383\ \mathrm{Ra}^{*0.244} H^{-0.308} K^{0.42} \tag{8}$$

for $\mathrm{Ra}^* \leq 1 \times 10^7$. And, the conduction regime is delimited by

$$\mathrm{Ra}^* \leq 150\, H^{1.43} K^{0.05} \tag{9}$$

By incorporating the Nusselt number dependence on aspect and radius ratios as reported by Thomas and de Vahl Davis in their results, Keyhani et al. [1] proposed a coefficient of 0.291 $H^{-0.238}\ K^{0.442}$ for the Ra* in Eq. (8). This was done based on the assumptions that the effect of geometric parameters is independent of the boundary conditions, and proper adjustment of the leading constant, for a short range of K and H values, would lead to acceptable results when the Nusselt number is defined in terms of Ra*. These assumptions were partially substantiated by the favorable agreement between Nusselt numbers obtained from their proposed correlation and the experimental results of Sheriff [2], and Landis and Yanowitz [3].

The present results, in tabulated form, are compared to those of Sheriff [2], and Landis and Yanowitz [3] in Table 3. Nusselt numbers obtained from the equation proposed by Keyhani et al. are given. In general, equation (8) leads to a better agreement with experimental values of other investigators as compared to the Nusselt numbers obtained from [1]. This is to be expected, since the correlation from [1] was based on one set of aspect and radius ratios augmented with the H and K effects as reported by Thomas and de Vahl Davis.

In order to determine the effect of constant heat flux boundary condition as opposed to an isothermal one, experimental results of Eckert and Carlson [8] for thermal convection in a vertical air layer are available. Equation (6) for $H = 15$, and $K = 1$, at $\mathrm{Ra} = 10^5$ results in a Nusselt number 32 percent higher than that given by Eckert and Carlson.

Conclusion

The correlations obtained in the present work show that the average Nusselt number in tall vertical annuli, in which the inner wall is at constant heat flux and the outer wall is at constant temperature, is strongly dependent on the geometry of the system. In the conduction regime, Nu is a weak function of Ra and H, but in the boundary layer regime is a strong function of both these parameters. In either flow regime, Nu is a strong function of radius ratio.

Three sets of data points for H and K are used in the present study to obtain the exponents of aspect radius ratios in equations (5), (6), (7), and (8). The results are in good agreement with the related studies in the literature. However, more sets of experimental data points for H and K are needed in order to refine the reported exponents. A mixed boundary condition, as in the present study, results in Nusselt numbers as much as 32 percent higher than those of an isothermal one.

Acknowledgment

We gratefully acknowledge the support of this work by The Office of Nuclear Waste Isolation under Contract E512-03900 to The Ohio State University Research Foundation.

References

1 Keyhani, M., Kulacki, F. A., and Christensen, R. N., "Free Convection in a Vertical Annulus With Constant Heat Flux on the Inner Wall," ASME JOURNAL OF HEAT TRANSFER, Vol. 105, 1983, pp. 454-459.

2 Sheriff, N., "Experimental Investigation of Natural Convection in a Single and Multiple Vertical Annuli With High Pressure Carbon Dioxide," *Proceedings, Third International Heat Transfer Conference*, Vol. 2, 1966, pp. 132-138.

3 Landis, F., and Yanowitz, H., "Transient Natural Convection in a Narrow Vertical Cell," *Proceedings, Third International Heat Transfer Conference*, Vol. 2, 1966, pp. 139-151.

4 MacGregor, R. K., and Emery, A. F., "Free Convection Through Vertical Plane Layers-Moderate and High Prandtl Number Fluids," *Journal of Heat Transfer*, Vol. 91, 1969, pp. 391-403.

5 Thomas, R. W., and de Vahl Davis, G., "Natural Convection in Annular and Rectangular Cavities, A Numerical Study," *Proceedings, Fourth International Heat Transfer Conference*, Vol. 4, Paper NC2.4, Elsevier, Amsterdam, 1970.

6 de Vahl Davis, G., and Thomas, R. W., "Natural Convection Between Concentric Vertical Cylinder," *High Speed Computing in Fluid Dynamics, Physics of Fluids*, Supplement II, 1969, pp. 198-207.

7 Bhushan, R., "Heat Transfer Within Spent Fuel Canisters," M.Sc. thesis in Nuclear Engineering, The Ohio State University, 1981.

8 Eckert, E. R. G., and Carlson, W. O., "Natural Convection in an Air Layer Enclosed Between Two Vertical Plates with Different Temperatures," *International Journal of Heat and Mass Transfer*, Vol. 2, 1961, pp. 106-120.

Natural Convection Heat Transfer in Complex Enclosures at Large Prandtl Number

M. W. Nansteel[1] and R. Greif[2]

Nomenclature

A = aspect ratio, H/L

A_p = aperture ratio, h/H

[1] Department of Mechanical Engineering and Applied Mechanics, University of Pennsylvania, Philadelphia, Pa. 19104

[2] Mechanical Engineering Department, University of California, Berkeley, Berkeley, Calif. 94720

Contributed by the Heat Transfer Division for publication in the JOURNAL OF HEAT TRANSFER. Manuscript received by the Heat Transfer Division December 13, 1982.

Table 3 Comparison of present results with those of other investigators

H	K	Ra*	Nu			
			Sheriff [2]	Landis and Yanowitz [3]	Keyhani et al. [1]	Present study, of equation (8)
38	1.23	10^6	4.15	------	3.91	3.97
		10^7	7.05	------	6.85	6.96
20	1.	10^4	----	1.44	1.35	1.44
		10^6	----	3.94	4.15	4.43
38.38	8.28	10^6	----	------	9.05	8.81
52.82	2.77	10^6	----	------	5.17	5.04

Conduction Regime:

$$\mathrm{Nu} = 0.845\ \mathrm{Ra}^{0.092} H^{-0.087} K^{0.467} \tag{5}$$

Boundary Layer Regime:

$$\mathrm{Nu} = 0.281\ \mathrm{Ra}^{0.322} H^{-0.407} K^{0.555} \tag{6}$$

In these correlations, the regression coefficients are both greater than 0.99, with a t-value for all parameters greater than 2.0. Table 2 presents a summary of the results of the multiple regression analysis.

Equations (5), (6) in terms of modified Rayleigh number, $\mathrm{Ra}^* = (g\beta/\alpha\nu)\ (q_c/k)\ (R_o - R_i)^4$, where q_c is the convective heat flux based on the surface of the inner cylinder, become:

Conduction Regime:

$$\mathrm{Nu} = 0.857\ \mathrm{Ra}^{*0.084} H^{-0.080} K^{0.428} \tag{7}$$

Boundary Layer Regime:

$$\mathrm{Nu} = 0.383\ \mathrm{Ra}^{*0.244} H^{-0.308} K^{0.42} \tag{8}$$

for $\mathrm{Ra}^* \leq 1 \times 10^7$. And, the conduction regime is delimited by

$$\mathrm{Ra}^* \leq 150\, H^{1.43} K^{0.05} \tag{9}$$

By incorporating the Nusselt number dependence on aspect and radius ratios as reported by Thomas and de Vahl Davis in their results, Keyhani et al. [1] proposed a coefficient of 0.291 $H^{-0.238}\ K^{0.442}$ for the Ra* in Eq. (8). This was done based on the assumptions that the effect of geometric parameters is independent of the boundary conditions, and proper adjustment of the leading constant, for a short range of K and H values, would lead to acceptable results when the Nusselt number is defined in terms of Ra*. These assumptions were partially substantiated by the favorable agreement between Nusselt numbers obtained from their proposed correlation and the experimental results of Sheriff [2], and Landis and Yanowitz [3].

The present results, in tabulated form, are compared to those of Sheriff [2], and Landis and Yanowitz [3] in Table 3. Nusselt numbers obtained from the equation proposed by Keyhani et al. are given. In general, equation (8) leads to a better agreement with experimental values of other investigators as compared to the Nusselt numbers obtained from [1]. This is to be expected, since the correlation from [1] was based on one set of aspect and radius ratios augmented with the H and K effects as reported by Thomas and de Vahl Davis.

In order to determine the effect of constant heat flux boundary condition as opposed to an isothermal one, experimental results of Eckert and Carlson [8] for thermal convection in a vertical air layer are available. Equation (6) for $H = 15$, and $K = 1$, at $\mathrm{Ra} = 10^5$ results in a Nusselt number 32 percent higher than that given by Eckert and Carlson.

Conclusion

The correlations obtained in the present work show that the average Nusselt number in tall vertical annuli, in which the inner wall is at constant heat flux and the outer wall is at constant temperature, is strongly dependent on the geometry of the system. In the conduction regime, Nu is a weak function of Ra and H, but in the boundary layer regime is a strong function of both these parameters. In either flow regime, Nu is a strong function of radius ratio.

Three sets of data points for H and K are used in the present study to obtain the exponents of aspect radius ratios in equations (5), (6), (7), and (8). The results are in good agreement with the related studies in the literature. However, more sets of experimental data points for H and K are needed in order to refine the reported exponents. A mixed boundary condition, as in the present study, results in Nusselt numbers as much as 32 percent higher than those of an isothermal one.

Acknowledgment

We gratefully acknowledge the support of this work by The Office of Nuclear Waste Isolation under Contract E512-03900 to The Ohio State University Research Foundation.

References

1 Keyhani, M., Kulacki, F. A., and Christensen, R. N., "Free Convection in a Vertical Annulus With Constant Heat Flux on the Inner Wall," ASME JOURNAL OF HEAT TRANSFER, Vol. 105, 1983, pp. 454-459.

2 Sheriff, N., "Experimental Investigation of Natural Convection in a Single and Multiple Vertical Annuli With High Pressure Carbon Dioxide," *Proceedings, Third International Heat Transfer Conference*, Vol. 2, 1966, pp. 132-138.

3 Landis, F., and Yanowitz, H., "Transient Natural Convection in a Narrow Vertical Cell," *Proceedings, Third International Heat Transfer Conference*, Vol. 2, 1966, pp. 139-151.

4 MacGregor, R. K., and Emery, A. F., "Free Convection Through Vertical Plane Layers-Moderate and High Prandtl Number Fluids," *Journal of Heat Transfer*, Vol. 91, 1969, pp. 391-403.

5 Thomas, R. W., and de Vahl Davis, G., "Natural Convection in Annular and Rectangular Cavities, A Numerical Study," *Proceedings, Fourth International Heat Transfer Conference*, Vol. 4, Paper NC2.4, Elsevier, Amsterdam, 1970.

6 de Vahl Davis, G., and Thomas, R. W., "Natural Convection Between Concentric Vertical Cylinder," *High Speed Computing in Fluid Dynamics, Physics of Fluids*, Supplement II, 1969, pp. 198-207.

7 Bhushan, R., "Heat Transfer Within Spent Fuel Canisters," M.Sc. thesis in Nuclear Engineering, The Ohio State University, 1981.

8 Eckert, E. R. G., and Carlson, W. O., "Natural Convection in an Air Layer Enclosed Between Two Vertical Plates with Different Temperatures," *International Journal of Heat and Mass Transfer*, Vol. 2, 1961, pp. 106-120.

Natural Convection Heat Transfer in Complex Enclosures at Large Prandtl Number

M. W. Nansteel[1] and R. Greif[2]

Nomenclature

A = aspect ratio, H/L

A_p = aperture ratio, h/H

[1] Department of Mechanical Engineering and Applied Mechanics, University of Pennsylvania, Philadelphia, Pa. 19104

[2] Mechanical Engineering Department, University of California, Berkeley, Berkeley, Calif. 94720

Contributed by the Heat Transfer Division for publication in the JOURNAL OF HEAT TRANSFER. Manuscript received by the Heat Transfer Division December 13, 1982.

B = enclosure breadth
c_p = constant pressure specific heat
g = acceleration due to gravity
H = enclosure height
h = distance from enclosure floor to partition
k = thermal conductivity
k_p = thermal conductivity of partition
k_p^* = nondimensional partition conductance, $(k_p/k)(L/\Delta x)/\mathrm{Nu}_L$
L = enclosure width
Nu_L = Nusselt number, $qL/(T_h - T_c)k$
Pr = Prandtl number, $\frac{\nu}{\alpha}$
Q = heat transfer across enclosure, $(Q_h + Q_c)/2$
q = average heat flux, $Q/(B \cdot H)$
Ra_L = Rayleigh number, $g\beta L^3(T_h - T_c)/\nu\alpha$
T = temperature
x = horizontal position coordinate
Δx = thickness of partial division
y = vertical position coordinate
α = thermal diffusivity
β = coefficient of thermal expansion
μ = dynamic viscosity
ν = kinematic viscosity
ρ = density

Subscripts

c = cold wall
h = hot wall

1 Introduction

Interest in natural convection within complex enclosures is growing rapidly. Such geometries are of practical importance in the design of passive solar heating systems, in fire research, and in thermal insulation. Heat transfer within enclosures containing partitions or baffles has been addressed in only a few investigations [1-11, 18]. Duxbury [1] experimentally studied the flow and heat transfer in rectangular air-filled cells fitted with vertical and horizontal partitions. Emery [5] carried out experiments in liquid-filled enclosures fitted with a partial vertical baffle at the center of the cavity. In [6] and [10], Nansteel and Greif experimentally studied the flow, temperature, and heat transfer in a water-filled cavity fitted with vertical partitions of various lengths and thermal conductances located either on the floor or on the ceiling of the cavity for Rayleigh numbers over the range $10^{10} \leq \mathrm{Ra}_L \leq 10^{11}$. Winters [7] and Chang et al. [8] used finite element and finite difference methods, respectively, in studying the flow in gas-filled enclosures fitted with vertical partitions. In [8] calculations were carried out for Grashof numbers as high as 10^8, while the calculations of Winters [7] were restricted to Rayleigh numbers less than 4×10^6. Recently, Lin and Bejan [18] experimentally studied the fluid flow and heat transfer in a rectangular enclosure ($A = 0.305$) with a vertical partition extending upward from the enclosure floor over the full range of aperture ratios, $1 \geq A_p \geq 0$ and $\mathrm{Ra}_L = 0(10^{11})$.

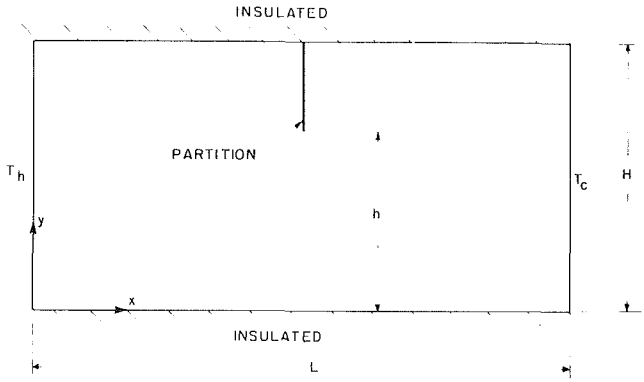

Fig. 1 Sketch of the two-dimensional, partially divided cavity

In this study, experiments are described in which vertical, low conductivity, ceiling-mounted partitions of various lengths partially divide a rectangular cavity (see Fig. 1) filled with silicone oil ($620 \leq \mathrm{Pr} \leq 910$). Experiments are carried out under steady conditions over the range $1.55 \times 10^9 \leq \mathrm{Ra}_L \leq 5.86 \times 10^9$, for undivided and partially divided enclosures of aspect ratio one-half. Correlations are obtained giving the dependence of the Nusselt number on the Rayleigh number and partition length.

2 Experimental Apparatus and Procedure

The experimental apparatus consisted of a rectangular plexiglass enclosure of height, $H = 15.2$ cm, width, $L = 30.5$ cm, and breadth, $B = 83.8$ cm, as described in [6]. Polystyrene foam partitions extended downward from the center of the enclosure ceiling and traversed the full breadth of the enclosure in order to achieve, as nearly as possible, a two-dimensional system. The use of foam partitions in conjunction with silicone oil as the test fluid resulted in nondimensional partition conductances of $k_p^* \lesssim 0.1$. The nondimensional partition conductance, $k_p^* = (k_p/k)(L/\Delta x)/\mathrm{Nu}_L$, is a measure of the fraction of the total cross-cavity heat transfer that is due to conduction through the partition; i.e., k_p^* indicates the magnitude of the thermal conductance of the partition relative to the conductance of the entire convection cell. The hot and cold vertical walls of the enclosure were maintained isothermal while the floor, ceiling, and endwalls were insulated. Energy input at the hot wall was measured with wattmeters (± 3 percent accuracy), while the energy removed from the cavity at the cold wall was determined by measuring the flow rate and temperature change of the cooling water that flowed through the cold wall. Uncertainty

Table 1 Thermodynamic and transport properties of General Electric SF-96(100) silicone oil

T (°C)	k (W/m − °C)	c_p (J/kg − °C)	ν (m^2/s)	ρ (kg/m^3)	β (1/K)	Pr
20	0.133	1550	1.11×10^{-4}	973	1.27×10^{-3}	1250
40	0.128	1560	7.61×10^{-5}	950	1.23×10^{-3}	884.6
60	0.122	1580	5.46×10^{-5}	927	1.21×10^{-3}	654.3
80	0.117	1600	4.07×10^{-5}	905	1.18×10^{-3}	503.7

Table 2 Silicone oil heat transfer data, $A_p = h/H = 1$

Run	Ra_L	Pr	Nu_L	Q_h (W)	Q_c (W)	$\frac{Q_h - Q_c}{Q_h}$	T_h (°C)	T_c (°C)	$T_h - T_c$ (°C)
1	4.85×10^9	660	130	474	389	18%	92.2	27.3	64.9
2	3.49×10^9	710	119	344	280	19%	79.9	29.1	50.8
3	2.49×10^9	770	108	251	204	19%	68.5	28.5	40.0
4	1.74×10^9	830	98.1	180	133	26%	59.3	29.2	30.1
5	5.78×10^9	630	137	562	458	19%	99.9	26.8	73.1

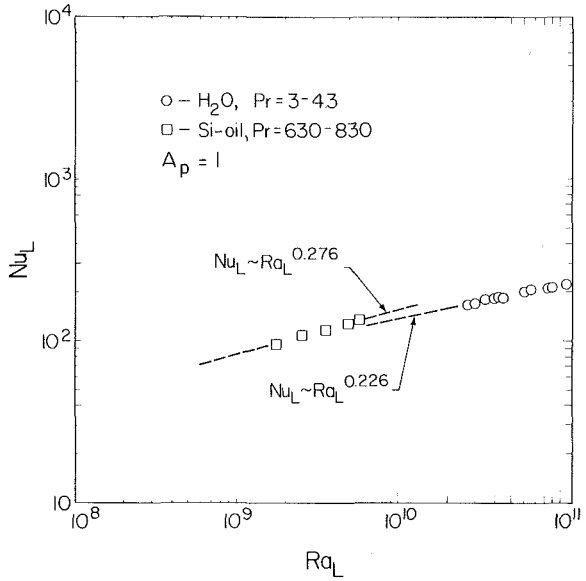

Fig. 2 Heat transfer in the undivided enclosure, water and silicone oil data

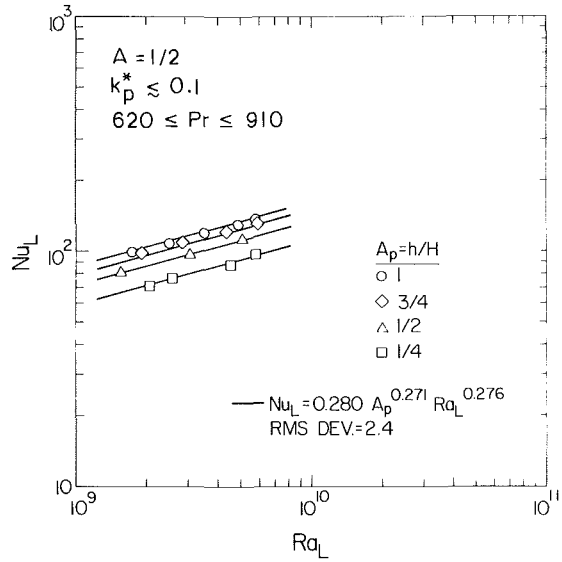

Fig. 4 Heat transfer in the partially divided, silicone oil-filled cavity, $A = 1/2, k_p^* \leq 0.1, 620 \leq Pr \leq 910$

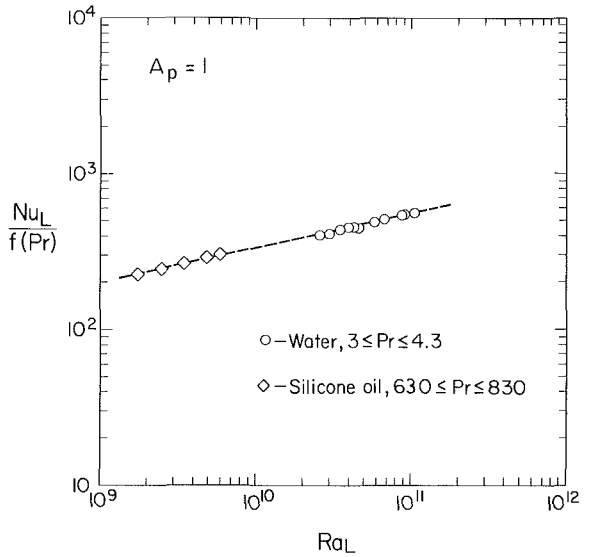

Fig. 3 Heat transfer data of Fig. 2 reported as $Nu_L/f(Pr)$ versus Ra_L, $f(Pr)$ defined in equation (1), dashed curve given by equation (2).

in the reported values of the Nusselt numbers due to measurement uncertainty and heat loss from the enclosure is estimated to be less than ± 10 percent in most cases. Physical properties of the working fluid (General Electric Silicone Oil SF-96(100)) are listed in Table 1. Further details of the experimental apparatus and procedure may be found in [6].

3 Results and Discussion

Heat transfer results were obtained over the ranges, $1.55 \times 10^9 \leq Ra_L \leq 5.86 \times 10^9$, $620 \leq Pr \leq 910$, for aperture ratios, $A_p = h/H = 1/4$, 1/2, 3/4, and 1 ($A_p = 1$ corresponds to the undivided case). The heat transfer results for the five tests in the undivided cavity ($A_p = 1$) are listed in Table 2 and are also presented along with the water data of [6] in Fig. 2. Note that the high Prandtl number silicone oil results in a somewhat greater slope and slightly increased heat transfer when compared with an extrapolation of the water data of [6] on the Nu_L versus Ra_L plot of Fig. 2. The effect of Prandtl number on the heat transfer may be accounted for by replotting the data of Fig. 2 as in Fig. 3 with $Nu_L/f(Pr)$ as ordinate. The Prandtl number function, $f(Pr)$, is given by equation (1) and is of the general form suggested by Churchill and Usagi [12]and used by Raithby, Hollands, and Unny [13] in their approximate study of the heat transfer in undivided cavities of aspect ratio, $A \gtrsim 5$

$$f(Pr) = \frac{0.446}{\left[1 + \left(\frac{1.24}{Pr^{1/4}}\right)^{11/2}\right]^{2/11}} \quad (1)$$

The form used here, equation (1), was modified [14] from that used in [13] in order to better correlate experimental and numerical heat transfer data available for undivided and partially divided enclosures with $A \simeq 1/2$, $10^5 \leq Ra_L \leq 10^{11}$, and $Pr \geq 0.1$. The dashed curve in Fig. 3 is given by the relation

$$Nu_L = 1.95 f(Pr) Ra_L^{0.224} \quad (2)$$

In Fig. 4, heat transfer data are shown for the silicone oil-filled cavity for the undivided configuration (i.e., $A_p = 1$) and for the partially divided configuration with $A_p = 3/4$, 1/2, and 1/4. Note that there is a substantial reduction in the cross-cavity heat transfer as partition length is increased (i.e., as A_p is decreased). However, the dependence of Nu_L on A_p is somewhat smaller for silicone oil than for water [6]. From Fig. 4

$$\mathrm{Nu}_L \sim A_p^{0.271} (620 \leq \mathrm{Pr} \leq 910) \tag{3}$$

while for water [6]

$$\mathrm{Nu}_L \sim A_p^{0.473} (3 \leq \mathrm{Pr} \leq 4.3) \tag{4}$$

The difference in the aperture ratio dependence of the heat transfer between the oil data and the water data may be a direct consequence of the different values of the Prandtl number for the two working fluids. However, it seems unlikely that such a substantial change in the aperture ratio dependence could be caused by a variation in Prandtl number at the relatively large values of Pr studied. It is generally accepted, at least in the case of an undivided cavity, that Nusselt number becomes virtually independent of Prandtl number for $\mathrm{Pr} \gtrsim 5$ [15-17]. Another effect which may have contributed to the difference in the aperture ratio dependence is the nondimensional partition conductance, k_p^*. For the experiments with water [6], $k_p^* \lesssim 0.02$, while for the present experiments with silicone oil, $k_p^* \lesssim 0.1$. It was shown in the experiments of [6] that the dependence of the cross-cavity heat transfer on the aperture ratio increases for decreased values of k_p^*. According to [6], the Nusselt number dependence on the aperture ratio increases from $A_p^{0.256}$ for divisions with a high relative conductance ($k_p^* >> 1$) to $A_p^{0.473}$ for divisions of low relative conductance ($k_p^* << 1$), all other parameters held fixed. This behavior is attributed in [6] to a reduction in recirculation strength in the upper left-hand quadrant of the partially divided enclosure (as division conductance decreases) and therefore to reduced convection adjacent to the upper part of the hot wall. Hence, insulating divisions represent an increased resistance to the heat transfer across the enclosure with a greater resulting sensitivity to the aperture ratio.

Extrapolation of the present results to other aperture ratios ($A_p < 1/4$) and aspect ratios ($A \neq 1/2$) should be done with caution. For example, for aperture ratios approaching $A_p = 0$ (i.e., the completely divided enclosure) the heat transfer must deviate from the power laws (3) and (4) when the partition has a finite thermal conductance, for then $\mathrm{Nu}_L > 0$ when $A_p = 0$. For the case $A_p = 0$, when the thermal resistance of the partition far exceeds the thermal resistance of the two adjoining fluid regions,[3] it is expected that these regions will be roughly isothermal at the temperatures T_h and T_c to the left and right of the partition, respectively. Then $\mathrm{Nu}_L \simeq (k_p/k)(L/\Delta x)$, where Δx is the partition thickness. On the other hand, the data of [1] indicates that when the fluid regions represent the major thermal resistances, the heat transfer across the completely divided enclosure ($A_p = 0$) corresponds roughly to the heat transfer across an undivided enclosure of height, H, and width, $L/2$, across which a temperature differential, $(T_h - T_c)/2$, is maintained. Thus, the heat transfer is as if the partition is isothermal at the temperature $(T_h + T_c)/2$. With respect to aspect ratio, there seems to be little information available concerning the effect of A on the heat transfer in partially divided enclosures.

[3] In this case the thermal resistance of the overall cell is practically equal to the resistance of the partition and therefore $k_p^* \simeq 1$.

4 Conclusions

From the results presented here for $620 \leq \mathrm{Pr} \leq 910$ and the lower Prandtl number data of [6], it is concluded that for undivided cavities of aspect ratio one-half, relations (1) and (2) correlate the heat transfer data over the range, $10^9 \leq \mathrm{Ra}_L \leq 10^{11}$. It was found that the aperture ratio dependence of the cross-cavity heat transfer is rather sensitive to the relative conductance of the partial division over the range tested: namely, $0.02 \lesssim k_p^* \lesssim 0.10$. The aperture ratio dependence may also be influenced by the Prandtl number.

Acknowledgment

This work has been supported in part by the Assistant Secretary for Conservation and Renewable Energy, Office of Solar Heat Technologies, Passive and Hybrid Solar Energy Division, U.S. Department of Energy, under contract number DE-AC03-76SF00098. The authors also wish to acknowledge Fred Bauman of the Passive Solar Research and Development Group, Lawrence Berkeley Laboratory, for his assistance during the early stages of this research.

References

1 Duxbury, D., "An Interferometric Study of Natural Convection in Enclosed Plane Air Layers With Complete and Partial Central Vertical Divisions," Ph.D. thesis, University of Salford, 1979.

2 Lynch, N. P., and Lloyd, J. R., "An Experimental Investigation of the Transient Build-Up of Fire in a Room-Corridor Geometry," 18th International Symposium on Combustion, The Combustion Institute, Pittsburgh, Pa., 1980.

3 Ku, A. C., Doria, M. L., and Lloyd, J. R., "Numerical Modeling of Unsteady Buoyant Flows Generated by Fire in a Corridor," *Proceedings of the 16th International Symposium on Combustion*, The Combustion Institute, Pittsburgh, Pa., 1976, pp. 1373-1384.

4 Janikowski, H. E., Ward, J., and Probert, S. D., "Free Convection in Vertical Air-Filled Rectangular Cavities Fitted with Baffles," *Proceedings of the 6th International Heat Transfer Conference*, Toronto, Vol. 2, pp. 257-262.

5 Emery, A. F., "Exploratory Studies of Free Convection Heat Transfer Through an Enclosed Vertical Liquid Layer with a Vertical Baffle," ASME JOURNAL OF HEAT TRANSFER, Vol. 91, 1969, pp. 163-165.

6 Nansteel, M. W., and Greif, R., "Natural Convection in Undivided and Partially Divided Rectangular Enclosures," ASME JOURNAL OF HEAT TRANSFER, Vol. 103, 1981, pp. 623-629.

7 Winters, K. H., "The Effect of Conducting Divisions on the Natural Convection of Air in a Rectangular Cavity with Heated Side Walls," 3rd Joint AIAA/ASME Thermophysics, Fluids, Plasma and Heat Transfer Conf., St. Louis, 1982.

8 Chang, L. C., Lloyd, J. R., and Yang, K. T., "A Finite Difference Study of Natural Convection in Complex Enclosures," *Proceedings of the Seventh Int. Heat Transfer Conf.*, Munich, Germany, 1982, pp. 183-188.

9 Nansteel, M. W., "Natural Convection in Enclosures," Ph.D. thesis, University of California, Berkeley, 1982.

10 Nansteel, M. W., and Greif, R., "An Investigation of Natural Convection in Enclosures with Two- and Three-Dimensional Partitions," to appear in *International Journal of Heat and Mass Transfer*.

11 Bauman, F., Gadgil, A., Kammerud, R., and Greif, R., "Buoyancy Driven Convection in Rectangular Enclosures: Experimental Results and Numerical Calculations," ASME Paper No. 80-HT-66, 1980.

12 Churchill, S. W., and Usagi, R., "A General Expression for the Correlation of Rates of Transfer and Other Phenomena," *AIChE J.*, Vol. 18, No. 6, 1972, pp. 1121-1128.

13 Raithby, G. D., Hollands, K. G. T., and Unny, T. E., "Analysis of Heat Transfer by Natural Convection Across Vertical Fluid Layers," ASME *Journal of Heat Transfer*, Vol. 99, 1977, pp. 287-293.

14 Nansteel, M. W., "An Attempt to Determine, Approximately, the Effects of Prandtl Number on Heat Transfer in the Partially Divided Enclosure of Aspect Ratio One-Half," Technical Note No. 25, Passive Solar Group, Lawrence Berkeley Laboratory, Nov. 1981.

15 de Vahl Davis, G., "Laminar Natural Convection in an Enclosed Rectangular Cavity," *International Journal of Heat and Mass Transfer*, Vol. 11, 1968, pp. 1675-1693.

16 MacGregor, R. K., and Emery, A. F., "Free Convection through Vertical Plane Layers, Moderate and High Prandtl Number Fluids," ASME JOURNAL OF HEAT TRANSFER, Vol. 91, 1969, pp. 391-403.

17 Rubel, R., and Landis, F., "Numerical Study of Natural Convection in a Vertical Rectangular Enclosure," *Physics of Fluids Supplement II*, Vol. 12, 1969, pp. 203-213.

18 Lin, N., and Bejan, A., "Natural Convection in a Partially Divided Enclosure," personal communication.

The "Heatline" Visualization of Convective Heat Transfer

S. Kimura[1] and A. Bejan[1]

Nomenclature

- c_p = specific heat at constant pressure
- Gr = Grashof number, Ra/Pr
- H = heat function, defined by equations (4) and (5)
- k = fluid thermal conductivity
- L = height of the square cavity
- Nu = Nusselt number; actual heat transfer rate divided by the pure conduction estimate
- Pr = Prandtl number, ν/α
- Ra = Rayleigh number, $g\beta L^3 (T_H - T_C)/(\alpha\nu)$
- T = temperature
- u = horizontal velocity
- v = vertical velocity
- x = horizontal position
- y = vertical position
- α = thermal diffusivity
- β = coefficient of thermal expansion
- ν = kinematic viscosity
- ρ = density of the fluid
- ζ = vorticity
- ψ = stream function

Subscripts

- H = hot wall
- C = cold wall
- $*$ = nondimensional variable

The object of this note is to propose a new approach to visualizing the transfer of heat by fluid flow. This new approach represents the energy-analog of the use of "stream function" and "streamlines" to visualize fluid flow. In a two-dimensional Cartesian convection heat transfer configuration, for example, it has become common practice to define a stream function $\psi(x,y)$ as [1]

$$u = \frac{\partial \psi}{\partial y}, \quad v = -\frac{\partial \psi}{\partial x} \tag{1}$$

such that the mass continuity equation for incompressible flow is satisfied identically by ψ

$$\frac{\partial u}{\partial x} + \frac{\partial v}{\partial y} = 0 \tag{2}$$

The actual flow is locally parallel to the ψ = constant line: therefore, although there is no substitute for (u,v) as bearers of precise information regarding the local flow, the family of ψ = constant streamlines provides a very useful birds-eye-view of the entire flow field and its main characteristics.

In convection, the transport of energy through the flow field is a combination of both thermal diffusion and enthalpy flow. For any such field one can define a function $H(x,y)$ such that the net flow of energy (thermal diffusion plus enthalpy flow) across each H = constant line is zero. The mathematical definition of the *heat function*, H, follows in the steps of equation (1) if, this time, the aim is to satisfy the energy equation. For steady-state convection through a constant-property homogeneous fluid [2], or through a volume-averaged homogeneous porous medium [3], the energy equation is

$$u\frac{\partial T}{\partial x} + v\frac{\partial T}{\partial y} = \alpha\left(\frac{\partial^2 T}{\partial x^2} + \frac{\partial^2 T}{\partial y^2}\right) \tag{3}$$

The heat function, H, is defined as

$$\frac{\partial H}{\partial y} = \rho c_p u T - k\frac{\partial T}{\partial x}, \text{ net energy flow in the } x\text{-direction} \tag{4}$$

$$-\frac{\partial H}{\partial x} = \rho c_p v T - k\frac{\partial T}{\partial y}, \text{ net energy flow in the } y\text{-direction} \tag{5}$$

so that $H(x,y)$ satisfies equation (3) identically. In definitions (4, 5), ρ, c_p and k are the fluid density, specific heat, and thermal conductivity. If the energy equation (3) refers to convection through a porous medium, then k is the thermal conductivity of the porous matrix filled with stagnant fluid [3].

According to the heat function definition (4, 5) any H = constant "heatline" is locally parallel to the direction of net energy flow through the convection field. Again, there is no substitute for (u, v, T) as a record of detailed local information regarding the convection heat transfer phenomenon; however, as demonstrated shortly through an example, the family of H = constant heatlines illustrates at a glance the actual path of the flow of energy through the entire field.

It is worth noting that if the fluid flow subsides ($u = v = 0$), the "heatlines" become identical to the "heat flux lines" employed frequently in the study of conduction phenomena. Therefore, as a heat transfer visualization technique the use of heatlines is the convection counterpart or the generalization of a standard technique (heat flux lines) used in conduction. It is interesting to point out also that the contemporary use of T = constant lines is not a proper way to visualize heat transfer in the field of convection: isotherms are a proper heat transfer visualization tool only in the field of conduction (where, in fact, they have been invented), because only there they are locally orthogonal to the true direction of energy flow.

Example

The convective heat transfer visualization proposal outlined above is illustrated in Figs. 1 and 2 by application to the classical problem of natural convection in a square enclosure heated from the side [4]. In each figure, the convective heat transfer phenomenon is described by means of the traditional ψ = constant and T = constant patterns, vis-a-vis the heatlines H = constant calculated via equations (4, 5). Figure 1 shows a low Ra flow in which the transfer of heat is dominated by thermal diffusion; consequently, the heatlines are nearly orthogonal to the isotherms, showing that the fluid flow does little to disturb the direct flow of energy between the two walls. Figure 2 illustrates a high Ra case where, by definition, the end-to-end transfer of energy is dominated by convection. The heatlines show vividly that "heat rises" and that the true energy corridor consists of two vertical boundary layers connected through an energy tube positioned along the upper wall.

In both figures, the heatlines are parallel to the top and bottom walls which are adiabatic. Along the two isothermal vertical walls, the heatlines are normal to the wall because the near wall regions are dominated by conduction (both u and v vanish at the wall).

The heat function $H(x,y)$ of Figs. 1 and 2 was evaluated numerically by first constructing a Poisson-type equation analogous to the equation used for calculating the stream

[1]Department of Mechanical Engineering, University of Colorado, Boulder, Colo. 80309

Contributed by the Heat Transfer Division for publication in the JOURNAL OF HEAT TRANSFER. Manuscript received by the Heat Transfer Division December 13, 1982.

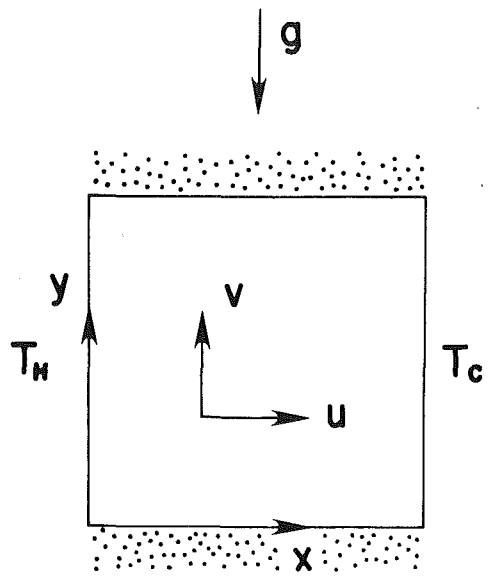

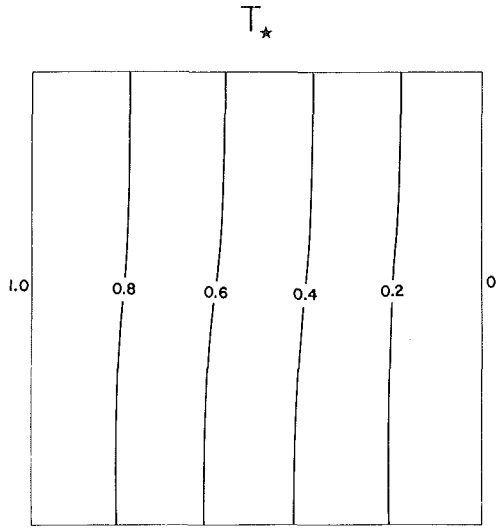

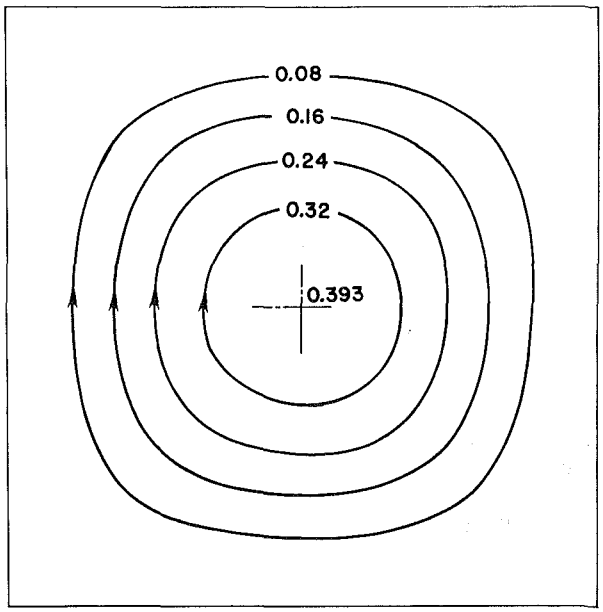

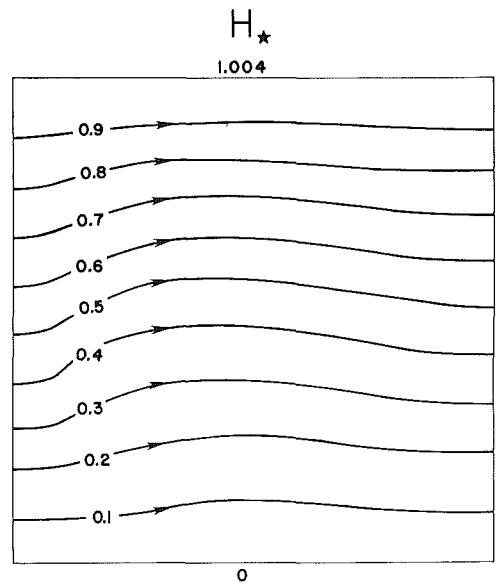

Fig. 1 Coordinate system for natural convection in a square enclosure, and patterns of streamlines, isotherms, and heatlines for a low-Rayleigh-number case, Ra = 140, Pr = 7

function. Differentiating equations (4) and (5) with respect to y and x, respectively, and subtracting the resulting equations side-by-side yields

$$\frac{\partial^2 H}{\partial x^2}+\frac{\partial^2 H}{\partial y^2}=\rho c_p\left[\frac{\partial}{\partial y}(uT)-\frac{\partial}{\partial x}(vT)\right] \tag{6}$$

In this equation the right-hand side is a quantity known from the solution to the convection problem (u,v,T): this quantity serves as "source" term. The (u,v,T) solution for the square box flow illustrated in Figs. 1 and 2 was obtained numerically based on the following dimensionless formulation:

(a) Governing equations

$$\frac{\partial}{\partial x_*}(u_* T_*)+\frac{\partial}{\partial y_*}(v_* T_*)=\frac{1}{\sqrt{\mathrm{Gr}}}\left(\frac{\partial^2 T_*}{\partial {x_*}^2}+\frac{\partial^2 T_*}{\partial {y_*}^2}\right) \tag{7}$$

$$\frac{\partial}{\partial x_*}(u_* \zeta_*)+\frac{\partial}{\partial y_*}(v_* \zeta_*)$$

$$=\frac{\mathrm{Pr}}{\sqrt{\mathrm{Gr}}}\left(\frac{\partial^2 \zeta_*}{\partial {x_*}^2}+\frac{\partial^2 \zeta_*}{\partial {y_*}^2}\right)+\mathrm{Pr}\frac{\partial T_*}{\partial x_*} \tag{8}$$

$$-\zeta_*=\frac{\partial^2 \psi_*}{\partial {x_*}^2}+\frac{\partial^2 \psi_*}{\partial {y_*}^2};\ u_*=\frac{\partial \psi_*}{\partial y_*};\ v_*=-\frac{\partial \psi_*}{\partial x_*} \tag{9}$$

(b) Boundary conditions

$$\begin{aligned} &T_*=1, \quad \psi_*=\frac{\partial \psi_*}{\partial x_*}=0 \quad \text{at } x_*=0\\ &T_*=0, \quad \psi_*=\frac{\partial \psi_*}{\partial x_*}=0 \quad \text{at } x_*=1\\ &\frac{\partial T_*}{\partial y_*}=0, \quad \psi_*=\frac{\partial \psi_*}{\partial y_*}=0 \quad \text{at } y_*=0,1 \end{aligned} \tag{10}$$

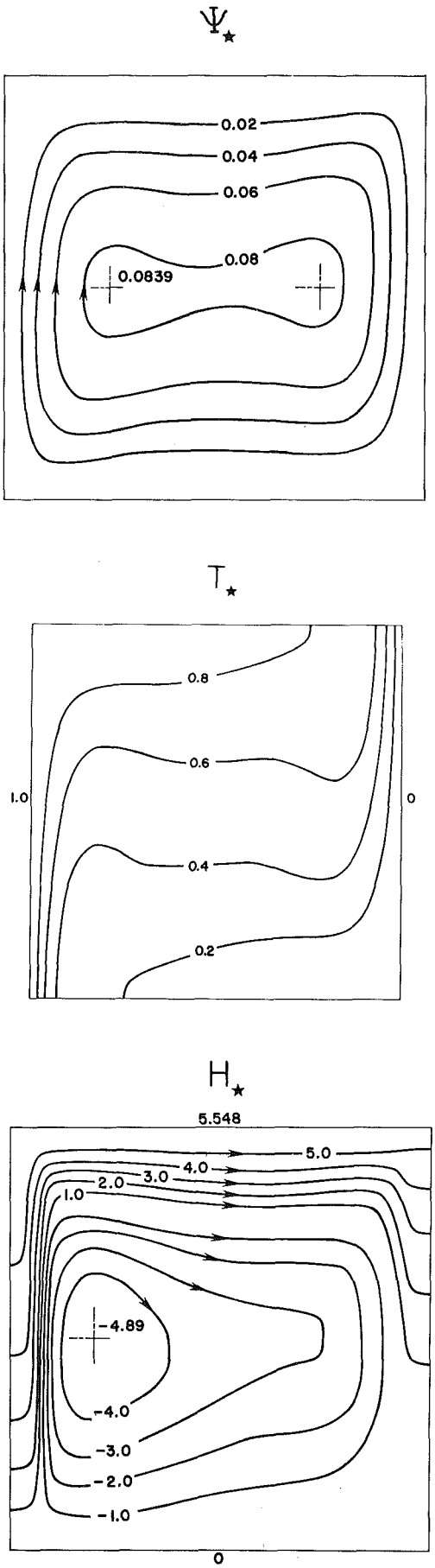

Fig. 2 Streamlines, isotherms, and heatlines for a high-Rayleigh-number case, Ra = 1.4 × 10^5, Pr = 7

(*c*) Dimensionless parameters

$$(x_*, y_*) = \frac{(x,y)}{L}; \; (u_*, v_*) = \frac{(u,v)L}{\alpha\sqrt{\mathrm{Gr}}}; \; T_* = \frac{T - T_c}{T_H - T_c}$$

$$\mathrm{Gr} = \mathrm{Ra}/\mathrm{Pr}; \; \mathrm{Pr} = \nu/\alpha; \; \mathrm{Ra} = \frac{g\beta L^3 (T_H - T_c)}{\alpha\nu} \tag{11}$$

The foregoing formulation is based on recommendations by Chow and Tien [5] and Torrance and Rockett [6]. Equations (7) and (8) were solved numerically using the Allen-Southwell finite difference scheme, which is described in detail in [5]. The numerical results agree very well with calculations made previously for natural convection in a square enclosure. For example, the present solution yielded Nu = 5.548 for the case (Gr = 2 × 10^4, Pr = 7), whereas Cormack et al. [7] reported Nu = 5.55 for (Gr = 2 × 10^4, Pr = 6.983).

To calculate the heat function, equation (6) was first written in dimensionless form as

$$\frac{\partial^2 H_*}{\partial x_*^{\,2}} + \frac{\partial^2 H_*}{\partial y_*^{\,2}} = \sqrt{\mathrm{Gr}}\left[\frac{\partial}{\partial y_*}(u_* T_*) - \frac{\partial}{\partial x_*}(v_* T_*)\right] \tag{12}$$

where

$$H_*(x_*, y_*) = \frac{H(x,y)}{k(T_H - T_c)} \tag{13}$$

The boundary conditions on H_* follow from the definition of heat function, equations (4, 5):

$$H_* = \int_0^{y_*} \left(-\frac{\partial T_*}{\partial x_*}\bigg|_{x_*=0}\right) dy_* \text{ and } \frac{\partial H_*}{\partial x_*} = 0 \quad \text{at } x_* = 0 \text{ and } 1$$

$$H_* = 0 \text{ and } \frac{\partial H_*}{\partial y_*} = -\frac{\partial T_*}{\partial x_*} \quad \text{at } y_* = 0 \tag{14}$$

$$H_* = \mathrm{Nu} \text{ and } \frac{\partial H_*}{\partial y_*} = -\frac{\partial T_*}{\partial x_*} \quad \text{at } y_* = 1$$

Equation (12) was discretized by means of the centered finite difference scheme. The resulting algebraic equation was solved by successive overrelaxation.

It is worth noting also that the heatline patterns of Figs. 1 and 2 do not exhibit the "centrosymmetry property" of streamline and isotherm patterns of natural convection in enclosures with centrosymmetric boundary conditions. In the present example, the centrosymmetry of streamlines and isotherms means

$$u(x,y) = -u(1-x, 1-y) \tag{15}$$

$$v(x,y) = -v(1-x, 1-y) \tag{16}$$

$$T(x,y) - \frac{1}{2} = -\left[T(1-x, 1-y) - \frac{1}{2}\right] \tag{17}$$

The heatline pattern would also be centrosymmetric if $H(x,y) = H(1-x, 1-y)$ or, in terms of derivatives, if

$$\left(\frac{\partial H}{\partial x}\right)_{x,y} = -\left(\frac{\partial H}{\partial x}\right)_{1-x,1-y} \tag{18}$$

$$\left(\frac{\partial H}{\partial y}\right)_{x,y} = -\left(\frac{\partial H}{\partial y}\right)_{1-x,1-y} \tag{19}$$

However, conditions (18, 19) are not satisfied by $H(x,y)$: for example, applying the transformation $(x,y) \rightarrow (1-x, 1-y)$ to definition (4) yields

$$\left(\frac{\partial H}{\partial y}\right)_{x,y} = \left(\rho c_p u T - k\frac{\partial T}{\partial x}\right)_{x,y}$$

$$= \left(-\rho c_p u(1-T) - k\frac{\partial T}{\partial x}\right)_{1-x,1-y} \neq -\left(\frac{\partial H}{\partial y}\right)_{1-x,1-y} \tag{20}$$

Another way to prove that $H(x,y)$ is not centrosymmetric, is to show that equation (6) is not invariant with respect to the transformation $(x,y) \rightarrow (1-x,1-y)$.

One interesting contribution of the heatline pattern is that it shows graphically the magnitude of the Nusselt number: note that the conduction-referenced Nusselt number appears on Figs. 1 and 2 as the value of maximum H_* on the top heatline of each heat function plot. Note further that the heatline pattern for the high-Rayleigh-number case, Fig. 2, shows graphically for the first time the flow of energy downward through the core.

In conclusion, the example of Figs. 1 and 2 shows the place and usefulness of heatline patterns in the art of illustrating convective heat transfer. The real value of this method, however, can only be assessed by application to more problems, other than the natural convection example illustrated in this note.

Acknowledgment

This work was supported in part by NSF Grant No. MEA-82-07779.

References

1 Kays, W. M., and Crawford, M. E., *Convective Heat and Mass Transfer*, 2d ed., McGraw-Hill, New York, 1980, p. 75.

2 Kays, W. M., and Crawford, M. E., Op. Cit., p. 36.

3 Cheng, P., "Heat Transfer in Geothermal Systems," *Advances in Heat Transfer*, Vol. 14, 1978, pp. 1-105.

4 Catton, I., "Natural Convection in Enclosures," *Proceedings of the 6th International Heat Transfer Conference*, Toronto 1978, Vol. 6, 1979, pp. 13-43.

5 Chow, L. C., and Tien, C. L., "An Examination of Four Differencing Schemes for Some Elliptic-Type Convection Equations," *Numerical Heat Transfer*, Vol. 1, 1978, pp. 87-100.

6 Torrance, K. E., and Rockett, J. A., "Numerical Study of Natural Convection in an Enclosure with Localized Heating From Below-Creeping Flow to the Onset of Laminar Instability," *Journal of Fluid Mechanics*, Vol. 36, 1969, pp. 33-54.

7 Cormack, D. E., Leal, L. G., and Seinfeld, J. H., "Natural Convection in a Shallow Cavity With Differentially Heated Endwalls. Part 2: Numerical Solutions," *Journal of Fluid Mechanics*, Vol. 65, 1974, pp. 231-246.

Forced Convection in Non-Newtonian Flow Past A Nonisothermal Needle

J. L. S. Chen[1] and J. W. Kearns, Jr.[2]

An analysis of the laminar steady-state forced convection heat transfer from a nonisothermal thin needle in an accelerating incompressible non-Newtonian fluid is presented. Similarity temperature profile and heat transfer characteristics are obtained for needles with axial power-law variations in surface temperature and surface heat flux. Effects of the needle size, the non-Newtonian flow behavior, and the generalized Prandtl number of the thermal characteristics of the flow are examined in detail.

1 Introduction

The flow behavior of non-Newtonian fluids past a thin needle has been recently reported by Chen and Kubler [1]. The study presented here is an attempt to understand the thermal characteristics of such flows. Increased basic understanding has important implications concerning the general nature of heat transfer in non-Newtonian fluids.

In recent years, considerable efforts have been usefully devoted to forced convection [2-4] and free convection [5-11], as well as combined convection heat transfer [12, 13], from a thin needle or a slender body of revolution. However, most of these investigations were only concerned with Newtonian fluid flow past an isothermal or uniform wall heat flux needle.

In this paper, we investigate the laminar forced convection in a power-law, non-Newtonian fluid from a thin needle having a surface with (*i*) nonuniform temperature, and (*ii*) nonuniform heat flux. It is shown that when the external flow is of the form $U(x) = u_1 x^m$ (where x is the axial coordinate, u_1 and m are arbitrary constants) and the wall temperature or wall heat flux distribution has an arbitrary power-law variation along the needle, similarity solutions exist for the following two problems: (*a*) the power-law variations in external flow and the wall thermal distribution being arbitrary if the fluid is Newtonian, and (*b*) an accelerating external flow for $m = 1/3$ if the fluid is non-Newtonian. Although the latter is limited to only one external flow case ($m = 1/3$), the similarity solutions obtained would provide us with a remarkable opportunity to gain physical insight concerning the effects of the non-Newtonian flow behavior, the needle size, and the thermal nonuniformity of the surface on the thermal behavior of such flows.

2 The Similarity Analysis

The needle under consideration is assumed to be thin. Thus, the effect of transverse curvature is of importance, but the pressure gradient along the needle surface may be neglected, except in the region near the front stagnation [1-3] (hence, the solution so obtained is expected invalid in this region). However, in order to study a more general flow with axial pressure gradient and to explore the possibility of similarity solutions of the problem, we impose a variable mainstream velocity of the form $U(x) = u_1 x^m$. Under the assumption of constant fluid properties, the governing boundary-layer equations of continuity, momentum, and energy for the steady, laminar, incompressible axisymmetrical flow are, respectively

$$\frac{\partial(ru)}{\partial x} + \frac{\partial(rv)}{\partial r} = 0 \tag{1}$$

$$u\frac{\partial u}{\partial x} + v\frac{\partial u}{\partial r} = \frac{1}{\rho r}\frac{\partial}{\partial r}(r\tau_{rx}) + U\frac{dU}{dx} \tag{2}$$

$$u\frac{\partial T}{\partial x} + v\frac{\partial T}{\partial r} = \frac{\alpha}{r}\frac{\partial}{\partial r}\left(r\frac{\partial T}{\partial r}\right) \tag{3}$$

where (x,r) are the axial and radial coordinates, respectively, and both are measured from the front stagnation point of the needle; (u,v), the velocity components in these directions; ρ is the fluid density; α, the fluid thermal diffusivity; T is the fluid temperature; and τ_{rx}, the axial component of the shear stresses. Using Prandtl's order-of-magnitude arguments, it can be readily shown that the equation of state for the power-law, non-Newtonian fluids simplifies to

$$\tau_{rx} = K\left(\frac{\partial u}{\partial r}\right)^n \tag{4}$$

where K and n are the respective consistency index and flow behavior index of the power-law fluids. The mainstream temperature is maintained at a constant temperature, T_∞. Thus, the boundary conditions at the outer edge of the boundary layer are

[1] Associate Professor, Department of Mechanical Engineering, University of Pittsburgh, Pittsburgh, Pa., 15261. Mem. ASME.

[2] Engineer, Nuclear Technology Division, Westinghouse Electric Corp., Pittsburg, Pa. 15235.

Contributed by the Heat Transfer Division for publication in the JOURNAL OF HEAT TRANSFER. Manuscript received by the Heat Transfer Division January 26, 1982.

Another way to prove that $H(x,y)$ is not centrosymmetric, is to show that equation (6) is not invariant with respect to the transformation $(x,y) \rightarrow (1-x,1-y)$.

One interesting contribution of the heatline pattern is that it shows graphically the magnitude of the Nusselt number: note that the conduction-referenced Nusselt number appears on Figs. 1 and 2 as the value of maximum H_* on the top heatline of each heat function plot. Note further that the heatline pattern for the high-Rayleigh-number case, Fig. 2, shows graphically for the first time the flow of energy downward through the core.

In conclusion, the example of Figs. 1 and 2 shows the place and usefulness of heatline patterns in the art of illustrating convective heat transfer. The real value of this method, however, can only be assessed by application to more problems, other than the natural convection example illustrated in this note.

Acknowledgment

This work was supported in part by NSF Grant No. MEA-82-07779.

References

1 Kays, W. M., and Crawford, M. E., *Convective Heat and Mass Transfer*, 2d ed., McGraw-Hill, New York, 1980, p. 75.

2 Kays, W. M., and Crawford, M. E., Op. Cit., p. 36.

3 Cheng, P., "Heat Transfer in Geothermal Systems," *Advances in Heat Transfer*, Vol. 14, 1978, pp. 1-105.

4 Catton, I., "Natural Convection in Enclosures," *Proceedings of the 6th International Heat Transfer Conference*, Toronto 1978, Vol. 6, 1979, pp. 13-43.

5 Chow, L. C., and Tien, C. L., "An Examination of Four Differencing Schemes for Some Elliptic-Type Convection Equations," *Numerical Heat Transfer*, Vol. 1, 1978, pp. 87-100.

6 Torrance, K. E., and Rockett, J. A., "Numerical Study of Natural Convection in an Enclosure with Localized Heating From Below-Creeping Flow to the Onset of Laminar Instability," *Journal of Fluid Mechanics*, Vol. 36, 1969, pp. 33-54.

7 Cormack, D. E., Leal, L. G., and Seinfeld, J. H., "Natural Convection in a Shallow Cavity With Differentially Heated Endwalls. Part 2: Numerical Solutions," *Journal of Fluid Mechanics*, Vol. 65, 1974, pp. 231-246.

Forced Convection in Non-Newtonian Flow Past A Nonisothermal Needle

J. L. S. Chen[1] and J. W. Kearns, Jr.[2]

An analysis of the laminar steady-state forced convection heat transfer from a nonisothermal thin needle in an accelerating incompressible non-Newtonian fluid is presented. Similarity temperature profile and heat transfer characteristics are obtained for needles with axial power-law variations in surface temperature and surface heat flux. Effects of the needle size, the non-Newtonian flow behavior, and the generalized Prandtl number of the thermal characteristics of the flow are examined in detail.

1 Introduction

The flow behavior of non-Newtonian fluids past a thin needle has been recently reported by Chen and Kubler [1]. The study presented here is an attempt to understand the thermal characteristics of such flows. Increased basic understanding has important implications concerning the general nature of heat transfer in non-Newtonian fluids.

In recent years, considerable efforts have been usefully devoted to forced convection [2-4] and free convection [5-11], as well as combined convection heat transfer [12, 13], from a thin needle or a slender body of revolution. However, most of these investigations were only concerned with Newtonian fluid flow past an isothermal or uniform wall heat flux needle.

In this paper, we investigate the laminar forced convection in a power-law, non-Newtonian fluid from a thin needle having a surface with (*i*) nonuniform temperature, and (*ii*) nonuniform heat flux. It is shown that when the external flow is of the form $U(x) = u_1 x^m$ (where x is the axial coordinate, u_1 and m are arbitrary constants) and the wall temperature or wall heat flux distribution has an arbitrary power-law variation along the needle, similarity solutions exist for the following two problems: (*a*) the power-law variations in external flow and the wall thermal distribution being arbitrary if the fluid is Newtonian, and (*b*) an accelerating external flow for $m = 1/3$ if the fluid is non-Newtonian. Although the latter is limited to only one external flow case ($m = 1/3$), the similarity solutions obtained would provide us with a remarkable opportunity to gain physical insight concerning the effects of the non-Newtonian flow behavior, the needle size, and the thermal nonuniformity of the surface on the thermal behavior of such flows.

2 The Similarity Analysis

The needle under consideration is assumed to be thin. Thus, the effect of transverse curvature is of importance, but the pressure gradient along the needle surface may be neglected, except in the region near the front stagnation [1-3] (hence, the solution so obtained is expected invalid in this region). However, in order to study a more general flow with axial pressure gradient and to explore the possibility of similarity solutions of the problem, we impose a variable mainstream velocity of the form $U(x) = u_1 x^m$. Under the assumption of constant fluid properties, the governing boundary-layer equations of continuity, momentum, and energy for the steady, laminar, incompressible axisymmetrical flow are, respectively

$$\frac{\partial(ru)}{\partial x} + \frac{\partial(rv)}{\partial r} = 0 \tag{1}$$

$$u\frac{\partial u}{\partial x} + v\frac{\partial u}{\partial r} = \frac{1}{\rho r}\frac{\partial}{\partial r}(r\tau_{rx}) + U\frac{dU}{dx} \tag{2}$$

$$u\frac{\partial T}{\partial x} + v\frac{\partial T}{\partial r} = \frac{\alpha}{r}\frac{\partial}{\partial r}\left(r\frac{\partial T}{\partial r}\right) \tag{3}$$

where (x,r) are the axial and radial coordinates, respectively, and both are measured from the front stagnation point of the needle; (u,v), the velocity components in these directions; ρ is the fluid density; α, the fluid thermal diffusivity; T is the fluid temperature; and τ_{rx}, the axial component of the shear stresses. Using Prandtl's order-of-magnitude arguments, it can be readily shown that the equation of state for the power-law, non-Newtonian fluids simplifies to

$$\tau_{rx} = K\left(\frac{\partial u}{\partial r}\right)^n \tag{4}$$

where K and n are the respective consistency index and flow behavior index of the power-law fluids. The mainstream temperature is maintained at a constant temperature, T_∞. Thus, the boundary conditions at the outer edge of the boundary layer are

[1] Associate Professor, Department of Mechanical Engineering, University of Pittsburgh, Pittsburgh, Pa., 15261. Mem. ASME.

[2] Engineer, Nuclear Technology Division, Westinghouse Electric Corp., Pittsburg, Pa. 15235.

Contributed by the Heat Transfer Division for publication in the JOURNAL OF HEAT TRANSFER. Manuscript received by the Heat Transfer Division January 26, 1982.

$$r \to \infty: u = U(x);\ T = T_\infty \tag{5}$$

and at the needle surface

$$r = r(x): \quad u = v = 0;$$

$$T = T_w(x) \tag{6}$$

or

$$\frac{\partial T}{\partial r} = -\frac{q_w(x)}{k} \tag{7}$$

in which k is the thermal conductivity of the fluid, $T_w = T_\infty + T_o x^s$ and $q_w = q_o x^p$ are, respectively, the variable wall temperature or wall heat flux along the needle, depending on which one is prescribed.

To transform (1) to (7), we introduce the axisymmetric stream function, ψ, similarity variable, z, and dimensionless temperature, θ

$$\psi = A_1 x f(z); \quad z = A_2 x^{m-1} r^2 \tag{8}$$

$$\theta(z) = \frac{T - T_\infty}{T_w - T_\infty} \text{ or } \theta(z) = 2a^{\frac{1}{2}}\,\mathrm{Re}^{\frac{1}{n+1}}\frac{T - T_\infty}{xq_w/k} \tag{9}$$

where

$$A_1 \equiv \left(\frac{K}{\rho}\right)^{\frac{2}{n+1}} u_1^{\frac{3(n-1)}{n+1}}, \quad A_2 \equiv \left(\frac{\rho}{K} u_1^{2-n}\right)^{\frac{2}{n+1}} \tag{10}$$

Table 1 Local skin-friction coefficient for $m = \frac{1}{3}$

$a =$		0.01		0.1	
n	$f''(a)$	$C_f \mathrm{Re}^{\frac{1}{n+1}}$	$f''(a)$	$C_f \mathrm{Re}^{\frac{1}{n+1}}$
0.5	28.3061	6.7298	3.4569	4.1822
1.0	9.9479	7.9583	1.6155	4.0869
1.5	6.1786	7.7706	1.1959	3.7212

Table 2 Values of $\mathrm{NuRe}^{\frac{-1}{n+1}}$ for variable surface temperature needles with $m = \frac{1}{3}$ (values in parentheses are of $\theta'(a)$

		n	0.5		1.0		1.5	
s	Pr	a	0.01	0.1	0.01	0.1	0.01	0.1
0.0	0.733		3.4194 (−17.0970)	1.6445 (−2.6002)	3.3240 (−16.6200)	1.5865 (−2.5084)	3.2646 (−16.3230)	1.5450 (−2.4428)
	10.0		5.4122 (−27.0610)	2.9645 (−4.6879)	4.9716 (−24.8580)	2.6898 (−4.2530)	4.7954 (−23.9770)	2.5986 (−4.1088)
	100.0		9.0160 (−45.0799)	5.4929 (−8.6850)	7.7232 (−38.6160)	4.6964 (−7.4256)	7.2320 (−36.1600)	4.4317 (−7.0072)
	500.0		13.6270 (−68.1350)	8.8354 (−13.9700)	11.0995 (−55.4975)	7.3162 (−11.5680)	10.1740 (−50.8700)	6.8115 (−10.7700)
1.0	0.733		4.0109 (−20.0545)	2.0211 (−3.1956)	3.8315 (−19.1577)	1.9113 (−3.0221)	3.7592 (−18.7962)	1.8756 (−2.9656)
	10.0		6.6463 (−33.2316)	3.8067 (−6.0189)	5.9381 (−29.6904)	3.3719 (−5.3314)	5.6609 (−28.3043)	3.2263 (−5.1012)
	100.0		11.5163 (−57.5813)	7.2655 (−11.4878)	9.5817 (−47.9085)	6.1007 (−9.6461)	8.8615 (−44.3077)	5.7130 (−9.0331)
	500.0		17.8196 (−89.0979)	11.8274 (−18.7008)	14.1467 (−70.7333)	9.6645 (−15.2809)	12.8146 (−64.0730)	8.9473 (−14.1469)

Table 3 Values of $\mathrm{NuRe}^{-\frac{1}{n+1}}$ for variable surface heat flux needles with $m = \frac{1}{3}$ (values in parentheses are of $\theta(a)$

		n	0.5		1.0		1.5	
p	Pr	a	0.01	0.1	0.01	0.1	0.01	0.1
0.0	0.733		3.6664 (0.0546)	1.8065 (0.3501)	3.5492 (0.0564)	1.7299 (0.3656)	3.4990 (0.0572)	1.7034 (0.3713)
	10.0		5.9559 (0.0336)	3.3044 (0.1914)	5.4245 (0.0369)	2.9679 (0.2131)	5.1680 (0.0387)	2.8515 (0.2218)
	100.0		10.1833 (0.0196)	6.2005 (0.1020)	8.6022 (0.0233)	5.2573 (0.1203)	7.9681 (0.0251)	4.9488 (0.1278)
	500.0		15.1172 (0.0132)	10.0549 (0.0629)	12.4533 (0.0161)	8.2771 (0.0764)	11.1297 (0.0180)	7.6485 (0.0827)
1.0	0.733		4.1667 (0.0480)	2.1110 (0.2996)	3.9580 (0.0505)	1.9882 (0.3181)	3.8700 (0.0517)	1.9490 (0.3245)
	10.0		6.9662 (0.0287)	4.0080 (0.1578)	6.1406 (0.0326)	3.5333 (0.1790)	5.8651 (0.0341)	3.3731 (0.1875)
	100.0		11.8694 (0.0169)	7.5562 (0.0837)	10.0000 (0.0200)	6.3595 (0.0995)	9.1324 (0.0219)	5.9497 (0.1063)
	500.0		18.1159 (0.0110)	12.2855 (0.0515)	14.5985 (0.0137)	10.0009 (0.0632)	13.1926 (0.0152)	9.3022 (0.0680)

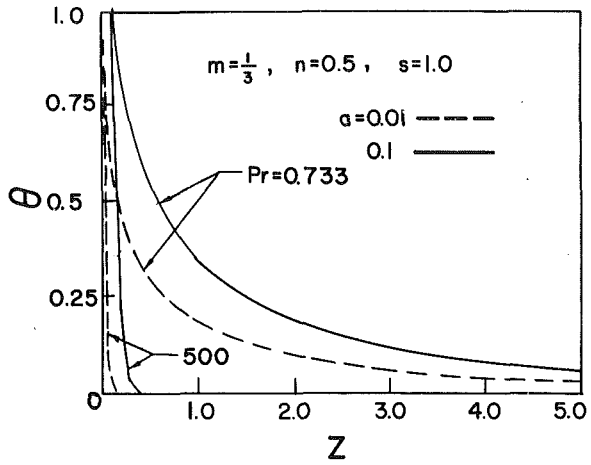

Fig. 1 Temperature profiles for a pseudoplastic fluid ($n = 0.5$) past needles with linear wall temperature

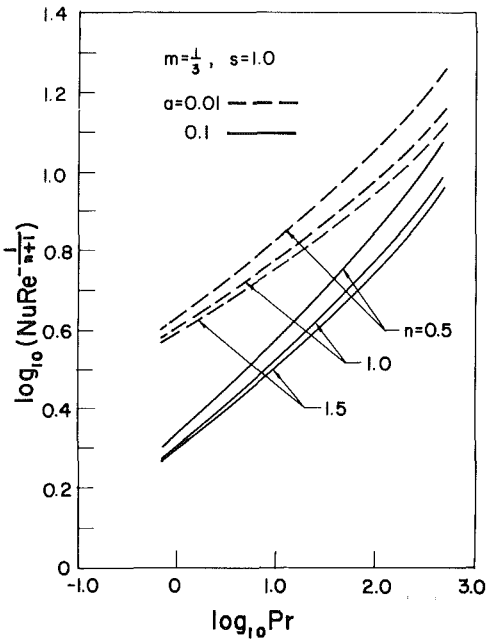

Fig. 2 Film heat transfer coefficients for needles with linear surface temperature distribution ($s = 1.0$)

and $\mathrm{Re} = \rho U^{2-n}x^n/K$ is the generalized local Reynolds number. By setting $z = a$ in the second equation of (8), where a is numerically small for a thin needle, a surface of revolution is represented which refers to the wall of the needle. Use of (8) to (10) transforms (2) to (7) to, under the restriction of either $n = 1$ or $m = 1/3$,

$$2n(4)^n z^{\frac{n+1}{2}}(f'')^{n-1}f''' + 4^n(n+1)z^{\frac{n-1}{2}}(f'')^n + 4ff'' - 4m(f')^2 + m = 0 \tag{11}$$

$$2z\theta'' + 2\theta' + \mathrm{Pr}(f\theta' - Bf'\theta) = 0 \tag{12}$$

$$f(a) = f'(a) = 0;\ \theta(a) = 1 \text{ or } \theta'(a) = -1$$

$$f(\infty) = \frac{1}{2};\ \theta(\infty) = 0 \tag{13}$$

where $B = s$ or $= p + (1-m)/2$, $\mathrm{Pr} = A_1/\alpha$ is the generalized Prandtl number, and the primes denote differentiation with respect to z. Thus, similarity solution exists for an arbitrary power-law flow past a needle when the fluid is Newtonian, but only for an accelerating flow with $m = 1/3$ when the fluid is non-Newtonian.

The local skin-friction coefficient is obtained as

$$C_f = \frac{K\left(\frac{\partial u}{\partial r}\right)^n_{z=a}}{\frac{1}{2}\rho U^2} = 2(4)^n a^{n/2}\mathrm{Re}^{\frac{-1}{n+1}}[f''(a)]^n \tag{14}$$

and the local Nusselt number is,

$$\mathrm{Nu} = -\frac{x\left(\frac{\partial T}{\partial r}\right)_{z=a}}{T_w - T_\infty} = -2a^{\frac{1}{2}}\mathrm{Re}^{\frac{1}{n+1}}\theta'(a) \tag{15}$$

or

$$\mathrm{Nu} = \frac{xq_w}{k(T_w - T_\infty)} = 2a^{\frac{1}{2}}\mathrm{Re}^{\frac{1}{n+1}}\theta^{-1}(a) \tag{16}$$

3 Results and Discussion

As noted earlier, similarity solutions exist only for the cases of $n = 1$ (Newtonian fluid) and $m = 1/3$ with arbitrary n. The former has been reported by Chen and Smith [2]; thus, the results presented herein are for the latter.

The local skin-friction coefficients for $m = 1/3$ with $a = 0.01$, 0.1 and $n = 0.5$, 1.0, 1.5 are tabulated in Table 1. It is noted that the non-Newtonian flow behavior along a thin needle has been discussed in detail in [1], thus, our present attention is focused on the thermal characteristics of the flow.

For the two cases considered, needles with either variable surface temperature or variable surface heat flux, the local heat transfer results along with their respective dimensionless wall temperature gradient and dimensionless wall temperature are tabulated in Tables 2 and 3 for $m = 1/3$ and various values of n, a, Pr, and s or p. These similarity results, it is hoped, may serve as a numerical checking guide for the general case of $m \neq 1/3$ for which only nonsimilarity solutions are feasible and an approximate method may be necessary for its solution.

To conserve space, we present graphically the dimensionless temperature profiles and local heat transfer results in Figs. 1 and 2, respectively, only for the case of variable surface temperature needles. At a given Pr, the effect of needle size is clearly seen; the more slender the needle the thinner the thermal boundary layer, and hence, the higher the wall heat flux. At a given needle size and Pr, the smaller the flow index, n, the higher the film heat transfer coefficient. It is also noted the coefficient increases with increasing Pr, as is expected.

References

1 Chen, J. L. S., and Kubler, E. A., "Non-Newtonian Flow Along Needles," *Physical of Fluids*, Vol. 21, No. 5, 1978, pp. 749-751.

2 Chen, J. L. S., and Smith, T. M., "Forced Convection Heat Transfer From Non-Isothermal Thin Needles," ASME JOURNAL OF HEAT TRANSFER, Vol. 100, 1978, pp. 358-362.

3 Narain, J. P., and Uberoi, M. S., "Forced Heat Transfer Over Thin Needles," ASME JOURNAL OF HEAT TRANSFER, Vol. 94, 1972, pp. 240-242.

4 Tam, K. K., "On the Asymptotic Solution of Viscous Incompressible Flow Past a Heated Paraboloid of Revolution," *SIAM Journal of Appl. Math.*, Vol. 20, No. 4, 1971, pp. 417-472.

5 Chen, J. L. S., "Natural Convection from Needles With Variable Wall Temperature," ASME paper No. 80-HT-72, 1980.

6 Raithby, G. D., and Hollands, K. G. T., "Free Convection Heat Transfer From Vertical Needles," ASME JOURNAL OF HEAT TRANSFER, Vol. 98, 1976, pp. 522-523.

7 Govindarajula, T., "Comments on Laminar Free-Convection from a Needle," *Physics of Fluids*, Vol. 15, No. 1, Jan., 1972, pp. 211-212.

8 Narain, J. P., and Uberoi, M. S., "Laminar Free-Convection From Thin Vertical Needles," *Physics of Fluids*, Vol. 15, No. 5, May 1972, pp. 928-929.

9 Van Dyke, M., "Free Convection From a Vertical Needle," *Problems of*

Hydrodynamics and Continum Mechanics, edited by I. E. Block, 1970, pp. 748–761.

10 Cebeci, T., and Na, T. Y., "Laminar Free-Convection Heat Transfer From a Needle," *Physics of Fluids*, Vol. 12, No. 2, Feb., 1969, pp. 463–465.

11 Cebeci, T., and Na., T. Y., "Erratum: Laminar Free-Convection Heat Transfer From a Needle," *Physics of Fluids*, Vol. 13, 1970, p. 563.

12 Narain, J. P., and Uberoi, M. S., "Combined Forced and Free-Convection Over Thin Needles," *International Journal of Heat and Mass Transfer*, Vol. 16, No. 8, Aug., 1973, pp. 1505–1511.

13 Narain, J. P., and Uberoi, M. S., "Combined Forced and Free-Convection Heat Transfer From Thin Needles in a Uniform Stream," *Physics of Fluids*, Vol. 15, No. 11, Nov. 1972, pp. 1879–1882.

Analysis of Transient Laminar Convective Heat Transfer Inside a Circular Duct

S. C. Chen,[1] N. K. Anand,[2] and D. R. Tree[3]

Introduction

In the literature, the transient heat transfer for laminar flow inside a flat or a circular duct following a step change in the wall temperature or wall heat flux has been presented analytically by the method of characteristics [1–4]. Lin [5] obtained a direct numerical solution to the transient laminar heat transfer in a tube subjected to a step change in ambient temperature. In this note, a direct numerical solution to the transient laminar heat transfer inside a circular duct subjected to a step change in either the wall temperature or heat flux will be discussed.

Formulation of the Problem and Solution Technique

A hydrodynamically developed laminar flow is considered. The velocity profile, u, is represented by

$$u = 2\bar{U}(1 - r^2/R^2) \tag{1}$$

where $\bar{U}$ is the mean fluid velocity, r is the radial coordinate, and R is the radius. In this analysis, flow is incompressible and physical properties of the fluid are constant. Viscous dissipation and conduction heat transfer along the direction of fluid flow are neglected. Initially, the fluid and the wall are assumed to be at same temperature, and at time = 0, the wall is subjected to a step change in temperature or heat flux. With these simplifying assumptions, the governing energy equation and the initial and boundary conditions in dimensionless form are

$$\frac{\partial\theta}{\partial F} + (1-\eta^2)\frac{\partial\theta}{\partial x} = \frac{1}{\eta}\frac{\partial\theta}{\partial\eta} + \frac{\partial^2\theta}{\partial\eta^2} \tag{2}$$

Case A: Step change in the wall temperature

Initial condition,

$$\theta(x,\eta,0) = 0$$

Boundary conditions,

$$\theta(0,\eta,F) = 0$$

$$\theta(x,1,F) = 1$$

$$\left.\frac{\partial\theta}{\partial\eta}\right|_{\eta=0} = 0 \tag{3}$$

Case B: Step change in the wall heat flux

Initial condition,

$$\theta(x,\eta,0) = 0$$

Boundary conditions,

$$\theta(0,\eta,F) = 0$$

$$\left.\frac{\partial\theta}{\partial\eta}\right|_{\eta=1} = 1$$

$$\left.\frac{\partial\theta}{\partial\eta}\right|_{\eta=0} = 0 \tag{4}$$

The dimensionless variables are defined below

$$\theta = \frac{T - T_i}{T_w - T_i} \text{ for case } A, \quad = \frac{T - T_i}{qR/k} \text{ for case } B$$

$$F = t\nu/R^2\text{Pr}; \quad \eta = r/R; \quad x = (Z/R)/(\text{RePr})$$

The Reynolds number $\text{Re} = 2\bar{U}R/\nu$, the Prandtl number is $\text{Pr} = \nu/\alpha$, T is temperature, T_i the constant entering fluid temperature, T_w the wall temperature, q the heat flux at the wall, k the thermal conductivity of the fluid, ν the kinematic viscosity, α the thermal diffusivity, t the time, and Z the axial coordinate.

The energy equation (2) is parabolic in time and in the axial direction, and elliptic in the radial direction. The storage and advection terms were represented by forward and upwind difference respectively. The central difference form was used to represent the radial diffusion term. For the reasons of stability, a fully implicit formulation in time was adopted. From the known temperature field at nth time, the temperature field at $(n+1)$th time was computed by marching in

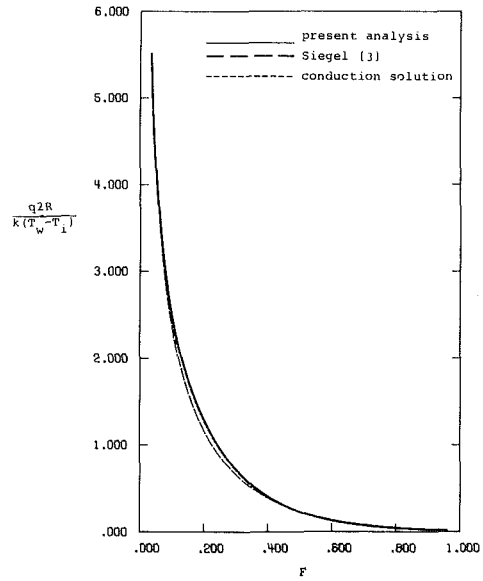

Fig. 1 Comparison of initial transient results in a circular tube with conduction transient

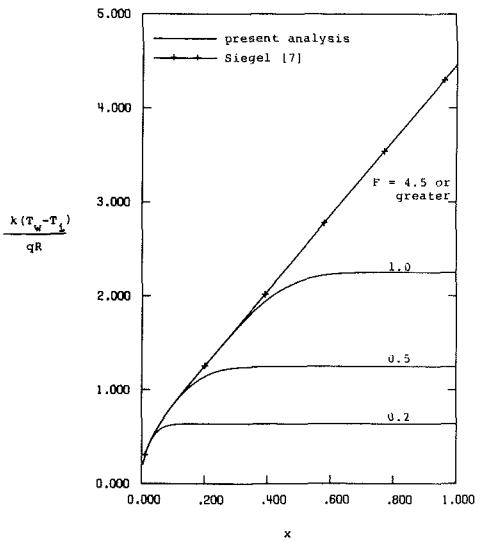

Fig. 2 Transient distribution in the wall temperature following a step change in the wall heat flux

[1] Graduate Research Assistant, Purdue University, Student Mem. ASME.

[2] Graduate Research Assistant, Purdue University.

[3] Professor and Assistant Head, Ray W. Herrick Laboratories, School of Mechanical Engineering, Purdue University, West Lafayette, Ind. 47907

Contributed by the Heat Transfer Division for publication in the JOURNAL OF HEAT TRANSFER. Manuscript received by the Heat Transfer Division March 29, 1983.

Hydrodynamics and Continum Mechanics, edited by I. E. Block, 1970, pp. 748–761.

10 Cebeci, T., and Na, T. Y., "Laminar Free-Convection Heat Transfer From a Needle," *Physics of Fluids*, Vol. 12, No. 2, Feb., 1969, pp. 463–465.

11 Cebeci, T., and Na., T. Y., "Erratum: Laminar Free-Convection Heat Transfer From a Needle," *Physics of Fluids*, Vol. 13, 1970, p. 563.

12 Narain, J. P., and Uberoi, M. S., "Combined Forced and Free-Convection Over Thin Needles," *International Journal of Heat and Mass Transfer*, Vol. 16, No. 8, Aug., 1973, pp. 1505–1511.

13 Narain, J. P., and Uberoi, M. S., "Combined Forced and Free-Convection Heat Transfer From Thin Needles in a Uniform Stream," *Physics of Fluids*, Vol. 15, No. 11, Nov. 1972, pp. 1879–1882.

Analysis of Transient Laminar Convective Heat Transfer Inside a Circular Duct

S. C. Chen,[1] N. K. Anand,[2] and D. R. Tree[3]

Introduction

In the literature, the transient heat transfer for laminar flow inside a flat or a circular duct following a step change in the wall temperature or wall heat flux has been presented analytically by the method of characteristics [1–4]. Lin [5] obtained a direct numerical solution to the transient laminar heat transfer in a tube subjected to a step change in ambient temperature. In this note, a direct numerical solution to the transient laminar heat transfer inside a circular duct subjected to a step change in either the wall temperature or heat flux will be discussed.

Formulation of the Problem and Solution Technique

A hydrodynamically developed laminar flow is considered. The velocity profile, u, is represented by

$$u = 2\bar{U}(1 - r^2/R^2) \tag{1}$$

where $\bar{U}$ is the mean fluid velocity, r is the radial coordinate, and R is the radius. In this analysis, flow is incompressible and physical properties of the fluid are constant. Viscous dissipation and conduction heat transfer along the direction of fluid flow are neglected. Initially, the fluid and the wall are assumed to be at same temperature, and at time = 0, the wall is subjected to a step change in temperature or heat flux. With these simplifying assumptions, the governing energy equation and the initial and boundary conditions in dimensionless form are

$$\frac{\partial\theta}{\partial F} + (1-\eta^2)\frac{\partial\theta}{\partial x} = \frac{1}{\eta}\frac{\partial\theta}{\partial\eta} + \frac{\partial^2\theta}{\partial\eta^2} \tag{2}$$

Case A: Step change in the wall temperature

Initial condition,

$\theta(x,\eta,0) = 0$

Boundary conditions,

$\theta(0,\eta,F) = 0$

$\theta(x,1,F) = 1$

$\left.\frac{\partial\theta}{\partial\eta}\right|_{\eta=0} = 0$ (3)

Case B: Step change in the wall heat flux

Initial condition,

$\theta(x,\eta,0) = 0$

Boundary conditions,

$\theta(0,\eta,F) = 0$

$\left.\frac{\partial\theta}{\partial\eta}\right|_{\eta=1} = 1$

$\left.\frac{\partial\theta}{\partial\eta}\right|_{\eta=0} = 0$ (4)

The dimensionless variables are defined below

$$\theta = \frac{T - T_i}{T_w - T_i} \text{ for case } A, \quad = \frac{T - T_i}{qR/k} \text{ for case } B$$

$$F = t\nu/R^2\text{Pr}; \quad \eta = r/R; \quad x = (Z/R)/(\text{RePr})$$

The Reynolds number $\text{Re} = 2\bar{U}R/\nu$, the Prandtl number is $\text{Pr} = \nu/\alpha$, T is temperature, T_i the constant entering fluid temperature, T_w the wall temperature, q the heat flux at the wall, k the thermal conductivity of the fluid, ν the kinematic viscosity, α the thermal diffusivity, t the time, and Z the axial coordinate.

The energy equation (2) is parabolic in time and in the axial direction, and elliptic in the radial direction. The storage and advection terms were represented by forward and upwind difference respectively. The central difference form was used to represent the radial diffusion term. For the reasons of stability, a fully implicit formulation in time was adopted. From the known temperature field at nth time, the temperature field at $(n+1)$th time was computed by marching in

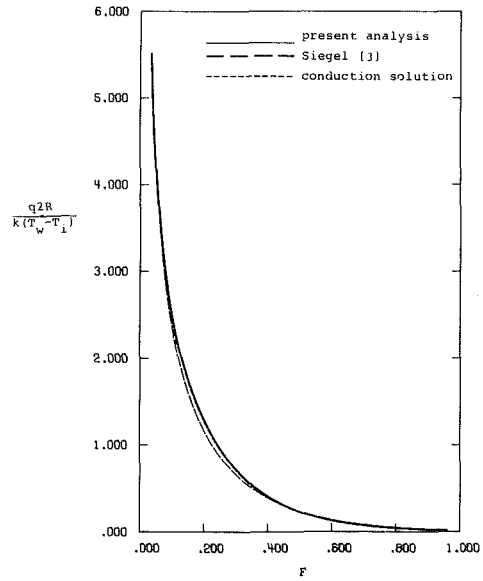

Fig. 1 Comparison of initial transient results in a circular tube with conduction transient

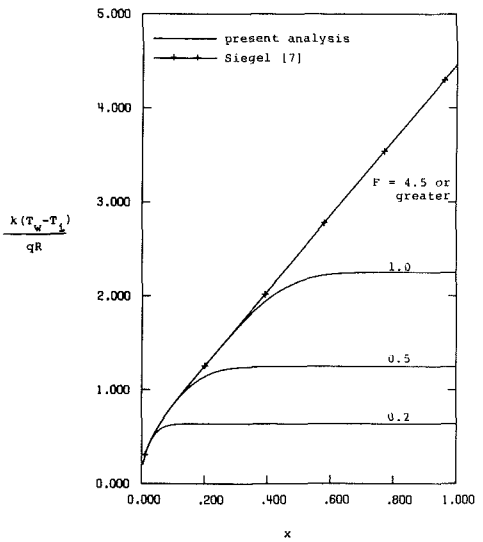

Fig. 2 Transient distribution in the wall temperature following a step change in the wall heat flux

[1] Graduate Research Assistant, Purdue University, Student Mem. ASME.

[2] Graduate Research Assistant, Purdue University.

[3] Professor and Assistant Head, Ray W. Herrick Laboratories, School of Mechanical Engineering, Purdue University, West Lafayette, Ind. 47907

Contributed by the Heat Transfer Division for publication in the JOURNAL OF HEAT TRANSFER. Manuscript received by the Heat Transfer Division March 29, 1983.

the axial direction. Because of the implicit formulation in time a set of simultaneous equations must be solved at each axial location. Each set of simultaneous equations was solved using the tridiagonal matrix algorithm.

Only the finite difference representation of the boundary condition ($\partial\theta/\partial\eta\,|_{\eta=1} = 1$) for case B needs some discussion. As $\eta \to 1$, the energy equation (2) takes the form

$$\frac{\partial\theta}{\partial F} = \frac{\partial\theta}{\partial\eta}\Big|_{\eta=1} + \frac{\partial^2\theta}{\partial\eta^2}\Big|_{\eta=1} \tag{5}$$

The temperature at the node adjacent to the wall ($\theta_{I,W-1}$) is expressed by means of the Taylors series expansion at the nodal temperature at the wall ($\theta_{I,W}$), where the subscript I means Ith node along the x-axis, and the subscript W means Wth node along the η-axis. The first three terms of the Taylors series give

$$\theta_{I,W-1} = \theta_{I,W} - \frac{\partial\theta_{I,W}}{\partial\eta}\Delta\eta + \frac{1}{2}\frac{\partial^2\theta_{I,W}}{\partial\eta^2}\Delta\eta^2 \tag{6}$$

Combining $\partial\theta/\partial\eta\,|_{\eta=1} = 1$ with equations (5) and (6) results in

$$\frac{\partial\theta_{I,W}}{\partial F} = 1 + \frac{2}{\Delta\eta^2}[\theta_{I,W-1} - \theta_{I,W} + \Delta\eta] \tag{7}$$

As stated earlier the method adopted is fully implicit in time, hence, equation (7) is represented in difference form as

$$-\frac{2}{\Delta\eta^2}\theta^{n+1}_{I,W-1} + \left(\frac{1}{\Delta F} + \frac{2}{\Delta\eta^2}\right)\theta^{n+1}_{I,W} = \frac{1}{\Delta F}\theta^{n}_{I,W} + 1 + \frac{2}{\Delta\eta} \tag{8}$$

This repesentation of the boundary condition $\partial\theta/\partial\eta\,|_{\eta=1} = 1$, has second-order accuracy and retains the tridiagonal nature of the system of simultaneous equations.

In the radial direction, 41 uniformly spaced nodes were deployed. The dimensionless space step in the axial direction (Δx) was fixed at .005. A series of numerical experiments showed the solution to be very sensitive to the time step during the early part of the transient. To ensure accuracy and at the same time to reduce computation time, a time step size of .005 was used for $0 < F \leq 1.0$ and 0.05 for $F > 1.00$.

Results and Discussion

The numerical algorithm has been compared with the following two limiting cases in order to verify its validity.

(i) Initial Transient Solution After a Step Change in the Wall Temperature. The exact solution for the initial transient is that resulting from suddenly changing the surface temperature of an infinitely long solid cylinder [3]. The surface heat flux variation for this case is [6]

$$\frac{q2R}{k(T_w - T_i)} = 4\sum_{n=0}^{\infty} e^{-\epsilon_n^2 F} \tag{9}$$

where ϵ_n are the zeros of the Bessel function, J_0. The surface heat flux at $x = 1.005$ obtained from the present numerical solution technique is compared with both equation (9) for a seven-term approximation and the initial transient solution in [3], as shown in Fig. 1. The agreement is generally quite good.

(ii) Steady State. The comparison between our solution at $F = 4.5$ with the steady-state solution by Siegel [7] for constant wall heat flux is shown in Fig. 2. The agreement is very good.

It is felt, therefore, that the present numerical algorithm not only gives sufficiently good results in the initial transient region, but also in the steady state.

Figure 2 also shows the transient distribution of T_w for case B. The transient variation of T_w for the same case is shown in Fig. 3. The transient wall heat flux for case A is compared with approximate solutions obtained by Siegel [3] for a seven-term approximation, as shown in Figs. 4 and 5. It is clear from Figs. 4 and 5 that the agreement is quite good for large x and F. As for very small F or very small x, the axial conduction effects may be important. Hence, the present results are not applicable to regions where F and x are both small. Figure 4 also shows good agreement with the solution in [5] for the case of a step change in the ambient temperature at an outside Nusselt number, $\mathrm{Nu}_o = 100$, where $\mathrm{Nu}_o = HR/k$, H is the outside heat transfer coefficient. The reason is that the

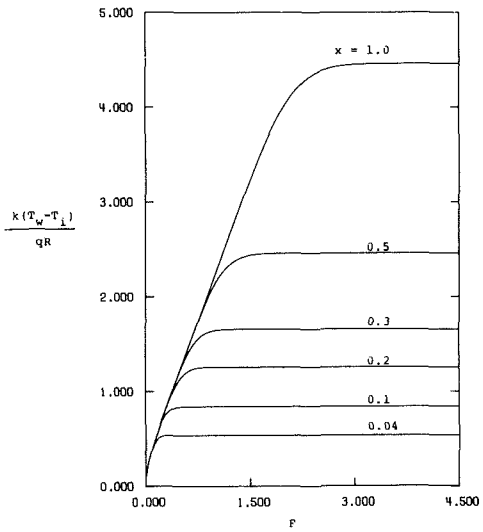

Fig. 3 Transient variation in the wall temperature following a step change in the wall heat flux

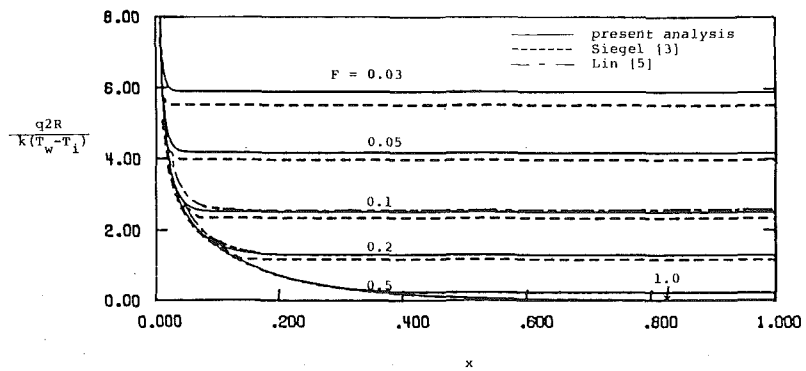

Fig. 4 Transient distribution in the wall heat flux following a step change in the wall temperature

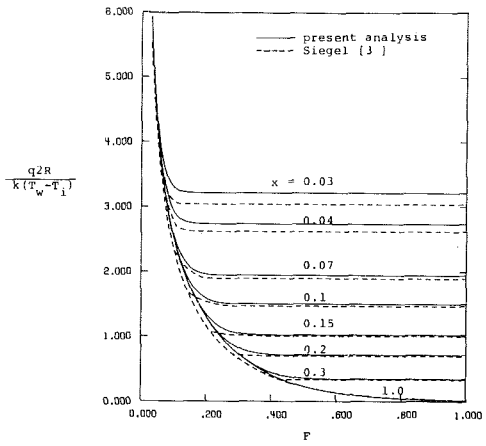

Fig. 5 Transient variation in the wall heat flux following a step change in the wall temperature

larger the outside Nusselt number, the better a step change in the ambient temperature can be approximated by a step change at the wall temperature.

Acknowledgments

The authors are grateful to the U.S. Department of Energy for their financial support of this overall research project. Also, the authors would like to express their thanks to Dr. R. Siegel of NASA Lewis Research Center for his valuable suggestions during the preparation of this paper.

References

1 Sparrow, E. M., and Siegel, R., "Thermal Entrance Region of a Circular Tube under Transient Heat Conditions," *Proceedings of United States National Congress of Applied Mechanics*, Vol. 3, 1958, pp. 817–826.

2 Siegel, R., and Sparrow, E. M., "Transient Heat Transfer for Laminar Forced Convection in the Thermal Entrance Region of Flat Ducts," ASME *Transactions*, Vol. 81, 1959, pp. 29–36.

3 Siegel, R., "Heat Transfer for Laminar Flow in Ducts With Arbitrary Time Variations in Wall Temperature," ASME *Journal of Applied Mechanics*, Vol. 27, 1960, pp. 241–249.

4 Kalinin, E. K., and Dreitser, G. A., "Unsteady Convective Heat Transfer and Hydrodynamics in Channels," *Advances in Heat Transfer*, Vol. 6, 1970, pp. 367–502.

5 Lin, T. F., "Theoretical and Experimental Study of Heat Transfer Characteristics of Cabinet Calorimeter System," Ph.D. thesis, Purdue University, 1982.

6 Millsaps, K., and Pohlhausen, K., "Heat Transfer to Hagen-Poiseuille Flows," *Proceedings of Conference on Differential Equations*, University of Maryland, March, 1955.

7 Siegel, R., Sparrow, E. M., and Hallman, T. M., "Steady Laminar Heat Transfer in a Circular Tube with Prescribed Wall Heat Flux," *Applied Science Research*, Sect. A., Vol. 7, 1958, pp. 386–392.

Buoyancy Effects in the Entrance Region of Horizontal Rectangular Channels

M. M. Abou-Ellail[1] and S. M. Morcos[2]

Nomenclature

a,b = width and height of a rectangular channel, respectively
AR = aspect ratio of a rectangular channel, a/b
c_p = constant pressure specific heat
D_e = equivalent hydraulic diameter
Gr = Grashof number
g = gravitational acceleration
h = average heat transfer coefficient
k = thermal conductivity
Nu = average Nusselt number
p = pressure in the cross-stream momentum equations
$\bar{p}$ = pressure in the axial momentum equation
Pr = Prandtl number
q_w = uniform wall heat flux
Ra = Rayleigh number
Re = Reynolds number
T = temperature
T_b = fluid bulk temperature
T_w = wall temperature
u,v,w = velocity component in x-, y-, and z-directions, respectively
U,V,W = dimensionless velocity components
x,y = cross-stream Cartesian coordinates
z = distance in the main flow direction
Z = dimensionless distance in the main flow direction
β = coefficient of thermal expansion
ΔT_e = equivalent temperature difference
$\Delta x, \Delta y, \Delta z$ = dimensions of a typical cell
θ = dimensionless temperature difference
μ = viscosity
ν = kinematic viscosity
ρ = density

Subscripts

0 = inlet condition

Superscripts

$-$ = average value

Introduction

The process of combined forced and free laminar convection in horizontal tubes with uniform wall heat flux has been investigated both analytically [1–4] and experimentally [4–7] in recent years. When a flowing fluid is heated in a horizontal tube, the fluid near the wall is warmer, and therefore lighter, than the bulk fluid in the core. As a consequence, two upward currents flow along the side walls, and, by continuity, the heavier fluid near the center of the tube flows downward. This sets up two spiralling vortices which are symmetrical about a vertical meridional plane. The gross result of this combined forced and free convection flow is to greatly enhance the convective heat transfer coefficient over the pure forced convection value [4, 5].

As for the problem of combined forced and free laminar convection in rectangular channels, the only available analytical solutions include Cheng and Hwang [8] for horizontal, Ostrach [9] and Han [10] for vertical, and Ou et al. [11] for inclined orientations. All these studies are concerned only with fully developed velocity and temperature

[1] Associate Professor, Mechanical Engineering Department, Cairo University, Cairo, Egypt

[2] Associate Professor, Mechanical Engineering Department, Cairo University, Cairo, Egypt, Assoc. Mem. ASME

Contributed by the Heat Transfer Division for publication in the JOURNAL OF HEAT TRANSFER. Manuscript received by the Heat Transfer Division December 16, 1980.

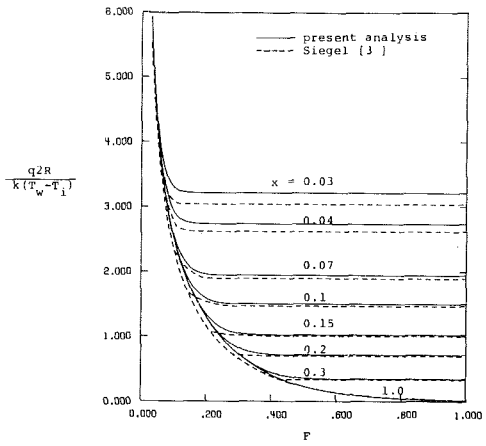

Fig. 5 Transient variation in the wall heat flux following a step change in the wall temperature

larger the outside Nusselt number, the better a step change in the ambient temperature can be approximated by a step change at the wall temperature.

Acknowledgments

The authors are grateful to the U.S. Department of Energy for their financial support of this overall research project. Also, the authors would like to express their thanks to Dr. R. Siegel of NASA Lewis Research Center for his valuable suggestions during the preparation of this paper.

References

1 Sparrow, E. M., and Siegel, R., "Thermal Entrance Region of a Circular Tube under Transient Heat Conditions," *Proceedings of United States National Congress of Applied Mechanics*, Vol. 3, 1958, pp. 817–826.

2 Siegel, R., and Sparrow, E. M., "Transient Heat Transfer for Laminar Forced Convection in the Thermal Entrance Region of Flat Ducts," ASME *Transactions*, Vol. 81, 1959, pp. 29–36.

3 Siegel, R., "Heat Transfer for Laminar Flow in Ducts With Arbitrary Time Variations in Wall Temperature," ASME *Journal of Applied Mechanics*, Vol. 27, 1960, pp. 241–249.

4 Kalinin, E. K., and Dreitser, G. A., "Unsteady Convective Heat Transfer and Hydrodynamics in Channels," *Advances in Heat Transfer*, Vol. 6, 1970, pp. 367–502.

5 Lin, T. F., "Theoretical and Experimental Study of Heat Transfer Characteristics of Cabinet Calorimeter System," Ph.D. thesis, Purdue University, 1982.

6 Millsaps, K., and Pohlhausen, K., "Heat Transfer to Hagen-Poiseuille Flows," *Proceedings of Conference on Differential Equations*, University of Maryland, March, 1955.

7 Siegel, R., Sparrow, E. M., and Hallman, T. M., "Steady Laminar Heat Transfer in a Circular Tube with Prescribed Wall Heat Flux," *Applied Science Research*, Sect. A., Vol. 7, 1958, pp. 386–392.

Buoyancy Effects in the Entrance Region of Horizontal Rectangular Channels

M. M. Abou-Ellail[1] and S. M. Morcos[2]

Nomenclature

a,b = width and height of a rectangular channel, respectively
AR = aspect ratio of a rectangular channel, a/b
c_p = constant pressure specific heat
D_e = equivalent hydraulic diameter
Gr = Grashof number
g = gravitational acceleration
h = average heat transfer coefficient
k = thermal conductivity
Nu = average Nusselt number
p = pressure in the cross-stream momentum equations
$\bar{p}$ = pressure in the axial momentum equation
Pr = Prandtl number
q_w = uniform wall heat flux
Ra = Rayleigh number
Re = Reynolds number
T = temperature
T_b = fluid bulk temperature
T_w = wall temperature
u,v,w = velocity component in x-, y-, and z-directions, respectively
U,V,W = dimensionless velocity components
x,y = cross-stream Cartesian coordinates
z = distance in the main flow direction
Z = dimensionless distance in the main flow direction
β = coefficient of thermal expansion
ΔT_e = equivalent temperature difference
$\Delta x, \Delta y, \Delta z$ = dimensions of a typical cell
θ = dimensionless temperature difference
μ = viscosity
ν = kinematic viscosity
ρ = density

Subscripts

0 = inlet condition

Superscripts

$-$ = average value

Introduction

The process of combined forced and free laminar convection in horizontal tubes with uniform wall heat flux has been investigated both analytically [1–4] and experimentally [4–7] in recent years. When a flowing fluid is heated in a horizontal tube, the fluid near the wall is warmer, and therefore lighter, than the bulk fluid in the core. As a consequence, two upward currents flow along the side walls, and, by continuity, the heavier fluid near the center of the tube flows downward. This sets up two spiralling vortices which are symmetrical about a vertical meridional plane. The gross result of this combined forced and free convection flow is to greatly enhance the convective heat transfer coefficient over the pure forced convection value [4, 5].

As for the problem of combined forced and free laminar convection in rectangular channels, the only available analytical solutions include Cheng and Hwang [8] for horizontal, Ostrach [9] and Han [10] for vertical, and Ou et al. [11] for inclined orientations. All these studies are concerned only with fully developed velocity and temperature

[1] Associate Professor, Mechanical Engineering Department, Cairo University, Cairo, Egypt

[2] Associate Professor, Mechanical Engineering Department, Cairo University, Cairo, Egypt, Assoc. Mem. ASME

Contributed by the Heat Transfer Division for publication in the JOURNAL OF HEAT TRANSFER. Manuscript received by the Heat Transfer Division December 16, 1980.

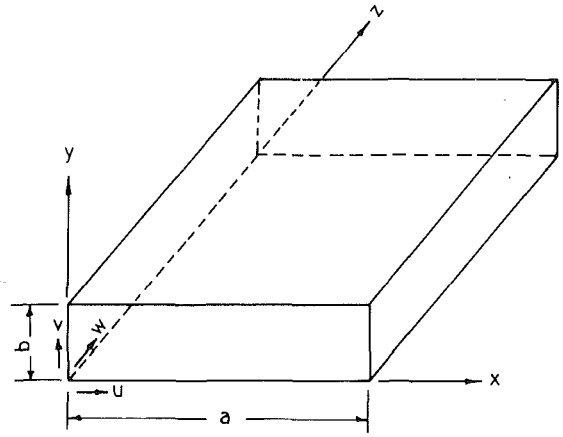

Fig. 1 Coordinate system for a horizontal rectangular channel

profiles under the thermal boundary condition of uniform wall heat flux. However, the assumption of fully developed profiles can only be established if the channel is very long. In spite of its practical importance, the only available analytical solution for the entrance region of a horizontal rectangular channel with significant buoyancy effects is that of Cheng et al. [12], which is limited to the case of large Prandtl number fluids. Recently, Abou-Ellail and Morcos [13-14] presented a prediction procedure for combined forced and free laminar convection in the entrance region of an inclined rectangular channel which can be extended in the horizontal channel case.

The purpose of the present investigation is to study numerically the buoyancy effect on laminar forced convection heat transfer in the entrance region of horizontal rectangular channels having aspect ratios 1 and 4 for different values of Prandtl number. The peripheral and axial wall heat fluxes are taken to be uniform. When the Prandtl number is large, all the convective terms in the momentum equations can be neglected which simplifies the numerical solution. In the present numerical procedure, however, these convective terms are retained, and the numerical results are therefore applicable to a wide range of Prandtl number fluids.

Governing Equations

Consideration is given to a steady laminar flow in the entrance of a horizontal rectangular channel with a uniform wall heat flux, as shown in Fig. 1. The thermodynamical properties of fluid are assumed constant. The density is also considered constant in all of the terms in the governing equations, except for its variation in the buoyancy term. The assumption of constant properties is only made for simplicity; however, in the present numerical procedure the properties can also be varied with coordinate directions. The viscous dissipation and compressibility effects in the energy equation will be neglected. Under the foregoing assumptions, the governing equations with reference to Cartesian coordinates x, y, z are:

Continuity equation

$$\frac{\partial}{\partial x}(\rho u)+\frac{\partial}{\partial y}(\rho v)+\frac{\partial}{\partial z}(\rho w)=0 \tag{1}$$

Momentum equations

$$\frac{\partial}{\partial x}(\rho u^2)+\frac{\partial}{\partial y}(\rho vu)+\frac{\partial}{\partial z}(\rho wu)-\frac{\partial}{\partial x}\left(\mu\frac{\partial u}{\partial x}\right)-\frac{\partial}{\partial y}\left(\mu\frac{\partial u}{\partial y}\right)-\frac{\partial}{\partial z}\left(\mu\frac{\partial u}{\partial z}\right)=-\frac{\partial p}{\partial x} \tag{2}$$

$$\frac{\partial}{\partial x}(\rho uv)+\frac{\partial}{\partial y}(\rho v^2)+\frac{\partial}{\partial z}(\rho wv)-\frac{\partial}{\partial x}\left(\mu\frac{\partial v}{\partial x}\right)-\frac{\partial}{\partial y}\left(\mu\frac{\partial v}{\partial y}\right)-\frac{\partial}{\partial z}\left(\mu\frac{\partial v}{\partial z}\right)=-\frac{\partial p}{\partial y}+g.\rho_0.\beta.(T-T_0) \tag{3}$$

$$\frac{\partial}{\partial x}(\rho uw)+\frac{\partial}{\partial y}(\rho vw)+\frac{\partial}{\partial z}(\rho w^2)-\frac{\partial}{\partial x}\left(\mu\frac{\partial w}{\partial x}\right)-\frac{\partial}{\partial y}\left(\mu\frac{\partial w}{\partial y}\right)-\frac{\partial}{\partial z}\left(\mu\frac{\partial w}{\partial z}\right)=-\frac{\partial \bar{p}}{\partial z} \tag{4}$$

Energy equation

$$\frac{\partial}{\partial x}(\rho uT)+\frac{\partial}{\partial y}(\rho vT)+\frac{\partial}{\partial z}(\rho wT)-\frac{\partial}{\partial x}\left(\frac{k}{c_p}\frac{\partial T}{\partial x}\right)-\frac{\partial}{\partial y}\left(\frac{k}{c_p}\frac{\partial T}{\partial y}\right)-\frac{\partial}{\partial z}\left(\frac{k}{c_p}\frac{\partial T}{\partial z}\right)=0 \tag{5}$$

Because of symmetry, it suffices to consider only one-half of the rectangular channel. Consequently, the boundary conditions can be written as

$u=v=w=0$, and $\dfrac{\partial T}{\partial n}=-q_w/k$ — at channel walls

$u=\dfrac{\partial v}{\partial x}=\dfrac{\partial w}{\partial x}=\dfrac{\partial T}{\partial x}=0$ — at plane of symmetry $(x=a/2)$

$w=w_0$, and $T=T_0$ — at channel entrance $(z=0)$

where u, v, and w are the velocity components in the x-, y-, and z-directions, respectively, T is the fluid temperature, w_0 and T_0 are the uniform fluid axial velocity and temperature at the entrance, respectively, and q_w is the uniform wall heat flux.

The foregoing set of governing conservation equations are elliptic in nature. However, neglection of the second-derivative terms in the axial direction for the momentum and energy equations are implemented in the solution procedure described below. Moreover, two symbols, p and $\bar{p}$, have been deliberately used for pressure, while p is the local pressure in the x-y-plane, $\bar{p}$ is a space average pressure over a cross-section normal to main flow direction [15]. In this way, the flow in the horizontal channels is basically parabolic with a predominant axial direction.

Solution Procedure

The present method of solution entails subdividing the rectangular channel into a number of finite volumes or cells, each of which encloses an imaginary grid node at which all scaler variables are stored, while the velocity components are chosen to lie on the cell boundaries where they are needed for mass flux calculations.

The preceding set of governing differential equations are integrated to yield the finite difference equations. The procedure used to solve the finite difference equations is a combined iterative-marching integration technique as described by Patankar and Spalding [15], with slight modifications to ensure convergence in the cross-stream plane before marching to the downstream plane as described in more detail in [14, 16].

Since the finite difference equations are actually nonlinear, their solution is repeated a few times before marching downstream to the next cross-stream plane. The iteration in the cross-stream plane is terminated when the current

solution satisfies the difference equation to within 1 percent or less. The number of iterations needed to obtain a converged solution at each cross-stream plane depends on the forward axial step, Δz. If Δz is chosen small enough, one or two iterations are needed before marching downstream to the next x-y-plane, which proved to be more economical in terms of overall computation time. The criterion for choosing the forward step is that the axial convection ($\rho w\, \Delta x\, \Delta y$) is greater than the cross-stream diffusion ($\mu\, \Delta x\, \Delta z/\delta y$) for fast convergence, i.e.,

$$\Delta z < (\rho\, w\, \Delta y.\, \delta y/\mu) \tag{6}$$

where Δx and Δy are the dimensions of a typical cell in the x-y-plane, and δy is the distance between two neighboring grid nodes.

In presenting the numerical results, the following dimensionless variables and parameters will be used:

$$U=u/(\nu/D_e), \qquad V=v/(\nu/D_e), \qquad W=w/w_0,$$

$$\theta=(T-T_0)/\Delta T_e, \quad \mathrm{Re}_o=\rho D_e w_0/\mu, \qquad \mathrm{Pr}=c_p\mu/k,$$

$$Z=z/(D_e \mathrm{Re}_0 \mathrm{Pr}), \quad \mathrm{Gr}=g\,\beta\,\Delta T_e D_e^3/\nu^2, \quad \mathrm{Ra}=\mathrm{Gr}\,\mathrm{Pr}$$

where $D_e = 2ab/(a+b)$ and $\Delta T_e = q_w D_e/k$.

Following the usual definition, the average Nusselt number over the perimeter at any given cross section can be written as

$$\mathrm{Nu}=\frac{h\,D_e}{k}=\frac{q_w D_e}{k(\bar{T}_w-T_b)}$$

where h is the average heat transfer coefficient, $\bar{T}_w$ is the average wall temperature, and T_b is the fluid bulk temperature.

Results and Discussion

The numerical calculations in this study is carried out for water flowing in horizontal rectangular channels having aspect ratio, $AR = 1$ and 4. The reference temperature of water at the entrance is taken as $T_0 = 40°C$ with a value of Pr = 4. The dimensions of the rectangular channels and the water flow rates are chosen such that $\mathrm{Re}_c = 275$.

The numerical results of the buoyancy effects on the local Nusselt number in the entrance region of horizontal rectangular channels are depicted in Fig. 2 for both $AR = 1$ and 4. The variation of Nusselt number along the channel axis showed that the buoyancy effects are negligible up to a certain axial distance from the entrance dependeng on the magnitude of Rayleigh number. After such distance, the Nusselt number is seen to deviate from the constant property solution as a result of the developed secondary flow motion caused by the buoyancy forces. After reaching a minimum value, the Nusselt number approaches asymptotically a constant value corresponding to the fully developed velocity and temperature profiles. The effect of increasing Rayleigh number is to decrease the entrance length and increase Nusselt number. The value of Nusselt number in the developed region at Ra = 10^5 is about 200 percent above the constant property prediction. Numerical instability was encountered at high values of Rayleigh number near the fully developed region.

A comparison between the results of Fig. 2 for $AR = 1$ and 4 shows that the effect of increasing the aspect ratio is to increase the entrance length. Moreover, the values of Nusselt number for $AR = 4$ are higher than those for $AR = 1$ at the corresponding value of Rayleigh number. In the figure, the numerical results check exactly with the limiting Nusselt number for fully developed pure forced convection Nu_0 = 3.091 and 2.93 [18] for $AR = 1$ and 4, respectively, confirming the accuracy of the present numerical results.

Secondary flow patterns in the x-y-plane at an axial location $Z = 0.0178$ are presented by way of a set of vectors for the case of Ra = 3×10^4 in Fig. 3 for $AR = 1$ and 4. This

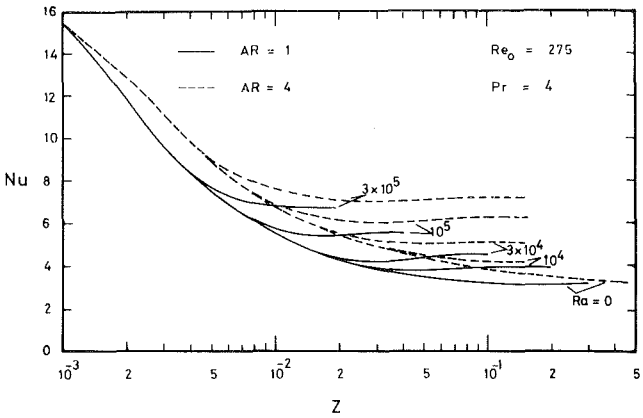

Fig. 2 Nusselt number variation in the entrance region of a horizontal rectangular channel with $AR = 1$ and 4

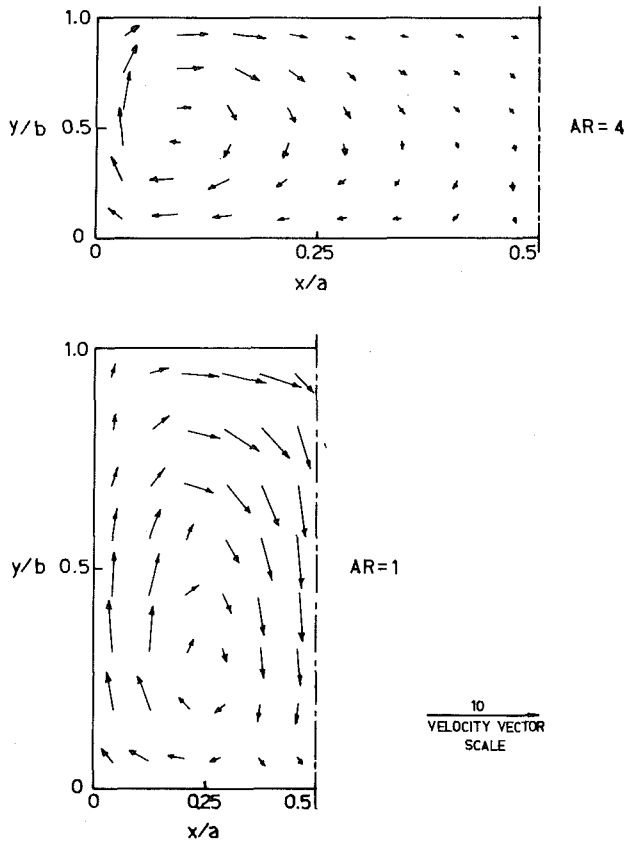

Fig. 3 Secondary flow vector plot in the entrance region of a horizontal rectangular channel at $Z = 0.0178$ for Ra = 3×10^4

axial distance is near the location where the curve for Nusselt number starts to branch out from the pure forced convection one, as described in Fig. 2. Figure 3 shows that for large aspect ratio, the secondary flow moves upward with a high velocity near the side wall and then decreases gradually as it moves downward along the center line axis with the center of the secondary flow being close to the side wall. For low aspect ratio, the secondary flow moves upward along the side wall and downward along the center line axis with relatively high velocities. The center of the secondary flow is seen to be close to the lower wall of the channel.

The wall temperature distributions in the entrance region of a horizontal rectangular channel for the case of Ra = 3×10^4 are shown in Fig. 4 for both $AR = 1$ and 4. Near the entrance, the wall temperature distribution is nearly symmetrical about the axis $y/b = 0.5$, with hot spots at the two corners of the

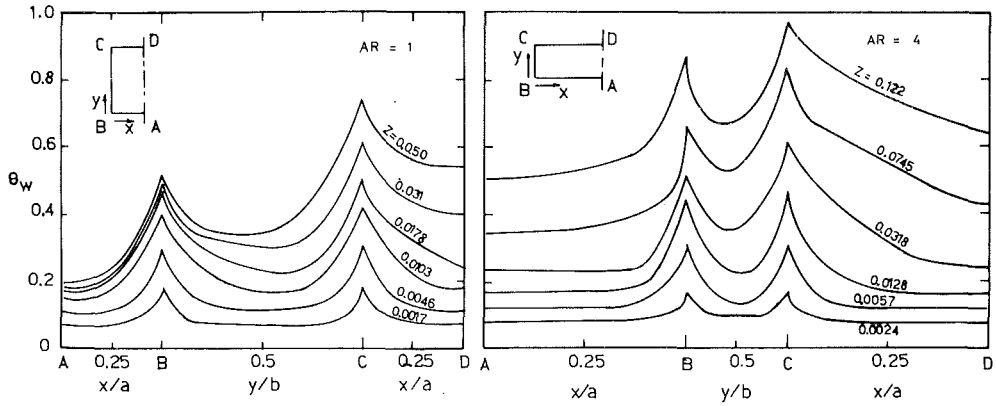

Fig. 4 Wall temperature distribution in the entrance region of a horizontal rectangular channel for Ra = 3 × 10^4

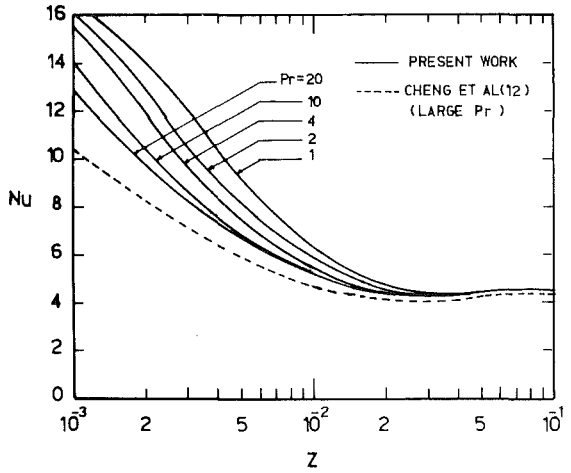

Fig. 5 Prandtl number effect on the Nusselt number variation in the entrance reigon of a horizontal rectangular channel with *AR* = 1 for Ra = 3 × 10^4

channel. However, at higher values of Z, the upper wall temperature gradually increases over the lower wall temperature and the highest wall temperature is located at the upper corner as a result of the secondary flow motion.

The effect of Prandtl number on the Nusselt number variation in the entrance region of a horizontal rectangular channel with $AR = 1$ is shown in Fig. 5 for the case of Ra = 3 × 10^4 and for values of Prandtl number ranging from 1 to 20. Figure 5 indicates that higher values of Prandtl number yield lower values of Nusselt number for the same dimensionless axial distance Z in the entrance region. However, all the curves for different Prandtl numbers approach asymptotically the same value for Nusselt number corresponding to the fully developed condition.

A comparison between the present numerical results and those of Cheng et al. [12] is also shown in Fig. 5 for the case of $AR = 1$ and Ra = 3 × 10^4. According to Cheng et al., their numerical results in the entrance region of a horizontal rectangular channel are valid for Prandtl number greater than 10. However, the comparison with the present numerical results shows clearly that their results in the entrance region are applicable for Prandtl numbers higher than 20.

Conclusions

In the present numerical procedure, the convective terms in the governing equations are retained, and the numerical results are, therefore, valid for a wide range Prandtl number fluids.

The heat transfer results showed that Nusselt number in the entrance region of a horizontal rectangular channel deviates from the pure forced convection solution at a certain axial distance depending on the magnitude of Rayleigh number. The effect of increasing Rayleigh number is to decrease the entrance length and increase Nusselt number. The value of Nusselt number in the developed region at Ra = 10^5 is about 200 percent above the constant property prediction.

The numerical results also indicated that the effect of increasing the aspect ratio is to increase both the entrance length and Nusselt number. Moreover, higher values of Prandtl number yield lower values of Nusselt number for the same dimensionless axial distance Z in the entrance region. However, all the curves for different Prandtl numbers approach asymtotically the same value for Nusselt number corresponding to the fully developed condition.

References

1 Mori, Y., and Futagami, K., "Forced Convective Heat Transfer in Uniformly Heated Horizontal Tubes (2nd Report, Theoretical Study)," *International Journal of Heat and Mass Transfer*, Vol. 10, 1967, pp. 1801–1813.

2 Hwang, G. J., and Cheng, K. C., "Boundary Vorticity Method for Convective Heat Transfer With Secondary Flow-Application to the Combined Free and Forced Laminar Convection in Horizontal Tubes," *Heat Transfer 1970*, Vol. 4, Paper No. NC3.5, Elsevier Publishing Co., Amsterdam, 1970.

3 Newell, P. H., Jr., and Bergles, A. E., "Analysis of Combined Free and Forced Convection for Fully Developed Laminar Flow in Horizontal Tubes," ASME *Journal of Heat Transfer*, Vol. 92, 1970, pp. 83–89.

4 Hong, S. W., Morcos, S. M., and Bergles, A. E., "Analytical and Experimental Results for Combined Forced and Free Laminar Convection in Horizontal Tubes," *Heat Transfer 1974*, Vol. 3, Paper No. NC4.6, Tokyo, 1974.

5 Morcos, S. M., and Bergles, A. E., "Experimental Investigation of Combined Forced and Free Laminar Convection in Horizontal Tubes," ASME *Journal of Heat Transfer*, Vol. 97, 1975, pp. 212–219.

6 Depew, C. A., Franklin, J. L., and Ito, C. H., "Combined Free and Forced Convection in Horizontal, Uniformly Heated Tubes," ASME Paper No. 75-HT-17, 1975.

7 Petukhov, B. S., and Polyakov, A. F., "Effect of Free Convection on Heat Transfer During Forced Flow in Horizontal Pipes," *High Temperature*, Vol. 5, 1967, pp. 348–351.

8 Cheng, K. C., and Hwang, G. J., "Numerical Solution for Combined Free and Forced Laminar Convection in Horizontal Rectangular Channels," ASME *Journal of Heat Transfer*, Vol. 91, 1969, pp. 59–66.

9 Ostrach, S., "Combined Natural and Forced Convection Laminar Flow and Heat Transfer of Fluids With and Without Heat Sources in Channels With Linearly Varying Wall Temperatures," NACA TN3141, 1954.

10 Han, L. S., "Laminar Heat Transfer in Rectangular Channels," ASME *Journal of Heat Transfer*, Vol. 81, 1959, pp. 121–128.

11 Ou, J. W., Cheng, K. C., and Lin, R. C., "Combined Free and Forced Laminar Convection in Inclined Rectangular Channels," *International Journal of Heat and Mass Transfer*, Vol. 19, 1976, pp. 277–283.

12 Cheng, K. C., Hong, S. W., and Hwang, G. J., "Buoyancy Effects on Laminar Heat Transfer in the Thermal Entrance Region of Horizontal Rectangular Channels With Uniform Wall Heat Flux for Large Prandtl Number Fluids," *International Journal of Heat and Mass Transfer*, Vol. 15, 1972, pp. 1819–1836.

13 Abou-Ellail, M. M. M., and Morcos, S. M., "A Prediction Procedure for

Combined Forced and Free Laminar Convection in the Entrance Region of an Inclined Rectangular Channel Solar Collector," *Proceedings of Izmir International Symposium-II on Solar Energy Fundamentals and Applications*, Izmir, Turkey, Aug. 1979.

14 Abou-Ellail, M. M. M., and Morcos, S. M., "Combined Forced and Free Laminar Convection in the Entrance Region of Inclined Rectangular Channels," *Numerical Methods for Non-Linear Problems*, Pineridge Press, Swansea, U.K., 1980, pp. 807-820.

15 Patankar, V. S., and Spalding, D. B., "A Calculation Procedure for Heat, Mass and Momentum Transfer in Three-Dimensional Parabolic Flows," *International Journal of Heat and Mass Transfer*, Vol. 15, 1972, pp. 1787-1806.

16 Abou-Ellail, M. M. M., Gosman, A. D., Lockwood, F. C., and Megahed, I. E. A., "Description and Validation of a Three-Dimensional Procedure for Combustion Chamber Flows," *Journal of Energy*, Vol. 2, No. 2, Mar.-Apr. 1978, pp. 71-80.

17 Caretto, L. S., Gosman, A. D., Patankar, S. V., and Spalding, D. B., "Two Calculation Procedures for Steady, Three-Dimensional Flows with Recirculation," *Proceedings of the 3rd International Conference on Numerical Methods in Fluid Dynamics*, Springer Verlag, New York, 1972, pp. 60-68.

18 Shah, R. K., and London, A. L., "Thermal Boundary Conditions and Some Solutions for Laminar Duct Flow Forces Convection," ASME *Journal of Heat Transfer*, Vol. 96, 1974, pp. 159-165.

The Use of a Simple Heat Transfer Model for Separated Flows in Tubes

J. A. Caton[1]

Nomenclature

A = surface area
C_p = specific heat capacity
d_e = eddy diameter
d_o = orifice diameter
D = port, pipe or tube diameter
h = convective heat transfer coefficient
k = thermal conductivity
l_{wiped} = distance swept by eddy
Nu = Nusselt number, equal to $\frac{hD}{k}$
q_o = instantaneous surface heat transfer rate
q_{avg} = average surface heat transfer rate
Pr = Prandtl number, equal to $\frac{\nu}{\alpha}$
Re = Reynolds number, equal to $\frac{VD}{\nu}$
t = time
T = temperature
ΔT = temperature difference
V_j = jet velocity
V_o = velocity through port
α = thermal diffusivity, equal to $\frac{k}{\rho C_p}$
ν = kinematic viscosity
ρ = gas density
τ_l = contact time during the wiping process

[1]Department of Mechanical Engineering, Texas A&M University, College Station, Tex. 77843, Assoc. Mem. ASME

Contributed by the Heat Transfer Division for publication in the JOURNAL OF HEAT TRANSFER. Manuscript received by the Heat Transfer Division January 17, 1983.

Introduction and Background

Heat transfer correlations for turbulent flows in tubes or pipes are generally applicable only to those heat transfer processes which are governed by the turbulence generated by the wall shear stresses. This wall-generated turbulence may not always be the only source of turbulence. When other sources of turbulence exist, the pipe flow heat transfer correlations are not valid. Other sources of turbulence include flows with separation such as downstream of bluff-bodies or restrictions. For flows with separation, heat transfer correlations are often unavailable. The few correlations that are available are restricted to specific geometries and offer little insight into the nature of the heat transfer process. This note describes the use of a simple heat transfer model for separated flows in tubes and pipes.

Flow separation is often characterized by regions of recirculation and large-scale coherent fluid structures with resulting local regions of relatively high heat transfer. Separated flows in tubes occur in many engineering applications due to baffles, orifices, valves, abrupt expansions, and abrupt contractions. Although turbulent heat transfer in tubes and pipes is well understood, relatively little experimental work has been reported for separated flows and no analytical work has been reported.

Krall and Sparrow [1] reported one of the first detailed experimental investigations of heat transfer for flows with separation in a tube. They examined the local heat transfer resulting from flow downstream of an orifice. Other closely related experimental heat transfer studies for flows with separation in tubes consist of flows with turbulence promoters [2] and flows with symmetric and unsymmetric tube blockages [3, 4]. A few other associated experimental heat transfer investigation are available (e.g., [5-7]) but the common weakness is that each study is limited to a particular geometry.

Flow separation processes often produce identifiable fluid structures (e.g., eddies) in the flow. These coherent, organized structures interact with the fluid near the wall and play an important, if not dominant, role in the heat transfer processes. To characterize heat transfer processes for flows with separation, the coherent fluid structures need to be related to the flow geometry.

Modeling Approach

Of the several possible modeling techniques, a relatively simple phenomenological model is available for the heat transfer processes for separated flows based on the surface renewal or penetration approach [8, 9]. The surface renewal or penetration approach models the turbulent transport process as a succession of quasi-steady interactions between the bulk fluid and the wall. Turbulent "eddies" are assumed to intermittently move from the main or core region to the close vicinity of the wall. At the wall, one-dimensional unsteady molecular transport is assumed to dominate the transport processes [8]. The alternative approach of developing a detailed, sophisticated model has several disadvantages. First, these models are complex and are not used on a routine basis by engineers in industry. Furthermore, these models are often geometry specific, require turbulent flow details as inputs, and mask an understanding of the dominant processes. The simpler, more direct approach, therefore, is often the most useful overall.

Past investigations [8, 9] which have used the surface renewal model were limited to flows where the turbulence was generated by wall shear stresses. The use of the surface renewal model to applications where the turbulence is generated by other than wall shear stresses has not been reported. This note describes the use of the surface renewal model for two different flow processes where the turbulence

Combined Forced and Free Laminar Convection in the Entrance Region of an Inclined Rectangular Channel Solar Collector," *Proceedings of Izmir International Symposium-II on Solar Energy Fundamentals and Applications*, Izmir, Turkey, Aug. 1979.

14 Abou-Ellail, M. M. M., and Morcos, S. M., "Combined Forced and Free Laminar Convection in the Entrance Region of Inclined Rectangular Channels," *Numerical Methods for Non-Linear Problems*, Pineridge Press, Swansea, U.K., 1980, pp. 807-820.

15 Patankar, V. S., and Spalding, D. B., "A Calculation Procedure for Heat, Mass and Momentum Transfer in Three-Dimensional Parabolic Flows," *International Journal of Heat and Mass Transfer*, Vol. 15, 1972, pp. 1787-1806.

16 Abou-Ellail, M. M. M., Gosman, A. D., Lockwood, F. C., and Megahed, I. E. A., "Description and Validation of a Three-Dimensional Procedure for Combustion Chamber Flows," *Journal of Energy*, Vol. 2, No. 2, Mar.-Apr. 1978, pp. 71-80.

17 Caretto, L. S., Gosman, A. D., Patankar, S. V., and Spalding, D. B., "Two Calculation Procedures for Steady, Three-Dimensional Flows with Recirculation," *Proceedings of the 3rd International Conference on Numerical Methods in Fluid Dynamics*, Springer Verlag, New York, 1972, pp. 60-68.

18 Shah, R. K., and London, A. L., "Thermal Boundary Conditions and Some Solutions for Laminar Duct Flow Forces Convection," ASME *Journal of Heat Transfer*, Vol. 96, 1974, pp. 159-165.

The Use of a Simple Heat Transfer Model for Separated Flows in Tubes

J. A. Caton[1]

Nomenclature

A = surface area
C_p = specific heat capacity
d_e = eddy diameter
d_o = orifice diameter
D = port, pipe or tube diameter
h = convective heat transfer coefficient
k = thermal conductivity
l_{wiped} = distance swept by eddy
Nu = Nusselt number, equal to $\frac{hD}{k}$
q_o = instantaneous surface heat transfer rate
q_{avg} = average surface heat transfer rate
Pr = Prandtl number, equal to $\frac{\nu}{\alpha}$
Re = Reynolds number, equal to $\frac{VD}{\nu}$
t = time
T = temperature
ΔT = temperature difference
V_j = jet velocity
V_o = velocity through port
α = thermal diffusivity, equal to $\frac{k}{\rho C_p}$
ν = kinematic viscosity
ρ = gas density
τ_l = contact time during the wiping process

[1]Department of Mechanical Engineering, Texas A&M University, College Station, Tex. 77843, Assoc. Mem. ASME

Contributed by the Heat Transfer Division for publication in the JOURNAL OF HEAT TRANSFER. Manuscript received by the Heat Transfer Division January 17, 1983.

Introduction and Background

Heat transfer correlations for turbulent flows in tubes or pipes are generally applicable only to those heat transfer processes which are governed by the turbulence generated by the wall shear stresses. This wall-generated turbulence may not always be the only source of turbulence. When other sources of turbulence exist, the pipe flow heat transfer correlations are not valid. Other sources of turbulence include flows with separation such as downstream of bluff-bodies or restrictions. For flows with separation, heat transfer correlations are often unavailable. The few correlations that are available are restricted to specific geometries and offer little insight into the nature of the heat transfer process. This note describes the use of a simple heat transfer model for separated flows in tubes and pipes.

Flow separation is often characterized by regions of recirculation and large-scale coherent fluid structures with resulting local regions of relatively high heat transfer. Separated flows in tubes occur in many engineering applications due to baffles, orifices, valves, abrupt expansions, and abrupt contractions. Although turbulent heat transfer in tubes and pipes is well understood, relatively little experimental work has been reported for separated flows and no analytical work has been reported.

Krall and Sparrow [1] reported one of the first detailed experimental investigations of heat transfer for flows with separation in a tube. They examined the local heat transfer resulting from flow downstream of an orifice. Other closely related experimental heat transfer studies for flows with separation in tubes consist of flows with turbulence promoters [2] and flows with symmetric and unsymmetric tube blockages [3, 4]. A few other associated experimental heat transfer investigation are available (e.g., [5-7]) but the common weakness is that each study is limited to a particular geometry.

Flow separation processes often produce identifiable fluid structures (e.g., eddies) in the flow. These coherent, organized structures interact with the fluid near the wall and play an important, if not dominant, role in the heat transfer processes. To characterize heat transfer processes for flows with separation, the coherent fluid structures need to be related to the flow geometry.

Modeling Approach

Of the several possible modeling techniques, a relatively simple phenomenological model is available for the heat transfer processes for separated flows based on the surface renewal or penetration approach [8, 9]. The surface renewal or penetration approach models the turbulent transport process as a succession of quasi-steady interactions between the bulk fluid and the wall. Turbulent "eddies" are assumed to intermittently move from the main or core region to the close vicinity of the wall. At the wall, one-dimensional unsteady molecular transport is assumed to dominate the transport processes [8]. The alternative approach of developing a detailed, sophisticated model has several disadvantages. First, these models are complex and are not used on a routine basis by engineers in industry. Furthermore, these models are often geometry specific, require turbulent flow details as inputs, and mask an understanding of the dominant processes. The simpler, more direct approach, therefore, is often the most useful overall.

Past investigations [8, 9] which have used the surface renewal model were limited to flows where the turbulence was generated by wall shear stresses. The use of the surface renewal model to applications where the turbulence is generated by other than wall shear stresses has not been reported. This note describes the use of the surface renewal model for two different flow processes where the turbulence

was caused by a high velocity jet and by a flow blockage, respectively.

High-Velocity Jet. In this case, the heat transfer process in an exhaust port of an internal combustion engine was examined [10–12]. The flow into the exhaust port was approximately a convergent, conical jet. Exhaust flow visualization experiments indicated that the high jet velocities produced a region of separation with large-scale motion in the exhaust port [13, 14]. This motion was suggestive of an eddylike fluid structure with a scale roughly half the port diameter. This motion, therefore, was not a result of wall-generated turbulence and would result in increased heat transfer rates. Figure 1 is a schematic illustration of the exhaust port with the large-scale motion depicted.

Since no empirical or analytical correlation existed in the literature for the heat transfer caused by the large-scale motion in the exhaust port, an analytical expression was developed which incorporated the major effects of the motion. This order-of-magnitude analysis was suggested for this application by Mikic [15] and followed the spirit of the surface renewal approach. Following results from the exhaust flow visualization experiments [13, 14], the large-scale motion was approximated as a series of eddies with diameters equal to half the port diameter, local velocities equal to the instantaneous jet velocities, and gas temperature equal to the local instantaneous temperature. These eddies were assumed to "wipe" the surface for a length equal to their diameter.

During the "wiping" process, higher temperature gas from the bulk flow is brought into contact with the lower temperature gas near the surface. For the surface renewal model, this process is assumed to be similar to the unsteady heat conduction of a semi-infinite solid with a step change in surface temperature. This similarity is most accurate to the degree that an eddy possesses no internal motion [8]. In the wiping process, the initial temperature, T_i, is approximated as the wall temperature and the surface temperature, T_o, is suddenly raised to the local mean bulk gas temperature. The solution for the surface heat transfer [16] at any time, t, is

$$q_o = \frac{kA(T_o - T_i)}{(\pi\alpha t)^{0.5}} \tag{1}$$

The average heat flux during the time that the eddy "wipes" the surface is

$$\frac{q_{\text{avg}}}{A} = \frac{1}{\tau_t}\int_o^{\tau_t} q_o dt = \frac{2k(T_o - T_i)}{(\pi\alpha\tau_t)^{0.5}} \tag{2}$$

The approximate time that the eddy is in contact with the wall is

$$\tau_t = \frac{l_{\text{wiped}}}{\text{velocity}} = \frac{D/2}{V_j} \tag{3}$$

The contact time of the eddy with the wall was estimated to be at most one-tenth of the average residence time of the eddy in the port [10]. A nondimensional expression was obtained from the Nusselt number definition

$$\text{Nu} = \frac{h\ D}{k} = \frac{(q/A)_{\text{avg}} D}{k\ \Delta T} \tag{4}$$

Combining equations (2), (3), and (4)

$$\text{Nu} = \frac{2k\ \Delta T}{\left(\pi\alpha \dfrac{D/2}{V}\right)^{0.5}} \left(\frac{D}{k\ \Delta T}\right) \tag{5}$$

Rearranging and introducing definitions

$$\text{Nu} = \left(\frac{8}{\pi}\right)^{0.5} \text{Re}_j^{0.5}\,\text{Pr}^{0.5} \tag{6}$$

where

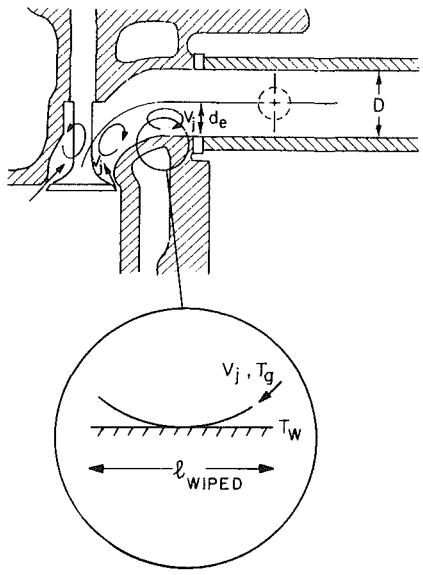

Fig. 1 Schematic illustration of the large-scale motion in the engine exhaust port

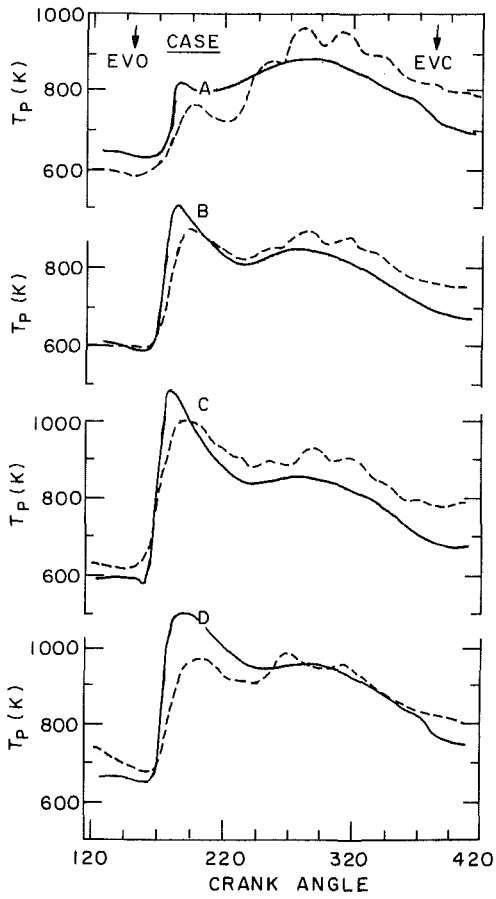

Fig. 2 Computed (——) and measured (····) exhaust port gas temperatures as a function of time (or crank angle) for four engine conditions

$$\text{Re}_j = \frac{V_j D}{\nu}$$

The final relation, then, describes the exhaust port heat transfer resulting from the large scale motion which was generated by the high-velocity jet.

To explore the usefulness of this simple model, equation (6)

was used to predict the port exit temperatures, T_p, for a range of engine conditions. These computed temperatures were compared to measured values as a form of model validation. The procedures and apparatus for the comparison and measurements are described elsewhere [12]. Figure 2 shows the computed and measured exhaust port exit gas temperatures as a function of crank angle for four different engine operating conditions. The comparison resulted in good agreement but the model slightly underpredicted the heat loss. Note that better agreement would have been obtained if the eddy size was approximated as one-third the port diameter; but this level of detail would have been somewhat arbitrary. Figure 2 shows that agreement was best during the initial periods of the exhaust process. This is the period with the highest jet velocities and the model would be expected to be most appropriate. Later periods of the exhaust process were better modeled with alternative expressions [12].

Flow Blockage. A second example of this modeling procedure utilized the data of Krall and Sparrow [1]. Krall and Sparrow determined an empirical correlation for the peak heat transfer in a tube due to flow separation downstream of a simple orifice for a Prandtl number of 3

$$\mathrm{Nu}_{\max} = 0.398\mathrm{Re}_o^{2/3} \tag{7}$$

where Re_o is the Reynolds number based on the orifice hole diameter. By assuming that the coherent fluid structures were produced in the flow through the orifice, an analytical correlation may be derived by using the surface renewal approach. The maximum Nusselt number is the appropriate parameter to compare to this model since the eddy/wall interaction is anticipated to dominate the maximum heat transfer process.

This development follows the previously described example of jet flow into an exhaust port. The major differences are in estimating the eddylike structure and its interaction with the wall. In this case, the eddy will be assumed to scale with the "step"

$$d_e = \frac{D - d_o}{2} \tag{8}$$

where d_e is the eddy diameter, D is the tube or pipe diameter, and d_o is the orifice diameter. Although no experimental data was available for this estimation, the eddy size scaling has the proper limits. As the orifice diameter approaches the pipe diameter, the eddy size approaches zero (no eddies due to flow separation). As the orifice diameter approaches zero, the eddy size approaches one-half the pipe diameter (which is consistent with the previously discussed observations of a jet into an exhaust port [13, 14]). The eddy velocity during the wall interaction was assumed to be one-half the velocity through the orifice. Again, no experimental data was available for this estimation but some decrease of the eddy velocity was anticipated during the wall interaction. The eddy also was assumed to complete one revolution during its interaction with the wall. Using these assumptions, the approximate time that the eddy is in contact with the wall is

$$\tau_l = \frac{\text{distance}}{\text{velocity}} = \frac{\pi d_e}{\frac{1}{2} V_o} = \pi \frac{(D - d_o)}{V_o} \tag{9}$$

Combining equation (9) with equation (2) and equation (4) yields

$$\mathrm{Nu} = \left(\frac{2}{\pi}\right) \mathrm{Re}_o^{1/2} \mathrm{Pr}^{1/2} \frac{D}{d_o} \left[\frac{d_o}{D - d_o}\right]^{1/2} \tag{10}$$

where

$$\mathrm{Re}_o = \frac{V_o d_o}{\nu}$$

For $\mathrm{Pr} = 3$

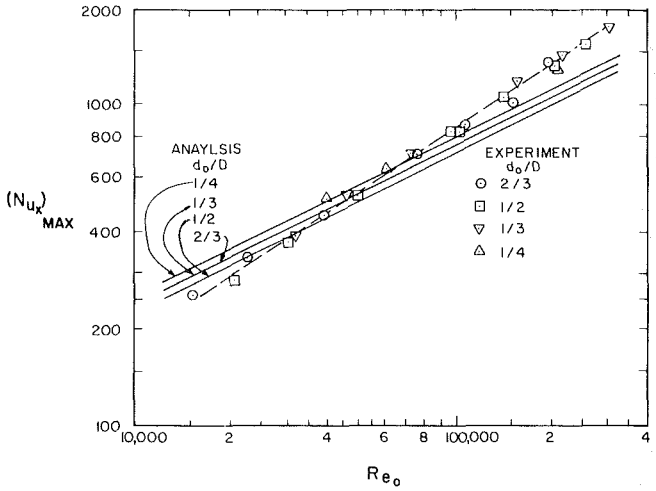

Fig. 3 Computed (——) and measured [1] (····) values for the maximum Nusselt number as a function of Reynolds number

$$\mathrm{Nu} = 1.10\,\mathrm{Re}_o^{1/2} \frac{D}{d_o} \left[\frac{d_o}{D - d_o}\right]^{1/2} \tag{11}$$

This expression has been evaluated for the orifice-to-pipe diameter ratios examined by Krall and Sparrow [1]. Figure 3 shows the results of the experiment [1] and the results of equation (11). The overall agreement is good, although the dependence on Reynolds number could be improved by incorporating second order effects. For example, a portion of the flow interacts with the wall due to wall generated turbulence, and this means the heat transfer has a dependence on Reynolds number to the 0.8 power. By combining these two heat transfer models, the dependency on Reynolds number would be in better agreement with the experiment. Improvements of this nature are not warranted at this time due to uncertainties concerning the flow, but such combinations may be as simple as adding together the proper fractions of each mechanism (e. g., $\mathrm{Nu} = a\,\mathrm{Re}^{0.5} + b\,\mathrm{Re}^{0.8}$). The model's dependence on the orifice-to-pipe diameter ratio is slight for the range of values examined and can neither be substantiated nor refuted.

Summary and Conclusions

The simple surface renewal or penetration model was used to estimate the turbulent heat transfer for flows with separation. For two different experiments, reasonable agreement was obtained. This approach is an order-of-magnitude technique which is based on assumptions (or experimental information) on the velocity and scale of turbulent eddies.

References

1 Krall, K. M., and Sparrow, E. M., "Turbulent Heat Transfer in the Separated, Reattached, and Redevelopment Regions of a Circular Tube," ASME JOURNAL OF HEAT TRANSFER, Vol. 88, Feb. 1966, pp. 131–136.

2 Thomas, D. G., "Enhancement of Forced Convection Heat Transfer Coefficient Using Detached Turbulence Promoters," *I & EC Process Design and Development*, Vol. 6, July 1967, pp. 385–390.

3 Koram, K. K., and Sparrow, E. M., "Turbulent Heat Transfer Downstream of an Unsymmetric Blockage in a Tube," ASME JOURNAL OF HEAT TRANSFER, Vol. 100, Nov. 1978, pp. 588–594.

4 Sparrow, E. M., Koram, K. K., and Charmchi, M., "Heat Transfer and Pressure Drop Characteristics Induced by a Slat Blockage in a Circular Tube," ASME JOURNAL OF HEAT TRANSFER, Vol. 102, Apr. 1970, pp. 64–70.

5 Dyban, E. P., and Epik, E. Ya., "Making Allowances for Stream Turbulence in Calculating Heat Transfer After an Orifice Plate in a Tube," *International Chemical Engineering*, Vol. 10, Apr. 1970, pp. 198–201.

6 Ota, T., and Kon, N., "Heat Transfer in the Separated and Reattached

Flow Over Blunt Flat Plates - Effects of Nose Shape," *International Journal of Heat and Mass Transfer*, Vol. 22, 1979, pp. 197-206.

7 Sparrow, E. M., and O'Brien, J. E., "Heat Transfer Coefficient on the Downstream Face of and Abrupt Enlargement or Inlet Constriction in a Pipe," ASME JOURNAL OF HEAT TRANSFER, Vol. 102, Aug. 1980, pp. 408-414.

8 Chung, B. T. F., Fan, L. T., and Hwang, C. L., "General Mathematical Models of Transport Processes with and without Chemical Reactions," The Canadian *Journal of Chemical Engineering*, Vol. 49, June 1971, pp. 340-345.

9 Sideman, S., and Pinezewski, W. V., "Turbulent Heat and Mass Transfer at Interfaces: Transport Models and Mechanisms," *Topics in Transport Phenomena*, edited by C. Gutfinger, Hemisphere Publishing Corp., 1975, pp. 47-207.

10 Caton, J. A., "Heat Transfer, Mixing and Hydrocarbon Oxidation in an Engine Exhaust Port," Ph.D thesis, Massachusetts Institute of Technology, Feb. 1980.

11 Caton, J. A., and Heywood, J. B., "Models for Heat Transfer, Mixing and Hydrocarbon Oxidation in an Exhaust Port of a Spark-Ignited Engine," SAE paper 800290, Feb. 1980.

12 Caton, J. A., and Heywood, J. B., "An Experimental and Analytical Study of Heat Transfer in an Engine Exhaust Port," *International Journal of Heat and Mass Transfer*, Vol. 24, No. 4, Apr. 1981, pp. 581-595.

13 Tanka, K., "Airflow Through Exhaust Valve of Conical Seat," *Proceedings of Third International Congress for Applied Mechanics*, Vol. 1., 1931, pp. 287-295.

14 Harrington, J. W., "Visualization of the Flow of Exhaust Through an Internal Combustion Engine Exhaust Port," BSME thesis, Massachusetts Institute of Technology, May 1979.

15 Mikic, B. B., personal communication, Mar. 1979.

16 Holman, J. P., *Heat Transfer*, McGraw-Hill 2d ed., 1968.

A Monte Carlo-Finite Difference Method for Coupled Radiation-Conduction Heat Transfer in Semitransparent Media

A. Al Abed[1] and J.-F. Sacadura[2]

Nomenclature

F = net radiative heat flux
I = intensity of radiation
N = radiation to conduction parameter, $\frac{4\,\bar{\sigma}\,T_1^3}{\lambda\beta}$
q = total heat flux
q_a = energy absorbed in the medium
q_s = energy emitted in the medium
R = random number in the (0-1) range
t = time, s
T = temperature, Kelvin
T_1 = temperature at surface 1
T_2 = temperature at surface 2
X = normal distance measured from surface 1
α = scattering angle or thermal diffusivity
β = extinction coefficient
β' = angle between the planes of incidence and scattering
Δt = time increment, s
Δx = element thickness, m
ϵ = surface emissivity
η = bundle angle after scattering
η' = angle of emitted bundle with the normal
θ = angle of a pencil of rays with the normal
Θ = dimensionless temperature: T/T_1
κ = absorption coefficient, m^{-1}
λ = thermal conductivity
μ = $\cos\theta$
$\bar{\sigma}$ = Stefan-Boltzmann constant
τ_o = optical depth = $\int_o^x \beta dx$
τ = optical thickness = $\int_o^D \beta dx$
ϕ = dimensionless radiant energy flux, $\frac{F(\tau)}{\bar{\sigma}T_1^4}$
ψ = dimensionless heat flux, $\frac{q}{\lambda\beta T_1}$
ω_0 = albedo
Ω = solid angle

Superscript

τ = time step number

Introduction

Simultaneous conduction-radiation heat transfer in participating media is an important problem. Applications include, among many, heat transfer in fibers used as insulators and reentry heating problems.

Some simplifications of the mathematical complexity of an analytical solution of the general problem has been introduced. This resulted in a number of methods that can be applied in some cases, but not in others. Only a few of such methods obtained complete solutions; among these are those for temperature distribution in the medium and heat flux at the boundary.

The steady-state case was investigated in several papers [1, 2, 3]. Viskanta [1] used a numerical method, while Bergquam and Seban [2] used a two-flux method. In [3], a differential approximation was employed.

The transient state problem was treated by Lick [4] who used a kernel substitution. Both Hazzah and Beck [5] and Chang and Kang [3] have used a differential approximation. In [6], a numerical solution of the problem was obtained, while in [7] the discrete coordinates method was employed. The idempodent method was chosen by Weston and Hauth [8] for their solution and the normal mode by Lii and Ozisik for theirs [9].

The Monte Carlo method has been used by Perlmutter and Howell [10] to solve the pure radiation problem and by Howell et al. [11] for the coupled radiation-convection problem in the steady state.

In this paper the Monte Carlo method is coupled with the finite difference method to solve the energy transfer in a homogeneous gray solid for cases in which radiation is an important mode of heat transfer. Both the transient and steady-states solutions are obtained.

To reduce the complexity of the problem, a one-dimensional plane geometry is used. Thermophysical and radiative properties are considered constant in the medium and do not vary with temperature.

The Monte Carlo method consists of following a bundle of energy through a probable path until final absorption in the system. Sufficient bundles are followed to give statistically meaningful results.

[1] Graduate Student, Laboratoire de Mécanique des Fluides et Thermique, Institut National des Sciences Appliqueés de Lyon, F 69621 Villeurbanne Cédex, France

[2] Maître-Assistant, Docteur ès-Sciences, Laboratoire de Mécanique des Fluides et Thermique, Institut National des Sciences Appliquees de Lyon, F 69621 Villeurbanne Cédex, France

Contributed by the Heat Transfer Division for publication in the JOURNAL OF HEAT TRANSFER. Manuscript received by the Heat Transfer Division August 2, 1982.

Flow Over Blunt Flat Plates - Effects of Nose Shape," *International Journal of Heat and Mass Transfer*, Vol. 22, 1979, pp. 197-206.

7 Sparrow, E. M., and O'Brien, J. E., "Heat Transfer Coefficient on the Downstream Face of and Abrupt Enlargement or Inlet Constriction in a Pipe," ASME JOURNAL OF HEAT TRANSFER, Vol. 102, Aug. 1980, pp. 408-414.

8 Chung, B. T. F., Fan, L. T., and Hwang, C. L., "General Mathematical Models of Transport Processes with and without Chemical Reactions," The Canadian *Journal of Chemical Engineering*, Vol. 49, June 1971, pp. 340-345.

9 Sideman, S., and Pinezewski, W. V., "Turbulent Heat and Mass Transfer at Interfaces: Transport Models and Mechanisms," *Topics in Transport Phenomena*, edited by C. Gutfinger, Hemisphere Publishing Corp., 1975, pp. 47-207.

10 Caton, J. A., "Heat Transfer, Mixing and Hydrocarbon Oxidation in an Engine Exhaust Port," Ph.D thesis, Massachusetts Institute of Technology, Feb. 1980.

11 Caton, J. A., and Heywood, J. B., "Models for Heat Transfer, Mixing and Hydrocarbon Oxidation in an Exhaust Port of a Spark-Ignited Engine," SAE paper 800290, Feb. 1980.

12 Caton, J. A., and Heywood, J. B., "An Experimental and Analytical Study of Heat Transfer in an Engine Exhaust Port," *International Journal of Heat and Mass Transfer*, Vol. 24, No. 4, Apr. 1981, pp. 581-595.

13 Tanka, K., "Airflow Through Exhaust Valve of Conical Seat," *Proceedings of Third International Congress for Applied Mechanics*, Vol. 1., 1931, pp. 287-295.

14 Harrington, J. W., "Visualization of the Flow of Exhaust Through an Internal Combustion Engine Exhaust Port," BSME thesis, Massachusetts Institute of Technology, May 1979.

15 Mikic, B. B., personal communication, Mar. 1979.

16 Holman, J. P., *Heat Transfer*, McGraw-Hill 2d ed., 1968.

A Monte Carlo-Finite Difference Method for Coupled Radiation-Conduction Heat Transfer in Semitransparent Media

A. Al Abed[1] and J.-F. Sacadura[2]

Nomenclature

F = net radiative heat flux
I = intensity of radiation
N = radiation to conduction parameter, $\frac{4\,\bar{\sigma}\,T_1^3}{\lambda\beta}$
q = total heat flux
q_a = energy absorbed in the medium
q_s = energy emitted in the medium
R = random number in the (0-1) range
t = time, s
T = temperature, Kelvin
T_1 = temperature at surface 1
T_2 = temperature at surface 2
X = normal distance measured from surface 1
α = scattering angle or thermal diffusivity
β = extinction coefficient
β' = angle between the planes of incidence and scattering
Δt = time increment, s
Δx = element thickness, m
ϵ = surface emissivity
η = bundle angle after scattering
η' = angle of emitted bundle with the normal
θ = angle of a pencil of rays with the normal
Θ = dimensionless temperature: T/T_1
κ = absorption coefficient, m^{-1}
λ = thermal conductivity
μ = $\cos\theta$
$\bar{\sigma}$ = Stefan-Boltzmann constant
τ_o = optical depth = $\int_o^x \beta dx$
τ = optical thickness = $\int_o^D \beta dx$
ϕ = dimensionless radiant energy flux, $\frac{F(\tau)}{\bar{\sigma}T_1^4}$
ψ = dimensionless heat flux, $\frac{q}{\lambda\beta T_1}$
ω_0 = albedo
Ω = solid angle

Superscript

τ = time step number

Introduction

Simultaneous conduction-radiation heat transfer in participating media is an important problem. Applications include, among many, heat transfer in fibers used as insulators and reentry heating problems.

Some simplifications of the mathematical complexity of an analytical solution of the general problem has been introduced. This resulted in a number of methods that can be applied in some cases, but not in others. Only a few of such methods obtained complete solutions; among these are those for temperature distribution in the medium and heat flux at the boundary.

The steady-state case was investigated in several papers [1, 2, 3]. Viskanta [1] used a numerical method, while Bergquam and Seban [2] used a two-flux method. In [3], a differential approximation was employed.

The transient state problem was treated by Lick [4] who used a kernel substitution. Both Hazzah and Beck [5] and Chang and Kang [3] have used a differential approximation. In [6], a numerical solution of the problem was obtained, while in [7] the discrete coordinates method was employed. The idempodent method was chosen by Weston and Hauth [8] for their solution and the normal mode by Lii and Ozisik for theirs [9].

The Monte Carlo method has been used by Perlmutter and Howell [10] to solve the pure radiation problem and by Howell et al. [11] for the coupled radiation-convection problem in the steady state.

In this paper the Monte Carlo method is coupled with the finite difference method to solve the energy transfer in a homogeneous gray solid for cases in which radiation is an important mode of heat transfer. Both the transient and steady-states solutions are obtained.

To reduce the complexity of the problem, a one-dimensional plane geometry is used. Thermophysical and radiative properties are considered constant in the medium and do not vary with temperature.

The Monte Carlo method consists of following a bundle of energy through a probable path until final absorption in the system. Sufficient bundles are followed to give statistically meaningful results.

[1] Graduate Student, Laboratoire de Mécanique des Fluides et Thermique, Institut National des Sciences Appliqueés de Lyon, F 69621 Villeurbanne Cédex, France

[2] Maître-Assistant, Docteur ès-Sciences, Laboratoire de Mécanique des Fluides et Thermique, Institut National des Sciences Appliquees de Lyon, F 69621 Villeurbanne Cédex, France

Contributed by the Heat Transfer Division for publication in the JOURNAL OF HEAT TRANSFER. Manuscript received by the Heat Transfer Division August 2, 1982.

Analysis and Results

A slab of a solid material confined between two parallel planes is used in this study. The bounding planes are supposedly isothermal and diffusely emit and reflect radiation. The solid material is considered capable of absorbing, emitting, and scattering radiation isotropically.

Solutions are obtained for the temperature distribution and the heat fluxes at the boundaries. The basic equations pertaining to this problem can be written as

$$\rho C_p \frac{DT}{Dt} = -\nabla . \mathbf{q} \tag{1}$$

where

$$\mathbf{q} = -\lambda \nabla \mathbf{T} + \mathbf{F} \tag{2}$$

where the following boundary conditions

$$\begin{aligned} T &= T_1, \quad \tau = 0 \\ T &= T_2, \quad \tau = \tau_o \end{aligned} \tag{3}$$

for the steady state and

$$\left.\begin{aligned} T(\tau,0) &= 0 \\ T(0,t) &= T_1 \\ T(\tau_o,t) &= T_2 \end{aligned}\right\} \begin{aligned} t &= 0 \\ t &> 0 \end{aligned} \tag{4}$$

for the transient case.

The radiative flux, F, in a given direction $\mathbf{n}$ ($F = \mathbf{F} \cdot \mathbf{n}$) can be expressed in terms of the intensity of radiation, I, as

$$F = \int_{\Omega = 4\pi} I(\tau,\mu)\, \mu\, d\,\Omega \tag{5}$$

The intensity, I, is the solution of the equation of transfer

$$\mu \frac{dI}{d\tau} + I = (1-\omega_o) I_b(T) + \frac{\omega_o}{2} \int_{-1}^{+1} I(\tau,\mu')\, d\,\mu' \tag{6}$$

subject to the boundary conditions

$$\begin{aligned} I(\tau,\mu) &= I(0) \quad \tau = 0 \\ I(\tau,\mu) &= I(\tau_o) \quad \tau = \tau_o \end{aligned} \tag{7}$$

$I(0)$ and $I(\tau_o)$ can be expressed as functions of the boundaries properties (emissivity, temperature).

The simultaneous solution of the preceding equations yields the exact analytical solution of the problem. It is obvious, however, that such a solution is hard to obtain. Moreover, introduction of simplifying hypotheses is not always justified. Then, when a high degree of accuracy is not required, the Monte Carlo method is very efficient for its relative simplicity.

The method of solution consists of dividing the slab into a number of smaller elements as in the classical finite difference method. The elements being represented by nodes are considered isothermal. By virtue of its temperature, each element emits a number of bundles of energy. The bundles are followed throughout the medium until absorption. The history of a bundle passes through different phases.

It is first emitted; its direction of emission is calculated from equation (A1) in the appendix. Then its path length, calculated from (A2), is compared to its actual distance from the wall. If it is found bigger, a test is made to determine whether it is reflected or absorbed at the wall (A3). If the path length is smaller, a test is made to find whether it is scattered or absorbed by the medium (A4). If scattered, the new bundle direction is obtained from (A5), and if absorbed, it is tallied and its life ends.

Although the state of local thermodynamic equilibrium applies in our case, the bundle is not reemitted after absorption in the medium because the reemission was accounted for originally, when the number of bundles was calculated for each element.

The elements that have their nodes on the boundaries have fixed temperature values. The size of these elements was reduced so that absorption in them is due to the surface only.

$$\begin{aligned} q_{s_i} &= 4\, \kappa\, \Delta x\, \bar{\sigma}\, T_i^4 \quad i = 2,3, \ldots, I-1 \\ q_{s_i} &= \epsilon_i \bar{\sigma}\, T_i^4 \qquad i = 1 \text{ or } i = I \end{aligned} \tag{8}$$

where I is the number of elements, and i refers to the element number.

Heat balance is made on each element and is expressed under the finite difference form in the steady state

$$\Delta x\, 4\kappa\, \bar{\sigma}\, T_i^4 = q_{a_i} + \left[-\frac{\lambda}{\Delta x}(T_i - T_{i-1})\right] - \left[-\frac{\lambda}{\Delta x}(T_{i+1} - T_i)\right] \tag{9}$$

$$i = 2,3, \ldots, I-1$$

The resulting equations are solved simultaneously for the temperatures.

Since the number of emitted bundles depends on the temperature in each element (equation (8)), an iterative scheme was required. An initial approximation for the temperature distribution (a linear one, for instance) was given. A distribution of the absorption (q_{a_i}) in the medium resulted from applying the Monte Carlo method. This was used to determine a new distribution of temperature (equation (9)). The procedure was repeated until convergence.

For the transient case, an implicit finite difference scheme was used, so as not to be limited in choosing the time step. Only accuracy considerations dictated the size of the time step. In this case, equation (9), valid for the steady state only, is replaced by

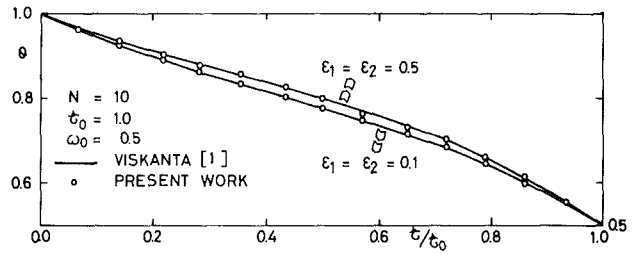

Fig. 1 Steady-state temperature distribution: $\omega_o = 0.5$, $\tau_o = 1.0$, $N = 10$, $\epsilon_1 = \epsilon_2 = 0.1, 0.5$

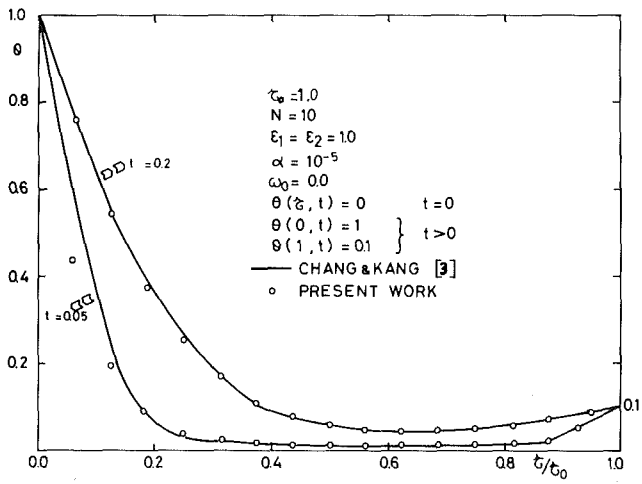

Fig. 2 Temperature distribution in the transient state: $\omega_o = 0$, $\tau_o = 1.0$, $N = 10$, $\epsilon_1 = \epsilon_2 = 1.0$, $\alpha = 10^{-5}$

Table 1 Conductive and radiative heat fluxes: $N = 10$, $\tau_o = 1.0$, $\epsilon_1 = \epsilon_2 = 1.0$, $t = 0.5$, $\alpha = 10^{-4}$ $\Theta(\tau,t) = 0.0$ $t = 0$; $\Theta(0,t) = 1.0$, $\Theta(1,t) = 0.0$ $t > 0$

Method	$-\partial\Theta/\partial\tau\|_{\tau=0}$	$\phi(\tau)\|_{\tau=0}$	ω_o
Monte Carlo	2.293	0.859	0.0
[9]	2.297	0.856	
Monte Carlo	2.470	0.664	0.5
[9]	2.439	0.657	

$$-q^{\tau}_{a_i} + \lambda \frac{T^{\tau}_i - T^{\tau}_{i-1}}{\Delta x} - \lambda \frac{T^{\tau}_{i+1} - T^{\tau}_i}{\Delta x} + 4\kappa\, \Delta x\, \bar{\sigma}\, T^{\tau 4}_i + \rho C_p \Delta x \frac{T^{\tau}_i - T^{\tau-1}_i}{\Delta t} = 0 \tag{10}$$

The same procedure just explained is followed for each time step to obtain the temperature distribution.

It has been found that the method of superposition [5], which consists of dividing the problem into two smaller ones, one problem without heat sources but with boundary temperature nonzero and the other one with heat sources in the medium and boundary temperatures zero, does not work here. The reason for this is that radiative heat sources in this problem are due to conduction; in other words, they depend on the temperature gradient in the medium. When the temperature gradient is constant, heat sources would vanish, and when it is decreasing, heat sources turn out to be negative. As can be seen clearly in the results, the temperature gradient is constant in some portions of the medium and sometimes decreasing; this yields vanishing or negative heat sources, respectively, which obviously makes little sense as heat sources are the generators of bundles.

In addition, we are treating a nonlinear problem where superposition techniques cannot be applied. Temperature distribution in the medium, and heat fluxes at the boundaries, were obtained for several values of medium properties (albedo) and boundary conditions (temperature, emissivity). Comparisons with results given by other methods show excellent agreement. A sample of these results is given in Figs. 1, 2 and Table (1).

Convergence of the solution was ensured by increasing the number of energy bundles and the number of nodes, and then observing that no change in the solution occurred. Calculations were conducted on an IRIS 80 digital computer. Program running time was of the order of 1-2 min for each time step. Running time depended, of course, on the initial guess for the temperature distribution and on the number of bundles employed.

References

1 Viskanta, R., "Heat Transfer by Conduction and Radiation in Absorbing and Scattering Materials," ASME JOURNAL OF HEAT TRANSFER, Feb. 1965, pp. 143-150.

2 Bergquam, J. B., and Seban, R. A., "Heat Transfer by Conduction and Radiation in Absorbing and Scattering Materials," ASME JOURNAL OF HEAT TRANSFER, May 1971, pp. 236-239.

3 Chang, Y. P., and Kang, C. S., "Transient and Steady Heat Transfer in a Conducting and Radiation Medium," *AIAA Journal*, Apr. 1970, p. 609-613.

4 Lick, W., "Transient Energy Transfer by Radiation and Conduction," *International Journal of Heat and Mass Transfer*, Vol. 8, 1965, pp. 119-127.

5 Hazzah, A. S., and Beck, J. V., "Unsteady Combined Conduction-Radiation Energy Transfer Using a Rigorous Differential Method," *International Journal of Heat and Mass Transfer*, Vol. 13, 1970, pp. 517-522.

6 Doornink, D. G., and Hering, R. G., "Transient Combined Conductive and Radiative Heat Transfer," ASME JOURNAL OF HEAT TRANSFER, Nov. 1972, pp. 473-478.

7 Roux, J. A., and Smith, A. M., "Combined Conductive and Radiative Heat Transfer in the Absorbing and Scattering Infinite Slab," ASME JOURNAL OF HEAT TRANSFER, Feb. 1978, pp. 98-104.

8 Weston, K. C., and Hauth, J. L., "Unsteady Combined Radiation and Conduction in an Absorbing, Scattering and Emitting Medium, ASME JOURNAL OF HEAT TRANSFER, Aug. 1973, pp. 357-364.

9 Lii, C. C., and Ozisik, "Transient Radiation and Conduction in an Absorbing Emitting, Scattering Slab With Reflective Boundaries," *International Journal of Heat and Mass Transfer*, Vol. 15, 1972, pp. 1175-1179.

10 Howell, J. R., and Perlmutter, M., "Monte-Carlo Solution of Thermal Transfer Through Radiant Media Between Gray Walls," ASME JOURNAL OF HEAT TRANSFER, Feb. 1964, pp. 116-122.

11 Howell, J. R., Strite, M. K., and Renkel, H., "Heat Transfer Analysis of Rocket Nozzles Using Very High Temperature Propellants," *AIAA Journal*, Vol. 3, 1965, pp. 669-673.

12 Al Abed, A., "Application de la méthode de Monte-Carlo au calcul du transfert de chaleur par conduction et rayonnement couplés dans un milieu semi-transparent solide," Dissertation, D. E. A. de mécanique, University of Lyon, 1982.

APPENDIX

MONTE CARLO Relations

Direction of emission from a diffuse surface:

$$\eta' = \cos^{-1}\sqrt{R_{\eta'}} \tag{A1a}$$

Direction of emission from a volume element:

$$\eta' = \cos^{-1}(1 - 2R_{\eta'}) \tag{A1b}$$

Bundle path length to absorption or scattering:

$$l = -\frac{1}{\beta} ln(R_l) \tag{A2}$$

Test for reflection or absorption at the wall:

$$\begin{aligned} R_\epsilon &\leqslant \epsilon \quad \text{absorption} \\ R_\epsilon &> \epsilon \quad \text{reflection} \end{aligned} \tag{A3}$$

Test for scattering or absorption by the medium:

$$\begin{aligned} R_\omega &\leqslant \omega_o \quad \text{scattering} \\ R_\omega &> \omega_o \quad \text{absorption} \end{aligned} \tag{A4}$$

New direction after scattering:

$$\cos\eta = \cos\eta' \cos\alpha + \sin\eta' \sin\alpha \cos\beta' \tag{A5}$$

Finite Element Solution of Radiative Heat Transfer in a Two-Dimensional Rectangular Enclosure With Gray Participating Media

M. M. Razzaque[1], D. E. Klein[2], and J. R. Howell[2,3]

Introduction

Much work on radiative transfer in absorbing-emitting media, including previous finite element applications [1-3], has been confined due to the complexity of the problem, to the one-dimensional radiative case. Other methods have been applied to multidimensional computations with varying degrees of accuracy.

The present work provides an exact solution of radiative heat transfer in a two-dimensional rectangular geometry with a gray participating medium. Ratzel [4] has used the *P-N* approximation to predict the temperature distribution in a medium and the heat flux distribution at all bounding sur-

[1] Virginia Electric and Power Company, Richmond, Va. 23261

[2] Department of Mechanical Engineering, The University of Texas at Austin, Autsin, Texas 78712, Mem. ASME

[3] Fellow ASME

Contributed by the Heat Transfer Division for publication in the JOURNAL OF HEAT TRANSFER. Manuscript received by the Heat Transfer Division December 13, 1982.

Table 1 Conductive and radiative heat fluxes: $N = 10$, $\tau_o = 1.0$, $\epsilon_1 = \epsilon_2 = 1.0$, $t = 0.5$, $\alpha = 10^{-4}$ $\Theta(\tau,t) = 0.0$ $t = 0$; $\Theta(0,t) = 1.0$, $\Theta(1,t) = 0.0$ $t > 0$

Method	$-\partial\Theta/\partial\tau\|_{\tau=0}$	$\phi(\tau)\|_{\tau=0}$	ω_o
Monte Carlo	2.293	0.859	0.0
[9]	2.297	0.856	
Monte Carlo	2.470	0.664	0.5
[9]	2.439	0.657	

$$-q^{\tau}_{a_i} + \lambda\frac{T^{\tau}_i - T^{\tau}_{i-1}}{\Delta x} - \lambda\frac{T^{\tau}_{i+1} - T^{\tau}_i}{\Delta x} + 4\kappa\,\Delta x\,\bar{\sigma}\,T^{\tau 4}_i + \rho C_p \Delta x \frac{T^{\tau}_i - T^{\tau-1}_i}{\Delta t} = 0 \tag{10}$$

The same procedure just explained is followed for each time step to obtain the temperature distribution.

It has been found that the method of superposition [5], which consists of dividing the problem into two smaller ones, one problem without heat sources but with boundary temperature nonzero and the other one with heat sources in the medium and boundary temperatures zero, does not work here. The reason for this is that radiative heat sources in this problem are due to conduction; in other words, they depend on the temperature gradient in the medium. When the temperature gradient is constant, heat sources would vanish, and when it is decreasing, heat sources turn out to be negative. As can be seen clearly in the results, the temperature gradient is constant in some portions of the medium and sometimes decreasing; this yields vanishing or negative heat sources, respectively, which obviously makes little sense as heat sources are the generators of bundles.

In addition, we are treating a nonlinear problem where superposition techniques cannot be applied. Temperature distribution in the medium, and heat fluxes at the boundaries, were obtained for several values of medium properties (albedo) and boundary conditions (temperature, emissivity). Comparisons with results given by other methods show excellent agreement. A sample of these results is given in Figs. 1, 2 and Table (1).

Convergence of the solution was ensured by increasing the number of energy bundles and the number of nodes, and then observing that no change in the solution occurred. Calculations were conducted on an IRIS 80 digital computer. Program running time was of the order of 1-2 min for each time step. Running time depended, of course, on the initial guess for the temperature distribution and on the number of bundles employed.

References

1 Viskanta, R., "Heat Transfer by Conduction and Radiation in Absorbing and Scattering Materials," ASME JOURNAL OF HEAT TRANSFER, Feb. 1965, pp. 143-150.

2 Bergquam, J. B., and Seban, R. A., "Heat Transfer by Conduction and Radiation in Absorbing and Scattering Materials," ASME JOURNAL OF HEAT TRANSFER, May 1971, pp. 236-239.

3 Chang, Y. P., and Kang, C. S., "Transient and Steady Heat Transfer in a Conducting and Radiation Medium," *AIAA Journal*, Apr. 1970, p. 609-613.

4 Lick, W., "Transient Energy Transfer by Radiation and Conduction," *International Journal of Heat and Mass Transfer*, Vol. 8, 1965, pp. 119-127.

5 Hazzah, A. S., and Beck, J. V., "Unsteady Combined Conduction-Radiation Energy Transfer Using a Rigorous Differential Method," *International Journal of Heat and Mass Transfer*, Vol. 13, 1970, pp. 517-522.

6 Doornink, D. G., and Hering, R. G., "Transient Combined Conductive and Radiative Heat Transfer," ASME JOURNAL OF HEAT TRANSFER, Nov. 1972, pp. 473-478.

7 Roux, J. A., and Smith, A. M., "Combined Conductive and Radiative Heat Transfer in the Absorbing and Scattering Infinite Slab," ASME JOURNAL OF HEAT TRANSFER, Feb. 1978, pp. 98-104.

8 Weston, K. C., and Hauth, J. L., "Unsteady Combined Radiation and Conduction in an Absorbing, Scattering and Emitting Medium, ASME JOURNAL OF HEAT TRANSFER, Aug. 1973, pp. 357-364.

9 Lii, C. C., and Ozisik, "Transient Radiation and Conduction in an Absorbing Emitting, Scattering Slab With Reflective Boundaries," *International Journal of Heat and Mass Transfer*, Vol. 15, 1972, pp. 1175-1179.

10 Howell, J. R., and Perlmutter, M., "Monte-Carlo Solution of Thermal Transfer Through Radiant Media Between Gray Walls," ASME JOURNAL OF HEAT TRANSFER, Feb. 1964, pp. 116-122.

11 Howell, J. R., Strite, M. K., and Renkel, H., "Heat Transfer Analysis of Rocket Nozzles Using Very High Temperature Propellants," *AIAA Journal*, Vol. 3, 1965, pp. 669-673.

12 Al Abed, A., "Application de la méthode de Monte-Carlo au calcul du transfert de chaleur par conduction et rayonnement couplés dans un milieu semi-transparent solide," Dissertation, D. E. A. de mécanique, University of Lyon, 1982.

APPENDIX

MONTE CARLO Relations

Direction of emission from a diffuse surface:

$$\eta' = \cos^{-1}\sqrt{R_{\eta'}} \tag{A1a}$$

Direction of emission from a volume element:

$$\eta' = \cos^{-1}(1 - 2R_{\eta'}) \tag{A1b}$$

Bundle path length to absorption or scattering:

$$l = -\frac{1}{\beta}\ln(R_l) \tag{A2}$$

Test for reflection or absorption at the wall:

$$\begin{aligned} R_\epsilon &\leqslant \epsilon \quad \text{absorption} \\ R_\epsilon &> \epsilon \quad \text{reflection} \end{aligned} \tag{A3}$$

Test for scattering or absorption by the medium:

$$\begin{aligned} R_\omega &\leqslant \omega_o \quad \text{scattering} \\ R_\omega &> \omega_o \quad \text{absorption} \end{aligned} \tag{A4}$$

New direction after scattering:

$$\cos\eta = \cos\eta'\cos\alpha + \sin\eta'\sin\alpha\cos\beta' \tag{A5}$$

Finite Element Solution of Radiative Heat Transfer in a Two-Dimensional Rectangular Enclosure With Gray Participating Media

M. M. Razzaque[1], D. E. Klein[2], and J. R. Howell[2,3]

Introduction

Much work on radiative transfer in absorbing-emitting media, including previous finite element applications [1-3], has been confined due to the complexity of the problem, to the one-dimensional radiative case. Other methods have been applied to multidimensional computations with varying degrees of accuracy.

The present work provides an exact solution of radiative heat transfer in a two-dimensional rectangular geometry with a gray participating medium. Ratzel [4] has used the *P-N* approximation to predict the temperature distribution in a medium and the heat flux distribution at all bounding sur-

[1] Virginia Electric and Power Company, Richmond, Va. 23261

[2] Department of Mechanical Engineering, The University of Texas at Austin, Autsin, Texas 78712, Mem. ASME

[3] Fellow ASME

Contributed by the Heat Transfer Division for publication in the JOURNAL OF HEAT TRANSFER. Manuscript received by the Heat Transfer Division December 13, 1982.

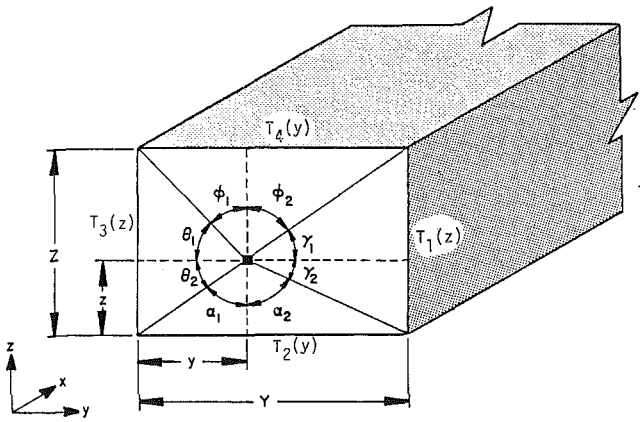

Fig. 1 Rectangular enclosure with the differential volume element and the surrounding triangular regions

faces of a rectangular enclosure. Crosbie and Schrenker [5] have presented some exact solutions to the same problem. The FEM results in the present study are compared with those of [4, 5]. The finite element solution of the present problem has not been attempted earlier, and the results for non-black walls from this work are not available elsewhere.

Analysis

If radiation is the sole mode of heat transfer and there is internal heat generation within the medium, the heat balance in nondimensional form for a gray absorbing-emitting gas with constant absorption coefficient becomes (see Fig. 1):

$$
\begin{aligned}
2\pi u^4 &\int_{-\alpha_1}^{\alpha_2} \psi_{o,lo} S_1\left(\frac{z}{\cos\alpha}\right) d\alpha \\
&+ \int_0^z \int_{-\alpha_1}^{\alpha_2} u^4 \frac{1}{\cos\alpha} S_0\left(\frac{z-z^*}{\cos\alpha}\right) d\alpha dz^* \\
&+ \int_{-\phi_1}^{\phi_2} \psi_{o,u} S_1\left(\frac{Z-z}{\cos\phi}\right) d\phi \\
&+ \int_z^Z \int_{-\phi_1}^{\phi_2} u^4 \frac{1}{\cos\phi} S_0\left(\frac{z^*-z}{\cos\phi}\right) d\phi dz^* \\
&+ \int_{\theta_1}^{\theta_2} \psi_{o,l} S_1\left(\frac{y}{\cos\theta}\right) d\theta \\
&+ \int_0^y \int_{-\theta_1}^{\theta_2} u^4 \frac{1}{\cos\theta} S_0\left(\frac{y-y^*}{\cos\theta}\right) d\theta dy^* \\
&+ \int_{-\gamma_1}^{\gamma_2} \psi_{o,rt} S_1\left(\frac{Y-y}{\cos\gamma}\right) d\gamma \\
&+ \int_y^Y \int_{-\gamma_1}^{\gamma_2} u^4 \frac{1}{\cos\gamma} S_0\left(\frac{y^*-y}{\cos\gamma}\right) d\gamma dy^* + S \qquad (1)
\end{aligned}
$$

where u is the nondimensional temperature (T/T_2), ψ is the energy flux, S_0, S_1, and S are heat source terms, z and y are optical thickness coordinates, Z and Y are the optical length and height of the enclosure, and z^* and y^* are dummy variables of integration. The nondimensional outgoing radiative heat fluxes for lower (l_o), upper (u), left (l), and right (rt) walls are given for diffusely emitting and reflecting gray surfaces by

$$
\psi_{o,i} = u_i^4 - \left(\frac{1-\epsilon}{\epsilon}\right)\psi_{r,i} \qquad (2)
$$

$$
i = lo, rt, u, l
$$

The physical conditions (temperature and emissivity) of the lower, upper, left, and right walls of the rectangular enclosure

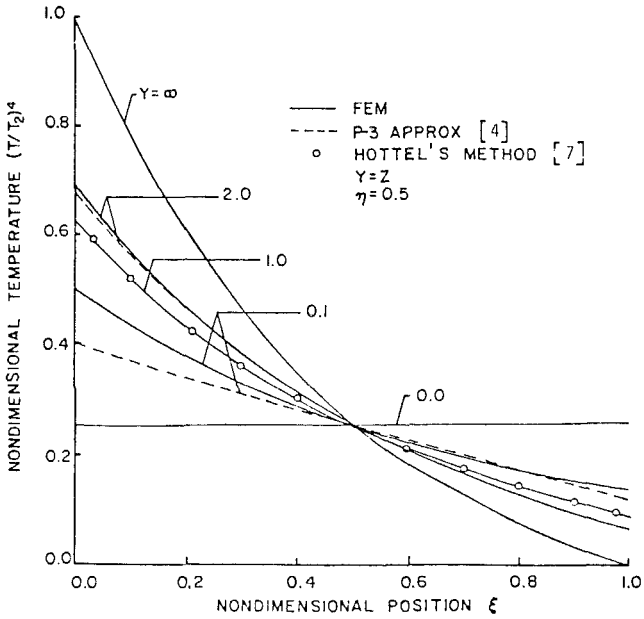

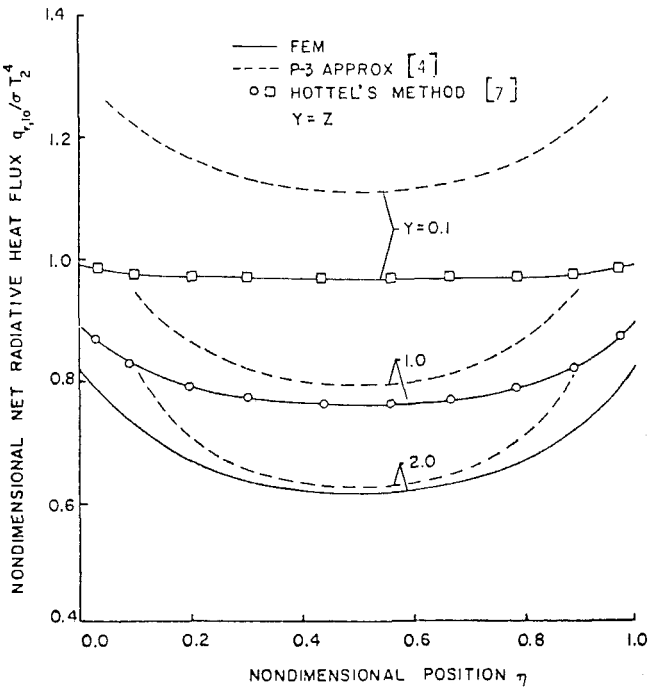

Fig. 2 Radiative transfer in square enclosures with different optical thickness. Black boundaries, bottom boundary at dimensionless temperature $u = 1.0$, other boundaries at $u = 0$. (*a*) centerline emissive power profile. (*b*) dimensionless radiative flux at hot boundary.

enter equation (1) through $\psi_{o,lo}$, $\psi_{o,u}$, $\psi_{o,l}$, and $\psi_{o,rt}$, respectively. Since the heat balance equation is an integral equation, the medium temperature will not match with the wall temperature (the "slip" condition).

The S_0 and S_1 functions in equation (1) are defined by

$$
S_n(g) = \int_1^\infty \mathrm{Exp}(-gt) \frac{dt}{t^{n+1}\sqrt{t^2-1}}
$$

The Galerkin finite element formulation is applied to equation (1) by writing it in a form that is linear in u^4

$$
u^4 = f(z, y, u^4) \qquad (3)
$$

Table 1 Pure radiation results

Nondimensional net radiative heat fluxes in a square enclosure with black walls, bottom wall at nondimensional temperature, $u = 1.0$, other walls at $u = 0.0$: $Y = Z = 1.0$, $S = 0$

Nondimensional position η	Bottom (hot) wall this work	Bottom (hot) wall [5][a]	Side (cold) wall this work	Side (cold) wall [5][a]	Top (cold) wall this work	Top (cold) wall [5][a]
0.1	0.828	0.827	−0.518	−0.518	−0.190	−0.190
0.2	0.792	0.796	−0.431	−0.433	−0.213	−0.213
0.3	0.776	0.777	−0.366	−0.366	−0.230	−0.230
0.4	0.765	0.767	−0.308	−0.309	−0.240	−0.240
0.5	0.762	0.764	−0.259	−0.260	−0.244	−0.244
0.6	0.765	0.767	−0.217	−0.218	−0.240	−0.240
0.7	0.776	0.777	−0.181	−0.181	−0.230	−0.230
0.8	0.792	0.796	−0.149	−0.149	−0.213	−0.213
0.9	0.828	0.827	−0.119	−0.119	−0.190	−0.190

Total nondimensional heat fluxes

Bottom wall	0.791
Side wall (each)	−0.287
Top wall	−0.218
Total	0.001
% error	0.120

[a] By linear interpolation to corresponding η

The standard application of the Galerkin method to equation (3) results in a set of linear algebraic equations

$$\sum_{j=1}^{N} K_{ij}\alpha_j = f_i; \quad i = 1,2, \ldots .N \tag{4}$$

where

$$K_{ij} = \int_V \phi_j \phi_i dV; \quad f_i = \int_V f(y,z,U^4)\phi_i dV$$

and α_j are unknown coefficients to be found by solution of equation (4). The ϕ's are the "shape functions." When this is done, u^4 is given by

$$u^4(y,z) \approx U^4(y,z) = \sum_{j=1}^{N} \alpha_j \phi_j(y,z) \tag{5}$$

In the present analysis, the shape function was taken to be isoparametric and biquadratic in form on quadrilateral elements; each element had nine nodes. This choice allowed the temperature within each element to vary quadratically in both the y-and z-directions, giving an accurate representation of the full temperature field in the medium with few elements. Details of the analysis are given in [6].

For all solutions given, four quadrilateral elements provided good results. Sixteen elements were used as a check on selected cases and changed the results by less than 1 percent, while quadrupling the computer time requirements. In all cases, the relative change in u^4 between the final iterations was less than 0.001 at all nodes. Second-order Gaussian quadrature was used for all integrations. For the four-element solutions, less than 100 s of CPU time on the CDC Dual Cyber computer were required for convergence. This is somewhat more than is required for the Hottel method, and is comparable to that for the P-3 results.

Results and Conclusions

Figure 2 presents the temperature profiles and lower (hot) wall heat flux distributions, respectively, for a square enclosure. Comparison with Hottel's method [7] and the results of [5] for both temperature and heat flux profiles show excellent agreement. The P-3 approximation results [4] agree quite well for large optical thickness, but deviate for smaller optical thickness, particularly for heat flux calculations. Notice that the deviation of the heat flux profile predicted by the P-3 approximation is larger near the walls. The results of [5] for $Y = 1$ and 2 are indistinguishable from the present results on Fig. 2. Table 1 shows further comparison with the results of [5], which are given at uneven η intervals. Although the results of [5] are given to four figures, they are here truncated to three because of the inaccuracy of the linear interpolation required. More complete results, including the effects of wall reflectivity, enclosure aspect ratio and internal uniform sources, are given in [6] and [8].

The method used here provides accurate temperature distributions in the medium and wall heat flux distributions, even for media with very small opacities where most of the approximation methods break down. The only noteworthy drawback is that for very low values of wall emissivity, a substantial amount of computer time is needed. The method can be extended to nongray gases and isotropically scattering media, but anisotropic media will require a more complicated analysis. As discussed in [9, 10], accurate solution requires accurate integration. The curvilinear shape function (the biquadratic shape function) was found to be the best compromise between the accuracy of results and the computer time requirement.

References

1 Wu, S. T., Ferguson, R. E., and Altgilbers, L. L., "Application of Finite Element Techniques to the Interaction of Conduction and Radiation in Participating Medium," *Heat Transfer and Thermal Control*, edited by A. L. Crosbie, Vol. 78 of *Progress in Astronautics and Aeronautics*, AIAA, New York, 1980, pp. 61-91.

2 Fernandes, R. L., Francis, J., and Reddy, J. N., "A Finite-Element Approach to Combined Conductive and Radiative Heat Transfer in a Planar Medium," *Heat Transfer and Thermal Control*, edited by A. L. Crosbie, Vol. 78 of *Progress in Astronautics and Aeronautics*, AIAA, New York, 1980, pp. 92-109.

3 Fernandes, R. L., and Francis, J. E., "Combined Radiative and Conductive Heat Transfer in a Planar Medium With a Flux Boundary Condition Using Finite Elements," AIAA Paper 92-0910, St. Louis, June 7, 1982.

4 Ratzel, A. C., "*P-N* Differential Approximation for Solution of One- and Two-Dimensional Radiation and Conduction Energy Transfer in Gray Participating Media," Ph.D. dissertation, The University of Texas at Austin, 1981.

5 Crosbie, A. L., and Schrenker, R. G., "Radiative Transfer in a Two-Dimensional Rectangular Medium Exposed to Diffuse Radiation," *JQSRT*, (to appear).

6 Razzaque, M. M., *Finite Element Analysis of Combined Mode Heat Transfer, Including Radiation in Gray Participating Media*, Ph.D. dissertation, Department of Mechanical Engineering, The University of Texas at Austin, May 1982.

7 Larsen, M., Hottel Zone Code, developed for Ph.D. research at The University of Texas at Austin, Aug. 1981.

8 Razzaque, M. M., Howell, J. R., and Klein, D. E., "Finite Element Solution of Radiative Heat Transfer in a Two-Dimensional Rectangular Enclosure With Gray Participating Media," ASME Paper 82-WA/HT-51, presented at 1982 ASME Winter Annual Meeting, St. Louis, Dec. 1982.

9 Razzaque, M. M., Howell, J. R., and Klein, D. E., "Finite Element Solution of Combined Radiative, Convective and Conductive Heat Transfer Problems," *Trans. Am. Nucl. Soc.*, Vol. 38, 1981, pp. 334-336.

10 Razzaque, M. M., Howell, J. R., and Klein, D. E., "Finite Element Solution of Heat Transfer for Gas Flow Through a Tube," *AIAA Journal*, Vol. 20, No. 7, July, 1982, pp. 1015-1019.

Cooling of a Slab With Thermal Contraction and Progressive Loss of Contact With a Cold Surface[1]

L. W. Hunter[2] and J. R. Kuttler[2]

Introduction

The cooling of a slab is considered, the surfaces of which, Fig. 1, initially make perfect thermal contact with two cold walls; but as the slab contracts, it breaks contact with one of the walls. Then the heat flow decreases across the regressing face of the slab, and the subsequent cooling of the slab is retarded. This problem can arise in casting applications when a metal shrinks away from a mold. The mathematical difficulty is that the location of the receding face is unknown in advance.

In the representative model, the heat transfer across the gap is assumed to occur by radiation and conduction through gas [1]. It is shown how the thickness of the slab and its temperature distribution may be calculated as a function of time. The approach applies a transformation [2] to coordinates that follow the motion. The transformed problem has fixed boundaries and may be solved in a straightforward manner.

It appears that this problem has not been treated fully before despite its practical importance. The approach suggested by Meyer [3] neglects the motion of the solid. Shamsunder and Sparrow [4] treated a loss of contact problem that arises when a material contracts as a result of a phase change from liquid to solid. The receding surface was assumed to be adiabatic. The numerical grid did not adapt to the changing size of the material and so the boundary conditions could not be applied at fixed grid points.

Governing Equations

The governing equations of heat and mass conservation determine the local temperature, T, and velocity, v, in the slab, and the thickness, X, of the slab. In terms of space-fixed coordinates, x, (see Fig. 1) and time, t, these equations are

$$\frac{\partial T}{\partial t}+v\frac{\partial T}{\partial x}=\frac{k}{\rho\hat{C}}\frac{\partial^2 T}{\partial x^2},\quad \text{for } 0<x<X \tag{1}$$

$$\frac{\partial \rho}{\partial t}+\frac{\partial}{\partial x}(\rho v)=0,\quad \text{for} <x<X \tag{2}$$

$$T=T_w \text{ and } v=0,\quad \text{at } =0 \tag{3}$$

$$k\frac{\partial T}{\partial x}=-k_g\left(\frac{T-T_w}{X_o-X}\right)-\epsilon\sigma(T^4-T_w^4),\quad \text{at } x=X \tag{4}$$

$$T=T_0,\quad \text{at } t=0 \tag{5}$$

$$X=X_o,\quad \text{at } t=0 \tag{6}$$

Here $\rho=\rho(T)$ is the density of the slab, $\hat{C}$ is its (constant) specific heat, and k is its (constant) thermal conductivity. In addition, T_w is the temperature of the cold walls, T_o is the initial temperature of the slab, X_o is the initial thickness of the slab, k_g is the thermal conductivity of the gas or vapor in the gap, ϵ is an emissivity, and σ is the Stefan-Boltzmann constant.

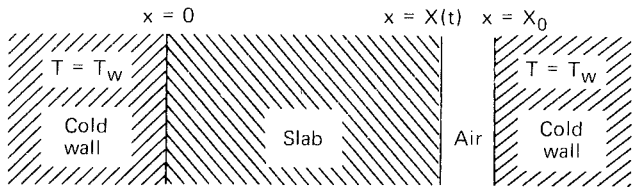

Fig. 1 The contracting slab

The conduction term in equation (4) assumes that the gas or vapor in the gap is stationary. This assumption is consistent with [1] and is thought to be reasonable considering the small size of the gap. While it is possible to approximate equation (4) by a convective boundary condition, this would conceal the fact that the heat flow depends on the distance across the gap. As written, equation (4) will make it possible to compare the relative importance of conduction and radiation.

Coordinates that follow the motion are now defined by [2]

$$\xi=\int_0^x dx'\,\frac{\rho(T(x',t))}{\rho(T_o)} \tag{7}$$

in which x' is a dummy space-fixed coordinate. The reader may verify that the velocity, v, drops out of the transformed equations, and conservation of mass is satisfied identically. In addition, the boundary locations become fixed and known. The transformed equations are as follows

$$\frac{\partial\theta}{\partial t^*}=\frac{\partial}{\partial\xi^*}\left(\rho^*\frac{\partial\theta}{\partial\xi^*}\right),\quad \text{for } 0<\xi^*<1 \tag{8}$$

$$\theta=\theta_w,\quad \text{at } \xi^*=0 \tag{9}$$

$$\rho^*\frac{\partial\theta}{\partial\xi^*}=-k_g^*\left(\frac{\theta-\theta_w}{1-X^*}\right)-\beta(\theta^4-\theta_w^4),\quad \text{at } \xi^*=1 \tag{10}$$

$$\theta=1\quad \text{at } t^*=0 \tag{11}$$

$$X^*=\int_0^1\frac{d\xi^*}{\rho^*} \tag{12}$$

in which the nondimensional variables are

$$\theta=\frac{T}{T_o},\quad \rho^*=\frac{\rho(T)}{\rho(T_o)},\quad X^*=\frac{X}{X_0} \tag{13}$$

$$\xi^*=\frac{\xi}{X_o},\quad t^*=\frac{kt}{\rho(T_o)\hat{C}X_0^2}=\text{Fourier number} \tag{14}$$

$$\beta=\frac{\epsilon X_0\sigma T_0^3}{k},\quad \theta_w=\frac{T_w}{T_o},\quad k_g^*=\frac{k_g}{k} \tag{15}$$

The density is written in terms of a constant coefficient of thermal expansion, α

$$\frac{1}{\rho^*}=1-\alpha^*(1-\theta) \tag{16}$$

where

$$\alpha^*=\alpha T_o \tag{17}$$

Equations (8-12) and (16) now determine $\theta=\theta(\xi^*,t^*)$ and $X^*=X^*(t^*)$. While it is straightforward to transform θ back to space-fixed coordinates, it is chosen to keep ξ^* here, noting that a thermocouple attached to the slab moves with constant ξ^*.

[1] This work was supported by the Naval Sea Systems Command, U.S. Department of the Navy, under Contract N00024-83-C-5301.

[2] Applied Physics Laboratory, The Johns Hopkins University, Laurel, Md. 20707.

Contributed by the Heat Transfer Division for publication in the JOURNAL OF HEAT TRANSFER. Manuscript received by the Heat Transfer Division March 14, 1983.

9 Razzaque, M. M., Howell, J. R., and Klein, D. E., "Finite Element Solution of Combined Radiative, Convective and Conductive Heat Transfer Problems," *Trans. Am. Nucl. Soc.*, Vol. 38, 1981, pp. 334-336.

10 Razzaque, M. M., Howell, J. R., and Klein, D. E., "Finite Element Solution of Heat Transfer for Gas Flow Through a Tube," *AIAA Journal*, Vol. 20, No. 7, July, 1982, pp. 1015-1019.

Cooling of a Slab With Thermal Contraction and Progressive Loss of Contact With a Cold Surface[1]

L. W. Hunter[2] and J. R. Kuttler[2]

Introduction

The cooling of a slab is considered, the surfaces of which, Fig. 1, initially make perfect thermal contact with two cold walls; but as the slab contracts, it breaks contact with one of the walls. Then the heat flow decreases across the regressing face of the slab, and the subsequent cooling of the slab is retarded. This problem can arise in casting applications when a metal shrinks away from a mold. The mathematical difficulty is that the location of the receding face is unknown in advance.

In the representative model, the heat transfer across the gap is assumed to occur by radiation and conduction through gas [1]. It is shown how the thickness of the slab and its temperature distribution may be calculated as a function of time. The approach applies a transformation [2] to coordinates that follow the motion. The transformed problem has fixed boundaries and may be solved in a straightforward manner.

It appears that this problem has not been treated fully before despite its practical importance. The approach suggested by Meyer [3] neglects the motion of the solid. Shamsunder and Sparrow [4] treated a loss of contact problem that arises when a material contracts as a result of a phase change from liquid to solid. The receding surface was assumed to be adiabatic. The numerical grid did not adapt to the changing size of the material and so the boundary conditions could not be applied at fixed grid points.

Governing Equations

The governing equations of heat and mass conservation determine the local temperature, T, and velocity, v, in the slab, and the thickness, X, of the slab. In terms of space-fixed coordinates, x, (see Fig. 1) and time, t, these equations are

$$\frac{\partial T}{\partial t}+v\frac{\partial T}{\partial x}=\frac{k}{\rho\hat{C}}\frac{\partial^2 T}{\partial x^2},\quad \text{for } 0<x<X \tag{1}$$

$$\frac{\partial \rho}{\partial t}+\frac{\partial}{\partial x}(\rho v)=0,\quad \text{for } <x<X \tag{2}$$

$$T=T_w \text{ and } v=0,\quad \text{at } =0 \tag{3}$$

$$k\frac{\partial T}{\partial x}=-k_g\left(\frac{T-T_w}{X_o-X}\right)-\epsilon\sigma(T^4-T_w^4),\quad \text{at } x=X \tag{4}$$

$$T=T_0,\quad \text{at } t=0 \tag{5}$$

$$X=X_o,\quad \text{at } t=0 \tag{6}$$

Here $\rho=\rho(T)$ is the density of the slab, $\hat{C}$ is its (constant) specific heat, and k is its (constant) thermal conductivity. In addition, T_w is the temperature of the cold walls, T_o is the initial temperature of the slab, X_o is the initial thickness of the slab, k_g is the thermal conductivity of the gas or vapor in the gap, ϵ is an emissivity, and σ is the Stefan-Boltzmann constant.

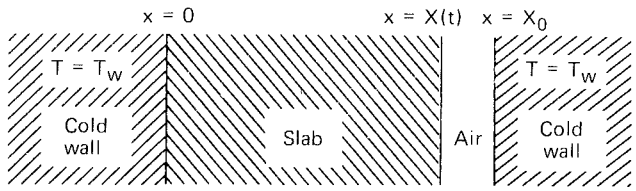

Fig. 1 The contracting slab

The conduction term in equation (4) assumes that the gas or vapor in the gap is stationary. This assumption is consistent with [1] and is thought to be reasonable considering the small size of the gap. While it is possible to approximate equation (4) by a convective boundary condition, this would conceal the fact that the heat flow depends on the distance across the gap. As written, equation (4) will make it possible to compare the relative importance of conduction and radiation.

Coordinates that follow the motion are now defined by [2]

$$\xi=\int_0^x dx'\,\frac{\rho(T(x',t))}{\rho(T_o)} \tag{7}$$

in which x' is a dummy space-fixed coordinate. The reader may verify that the velocity, v, drops out of the transformed equations, and conservation of mass is satisfied identically. In addition, the boundary locations become fixed and known. The transformed equations are as follows

$$\frac{\partial\theta}{\partial t^*}=\frac{\partial}{\partial\xi^*}\left(\rho^*\frac{\partial\theta}{\partial\xi^*}\right),\quad \text{for } 0<\xi^*<1 \tag{8}$$

$$\theta=\theta_w,\quad \text{at } \xi^*=0 \tag{9}$$

$$\rho^*\frac{\partial\theta}{\partial\xi^*}=-k_g^*\left(\frac{\theta-\theta_w}{1-X^*}\right)-\beta(\theta^4-\theta_w^4),\quad \text{at } \xi^*=1 \tag{10}$$

$$\theta=1\quad \text{at } t^*=0 \tag{11}$$

$$X^*=\int_0^1\frac{d\xi^*}{\rho^*} \tag{12}$$

in which the nondimensional variables are

$$\theta=\frac{T}{T_o},\quad \rho^*=\frac{\rho(T)}{\rho(T_o)},\quad X^*=\frac{X}{X_0} \tag{13}$$

$$\xi^*=\frac{\xi}{X_o},\quad t^*=\frac{kt}{\rho(T_o)\hat{C}X_0^2}=\text{Fourier number} \tag{14}$$

$$\beta=\frac{\epsilon X_0\sigma T_0^3}{k},\quad \theta_w=\frac{T_w}{T_o},\quad k_g^*=\frac{k_g}{k} \tag{15}$$

The density is written in terms of a constant coefficient of thermal expansion, α

$$\frac{1}{\rho^*}=1-\alpha^*(1-\theta) \tag{16}$$

where

$$\alpha^*=\alpha T_o \tag{17}$$

Equations (8-12) and (16) now determine $\theta=\theta(\xi^*,t^*)$ and $X^*=X^*(t^*)$. While it is straightforward to transform θ back to space-fixed coordinates, it is chosen to keep ξ^* here, noting that a thermocouple attached to the slab moves with constant ξ^*.

[1] This work was supported by the Naval Sea Systems Command, U.S. Department of the Navy, under Contract N00024-83-C-5301.

[2] Applied Physics Laboratory, The Johns Hopkins University, Laurel, Md. 20707.

Contributed by the Heat Transfer Division for publication in the JOURNAL OF HEAT TRANSFER. Manuscript received by the Heat Transfer Division March 14, 1983.

Numerical Methods

The governing equations (8–12) lend themselves to straightforward numerical solution. The implicit finite difference method of Crank and Nicholson [5] is used with a standard tridiagonal equation solver [7]. The length, X^*, and density, ρ^*, at the current time step are taken as the first estimates of X^* and ρ^* at the next time step. Iteration then refines these estimates. The details are as follows.

Let $h=N^{-1}$ be the space step for integer, N, and let k be the time step. Let

$$\theta_{i,j}=\theta(ih,jk),\ \rho^*_{i,j}=\rho^*(ih,jk),\ X^*_j=X^*(jk)$$

Initially, for $j=0$, θ, ρ^*, and X^* are specified by

$$\theta_{o,o}=\theta_w,\ \rho^*_{o,o}=(1-\alpha(1-\theta_w))^{-1},$$
$$\theta_{i,o}=1,\ \rho^*_{i,o}=1,\ i=1,2,\ldots,N, \tag{18}$$
$$X^*_o=h\sum_{i=0}{}'\,\rho^{*-1}_{i,0}$$

where $'$ indicates the $i=0$ and $i=N$ terms are given half-weight. To proceed from the jth step to the $(j+1)$st time step, we use a Crank-Nicholson type difference equation to approximate (8)

$$\frac{\theta_{i,j+1}-\theta_{i,j}}{k}=\frac{1}{4h^2}\Big\{(\rho^*_{i+1,j+1}+\rho^*_{i,j+1})(\theta_{i+1,j+1}-\theta_{i,j+1})$$
$$-(\rho^*_{i,j+1}+\rho^*_{i-1,j+1})(\theta_{i,j+1}-\theta_{i-1,j+1})$$
$$+(\rho^*_{i+1,j}+\rho^*_{i,j})(\theta_{i+1,j}-\theta_{i,j})$$
$$-(\rho^*_{i,j}+\rho^*_{i-1,j})(\theta_{i,j}-\theta_{i-1,j})\Big\},$$
$$i=1,2,\ldots,N-1 \tag{19}$$

with

$$\theta_{o,j+1}=\theta_w,\ \rho^*_{o,j+1}=(1-\alpha(1-\theta_w))^{-1}$$

This difference scheme is unconditionally stable [6] and approximates (8) with local truncation error proportional to h^2+k^2. For $i=N$, the boundary condition (10) is used in the form

$$\rho^*_{N,j+1}\left(\frac{3\theta_{N,j+1}-4\theta_{N-1,j+1}+\theta_{N-2,j+1}}{2h}\right)$$
$$=-k^*_g\left(\frac{\theta_{N,j+1}-\theta_w}{1-X^*_{j+1}}\right)-\beta(\theta^4_{N,j+1}-\theta^4_w) \tag{20}$$

Now equations (19) and (20) are nonlinear because ρ^* and X^* depend on θ and so they are solved iteratively as follows. Initially, set

$$\theta_{N,j+1}=\theta_{N,j},\ X^*_{j+1}=X^*_j,\ \rho^*_{i,j+1}=\rho^*_{i,j}$$

and solve the tridiagonal system of equations resulting from (19) for $\theta_{i,j+1}$, $i=1, 2, \ldots, N-1$. Then, (20) is solved for $\theta_{N,j+1}$ (except that the old value of $\theta_{N,j+1}$ is employed in the nonlinear $\beta(\theta^4-\theta^4_w)$ term). Then, calculate new values of ρ^* and X^* from

$$\rho^*_{i,j+1}=(1-\alpha(1-\theta_{i,j+1}))^{-1},$$
$$i=1,2,\ldots,N \tag{21}$$
$$X^*_{j+1}=h\sum_{i=0}{}'\,\rho^{*-1}_{i,j+1}. \tag{22}$$

The process is repeated until two successive values of X^*_{j+1} agree within 10^{-8}. In practice, this occurred within 20 iterations.

Several sizes of space and time steps were tried until the procedure gave consistent results. The results reported are for $N=100$, $k=0.001$. On an IBM system 3033, 1000 time steps took less than 18 s of CPU time.

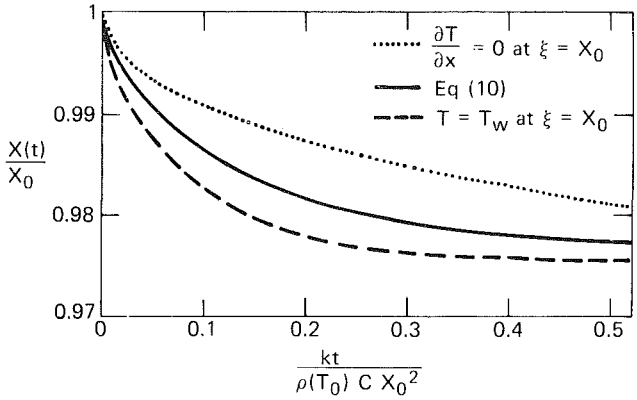

Fig. 2 The thickness of the slab

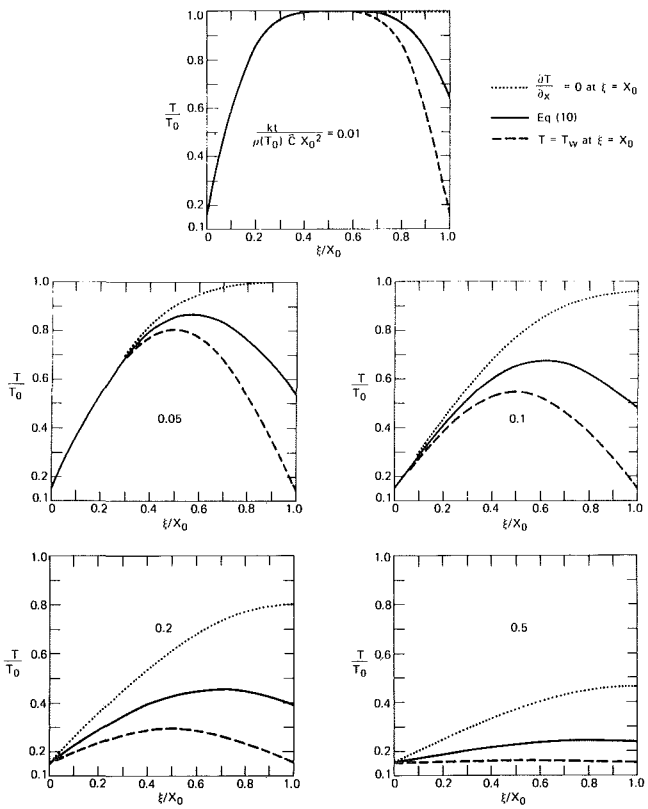

Fig. 3 The temperature in the slab

Numerical Results

The parameters of the problem are α^*, θ_w, k^*_g, and β, of which α^* characterizes the material and θ_w characterizes the initial conditions while k^*_g and β control conduction and radiation across the gap.

The parameters are assigned the nominal values $\alpha^*=2.9\times10^{-2}$, $\theta_w=1.5\times10^{-1}$, $k^*_g=4.9\times10^{-4}$, and $\beta=1.7\times10^{1}$. These values represent a rod of iron 100 in. long at 2800°F (3260°R) then cooled to 32°F (492°R). The emissivity is set equal to 1 in β.

For these values, the numerical results show that the radiation is more important than the conduction across the gap. Then the heat flux across the interface is simply the term multiplied by β in equation (10). In the limit where $\epsilon=0$, the receding face of the slab quickly becomes effectively insulated.

Figure 2 shows the decreasing thickness of the slab as it

contracts to 97.535 percent of its original length (solid curve). The rate of contraction is slower when the free end is insulated (dotted curve) and faster when the right-hand wall recedes with the slab to maintain perfect thermal contact (dashed curve). The full boundary condition of equation (10), with conduction and radiation across the gap, gives results which lie between the two extremes.

Figures 3–7 show temperature distributions in the slab at successive times. In each chart, the results with the full boundary condition, equation (10), are compared with the two other limiting boundary conditions. While the temperatures with the free end insulated are always higher than with perfect contact, the spread is so large that neither limit is a practical approximation to the full results.

The results in the insulated limit (dotted curves) are close to results for $\epsilon = 0$. Thus, the spread between the dotted curves and the solid curves shows the effect of ϵ.

Numerical values are obtainable from the authors.

Conclusion

The temperatures in a contracting slab have been examined. In the case of primary interest, the slab breaks contact with a cold wall but heat transfer continues mainly by radiation and partly by conduction through gas or vapor which fills the gap. In a second case, the cold wall recedes with the slab to maintain perfect thermal contact. In the remaining case, the receding face is insulated. The temperature profiles in all three cases show the same qualitative features as the corresponding constant density profiles. The differences between the three cases can be substantial throughout most of the history of the cooling. The principal mathematical difficulty common to the three problems is the fact that the location of the receding face is unknown in advance. The paper shows how to overcome this difficulty by using mass-weighted coordinates that follow the motion. This permits precise calculations of the thickness of the slab as a function of time.

References

1 Schneider, P. J., "Conduction," section 3, *Handbook of Heat Transfer*, edited by W. M. Rohsenow and J. P. Hartnett, McGraw-Hill, New York, 1973.

2 Hunter, L. W., "Transient Thermal Expansion of Solids During Inert Heating, Phase Change and Surface Gasification," JOURNAL OF HEAT TRANSFER, Vol. 103, 1981, pp. 601–602.

3 Meyer, G. H., "A Numerical Method for Heat Transfer in an Expanding Rod," *International Journal of Heat and Mass Transfer*, Vol. 21, 1978, pp. 824–826.

4 Shamsundar, N., and Sparrow, E. M., "Effect of Density Change on Multidimensional Conduction Phase Change," JOURNAL OF HEAT TRANSFER, Vol. 98, 1976, pp. 550–557.

5 Crank, J., and Nicholson, P., "A Practical Method for Numerical Evaluation of Solutions of Partial Differential Equations of the Heat Conduction Type," *Proc. Cambridge Philosophical Soc.*, Vol. 43, 1947, pp. 50–67.

6 Forsythe, G. F., and Wasow, W. R., *Finite Difference Methods for Partial Differential Equations*, John Wiley, New York, 1960.

7 Dongarra, J. J., Bunch, J. R., Moler, C. B., and Stewart, G. W., *Linpack User's Guide*, SIAM, Philadelphia, 1979.

Journal of Heat Transfer

Discussion

Crystalline Fouling Studies[1]

N. Epstein.[2] In his recent paper, R. B. Ritter presents the following three empirical equations for the fouling of aqueous calcium sulfate solutions undergoing sensible heating

$$\theta = \frac{0.15}{k_l(\Delta C/C_s)^2}, \text{ hr} \tag{4}$$

$$F_r = (3.8\times10^{-5})k_l(\Delta C/C_s)^2, (\text{ft}^2)(^\circ\text{F})/\text{Btu} \tag{5}$$

with standard deviations of ± 64 and ± 42 percent, respectively, and

$$F_r = (1.3\times10^{-3})\theta^{-0.6}, (\text{ft}^2)(^\circ\text{F})/\text{Btu} \tag{8}$$

with an unstated standard deviation. (The units of each of the variables in equations (4), (5), and (8) are given in the Nomenclature.)

If we multiply equation (4) by equation (5), the result is

$$F_r = (5.7\times10^{-6})\theta^{-1}, (\text{ft}^2)(^\circ\text{F})/\text{Btu} \tag{i}$$

It is clear to start with that equation (*i*), with a power of −1 on the θ, contradicts equation (8), where the power on θ is −0.6. However, this apparent inconsistency may arise from the large standard deviations associated with equations (4) and (5), from which (*i*) was derived. More troubling is the very large discrepancy in the magnitudes of the coefficients in equations (8) and (*i*). The values of F_r which result from these two equations, over the reported measured induction time range of 0.15–50 hrs, are shown in the following table

θ hours	$F_r\times10^3$ equation (8)	$F_r\times10^3$ equation (*i*)
0.15	4.06	0.038
1	1.3	0.0057
50	0.124	0.000114

The measured values of $F_r\times10^3$ ranged from 0 to 3, with F_r in $(\text{ft}^2)(^\circ\text{F})/\text{Btu}$, which is consistent with the results shown by equation (8) but is at least two orders of magnitude greater than those from equation (*i*). Evidently the values of the empirical constants in equation (4) and/or (5) are in error.

To determine the probable source of the error, F_r was first evaluated by equation (5) over the reported range of k_l = 16–140 $\text{lb}/(\text{ft}^2)$ (hr) and $\Delta C/C_s$ = 0.09–1.70. The resulting possible range of F_r is then $(3.8\times10^{-5})(16)(0.09)^2$ or 4.92×10^{-6} $(\text{ft}^2)(^\circ\text{F})/\text{Btu}$ at a minimum and $(3.8\times10^{-5})(140)(1.70)^2 = 15.4\times10^{-3}$ $(\text{ft}^2)(^\circ\text{F})/\text{Btu}$ at a maximum. Since the measured values of fouling rate, F_r, actually ranged from very small to 3×10^{-3} $(\text{ft}^2)(^\circ\text{F})/\text{Btu}$, it is likely that equation (5), which encompasses this range, is not in error. Equation (4) was then subjected to similar scrutiny, by evaluating θ via this equation over the same ranges of k_l and $\Delta C/C_s$. The resulting possible range of θ is then $0.15/(140)(1.70)^2$ or 3.71×10^{-4} hr at a minimum and $0.15/(16)(0.09)^2$ or 1.16 hrs at a maximum. Since the measured values of the induction period, θ, actually ranged from 0.15 to 50 hrs, it seems very likely that the constant, 0.15, in equation (4) is low by some two orders of magnitude.

Nomenclature

- $\Delta C/C_s$ = supersaturation at surface, dimensionless
- F_r = fouling rate, $(\text{ft}^2)(^\circ\text{F})/\text{Btu}$
- k_l = mass transfer coefficient, $\text{lb}/(\text{ft}^2)(\text{hr})$
- θ = induction period, hr

[1] By R. B. Ritter, published in the May 1983 issue of the JOURNAL OF HEAT TRANSFER, Vol. 105, No. 2, pp. 374–378.

[2] Department of Chemical Engineering, University of British Columbia, Vancouver, B. C. V6T 1W5, Canada

Author's Closure

Professor Epstein is correct in pointing out an error in the constant of equation (4). The value of the constant, A, should be 55 when k_l is expressed as lb/ft^2 hr, or 0.075 for k_l in S.I. units, kg/m^2 s. The product of equations (4) and (5), expressed as equation (*i*) in Epstein's discussion, then becomes

$$F_r = (2.1\times10^{-3})\theta^{-1}, (\text{ft}^2)(^\circ\text{F})\text{Btu} \tag{i}$$

This equation and equation (8) give identical results at a midrange induction period, θ, of 3.3 hrs. The standard deviation of equation (8) was ± 85 percent.

Professor Epstein's careful analysis is certainly appreciated. We thank him for uncovering this error.

